frontiers | Research Topics

Advanced water splitting technologies development: Best practices and protocols

Edited by
Ellen B. Stechel, Kathy Ayers, Brendan Bulfin, Marcelo Carmo,
Olga A. Marina, Roel Van de Krol, Chengxiang Xiang and Julie Mougin

Published in
Frontiers in Energy Research

ISSN 1664-8714
ISBN 978-2-83251-964-6
DOI 10.3389/978-2-83251-964-6

About Frontiers

Frontiers is more than just an open access publisher of scholarly articles: it is a pioneering approach to the world of academia, radically improving the way scholarly research is managed. The grand vision of Frontiers is a world where all people have an equal opportunity to seek, share and generate knowledge. Frontiers provides immediate and permanent online open access to all its publications, but this alone is not enough to realize our grand goals.

Frontiers journal series

The Frontiers journal series is a multi-tier and interdisciplinary set of open-access, online journals, promising a paradigm shift from the current review, selection and dissemination processes in academic publishing. All Frontiers journals are driven by researchers for researchers; therefore, they constitute a service to the scholarly community. At the same time, the *Frontiers journal series* operates on a revolutionary invention, the tiered publishing system, initially addressing specific communities of scholars, and gradually climbing up to broader public understanding, thus serving the interests of the lay society, too.

Dedication to quality

Each Frontiers article is a landmark of the highest quality, thanks to genuinely collaborative interactions between authors and review editors, who include some of the world's best academicians. Research must be certified by peers before entering a stream of knowledge that may eventually reach the public - and shape society; therefore, Frontiers only applies the most rigorous and unbiased reviews. Frontiers revolutionizes research publishing by freely delivering the most outstanding research, evaluated with no bias from both the academic and social point of view. By applying the most advanced information technologies, Frontiers is catapulting scholarly publishing into a new generation.

What are Frontiers Research Topics?

Frontiers Research Topics are very popular trademarks of the *Frontiers journals series*: they are collections of at least ten articles, all centered on a particular subject. With their unique mix of varied contributions from Original Research to Review Articles, Frontiers Research Topics unify the most influential researchers, the latest key findings and historical advances in a hot research area.

Find out more on how to host your own Frontiers Research Topic or contribute to one as an author by contacting the Frontiers editorial office: frontiersin.org/about/contact

Advanced water splitting technologies development: Best practices and protocols

Topic editors
Ellen B. Stechel — Arizona State University, United States
Kathy Ayers — Other, United States
Brendan Bulfin — ETH Zürich, Switzerland
Marcelo Carmo — Nel, Norway
Olga A. Marina — Pacific Northwest National Laboratory (DOE), United States
Roel Van de Krol — Helmholtz Center Berlin for Materials and Energy, Helmholtz Association of German Research Centers (HZ), Germany
Chengxiang Xiang — Department of Applied Physics and Materials Science, Division of Engineering and Applied Science, California Institute of Technology, United States
Julie Mougin — CEA/LITEN, France

Citation
Stechel, E. B., Ayers, K., Bulfin, B., Carmo, M., Marina, O. A., Van de Krol, R., Xiang, C., Mougin, J., eds. (2023). *Advanced water splitting technologies development: Best practices and protocols*. Lausanne: Frontiers Media SA.
doi: 10.3389/978-2-83251-964-6

Table of contents

Frontiers in Energy Research

TYPE Editorial
PUBLISHED 06 March 2023
DOI 10.3389/fenrg.2023.1149688

Editorial: Advanced water splitting technologies development: Best practices and protocols

Brendan Bulfin[1], Marcelo Carmo[2], Roel Van de Krol[3], Julie Mougin[4], Kathy Ayers[2]*, Karl J. Gross[5], Olga A. Marina[6]*, George M. Roberts[2], Ellen B. Stechel[7]* and Chengxiang Xiang[8]*

[1]Department of Mechanical and Process Engineering, ETH Zurich, Zurich, Switzerland, [2]Nel Hydrogen, Wallingford, CT, United States, [3]Institute for Solar Fuels, Helmholtz-Zentrum Berlin für Materialien und Energie, Berlin, Germany, [4]University Grenoble Alpes, CEA, Grenoble, France, [5]H_2 Technology Consulting, Alamo, CA, United States, [6]Pacific Northwest National Laboratory, Richland, WA, United States, [7]ASU LightWorks® and the School of Molecular Sciences, Arizona State University, Tempe, AZ, United States, [8]Division of Engineering and Applied Science, California Institute of Technology, Pasadena, CA, United States

OPEN ACCESS

EDITED AND REVIEWED BY
Fenglong Wang,
Shandong University, China

*CORRESPONDENCE
Kathy Ayers,
✉ kayers@nelhydrogen.com
Olga A. Marina,
✉ Olga.Marina@pnnl.gov
Ellen B. Stechel,
✉ Ellen.Stechel@asu.edu
Chengxiang Xiang,
✉ cxx@caltech.edu

SPECIALTY SECTION
This article was submitted to Hydrogen Storage and Production, a section of the journal Frontiers in Energy Research

RECEIVED 22 January 2023
ACCEPTED 14 February 2023
PUBLISHED 06 March 2023

CITATION
Bulfin B, Carmo M, Van de Krol R, Mougin J, Ayers K, Gross KJ, Marina OA, Roberts GM, Stechel EB and Xiang C (2023), Editorial: Advanced water splitting technologies development: Best practices and protocols.
Front. Energy Res. 11:1149688.
doi: 10.3389/fenrg.2023.1149688

KEYWORDS

hydrogen, water splitting, benchmarking, low temperature electrolysis, high temperature electrolysis, photoelectrochemical, solar thermochemical water splitting, protocol

Editorial on the Research Topic
Advanced water splitting technologies development: Best practices and protocols

As the level of deployment and utilization of renewable energy sources, including wind and solar, continues to rise, large-scale, long-term energy storage technologies that could accommodate weekly and seasonal energy fluctuations will play a significant role in the overall deployment of renewable energies in the future. Harnessing and storing renewable energy resources *via* electrochemical, photoelectrochemical, or thermochemical processes by converting renewable energy into sustainable (energy storage) fuels have the potential to meet the long-term, terawatt scale energy storage challenge. Renewable hydrogen production is the cornerstone for sustainable fuel production and deep decarbonization of multiple sectors in our society. Cost-competitive clean hydrogen provides value to applications, such as 1) in the transportation sector for fuel cell vehicles, 2) in the electric grid sector for system stability and load balancing, and 3) in the industrial sector with metal refineries, cement production, and biomass upgrading (carbon-free fertilizer production). In addition, coupling clean renewable hydrogen with the carbon and nitrogen cycles enables known and well-established thermal-chemical processes to generate renewable hydrocarbon fuels and ammonia. The Advanced Water Splitting Technologies (AWST): low temperature electrolysis (LTE), high temperature electrolysis (HTE), photoelectrochemical (PEC) and solar thermo-chemical hydrogen (STCH) provide four unique and parallel approaches to produce low cost, low greenhouse gas (GHG) emission hydrogen at scale (Figure 1). Cost competitive clean hydrogen production using these four technologies is a current high priority focus for governments and industry. In June of 2022, the U.S. Department of Energy (DOE) launched the first in a series of Earthshot Initiatives. The Hydrogen Shot, “1 1 1” aims to reduce the cost of clean hydrogen by more than 80% to one dollar per one kilogram in 1 decade (\$1/kg H_2). The European Green Deal and the International Energy Agency (IEA)

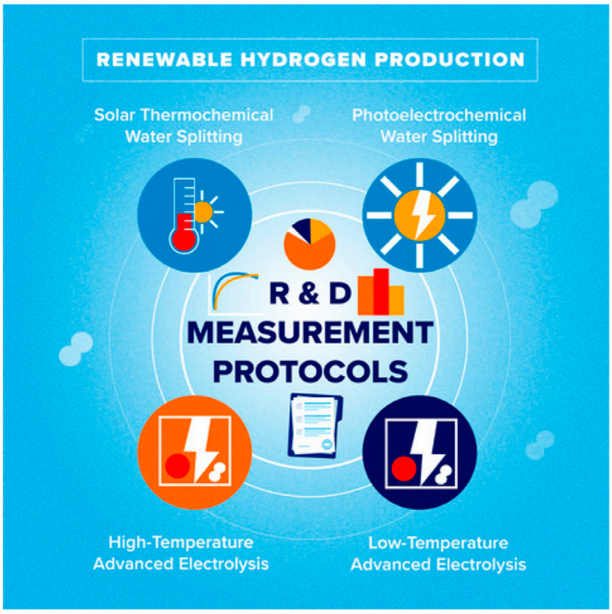

FIGURE 1
Advanced water splitting technologies for renewable hydrogen production.

have implemented a strong focus on green hydrogen production for a clean and secure energy future.

In LTE, an electrochemical process produces hydrogen gas from water. H_2 is produced at the cathode and O_2 at the anode electrochemically under a voltage bias, typically operating between 50 and 80°C. In commercial systems, either a membrane or a porous fabric-like separator separates the cathode from the anode. Among various LTE configurations, three types of LTE systems include alkaline, proton exchange membrane (PEM) based, and hydroxide exchange membrane based water electrolysis. These configurations are the most utilized systems. Alkaline and PEM electrolyzers have been deployed commercially at multi-megawatt scale (thousands to tens of thousands of metric tons per year H_2 production capacity for the largest projects) while hydroxide membrane electrolyzers are mostly pre-commercial.

The operating principle of HTE is similar to LTE. The HTE cells include a cathode for water reduction and hydrogen production, an anode for oxygen generation, and a solid ceramic electrolyte for selective transport of oxygen or proton ions at elevated temperatures of 400–850°C. HTE systems operate at low voltages of ≤ 1.3 V and current densities of 1–1.5 A cm^{-2} and can achieve 90%–95% stack electrical efficiency. Current SOEC technology is pre-commercial; the largest demonstrated scale for HTE is 0.72 MW projected to increase to a 2.6 MW demo plant in 2023, which corresponds to a generation rate of ~ 525 metric tons per year.

While LTE and HTE use renewable electrons from solar, wind, and/or hydroelectric power (or carbon free electrons from nuclear) to generate clean hydrogen, PEC and STCH produce clean H_2 directly from sunlight. PEC water-splitting integrates light absorption, photo-generated carrier transport, electrocatalysis, ionic transport, and product separation in an integrated photoelectrochemical device for hydrogen generation, (water plus sunshine-in and renewable-hydrogen-out solar panel). In a more in-depth perspective: PEC devices often operate at much lower current densities compared with LTE or HTE to match the solar flux, while high current density PEC devices with an operating current density close to 1 A cm^{-2} have been demonstrated in conjunction with solar concentrators. A portfolio of PEC devices have achieved a solar to hydrogen conversion efficiency of >10% with an overall device stability ranging from tens of hours to hundreds of hours. For the moment, PEC devices have only been demonstrated at a laboratory scale <<1 kg/day H_2.

In contrast, solar thermochemical hydrogen (STCH) cycles use the heat from sunlight to produce hydrogen and oxygen from water. A popular STCH pathway uses two-step redox active metal oxide (MO_x) thermochemical cycles to produce H_2 and O_2 sequentially in two different chemical reactions. STCH has been demonstrated at −1 kg/day. In the two-step cycle, a redox-active MO_x is first heated, generally using concentrated solar radiation, to temperatures typically exceeding 1500 K and often close to 1800 K at a low partial pressure of oxygen (pO_2), at which point the material becomes reduced to a more O-poor metal oxide. In the second step, the reduced metal oxide cools to a temperature where re-oxidation is favorable when exposed to superheated H_2O vapor (aka steam), which leads to water splitting and regeneration of the original MO_x. Off-stoichiometric metal oxides form and fill oxygen vacancies during the thermal reduction and water splitting (or re-oxidation) steps, respectively, without undergoing major structural bulk phase transitions, thus promoting faster kinetics, cyclability, and durability.

It is important to understand that LTE, HTE, PEC, and STCH water splitting technologies have different technical readiness levels and face different technical challenges. However, a common and absolutely vital need in each and all of these (and many other) basic research to commercial development efforts, is a concerted effort to come together and produce a path for the most trust-worthy, reliable, and reproducible results. This coordination will lead ultimately to the most rapid development of these life-changing beneficial technologies.

In this light, Benchmarking including the developing and documenting the best practice procedures and protocols are vital for creating an advanced R&D foundation for the broader research community in all four pathways and, potentially, in the R&D community in general. The development of standard protocols that integrate and harmonize independently funded work across the world is vital for accelerating the materials development as well as for the commercialization of each technology. This statement is particularly true given the enormous new interest in clean or green hydrogen. There exists at this moment a critical need for consistency in testing protocols, reference materials, and standard testing cells within and across all four technological pathways. To present a clear perspective, standard protocol development and the use of reference materials and cells for testing at the materials level, component level, and device level have proved to be critical in the development of similar technologies including fuel cells, advanced batteries, *etc.* Standard protocols, when successfully established and utilized within and across communities and technologies, can significantly reduce inconsistencies in results from different research groups due to different and varying testing procedures. The incorporation and adherence to a set of standardized protocols enables true cross comparison among newly discovered or developed materials and components. Standard protocols can also quantitatively gauge the progress made in each technology and are a vital part of developing an overall roadmap designed to achieve high level \$/kg H_2 goals that are desperately needed.

Through this collaborative Benchmarking, Protocol, Best Practices, and Road mapping project, an improved efficiency, reliability, and most effective pathway towards solving serious future energy issues has taken form and is being implemented. Critical for this effort was bringing the four technologies together to effectively facilitate cross-cutting opportunities. Low TRL technologies with a current emphasis on materials level development can learn scale up strategies, balance of system designs, and methods of estimating cost from higher TRL technologies, while high TRL technologies with the current emphasis on the system level development can benefit from fundamental materials knowledge gained in low TRL technologies.

To provide a specific example of the benefits and success in these efforts; the standard protocols that benchmark membrane properties, such as water content, gas permeability, and ion exchange capacity in LTE, can be adapted by the PEC community to include additional considerations on stability under illumination and conductivity for cations and anions other than proton or hydroxide for near-neutral pH operations. Similarly, HTE is learning from LTE about cell and system scale-up, testing on comparable cell and device levels, and corresponding testing protocols.

At the same time, through this widening of communications and support, expertise in PEC has opened new possibilities for LTE. For example, earth abundant electro-catalytic materials development in the PEC community is largely translatable to LTE and can in principle provide options for non-platinum group metal (PGM) catalysts for incorporation in LTE. There is a lot of similarities in materials requirements in HTE and STCH. Examples of common R&D interests in system level considerations for PEC and STCH include sunlight spectrum utilization, overall solar to hydrogen conversion efficiency, operational conditions, and constraints of each system under sunlight, can cross-fertilize advances in both technologies. Cross-communication, collaboration, and unilateral support of R&D advancements towards a clean energy future is vital for all our futures. This project and this publication platform provide an opportunity to collaborate and collectively improve the community's R&D efforts to ensure that we are all working most effectively towards a sustainable clean energy future.

Research Topic in Frontiers in Energy: This on-line, peer reviewed journal, provides open access to rapidly developing standardized testing protocols for the AWST R&D community. In this issue, authors offer a collection of standard protocols in the fields of LTE, HTE, PEC, and STCH advanced water-splitting technologies for clean hydrogen production. To track and report on progress and to set global priorities for advanced water splitting hydrogen research, this issue is a step intended to address the need to gain consistency within and across individual technology pathways so that researchers can reliably evaluate and compare the potential for each pathway. In addition, time is not our friend, and the lack of consistency and agreed upon benchmarks, protocols, standards, or roadmaps creates a large activation barrier for entry, for communicating to decision makers, and for general outreach.

In the interest of lowering the barriers and disseminating best practices in characterizing and benchmarking advanced water splitting materials, creating a foundation in accelerated materials, device, and systems research, development and deployment for the broader research community, this research topic asked the community for articles that describe comparisons, materials screening, characterization protocols, benchmarks, techno-economics, system analyses, and roadmaps for any and all advanced water splitting pathways, in which the primary energy is renewable (or at least carbon-free).

Current LTE protocols focus on *ex-situ* material screening methods as a first step in any new exploration to ensure that minimum criteria are met before investing additional time and resources in more complex tests. Some of these measurements are very technique dependent and require careful methods to obtain accurate results, such as catalyst activity *via* rotating disk electrodes. Other property measurements include ion exchange capacity, and oxidative stability of anion exchange membranes, and physical properties of porous transport layers. A final protocol addresses standard teardown of full cells for analysis. These protocols form a framework to build from for in cell component testing and durability.

PEC currently has five topical protocol reports that include benchmarking solar-to-hydrogen conversion efficiency of photoelectrodes, measurements of ion exchange membranes for solar fuel applications, comprehensive evaluation of optical, electrical, photoelectrochemical and spectroscopic properties of protective coatings, incident photo-to-current efficiency measurements and long term photoelectrode stability measurement protocols for PEC water splitting.

Presented HTE protocols focus on methods of solid oxide cell materials properties' characterization, such as measuring sample density, determining oxide electrical properties, separating the contributions of different charge carriers to the total conductivity as well as describing effective ways of solid oxide cell sealing, operating, and leak testing. In addition, one of the protocols compares several different steam generators to ensure stable and reliable steam supply to HTE, which is vital to ensure a uniform hydrogen production rate and to report degradations accurately.

STCH protocols in this issue include one paper on performance indicators ("Performance Indicators for Benchmarking Solar Thermochemical Fuel Processes and Reactors.") The solar reactor for operationalizing STCH is the key component and the performance of that reactor can be the deciding factor in assessing technical and economic feasibility. Important indicators discussed in this paper are conversion, selectivity, efficiency, and stability. The issue also includes a paper on determining the off-stoichiometry with temperature and partial pressure of oxygen ("A Thermogravimetric Temperature-Programmed Thermal Redox Protocol for Rapid Screening of Metal Oxides for Solar Thermochemical Hydrogen Production,") The authors show that temperature-programmed thermal reduction can provide a simple thermogravimetric analysis-based single-run experiment that measures the redox behavior of a specimen under thermal reduction and reoxidation conditions relevant to STCH. Lastly, the issue includes a paper on synchrotron-base characterization ("Synchrotron-based techniques for characterizing STCH water-splitting materials.") Synchrotron radiation is a powerful tool for characterizing STCH materials. X-ray absorption spectroscopy can identify those cations that are redox active and the extent of reduction in quenched conditions.

In summary, this issue contains nineteen articles and ninety different authors. Additional protocols are still in development and will be published later. We look forward to extensive international use of the protocols presented in this Research Topic and new ones as they become available. We also highly encourage participation by the wider community in improving and giving feedback on the current protocols and the continued creation of advanced protocols for AWST materials, component, and systems research and development.

Author contributions

KA, OM, ES, and CX contributed to the manuscript equally.

Conflict of interest

Authors MC, KA, and GR are employed by Nel Hydrogen. KJG was employed by H_2 Technology Consulting.

The remaining authors declares that the research was conducted in the absence of any commercial or financial relationships that could be construed as a potential conflict of interest.

Publisher's note

frontiers
in Energy Research

METHODS
published: 21 July 2021
doi: 10.3389/fenrg.2021.677980

Performance Indicators for Benchmarking Solar Thermochemical Fuel Processes and Reactors

Brendan Bulfin[1]*, **Miguel Miranda**[2] and **Aldo Steinfeld**[1]

[1]Departoment of Mechanical and Process Engineering, ETH Zurich, Zurich, Switzerland, [2]National Laboratory of Energy and Geology (LNEG), Lisbon, Portugal

Concentrated solar energy offers a source for renewable high-temperature process heat that can be used to efficiently drive endothermic chemical processes, converting the entire spectrum of solar radiation into chemical energy. In particular, solar-driven thermochemical processes for the production of fuels include reforming of methane and other hydrocarbons, gasification of biomass, coal, and other carbonaceous feedstock, and metal oxide redox cycles for splitting H_2O and CO_2. A notable issue in the development of these processes and their associated solar reactors is the lack of consistent reporting methods for experimental demonstrations and modelling studies, which complicates the benchmarking of the corresponding technologies. In this work we formulate dimensionless performance indicators based on mass and energy balances of such reacting systems, namely: energy efficiency, conversion extent, selectivity, and yield. Examples are outlined for the generic processes mention above. We then provide guidelines for reporting on such processes and reactors and suggest performance benchmarking on four key criteria: energy efficiency, conversion extent, product selectivity, and performance stability.

Keywords: concentrated solar power, solar fuels and chemicals, solar reactors, benchmarking, thermochemical processes

Edited by:
Thomas Alan Adams,
McMaster University, Canada

Reviewed by:
Jonathan Scheffe,
University of Florida, United States
Srirat Chuayboon,
King Mongkut's Institute of Technology Ladkrabang, Thailand

***Correspondence:**
Brendan Bulfin
bulfinb@ethz.ch

Specialty section:
This article was submitted to Process and Energy Systems Engineering,
a section of the journal Frontiers in Energy Research

Received: *08 March 2021*
Accepted: *06 July 2021*
Published: *21 July 2021*

Citation:
Bulfin B, Miranda M and Steinfeld A (2021) Performance Indicators for Benchmarking Solar Thermochemical Fuel Processes and Reactors. Front. Energy Res. 9:677980. doi: 10.3389/fenrg.2021.677980

INTRODUCTION

Concentrated solar power plants have been established for large-scale renewable power generation in areas with high direct normal irradiance (DNI). These plants convert the entire spectrum of DNI into high-temperature heat, which in turn is used by a heat engine to generate electricity. Alternatively, heat can be used to drive endothermic chemical processes (Romero and Steinfeld, 2012; Yadav and Banerjee 2016; Rodat et al., 2020), converting solar energy into chemical energy, with the chemical products acting as energy carriers. A promising application in this area is the production of solar fuels. In particular, syngas–a mixture of H_2 and CO–can be produced via a number of routes as illustrated in **Figure 1**, and further processed to drop-in transportation fuels such as gasoline and kerosene via established gas-to-liquid technologies (Steinfeld 2012; Agrafiotis et al., 2015). Examples of thermochemical processes for solar fuels production include the gasification of biomass, coal, and other carbonaceous feedstock (Nzihou et al., 2012; Piatkowski et al., 2011, Loutzenhiser and Muroyama 2017, Abanades et al., 2021), reforming of hydrocarbons (Agrafiotis et al., 2014; Sheu et al., 2015), and thermochemical redox cycles for splitting H_2O and CO_2 (Romero and Steinfeld, 2012; Lu et al., 2019; Boretti 2021). The study of these solar driven chemical processes is a growing field of research (Kodama 2003;

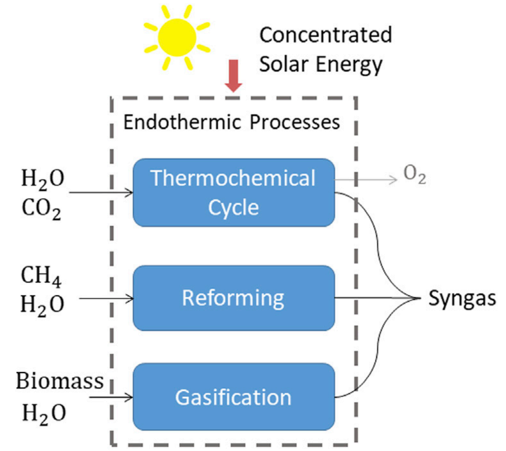

FIGURE 1 | Main process routes for the solar thermochemical production of syngas–a mixture of H_2 and CO that can be further processed to drop-in transportation fuels.

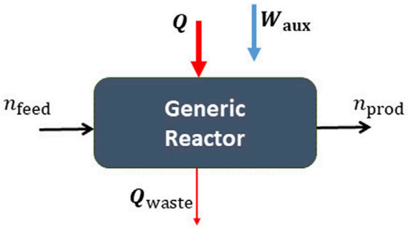

FIGURE 2 | Generic thermochemical reactor with a feedstock n_{feed} (moles or molar flow rates), a product stream n_{prod}, a heat input Q, a waste heat output Q_{waste}, and some auxiliary work associated with operating the reactor W_{aux}. The heat input is supplied by concentrated solar energy.

Steinfeld 2014; Mao et al., 2020) with an increasing rate of publications in recent years (Safari and Dincer 2020).

The solar reactor for effecting these processes is the key component and its performance can be the deciding factor in assessing its technical and economic feasibility. Thus, when reporting on the R&D of such reactors it is beneficial to follow standard conventions and procedures to facilitate benchmarking progress.

A generic solar thermochemical reactor can be defined as a system with both an energy and mass flow input (see **Figure 2**), with a thermochemical transformation consuming energy in the form of heat and converting chemical species. It is convenient in chemical engineering to define dimensionless parameters to describe the energy and mass balances which are independent of scale and process, and can be used as performance indicators to benchmark the system. These are the energy efficiency for the energy balance, and the conversion extent, selectivity and yield for the mass balance. In addition, we are interested in the stability of the process, i.e., its performance over time. All of these aspects will affect the investment capital and operating cost of any scaled up fuel production process. In an opinion article in *Advanced Science Views*, Ozin highlighted the importance of reporting all of these performance indicators to assess the feasibility of renewable fuel production technologies (Ozin 2018), and notes that seldom are all four: conversion, selectivity, efficiency and stability, reported on. When they are reported on, the definitions of these parameters often vary, in particular for the efficiency, but also for standard chemical process parameters such as selectivity and yield. This article aims to tackle these issues by providing clear protocols and definitions of the dimensionless parameters that can be used as performance indicators for reporting on solar fuel reactors. To do this we propose a standardized efficiency definition, and outline the already standardized chemical process parameters of conversion extent, selectivity and yield. Examples for applying them to the solar thermochemical processes shown in **Figure 1** are provided.

ENERGY EFFICIENCY

Consider a generic thermochemical reactor as illustrated in **Figure 2**, which has a feedstock input, a product output, energy inputs in the form of heat and auxiliary work, and waste heat output. To illustrate the definitions, we consider a batch process (or an integral over time of a continuous process) and define efficiencies in terms of the number of moles and quantities of heat and work supplied. For a continuous process molar flow rates, and heat and work flow rates can also be used. We can draw a boundary around the reactor illustrated in **Figure 2** and treat it as our system. The heat input Q is assumed to be provided by concentrated solar energy, either by direct solar irradiation or by using an indirect method of heat transfer from a solar receiver via heat transfer media. The waste heat can include radiation, conduction, and convection losses, and unrecovered sensible and latent heat in the reaction products and materials of construction. The auxiliary work W_{aux} is the additional work that is required for the operation of the reactor, for example pumping work to overcome pressure drops or to operate at vacuum/high pressures or the energy required to separate undesired products or the inert gas that is consumed during the process.

We set two criteria for the energy efficiency definition, namely: i) it should reflect the fraction of the supplied energy which is available in the produced fuel, and ii) it should always take a value between zero and one to emphasize the conservation of energy, $\eta \in (0, 1)$. A generic energy efficiency can thus be defined as,

$$\eta = 1 - \frac{Q_{waste}}{E_{total}} \tag{1}$$

where $E_{total} = Q + W_{aux}$, is the total energy supplied to the system and Q_{waste} is the heat that leaves the system to the surroundings unused. Evidently, η should always have a value between 0 and 1 using **Eq. 1**, unless some component of the supplied energy is

TABLE 1 | Efficiency definitions in the literature, with the process type, the type of efficiency equation used, whether they use LHV or HHV, and if they include auxiliary work directly or convert it to heat.

References	Process	Equation[a]	LHV/HHV	W_{aux}/Q_{aux}
Bhosale et al. (2017)	Thermochemical cycle	(5) or (6)	HHV	Q
Bhosale (2019)	Thermochemical cycle	(5) or (6)	HHV	Q
Binnoti et al. (2017)	Thermochemical cycle	(5) or (6)	HHV	Q
Bulfin et al. (2016)	Thermochemical cycle	(5) or (6)	HHV	Q
Chuayboon et al. (2019)	Gasification	(6)	LHV	–
Chuayboon et al. (2019a)	Reforming	Other	LHV	–
Falter (2017)	Thermochemical cycle	(5) or (6)	HHV	Q
Falter and Pitz-Paal, (2017)	Thermochemical cycle	(5) or (6)	HHV	Q
Foshheim et al. (2019)	Reforming	(5)	HHV	Q
Fletcher and Moen (1977)	Thermolysis	(3)	–	–
Gokon et al. (2014)	Gasification	(5)	–	–
Hathaway and Davidson, (2017)	Gasification	(6)	LHV	–
Hathaway et al. (2016)	Thermochemical cycle	(5) or (6)	HHV	Q
Jarrett et al. (2016)	Thermochemical cycle	(5) or (6)	HHV	W
Jin et al., 2018	Reforming	(5)	–	–
Koepf et al. (2016)	Thermochemical cycle	(5) or (6)	–	W
Kong et al. (2016)	Reforming	(5)	HHV	–
Kong et al. (2018)	Thermochemical cycle	(5) or (6)	HHV	Q
Lapp et al. (2012)	Thermochemical cycle	(5) or (6)	HHV	Q
Li et al. (2021)	Thermochemical cycle	(5) or (6)	HHV	Q
Marxer et al. (2017)	Thermochemical cycle	(5) or (6)	HHV	Q
Müller et al. (2017)	Gasification	(6)	LHV	-
Müller et al. (2018)	Gasification	(6)	LHV	–
Muroyama et al. (2018)	Gasification	(6)	LHV	–
Palumbo et al. (2015)	Reforming/Gasification	(6)	LHV	–
Piatkowski et al. (2011)	Gasification	(6)	LHV	–
Yuan et al. (2015)	Thermochemical cycle	(5) or (6)	HHV	W
Z'Graggen et al. (2006)	Gasification	(5)	–	–
Z'Graggen et al. (2008)	Gasification	(5)	–	–
Zheng et al. (2015)	Reforming	(5)	HHV	–
Zhu et al. (2016)	Membrane reactor	Other	HHV	–
Zoller et al. (2019)	Thermochemical cycle	(5) or (6)	HHV	Q

[a] *The definitions given by* ***Eqs 5, 6*** *are equivalent when the feedstock has a heating value of zero.*

overlooked. However, efficiency is rarely defined explicitly as in **Eq. 1** because Q_{waste} is not usually a term that can be directly measured.

Before considering other efficiency definitions, it is important to first discuss the auxiliary work, as there is some variance in the treatment of this term in the literature. The auxiliary work W_{aux} is not necessarily an energy consumption taking place within the reactor itself, however it is work that must be done in order for the reactor to operate, such as pumping or recycling sweep gas. It should therefore be included in the energy demand, E_{total}. However, in solar thermochemical fuel processes, the total energy is most often given as a purely thermal energy (see **Table 1**). Thus, W_{aux} is substituted by an equivalent thermal energy input Q_{aux}, calculated using a heat-to-work efficiency,

$$Q_{\mathrm{aux}} = \frac{W_{\mathrm{aux}}}{\eta_{\mathrm{heat-to-work}}}. \tag{2}$$

The total energy then includes the heat supplied to the reactor and the heat demand to perform the auxiliary work, $E_{\mathrm{total}} = Q + Q_{\mathrm{aux}}$, which in principal includes a power cycle within the system boundaries.

A range of values for the heat-to-work efficiency can be found in the literature, and here we are suggesting a value of $\eta_{\mathrm{heat-to-work}} = 0.4$ (Marxer et al., 2017). This conversion is academic in nature, while in practice grid electricity is typically used for auxiliary work or bottled gases in the case of sweep gas requirements. Even for a scaled up industrial plant it may be more economical and flexible to rely on grid electricity if it is available. Indeed, some studies have chosen to include the work directly in the total energy demand, as can be seen in **Table 1**. However, since the majority of researchers apply this conversion of work to an equivalent heat demand, we include it in the efficiency definitions described here.

We can now look at some common efficiency definitions seen in the literature and discuss the pros and cons of each. We first consider a definition based around the second law of thermodynamics,

$$\eta = \frac{\sum_i^{\mathrm{prod}} \mathrm{n_i} G_{\mathrm{i}} - \sum_i^{\mathrm{feed}} \mathrm{n_i} G_{\mathrm{i}}}{E_{\mathrm{total}}}, \tag{3}$$

where $\sum\limits_i^{\mathrm{prod}} \mathrm{n_i} G_{\mathrm{i}}$ is the total Gibbs free energy of the products, and $\sum\limits_i^{\mathrm{feed}} \mathrm{n_i} G_{\mathrm{i}}$ is the total Gibbs free energy of the feedstock. Thus, the numerator represents the change in Gibbs free energy of the process, which is equivalent to the theoretical maximum *work* that can potentially be performed by the reverse process. This definition was often used in the pioneering research of Fletcher on solar-driven processes (Noring and Fletcher 1982). Fletcher also derived a theoretical upper bound for this efficiency, given by:

$$\eta_{\max} = \left(1 - \frac{\sigma T_{\mathrm{H}}^4}{IC}\right)\left(1 - \frac{T_{\mathrm{L}}}{T_{\mathrm{H}}}\right), \tag{4}$$

where I is the DNI, C is the solar concentration ratio, T_{H} and T_{L} are the temperatures of the upper and lower thermal reservoirs of an equivalent heat engine, and σ is the Stefan-Boltzmann constant (Fletcher and Moen 1977). This upper bound results from multiplying of the maximum solar absorption efficiency of a perfectly-insulated blackbody cavity-receiver (taking into account only radiation losses), and the Carnot efficiency for the maximum conversion of heat to work. One issue with the efficiency according to **Eq. 3** is that it relates to the fuel's potential to perform work, but the energy available in a fuel is usually quantified in terms of its heating value, which leads to an alternative efficiency definition, given by:

$$\eta = \frac{\sum_i^{\mathrm{prod}} n_i \mathrm{HHV_i} - \sum_i^{\mathrm{feed}} n_i \mathrm{HHV_i}}{E_{\mathrm{total}}} \tag{5}$$

where HHV denotes the higher heating value and the numerator denotes the change in the heating value between the products and the feedstock. Note that lower heating value (LHV) can also be used, as discussed later. The numerator in this case is equivalent to the enthalpy change of the reaction. This efficiency definition has a direct relation to the fuel properties and has been applied in publications on both natural gas reforming and biomass gasification (Jin et al., 2018; Z'Graggen and Steinfeld 2008).

One issue with **Eq. 5** is that it can take negative values for some processes. Take for example solar biomass gasification in a hybrid reactor that can switch between solar thermal operation and auto-thermal operation by supplying some oxygen when off Sun (Muroyama et al. (2018), Boujjat et al., 2020). When such a hybrid system is in auto-thermal operation, the heating value of the feedstock would be decreased by the process and the efficiency according to **Eq. 5** would be negative. Another interesting example is solar fast pyrolysis of biomass (Zeng, et al., 2017; Bashir et al., 2017), in which the biomass is thermally decomposed in the absence of an oxidizing agent such as steam or oxygen. Depending on the feedstock, this process can become net exothermic (Di Blasi et al., 2017), but a heat source is still required for the rapid heating of the feedstock and starting the decomposition. In this case the efficiency according to **Eq. 5** would become negative even during solar operation.

To avoid the possibility of negative efficiencies we can consider the heating value of the feedstock as an energy input to the system, and include it in the denominator, E_{total}. For H_2O and CO_2 splitting cycles, the corresponding heating values are zero. But this is not the case for example for the gasification of biomass or for the reforming of hydrocarbons (Piatkowski et al., 2011; Muroyama et al., 2018; Müller et al., 2017). The efficiency is then defined as,

$$\eta = \frac{\sum_i^{\mathrm{prod}} n_i \mathrm{HHV_i}}{E_{\mathrm{total}}}, \tag{6}$$

where the total energy now includes the solar heat supplied to the reactor, the equivalent heat for auxiliary work, and the heating value in the feedstock, $E_{\mathrm{total}} = Q + Q_{\mathrm{aux}} + \sum_i^{\mathrm{feed}} n_{\mathrm{i}} \mathrm{HHV_i}$. **Eq. 6** is equivalent to **Eq. 5** if the feedstock itself has no heating value (e.g., H_2O or CO_2). This definition is equivalent to **Eq. 1**, in that it tracks the fraction of waste heat released in the process as the difference between the denominator and numerator. The heat losses can be radiation, convection, and conduction losses, losses in sensible heat from the products, and waste heat from the generation of W_{aux} (see **Eq. 2**). Thus, **Eq. 6** can be generally applied to any solar thermochemical fuel production process described in **Figure 1**, will always take a value between 0 and 1, and reflects the fraction of the energy supplied which is available in the fuel.

An interesting point to note is that **Eqs 5**, **6** are *heat-to-heat* efficiencies and can have a larger value than the *heat-to-work* efficiency given by **Eqs 3**, **4**. They are bounded by only the first bracketed term of **Eq. 4**, which is the maximum absorption efficiency. Thus, while the second law of thermodynamics places a limit on the efficiency according to **Eq. 3**, only the first law of thermodynamics places a limit on the efficiency according to **Eqs 5**, **6**. This fact is very frequently overlooked, where many studies use a *heat-to-heat* efficiency definition and state **Eq. 3** as an upper bound.

Another point worth noting is that some cases have a number of options for what is included as part of the products in the numerator of the efficiency definition given in **Eq. 6**. This can require some additional thought, and as a general rule we suggest only the products that are considered to be the produced fuel should be included, while the heating value of unusable byproducts or unreacted feed that cannot be recycled should be neglected. Take for example the thermal cracking of methane for the production of hydrogen (Maag et al., 2009; Rodat et al., 2011),

$$CH_4 \rightarrow C(s) + 2H_2, \tag{7}$$

which forms gaseous hydrogen and solid phase carbon as a byproduct. If only the produced hydrogen is intended to be used as a fuel, and the carbon is sequestered, then the heating value of the carbon byproduct should not be included in the numerator. Similarly, if there is unconverted methane which cannot be recycled or used in the final fuel it should also be omitted from the numerator giving an efficiency,

$$\eta = \frac{n_{\mathrm{H_2}} \mathrm{HHV_{H_2}}}{Q + Qaux + n_{\mathrm{CH_4}} \mathrm{HHV_{CH_4}}}. \tag{8}$$

The heating value of the byproduct and the heating value of the unconverted feedstock would then be considered part of the waste heat in the efficiency according to **Eq. 1**, which effectively closes the energy balance.

When choosing the efficiency, we should also consider the prevalence of each definition in the literature, as past work does set some precedent. A selection of publications with explicitly defined efficiencies are shown in **Table 1**. We distinguish the equations quite generally by whether the use change in Gibbs free energy as in **Eq. 3**, the change in heating value or enthalpy as in **Eq. 5**, or include the heating value of the feed in the denominator as in **Eq. 6**.

From **Table 1**, it can be seen that both **Eqs 5**, **6** are frequently applied in gasification and reforming processes. **Eq. 6** is the most general formulae, in that it can be applied to a reactor or an entire process chain, as well as solar and non-solar processes. Consider for example a conventional oil refinery where some of the feed is combusted to provide the heat required for the plant. In this case we cannot apply **Eq. 3** or **Eq. 5** as they will both give a negative efficiency, but **Eq. 6** would be suitable. Similarly, if we consider a complete solar fuel production process consisting of the endothermic solar gasification of biomass followed by exothermic Fischer-Tropsch synthesis and subsequent refining of the hydrocarbons, the end product can have less heating value than the original biomass. Again we cannot apply **Eq. 3** or **Eq. 5** to this complete process as they would give negative values. Therefore, as the most general formula which is already commonly applied, **Eq. 6** is the recommended efficiency definition for future studies.

It is often the case that authors want to gauge the solar energy demand per unit of fuel produced, as the solar concentrating infrastructure can make up for a significant part of the capital investment. For gasification and reforming processes, the efficiency defined by **Eq. 6** does not provide this directly. To provide this information one can further define dimensionless energy factors (Jarret et al., 2016, Li et al., 2021),

$$F_i = \frac{Q_\mathrm{i}}{\sum_i^\mathrm{prod} n_i \mathrm{HHV_i}}, \tag{9}$$

which gives a specific energy demand relative to the fuel's heating value. The efficiency is then related to the energy factors by $\eta = \frac{1}{\sum_i F_i}$. The solar energy factor would then be $F_\mathrm{solar} = \frac{Q_\mathrm{solar}}{\sum_i^\mathrm{products} n_i \mathrm{HHV_i}}$. Similarly one can give a more detailed breakdown of the energy demands by giving factors for subsystems such as the auxiliary work $F_\mathrm{aux} = \frac{W_\mathrm{aux}}{\sum_i^\mathrm{prod} n_i \mathrm{HHV_i}}$, or the heating value of the feedstock $F_\mathrm{feed} = \frac{\sum_i^\mathrm{feed} n_i \mathrm{HHV_i}}{\sum_i^\mathrm{prod} n_i \mathrm{HHV_i}}$. In this way, a more complete breakdown of the energy balance can be reported together with the efficiency.

Note that other efficiency definitions are found in the literature, some of which are difficult to interpret and should be avoided. For example, subtracting the auxiliary work term from the numerator rather than including it in the denominator (Zhu et al., 2016),

$$\eta = \frac{\sum_i^\mathrm{feed} n_\mathrm{i} \mathrm{HHV_i} - W_\mathrm{aux}}{Q + \sum_i^\mathrm{prod} n_i \mathrm{HHV_i}}, \tag{10}$$

as this leads to an equation which can easily have negative values. Another variation encountered is the inclusion of the conversion extent of the feedstock X_feed in the denominator of the efficiency definition (Chuayboon et al., 2019)

$$\eta = \frac{\sum_i^\mathrm{prod} n_i \mathrm{HHV_i}}{X_\mathrm{feed} n_\mathrm{feed} \mathrm{HHV_{feed}} + Q + Q_\mathrm{aux}}. \tag{11}$$

which mixes up the benchmarks for mass balance with that of the energy balance.

Higher heating value (HHV) vs. *lower heating value (LHV)*– Some sources use LHV instead of HHV (**Table 1**). If there is hydrogen or hydrocarbons in the products this will lead to lower efficiency values. The use of HHV is recommended because it offers a strict upper-bound for the useful thermal energy that can be extracted from the fuel in all applications.

CONVERSION EXTENT, SELECTIVITY, AND YIELD

These performance indicators are based on the mass balance and are used to keep track of the chemical reactions taking place, and they are, along with energy efficiency, the most important metrics for assessing the performance of chemical reactors. The conversion extent monitors how much of the feedstock supplied undergoes a chemical change within the reactor, while the selectivity gauges the extent of unwanted side reactions. The yield is the product of conversion and selectivity, and it gives the amount of the desired product formed relative to the stoichiometric maximum product formation, and thus provides information about the purity of the fuel produced. This means that reporting conversion extent and selectivity (or yield) gives the information needed to benchmark the system, while only reporting one of them leaves ambiguity about the other two. Together, these mass balance metrics have very useful implications for reactor design, including relating the reactor free volume and flow rates to production rates, which in turn can be used to rule out processes as unfeasible for large scale industrial production (Lange 2016). For example, a process can exhibit total (100%) selectivity for the conversion of CO_2 to CO, but if its conversion extent is low, it will lead to a fuel of little practical application because of the high dilution in unreacted CO_2. Although these metrics can be considered the nuts and bolts of chemical engineering research, they are often omitted in solar reactor studies.

We first define these indicators for a generic chemical reactor and then give examples for the solar fuel production processes discussed. We follow the definitions formulated in the seminal chemical reactor engineering text book by Levenspiel (2001). The conversion extent is generally formulated in terms of a limiting reactant. The limiting reactant is the reactant fed to the reactor which can be completely consumed according to the chemical reaction stoichiometry and input flow rates. For a trivial chemical process, such as

$$\mathrm{A} \rightarrow \mathrm{B}, \tag{12}$$

with only one feedstock, species *A* is the limiting reactant and *B* is the desired product. A chemical reactor for this processes is illustrated in **Figure 3**.

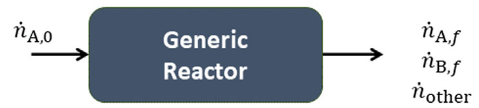

FIGURE 3 | A continuous-flow thermochemical reactor with an input molar feed rate of $\dot{n}_{A,0}$, and a product stream with outflows $\dot{n}_{A,f}$, $\dot{n}_{B,f}$ and.$\dot{n}_{other}$.

The conversion extent for this process can be defined as the relative change in the number of moles of the limiting reactant,

$$X_A = 1 - \frac{\dot{n}_{A,f}}{\dot{n}_{A,0}}. \tag{13}$$

where the subscript 0 indicates an input flow rate and the subscript f indicates the final flow rate at the exit of the reactor. For a batch reactor we can use the same formulae but with the number of initial and final moles, instead of molar flow rates. The importance of the conversion extent as a performance indicator is highlighted in classical text's where the *performance equation* of a chemical reactor gives the relation between the free volume, species flow rates and the conversion extent (Levenspiel 2001). For example, if we can only achieve a low conversion extent of say 10%, and we assume perfect selectivity, then we must have a feedstock flow rate which is 10 times higher than the desired production rate, and a large volume reactor to accommodate the flow, which has obvious implications for the cost and practical feasibility of a process.

As well as the desired reaction there can also be undesired reactions, for example,

$$A + B \rightarrow C, \tag{14}$$

where A is the reactant, B is the desired product, and C is an undesired product. The selectivity of the reactor towards species B is defined as the production rate of the desired product B relative to consumption rate of the feedstock A,

$$S_B = \frac{\dot{n}_{B,f}}{\dot{n}_{A,0} - \dot{n}_{A,f}}. \tag{15}$$

If there are no side reactions we would have $\dot{n}_{B,f} = \dot{n}_{A,0} - \dot{n}_{A,f}$, resulting in a selectivity of 1. The yield is the amount of desired product formed relative to the maximum amount of desired product that can be formed, i.e., it is the product of conversion extent and selectivity,

$$Y_B = X_A S_B = \frac{\dot{n}_{B,f}}{\dot{n}_{A,0}}. \tag{16}$$

Note then that reporting conversion extent, selectivity, and feed rates can offer a complete description of the chemical transformation in the reactor. However, if the system does not have an ideal selectivity of $S = 1$, it is also recommended to report the yield too.

Another point worth noting is that the selectivity and yield need to be adjusted by the relative stoichiometry of the product to the limiting reactant. For example, for the reaction $A \rightarrow 2B$, the selectivity would be given by $S_B = \frac{1}{2}\frac{\dot{n}_{B,f}}{\dot{n}_{A,0} - \dot{n}_{A,f}}$, where the factor of one half accounts for the 2 moles of B formed for every 1 mole of A reacted.

When reporting on the mass balance for reactor demonstrations it is recommend to report.

a) The feedstock molar flow rates (or mass flow rates for biomass).
b) The conversion extent of the feedstock in terms of the limiting reactant.
c) The selectivity towards the desired product, and the yield.

In trivial cases where the selectivity can be assumed to have a value of 1, then the conversion extent and yield will be equal. In such cases this should be clearly stated in the results.

STABILITY

The reactor's performance stability can be reported using the same mass and energy balance performance indicators described above, by giving their values as a function of time (or cycle # for cyclic processes). In other words, the efficiency η given by **Eq. 6**, conversion extent X_i given by **Eq. 13**, the selectivity S_i given by **Eq. 15**, and the yield given by **Eq. 16**, should all be monitored over time to gauge the stability of the performance. Other stability issues such as degradation or complete failure of components are much more difficult to report in a consistent way, as there are no scalable measurements of such faults that can be broadly applied. We therefore restrict our recommendations to recording the performance indicators over time.

EXAMPLES OF THE PERFORMANCE INDICATORS

Here we outline the performance indicators for some example processes that have been investigated in the literature, namely: solar reforming, thermochemical redox cycles and solar biomass gasification.

Solar methane reforming–Methane can be converted to syngas by reacting it with steam at high temperatures via the endothermic reforming reaction,

$$CH_4 + H_2O \rightarrow CO + 3H_2, \tag{17}$$

The heat for this reaction can be supplied by concentrated solar energy (Agrafiotis et al., 2014). This can be performed with a continuous flow reactor as illustrated in **Figure 4**. The process can also have numerous side reactions such as the reverse water-gas shift,

$$CO + H_2O \rightarrow CO_2 + H_2. \tag{18}$$

For this process we consider the syngas components CO and H_2 to be the produced fuel and the unreacted methane to be lost, so that the efficiency is given as (**Eq. 6**);

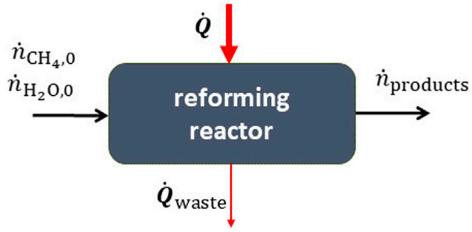

FIGURE 4 | A thermochemical reactor for the steam reforming of methane. The heat input is supplied by concentrated solar energy.

$$\eta = \frac{\dot{n}_{H_2}HHV_{H_2} + \dot{n}_{CO}HHV_{CO}}{\dot{n}_{CH_4,0}HHV_{CH_4} + \dot{Q}}. \tag{19}$$

where the sum in the numerator is over the species flow rates in the products times their HHVs. To avoid coking, steam is used in excess with $\dot{n}_{H_2O} > \dot{n}_{CH_4}$ and methane as the limiting reactant, with conversion extent given by,

$$X_{CH_4} = 1 - \frac{\dot{n}_{CH_4,f}}{\dot{n}_{CH_4,0}}. \tag{20}$$

The presence of side reactions means that we should also consider the selectivity towards the syngas products CO and H_2, given by:

$$S_{CO} = \frac{\dot{n}_{CO,f}}{\dot{n}_{CH_4,0} - \dot{n}_{CH_4,f}} \text{ and } S_{H_2} = \frac{\dot{n}_{H_2,f}}{3\left(\dot{n}_{CH_4,0} - \dot{n}_{CH_4,f}\right)}. \tag{21}$$

Solid phase carbon is an unwanted product which can form due to the Boudouard reaction or methane cracking. If present, this can be quantified using the carbon yield (Bulfin et al., 2021),

$$Y_C = \frac{\dot{n}_C}{\dot{n}_{CH_4,0}}, \tag{22}$$

but ideally it should be zero. Note the formulae given can be re-arranged to be in terms of feed rate, and mole fractions in the product stream, as required by the type of measurements taken in the experiment. However, it should be checked that definitions used are equivalent to the standard versions given here.

Thermochemical redox cycles–Two-step metal oxide redox cycles can be used to split H_2O and CO_2, producing H_2 and CO (Romero and Steinfeld, 2012; Bulfin et al., 2017). A metal oxide first undergoes reduction at high temperature and low oxygen partial pressures,

$$MO_{ox} \rightarrow MO_{red} + \frac{\delta}{2}O_2 \tag{23}$$

and is then reacted at lower temperature with H_2O or CO_2 to form H_2 and CO,

$$MO_{red} + CO_2 \rightarrow MO_{ox} + CO \tag{24}$$

$$MO_{red} + H_2O \rightarrow MO_{ox} + H_2 \tag{25}$$

Both redox reactions can be performed in the same fixed-bed reactor but at different times in a cyclic sequential mode (Hathaway et al., 2016; Haeussler et al., 2020; Marxer et al., 2017). Alternatively, it could be operated continuously using a particle transport reactor (Ermanoski et al., 2013; Singh et al., 2017; Welte et al.,2016). The process is illustrated in **Figure 5**, where it is important to note that reduction and oxidation are either taking place at different times or in separate reaction chambers.

In the fixed bed case, the system parameters; temperature, pressure, input power, conversion extent, auxiliary work *etc*., are varying in time. Therefore, integrals are taken over an entire cycle to obtain the desired performance parameters. For CO_2-splitting, we define the efficiency as,

$$\eta = \frac{HHV_{CO}\int_0^{t_{cycle}} \dot{n}_{CO}(t)\,dt}{\int_0^{t_{cycle}} \dot{Q}(t) + \dot{Q}_{aux}(t)\,dt}. \tag{26}$$

Auxiliary work may include vacuum pumping during reduction and the production of inert sweep gas. This definition is the same for water splitting, where CO is replaced by H_2. In this case the conversion extent is given by:

$$X_{CO_2} = 1 - \frac{\int_0^{t_{cycle}} \dot{n}_{CO_2,f}\,dt}{\int_0^{t_{cycle}} \dot{n}_{CO_2,0}\,dt}. \tag{27}$$

The selectivity towards CO is given by:

$$S_{CO} = \frac{\int_0^{t_{cycle}} \dot{n}_{CO,f}\,dt}{\int_0^{t_{cycle}} \dot{n}_{CO_2,0} - \dot{n}_{CO_2,f}\,dt}. \tag{28}$$

The yield is given by $Y_{CO} = X_{CO_2}S_{CO}$.

The literature on thermochemical redox cycles is perhaps the most problematic in terms of reporting standards due to the more complex nature of the cyclic process. There are a few articles in the literature which address all the performance indicators described here, with the work of Marxer *et al.* a notable example (Marxer et al., 2017). However, many studies omit the conversion extent, selectivity and yield as defined here, and instead only report the moles of H_2 or CO produced per gram of the cycled redox material as the yield (Agrafiotis et al., 2005; Hathaway et al., 2016; Haeussler et al., 2020). Reporting the mass balance using the performance indicators defined here together with the efficiency will offer a more complete picture of the performance. As additional

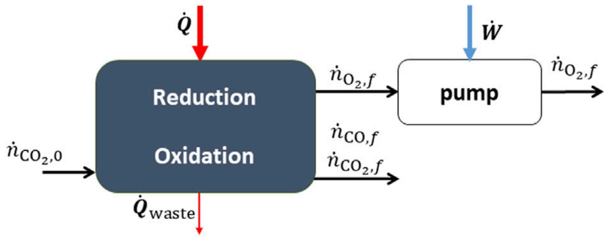

FIGURE 5 | A thermochemical reactor for the redox splitting of CO_2. The heat input is supplied by concentrated solar energy.

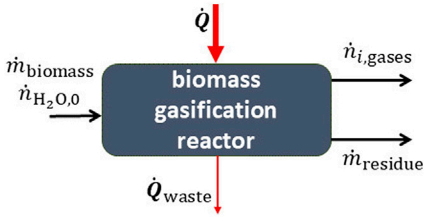

FIGURE 6 | A reactor for the gasification of biomass. The high-temperature heat input is supplied by concentrated solar energy.

information the moles of fuel per mole of redox material can also be reported, but to avoid confusion this parameter should not be referred to as the yield.

An interesting example that emphasizes the importance of reporting both energy and mass balance performance indicators is that of isothermal redox cycles. In this case both redox steps are conducted at the same temperature by performing a pressure swing. Studies have focused on the energy efficiency (Ermanoski et al., 2014) and experimental demonstrations of the process (Muhich et al., 2013; Hathaway et al., 2016; Hoskins et al., 2019). The conversion extent in the demonstrations are typically not reported, but at the operating conditions considered it is known to be thermodynamically limited to low values on the order of $X \approx 0.01$ (Ermanoski et al., 2014; Bulfin et al., 2016). The feedstock flow rate of H_2O or CO_2 required for a given output is inversely proportional to the conversion extent, with such low values resulting in considerable practical limitations for scaling-up the process. Low conversion extents lead to large feedstock flow rates, which in turn lead to larger reactors with increased capital cost and impractical design constraints. For this reason, classical chemical reactor engineering texts put a large emphasis on the conversion extent as a performance indicator (Levenspiel 2001).

Solar biomass gasification–Biomass, coal, or carbonaceous materials can be reacted with steam at high temperatures to produce syngas, as illustrated in **Figure 6** (Piatkowski et al., 2011). Since biomass does not have a simple chemical composition, the mass balance is more complex than the previous examples. Proximate and ultimate analysis are required to determine the chemical breakdown of the biomass (Müller et al., 2018; Muroyama et al., 2018).

Biomass gasification is a combination of many independent reactions with the net reaction summarized by the formula,

$$C_nH_mO_k + yH_2O \rightarrow x_1CO + x_2CO_2 + x_3H_2 + x_4CH_4 + \text{other gases} + \text{residue}, \tag{29}$$

where $C_nH_mO_k$ represents biomass. The biomass generally contains sulphur and nitrogen impurities on the order of 1% by mass. The efficiency can be expressed as;

$$\eta = \frac{\sum_i^{\text{prod}} \dot{m}_i \text{HHV}_i}{\dot{Q} + \dot{m}_{\text{biomass}} \text{HHV}_{\text{biomass}}}. \tag{30}$$

where we only sum the heating value of the gasified products, as the residue is an ash like byproduct and not a fuel. Note that the HHV are per unit mass and not per mole as in other formulae, which is due to the fact that the feed does not have a well-defined stoichiometric chemical formula. In this case an upgrade factor is also often reported, defined by the relative change in the heating value between the products and feedstock,

$$U = \frac{\sum_i^{\text{prod}} \dot{m}_i \text{HHV}_i}{\dot{m}_{\text{biomass}} \text{HHV}_{\text{biomass}}}. \tag{31}$$

The value of U depends on the type of feedstock and the syngas yield. This value can offer non-redundant information on the energy balance when reported together with the efficiency. For carbonaceous materials, the conversion extent is usually defined in terms of the carbon conversion extent (Müller et al., 2018),

$$X_C = 1 - \frac{\dot{m}_{\text{C-residue}}}{\dot{m}_{\text{C},0}}, \tag{32}$$

where $\dot{m}_{\text{C},0}$ is the mass flow rate of carbon in the biomass feed (determined by ultimate analysis), and $\dot{m}_{\text{C-residue}}$ is the mass of carbon in the residue (the unreacted carbon), which can be made up of tar and ash. The carbon to syngas yield can be expressed using molar flow rates of carbon containing species in the gas stream,

$$Y_{\text{syngas}} = \frac{\sum_i^{\text{gases}} \nu_{i,C} \dot{n}_{\text{i,gas}}}{\dot{n}_{\text{C},0}} = \frac{\dot{n}_{\text{CO}} + \dot{n}_{\text{CO}_2} + \dot{n}_{\text{CH}_4} + 2\dot{n}_{\text{C}_2\text{H}_6} + \ldots}{\dot{n}_{\text{C},0}}. \tag{33}$$

where $\nu_{i,C}$ is the stoicheometric number of carbon in the gas species. Often this sum is only performed for CO, CO_2, and CH_4, which differentiates it from the conversion extent defined above. Given the large number of reactions present there are a number of different selectivity's which may be of interest. For downstream gas-to-liquid processes, CO may be favored over CO_2 and CH_4, in which case the selectivity towards CO can be defined as,

$$S_{\text{CO}} = \frac{\dot{n}_{\text{CO}}}{\sum_i^{\text{gases}} \nu_{i,C} \dot{n}_{\text{i,gas}}} = \frac{\dot{n}_{\text{CO}}}{\dot{n}_{\text{CO}} + \dot{n}_{\text{CO}_2} + \dot{n}_{\text{CH}_4}}. \tag{34}$$

SUMMARY OF REPORTING PROTOCOLS

The dimensioned parameters required to described the reactor system are:

1) The reactor volume and free volume.
2) Mass loading of cycled redox material or catalyst.
3) The operating conditions of the reactor (e.g., temperature, pressure, etc.).
4) The molar/mass flow rates of feedstock into the reactor.
5) The total heat supply to the reactor, Q (e.g., solar heat, etc.).
6) Auxiliary work demands, W_{aux}, (e.g., pumping work, inert gas production, etc.).

TABLE 2 | The performance indicatoars for the example solar fuel processes discussed in this work.

Reactor type	Efficiency η	Conversion extent X_i	Selectivity (or Yield) S (or Y)
Thermochemical redox CO_2 splitting	$\frac{\mathrm{HHV_{CO}} \int_0^{t_{\mathrm{cycle}}} \dot{n}_{\mathrm{CO}}(t)dt}{\int_0^{t_{\mathrm{cycle}}} \dot{Q}(\mathrm{t})+\dot{Q}_{\mathrm{aux}}(t)dt}$	$1-\frac{\int_0^{t_{\mathrm{cycle}}} \dot{n}_{\mathrm{CO_2},f}dt}{\int_0^{t_{\mathrm{cycle}}} \dot{n}_{\mathrm{CO_2},0}dt}$	$\frac{\int_0^{t_{\mathrm{cycle}}} \dot{n}_{\mathrm{CO},f}dt}{\int_0^{t_{\mathrm{cycle}}} \dot{n}_{\mathrm{CO_2},0}-\dot{n}_{\mathrm{CO_2},f}dt}$
Solar methane reforming	$\frac{\sum_i^{\mathrm{products}} \dot{n}_{\mathrm{i}}\mathrm{HHV_i}}{\dot{Q}+\dot{n}_{\mathrm{CH_4},0}\mathrm{HHV_{CH_4}}}$	$1-\frac{\dot{n}_{\mathrm{CH_4},f}}{\dot{n}_{\mathrm{CH_4},0}}$	$\frac{\dot{n}_{\mathrm{CO},f}}{\dot{n}_{\mathrm{CH_4},0}-\dot{n}_{\mathrm{CH_4},f}}$
Biomass gasification	$\frac{\sum_i^{\mathrm{prod}} \dot{m}_{\mathrm{i}}\mathrm{HHV_i}}{\dot{Q}+\dot{m}_{\mathrm{biomass}}\,\mathrm{HHV_{biomass}}}$	$1-\frac{\dot{m}_{\mathrm{C-residue}}}{\dot{m}_{\mathrm{C},0}}$	$\left(Y_{\mathrm{syngas}}=\frac{\sum_i^{\mathrm{gases}} \nu_{i,C}\dot{n}_{\mathrm{i,gas}}}{\dot{n}_{\mathrm{C},0}}\right)$
Generic **A → B**	$\frac{\dot{n}_{\mathrm{B}}\mathrm{HHV_B}}{\dot{Q}+\dot{Q}_{\mathrm{aux}}+\dot{n}_{\mathrm{A}}\mathrm{HHV_A}}$	$1-\frac{\dot{n}_{A,f}}{\dot{n}_{\mathrm{A},0}}$	$\frac{\dot{n}_{\mathrm{B},f}}{\dot{n}_{\mathrm{A},0}-\dot{n}_{\mathrm{A},f}}$

This information should enable the study to be reproduced or modelled by other researchers. The energy and mass balance performance indicators outlined in the previous sections allows for the system to be benchmarked. These are:

1) The energy efficiency: $\eta = \frac{\sum_i^{\mathrm{prod}} n_i \mathrm{HHV_i}}{Q + Q_{\mathrm{aux}} + \sum_i^{\mathrm{feed}} n_i \mathrm{HHV_i}}$. For solar-upgrading processes such as gasification and reforming, report additionally the upgrade factor: $U = \frac{\sum_i^{\mathrm{prod}} n_i \mathrm{HHV_i}}{\sum_i^{\mathrm{feed}} n_i \mathrm{HHV_i}}$.
2) The conversion extent: $X_{\mathrm{A}} = 1 - \frac{\dot{n}_{\mathrm{A},f}}{\dot{n}_{\mathrm{A},0}}$.
3) The selectivity towards the desired product: $S_{\mathrm{B}} = \frac{\dot{n}_{\mathrm{B},f}}{\dot{n}_{\mathrm{A},0}-\dot{n}_{\mathrm{A},f}}$, or the yield of the desired product: $Y_{\mathrm{B}} = \frac{\dot{n}_{\mathrm{B},f}}{\dot{n}_{\mathrm{A},0}}$, for the case that the selectivity is not reported.
4) Performance stability, *i.e.,* report the above indicators over time.

The example definitions given for these performance indicators are summarized in **Table 2**.

Conversion extent, product selectivity, and energy efficiency, combined with mass flow rates offer a complete description of the reactor performance, while the performance over time can be used to gauge stability. For cyclic processes, the benchmarks should use integrals of the performance indicators over an entire cycle as outlined here. Similarly, for continuous processes, the benchmarks should use steady-state or integrals over time of the heat and mass flow rates when calculating the performance indicators.

DATA AVAILABILITY STATEMENT

The original contributions presented in the study are included in the article/Supplementary Material, further inquiries can be directed to the corresponding author.

AUTHOR CONTRIBUTIONS

BB wrote the manuscript and assisted in the planning of the study. MM performed a review of the solar fuel production literature and assisted in writing the article. AS assisted in the planning of the study and in the writing of the article.

FUNDING

This research work was funded by the European Union's Horizon 2020 Research Infrastructure Programme (Project SFERA-III–Grant Nr. 823802) and by the Swiss Federal Office of Energy (Project SOLIFUEL-Grant Nr. SI/501213-01).

ACKNOWLEDGMENTS

We would like to thank Martin Roeb, Valéry Vuillerme, Silvane Rodat, Ricardo Sanchez and other members of the SFERA III consortium who offered feedback on the formulation of standardized reporting protocols for solar fuel processes and reactors.

REFERENCES

Abanades, S., Rodat, S., and Boujjat, H. (2021). Solar Thermochemical Green Fuels Production: A Review of Biomass Pyro-Gasification, Solar Reactor Concepts and Modelling Methods. *Energies* 14 (5), 1494. doi:10.3390/en14051494

Agrafiotis, C., Roeb, M., Konstandopoulos, A. G., Nalbandian, L., Zaspalis, V. T., Sattler, C., et al. (2005). Solar Water Splitting for Hydrogen Production with Monolithic Reactors. *Solar Energy* 79 (4), 409–421. doi:10.1016/j.solener.2005.02.026

Agrafiotis, C., Roeb, M., and Sattler, C. (2015). A Review on Solar thermal Syngas Production via Redox Pair-Based Water/carbon Dioxide Splitting Thermochemical Cycles. *Renew. Sust. Energ. Rev.* 42, 254–285. doi:10.1016/j.rser.2014.09.039

Agrafiotis, C., von Storch, H., Roeb, M., and Sattler, C. (2014). Solar thermal Reforming of Methane Feedstocks for Hydrogen and Syngas Production-A Review. *Renew. Sust. Energ. Rev.* 29, 656–682. doi:10.1016/j.rser.2013.08.050

Bashir, M., Yu, X., Hassan, M., and Makkawi, Y. (2017). Modeling and Performance Analysis of Biomass Fast Pyrolysis in a Solar-thermal Reactor. *ACS Sust. Chem. Eng.* 5 (5), 3795–3807. doi:10.1021/acssuschemeng.6b02806

Bhosale, R., Kumar, A., AlMomani, F., and Gupta, R. B. (2017). Solar Thermochemical ZnO/ZnSO4 Water Splitting Cycle for Hydrogen Production. *Int. J. Hydrogen Energ.* 42 (37), 23474–23483. doi:10.1016/j.ijhydene.2017.02.190

Bhosale, R. R. (2019). Thermochemical H2 Production via Solar Driven Hybrid SrO/SrSO4 Water Splitting Cycle. *Int. J. Hydrogen Energ.* 44 (1), 118–127. doi:10.1016/j.ijhydene.2018.02.053

Binotti, M., Di Marcoberardino, G., Biassoni, M., and Manzolini, G. (2017). Solar Hydrogen Production With Cerium Oxides Thermochemical Cycle". In AIP Conference Proceedings (AIP Publishing LLC), 100002.

Boretti, A. (2021). Technology Readiness Level of Solar Thermochemical Splitting Cycles. *ACS Energ. Lett.* 6 (4), 1170–1174. doi:10.1021/acsenergylett.1c00181

Boujjat, H., Yuki Junior, G. M., Rodat, S., and Abanades, S. (2020). Dynamic Simulation and Control of Solar Biomass Gasification for Hydrogen-Rich Syngas Production during Allothermal and Hybrid Solar/autothermal Operation. *Int. J. Hydrogen Energ.* 45 (48), 25827–25837. doi:10.1016/j.ijhydene.2020.01.072

Bulfin, B., Ackermann, S., Furler, P., and Steinfeld, A. (2021). Thermodynamic Comparison of Solar Methane Reforming via Catalytic and Redox Cycle Routes. *Solar Energy* 215, 169–178.

Bulfin, B., Lange, M., de Oliveira, L., Roeb, M., and Sattler, C. (2016). Solar Thermochemical Hydrogen Production Using Ceria Zirconia Solid Solutions: Efficiency Analysis. *Int. J. Hydrogen Energ.* 41 (42), 19320–19328. doi:10.1016/j.ijhydene.2016.05.211

Bulfin, B., Vieten, J., Agrafiotis, C., Roeb, M., and Sattler, C. (2017). Applications and Limitations of Two Step Metal Oxide Thermochemical Redox Cycles; a Review. *J. Mater. Chem. A.* 5 (36), 18951–18966. doi:10.1039/c7ta05025a

Chuayboon, S., Abanades, S., Rodat, S., and Boujjat, H. (2019). "Experimental Assessment of Biomass Feedstock Gasification in a High-Temperature Continuous Solar Gasifier," in AIP Conference Proceedings (AIP Publishing LLC, Casablanca, Morocco, October 2–5, 2018), 180006. doi:10.1016/j.solener.2020.11.076

Chuayboon, S., Abanades, S., and Rodat, S. (2019a). Syngas Production via Solar-Driven Chemical Looping Methane Reforming from Redox Cycling of Ceria Porous Foam in a Volumetric Solar Reactor. *Chem. Eng. J.* 356, 756–770. doi:10.1016/j.cej.2018.09.072

Di Blasi, C., Branca, C., and Galgano, A. (2017). On the Experimental Evidence of Exothermicity in Wood and Biomass Pyrolysis. *Energy Technol.* 5 (1), 19–29.

Ermanoski, I., Miller, J. E., and Allendorf, M. D. (2014). Efficiency Maximization in Solar-Thermochemical Fuel Production: Challenging the Concept of Isothermal Water Splitting. *Phys. Chem. Chem. Phys.* 16 (18), 8418–8427. doi:10.1039/c4cp00978a

Ermanoski, I., Siegel, N. P., and Stechel, E. B. (2013). A New Reactor Concept for Efficient Solar-Thermochemical Fuel Production. *J. Solar Energ. Eng.* 135 (3), 031002. doi:10.1115/1.4023356

Falter, Christoph. (2017). *Efficiency Potential of Solar Thermochemical Reactor Concepts with Ecological and Economical Performance Analysis of Solar Fuel Production*. Aachen, Germany: Diss. RWTH Aachen. doi:10.18154/RWTH-2017-06526

Falter, C. P., and Pitz-Paal, R. (2017). A Generic Solar-Thermochemical Reactor Model with Internal Heat Diffusion for Counter-flow Solid Heat Exchange. *Solar Energy* 144, 569–579. doi:10.1016/j.solener.2017.01.063

Fletcher, E. A., and Moen, R. L. (1977). Hydrogen- and Oxygen from Water. *Science* 197 (4308), 1050–1056. doi:10.1126/science.197.4308.1050

Fosheim, J. R., Hathaway, B. J., and Davidson, J. H. (2019). High Efficiency Solar Chemical-Looping Methane Reforming with Ceria in a Fixed-Bed Reactor. *Energy* 169, 597–612. doi:10.1016/j.energy.2018.12.037

Gokon, N., Izawa, T., Abe, T., and Kodama, T. (2014). Steam Gasification of Coal Cokes in an Internally Circulating Fluidized Bed of thermal Storage Material for Solar Thermochemical Processes. *Int. J. Hydrogen Energ.* 39 (21), 11082–11093. doi:10.1016/j.ijhydene.2014.05.124

Haeussler, A., Abanades, S., Julbe, A., Jouannaux, J., and Cartoixa, B. (2020). Solar Thermochemical Fuel Production from H2O and CO2 Splitting via Two-step Redox Cycling of Reticulated Porous Ceria Structures Integrated in a Monolithic Cavity-type Reactor. *Energy* 201, 117649. doi:10.1016/j.energy.2020.117649

Hathaway, B. J., Bala Chandran, R., Gladen, A. C., Chase, T. R., and Davidson, J. H. (2016). Demonstration of a Solar Reactor for Carbon Dioxide Splitting via the Isothermal Ceria Redox Cycle and Practical Implications. *Energy Fuels* 30 (8), 6654–6661. doi:10.1021/acs.energyfuels.6b01265

Hathaway, B. J., and Davidson, J. H. (2017). Demonstration of a Prototype Molten Salt Solar Gasification Reactor. *Solar Energy* 142, 224–230. doi:10.1016/j.solener.2016.12.032

Hoskins, A. L., Millican, S. L., Czernik, C. E., Alshankiti, I., Netter, J. C., Wendelin, T. J., et al. (2019). Continuous On-Sun Solar Thermochemical Hydrogen Production via an Isothermal Redox Cycle. *Appl. Energ.* 249, 368–376. doi:10.1016/j.apenergy.2019.04.169

Jarrett, C., Chueh, W., Yuan, C., Kawajiri, Y., Sandhage, K. H., and Henry, A. (2016). Critical Limitations on the Efficiency of Two-Step Thermochemical Cycles. *J. Sol. Energy* 123, 57–73.

Jin, J., Wei, X., Liu, M., Yu, Y., Li, W., Kong, H., et al. (2018). A Solar Methane Reforming Reactor Design with Enhanced Efficiency. *Appl. Energ.* 226, 797–807. doi:10.1016/j.apenergy.2018.04.098

Kodama, T. (2003). High-temperature Solar Chemistry for Converting Solar Heat to Chemical Fuels. *Prog. Energ. combustion Sci.* 29 (6), 567–597. doi:10.1016/s0360-1285(03)00059-5

Koepf, E., Villasmil, W., and Meier, A. (2016). Pilot-scale Solar Reactor Operation and Characterization for Fuel Production via the Zn/ZnO Thermochemical Cycle. *Appl. Energ.* 165, 1004–1023. doi:10.1016/j.apenergy.2015.12.106

Kong, H., Hao, Y., and Jin, H. (2018). Isothermal versus Two-Temperature Solar Thermochemical Fuel Synthesis: A Comparative Study. *Appl. Energ.* 228, 301–308. doi:10.1016/j.apenergy.2018.05.099

Kong, H., Hao, Y., and Wang, H. (2016). A Solar Thermochemical Fuel Production System Integrated with Fossil Fuel Heat Recuperation. *Appl. Therm. Eng.* 108, 958–966. doi:10.1016/j.applthermaleng.2016.03.170

Lange, J.-P. (2016). Catalysis for Biorefineries - Performance Criteria for Industrial Operation. *Catal. Sci. Technol.* 6 (13), 4759–4767. doi:10.1039/c6cy00431h

Lapp, J., Davidson, J. H., and Lipiński, W. (2012). Efficiency of Two-step Solar Thermochemical Non-stoichiometric Redox Cycles with Heat Recovery. *Energy* 37 (1), 591–600. doi:10.1016/j.energy.2011.10.045

Levenspiel, O. (2001). *Chemical Reaction Engineering*. 3rd edition. New York, NY: John Willey and Sons.

Li, S., Wheeler, V. M., Kumar, A., Venkataraman, M. B., Muhich, C. L., Hao, Y., et al. (2021). Thermodynamic Guiding Principles for Designing Nonstoichiometric Redox Materials for Solar Thermochemical Fuel Production: Ceria, Perovskites, and beyond. *Energ. Tech.*, 2000925. doi:10.1002/ente.202000925

Loutzenhiser, P. G., and Muroyama, A. P. (2017). A Review of the State-Of-The-Art in Solar-Driven Gasification Processes with Carbonaceous Materials. *Solar Energy* 156, 93–100. doi:10.1016/j.solener.2017.05.008

Lu, Y., Zhu, L., Agrafiotis, C., Vieten, J., Roeb, M., and Sattler, C. (2019). Solar Fuels Production: Two-step Thermochemical Cycles with Cerium-Based Oxides. *Prog. Energ. Combustion Sci.* 75, 100785. doi:10.1016/j.pecs.2019.100785

Maag, G., Zanganeh, G., and Steinfeld, A. (2009). Solar thermal Cracking of Methane in a Particle-Flow Reactor for the Co-production of Hydrogen and Carbon. *Int. J. Hydrogen Energ.* 34 (18), 7676–7685. doi:10.1016/j.ijhydene.2009.07.037

Mao, Y., Gao, Y., Dong, W., Wu, H., Song, Z., Zhao, X., et al. (2020). Hydrogen Production via a Two-step Water Splitting Thermochemical Cycle Based on Metal Oxide - A Review. *Appl. Energ.* 267, 114860. doi:10.1016/j.apenergy.2020.114860

Marxer, D., Furler, P., Takacs, M., and Steinfeld, A. (2017). Solar Thermochemical Splitting of CO2 into Separate Streams of CO and O2 with High Selectivity, Stability, Conversion, and Efficiency. *Energy Environ. Sci.* 10 (5), 1142–1149. doi:10.1039/c6ee03776c

Muhich, C. L., Evanko, B. W., Weston, K. C., Lichty, P., Liang, X., Martinek, J., et al. (2013). Efficient Generation of H2 by Splitting Water with an Isothermal Redox Cycle. *Science* 341 (6145), 540–542. doi:10.1126/science.1239454

Müller, F., Patel, H., Blumenthal, D., Poživil, P., Das, P., Wieckert, C., et al. (2018). Co-production of Syngas and Potassium-Based Fertilizer by Solar-Driven Thermochemical Conversion of Crop Residues. *Fuel Process. Tech.* 171, 89–99. doi:10.1016/j.fuproc.2017.08.006

Müller, F., Poživil, P., Van Eyk, P. J., Villarrazo, A., Haueter, P., Wieckert, C., et al. (2017). A Pressurized High-Flux Solar Reactor for the Efficient Thermochemical Gasification of Carbonaceous Feedstock. *Fuel* 193, 432–443. doi:10.1016/j.fuel.2016.12.036

Muroyama, A. P., Guscetti, I., Schieber, G. L., Haussener, S., and Loutzenhiser, P. G. (2018). Design and Demonstration of a Prototype 1.5 kWth Hybrid Solar/autothermal Steam Gasifier. *Fuel* 211, 331–340. doi:10.1016/j.fuel.2017.09.059

Noring, J. E., and Fletcher, E. A. (1982). High Temperature Solar Thermochemical Processing-Hydrogen and Sulfur from Hydrogen Sulfide. *Energy* 7 (8), 651–666. doi:10.1016/0360-5442(82)90002-0

Nzihou, A., Flamant, G., and Stanmore, B. (2012). Synthetic Fuels from Biomass Using Concentrated Solar Energy - A Review. *Energy* 42 (1), 121–131. doi:10.1016/j.energy.2012.03.077

Ozin, G. (2018). Drop-In Solar Fuels from Carbon Dioxide and Water: Performance Indicators. Available at: https://www.advancedsciencenews.com/drop-in-solar-fuels-from-carbon-dioxide-and-water-performance-indicators.

Palumbo, A. W., Sorli, J. C., and Weimer, A. W. (2015). High Temperature Thermochemical Processing of Biomass and Methane for High Conversion and Selectivity to H2-Enriched Syngas. *Appl. Energ.* 157, 13–24. doi:10.1016/j.apenergy.2015.07.072

Piatkowski, N., Wieckert, C., Weimer, A. W., and Steinfeld, A. (2011). Solar-Driven Gasification of Carbonaceous Feedstock—A Review . *Energy Environ. Sci.* 4 (1), 73–82.

Rodat, S., Abanades, S., Boujjat, H., and Chuayboon, S. (2020). On the Path toward Day and Night Continuous Solar High Temperature Thermochemical Processes: A Review. *Renew. Sust. Energ. Rev.* 132, 110061. doi:10.1016/j.rser.2020.110061

Rodat, S., Abanades, S., and Flamant, G. (2011). Co-production of Hydrogen and Carbon Black from Solar thermal Methane Splitting in a Tubular Reactor Prototype. *Solar energy* 85 (4), 645–652. doi:10.1016/j.solener.2010.02.016

Romero, M., and Steinfeld, A. (2012). Concentrating Solar Thermal Power and Thermochemical Fuels. *Energ. Environ. Sci.* 5, 9234–9245. doi:10.1039/c2ee21275g

Safari, F., and Dincer, I. (2020). A Review and Comparative Evaluation of Thermochemical Water Splitting Cycles for Hydrogen Production. *Energ. Convers. Manag.* 205, 112182. doi:10.1016/j.enconman.2019.112182

Sheu, E. J., Mokheimer, E. M. A., and Ghoniem, A. F. (2015). A Review of Solar Methane Reforming Systems. *Int. J. Hydrogen Energ.* 40 (38), 12929–12955. doi:10.1016/j.ijhydene.2015.08.005

Singh, A., Lapp, J., Grobbel, J., Brendelberger, S., Reinhold, J. P., Olivera, L., et al. (2017). Design of a Pilot Scale Directly Irradiated, High Temperature, and Low Pressure Moving Particle Cavity Chamber for Metal Oxide Reduction. *Solar Energy* 157, 365–376. doi:10.1016/j.solener.2017.08.040

Steinfeld, A.. (2014) Solar Thermochemical Production of Hydrogen. in *Handbook of Hydrogen Energy*. Boca Raton, FL: CRC Press, Chapter 12, 421–443.

Steinfeld, A. (2012). Thermochemical Production of Syngas Using Concentrated Solar Energy. *Annu. Rev. Heat Transfer* 15. doi:10.1615/annualrevheattransfer.2012004537

Welte, M., Barhoumi, R., Zbinden, A., Scheffe, J. R., and Steinfeld, A. (2016). Experimental Demonstration of the Thermochemical Reduction of Ceria in a Solar Aerosol Reactor. *Ind. Eng. Chem. Res.* 55 (40), 10618–10625. doi:10.1021/acs.iecr.6b02853

Yadav, D., and Banerjee, R. (2016). A Review of Solar Thermochemical Processes. *Renew. Sust. Energ. Rev.* 54, 497–532. doi:10.1016/j.rser.2015.10.026

Yuan, C., Jarrett, C., Chueh, W., Kawajiri, Y., and Henry, A. (2015). A New Solar Fuels Reactor Concept Based on a Liquid Metal Heat Transfer Fluid: Reactor Design and Efficiency Estimation. *Solar Energy* 122, 547–561. doi:10.1016/j.solener.2015.08.019

Z'Graggen, A., Haueter, P., Maag, G., Vidal, A., Romero, M., and Steinfeld, A. (2006). "Hydrogen Production by Steam-Gasification of Petroleum Coke Using Concentrated Solar Power: Reactor Experimentation with Slurry Feeding". In International Solar Energy Conference, Denver, CO, July 8–13, 2006 (ASME). 23–27. doi:10.1115/ISEC2006-99029

Z'Graggen, A., and Steinfeld, A. (2008). Hydrogen Production by Steam-Gasification of Carbonaceous Materials Using Concentrated Solar Energy–V. Reactor Modeling, Optimization, and Scale-Up. *Int. J. Hydrogen Energ.* 33 (20), 5484–5492.

Zeng, K., Gauthier, D., Soria, J., Mazza, G., and Flamant, G. (2017). Solar Pyrolysis of Carbonaceous Feedstocks: A Review. *Solar Energy* 156, 73–92. doi:10.1016/j.solener.2017.05.033

Zheng, R., Diver, R., Caldwell, D., Fritz, B., Cameron, R., Humble, P., et al. (2015). Integrated Solar Thermochemical Reaction System for Steam Methane Reforming. *Energ. Proced.* 69, 1192–1200. doi:10.1016/j.egypro.2015.03.204

Zhu, L., Lu, Y., and Shen, S. (2016). Solar Fuel Production at High Temperatures Using Ceria as a Dense Membrane. *Energy* 104, 53–63. doi:10.1016/j.energy.2016.03.108

Zoller, S., Koepf, E., Roos, P., and Steinfeld, A. (2019). Heat Transfer Model of a 50 kW Solar Receiver–Reactor for Thermochemical Redox Cycling Using Cerium Dioxide. *J. Solar Energ. Eng.* 141 (2). doi:10.1115/1.4042059

Conflict of Interest: The authors declare that the research was conducted in the absence of any commercial or financial relationships that could be construed as a potential conflict of interest.

NOMENCLATURE

η	Energy efficiency
E_{total}	Total energy demand
Q	Quantity of heat
$\dot{Q}$	Heat flow rate
W	Quantity of work
$\dot{W}$	Work flow rate
n_i	Number of moles of species i
$\dot{n}_i$	Molar flow rate of species i
G_i	Gibbs free energy of species i
HHV_i	Higher heating value of species i
X_i	Conversion extent of reactant i
S_i	Selectivity towards product i
Y_i	Yield of product i
$\dot{n}_{i,0}$	Input flow rate of species i
$\dot{n}_{i,f}$	Output flow rate of species i
F_i	Energy factor of component i
U	Upgrade factor of the heating value

frontiers in Energy Research

ORIGINAL RESEARCH
published: 05 January 2022
doi: 10.3389/fenrg.2021.726069

Considerations for the Accurate Measurement of Incident Photon to Current Efficiency in Photoelectrochemical Cells

David S. Ellis[1]*, **Yifat Piekner**[2], **Daniel A. Grave**[1,3], **Patrick Schnell**[4,5] **and Avner Rothschild**[1]*

[1]Department of Materials Science and Engineering, Technion–Israel Institute of Technology, Haifa, Israel, [2]The Nancy & Stephen Grand Technion Energy Program (GTEP), Technion–Israel Institute of Technology, Haifa, Israel, [3]Department of Materials Engineering and Ilse Katz Institute for Nanoscale Science and Technology, Ben Gurion University of the Negev, Be'er Sheva, Israel, [4]Institute for Solar Fuels, Helmholtz-Zentrum Berlin für Materialien und Energie GmbH, Berlin, Germany, [5]Institute of Chemistry, Technische Universität Berlin, Berlin, Germany

Edited by:
Chengxiang Xiang,
California Institute of Technology,
United States

Reviewed by:
Anja Bieberle-Hütter,
Dutch Institute for Fundamental
Energy Research, Netherlands
Vinod Singh Amar,
South Dakota School of Mines and
Technology, United States

***Correspondence:**
David S. Ellis
ellis@technion.ac.il
Avner Rothschild
avnerrot@technion.ac.il

Specialty section:
This article was submitted to
Hydrogen Storage and Production,
a section of the journal
Frontiers in Energy Research

Received: 16 June 2021
Accepted: 08 December 2021
Published: 05 January 2022

Citation:
Ellis DS, Piekner Y, Grave DA, Schnell P
and Rothschild A (2022)
Considerations for the Accurate
Measurement of Incident Photon to
Current Efficiency in
Photoelectrochemical Cells.
Front. Energy Res. 9:726069.
doi: 10.3389/fenrg.2021.726069

In this paper we review some of the considerations and potential sources of error when conducting Incident Photon to Current Efficiency (IPCE) measurements, with focus on photoelectrochemical (PEC) cells for water splitting. The PEC aspect introduces challenges for accurate measurements often not encountered in dry PV cells. These can include slow charge transfer dynamics and, depending on conditions (such as a white light bias, which is important for samples with non-linear response to light intensity), possible composition changes, mostly at the surface, that a sample may gradually undergo as a result of chemical interactions with the aqueous electrolyte. These can introduce often-overlooked dependencies related to the timing of the measurement, such as a slower measurement requirement in the case of slow charge transfer dynamics, to accurately capture the steady-state response of the system. Fluctuations of the probe beam can be particularly acute when a Xe lamp with monochromator is used, and longer scanning times also allow for appreciable changes in the sample environment, especially when the sample is under realistically strong white light bias. The IPCE measurement system and procedure need to be capable of providing accurate measurements under specific conditions, according to sample and operating requirements. To illustrate these issues, complications, and solution options, we present example measurements of hematite photoanodes, leading to the use of a motorized rotating mirror stage to solve the inherent fluctuation and drift-related problems. For an example of potential pitfalls in IPCE measurements of metastable samples, we present measurements of $BiVO_4$ photoanodes, which had changing IPCE spectral shapes under white-light bias.

Keywords: IPCE, EQE, photoelectrochemical, device characterisation, measurement technique

1 INTRODUCTION

A standard measure to gauge the performance of photoactive devices, whereby an electron-hole pair is generated by a photon, leading to useful electrical current, is the Incident Photon to Current Efficiency (IPCE), synonymous with External Quantum Efficiency (EQE). IPCE is a measurement of the output current for a given number of incident photons at a given wavelength. Physically, this photocurrent spectrum comprises a combination of key characteristics of the device. These include the ability to concentrate incident photons in the active area (a function of the optical architecture of the whole device), the absorption coefficient within the active area, the nature of the excited electronic states as a result of the absorption (i.e., mobile charges, vs. non-mobile localized excitations), the ability to separate and transport these charges through the bulk to reach the surfaces, and efficiency of transferring charges across the surface interface vs. surface recombination. For methods of extracting these physical parameters from the IPCE spectrum and optical measurements, please refer to Piekner et al. and references therein (Piekner et al., 2021). Because of its importance in accessing and comparing the performance of photovoltaic and photoelectrochemical solar cells, previous works have sought to establish standards and protocol for the IPCE measurement, and examine various issues that can affect it (Chen et al., 2013; Reese et al., 2018; Saliba and Etgar 2020; Bahro et al., 2016; Timmereck et al., 2015; ASTM Standard E1021-15 2019). Chen et al. (2013) (Chen et al., 2013) were focused on measurements of perovskite solar cells in particular. They highlighted frequency and time-scale as issues affecting the accuracy, and concluded that a 10–20% consistency between IPCE and observed photocurrent was "reasonably accurate." Saliba and Etgar (2020) (Saliba and Etgar 2020) also dealt with mismatch between observed photocurrent and IPCE spectra in perovskite, citing both settling time and frequency dependences, as well as possible non-stability of the sample during measurements. Bahro et al. (2016) paper (Bahro et al., 2016) examined IPCE measurements of organic tandem devices, with emphasis in their discussion about the effect of light bias on the IPCE spectrum due to different charge carrier interactions.

In this paper we discuss these issues, and demonstrate with many actual examples from measurements of photoelectrochemical (PEC) cells for water splitting, based on (mostly) hematite photoanodes, that we accumulated over the course of the last few years. Many of the aforementioned problems we were able mitigate by modifications to the basic IPCE measurement system and procedure, which are presented herein. We include and expand upon several of the issues of time-scale and frequency considerations, sample stability, and white light bias. Since there can be significant differences between specific devices and material systems earmarked for IPCE measurements, we do not aim to provide a set of master rules and priorities–but rather provide illustrative examples, from our specific case, and leave it to the reader to decide how relevant each issue may be for their own type of cell and material.

Our paper is organized as follows. **Section 2** begins with the basic definition of IPCE and a general outline of a measuring system with a Xenon lamp and monochromator. The notable alternative of "flash" IPCE technology is also briefly described. Next, the validity of applying the small-signal IPCE spectrum to predict the large signal performance (photocurrent) is discussed at length, with an illustrative example of non-linear response of photocurrent to light intensity, and, for those latter cases, the strategy of measuring in white-light bias as a means to best capture the efficiency spectrum which most represents the actual performance. **Section 3** is about mitigating sources of error and noise. We emphasize that it is based on our own experiences with photo-electrochemical cells with hematite photoanodes, and using our Xe-lamp/monochromator light source, and not all of the issues might necessarily apply universally, but certainly (from the above literature survey) many are prevalent in other systems as well. The section is divided into subsections which deal with **Section 3.1** a detailed description and rationale for our IPCE measurement setup and procedure, **Section 3.2** optical power measurements including calibrated detectors, averaging, background subtraction, and the additional issue of harmonics in the case of monochromator-based system, **Section 3.3** example of photocurrent drift and our way of dealing with it, and the issue of system frequency response which would be important in the case of the lock-in amplifier approach, **Section 3.4** Xe-lamp drift and noise, including our (to our knowledge) unique solution and demonstration of repeatable and consistent results achieved in our "final" measurement system, and discussion of alternative the "flash" approach. **Section 3.5** is of a slightly different nature in that it deals with the "human error" factor and how interface software can be designed to mitigate it. While not directly related to evaluating the accuracy IPCE spectra itself, the sub-section may be skipped without loss of continuity, but contains user interface considerations of that can promote (or hinder, if neglected) more fruitful measurement sessions and may be of interest to system developers. The final **Section 4** is a case study of a measurement of a new (to us) sample, $BiVO_4$, which unexpectedly exhibited strong dependence on both bias light and time. While this presented a grave challenge, the fact that the final measurement system and technique was accurate and robust, as demonstrated in the prior sections, allowed us to rule out measurement error and attribute the observed systematic spectral evolution to the sample itself, that could lead to unique physical insight into the device operation.

2 BASIC DEFINITIONS AND THEIR SUBTLETIES

IPCE is not a single figure of merit, but rather a spectrum as a function of photon wavelength λ. Thus, the measurement usually takes the form of scanning the wavelength of a light source or bandpass filter, and measuring the current increase from that monochromatized light at each wavelength point. The two key observables, for each wavelength, are 1) the photogenerated current $\delta j_{ph}(\lambda)$, which is proportional to the amount of photogenerated holes (electrons) that reach the surface of the anode (cathode) and contribute to the photocurrent, which we denote (for holes) as $\delta n_h(\lambda)$, and 2) the incident optical power $\delta P(\lambda)$, which is proportional to the amount of photons $\delta n_{ph}(\lambda)$, multiplied by each photon's energy, the latter proportional to $1/\lambda$. Thus, we arrive at the unitless expression:

$$IPCE(\lambda) = \frac{\delta n_h(\lambda)}{\delta n_{ph}(\lambda)} = K \frac{\delta j_{ph}(\lambda)}{\lambda\, \delta P(\lambda)} \tag{1}$$

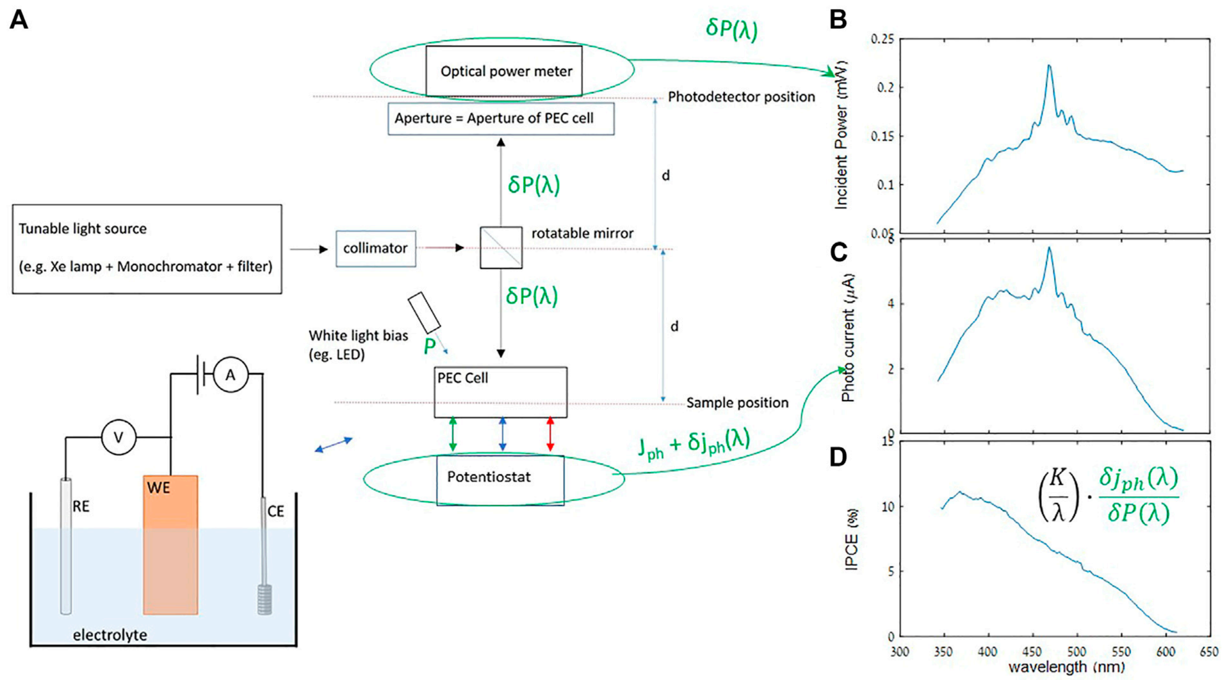

FIGURE 1 | (A) Basic IPCE setup. The three-electrode mode voltammetry measurement setup of the current –potential (J_{ph}-U) curve of the PEC cell (using a potentiostat) is illustrated schematically in the bottom left, with the sample serving as the working electrode (WE), a reference electrode (RE) and counter electrode (CE), all in contact with the electrolyte. Typical measurements of optical power **(B)** and photocurrent **(C)** spectra, resulting in IPCE spectrum **(D)**, computed from the above with **Eq. 1** Note that the bias light (of power P) from the LED leads to a bias photocurrent level (J_{ph}) produced by the PEC cell, but the IPCE is determined from only the small signal values.

where K is comprised of fundamental physical constants: $K = h.c/e$, where h is Planck's constant, c the speed of light, and e the charge of an electron. All of the above variables are written in small signal form, preceded by a "δ", because as a matter of practice the IPCE is measured only as small signals, even though this is not mentioned in most definitions that one might look up for IPCE or EQE. We also note that "per unit time" of the observables $\delta j_{ph}(\lambda)$ and $\delta P(\lambda)$ cancel out between numerator and denominator, and likewise "per unit area." Therefore, if $\delta P(\lambda)$ is actual power reading, then $\delta j_{ph}(\lambda)$ in **Eq. 1** likewise has units of current, as opposed to the usual current density; we avoided the usual "I" nomenclature for current in order to reserve that variable for optical intensity. It is therefore ideal that the effective areas accepting the incident light for optical power detection and current detection respectively be the same, which includes the center position relative to the beam profile. A typical IPCE setup is schematically depicted in **Figure 1A**, showing the light source, PEC cell with the sample and electrolyte. A potentiostat is used to measure $\delta j_{ph}(\lambda)$ in 3-electrode mode (**Figure 1C**) as well as characterize the J_{ph}-U curves, where U is the applied potential, and J_{ph} is the large-signal photocurrent. The latter is determined from the current in the total incident light (usually dominated by the white-light bias), minus the current measured in the dark. The dark current can become significant at high enough U. Also included is the optical power meter for $\delta P(\lambda)$ (**Figure 1B**) with aperture in front to maintain a light beam area consistent with that on the sample side, and a white-light bias source contributing broadband optical power P to the sample, whose importance is discussed below. The resultant IPCE spectrum is shown in **Figure 1D**, which is essentially **Figure 1C** normalized by **Figure 1B**, as per **Eq. 1**. The sharp peaks in **Figures 1B,C** are a result of the Xe lamp's spectrum, but are seen to cancel out in the IPCE shown in **Figure 1D**.

From the definition of IPCE as described by **Eq. 1**, it is common to relate the total expected photocurrent J_{ph} to the IPCE spectrum (where both J_{ph} and IPCE are measured at the same applied potential, U) by integrating the IPCE over the full wavelength range of the incident light spectrum $S(\lambda)$. This is used to validate the consistency between the IPCE and photocurrent voltammetry measurements. Then, the spectrum of the light source can be replaced by the standard spectrum of the sunlight (typically the NREL AM1.5G standard) to calculate the expected photocurrent under 1-sun illumination conditions. Omitting unit conversion factors, for $S(\lambda)$ units of photons per seconds per unit area per wavelength, we write for simplicity:

$$J_{ph}(U) \cong e \int S(\lambda) IPCE.(\lambda, U) d\lambda \tag{2}$$

While **Eq. 2** in many cases has been demonstrated to be exact within experimental error, and is indeed used as a standard check for consistency between the IPCE measurement and measured

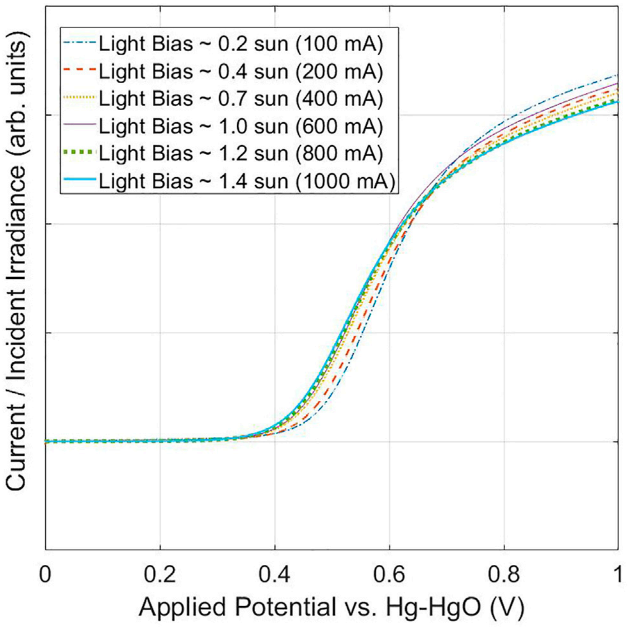

FIGURE 2 | Photocurrent normalized by light intensity vs. applied potential, for various intensities of the LED white light source. The light intensity was determined by a fitted calibration curve of light intensity vs. LED current, the former measured with a spectroradiometer and integrated over wavelength for the total irradiance. The sample was a 26 nm thick epitaxial 1% Ti-doped hematite deposited on platinized sapphire.

photocurrent, there are a number of subtleties to consider. In practice, because the monochromized (or sometimes also modulated) light signal $P(\lambda)$ for the IPCE measurement could be relatively weak, **Eq. 1** for IPCE should be considered to be a small-signal equation, measuring a small increase in current for a small increase in optical power. In contrast, J_{ph} in **Eq. 2** is a large signal quantity. **Eq. 2** would be exact if IPCE were a constant (for a given applied potential U), independent of light intensity, but in some cases the small-signal IPCE spectrum could be dependent on light intensity [8]. This light-bias dependence is readily apparent simply by inspecting the dependence of J_{ph}-U curves normalized by light bias. **Figure 2** shows an example of J_{ph}-U curves measured at different light intensities, and normalized by them, which cannot be explained by an intensity-independent IPCE spectrum at all applied potentials, even if one allows for series resistance to account for the photocurrent onset potential shifts. This issue regarding **Eq. 2**, has been highlighted previously (Christians et al., 2015; Shi et al., 2015), and up to 20% discrepancy can be commonly expected (Zimmermann et al., 2014). Before attempting to improve on **Eq. 2**, we should note that the mathematical complexity is increased because IPCE(λ) may not only be dependent on the light intensity at a given wavelength λ, but also on the total light intensity across all photon energies exceeding the bandgap. Physically, this determines the steady state photogenerated carriers, which can, in turn, affect the internal sample and surface conditions, and therefore have an influence on the IPCE.

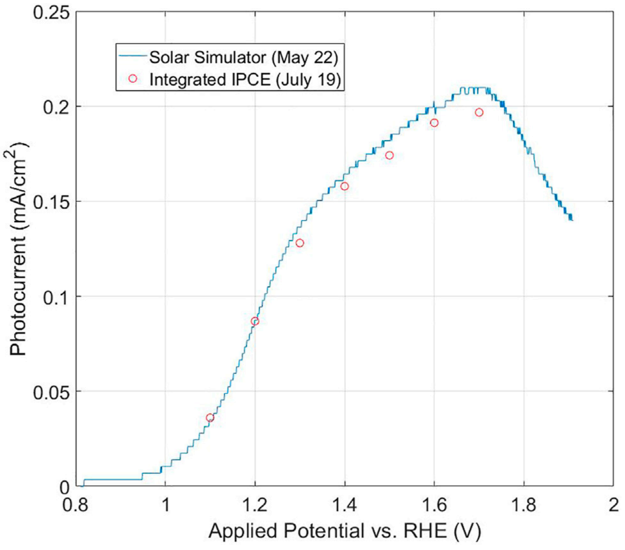

FIGURE 3 | Integrations of **Eq. 3b** for IPCE of a hematite photoanode (measured in white LED light bias) vs. potential, compared to the J_{ph}-U curve measured, on a different date, under solar simulator illumination. The sample was a 1% Sn-doped hematite layer, having 85 nm thickness, deposited on ITO, on an eagle glass substrate.

Notwithstanding, we can proceed to a more exact variation of **Eq. 2** if we consider a total-intensity-dependent IPCE (λ,U,β) where IPCE now also depends on total light intensity I via an intensity scaling factor β such that $I = \boldsymbol{\beta} \int S(\lambda)\cdot d\lambda$. In this way, we can envision a “thought-experiment” in which we gradually increment the total intensity, while maintaining the spectral shape of the light source, by increasing β continually from 0 to 1, which in turn gradually increases the photocurrent accordingly until it reaches the final value. With this picture in mind, we write:

$$J_{ph}(U) = \int_{\beta=0}^{\beta=1} \int S(\lambda) IPCE.(\lambda, U, \beta) d\lambda d\beta \tag{3a}$$

where the inner integral is over the full wavelength range determined on either side by the IPCE or S (λ) limits, whichever is more limiting. Re-writing to a form resembling the original **Eq. 2**:

$$J_{ph}(U) = \int S(\lambda)\overline{IPCE}.(\lambda, U) d\lambda \tag{3b}$$

where $\overline{IPCE}(\lambda, U) = \int_0^1 IPCE(\lambda, U, \beta) d\beta$ is the intensity-averaged IPCE spectrum, at applied potential U. Strictly speaking, this requires measuring IPCE at a number of different light biases to find the average. However, in the interest of saving time and reducing tedium, it may be an acceptable approximation to measure at half of the actual operating light bias, β = 0.5, to represent a kind of average. Many in the community may feel more comfortable intuitively to know the IPCE *at* 1-sun conditions $\beta = 1$, even though it may arguably be less representative of the required average of **Eq. 3b** than would be $\beta = 0.5$ light bias. This may nevertheless be acceptable in many cases, especially when the IPCE of the sample is almost independent of light intensity, which could also depend on applied potential and other conditions. **Figure 3** is an example of good agreement of integrations as compared to the photocurrent–potential curves for a hematite photoanode, even though the light bias for the IPCE measurement (white LED light bias) was different from the photocurrent measurement light bias (commercial solar simulator). The integration, of course, used the spectrum for the latter, under which the photocurrent was measured. Excellent agreement between photocurrent and integrations was also seen for our $BiVO_4$ photoanode measurements presented in **Section 3**, but as will be shown, stability of the IPCE within the spectral range of S (λ) is crucial.

Especially for new and relatively untried types of photoanodes, we highly recommend to at least once characterize the typical light-bias dependence of the current–potential curves (as in **Figure 2**) to begin with (and if warranted, measurement of IPCE at a number of different light biases), in order to avoid potential misuse or mis-interpretation when attempting to validate the IPCE and/or J_{ph} measurement with **Eq. 2**. So-motivated to measure IPCE under light bias, we caution that this introduces additional challenges in the measurement, but can be dealt with as shown in the next section. A final note regarding **Eq. 2** or **Eq. 3b** is that ideally, $S(\lambda)$ should be measured in the same sitting as the J_{ph}–U measurement, to ensure that the actual $S(\lambda)$ is used to integrate with the IPCE, not affected by possible changes in sample distance from the source, etc. This could be measured, for example, by a spectroradiometer put in place of the PEC cell. The IPCE measurement itself need not be done in the same sitting as the J_{ph}–U or light source measurements (for example, see the dates between measurements in **Figure 3**), as long as the sample is stable over time and conditions such as applied potential and electrolyte are well replicated.

3 MITIGATING SOURCES OF ERROR AND NOISE

3.1 Description of Basic System and Measurement Procedure

In the following sub-sections we list or state a number of measurement trouble-spots and possible solutions, some of which are straightforward and self-explanatory (but nevertheless warrant brief attention as a reminder), but others requiring more elaboration which we provide with specific demonstrations and examples. As a starting point of reference, we begin with a description of our base system and procedure (before introducing modifications in subsequent sections), whose elements are likely typical for many IPCE systems, with only minor variations (a majorly different scheme, however, will be briefly touched upon in **Section 3.4**). Our measuring system, depicted schematically in **Figure 1A**, is based around the Oriel QV-PV-SI "Quantum Efficiency Measurement Kit," by Newport. The work area at the IPCE station is enclosed in a black curtain and ambient light (as can be monitored on the power meter) is kept to a minimum; ambient light from instrumentation panels and computer screens is low enough for the power meter reading to be at its noise floor and likewise does not produce significant photocurrent (as a comparison, the few 100 μW of monochromatic light in **Figure 1B**, which in the dark looks quite bright on the sample, produces a few μA of photocurrent, but the ambient light is relatively dim, perhaps several hundred times less). The probe light is generated from a broadband Xe lamp source (up to 1 kW input power) monochromatized by a Cornerstone 260 monochromator. The output light is collimated and focused with the appropriate optics. Collimation of the beam plays the important role of decreasing the sensitivity of the beam cross-sectional profile to small changes that could inadvertently occur in distance between mirror and sample or power meter, in spite of efforts made to make these distances consistent. The aluminum mirror shown at the center of the system illustration presented in **Figure 1** could be manually rotated so as to direct the light to either the power meter or PEC cell (i.e., the sample), with grooves on the mirror stage restricting the possible angles to discrete values to ensure repeatability and proper placement of the angle. On the PEC cell side, the photoanode is placed in a "cappuccino" cell (Cesar 2007), and connected in 3-electrode mode to a potentiostat (Zahner Zennium in our system). Our typical sample has a transparent current collector layer (typically a doped tin oxide layer, fluorine-doped FTO or niobium-doped NTO, or a tin-doped indium oxide layer ITO), with the photoanode layer (i.e. hematite, and possible underlayers and overlayers) deposited over part of it. Typical hematite samples produced in our group were deposited by pulsed laser deposition either on a tin-doped indium oxide (ITO) (Piekner et al., 2018), niobium doped titanium oxide (NTO) conductive layer (Grave et al., 2016b), or platinum conductive layer (Grave et al., 2016a) on sapphire, or on eagle glass substrates for polycrystalline films. The working electrode lead is connected with an alligator clip to the exposed transparent correct collector layer, with the hematite layer partially in contact with the electrolyte (1M NaOH aqueous solution, pH 13.6), through the aperture (3.7 mm when measuring samples with sapphire substrates, or 6 mm diameter for larger samples having eagle glass substrates) of the cappuccino cell. An Hg/HgO/1M NaOH reference electrode (ALS model RE-61AP, appropriate for use in alkaline solutions), and platinum counter electrode (ALS model 012961), are immersed in the electrolyte and likewise connected to the potentiostat with alligator clips. This is shown schematically in the bottom left of **Figure 1A**.

Prior to making electrical connections, the optics is inspected to ensure that the (monochromatic) beam profile on the aperture to the power meter is identical to the beam profile incident to the aperture on the cappuccino cell. After connecting the alligator clips, the electrical connection is checked by, in our case, making an impedance measurement (typically at 10 kHz frequency, to bypass usual capacitive effects from electrochemical interfaces) using the a.c. capabilities of the potentiostat which is coupled to a frequency response analyzer (FRA) in our Zahner Zennium potentiostat. In the case of our typical samples, we consider 200 Ω and below to indicate a reasonably good connection; if our typical photocurrent is maximum 200 μA, then this amounts to an error of ~40 mV at most, which could represent a significant offset (i.e. see **Figure 2**), but on the other hand could be accounted for and does not qualitatively impact the measurement, as compared to a "bad connection" which is typically 1 kΩ and higher, and is usually a sign of an ill-placed or corroded alligator clip. The next step after the probe beam optics and electrical connections are set, is to arrange the white-light bias so as to produce an expected amount of photocurrent for a given applied potential. In our setup, a broadband, high power LED (Mightex Systems, 6500 K "glacial white" spectrum, 300 mW maximum radiant flux, which could output an order of ~1 sun equivalent intensity on the sample) is positioned to obliquely shine on the sample, as depicted in **Figure 1A**, so as not to block the incident monochromatic beam. The usual procedure is to modify the incident angle of the light bias to center its circular profile on the sample, monitoring the photocurrent in real time to maximize it. The light level can be subsequently adjusted by changing the LED current via software.

After the above preliminary checks and setups, a current-potential scan under light bias is performed. These may be repeated until the sample stabilizes (i.e. the current-potential curves are repeatable), and further adjustments to the light bias current may be made to achieve the desired condition for the IPCE measurement (i.e., typically to replicate a J_{ph}-U scan made elsewhere, or set β to a specific value). For our hematite samples, we found that 20 mV/s was an adequately slow sweep-rate, but this may vary depending on the sample. We note that the photocurrent is obtained by subtracting the dark current vs. applied potential scan from the scan made under light. Once the applied potential and white light bias are set for the IPCE measurement, a certain time may be allotted for stabilization, which may also be monitored in real time by continuous measurement of the photocurrent.

Having set the operating condition, including fixing the applied potential and light bias, the basic IPCE procedure is relatively simple. First the mirror is rotated to direct the monochromatic beam to the power meter, and a scan of optical power vs. wavelength is performed. Then, the mirror is rotated for sample illumination and the same wavelength scan repeated, but this time measuring current on the potentiostat. The baseline current, measured with the same light-bias, but without any monochromatic beam, is subtracted to produce $\delta j_{ph}(\lambda)$, and **Eq. 1** applied for the IPCE spectrum. Usually, another $P(\lambda)$ scan is done afterwards to check stability of the monochromator, discussed in **Section 3.4** below. We found this method to be adequate in the case of zero light bias ($\beta = 0$), whereby the LED would only be used to check the J_{ph}-U curve for the purpose of setting the applied potential to a certain operating point, but then turned off for the IPCE scans. However, in the case of light biases approaching 1-sun intensity ($\beta = 1$), it fails spectacularly. In the sub-sections below we discuss some of the finer points of different aspects of the measurement.

3.2 Optical Power Measurement

The basic optical power measurement is fairly straightforward. Here we just briefly review a few points. As described above, one should be careful to keep the optical power (i.e. beam-profile) the same on the power meter as on the sample, by use of appropriate apertures, and symmetric geometry etc., which should be confirmed by appropriate distance and height measurements and visual inspection, to verify proper centering of the incident beam profile on the sample and photodetector. The power meter should be calibrated according to wavelength, ideally NIST traceable, and informed of the correct wavelength at each point in the scan. As the power measurement time could be rather quick (several readings per second), fluctuations can be reduced by repeated averaging (or longer integration times) of measurement without much additional cost in scan time. To be optimal, this could be adjusted to be comparable to the overhead time of each wavelength point, or some fraction thereof. If the ambient environment is dark, there will usually be negligible background for most of the scan, but as can be seen from the Xe lamp (plus monochromator grating/filter) spectrum in **Figure 1B**, the power can fall off significantly at the extrema of the wavelength range. If the scan must necessarily include such low-power ranges, the electronic noise-floor of the power meter may dominate the reading. In this case, a background (in the dark) scan of the power meter should be done first and subtracted wavelength-per-wavelength. We found, however, that a few wavelength points plus linear interpolation, lasting only a few seconds total, are adequate for the background scan. Lastly in this section, although perhaps not solely a power issue, we emphasize the importance of correct use of optical filters (which cut off low wavelengths) appropriate to the wavelength range (or vice-versa) during the monochromatic scan, in order to block higher order diffraction passed by the monochromator gratings. Although the higher harmonics may have a relatively small effect on the total power, they can have a significant impact on the photocurrent–for example, if at a photon energy below the sample's optical bandgap, there should be practically no photocurrent, but a second harmonic could have energy above the bandgap, and produce significant (and misleading) photocurrent. Additionally, the typically wide-bandgap transparent conducting layers (i.e., FTO, ITO or NTO) may also activate from short-wavelength second harmonics.

3.3 Current Measurement and Current Drift

Current drift during measurement is the main killer when it comes to measuring in light bias, and is the likely reason many published works to date have avoided presenting IPCE measurements in light bias. Very simply, the optical power of the monochromatic probe beam is typically much weaker than the ~1 sun white-light bias intensity, and thus the resultant photocurrent signal is correspondingly weaker. A factor of 100 is not unusual, depending on the wavelength and lamp condition. Therefore, merely a few percent drift of the current under bias over the time of a typical wavelength scan (which could be ~½ h or more, depending on the wavelength stepsize, etc., and could easily be caused by gas bubbles or other effects) could produce a significant error, in either direction, to the measured δj_{ph} after subtracting the light bias contribution, and thus to the IPCE. This is illustrated in **Figure 4A**, which shows reasonable looking IPCE values for zero light bias (0 mA LED current), but an artifact decrease, even to negative IPCE values, at low wavelengths when a ~ 1-sun bias (1,000 mA LED current) is applied. The inset shows

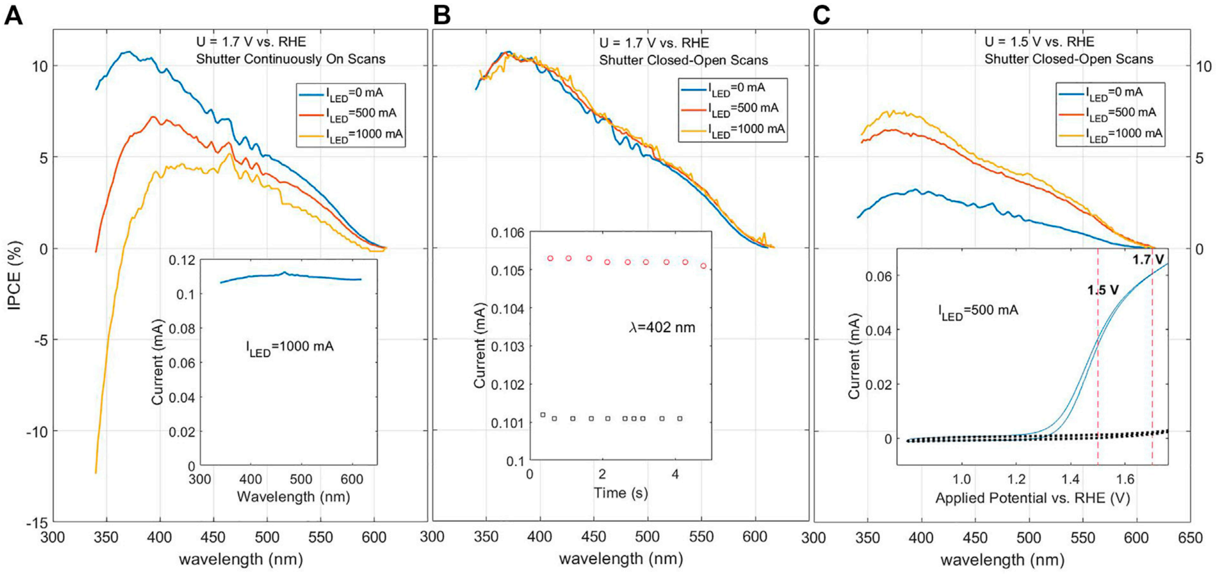

FIGURE 4 | IPCE scans on a 30 nm Ti-doped hematite film deposited on a platinized sapphire substrate, for different light bias intensities (1000 mA LED current is comparable to 1 sun). **(A)** Measured by the base system and method, before the shutter on-off method was implemented. In this case, the current is measured as the monochromator is incremented from high to low wavelengths. The inset shows the total measured current (including from the light bias) of such a scan under strong light bias. The applied potential was set to 1.7 V RHE, near the plateau region as indicated in the inset of **(C)**. **(B)** Using the shutter closed-open scheme. The inset shows the current vs. time measurements for one of the wavelength points, with shutter open in red **(upper)**, shutter closed in black **(lower)**. **(C)** Using the shutter open-closed scheme, but for the applied potential lowered to 1.5 V, which is below the plateau region of the J_{ph}-U curve, shown in the inset; dark current is shown as the black dashed line.

the measured total current under light bias, which looks relatively stable on an absolute scale, but the slight decrease near the end of the scan (from high to low wavelength) causes a precipitous decrease of the calculated IPCE, which is clearly an artifact.

One solution to take into account this current drift is to subtract the baseline current (the current under the light bias used, but without the monochromatic small signal light), such that the "mono-light on" and "mono-light off" current measurements are done at almost the same time (only a few seconds apart) at each wavelength. We initially implemented this by simply using the slits in the monochromator as an effective shutter: opening and closing them at each wavelength, and measuring current as a function of time for each of the shutter-open and shutter-closed states, as shown in the inset of **Figure 4B**. The improvement of using the shutter on-off scheme is immediately apparent in **Figure 4B**, where the measured IPCE spectrum does not change with light bias, even up to ~1 sun at LED current of 1,000 mA. **Figure 4C** shows that when the applied potential is lowered to be below the plateau region of the J_{ph}-U curve, indicated in the inset, there appears to be a systematic drop in the IPCE for this sample as the light bias is lowered. Given the consistency of the measurement in the plateau region shown in **Figure 4B**, we can plausibly make the distinction that this is truly a sample condition effect of non-linear sensitivity to light intensity in the near-onset region, and not a measuring artifact like in **Figure 4A**.

To examine more closely the dynamics that could occur in the PEC cell during the IPCE measurement, the current vs. time response upon opening or closing the monochromator shutter ($\lambda = 582$ nm), for another hematite sample, is shown in **Figures 5A,B** for zero light bias and ~1 sun white light bias, respectively. We note that $j_{ph}(\lambda)$ in **Figure 5B** is less than 1% of the current due to the light bias. For the case without light bias, **Figure 5A**, we see a relatively slow decay in the current response to opening and closing the monochromator shutter, lasting several seconds before the current reaches steady state. The photocurrent $j_{ph}(\lambda)$ is taken as the difference between the (approximately) steady state values. The dynamics with light bias, **Figure 5B** is somewhat faster, but still with a settling time of the order of ~1 s. This variation in settling time could be understood in terms of charging and loss mechanisms at the surface, which has also been demonstrated by modulated techniques and related distribution of relaxation time (DRT) analysis (Peter 2013; Klotz et al., 2016; Klotz et al., 2018). This sometimes-slow dynamics is a reason for caution related to using the popular phase-locked loop (PLL) technique with a lock-in amplifier for measuring the small-signal IPCE, which indeed can overcome the drift (and other) problems, but if the modulating frequency is higher than 1 Hz (which is typical for PLL), may miss such slow loss mechanisms, erroneously measuring the higher $\delta j_{ph}(\lambda)$ seen at the beginning of the transient response. This is more likely to occur at lower applied potentials where surface recombination dominates. Frequency dependence issues of IPCE have also been studied for perovskite materials (Ravishankar et al., 2018) and dye-sensitized solar cells (Xue et al., 2012).

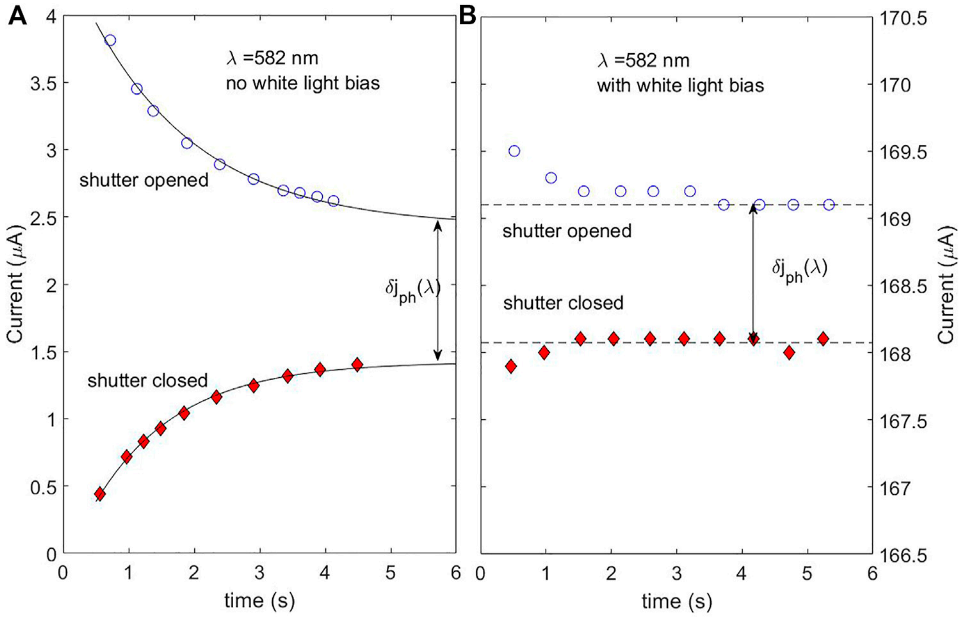

FIGURE 5 | Effect of light bias on small-signal photocurrent response to a step in the light intensity. The sample was a 1 µm thick, Ti-doped hematite layer over an FTO conductive layer, measured with monochromatic light incident on the back of the sample. The applied potential was set to 1.6 V RHE, well above the photocurrent onset (at ~1.2 V RHE, not shown), but near the onset of dark current **(A)** Without light bias **(B)** with ~1 sun white light bias, incident on the front of the sample. Note that the photocurrent scale spans the same 4 µA as in **(A)**, but offset by the current contribution from the LED bias (~ 166.5 µA).

3.4 Light Source Drift and Noise

Another source of error in the IPCE measurement, usually less dramatic than photocurrent drift, but still potentially significant, is drift and/or noise of the light source for the monochromatic beam. In many IPCE setups including our own, the light source is a Xe lamp. However, it is a fitting juncture to make mention of an alternative technology which was developed at the National Renewable Energy Laboratory (Young et al., 2008). In this concept, light from an array of several LED's, each emitting a different wavelength spanning the spectral range, is simultaneously focused on the sample. The LED's are each modulated with a different frequency, so data processing can isolate the contributions to the generated photocurrent from each wavelength via the Fourier transform of the photocurrent, which in Fourier space will have a peak for each modulation frequency. In this way, the whole spectral range is measured at once, drastically reducing the time required to measure each IPCE spectrum, and can be as short as a second (for high frequencies). This method is currently employed in a number of commercial systems. Many of the drift-related problems can be totally avoided, however the modulation frequencies (and thus speed) would still subject to the system frequency limitation described in the previous section. Anticipated disadvantage of an LED array as opposed to Xenon source plus monochromator, would be less access to the UV portion of the spectrum, and also somewhat less wavelength resolution (or sharpness) based on the inherent LED bandwidth limitations as compared to the monochromator, and discrete separation of the LEDs. Evaluating these quantitatively is beyond the scope of this paper. The approach certainly deserves serious consideration, depending on the system being measured, but we here we proceed to deal with the problems and procedures for using the conventional Xe lamp and monochromator.

A common practice is to allow an hour or half an hour time after turning on for the lamp to stabilize before commencing the IPCE scans. However, as shown in a sequence of repeated lamp scans over 6 hours in **Figure 6**, fluctuations in lamp power from one scan to another, can occur well past this initial warmup time. While several scans in a row show intensity that is relatively stable (~2% or better), occasionally larger shifts of lamp power also occur, of the order of ~10%. While this allows the viability of checking the lamp stability immediately before and after each $\delta j_{ph}(\lambda)$ measurement, should one be unlucky enough to have measured between the big jumps of the lamp, it would mean repeating the measurement/waiting until the lamp is stable again, amounting to a considerable cost in time.

The above problem would be largely circumvented if, similar to the shutter on-off measurements in the previous section, the optical power were also measured at every wavelength point. There are a number of different approaches to achieve this, each having advantages and drawbacks. One approach (Palma et al., 2015) used the optical architecture of a Lambda 35 spectrophotometer, which featured a beam splitter to divide the incident beam to simultaneously measure the incident power. A slight complication of the beam splitter approach is that, from surveying vendor's websites, even beam splitters designed for broadband applications seldom exhibit completely uniform or consistent splitting ratios over a wide wavelength range, so a careful calibration, requiring two calibrated (ideally identical) photodetectors, would be needed to characterize the

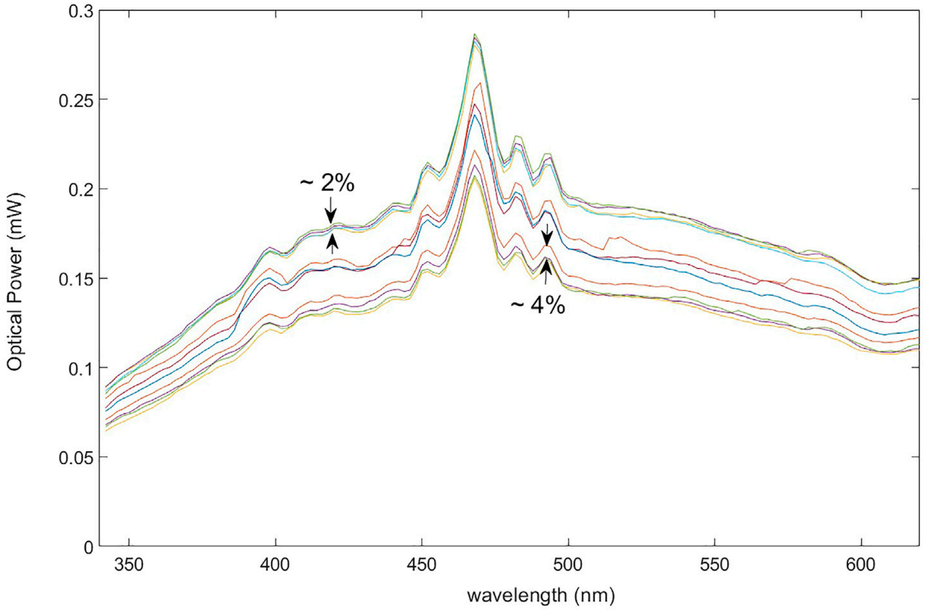

FIGURE 6 | Series of monochromator scans of a Xe lamp over a period of 6 h. Some typical shifts, during the periods of relative stability between the larger jumps of intensity, are indicated as a percent error.

splitting ratio as a function of wavelength. In principle, however, this calibration need be done only once.

As an alternative method, we automated the rotation of the mirror in our setup which was previously done by hand between scans, allowing the mirror to switch angles to direct the light between the power meter and the PEC cell for every wavelength. This has the advantage of measuring (in principle) the exact same light beam incident on the PEC cell, aside from possible errors in motor motion, or power fluctuations that could occur on a few-second scale, which in practice was usually not large (with exceptions, discussed below). The main challenge with this method is precise and consistent control of the motor angle. Our rotary stage was a HR-3 model from Newmark Systems, with an NSC-A1 stepper motor controller. Inclusion of an encoder which independently measured the angle was crucial for ensuring the correct angles, and we incorporated stabilization routines and checks in our software control. In practice, a 0.1° repeatability in angle was achieved with relatively fast motions (~1 s position switching time), resulting in negligible variation in detected power or current. Each time upon startup of the IPCE system, we performed a brief (few minutes) but effective angle zeroing procedure whereby a small aperture is temporarily placed in front of the monochromator output, and the mirror angle zeroed by back-reflecting the beam back unto the aperture. Even relatively tiny IPCE's could be resolved with relatively little fluctuation. This sensitivity is also largely thanks to the resolution of the Zennium potentiostat (by Zahner), which can accurately resolve down to the level of nA currents. The ability to measure low IPCE's could be useful, for example, to characterize device behavior outside the normal operational range, such as energies near or below the band-edge, or a low applied potentials. **Figure 7**, adopted from (Grave et al., 2021), shows IPCE spectra (**Figure 7B**) measured at different applied potentials along the J_{ph}-U curve (**Figure 7A**). As the cyan spectrum around 500 nm and scaling factors in the legend of **Figure 7B** show, IPCE spectra with values down to ~0.001% can be at least roughly measured. An added benefit of the motorized mirror method is that, in addition to measuring the optical power at each wavelength, the light-off current may also be measured by directing the beam away from the PEC cell, thus also filling or replacing the "shutter on/shutter off" role described in the previous section.

One situational disadvantage of the motorized mirror stage scheme, which might be in some respects better handled with the beam splitting approach, is if lamp fluctuations occurred over the same timescale as the delay between mirror rotations (typically a number of seconds). Ideally the Xe lamps are designed to not normally exhibit such fast intensity fluctuations, but we nevertheless found this to be the case from time to time. We noticed that in these situations, the spectra markedly improved and the noise disappeared in the evening hours, when other electronic devices in the building or vicinity were likely not as active. We consequently attributed the short-term fluctuations to electromagnetic interference (EMI) or other noise coming from the operation of other devices in the vicinity of the experiment, perhaps from adjacent rooms or floors, or outside. bXe arc lamps and similar plasma-based devices can be particularly sensitive to electrical noise including from EMI, in part due to thermal stresses and turbulent convection flows within the lamp, and there have been studies of these issues (Green et al., 1968; Rolt et al., 2016). Therefore, EMI could be a possible issue to consider, which could be mitigated by additional shielding or regulation, or

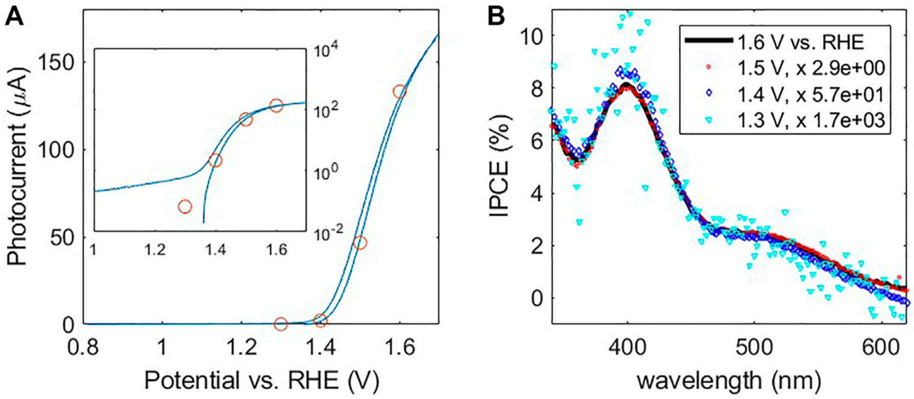

FIGURE 7 | IPCE measurements at different applied potentials along the J_{ph}-U curve of a 1% Sn-doped 7 nm hematite film deposited on ITO-coated glass substrate **(A)** J_{ph}-U curve, with circles indicating the applied potentials at which IPCE measurements were made and their corresponding integrations with the LED spectrum according to **Eq. 3b**. The inset plots the same, but with the photocurrent axis on a log scale. **(B)** IPCE spectra measured at the different applied potentials, in white light bias shown in the legend. The measured spectra were scaled up by multiplying by the factors indicated in the legend. Adapted from Supplementary Figure S4 of (Grave et al., 2021).

more simply by measuring in a time and/or place where less EMI or other external noise is likely to occur. Sensitivity to electronic noise may also be a function of the age of the lamp, which should be periodically replaced.

3.5 On Software: Handshaking With Machines but Holding Hands With Humans

We conclude this section by briefly digressing from the science/instrumentation side to discuss a nonetheless important part of effective IPCE measurements: the software interface. The core goal of IPCE software is to synchronize the actions of the rather diverse collection of instrumentation participating in an IPCE measurement–for the system outlined here this includes monochromator, potentiostat, optical power meter, and motorized mirror stage–integrating their control into a single program capable of properly orchestrating the measurement according to the experimenter's specifications. This could be implemented by such programs as Labview, as was done in this work. But to truly be effective, the "user friendliness" aspect should not be neglected. This includes an intuitive and easy-to-learn interface, active anticipation and prevention of common human error (such as checking if the typed data-save directory or filename exists before the scan starts, and prompting the user if there is a suspected problem with either files or devices to take corrective action), accommodation of situations such as the need to pause the scan mid-way to remove bubbles (especially important for measurements under light bias) and bubble-related spike-removal options, communicating and updating status (such as the applied potential) to the user so they can easily spot problems in real time, and convenient (but controlled) access to peripheral functions, such as opening popups that allow manual control of the monochromator or rotary stage, etc. In the case of Labview, a "stop" button is default to all programs, yet can present a hazard in that it allows users to arbitrarily and easily interrupt the program at any time, typically for reasons that could have been prevented or otherwise handled, and with potentially costly end-results of very possibly requiring resets of machines (and in the case of our rotary motor, even re-zeroing of the position). This button can be replaced with a more controlled abort and shutdown mechanism. In short, what we describe amounts to pro-active prevention of problems by tight control of the measuring process flow, but at the same allowing user flexibility in a "safe" manner. These features were implemented in our software, largely motivated by the experience (and frustrations) of ourselves and other colleagues and students measuring IPCE at various stages of development of the system. **Figure 8** shows some sample screenshots of our Labview interface including such features. Visual cues and audio cues (such as end-of-scan announcement) were also incorporated for enhanced awareness (and, a little bit, fun variety) during the measurements.

4 INCIDENT PHOTON TO CURRENT EFFICIENCY MEASUREMENTS OF $BiVO_4$ ULTRATHIN FILM PHOTOANODES UNDER WHITE LED BIAS

Recently, some of us undertook to measure the IPCE of $BiVO_4$ photoanodes under light bias. Light intensity dependence and photodegradation of $BiVO_4$ photoanodes under PEC operation is a well-known issue with these types of photoanodes, and has been studied by various groups of authors for more than a decade (and counting), including but not limited to references (Sayama et al., 2006; Abdi and van de Krol 2012; Toma et al., 2016; Zhang et al., 2019; Kou et al., 2020; Zhang et al., 2020). Nevertheless, the photocurrent under our white LED bias appeared to be relatively stable, decreasing ~3% during a typical scan. From this (deceptively) stable photocurrent, one might reasonably assume as a corollary of **Eq. 2** or **Eq. 3b** that the IPCE spectrum should likewise be stable. As later became apparent, this was not to be the case. Nevertheless, it makes for an

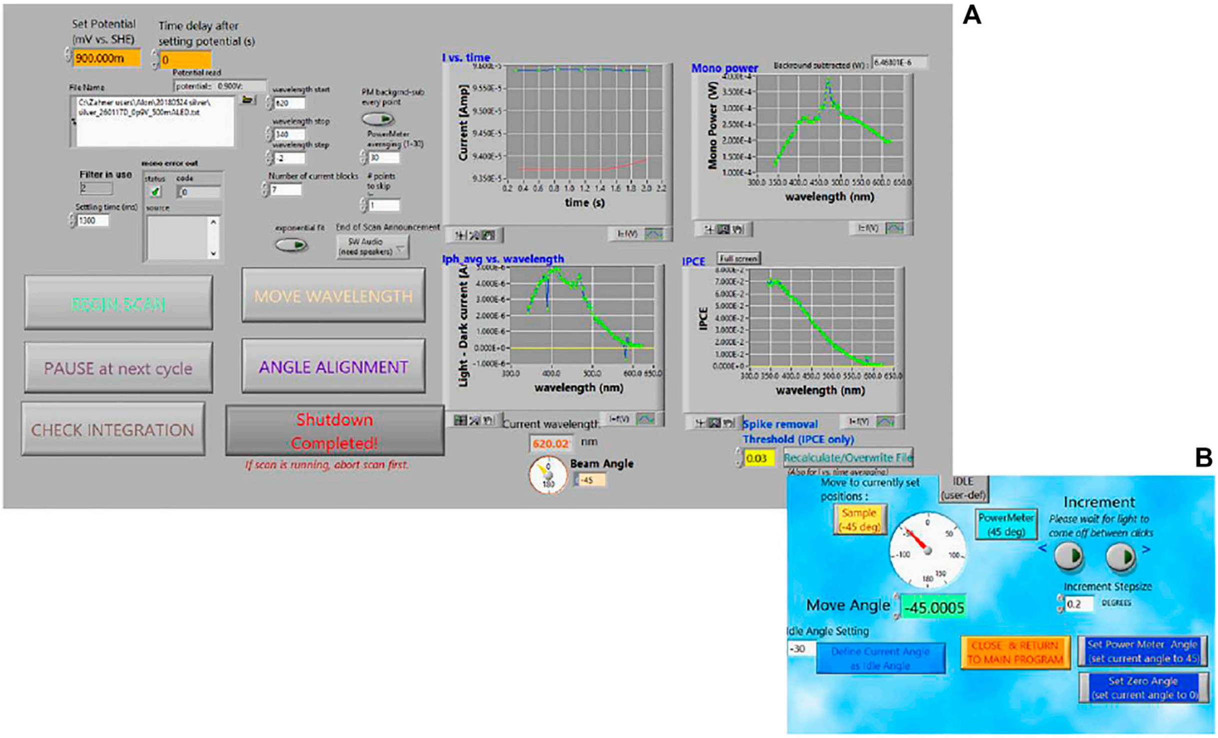
Set Potential (mV vs. SHE): 900.000m

Time delay after setting potential (s): 0

Potential read: potential= 0.900V

File Name: C:\Zahner users\Alon\20180524 silver\silver_260117D_0p9V_500mALED.txt

wavelength start: 620

wavelength stop: 340

wavelength step: -2

PM backgrnd-sub every point

PowerMeter averaging (1-30): 30

Number of current blocks: 7

points to skip: 1

Filter in use: 2

Settling time (ms): 1300

mono error out: status ✓ code 0 source

End of Scan Announcement: SW Audio (need speakers)

Background subtracted (W): 6.46801E-6

Current wavelength: 620.02 nm

Beam Angle: -45

Spike removal Threshold (IPCE only): 0.03

If scan is running, abort scan first.

Move Angle: -45.0005

Idle Angle Setting: -30

Increment Stepsize: 0.2 DEGREES

Please wait for light to come off between clicks

FIGURE 8 | Screenshots of the software interface used for the IPCE system: **(A)** Interface with scan settings and large buttons for the main, often-used functions, such as beginning the scan and pausing. Plots of the on-off transient current, photocurrent (before automatic spike removal, which can be user-specified), optical power, and resultant IPCE spectra update point-by-point during the scan. The large buttons also dynamically display messages such as status messages (like "setting potential," etc.), and/or instructional messages (like "press to resume scan" after pausing), or open pop-ups, such as **(B)** a pop-up window for manual control and calibration of the mirror angle.

interesting case study of an unexpected situation that can occur when measuring IPCE on unknown samples, and the IPCE data obtained may offer some new lines of investigation for further studies of the IPCE decrease, although the latter is beyond the scope of this manuscript, and from this point of view we present this final section.

The samples were 30 and 10 nm thick $BiVO_4$ films deposited by pulsed laser deposition (Kölbach et al., 2020) for which zero-light bias IPCE measurements of the 10 nm film were recently published (Grave et al., 2021). Our original intention for the latter work was to measure under light-bias, as was done for hematite photoanodes. We describe the procedure, which was approximately identical for both samples. The J_{ph}-U curves were measured with the LED current set to 1,000 mA, shown in **Figure 9A** as solid lines. This LED intensity roughly corresponded to an overall photon flux of the same order of magnitude as 1 sun intensity. The first IPCE measurements were done under the same light bias, with the applied potential set to the plateau region (as shown by the crosses in **Figure 9A**, which also correspond to **Eq. 3b** integrations). These initial IPCE spectra in strong light bias are shown as yellow lines in **Figures 9B,C** for the 30 and 10 nm samples, respectively. Then, the PEC cell was rotated 180° so as to illuminate the back of the sample with the monochromator light, while also moving the LED around so as to continue to illuminate with the light bias on the front, and IPCE measurements were done with back illumination (not shown). Additional UV measurements were performed (not shown), and the sample and LED once more re-positioned to repeat the front (monochromator) illumination scans. By the time the 2nd front-illumination IPCE scan was started, the sample had been under the LED illumination for approximately 2 h (with brief interruptions rotating the sample, etc). The 2nd IPCE scans with front illumination are shown as purple lines in **Figures 9B,C**. The 10 nm film especially showed dramatic decrease of the hump at low wavelengths between the two front illumination measurements. For the 30 nm film there is a significant change between 1st and 2nd measurements, but not as dramatic. This is likely because even before the first measurement, the sample was already under illumination for some time while trouble-shooting a technical issue with the alligator clip, so was already in a decreased-IPCE state (possibly light-soaked; see for example, Wing et al., 2015) by the time the first measurement commenced. After observing these dramatic changes, the electrodes and electrolyte were removed, and sample allowed until the next day (~14 h) to recover to their original surface state.

When the measurements commenced the following day, it was without exposing the sample to a strong light bias, in order to avoid the time-dependent effects observed above. Even the J_{ph}-U curves, usually done before each IPCE measurement to verify a consistent operating potential relative to them, were done with the LED current set to only 25 mA. These low-intensity curves are shown as dotted

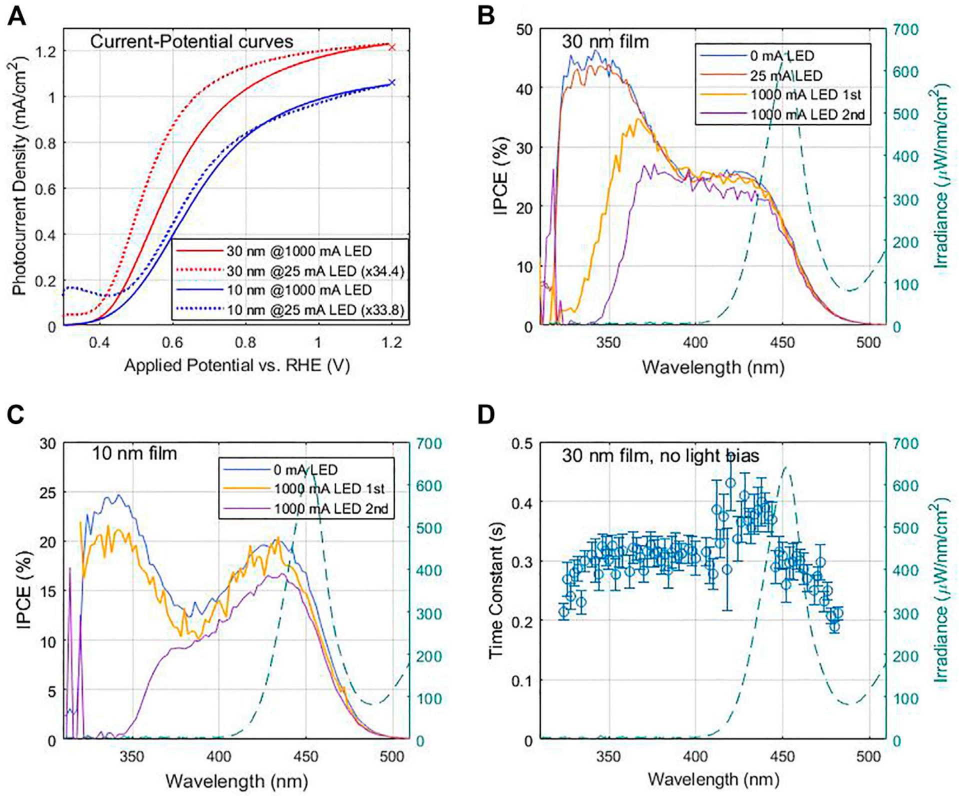

FIGURE 9 | Measurements of 30 and 10 nm thick $BiVO_4$ samples measured in a neutral buffer solution with a hole scavenger; details in (Grave et al., 2021). **(A)** J_{ph}-U curves for 30 nm (blue) and 10 nm (red) thicknesses, under white-light LED bias of ~1 sun (solid) and low-intensity (dotted). The x's at 1.2 V indicate the applied potential where the IPCE was measured as well as the resultant integrations of **Eq. 3b** **(B)** IPCE spectra for the 30 nm film at various light intensities. The measurement sequence is described in the text. The LED spectrum is overlaid on the right *y*-axis (teal color). Zero-bias IPCE data obtained from (Grave et al., 2021). **(C)** IPCE spectra for the 10 nm film at various light intensities. The measurement sequence is described in the text. The LED spectrum is overlaid on the right *y*-axis (teal color). Zero-bias IPCE data obtained from (Grave et al., 2021). **(D)** Fitted time constant of the step-response vs. wavelength, measured during the IPCE measurement without light bias, for the 30 nm film. The LED spectrum is overlaid on the right *y*-axis (teal color).

lines in **Figure 9A**, scaled as indicated in the legends by a factor of ~34 which was similar for both samples so the shapes and onset potentials may be compared. We attribute the larger potential shift for the 30 nm sample to a larger series resistance, but otherwise the shape of the J_{ph}-U curves were fairly consistent with the previous day's high-intensity scans. The IPCE curves for 25 and 0 mA LED biases, respectively, are plotted as red and blue curves in **Figures 9B** and a large low-wavelength hump appears, qualitatively similar to that of the 10 nm sample, approximately the same for both low intensities. For the 10 nm film in **Figure 9C**, the zero light-bias IPCE measurement (the 25 mA was skipped) showed very similar IPCE to the 1st light bias measurement the previous day. Repeated zero light-bias IPCE measurements for both films were found to be consistent, so the sample was stable in zero light-bias conditions.

These results together indicate that not only is there a light-bias effect, but also a slow decrease of parts of the IPCE spectrum in sustained light bias. But what appears to be the most unexpected and, in some sense, perplexing/counter-intuitive behavior, is that the spectral portion of the IPCE which is encompassed by the spectrum of the LED is relatively stable, while the unstable part is outside of the LED spectral coverage. The latter is plotted as dashed lines in **Figures 9B–D**, showing that the LED itself causes a dramatic decrease of the higher-energy (lower wavelength) part of the IPCE, which is well outside its own spectral range. A physical model that could explain this behavior is outside the scope of this manuscript. One additional indicator could perhaps be in the time constants of the photocurrent step-response (i.e., like plotted in **Figure 5A** for example). The step responses, recorded for each wavelength as part of the IPCE measurements described in **Section 3.3**, were fitted to an exponential decay for each wavelength and plotted in **Figure 9D**. The time resolution of our measurements was relatively poor, only 0.5 s intervals, and the 10 nm sample's response became stable too quickly for us to fit, but the 30 nm sample was slower (consistent with a larger series resistance, as indicated by the onset potential shift in **Figure 9A**), and the decay could be somewhat resolved and fitted at most wavelengths (far outliers were excluded from the plot). As **Figure 9D** shows, while the time constant is steady between 350 and 400 nm, there appears to be a distinct increase above ~410 nm and then falls off again beyond ~450 nm. Comparing against the IPCE curves in **Figure 9B** above, there might be some correlation between the time constants, and the stable and unstable regions of the IPCE spectrum. This could be an avenue to investigate in further studies using smaller time steps and more systematic measurements, which should also include dependence on applied potential as well. We note that similarly prepared samples, but with 90 nm thick $BiVO_4$ layers, were used in a recent photocorrosion study (Zhang et al., 2020). In our case, the relative stability of the IPCE within the LED spectrum gave rise to the observed stability of the photocurrent, which only changed a few percent during the scans. The crosses in **Figure 9A**, at 1.2 V, are the integration of the (10 and 30 nm) IPCE spectra with the LED spectrum according to **Eq. 3b** and which works well because the IPCE in the LED's spectral region is mostly independent of light-bias intensity of the LED, and is stable over time. Under a spectrum more resembling the solar spectrum, which has lower-wavelength spectral weight, the photocurrent would be expected to decrease with time more dramatically, as has indeed been observed in the literature. Subsequent to this preliminary measurement, we observed similar time dependence of the IPCE spectrum for thicker $BiVO_4$ samples under white light bias, which will be presented elsewhere.

In summary, we reviewed the basics and expanded on some of the finer technical points of IPCE measurements in PEC systems, using primarily hematite as a model system for examples. Emphasis was placed on demonstrating the importance (depending on the linearity of the photo-response) and difficulties of measuring the sample under white light bias, which along with applied potential sets the operating point to a large-signal photocurrent. The wavelength-resolved light source used for the small-signal probe was based on a Xe lamp with scanning monochromator. Because of the considerable amount of wavelength points for the scan, combined with upper limit on the photo-electrochemical frequency response (or lower limit on measurement time required), the total measurement time for an IPCE scan can take several minutes or even half an hour. During this time, two distinct problems can occur, drift of the large-signal photocurrent under white light bias, due to small changes in the sample or its environment, or change in the Xe lamp's output. These can be remedied by measuring the optical power, and the small-signal photocurrent (both with and without monochromatic light) at each wavelength point. We accomplished this by using a rotary mirror, but it is by no means the only possible solution, and the advantages and potential drawbacks of various alternatives, including the lock-in technique, beam-splitter, and the "flash" IPCE technique, were discussed. The IPCE spectra measured with our final system was demonstrated to be consistent (when integrated over the incident light spectra) with large signal photocurrent (**Figures 3**, **7A**), and spectral shape repeatable under light bias for different LED intensities (in the linear regime, **Figure 4B**), and applied potentials (and able to resolve miniscule signals, **Figure 7B**). In the case study of $BiVO_4$ photoanodes, the measuring system so-modified to minimize drift effects allowed us to attribute the observed time-dependence under light bias to actual behavior of the photo-electrochemical system under test, rather than to the measuring system.

DATA AVAILABILITY STATEMENT

The original contributions presented in the study are included in the article, further inquiries can be directed to the corresponding authors.

AUTHOR CONTRIBUTIONS

DE wrote the first draft of the manuscript and did the system development work described herein, and measured or closely guided assistants measuring the presented data. DG and YP. grew the various hematite samples measured, helped with some of the IPCE measurements, and helped with the subsequent drafts of the manuscript. PS grew the $BiVO_4$ samples and helped with the subsequent drafts of the manuscript. AR is the principle investigator who initiated this work and worked carefully especially on the initial edits of this manuscript.

FUNDING

The research leading to these results has received funding from the PAT Center of Research Excellence supported by the Israel Science Foundation (grant no: 1867/17). The IPCE measurements were carried out at the Technion's Photovoltaics Laboratory (HTRL), supported by the Russell Berrie Nanotechnology Institute (RBNI), the Nancy and Stephen Grand Technion Energy Program (GTEP) and the Adelis Foundation. Part of this research was carried out within the Helmholtz International Research School "Hybrid Integrated Systems for Conversion of Solar Energy" (HI-SCORE), an initiative co-funded by the Initiative and Networking Fund of the Helmholtz Association. Part of the work was funded by the Volkswagen Foundation. DG and DE acknowledge support from the Center for Absorption in Science at the Ministry of Aliyah and Immigrant Absorption in Israel. YP acknowledges support by the Levi Eshkol scholarship from the Ministry of Science and Technology of Israel. AR acknowledges the support of the L. Shirley Tark Chair in Science.

ACKNOWLEDGMENTS

DE would like to thank Yossi Levi who acquainted him with IPCE measurements and initial system, which was in large part set up by Gideon Segev, and introduced him to some of the issues discussed herein, and is grateful to Dr. Guy Ankonina for his constant technical support and willing assistance whenever needed or asked for in the Photovoltaics Laboratory at the Technion. Many thanks to Sofi Yanru, Ortal Tiurin, Rotem Yaniv and Alon Inbar for assisting with the measurements throughout the various stages of this work.

REFERENCES

Abdi, F. F., and van de Krol, R. (2012). Nature and Light Dependence of Bulk Recombination in Co-pi-catalyzed BiVO4 Photoanodes. *J. Phys. Chem. C* 116, 9398–9404. doi:10.1021/jp3007552

ASTM Standard E1021-15 (2019). *Standard Test Method for Spectral Responsivity Measurements of Photovoltaic Devices.* West Conshohocken, PA): ASTM International.

Bahro, D., Koppitz, M., and Colsmann, A. (2016). Tandem Organic Solar Cells Revisited. *Nat. Photon* 10, 354–355. doi:10.1038/nphoton.2016.96

Cesar, I. (2007). *Solar Photoelectrolysis of Water with Translucent Nanostructured Hematite Photoanodes*. Lausanne: EPFL.

Chen, Z., Deutsch, T. G., Dinh, H. N., Domen, K., Emery, K., Forman, A. J., et al. (2013). "Incident Photon-To-Current Efficiency and Photocurrent Spectroscopy," in *Photoelectrochemical Water Splitting Standards, Experimental Methods, and Protocols*. N. Gaillard, R. Garland, C. Heske, T. F. Jaramillo, A. Kleiman-Shwarsctein, E. Miller, et al. (New York: Springer), 87–97. doi:10.1007/978-1-4614-8298-7_7

Christians, J. A., Manser, J. S., and Kamat, P. V. (2015). Best Practices in Perovskite Solar Cell Efficiency Measurements. Avoiding the Error of Making Bad Cells Look Good. *J. Phys. Chem. Lett.* 6, 852–857. doi:10.1021/acs.jpclett.5b00289

Grave, D. A., Dotan, H., Levy, Y., Piekner, Y., Scherrer, B., Malviya, K. D., et al. (2016a). Heteroepitaxial Hematite Photoanodes as a Model System for Solar Water Splitting. *J. Mater. Chem. A.* 4, 3052–3060. doi:10.1039/c5ta07094e

Grave, D. A., Ellis, D. S., Piekner, Y., Kölbach, M., Dotan, H., Kay, A., et al. (2021). Extraction of mobile Charge Carrier Photogeneration Yield Spectrum of Ultrathin-Film Metal Oxide Photoanodes for Solar Water Splitting. *Nat. Mater.* 20, 833–840. doi:10.1038/s41563-021-00955-y

Grave, D. A., Klotz, D., Kay, A., Dotan, H., Gupta, B., Visoly-Fisher, I., et al. (2016b). Effect of Orientation on Bulk and Surface Properties of Sn-Doped Hematite (α-Fe2O3) Heteroepitaxial Thin Film Photoanodes. *J. Phys. Chem. C* 120, 28961–28970. doi:10.1021/acs.jpcc.6b10033

Green, M., Breeze, R. H., and Ke, B. (1968). Simple Power Supply System for Stable Xenon Arc Lamp Operation. *Rev. Scientific Instr.* 39, 411–412. doi:10.1063/1.1683394

Klotz, D., Ellis, D. S., Dotan, H., and Rothschild, A. (2016). Empirical in Operando Analysis of the Charge Carrier Dynamics in Hematite Photoanodes by PEIS, IMPS and IMVS. *Phys. Chem. Chem. Phys.* 18, 23438–23457. doi:10.1039/C6CP04683E

Klotz, D., Grave, D. A., Dotan, H., and Rothschild, A. (2018). Empirical Analysis of the Photoelectrochemical Impedance Response of Hematite Photoanodes for Water Photo-Oxidation. *J. Phys. Chem. Lett.* 9, 1466–1472. doi:10.1021/acs.jpclett.8b00096

Kölbach, M., Harbauer, K., Ellmer, K., and van de Krol, R. (2020). Elucidating the Pulsed Laser Deposition Process of BiVO4 Photoelectrodes for Solar Water Splitting. *J. Phys. Chem. C* 124, 4438–4447. doi:10.1021/acs.jpcc.9b11265

Kou, S., Yu, Q., Meng, L., Zhang, F., Li, G., and Yi, Z. (2020). Photocatalytic Activity and Photocorrosion of Oriented BiVO4 Single crystal Thin Films. *Catal. Sci. Technol.* 10, 5091–5099. doi:10.1039/d0cy00920b

Palma, G., Cozzarini, L., Capria, E., and Fraleoni-Morgera, A. (2015). A home-made System for IPCE Measurement of Standard and Dye-Sensitized Solar Cells. *Rev. Scientific Instr.* 86, 013112. doi:10.1063/1.4904875

Peter, L. M. (2013). Energetics and Kinetics of Light-Driven Oxygen Evolution at Semiconductor Electrodes: the Example of Hematite. *J. Solid State. Electrochem.* 17, 315–326. doi:10.1007/s10008-012-1957-3

Piekner, Y., Dotan, H., Tsyganok, A., Malviya, K. D., Grave, D. A., Kfir, O., et al. (2018). Implementing Strong Interference in Ultrathin Film Top Absorbers for Tandem Solar Cells. *ACS Photon.* 5, 5068–5078. doi:10.1021/acsphotonics.8b01384

Piekner, Y., Ellis, D. S., Grave, D. A., Tsyganok, A., and Rothschild, A. (2021). Wasted Photons: Photogeneration Yield and Charge Carrier Collection Efficiency of Hematite Photoanodes for Photoelectrochemical Water Splitting. *Energy Environ. Sci.* 14, 4584–4598. doi:10.1039/d1ee01772a

Ravishankar, S., Aranda, C., Boix, P. P., Anta, J. A., Bisquert, J., and Garcia-Belmonte, G. (2018). Effects of Frequency Dependence of the External Quantum Efficiency of Perovskite Solar Cells. *J. Phys. Chem. Lett.* 9, 3099–3104. doi:10.1021/acs.jpclett.8b01245

Reese, M. O., Marshall, A. R., and Rumbles, G. (2018). "Reliably Measuring the Performance of Emerging Photovoltaic Solar Cells," in *Nanostructured Materials for Type III Photovoltaics*. Editors P. Skabara and M. A. Malik (London: Royal Society of Chemistry), 1–32. doi:10.1039/9781782626749-00001

Rolt, S., Clark, P., Schmoll, J., and Shaw, B. J. R. (2016). Xenon Arc Lamp Spectral Radiance Modelling for Satellite Instrument Calibration. *Proc. SPIE* 9904, 99044V. doi:10.1117/12.2232299

Saliba, M., and Etgar, L. (2020). Current Density Mismatch in Perovskite Solar Cells. *ACS Energ. Lett.* 5, 2886–2888. doi:10.1021/acsenergylett.0c01642

Sayama, K., Nomura, A., Arai, T., Sugita, T., Abe, R., Yanagida, M., et al. (2006). Photoelectrochemical Decomposition of Water into H2and O2on Porous BiVO4Thin-Film Electrodes under Visible Light and Significant Effect of Ag Ion Treatment. *J. Phys. Chem. B* 110, 11352–11360. doi:10.1021/jp057539+

Shi, X., Cai, L., Ma, M., Zheng, X., and Park, J. H. (2015). General Characterization Methods for Photoelectrochemical Cells for Solar Water Splitting. *ChemSusChem* 8, 3192–3203. doi:10.1002/cssc.201500075

Timmreck, R., Meyer, T., Gilot, J., Seifert, H., Mueller, T., Furlan, A., et al. (2015). Characterization of Tandem Organic Solar Cells. *Nat. Photon* 9, 478–479. doi:10.1038/nphoton.2015.124

Toma, F. M., Cooper, J. K., Kunzelmann, V., McDowell, M. T., Yu, J., Larson, D. M., et al. (2016). Mechanistic Insights into Chemical and Photochemical Transformations of Bismuth Vanadate Photoanodes. *Nat. Commun.* 7, 12012. doi:10.1038/ncomms12012

Wing, D., Rothschild, A., and Tessler, N. (2015). Schottky Barrier Height Switching in Thin Metal Oxide Films Studied in Diode and Solar Cell Device Configurations. *J. Appl. Phys.* 118, 054501. doi:10.1063/1.4927839

Xue, G., Yu, X., Yu, T., Bao, C., Zhang, J., Guan, J., et al. (2012). Understanding of the Chopping Frequency Effect on IPCE Measurements for Dye-Sensitized Solar Cells: from the Viewpoint of Electron Transport and Extinction Spectrum. *J. Phys. D: Appl. Phys.* 45, 425104. doi:10.1088/0022-3727/45/42/425104

Young, D. L., Egaas, B., Pinegar, S., and Stradins, P. (2008). *New Real-Time Quantum Efficiency Measurement System*. San Diego Ca: 33rd IEEE PVSC. doi:10.1109/pvsc.2008.4922748

Zhang, S., Ahmet, I., Kim, S.-H., Kasian, O., Mingers, A. M., Schnell, P., et al. (2020). Different Photostability of BiVO4 in Near-pH-Neutral Electrolytes. *ACS Appl. Energ. Mater.* 3, 9523–9527. doi:10.1021/acsaem.0c01904

Zhang, S., Rohloff, M., Kasian, O., Mingers, A. M., Mayrhofer, K. J. J., Fischer, A., et al. (2019). Dissolution of BiVO4 Photoanodes Revealed by Time-Resolved Measurements under Photoelectrochemical Conditions. *J. Phys. Chem. C* 123, 23410–23418. doi:10.1021/acs.jpcc.9b07220

Zimmermann, E., Ehrenreich, P., Pfadler, T., Dorman, J. A., Weickert, J., and Schmidt-Mende, L. (2014). Erroneous Efficiency Reports Harm Organic Solar Cell Research. *Nat. Photon* 8, 669–672. doi:10.1038/nphoton.2014.210

Conflict of Interest: Author PS is employed by Helmholtz-Zentrum Berlin für Materialien und Energie GmbH. All authors declare no other competing interests.

frontiers in Energy Research

MINI REVIEW
published: 12 January 2022
doi: 10.3389/fenrg.2021.799776

Comprehensive Evaluation for Protective Coatings: Optical, Electrical, Photoelectrochemical, and Spectroscopic Characterizations

Xin Shen[1,2], *Rito Yanagi*[1,2], *Devan Solanki*[1,2], *Haoqing Su*[1,2], *Zhaohan Li*[1,2], *Cheng-Xiang Xiang*[3]* and *Shu Hu*[1,2]*

[1]Department of Chemical and Environmental Engineering, School of Engineering and Applied Sciences, Yale University, New Haven, CT, United States, [2]Energy Sciences Institute, Yale West Campus, West Haven, CT, United States, [3]Division of Engineering and Applied Science, California Institute of Technology, Pasadena, CA, United States

Numerous efficient semiconductors suffer from instability in aqueous electrolytes. Strategies utilizing protective coatings have thus been developed to protect these photoabsorbers against corrosion while synergistically improving charge separation and reaction kinetics. Recently, various photoelectrochemical (PEC) protective coatings have been reported with suitable electronic properties to ensure low charge transport loss and reveal the fundamental photoabsorber efficiency. However, protocols for studying the critical figures of merit for protective coatings have yet to be established. For this reason, we propose four criteria for evaluating the performance of a protective coating for PEC water-splitting: stability, conductivity, optical transparency, and energetic matching. We then propose a flow chart that summarizes the recommended testing protocols for quantifying these four performance metrics. In particular, we lay out the stepwise testing protocols to evaluate the energetics matching at a semiconductor/coating/(catalyst)/liquid interface. Finally, we provide an outlook for the future benchmarking needs for coatings.

Keywords: coating, performance evaluation, performance metrics, energetics, spectroscopy

Edited by:
Rahul R. Bhosale,
Qatar University, Qatar

Reviewed by:
Avner Rothschild,
Technion Israel Institute of Technology, Israel
Shankara Kalanur,
Ajou University, South Korea

Correspondence:
Cheng-Xiang Xiang
cxx@caltech.edu
Shu Hu
shu.hu@yale.edu

Specialty section:
This article was submitted to Hydrogen Storage and Production, a section of the journal Frontiers in Energy Research

Received: *22 October 2021*
Accepted: *17 December 2021*
Published: *12 January 2022*

Citation:
Shen X, Yanagi R, Solanki D, Su H, Li Z, Xiang C-X and Hu S (2022) Comprehensive Evaluation for Protective Coatings: Optical, Electrical, Photoelectrochemical, and Spectroscopic Characterizations. Front. Energy Res. 9:799776. doi: 10.3389/fenrg.2021.799776

INTRODUCTION

Energy conversion materials such as semiconductor photoabsorbers likely undergoe chemical, electrochemical, or photochemical corrosion during photoelectrochemical reductive or oxidative reactions (Chen and Wang, 2012; Zheng et al., 2019). Thus, protective coatings were developed to protect those otherwise unstable semiconductor photoabsorbers against corrosion (Walter et al., 2010; Paracchino et al., 2012; Hu et al., 2015; Gu et al., 2017). As the field evolved, stabilization coatings alone or in conjunction with co-catalysts have been developed to promote charge separation (Gu et al., 2016; Pan et al., 2019; Zhao et al., 2021), to improve charge transport kinetics, to passivate surface states (Le Formal et al., 2011), to form rectifying heterojunction (Scheuermann et al., 2016), and to boost surface reaction rates (Chen et al., 2020; Kawde et al., 2020; Pastukhova et al., 2021). However, the addition of coatings and co-catalysts creates new interfaces and new electronic states: one fundamental requirement is the energetic compatibility with the underlying photoabsorbers to reveal the photoabsorber fundamental performance and maximize solar-to-chemical conversion efficiency. Furthermore, the employment of coating is not limited to PEC water splitting, but a wider

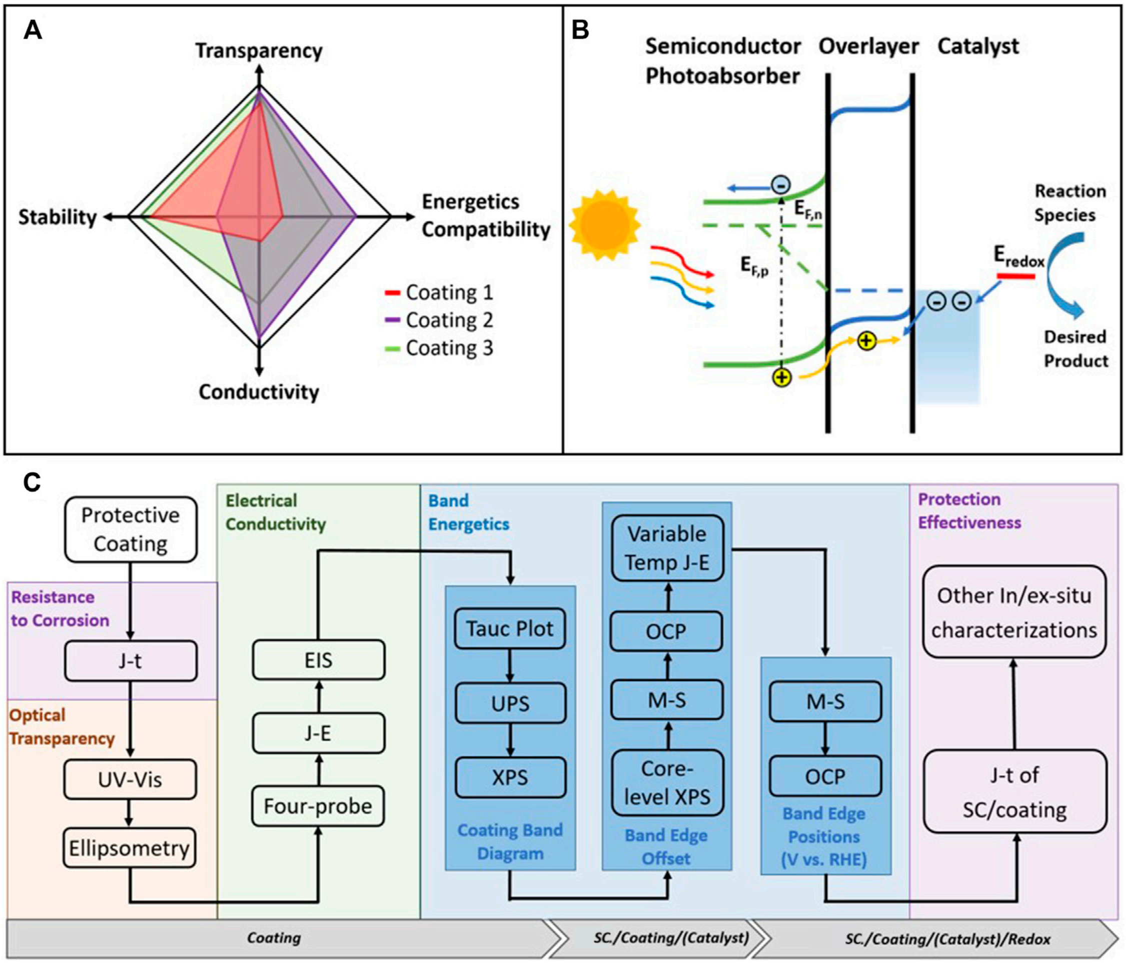

FIGURE 1 | (A) Illustration of the four performance metrics for evaluating protective coatings for PEC water-splitting devices. The performance metrics for three representative coatings are also shown. They include: stability (primarily lifetime/hours), optical transparency (primarily transmittance/%), conductivity (primarily resistance/ohm) and energetics compatibility (primarily charge transfer efficiency across interface/%); **(B)** Schematics for showing the concept of energetics compatibility (here, the photoanode case is used as an example); **(C)** Flow chart that summarizes the recommended testing protocols for quantitatively evaluating the four performance metrics of a protective coating. Abbreviations: current-time (J-t), current-potential (J–E), electrochemical impedance spectroscopy (EIS), ultraviolet photoelectron spectroscopy (UPS), X-ray photoelectron spectroscopy (XPS), Mott-Schottky (M–S), and open-circuit potential (OCP). SC stands for semiconductor.

fields such as dye sensitized PEC cells, perovskite solar cells, battery, and fuel cell devices, the materials and components of which have been reported with stability issues and require coating protection (Kay and Gratzel, 2002; Wang et al., 2008; Liu et al., 2015; Park and Zhu, 2020).

At the current stage, we recognize the challenges of comparing and evaluating the performance of coating strategies for different applications using a standardized approach. Protective coatings are often reported with various growth techniques and conditions and in combination with different underlying photoabsorbers and surface catalysts. The difficulty in deconvoluting the coating contribution from the overall performance of the coated device and interface (Hu et al., 2015). This results in a lack of data for the optical and electrical properties of the pure coating materials which hinder the progress of coating development. In addition, methods for evaluating device stability, coating stability, and optical properties are inconsistent among reports. In response to these inconsistencies, we present this work as an initiative to recommend comprehensive methodology for evaluating coating's performance.

Herein, we identify four performance metrics: stability, optical transparency, electrical conductivity, and energetics compatibility (**Figure 1A**) as the primary descriptors of protective coatings. In this paper, the concept of "stability" is two-fold: the coating's resistance to corrosion and its effectiveness at protecting the underlying photoabsorber. Resistance to corrosion includes both chemical and electrochemical resistances to corrosion, and it depends on the pH and local potentials. On the one hand, this photochemical stability criterion is firstly illustrated in a Pourbaix diagram (for electrochemical stability) for the thermodynamic corrosion potentials relative to the band edges (Chen and Wang, 2012; Hu et al., 2015). On the other hand, the stabilization efficiency (S), defined as the kinetic branching ratio of the local charge transfer current for desired reactions versus total light-induced current (Frese et al., 1981; Nandjou and Haussener, 2019), is often used to measure the coating's effectiveness for protecting the photoabsorber. The optical transparency is a unique requirement of the protective layer for sunlight driven processes. Any parasitic absorption and reflection from the protective layer would result in overall device efficiency loss. Depending on the detailed construct of the PEC cell, for example, the number of photoabsorbers and the bandgaps of the photoabsorbers, the requirement for the optical transparency could be very different. The electrical conductivity of a coating depends on in-plane and through-plane conductivity or resistance. The through-plane resistance consists of the contact resistance at the coating-absorber and the coating-liquid interfaces plus the coating bulk resistance, all of which need to be minimized to reduce the potential loss. Energetic compatibility is another critical aspect of protective coatings. It is achieved when the energy levels of charge carriers on both the photoabsorber side and the liquid interface side of the coating align, as shown in **Figure 1B**. The matching minimizes the energy barrier and the energy loss for charge transfer across the interface. Even though the photoabsorber and the protective layer may have excellent properties by themselves, a mismatch in the charge-transport energetic levels between the two can result in very low conversion efficiency.

While ideal coatings are expected to excel in all four categories, there are often inherent trade-offs when optimizing their properties. For example, conductivity often comes at the expense of transparency and stability: wide-bandgap oxides are usually more optical transparent and stable than narrow bandgap materials but at the cost of being more electrically insulating. The reason is that the electronic states for transporting charges through the coating and achieving energetic matching are often missing or lower in the density of states than narrow bandgap materials (Frese et al., 1980; Sze and Ng, 2007). One strategy to improve the conductivity of wide-bandgap oxide materials without sacrificing stability and optical transparency is to introduce intermediate band (IB) or in-gap defect states (Hu et al., 2016). Recently, methods for engineering intermediate bands (IB) or defect states in wide bandgap coatings avoid these trade-offs and allow for good transparency without sacrificing charge transport performance (Campet et al., 1989; Hu et al., 2014; Bein et al., 2019; Li et al., 2021). These coatings modify the interfacial thermodynamics, carrier dynamics, and surface reaction pathways, which require special characterization techniques to elucidate (Dai et al., 2020). This paper summarizes these characterization techniques and their measurement approaches to illustrate these coating characterization protocols.

To illustrate the application of the protocol, we consider three representative coatings and their corresponding four performance metrics as examples (**Figure 1**). Tunneling TiO_2 overlayers developed for metal-insulator-semiconductor (MIS) Si photoanode are illustrated as **Figure 1A** coating 1 (Chen et al., 2011; Scheuermann et al., 2013). This approach stabilized heavily p^+-doped Si for 8 h under both acidic and basic conditions (Lin et al., 2013). Despite the optical transparency of few-nanometer TiO_2, the energetic mismatch and low conductivity of this TiO_2 coating resulted in ~21 mV of added overpotentials at 1 mA cm^{-2} per nanometer of TiO_2 for thicknesses greater than ~2 nm. The primary mechanism of charge transport through this coating is by charge tunneling, as its energetics is incompatible with the photoabsorber and the water oxidation electrocatalyst. NiO_x (Sun et al., 2015c), illustrated as **Figure 1A** coating 2, was shown to stabilize Si photoanodes in 1 M KOH(aq) for 5 h. The long-term stability of NiO_x-protected Si photoanodes was inferior relative to other wide bandgap oxide coatings because the NiO_x layer underwent microstructure changes after redox cycling, which made the NiO_x layer ion-permeable (Lin and Boettcher, 2014). Despite that, NiO_x has its own strength in high transparency, metal-like conductivity, and negligible energy loss for the various efficient photoabsorbers performing light-induced charge transfer (Sun et al., 2015a; Sun et al., 2015b; Sun et al., 2015c). "Leaky" TiO_2 (Hu et al., 2014) (**Figure 1A**: coating 3) with Ni/NiO_x electrocatalysts is stable in 1M KOH(aq) for over thousands of hours (Shaner et al., 2015) and has an average 80% transmission in the visible light range (Hu et al., 2014). In this coating/co-catalyst combination, the TiO_2 has nearly thickness-independent hole-transport conductivity which is four orders of magnitude higher than the insulator TiO_2 reported above (Scheuermann et al., 2013; Scheuermann et al., 2016), and is energetically compatible with photoabsorbers such as Si and CdTe (Hu et al., 2014; Chen et al., 2020). So far, a few protective layers including the "leaky" TiO_2 achieve the stablility, transparency, conductivity, and the proper energetic matching for several technologically important photoabsorbers of <1.4 eV bandgaps. But further improvement is anticipated to further broaden coatings' practice with photoabsorbers of >1.7 eV bandgaps and enhancing its corrosion resistance and protection effectiveness.

We recommend a standard procedure to evaluate these four metrics, as shown in the flow chart **Figure 1C**. Quantification of the stability (primarily lifetime/hours), optical transparency (primarily transmittance/%), conductivity (primarily resistance/ohm) and energetics compatibility (primarily charge transfer efficient accorss interface/%) under the control of other aspects such as thickness and substrate, help to evaluate protective coating comprehensively and highlights the current deficiencies and constraints. Such an evaluation can help create guidelines for designing and developing more efficient and multifunctional coating materials. We note that corrosion resistance is a prerequisite for a coating material. Therefore, it is the first aspect to be investigated, while the remaining four criteria can be studied based on a specific application.

Stability

Both the coating's resistance to corrosion and its effectiveness at protecting the PEC device should be measured. However, in many articles, only the time-dependent current or potential behavior, which measures the effectiveness, is reported according to the PEC test protocol used in the last decade (Chen et al., 2013a). While stable device operation should imply coating's resistance to corrosion, an explicit study is still valuable, because 1) it is a primary screening tool and a prerequisite for developing a new coating (Siddiqi et al., 2018); 2) it helps distinguish the pitting corrosion of the underlying protected photoabsorber from the dissolution of the coating (Shen et al., 2021); and 3) it helps better understand the corrosion or failure mechanism of the coating stabilized interface (Gerischer, 1977; 1991). For testing the coating's resistance to corrosion, it is typical to grow coatings on conductive substrates initially and use electrochemistry methods. These methods include chronoamperometry to observe the current degradation and chronopotentiometry to test the potential deviation (Moehl et al., 2017; Siddiqi et al., 2018), in combination with various in-situation or ex-situ characterizations, such as XPS to compare the chemical change and electronic structure change after the test with those before (Moehl et al., 2017; Siddiqi et al., 2018).

For evaluating the effectiveness of protection, the porosity as part of the ion permeability test (Jung et al., 2018b) can be used for measuring how effectively the coating reduces the diffusion of reactive species from an electrolyte solution. Since the protection effectiveness directly reflects the operational stability, electrochemical methods are usually used to test the coated PEC device's operational lifetime, sometimes even imitating the practical conditions (e.g., biased, AM 1.5 one Sun illumination, neutral pH, simulated diurnal cycles, etc.). Thus, they are powerful and indispensable tools for studying a coating's stability as they consider realistic operating conditions for photoelectrochemistry applications.

The evaluation of device operational stability can be short term or long term. While short-term tests are primarily conducted under harsh conditions for examining the robustness of the coated photoabsorber and studying their corrosion mechanism, long-term tests are employed to demonstrate practical viability (Vanka et al., 2019). As the operational lifetime test alone cannot reveal the compositional or structural changes during operation, these tests are typically combined with a series of compositional, morphological, and topographical characterizations (both in-situ and ex-situ). Characterization techniques include morphological: AFM and ac mode AFM (for local metastable species) (Cheng et al., 2017; Ros et al., 2019; Vanka et al., 2019), Cross-section SEM (structural integrity) (Yu et al., 2018), TEM (nanoscale integrity) (Cheng et al., 2017); compositional: SEM-EDS (surface mapping of the composition) (Shen et al., 2021), XPS (surface atoms oxidation state change) (Pishgar et al., 2019; Cao et al., 2020), ICP-MS (Materials dissolution) (Pishgar et al., 2019).

Optical Properties

A comprehensive optical characterization of a protective coating includes the study of both the intrinsic properties, such as the dielectric constants (n, k) and the extrinsic properties, such as absorption, transmission, and reflection. Those optical characteristics depend on the coating's thickness and morphology.

The dielectric properties (n, k) of thin films can be determined by Ellipsometry which measures the change in polarization as light reflects or transmits from the sample. The polarization change is represented as an amplitude ratio and the phase difference. The measured complex dielectric constants are the thickness-independent optical property of a coating. They are closely related to the dopant concentration and oxidation states, and thus also serve as an important input parameter for optical simulations (e.g., Finite-Difference Time-Domain modeling) (Mohsin et al., 2020). Ellipsometry is an indirect method, where the (n, k) values are obtained by fitting the measured light amplitude ratio and the phase difference with a dielectric function model. Therefore, selecting the appropriate model based on the material type and wavelength used for analysis is crucial for obtaining meaningful results. For anisotropic or inhomogeneous coating materials, the Mueller matrix formalism should be used to account for depolarization (Fujiwara, 2007).

The extrinsic optical properties are commonly characterized by ultraviolet-visible spectroscopy (UV-Vis). Initial screening for low optical loss involves measuring the transmission, reflection and absorption spectra of a substrate with/without coating for comparing the effect of coating (Sun et al., 2015c). The coating reflectance is recommended to be measured by either diffuse reflectance spectroscopy (DRS) using an integrating sphere (when the interference effect need to be rule out), or specular reflectance (when the interference effect need to be taken into account) (Chen et al., 2013b). While the UV-Vis solid film measurement is conducted in air, it is most relevant for reflectance measurements when the coated sample is immersed in liquids, so the measurement responds to the PEC operational environment. Lastly, the absorption spectra can also be used to construct a Tauc plot for measuring the optical bandgap, which is crucial information of the energy band diagram (Makula et al., 2018).

It should be noted that the thin-film interference effect may influence the reflectance, transmittance, and absorption of the coated photoelectrode. If the coating thickness is comparable to the incident light wavelength and the phase delay between the reflected light at two interfaces of the thin film module as a function of coating thickness, the reflected and transmitted light intensity will constructive and destructive interfere alternatively (Wolter, 1966). The use of Ellipsometry to measure dielectric (n,k) properties elucidates the interference issue. Coatings should be compared at the same thickness outside of the interference regime (Kats et al., 2014; Xu et al., 2018). This way avoids the inaccurate assessment caused by this effect and compares the coating extrinsic optical properties fairly. In some cases, the surface morphology (roughness or special surface patterns) can also contribute to the UV-Vis spectra, and therefore this factor should be considered when benchmarking the coating optics (Xu et al., 2018).

Electrical Conductivity

The methods for characterizing in-plane and through-plane conductivity of bulk coatings include: 1) Electrochemical Impedance Spectroscopy (EIS), which quantitatively measures the through-plane conductivity. The precision of the EIS technique depends on the selection and fitting of equivalent circuits. Besides the coating through-plane resistance, a typical equivalent circuit also consists of solution series resistance, charge-transfer resistance, and space-charge and surface state capacitances in series or parallel. Given the multiple fitting parameters in the equivalent circuits, it is important to ensure all parameters have physical meanings. The selection accuracy and model validation can be referred to by Spyker and coworkers (Jiya et al., 2018); 2) Electrochemical cyclic voltammetry at the low bias region for through-plane conductivity, in which the resistance can be derived from the extrapolation of the linear region at low bias (Nunez et al., 2019). It should be noted that this method only applies when the coating resistance dominates the through-layer resistance; 3) Sheet resistance for in-plane conductivity, which can be measured by the four-point probe method (Hu et al., 2014); 4) Hall measurement for in-plane conductivity, a technique that employs a magnetic field perpendicular to the in-plane current flow, can be used to measure charge carrier density, electrical resistance, and carrier mobility for the bands of the films from which the conductivity can be derived (Hu et al., 2014). The through-plane resistance can limit the coating thickness selection, and therefore indirectly affect the stability and optical transparency of the device. Here, one typically assumes that coating conductivity is isotropic, which can be validated by the comparison of in-plane and through-plane resistivity.

In addition to providing information about coating resistance, conductivity studies can also be useful for revealing charge conduction mechanisms for the coating by: 1) solid-state I-V measurement of coatings deposited on the substrates of varying work functions; 2) alternating current-conductance of the through-layer device as a function of frequency under a fixed temperature and fixed applied bias, where the response can be used to fit the model for band-mediated charge transport, or model for charge transport via hopping, therefore help determine the charge transport pathway; 3) temperature-dependent direct current conductance. This temperature-dependent conductance can be used to determine the activation energy, which reveals the mechanism of tunneling or hopping based on charge transfer barrier and conduction mechanism (Nunez et al., 2019); 4) space-charge-limited current spectroscopy, where the conductivity of the coating in contact with the solution is measured over a range of gate potentials (Nunez et al., 2019). The potential-dependent conductivity is done by interdigitated electrodes in a field-effect transistor configuration, where I-V conductivity is measured with the varying Fermi-energy level (applied gate voltages) (Roest et al., 2002; Plana et al., 2013). This technique is also commonly used for studying the conduction mechanism in combination with the frequency and temperature varied conductance measurement (Nunez et al., 2019). The above techniques mainly focus on the macroscopic electrical properties of the coating. Last but not the least, conductive atomic force microscopy (c-AFM) can be used for testing local conductivity on the film surface or the cross-section for revealing coating inhomogeneity or detecting metastable phases (Yu et al., 2018; Ros et al., 2019).

Energetics Compatibility

The interfaces between the protective coating and the photoabsorber, with or without surface-attached catalysts (Walter et al., 2010; Hu et al., 2015; Bae et al., 2017) are vital for thermodynamics, charge separation, charge transfer and reaction kinetics (Thorne et al., 2015; Vanka et al., 2019). The protective coating's electrical properties should be tailored to the photoabsorber and the catalyst for minimizing energy conversion loss. In doing so, the band bending and defect band alignment across the SC/coating interface can be tailored towards efficient charge transfer, thus allowing for thicker protective coatings and eliminating manufacturing defects. Without proper energetics compatibility, charge transport through SC/coating interface would primarily rely on charge tunneling. Hence, the coating thickness is constrained to <3 nm (Scheuermann et al., 2016), which makes the protective coating prone to degradation.

Since energetics depends on interfacial chemistry, it is imperative to standardize surface treatment before the coating deposition to remove surface oxide and achieve reproducible substrate/coating interface conditions. Procedures for surface treatment requires the selection and standardization of photoabsorbers to ensure fair evaluation. For example, in the case of n^+ Si/TiO_2, the Si substrate has a well-established surface treatment protocol: an RCA SC-1 etch, followed by immersion in 5 M hydrofluoric (HF) acid, and an RCA SC-2 procedure (Hu et al., 2014). This series of surface treatments produce a SiO_2 tunnel interface, which passivates surface states responsible for non-radiative carrier recombination and aligns the Ti^{3+} defect band to the Si valence band.

Determination of the complete band energetic diagram of the coated PEC device follows a protocol with three major steps, each requiring a series of characterizations as illustrated in **Figure 2**. The first step (**Figures 2A,B**) for mapping band energetics is to measure the coating bulk band diagram in vacuum. Tauc plot ($h\nu - \alpha h\nu$ plot) by UV–Vis can be used to determine the optical band gap (**Figure 2A**). The film absorption coefficient α is measured as mentioned in the optical measurement section. Extrapolation of the linear region of the hν -$(\alpha h\nu)^{1/2}$ plot yields the energy of the optical bandgap of the amorphous material (Hu et al., 2014; Siddiqi et al., 2018). Alternatively, the electronic bandgap of some ultra wide bandgap oxides, such as SiO_x can be obtained by high energy XPS using the difference in energy between the elastic peak (e.g., oxygen peak) and the onset of inelastic losses (Nichols et al., 2014; Iatsunskyi et al., 2015). Ultraviolet photoelectron spectroscopy (UPS) can provide information including the work function, i.e., the Fermi level position versus the vacuum potential, and the surface density of states (Hu et al., 2014; Hu et al., 2016; Richter et al., 2021).

Both UPS and valence XPS can be used for determining the band edge position relative to the Fermi level. However, while UPS only probes the film's surface, valence XPS provides a more accurate means to analyze the bulk film's valence band position because the greater penetration depth of the XPS probe beam reduces the effect of spurious surface states during the analysis of the valence band position (Lichterman et al., 2015; Hu et al., 2016; Richter et al., 2021). For the valence XPS measurement, the coating sample surface needs to be partially covered by a gold foil and grounded to the stage. The scan range typically starts from −5 to 20 eV vs. 0 eV binding energy, defined as the Fermi level. The conductivity of the film sample needs to be ensured to avoid the electron charging effect, with the valence spectra of gold

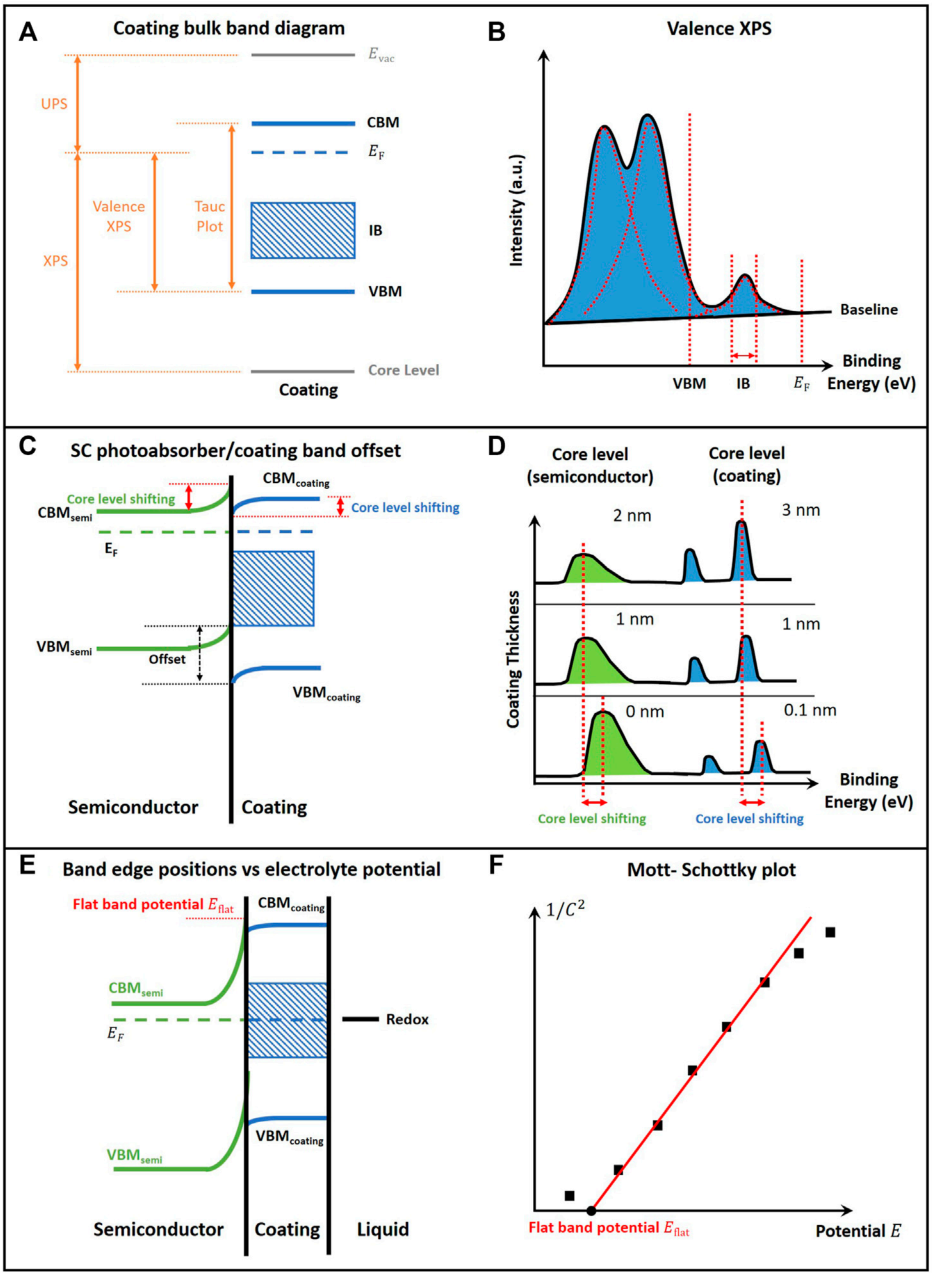

FIGURE 2 | The development of band-energy diagram of semiconductor photoabsorber/coating/(catalyst)/liquid electrolyte. **(A)** Band-energy diagram for bulk coating; **(B)** Valence XPS data with peak deconvolution results; **(C)** Band-energy diagram for semiconductor photoabsorber/coating integrace, which can be obtained from literature report, and the measured position of the peak from XPS at the interface (as indicated by the red arrow); **(D)** The characteristic XPS core level peak shifting for the semiconductor and the coating; **(E)** Band-energy diagram for semiconductor photo absorber/coating/(catalyst)/liquid; **(F)** Mott-Schottky plot, i.e., the reciprocal of the square of capacitance versus the potential between the bulk electrode and the bulk electrolyte.

or palladium measured as a reference for the binding-energy calibration (Sharpe et al., 2017).

Peak deconvolution of the raw valence spectra data can be achieved by software such as Casa XPS or Multipak. The assignment of the characteristic peaks should follow the previous report of the electronic study of the material or its component. The result of the valence XPS allows for the determination of the coating energy levels (including CB, VB, and IB) relative to the Fermi level of the material, while UPS determines the valence band position and the work function. This step completes the derivation of the energetics of bulk coating. The valence band edge (VBM) is determined by linear extrapolation of the characteristic peak. The intermediate band center position and width corresponds to the peak position of the intra gap electronic states, and its FWHM of measured XPS peaks. After the peak deconvolution analysis of valence XPS spectra and UPS (**Figure 2B**), a bulk energy diagram can be constructed (**Figure 2A**).

The second step (**Figures 2C,D**) for mapping band energetics is to derive the band edge offset between the SC photoabsorber and the coating. When a coating is applied to a semiconductor, the degree of band bending can be determined by comparing the shift of the core-level XPS peak positions for the samples with incremental increases of coating thickness (Klein et al., 2008; Hu et al., 2016; Richter et al., 2021). Usually, overlayer thicknesses of over 4 nm are not recommended because they block the substrate signal due to the limits of penetration depth or mean free path of the photoelectrons, unless using hard X-ray spectroscopy. The characteristic core-level XPS spectra can be measured for both the substrate and the coating. For example, in the case of Si/TiO_2, Si-2p core-level spectra can be measured for deriving the Si band bending, while the Ti-2p spectra can be obtained for the band bending on the protective coating. The magnitude of band bending is determined by the shift of the characteristic positions of the core-level peak that belong to the semiconductor photoabsorber, as shown in **Figure 2D**. For the protective coating, the band bending can be derived in the same manner by the binding energy difference between the bulk (when coating thickness is > 2 nm) and interface (when the coating is only few cycles by atomic layer deposition) (as indicated by the red arrow) (Klein et al., 2008; Hu et al., 2016). Assuming that the Fermi level of semiconductor and coating align under equilibrium in the dark, the band offset can be determined in conjunction with the characterization of band edge positions relative to the Fermi level. Then, the band bending values for both the semiconductor photoabsorber and coating can be obtained. An alternative option to obtain the band bending (barrier height) of the semiconductor photoabsorber is by the solid-state variable temperature J-V measurements (Hu et al., 2016), or light-dependent open-circuit potential (OCP) measurements (Chen et al., 2013b; Dai et al., 2020), or by Mott-Schottky analysis (Hu et al., 2016). These techniques are often combined to provide a full picture of the band energetics and to validate one another.

The third step (**Figures 2E,F**) for mapping the band energetics is to determine the band edge positions of coatings in contact with the electrolyte solution of interest. We assume that the band offset at the semiconductor/coating solid-solid interface is independent of the contacting electrolyte (Tan et al., 1994; Walter et al., 2010). For the semiconductor/coating/liquid interface, Mott-Schottky (M-S) analysis can be used for obtaining the flat band potential and band edge positions (**Figures 2E,F**) (Gelderman et al., 2007; Hankin et al., 2019; Chen et al., 2020) By using the M-S analysis, the entire energy band diagram with respect to electrolyte potential can be mapped. Light-dependent OCP is an alternative option for determining the flat-band potential, where the Fermi level approaching the flat-band potential at high light intensity (Hankin et al., 2019).

The open-circuit photovoltage, measured from the difference between the dark and light OCP, in various redox electrolytes can also help to study the junction type (Hu et al., 2016). For PEC application, a buried junction with a fixed barrier height is often desired. In this case, the barrier height of the semiconductor junction depends on doping and built-in potential. This junction energetics have been fully exploited to achieve the desired performance independent of local pH environment and redox potentials (Dai et al., 2014; Chen et al., 2015; Hu et al., 2015).

These are cases that when semiconductor/coating get immersed in liquids, the band edge positions of coating and semiconductor with respect to liquid potential shift together with the applied bias and liquid potential. In this case, the band offset at the solid-solid interface remains constant with a fixed barrier height. When surface states dominate, the band edge of the solid will not be fixed under applied bias or light illumination (Jung et al., 2018a). This case occurs when surface states dominate. Inserting a coating between photoabsorbers and liquids can mitigate the Fermi level pinning, but for some porous and ion-permeable coatings, partial Fermi-level pinning can occur (Lin and Boettcher, 2014). A “dual-working-electrode” (DWE) technique can be employed to measure the local surface potential of the catalyst (Lin and Boettcher, 2014; Nellist et al., 2016), or a sophisticated electrochemical atomic force microscopy approach for electrochemical potential sensing can be employed (Nellist et al., 2018; Laskowski et al., 2020).

The aforementioned steps allow the construction of a complete band diagram of a coating protected semiconductor photoelectrode. The following characterizations are optional, used to validate the band energetics, providing energetics at *operando* conditions or for a local region. These techniques include *in situ* or *operando* XPS, which provide a band energy diagram at applied bias condition (Lichterman et al., 2015); Operando AFM which provides information including local site potential and carrier dynamics (Nellist et al., 2018; Connor et al., 2020; Kalanur et al., 2021); Resonant X-ray Photoelectron Spectroscopy (ResPES) and Resonant X-ray Spectroscopy (RiXS) can be used to quantify the energetics between the coating/catalyst interface that is immersed in liquids (Richter et al., 2021). Besides, ResPES and RiXS measurements were reported to be helpful for a thick catalyst layer since they can penetrate the relatively thick metal layer and examine the VB states using resonant excitation of a particular element.

In addition to the four metrics we mentioned in the former paragraph, we also acknowledge that the other aspect of coating should be taken into account for a comprehensive and fair evaluation. For example, as we mention in the introduction, coating can form a p-n hetero-junction with the underlying absorber to promote the charge separation, therefore a desired coating candidate should have the opposite dopant type with appropriate doping concentration to form favorable band bending toward the corresponding surface reactions (Yang et al., 2019). Lastly, doped coating materials such as Fe doped TiO_2, can contains trap defects that quench the photo-generated carriers before they migrate to the coating surface. The non-radiative recombination through coating-absorber interfaces and charge-transport states should be minimized not to affect charge separation (Kautek et al., 1980; Singh et al., 2008).

CONCLUSION AND PERSPECTIVE

We recommended using the four metrics of stability, optical transparency, conductivity, energetics compatibility, and a series of protocols to evaluate protective coating materials systematically. These metrics can also serve as a helpful guide for the coating design and comparing performance across different coatings. We summarized the current methods reported in the literature for evaluating these four metrics, along with common pitfalls. Lastly, we discussed a stepwise procedure for deriving the complete band energy diagram for a complex SC photoabsorber/coating/liquid interface with or without catalysts.

We note that there are challenges that require further research, such as the inherent trade-off between the four metrics, as well as tailoring the intermediate-band states to specific needs. More advanced but less frequently utilized methods such as 1) comprehensive property observation under operando condition; 2) high throughput methods for screening and optimizing coating composition; 3) accelerated stress testing (AST) and corrosion mechanism study, which correlates the coating permeability with the coating protection effectiveness, can further be developed following the protocols stated in this paper.

AUTHOR CONTRIBUTIONS

C-XX and SH conceived the idea and designed this review. XS collected and reviewed the related literatures. XS and RY designed and made the schematics and figures with help from DS and HS. XS and DS wrote the manuscript. XS revised the manuscript with help from SH, CX and DS. SH revised the manuscript and oversaw the project. All authors contributed to the manuscript and provided feedback.

FUNDING

SH gratefully acknowledges the financial support of the National Science Foundation Award No. CBET-2055416. C-XX gratefully acknowledges the support from the Fuel Cell Technologies Office, of the United States Department of Energy, Energy Efficiency and Renewable Energy (EERE) under contract number DE-EE0008092. RY acknowledges fellowship support from Japan Student Services Organization.

REFERENCES

Bae, D., Seger, B., Vesborg, P. C. K., Hansen, O., and Chorkendorff, I. (2017). Strategies for Stable Water Splitting via Protected Photoelectrodes. *Chem. Soc. Rev.* 46, 1933–1954. doi:10.1039/c6cs00918b

Bein, N. S., Machado, P., Coll, M., Chen, F., Makarovic, M., Rojac, T., et al. (2019). Electrochemical Reduction of Undoped and Cobalt-Doped BiFeO3 Induced by Water Exposure: Quantitative Determination of Reduction Potentials and Defect Energy Levels Using Photoelectron Spectroscopy. *J. Phys. Chem. Lett.* 10, 7071–7076. doi:10.1021/acs.jpclett.9b02706

Campet, G., Puprichitkun, C., and Sun, Z. W. (1989). Protection of Photoanodes against Photocorrosion by Surface Deposition of Oxide Films. *J. Electroanalytical Chem. Interfacial Electrochemistry* 269, 435–445. doi:10.1016/0022-0728(89)85150-2

Cao, S. Y., Kang, Z., Yu, Y. H., Du, J. L., German, L., Li, J., et al. (2020). Tailored TiO2 Protection Layer Enabled Efficient and Stable Microdome Structured P-GaAs Photoelectrochemical Cathodes. *Adv. Energ. Mater.* 10. doi:10.1002/aenm.201902985

Chen, L., Yang, J., Klaus, S., Lee, L. J., Woods-Robinson, R., Ma, J., et al. (2015). p-Type Transparent Conducting Oxide/n-type Semiconductor Heterojunctions for Efficient and Stable Solar Water Oxidation. *J. Am. Chem. Soc.* 137, 9595–9603. doi:10.1021/jacs.5b03536

Chen, S., and Wang, L.-W. (2012). Thermodynamic Oxidation and Reduction Potentials of Photocatalytic Semiconductors in Aqueous Solution. *Chem. Mater.* 24, 3659–3666. doi:10.1021/cm302533s

Chen, X., Shen, X., Shen, S., Reese, M. O., and Hu, S. (2020). Stable CdTe Photoanodes with Energetics Matching Those of a Coating Intermediate Band. *ACS Energ. Lett.* 5, 1865–1871. doi:10.1021/acsenergylett.0c00603

Chen, Y. W., Prange, J. D., Dühnen, S., Park, Y., Gunji, M., Chidsey, C. E. D., et al. (2011). Atomic Layer-Deposited Tunnel Oxide Stabilizes Silicon Photoanodes for Water Oxidation. *Nat. Mater.* 10, 539–544. doi:10.1038/nmat3047

Chen, Z., Dinh, H. N., and Miller, E. (2013a). *Photoelectrochemical Water Splitting*. Springer.

Chen, Z., Dinh, H. N., Miller, E., and Springerlink (Online Service (2013b). "Photoelectrochemical Water Splitting Standards, Experimental Methods, and Protocols," in *SpringerBriefs in Energy*.

Cheng, Q., Benipal, M. K., Liu, Q., Wang, X., Crozier, P. A., Chan, C. K., et al. (2017). Al2O3 and SiO2 Atomic Layer Deposition Layers on ZnO Photoanodes and Degradation Mechanisms. *ACS Appl. Mater. Inter.* 9, 16138–16147. doi:10.1021/acsami.7b01274

Connor, P., Schuch, J., Kaiser, B., and Jaegermann, W. (2020). The Determination of Electrochemical Active Surface Area and Specific Capacity Revisited for the System MnOx as an Oxygen Evolution Catalyst. *Z. Physikalische Chemie-International J. Res. Phys. Chem. Chem. Phys.* 234, 979–994. doi:10.1515/zpch-2019-1514

Dai, P., Li, W., Xie, J., He, Y., Thorne, J., Mcmahon, G., et al. (2014). Forming Buried Junctions to Enhance the Photovoltage Generated by Cuprous Oxide in Aqueous Solutions. *Angew. Chem. Int. Ed.* 53, 13493–13497. doi:10.1002/anie.201408375

Dai, Y., Yu, J., Cheng, C., Tan, P., and Ni, M. (2020). Engineering the Interfaces in Water-Splitting Photoelectrodes - an Overview of the Technique Development. *J. Mater. Chem. A.* 8, 6984–7002. doi:10.1039/d0ta01670e

Frese, K. W., Madou, M. J., and Morrison, S. R. (1980). Investigation of Photoelectrochemical Corrosion of Semiconductors. 1. *J. Phys. Chem.* 84, 3172–3178. doi:10.1021/j100461a008

Frese, K. W., Madou, M. J., and Morrison, S. R. (1981). Investigation of Photoelectrochemical Corrosion of Semiconductors: II . Kinetic Analysis of Corrosion-Competition Reactions on. *J. Electrochem. Soc.* 128, 1527–1531. doi:10.1149/1.2127676

Fujiwara, H. (2007). *Spectroscopic Ellipsometry: Principles and Applications*. John Wiley & Sons.

Gelderman, K., Lee, L., and Donne, S. W. (2007). Flat-band Potential of a Semiconductor: Using the Mott-Schottky Equation. *J. Chem. Educ.* 84, 685–688. doi:10.1021/ed084p685

Gerischer, H. (1977). On the Stability of Semiconductor Electrodes against Photodecomposition. *J. Electroanalytical Chem. Interfacial Electrochemistry* 82, 133–143. doi:10.1016/s0022-0728(77)80253-2

Gerischer, H. (1991). *Photodecomposition of Semiconductors - a Thermodynamic Approach - a Citation-Classic Commentary on the Stability of Semiconductor*

Electrodes against Photodecomposition by Gerischer,H. Berlin: Current Contents/Physical Chemical & Earth Sciences, 10.

Gu, J., Aguiar, J. A., Ferrere, S., Steirer, K. X., Yan, Y., Xiao, C. X., et al. (2017). A Graded Catalytic-Protective Layer for an Efficient and Stable Water-Splitting Photocathode. *Nat. Energ.* 2. doi:10.1038/nenergy.2016.192

Gu, J., Yan, Y., Young, J. L., Steirer, K. X., Neale, N. R., and Turner, J. A. (2016). Water Reduction by a P-GaInP2 Photoelectrode Stabilized by an Amorphous TiO2 Coating and a Molecular Cobalt Catalyst. *Nat. Mater.* 15**,** 456, 460-+.doi:10.1038/nmat4511

Hankin, A., Bedoya-Lora, F. E., Alexander, J. C., Regoutz, A., and Kelsall, G. H. (2019). Flat Band Potential Determination: Avoiding the Pitfalls. *J. Mater. Chem. A.* 7, 26162–26176. doi:10.1039/c9ta09569a

Hu, S., Lewis, N. S., Ager, J. W., Yang, J., Mckone, J. R., and Strandwitz, N. C. (2015). Thin-Film Materials for the Protection of Semiconducting Photoelectrodes in Solar-Fuel Generators. *J. Phys. Chem. C* 119, 24201–24228. doi:10.1021/acs.jpcc.5b05976

Hu, S., Richter, M. H., Lichterman, M. F., Beardslee, J., Mayer, T., Brunschwig, B. S., et al. (2016). Electrical, Photoelectrochemical, and Photoelectron Spectroscopic Investigation of the Interfacial Transport and Energetics of Amorphous TiO2/Si Heterojunctions. *J. Phys. Chem. C* 120, 3117–3129. doi:10.1021/acs.jpcc.5b09121

Hu, S., Shaner, M. R., Beardslee, J. A., Lichterman, M., Brunschwig, B. S., and Lewis, N. S. (2014). Amorphous TiO 2 Coatings Stabilize Si, GaAs, and GaP Photoanodes for Efficient Water Oxidation. *Science* 344, 1005–1009. doi:10.1126/science.1251428

Iatsunskyi, I., Kempiński, M., Jancelewicz, M., Załęski, K., Jurga, S., and Smyntyna, V. (2015). Structural and XPS Characterization of ALD Al2O3 Coated Porous Silicon. *Vacuum* 113, 52–58. doi:10.1016/j.vacuum.2014.12.015

Jiya, I. N., Gurusinghe, N., and Gouws, R. (2018). Electrical Circuit Modelling of Double Layer Capacitors for Power Electronics and Energy Storage Applications: A Review. *Electronics* 7. doi:10.3390/electronics7110268

Jung, J.-Y., Yu, J.-Y., and Lee, J.-H. (2018a). Dynamic Photoelectrochemical Device Using an Electrolyte-Permeable NiOx/SiO2/Si Photocathode with an Open-Circuit Potential of 0.75 V. *ACS Appl. Mater. Inter.* 10, 7955–7962. doi:10.1021/acsami.7b16918

Jung, J. Y., Yu, J. Y., Yoon, S., Yoo, B., and Lee, J. H. (2018b). A Photoelectrochemical Device with Dynamic Interface Energetics: Understanding of Structural and Physical Specificities and Improvement of Performance and Stability. *Adv. Sust. Syst.* 2. doi:10.1002/adsu.201800083

Kalanur, S. S., Singh, R., and Seo, H. (2021). Enhanced Solar Water Splitting of an Ideally Doped and Work Function Tuned {002} Oriented One-Dimensional WO3 with Nanoscale Surface Charge Mapping Insights. *Appl. Catal. B-Environmental* 295. doi:10.1016/j.apcatb.2021.120269

Kats, M. A., Blanchard, R., Ramanathan, S., and Capasso, F. (2014). Thin-film Interference in Lossy, Ultra-thin Layers. *Opt. Photon. News* 25, 40–47. doi:10.1364/opn.25.1.000040

Kautek, W., Gerischer, H., and Tributsch, H. (1980). The Role of Carrier Diffusion and Indirect Optical Transitions in the Photoelectrochemical Behavior of Layer Type d-Band Semiconductors. *J. Electrochem. Soc.* 127, 2471–2478. doi:10.1149/1.2129499

Kawde, A., Annamalai, A., Sellstedt, A., Uhlig, J., Wågberg, T., Glatzel, P., et al. (2020). More Than protection: the Function of TiO2 Interlayers in Hematite Functionalized Si Photoanodes. *Phys. Chem. Chem. Phys.* 22, 28459–28467. doi:10.1039/d0cp04280c

Kay, A., and Grätzel, M. (2002). Dye-Sensitized Core−Shell Nanocrystals: Improved Efficiency of Mesoporous Tin Oxide Electrodes Coated with a Thin Layer of an Insulating Oxide. *Chem. Mater.* 14, 2930–2935. doi:10.1021/cm0115968

Klein, A., Mayer, T., Thissen, A., and Jaegermann, W. (2008). Photoelectron Spectroscopy in Materials Science and Physical Chemistry. *Sci. Phys. Chem. Bunsen-magazin* 10, 124–139.

Laskowski, F. A. L., Oener, S. Z., Nellist, M. R., Gordon, A. M., Bain, D. C., Fehrs, J. L., et al. (2020). Nanoscale Semiconductor/catalyst Interfaces in Photoelectrochemistry. *Nat. Mater.* 19**,** 69, 76-+.doi:10.1038/s41563-019-0488-z

Le Formal, F., Tétreault, N., Cornuz, M., Moehl, T., Grätzel, M., and Sivula, K. (2011). Passivating Surface States on Water Splitting Hematite Photoanodes with Alumina Overlayers. *Chem. Sci.* 2, 737–743. doi:10.1039/c0sc00578a

Li, J., Solanki, D., Zhu, Q., Shen, X., Callander, G., Kim, J., et al. (2021). Microstructural Origin of Selective Water Oxidation to Hydrogen Peroxide at Low Overpotentials: a Study on Mn-Alloyed TiO2. *J. Mater. Chem. A.* 9, 18498–18505. doi:10.1039/d1ta05451a

Lichterman, M. F., Hu, S., Richter, M. H., Crumlin, E. J., Axnanda, S., Favaro, M., et al. (2015). Direct Observation of the Energetics at a Semiconductor/liquid junction by Operando X-ray Photoelectron Spectroscopy. *Energy Environ. Sci.* 8, 2409–2416. doi:10.1039/c5ee01014d

Lin, C.-P., Chen, H., Nakaruk, A., Koshy, P., and Sorrell, C. C. (2013). Effect of Annealing Temperature on the Photocatalytic Activity of TiO2 Thin Films. *Energ. Proced.* 34, 627–636. doi:10.1016/j.egypro.2013.06.794

Lin, F., and Boettcher, S. W. (2014). Adaptive Semiconductor/electrocatalyst Junctions in Water-Splitting Photoanodes. *Nat. Mater.* 13, 81–86. doi:10.1038/nmat3811

Liu, H., Li, W., Shen, D., Zhao, D., and Wang, G. (2015). Graphitic Carbon Conformal Coating of Mesoporous TiO2 Hollow Spheres for High-Performance Lithium Ion Battery Anodes. *J. Am. Chem. Soc.* 137, 13161–13166. doi:10.1021/jacs.5b08743

Makula, P., Pacia, M., and Macyk, W. (2018). How to Correctly Determine the Band Gap Energy of Modified Semiconductor Photocatalysts Based on UV-Vis Spectra. *J. Phys. Chem. Lett.* 9, 6814–6817.

Moehl, T., Suh, J., Sévery, L., Wick-Joliat, R., and Tilley, S. D. (2017). Investigation of (Leaky) ALD TiO2 Protection Layers for Water-Splitting Photoelectrodes. *ACS Appl. Mater. Inter.* 9, 43614–43622. doi:10.1021/acsami.7b12564

Mohsin, A. S. M., Mobashera, M., Malik, A., Rubaiat, M., and Islam, M. (2020). Light Trapping in Thin-Film Solar Cell to Enhance the Absorption Efficiency Using FDTD Simulation. *J. Opt.* 49, 523–532. doi:10.1007/s12596-020-00656-w

Nandjou, F., and Haussener, S. (2019). Kinetic Competition between Water-Splitting and Photocorrosion Reactions in Photoelectrochemical Devices. *Chemsuschem* 12, 1984–1994. doi:10.1002/cssc.201802558

Nellist, M. R., Laskowski, F. A. L., Lin, F., Mills, T. J., and Boettcher, S. W. (2016). Semiconductor-Electrocatalyst Interfaces: Theory, Experiment, and Applications in Photoelectrochemical Water Splitting. *Acc. Chem. Res.* 49, 733–740. doi:10.1021/acs.accounts.6b00001

Nellist, M. R., Laskowski, F. A. L., Qiu, J., Hajibabaei, H., Sivula, K., Hamann, T. W., et al. (2018). Potential-sensing Electrochemical Atomic Force Microscopy for in Operando Analysis of Water-Splitting Catalysts and Interfaces. *Nat. Energ.* 3, 46–52. doi:10.1038/s41560-017-0048-1

Nichols, M. T., Li, W., Pei, D., Antonelli, G. A., Lin, Q., Banna, S., et al. (2014). Measurement of Bandgap Energies in Low-K Organosilicates. *J. Appl. Phys.* 115. doi:10.1063/1.4867644

Nunez, P., Richter, M. H., Piercy, B. D., Roske, C. W., Cabán-Acevedo, M., Losego, M. D., et al. (2019). Characterization of Electronic Transport through Amorphous TiO2 Produced by Atomic-Layer Deposition. *The J. Phys. Chem. C.* doi:10.1021/acs.jpcc.9b04434

Pan, Z., Röhr, J. A., Ye, Z., Fishman, Z. S., Zhu, Q., Shen, X., et al. (2019). Elucidating Charge Separation in Particulate Photocatalysts Using Nearly Intrinsic Semiconductors with Small Asymmetric Band Bending. *Sust. Energ. Fuels* 3, 850–864. doi:10.1039/c9se00036d

Paracchino, A., Mathews, N., Hisatomi, T., Stefik, M., Tilley, S. D., and Grätzel, M. (2012). Ultrathin Films on Copper(I) Oxide Water Splitting Photocathodes: a Study on Performance and Stability. *Energ. Environ. Sci.* 5, 8673–8681. doi:10.1039/c2ee22063f

Park, N.-G., and Zhu, K. (2020). Scalable Fabrication and Coating Methods for Perovskite Solar Cells and Solar Modules. *Nat. Rev. Mater.* 5, 333–350. doi:10.1038/s41578-019-0176-2

Pastukhova, N., Mavric, A., and Li, Y. B. (2021). Atomic Layer Deposition for the Photoelectrochemical Applications. *Adv. Mater. Inter.* 8. doi:10.1002/admi.202002100

Pishgar, S., Strain, J. M., Gulati, S., Sumanasekera, G., Gupta, G., and Spurgeon, J. M. (2019). Investigation of the Photocorrosion of N-GaP Photoanodes in Acid with *In Situ* UV-Vis Spectroscopy. *J. Mater. Chem. A.* 7, 25377–25388. doi:10.1039/c9ta10106c

Plana, D., Humphrey, J. J. L., Bradley, K. A., Celorrio, V., and Fermín, D. J. (2013). Charge Transport across High Surface Area Metal/Diamond Nanostructured Composites. *ACS Appl. Mater. Inter.* 5, 2985–2990. doi:10.1021/am302397p

Richter, M. H., Cheng, W.-H., Crumlin, E. J., Drisdell, W. S., Atwater, H. A., Schmeisser, D., et al. (2021). X-ray Photoelectron Spectroscopy and Resonant

X-ray Spectroscopy Investigations of Interactions between Thin Metal Catalyst Films and Amorphous Titanium Dioxide Photoelectrode Protection Layers. *Chem. Mater.* 33, 1265–1275. doi:10.1021/acs.chemmater.0c04043

Roest, A. L., Kelly, J. J., Vanmaekelbergh, D., and Meulenkamp, E. A. (2002). Staircase in the Electron Mobility of a ZnO Quantum Dot Assembly Due to Shell Filling. *Phys. Rev. Lett.* 89, 036801. doi:10.1103/PhysRevLett.89.036801

Ros, C., Carretero, N. M., David, J., Arbiol, J., Andreu, T., and Morante, J. R. (2019). Insight into the Degradation Mechanisms of Atomic Layer Deposited TiO2 as Photoanode Protective Layer. *ACS Appl. Mater. Inter.* 11, 29725–29735. doi:10.1021/acsami.9b05724

Scheuermann, A. G., Lawrence, J. P., Kemp, K. W., Ito, T., Walsh, A., Chidsey, C. E. D., et al. (2016). Design Principles for Maximizing Photovoltage in Metal-Oxide-Protected Water-Splitting Photoanodes. *Nat. Mater* **15**, 99, 105-+.doi:10.1038/nmat4451

Scheuermann, A. G., Prange, J. D., Gunji, M., Chidsey, C. E. D., and Mcintyre, P. C. (2013). Effects of Catalyst Material and Atomic Layer Deposited TiO2 Oxide Thickness on the Water Oxidation Performance of Metal-Insulator-Silicon Anodes. *Energ. Environ. Sci.* 6, 2487–2496. doi:10.1039/c3ee41178h

Shaner, M. R., Hu, S., Sun, K., and Lewis, N. S. (2015). Stabilization of Si Microwire Arrays for Solar-Driven H2O Oxidation to O2(g) in 1.0 M KOH(aq) Using Conformal Coatings of Amorphous TiO2. *Energ. Environ. Sci.* 8, 203–207. doi:10.1039/c4ee03012e

Sharpe, R., Counsell, J., and Bowker, M. (2017). Pd Segregation to the Surface of Au on Pd(111) and on Pd/TiO2(110). *Surf. Sci.* 656, 60–65. doi:10.1016/j.susc.2016.10.005

Shen, X., Yao, M., Sun, K., Zhao, T., He, Y., Chi, C.-Y., et al. (2021). Defect-Tolerant TiO2-Coated and Discretized Photoanodes for >600 H of Stable Photoelectrochemical Water Oxidation. *ACS Energ. Lett.* 6, 193–200. doi:10.1021/acsenergylett.0c02521

Siddiqi, G., Luo, Z., Xie, Y., Pan, Z., Zhu, Q., Röhr, J. A., et al. (2018). Stable Water Oxidation in Acid Using Manganese-Modified TiO2 Protective Coatings. *ACS Appl. Mater. Inter.* 10, 18805–18815. doi:10.1021/acsami.8b05323

Singh, A., Kumari, S., Shrivastav, R., Dass, S., and Satsangi, V. (2008). Iron Doped Nanostructured TiO2 for Photoelectrochemical Generation of Hydrogen. *Int. J. Hydrogen Energ.* 33, 5363–5368. doi:10.1016/j.ijhydene.2008.07.041

Sun, K., Kuang, Y., Verlage, E., Brunschwig, B. S., Tu, C. W., and Lewis, N. S. (2015a). Sputtered NiOx Films for Stabilization of P+n-InP Photoanodes for Solar-Driven Water Oxidation. *Adv. Energ. Mater.* 5. doi:10.1002/aenm.201402276

Sun, K., Mcdowell, M. T., Nielander, A. C., Hu, S., Shaner, M. R., Yang, F., et al. (2015b). Stable Solar-Driven Water Oxidation to O2(g) by Ni-Oxide-Coated Silicon Photoanodes. *J. Phys. Chem. Lett.* 6, 592–598. doi:10.1021/jz5026195

Sun, K., Saadi, F. H., Lichterman, M. F., Hale, W. G., Wang, H.-P., Zhou, X., et al. (2015c). Stable Solar-Driven Oxidation of Water by Semiconducting Photoanodes Protected by Transparent Catalytic Nickel Oxide Films. *Proc. Natl. Acad. Sci. USA* 112, 3612–3617. doi:10.1073/pnas.1423034112

Sze, S. M., and Ng, K. K. (2007). *Physics of Semiconductor Devices*. Hoboken, NJ: Wiley-Interscience.

Tan, M. X., Laibinis, P. E., Nguyen, S. T., Kesselman, J. M., Stanton, C. E., and Lewis, N. S. (1994). Principles and Applications of Semiconductor Photoelectrochemistry. *Prog. Inorg. Chem.* 41, 21–144.

Thorne, J. E., Li, S., Du, C., Qin, G., and Wang, D. (2015). Energetics at the Surface of Photoelectrodes and its Influence on the Photoelectrochemical Properties. *J. Phys. Chem. Lett.* 6, 4083–4088. doi:10.1021/acs.jpclett.5b01372

Vanka, S., Sun, K., Zeng, G., Pham, T. A., Toma, F. M., Ogitsu, T., et al. (2019). Long-term Stability Studies of a Semiconductor Photoelectrode in Three-Electrode Configuration. *J. Mater. Chem. A.* 7, 27612–27619. doi:10.1039/c9ta09926c

Walter, M. G., Warren, E. L., Mckone, J. R., Boettcher, S. W., Mi, Q., Santori, E. A., et al. (2010). Solar Water Splitting Cells. *Chem. Rev.* 110, 6446–6473. doi:10.1021/cr1002326

Wang, H., Turner, J. A., Li, X., and Teeter, G. (2008). Process Modification for Coating SnO2:F on Stainless Steels for PEM Fuel Cell Bipolar Plates. *J. Power Sourc.* 178, 238–247. doi:10.1016/j.jpowsour.2007.12.010

Wolter, H. (1966). Born,M - Principles of Optics Electromagnetic Theory of Propagation Interference and Diffraction of Light. *Z. Angew. Physik* 21, 565.

Xu, J., Nagasawa, H., Kanezashi, M., and Tsuru, T. (2018). UV-protective TiO2 Thin Films with High Transparency in Visible Light Region Fabricated via Atmospheric-Pressure Plasma-Enhanced Chemical Vapor Deposition. *ACS Appl. Mater. Inter.* 10, 42657–42665. doi:10.1021/acsami.8b15572

Yang, H., Bright, J., Kasani, S., Zheng, P., Musho, T., Chen, B., et al. (2019). Metal-organic Framework Coated Titanium Dioxide Nanorod Array P-N Heterojunction Photoanode for Solar Water-Splitting. *Nano Res.* 12, 643–650. doi:10.1007/s12274-019-2272-4

Yu, Y., Sun, C., Yin, X., Li, J., Cao, S., Zhang, C., et al. (2018). Metastable Intermediates in Amorphous Titanium Oxide: A Hidden Role Leading to Ultra-stable Photoanode Protection. *Nano Lett.* 18, 5335–5342. doi:10.1021/acs.nanolett.8b02559

Zhao, T. S., Yanagi, R., Xu, Y. J., He, Y. L., Song, Y. Q., Yang, M. Q., et al. (2021). A Coating Strategy to Achieve Effective Local Charge Separation for Photocatalytic Coevolution. *Proc. Natl. Acad. Sci. United States America* 118. doi:10.1073/pnas.2023552118

Zheng, J. Y., Zhou, H. J., Zou, Y. Q., Wang, R. L., Lyu, Y. H., Jiang, S. P., et al. (2019). Efficiency and Stability of Narrow-gap Semiconductor-Based Photoelectrodes. *Energ. Environ. Sci.* 12. doi:10.1039/c9ee00524b

Conflict of Interest: The authors declare that the research was conducted in the absence of any commercial or financial relationships that could be construed as a potential conflict of interest.

frontiers in Energy Research

BRIEF RESEARCH REPORT
published: 28 March 2022
doi: 10.3389/fenrg.2022.871851

Assessing the Oxidative Stability of Anion Exchange Membranes in Oxygen Saturated Aqueous Alkaline Solutions

Christopher G. Arges[1], Vijay Ramani[2]*, Zhongyang Wang[3] and Ryan J. Ouimet[4]

[1]Department of Chemical Engineering, Pennsylvania State University, University Park, PA, United States, [2]Department of Energy, Environmental and Chemical Engineering, Washington University in St. Louis, St. Louis, MO, United States, [3]Pritzker School of Molecular Engineering, University of Chicago, Chicago, IL, United States, [4]Nel Hydrogen, Wallingford, CT, United States

While anion exchange membrane water electrolyzers show promise as a source of green hydrogen using low-temperatures and non-platinum group metal catalysts, many concerns must be addressed. A primary challenge for the development of high-performance anion exchange membrane water electrolyzers is the fabrication of a stable membrane that will be able to survive long-term stability test while maintaining high anion conductivity, which is a necessity for a durable water electrolyzer. This method will present a standardized protocol that can be used by researchers to assess the quality of their AEM materials and be able to provide insight into how materials may be degrading and how to improve the quality of AEMs. Using Mohr or Volhard titration to measure ion-exchange capacity, EIS to determine the ionic conductivity, NMR and FTIR to understand the extent of membrane degradation over time, and mechanical analyzers to determine the strength of their AEMs, this standardized protocol will guide researchers to determining and improving upon the long-term durability and performance of their AEM materials.

Keywords: anion exchange membrane, conductivity, electrolysis, stability, protocol and guidelines

Edited by:
Roel Van de Krol,
Helmholtz Association of German Research Centers (HZ), Germany

Reviewed by:
Ryszard Wycisk,
Vanderbilt University, United States
Viatcheslav Freger,
Technion Israel Institute of Technology, Israel

****Correspondence:***
Vijay Ramani
ramani@wustl.edu

Specialty section:
This article was submitted to Process and Energy Systems Engineering,
a section of the journal Frontiers in Energy Research

Received: *08 February 2022*
Accepted: *11 March 2022*
Published: *28 March 2022*

Citation:
Arges CG, Ramani V, Wang Z and Ouimet RJ (2022) Assessing the Oxidative Stability of Anion Exchange Membranes in Oxygen Saturated Aqueous Alkaline Solutions.
Front. Energy Res. 10:871851.
doi: 10.3389/fenrg.2022.871851

INTRODUCTION

Anion exchange membrane water electrolyzers (AEMWEs) have many advantages when compared to other green hydrogen production methods. When compared to liquid alkaline electrolysis, the use of a membrane electrolyte allows for a significant reduction in ohmic overpotential and allows for AEMWEs to operate at high current densities (Ayers et al., 2019). In addition, AEMWEs can use the cost-effective non-platinum group metal catalysts that can lead to a significant reduction in catalyst costs while also utilizing low-cost cell hardware components when using a water feed. Based on these advantages, it is potentially feasible to reduce the cost of clean hydrogen production with AEMWEs.

Despite the advantages of AEMWEs, many challenges remain before they can become widely commercialized. A significant concern for AEMWE development is the chemical and mechanical stability of anion exchange membrane (AEM) materials (Varcoe et al., 2014). Since the hydroxide ion has lower mobility than protons, many AEM materials attempt to increase the ion exchange capacity and improve the ionic conductivity (Ayers et al., 2019). However, this can increase the water uptake of the membrane and lead to worsened mechanical stability. Additionally, when used in alkaline environments, the OH^- ions have been seen to severely degrade AEMs through direct nucleophilic reaction (S_N2) as nucleophiles (Varcoe et al., 2014). When AEM are exposed to oxygen molecules,

OH^- ions participate the generation of highly reactive superoxide anion radical and hydroxyl free radicals, which will accelerate the degradation of AEMs. The detailed reaction mechanism can be found in our previous reports. (Parrondo et al., 2016; Zhang et al., 2017). This poor oxidative stability significantly limits the durability of the AEMs and prevents long-term operation of AEMWEs.

While many researchers have begun to develop and characterize new AEM materials with the intent of improving the oxidative stability and ionic conductivity, it is important to follow a standard protocol for an accurate comparison of these new AEMs. This method article will present researchers with a standardized procedure for testing the oxidative stability of AEMs by placing AEM materials into oxygen saturated aqueous alkaline solutions and examining the ion exchange capacity over time using Mohr or Vohlard titration compared to a control sample. AEM samples can also be examined over time using NMR and FTIR techniques which can allow researchers the ability to understand the extent of AEM degradation over time and can provide insight into the possible degradation mechanisms that are occurring. This method also uses electrochemical impedance spectroscopy (EIS) to assist in the measurement of ionic conductivity. Lastly, this report describes a protocol of determining the mechanical stability of AEM materials using tensile test analyzers. It provides information for the mechanical properties of the AEM material, such as ultimate tensile strength and elongation of the AEM at the break point.

PROTOCOL SCOPE

Scope and Applicability

This procedure describes experimental methods for characterizing the chemical and mechanical stability of anion exchange membranes (AEMs) exposed to oxygen saturated aqueous alkaline solutions. The stability testing condition is aggressive, akin to an accelerated stress test (AST), and is used to assess the viability of a given AEM material to be stable in the presence of alkaline solutions containing dissolved oxygen at near saturation level. The testing procedure is based on previous publications by Arges, Ramani, and others (Arges et al., 2013; Arges et al., 2015; Parrondo et al., 2016). Their work showed accelerated degradation of quaternary ammonium based AEM materials in oxygen saturated aqueous alkaline solutions when compared to nitrogen saturated alkaline solutions. Since water electrolyzers using AEMs generate oxygen at the anode and operate under an alkaline environment, this procedure allows stability assessment of AEM materials under AEMWE conditions without having to test an AEM in a water electrolyzer cell.

Summary of Method

This method carries out chemical stability experiments of AEMs by immersing AEM samples in oxygen saturated alkaline solutions at elevated temperatures (e.g., 1 M KOH or 1 M NaOH at 80°C). Control experiments are performed by immersing AEM samples in nitrogen saturated alkaline solutions at elevated temperatures (i.e., identical conditions). After exposing the samples for a period time to the oxygen saturated and nitrogen saturated alkaline solutions, post-mortem analysis is performed on the AEMs to assess the extent of membrane degradation. This includes measuring ionic conductivity, ion-exchange capacity via titration, collecting NMR spectra (and/or FTIR spectra), and assessing mechanical properties (e.g., tensile test). The properties and spectra of the AEM samples before exposure to the alkaline solutions are compared against the AEM samples exposed to oxygen and nitrogen saturated alkaline solutions. The change in AEM properties when compared to the pristine AEM are quantified over exposure time to the alkaline solutions to determine degradation modes and rate of degradation.

Personnel Qualifications/Responsibilities

The person performing this procedure should have basic training in chemistry at the college level and should have taken a general chemistry class and lab along with an organic chemistry class and lab. All users are responsible for their safety and should be familiar with the safety data sheets (SDS) of the chemicals used during this method. All users should have training on the equipment that is being used and should understand the basics of titration, NMR, FTIR, and mechanical stress testing.

Health and Safety Warning

Be cautious when working with solutions that contain NaOH, KOH, and HCl as they are corrosive and can cause skin burns and damage metals and other equipment. d6-DMSO is flammable, and it can be adsorbed by skin and should not be inhaled. Other chemicals dissolved in d6-DMSO can penetrate the skin and body if direct contact with DMSO is made. Read through all relevant safety data sheets (SDS) before performing the experiments stated in this protocol.

Equipment and Supplies

- Personal protective equipment (PPE)—lab jacket, safety glasses, and safety gloves that protect against d6-DMSO and other caustic solutions
- 150 ml empty high-density polyethylene, polypropylene, or polytetrafluoroethylene jars with lids. You need one jar for each sample to be tested with oxygen saturated alkaline solutions and with nitrogen saturated alkaline solutions.
- KOH or NaOH pellets. The water content of the pellets should be noted so accurate 1 M solutions can be prepared.
- Polytetrafluoroethylene or polypropylene tweezers for handling AEM samples in and out of the jar.
- Deionized (DI) water (18.2 MΩ, < 10 ppb TOC). Water should be withdrawn the day the alkaline solutions are prepared.

The following items are needed for NMR characterization:

- NMR tubes
- Deuterated dimethyl sulfoxide (d6-DMSO)
- NMR spectrometer

The following items are needed for conductivity measurements:

- 500 ml beaker
- Potentiostat/galvanostat for conductivity measurements

The following items are needed for IEC titrations:

- 1 M sodium nitrate in deionized water
- 0.1 M silver nitrate in deionized water
- 14 wt% iron (III) nitrate in deionized water
- 0.1 M potassium thiocyanate in deionized water

Other required equipment for this protocol includes an FTIR spectrometer with a transmission sample holder as well as an Instron® (or other) dynamic mechanical analyzer for AEM mechanical property testing.

Nomenclature and Definitions

- AEM: anion exchange membranes
- AEMWE: anion exchange membrane water electrolyzer
- $AgNO_3$: silver nitrate
- AST: accelerated stress test
- d6-DMSO: deuterated dimethyl sulfoxide
- DI: deionized
- $Fe(NO_3)_3$: iron (III) nitrate
- FTIR: Fourier transform infrared spectroscopy
- HFR: high frequency resistance
- IEC: ion-exchange capacity
- KOH: potassium hydroxide
- KSCN: potassium thiocyanate
- M: molar
- MΩ: megaohm
- $NaNO_3$: sodium nitrate
- NaOH: sodium hydroxide
- NMR: nuclear magnetic resonance
- ppb: parts per billion
- PP: polypropylene
- PPE: personal protective equipment
- PTFE: polytetrafluoroethylene
- SOP: standard operating procedure
- TOC: total organic carbon

Recommended Reading

Other literature sources which may help understand the concepts listed in this protocol include:

Arges, Christopher G., and Vijay Ramani. 2012. “Two-dimensional NMR spectroscopy reveals cation-triggered backbone degradation in polysulfone-based anion exchange membranes.” *Proceedings of the National Academy of Sciences* 2,490–2,495.

Arges, Christopher G., Javier Parrondo, Graham Johnson, Athrey Nadhan, and Vijay Ramani. 2012. “Assessing the influence of different cation chemistries on ionic conductivity and alkaline stability of anion exchange membranes.” *Journal of Materials Chemistry* 3,733–3,744.

Becerra-Arciniegas, R.-A., R. Narducci, G. Ercolani, S. Antonaroli, E. Sgreccia, L. Pasquini, P. Knauth, and M.L. Di Vona. 2019. “Alkaline stability of model anion exchange membranes based on poly (phenyene oxide) (PPO) with grafted quaternary ammonium groups: Infulence of the functionalization route.” *Polymer* 121,931.

Cho, Min Kyung, Ahyoun Lim, So Young Lee, Hyoung-Juhn Kim, Sung Jong Yoo, Yung-Eun Sung, Hyun S. Park, and Jong Hyun Jang. 2017. “A Review on Membranes and Catalysts for Anion Exchange Membrane Water Electrolysis Single Cells.” *Journal of Electrochemical Science and Technology* 183–196.

PROCEDURE

Step-by-Step Procedure

1. Place 150–200 mg of AEM sample in a 150 ml empty high-density polyethylene, polypropylene, or polytetrafluoroethylene jar. The jar should be sealable using a screw lid. Replicate samples should be prepared for assessing sample stability at different time points, stability repeatability, and to benchmark against a control (i.e., alkaline solution saturated with nitrogen as opposed to oxygen).
2. For each sample being assessed, 100 ml of 1 M sodium hydroxide (NaOH) in deionized water (18.2 MΩ and <100 ppb TOC) should be prepared. KOH can be substituted for NaOH. Split the 1 M NaOH (or 1 M KOH) solution in half. For one of the 1 M NaOH (or 1 M KOH) solutions, bubble pure oxygen gas through it continuously for over 30 min. The liquid volume should not exceed over 500 ml. If more than 500 ml needs to be saturated with oxygen, then have two separate containers for bubbling oxygen gas through it. The orifice for bubbling the oxygen gas should be near the bottom of the container holding the 1 M NaOH (or 1 M KOH) solution to ensure the gas bubbles make adequate contact with the entire volume of the liquid solution. For the other 1 M NaOH (or 1 M KOH) solution not saturated with oxygen, bubble pure nitrogen through it continuously for over 30 min. The liquid volume should not exceed over 500 ml. If more than 500 ml needs to be saturated with nitrogen, then have two separate containers for bubbling nitrogen gas through it. The orifice for bubbling the nitrogen gas should be near the bottom of the container holding the 1 M NaOH (or 1 M KOH) solution to ensure the gas bubbles make adequate contact with the entire volume of the liquid solution.
3. For each jar containing a sample, 50 ml of the 1 M NaOH (or 1 M KOH) saturated with oxygen should be added to the jar. The addition of liquid solution to the jar should occur within 5 min after bubbling the gas. After adding the liquid solution, the jar needs to be sealed shut with the screw cap. The immersed AEM sample in the liquid solution stored in the jar should be stored in a 60°C oven. If an AEM candidate has demonstrated acceptable stability at 60°C, additional testing can be performed at 80°C or higher to further analyze that material.

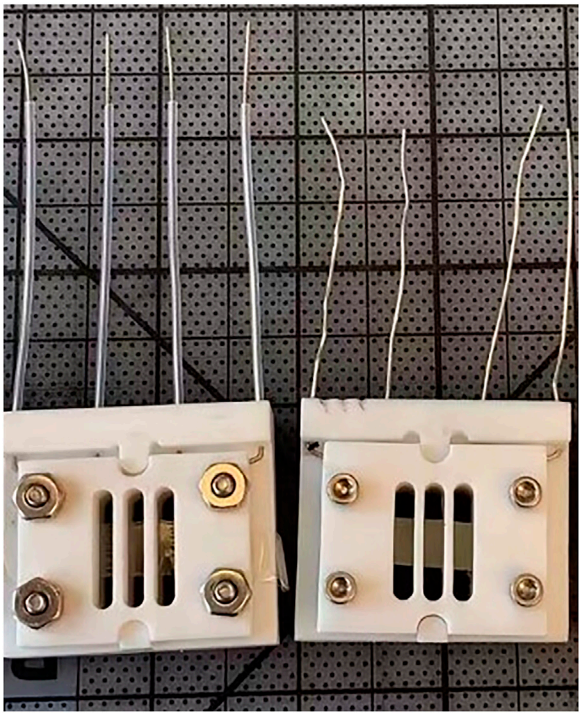

FIGURE 1 | Conductivity cells for in-plane ionic conductivity measurements using stand-alone membrane samples.

4. Repeat this procedure for replicate samples that can be used to assess the AEM stability at various time points and with nitrogen saturated 1 M NaOH (or 1 M KOH) solution.
5. After storing the AEM samples in gas saturated alkaline solutions for a given period at 60°C or 80°C, remove the jar sample from the oven. Let it cool for 30 min. Unscrew the lid and remove the AEM sample from the jar with a pair of PTFE (or PP) tweezers/forceps. Immerse the sample in 0.1 M HCl for 30 min followed by 1 M NaCl for 12–18 h. Then, rinse the AEM sample with deionized water and store in deionized water for 2 h. Remove the deionized water from the sample and add fresh deionized water for another 2 h. Then, store the AEM sample in an empty, clean jar with the lid open and let it dry in a fume hood for a day. The sample will be ready for IEC, NMR, ionic conductivity, and mechanical testing.
6. The AEM samples should be stored at 60°C or 80°C over a 4 week period. A sample should be withdrawn from the oven at 7, 14, and 28 days, etc.
7. All AEM samples (both virgin samples and samples which have been exposed to gas saturated alkaline solutions at elevated temperatures) should be characterized via the following methods:

i. Ion-exchange capacity via Mohr or Vohlard titration. The AEMs in chloride form (dry weight of approximately 0.1 g) should be immersed in 20 ml of 1 M $NaNO_3$ for 48 h. The amount of chloride ions exchanged can be determined by back titration using 0.1 M KSCN, after addition of 5 ml of 0.1 M $AgNO_3$. A control sample containing only 20 ml of 1M $NaNO_3$ should be also titrated as described above. $Fe(NO_3)_3$ is used as endpoint indicator (Arges et al., 2013).

ii. NMR and/or FTIR spectroscopy to characterize the change in the chemical structure of the samples (Arges et al., 2013; Varcoe et al., 2014; Arges et al., 2015). For NMR measurements, 3–5 mg of AEM samples with different immersion time should be dissolved in 1 ml d6-DMSO. Note that d6-DMSO is not a universal solvent that used to run NMR experiments. Operator should choose an appropriate deuterated solvent to dissolve the polymer. ^{1}H-NMR and ^{13}C-NMR spectrum can be coupled to analyze the degradation mechanisms both from the polymer backbone and the cationic groups. An example of using 2D NMR spectra to detect the degradation process of AEM can be found in **Supplementary Material**. The presence of functional groups can be qualitatively confirmed by using FTIR spectroscopy. An example of using FTIR spectroscopy to monitor the alkaline stability of AEM can be found in **Supplementary Material**.

iii. Ionic conductivity in deionized water at 25 °C with a 4-pt conductivity probe. In-plane ionic conductivity measurements can be carried out in a 4-point conductivity cell using electrochemical impedance spectroscopy (EIS) to measure the resistance. A 1 cm × 3 cm membrane is placed in the PTFE conductivity cell in contact with the four platinum electrodes and immersed in a temperature-controlled DI water bath. **Figure 1** shows 4-electrode measurements with membrane samples assembled in conductivity cells. A potentiostat is used to measure the impedance in the frequency range 100 kHz to 0.1 Hz. The high frequency resistance that is associated with ion transport is estimated from the Bode plots (corresponding to a phase angle close to zero) (Arges et al., 2013). Bode plots consist plots of the magnitude of the impedance and phase as a function of frequency. **Figure 2** shows an exemplary of Bode plots with ionic conduction characteristics (Vadhva et al., 2021)). An example of measuring ionic conductivity in an alkaline environment is shown in **Supplementary Material**.

iv. Stress-strain curve of the AEM by performing a tensile test or using a dynamic mechanical analyzer (DMA). The tensile tests for

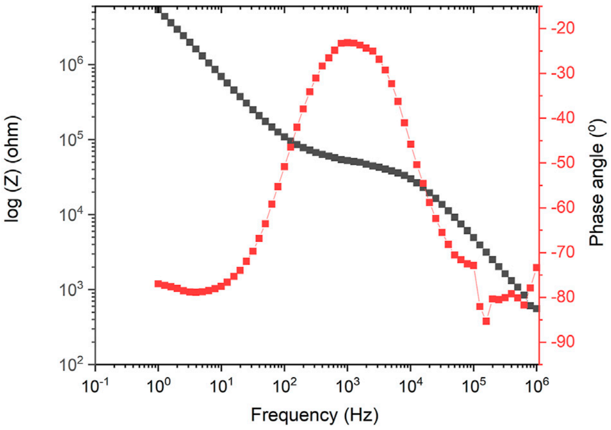

FIGURE 2 | Bode plot containing information of phase angle and impedance as a function of frequency.

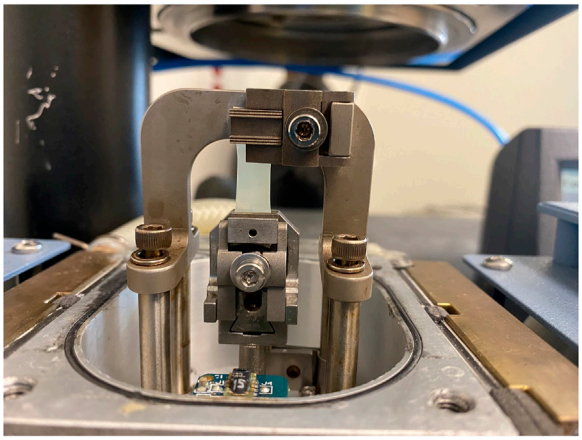

FIGURE 3 | Illustration of a membrane sample in clamps of a DMA.

the AEM can be performed using a differential mechanical analyzer. The membrane sample (approximate dimensions: 50 mm × 5 mm × 0.05 mm) is fixed in a film tension clamp using a certain torque. The experiments can be performed at 25 ˚C with different relative humidity values. The membrane can be stretched at 0.5 MPa/min until the sample fractures (Arges et al., 2013). **Figure 3** shows an example of a membrane sample in the clamps of a DMA (Bashir, 2021). Exemplary tensile test curves can be found in Figure 4 in our previous report (Wang et al., 2020).

Sample Preparation and Analysis

AEM samples should be cut so that the sample weight is approximately 150–200 mg. Enough samples should be cut so that samples can be placed in oxygen saturated alkaline solution, nitrogen saturated alkaline solution, and so that there are replicate samples that can be tested at various time intervals. During the IEC titration measurements, the samples should have an estimated dry weight of approximately 100 mg. For NMR measurements, the sample weight should be 3–5 mg. Samples that are to be used for measuring the ionic conductivity in water should be 10 mm × 30 mm so that they can fit within the PTFE conductivity cell. Samples to be used for the stress-strain measurement should have an approximate dimension of 50 mm × 5 mm x 0.05 mm. When preparing samples, ensure that there is enough virgin AEM material remaining for characterization.

RESULTS

From the data collected from step 4.1.7. i., the anion exchange capacity for the chloride counter ion can be calculated using the following equation:

$$IEC = 0.1\frac{V_C - V}{W}$$

In this equation, IEC is the anion exchange capacity (mmol/g), V_C is the volume (ml) of 0.1 M KSCN necessary to reach the equivalence point with the control sample, V is the volume (ml) of 0.1 M KSCN necessary to reach the equivalence point with the AEM sample, and W is the dry weight (g) of the AEM sample.

To determine the ionic conductivity of the AEM sample, the ionic resistance of the sample should first be determined using the collected EIS data. Since the high frequency resistance (HFR) measured with EIS is associated with the ionic resistance of the sample, the ionic resistance is measured by reading the resistance of the sample on a Bode plot when the phase angle is equal to zero. Once the ionic resistance is known, the ionic conductivity of the membrane can be determined using the following equation:

$$\sigma = \frac{L}{R \cdot t \cdot w}$$

In this equation, σ is the in-plane membrane conductivity (mS/cm), R is the in-plane membrane resistance determined from the HFR (mOhm), t is the thickness of the fully hydrated membrane sample (cm), w is the width of the fully hydrated membrane sample (cm), and L is the distance between the two inner electrodes (cm).

When performing the tensile tests with the AEM samples, a stress-strain curve should be recorded and presented. This plot will detail the stress applied to the AEM sample and the strain felt by the sample. This plot will allow the user to record the ultimate tensile strength and elongation at the break point.

QUALITY CONTROL AND QUALITY ASSURANCE

Instrument or Method Calibration and Standardization

Ionic conductivity measurements can be calibrated by measuring a well-studied ion conducting membrane such as Nafion® 212. For IEC measurements, Vohlard titration can be calibrated by titrating 0.1 M $AgNO_3$ solutions with no AEM samples and then titrating with 0.1 M KSCN. The volume of KSCN needed to reach the endpoint should be the same volume of added $AgNO_3$. Titration method can also be calibrated by measuring the IEC of a commercially available AEM such as Fumasep®. The same principle applies to the tensile test. When performing the spectroscopy methods, background corrections should be performed to account for environmental conditions.

Cautions

AEM samples that are too brittle to handle after removing from the jar with alkaline solutions should be discarded appropriately. Note that the sample did not mechanically survive the alkaline stability test at the specified temperature and time point.

Interferences

Do not use glass containers for storing or hold NaOH and KOH solutions as the caustic media can etch the glass leading to precipitates that interfere with the degradation analysis.

DISCUSSION

Plot ionic conductivity, IEC, and mechanical properties (stress or elongation at break) versus time. Create separate traces for samples exposed to oxygen saturated alkaline solutions versus nitrogen saturated alkaline solutions. Please refer to the results (**Figure 3** in page 4) published in our previous report (Parrondo et al., 2016). At t = 0 h, the initial point refers to IEC of the virgin AEM sample. If NMR characterization is possible, the ^{1}H NMR for the AEM sample at different time points should be compared. Peaks associated with backbone and cation integrity in the virgin AEM sample should be assigned and monitored in the ^{1}H NMR. An internal standard should be added to the AEM sample dissolved in a deuterated solvent such as d6-DMSO to quantify cation and backbone degradation products. Similarly, FTIR spectra can be compared versus the samples exposed to alkaline solutions and the virgin AEM sample.

Note that the membrane sample might suffer from mechanical failure during the stability test. For instance, membrane sample might break into pieces due to the degradation process from nucleophiles, which would result in the difficulty of continued ionic and mechanical measurements. It is still necessary to extract degradation information from the NMR characterization.

DATA AVAILABILITY STATEMENT

The original contributions presented in the study are included in the article/**Supplementary Material**, further inquiries can be directed to the corresponding author.

AUTHOR CONTRIBUTIONS

CA and ZW were responsible for draft writing and editing. VR and RO were responsible for reviewing and editing.

ACKNOWLEDGMENTS

The author VR would like to acknowledge with gratitude the Office of Naval Research (ONR grant no. N00014-16-1-2833) for funding this work. The author VR also acknowledges with gratitude generous support from the Roma B. and Raymond H. Wittcoff Distinguished University Professorship at Washington University in St. Louis. The author RO would like to acknowledge the U.S. Department of Energy and the funding support from project DOE-DE-EE0008092, Benchmarking Advanced Water Splitting Technologies: Best Practices in Materials Characterization.

SUPPLEMENTARY MATERIAL

The Supplementary Material for this article can be found online at: https://www.frontiersin.org/articles/10.3389/fenrg.2022.871851/full#supplementary-material

REFERENCES

Arges, C. G., Wang, L., Parrondo, J., and Ramani, V. (2013). Best Practices for Investigating Anion Exchange Membrane Suitability for Alkaline Electrochemical Devices: Case Study Using Quaternary Ammonium Poly(2,6-Dimethyl 1,4-phenylene)oxide Anion Exchange Membranes. *J. Electrochem. Soc.* 160, F1258–F1274. doi:10.1149/2.049311jes

Arges, C. G., Wang, L., Jung, M.-S., and Ramani, V. (2015). Mechanically Stable Poly(arylene Ether) Anion Exchange Membranes Prepared from Commercially Available Polymers for Alkaline Electrochemical Devices. *J. Electrochem. Soc.* 162, F686–F693. doi:10.1149/2.0361507jes

Ayers, K., Danilovic, N., Ouimet, R., Carmo, M., Pivovar, B., and Bornstein, M. (2019). Perspectives on Low-Temperature Electrolysis and Potential for Renewable Hydrogen at Scale. *Annu. Rev. Chem. Biomol. Eng.* 10, 219–239. doi:10.1146/annurev-chembioeng-060718-030241

Bashir, M. A. (2021). Use of Dynamic Mechanical Analysis (DMA) for Characterizing Interfacial Interactions in Filled Polymers. *Solids* 2, 108–120. doi:10.3390/solids2010006

Parrondo, J., Wang, Z., Jung, M.-S. J., and Ramani, V. (2016). Reactive Oxygen Species Accelerate Degradation of Anion Exchange Membranes Based on Polyphenylene Oxide in Alkaline Environments. *Phys. Chem. Chem. Phys.* 18, 19705–19712. doi:10.1039/c6cp01978a

Vadhva, P., Hu, J., Johnson, M. J., Stocker, R., Braglia, M., Brett, D. J. L., et al. (2021). Electrochemical Impedance Spectroscopy for All-Solid-State Batteries: Theory, Methods and Future Outlook. *ChemElectroChem* 8, 1930–1947. doi:10.1002/celc.202100108

Varcoe, J. R., Atanassov, P., Dekel, D. R., Herring, A. M., Hickner, M. A., Kohl, P. A., et al. (2014). Anion-exchange Membranes in Electrochemical Energy Systems. *Energy Environ. Sci.* 7, 3135–3191. doi:10.1039/c4ee01303d

Wang, Z., Parrondo, J., Sankarasubramanian, S., Bhattacharyya, K., Ghosh, M., and Ramani, V. (2020). Alkaline Stability of Pure Aliphatic-Based Anion Exchange Membranes Containing Cycloaliphatic Quaternary Ammonium Cations. *J. Electrochem. Soc.* 167, 124504. doi:10.1149/1945-7111/abac29

Zhang, Y., Parrondo, J., Sankarasubramanian, S., and Ramani, V. (2017). Detection of Reactive Oxygen Species in Anion Exchange Membrane Fuel Cells Using *In Situ* Fluorescence Spectroscopy. *ChemSusChem* 10, 3056–3062. doi:10.1002/cssc.201700760

Conflict of Interest: RO was employed by Nel Hydrogen

The remaining authors declare that the research was conducted in the absence of any commercial or financial relationships that could be construed as a potential conflict of interest.

frontiers | Frontiers in Energy Research

METHODS
published: 08 April 2022
doi: 10.3389/fenrg.2022.856943

A Thermogravimetric Temperature-Programmed Thermal Redox Protocol for Rapid Screening of Metal Oxides for Solar Thermochemical Hydrogen Production

Michael D. Sanders[1], *Anyka M. Bergeson-Keller*[1], *Eric N. Coker*[2] and *Ryan P. O'Hayre*[1]*

[1]Colorado School of Mines, Department of Metallurgy and Materials Engineering, Colorado Center for Advanced Ceramics, Golden, CO, United States, [2]Sandia National Laboratories, Albuquerque, NM, United States

As combinatorial and computational methods accelerate the identification of potentially suitable thermochemically-active oxides for use in solar thermochemical hydrogen production (STCH), the onus shifts to quickly evaluating predicted performance. Traditionally, this has required an experimental setup capable of directly carrying out a two-stage thermochemical water-splitting process. But this can be a difficult endeavor, as most off-the-shelf equipment cannot adequately deal simultaneously with the high temperatures, varying oxygen partial pressures, and high H_2O partial pressures required; achieving sufficient temporal sensitivity to accurately quantify the kinetics is also a major challenge. However, as proposed here, a less complicated experiment can be used as a first screening for thermochemical water splitting potential. Temperature-Programmed Thermal Redox (TPTR) using thermogravimetry evaluates the thermal reduction behavior of materials. This technique does not require water splitting or CO_2-splitting analogs but can nonetheless predict water-splitting performance. Three figures of merit are obtained from the TPTR experiment: reduction onset temperature, extent of reduction, and extent of recovery upon reoxidation. These metrics can collectively be used to determine if a material is capable of thermochemical water-splitting, and, to good approximation, predict whether the thermodynamics are favorable for use under more challenging high-conversion conditions. This paper discusses the pros and cons of using TPTR and proposes a protocol for use within the STCH community.

Keywords: concentrated solar, thermogravimetry, screening, perovskite, water splitting, hydrogen lcroduction

Edited by:
Ellen B. Stechel,
Arizona State University, United States

Reviewed by:
Alicia Bayon,
Arizona State University, United States
Juan M. Coronado,
Institute of Catalysis and Petrochemistry (CSIC), Spain

****Correspondence:***
Ryan P. O'Hayre
rohayre@mines.edu

Specialty section:
This article was submitted to Hydrogen Storage and Production, a section of the journal Frontiers in Energy Research

Received: *17 January 2022*
Accepted: *08 March 2022*
Published: *08 April 2022*

Citation:
Sanders MD, Bergeson-Keller AM, Coker EN and O'Hayre RP (2022) A Thermogravimetric Temperature-Programmed Thermal Redox Protocol for Rapid Screening of Metal Oxides for Solar Thermochemical Hydrogen Production. Front. Energy Res. 10:856943. doi: 10.3389/fenrg.2022.856943

INTRODUCTION

Solar thermochemical water splitting (STCH) is an emerging technology that can be used to produce hydrogen gas from steam using thermal energy from the Sun *via* a two-step reduction and oxidation cycle (Bayon et al., 2020). While STCH has been shown to have theoretically high efficiencies (Steinfeld, 2005; Wang et al., 2012; Cheng et al., 2021), these values have yet to be attained in practice (Muhich et al., 2018), in part due to the thermodynamic limitations of the ceramic oxide materials used to perform the water splitting. The current state-of-the-art material for STCH is fluorite-structured ceria (CeO_2) (Lu et al., 2019), however perovskite oxides also hold much promise due to their thermodynamic tunability, thermal and chemical stability over a wide range of temperatures and oxygen nonstoichiometries, and their compositional versatility (Scheffe and Steinfeld, 2014).

Many perovskite oxides have been explored in the context of STCH already (McDaniel et al., 2013; Barcellos et al., 2018), however benchmarking their performance relative to ceria is often a lengthy and unstandardized process. Efforts have been made to streamline the exploration of new STCH materials by comparing the oxygen vacancy formation energies (E_v) of prospective compounds relative to ceria [e.g., through thermodynamic computations using HSC (Abanades et al., 2006) and DFT (Emery et al., 2016; Bartel et al., 2019; Sai Gautam et al., 2020)] or by running thermochemical splitting experiments *via* thermogravimetry (TG) with CO_2 analogs (Nair and Abanades, 2018). However, these methods are often complex, time intensive and/or fall short of correctly predicting the water-splitting capability. Thus, it would be beneficial to the STCH community to find a new screening method that is relatively quick, simple, and provides sufficient information to reasonably predict a prospective material's water splitting potential. Here, we adopt a modified temperature-programmed reduction (TPR) methodology to quantify redox thermodynamics for this purpose.

TPR is most commonly associated with catalysis research (Hurst et al., 1982; Jones, 1986). In a typical TPR experiment, a sample is exposed to a flowing gas environment containing a reductant (hydrogen is the most prevalent) while the temperature of the sample is changed. The gas composition is monitored at the outlet of the reactor and the resulting changes in reductant concentration provide a "fingerprint" of the catalytic behavior. Other TPR implementations instead track changes in the mass of the sample being reduced or pressure changes in the reaction chamber.

In contrast to the general TPR approach described above, the TPR approach recommended for STCH materials discovery involves thermal rather than chemical reduction and incorporates a reoxidation step. To avoid confusion, it is therefore proposed that this technique be termed Temperature-programmed Thermal Redox (TPTR). TPTR offers significant benefits for STCH materials discovery as it is rapid (5.5 h per sample with only a few minutes of experiment setup) and it can be run on virtually any standard TG instrument without the need to add gas detection or advanced gas switching capabilities.

To illustrate the TPTR protocol, this study focuses on six candidate STCH compositions that span a broad range of possible STCH-relevant thermodynamic behavior. Three of the chosen compositions are perovskite structured manganates; $Sr_{0.95}Ce_{0.05}MnO_{3-\delta}$ (SCM05), $Sr_{0.9}Ca_{0.1}Ti_{0.7}Mn_{0.3}O_{3-\delta}$ (SCTM9173), and $Sr_{0.7}Ca_{0.3}Ti_{0.7}Mn_{0.3}O_{3-\delta}$ (SCTM7373). The two SCTM compositions were identified using the predicted performance from a STCH related Materials Project contribution (Vieten et al., 2019). Notably, the two end members STM and CTM were also later shown to be promising STCH candidates (Qian et al., 2020; Qian et al., 2021). In contrast, SCM05 was originally part of a broader study of the water-splitting SCM family (Bergeson-Keller et al., 2022), but it was predicted to have poor water splitting performance compared to higher Ce-content SCM compositions. In addition to the three manganates, two barium niobium ferrites, the double-perovskites $Ba_2FeNbO_{6-\delta}$ (BFN), and $Ba_2Ca_{0.66}Nb_{0.68}Fe_{0.66}O_{6-\delta}$ (BCNF), were selected due to the former's photocatalysis and CO_2 reduction potential (Voorhoeve et al., 1974; Zhang et al., 2017). Finally, CeO_2 (ceria) was included as a known state-of-the-art STCH material (Chueh et al., 2010) for comparison.

All compositions were screened using TPTR and the results analyzed using several different normalizations. The materials were also tested using an actual water-splitting test-stand to evaluate their water-splitting performance. The results from the two techniques were used to define target windows for the proposed figures of merit. This work will show that TPTR can accurately predict the water-splitting performance of new materials without the need for large sample quantities or specialized equipment.

EXPERIMENTAL

Powder Synthesis and Characterization

Powders used for this study were synthesized except for CeO_2, which was purchased (99.99% purity). SCM05 was synthesized *via* the sol-gel modified Pechini method described in detail elsewhere (Shang et al., 2013). Briefly, stoichiometric amounts of transition metal nitrates were weighted and dissolved in aqueous solution. Citric acid and Ethylenediaminetetraacetic acid (EDTA) were added to the solution as complexing agents in ratios of 3:1 to the metal cations. The reactants were dissolved in deionized water and ammonium hydroxide to achieve a pH close to 9, then the solution was heated to 350°C and stirred continuously until it became gelatinous. Finally, the gel was dried in a furnace held at 125°C overnight and calcined in air at 800°C for 10 h, then at 1,400°C for 5 h using a ramp rate of 5°C/min, and ground into a fine powder using a mortar and pestle.

The other compositions were synthesized using a solid-state reaction method. Briefly, stoichiometric amounts of various carbonates and oxides were mixed and dry planetary milled for 24 h then dried in air on a hot plate. The two SCTM compositions were pressed into pellets before calcination in air (500°C for 1 h, then 1,300°C for 12 h). The ferrites were directly pre-calcined (1,000°C for 10 h) before being wet planetary milled for 12 h then pressed into a pellet and calcined at 1,400°C for 10 h.

Powder X-ray diffraction (XRD) was conducted using Cu-Kα radiation (PANalytical/X'Pert PRO MPD, $\lambda = 1.5406$ Å, $2\theta = 20–120°$, $0.016\ s^{-1}$ scan rate, 45 kV/40 mA output) and the target phases were confirmed *via* Rietveld refinement using Fullprof software.

TPTR

Overview of Necessary Equipment

In general, almost any TG is capable of TPTR. If the furnace has a suitable maximum temperature (>1,300°C for reasonable results) and the reactor chamber can be purged of oxygen to at least an oxygen partial pressure of 1 mbar (although lower than 0.001 mbar is preferred), most of the TPTR protocol can be followed. Realtime oxygen sensing, either with a mass spectrometer or an oxygen sensor is helpful, especially for quantifying the actual reaction chamber pO_2, but this is not required. To fully carry out the experimental protocol, the TG should also be capable of changing gas environments while at temperature: specifically, flowing oxidizing gasses at temperatures of <1,000°C[1]. Most commercial TG balances have adequate resolution for TPTR as the experiments are designed to push the sample to high levels of oxygen non-stoichiometry. For instruments that have lower sensitivities, increased sample masses can often overcome this limitation (this and other sample considerations are discussed in more detail below). Unlike experiments designed to accurately capture the thermodynamics of reduction, TPTR is not as concerned with lower temperature non-stoichiometry behavior. For this reason, the need to control the chamber pressure using a back-pressure regulator is less important. Such regulation is far more important for long duration tests (tens of hours or days) and small mass losses (<100 μg).

Experimental Sample Considerations

Best results come from powder samples that have already experienced temperatures at least as high as those of the T_{red} step. This requirement is typically satisfied by the calcination procedure used during synthesis. This thermal stability requirement acts as an initial screen in case the composition cannot survive the temperatures used in the TPTR test (either due to decomposition, metal volatilization, or even melting). Particle size is not critically important, as long as the particles are <500 μm. Fine particles, like those that result from sol-gel synthesis, will give results closer to equilibrium, but in deeper powder beds, a fine powder size can lead to unreliable results due to gas diffusion effects. Sintering can also occur when using small powder sizes, although typically this has a relatively minor effect on the results.

Typical Experimental Conditions and Considerations

The TPTR experiments discussed in this study were conducted using a Setaram TGA (Setsys Evolution). Between 50 and 75 mg of sample powder was loaded into a platinum or alumina crucible. An initial oxygen burnout/reoxidation was performed in air up to 800°C and then the sample was cooled. The TPTR run begins with a ramp at 20°C min^{-1} to 1,350°C with a soak for 1 h in Ultra High Purity (UHP) N_2 at a flow rate of 100 sccm while the mass change due to thermal reduction is continuously monitored. The sample is then cooled at 20°C min^{-1} to 1,000°C and air is subsequently introduced for another hour to measure the reoxidation behavior, before finally cooling to 25°C at 10°C min^{-1}. Buoyancy effects are subtracted using a blank run of dense alumina balls of similar volume as the powder sample. Temperatures for the reduction and oxidation steps should be chosen based on the type of STCH cycle that is being investigated—here 1,350 and 1,000°C respectively, although higher or lower temperatures can also be examined. Many of the other parameters are chosen for convenience and can be adjusted with some consideration.

The optimal mass of sample is typically dictated by crucible volume, bed depth, and balance sensitivity. In principle, researchers should aim to use a sample mass and crucible configuration that produces a total mass loss two orders of magnitude larger than the noise floor of the instrument while yielding the shallowest possible bed depth to minimize gas diffusion effects. Higher signal-to-noise ratios are preferable, but not required. Exceptionally large amounts of sample can negatively impact test results. If powder beds are too deep, evolved oxygen may have trouble diffusing out of the bed, thereby elevating the local oxygen partial pressure and suppressing reduction. Even if the oxygen can escape the local sample area, if it cannot be properly swept out of the reaction chamber, oxygen build-up can again suppress reduction—thus the total volume of sample relative to the volume of the reaction chamber and the sweep-gas volumetric flow rate is also an important consideration.

The concerns discussed above motivate careful consideration of the impact of gas flow rates and heating rates. While low flow rates can assist in creating better TG traces, if the rate is too low, oxygen can accumulate in the chamber as mentioned above. Similarly, heating rates that are too fast can introduce a temperature lag into the sample (the reported temperature of the sample is not the actual temperature due to thermal diffusivity effects) and may also not allow enough time to sweep away evolved oxygen.

Because of the above considerations, it is recommended to run a couple of known samples under various experimental conditions to ensure that all necessary behavior is being captured. Ceria is a good choice to ensure that sample masses are adequate to capture low-reduction behavior. A few runs with decreasing amounts of sample can be used to identify when the mass loss can no longer be reliably measured. Most perovskites, especially an easily reduced compound like SCM05, will likely expel enough oxygen during reduction to affect the local oxygen partial pressure. A few experiments subjecting a known, easily-reduced STCH oxide (e.g., SCM05 or $Sr_aLa_{1\text{-}a}Mn_bAl_{1\text{-}b}O_{3-\delta}$) to increasing flow rates of gas can be used to identify a sufficiently high flow rate such that the amount of reduction remains constant from run to run, thereby ensuring that oxygen accumulation is not impacting results.

Water-Splitting Tests

Sandia National Laboratories' stagnation flow reactor (SFR) was used for water-splitting performance testing. The reactor employs a laser-based sample heater and utilizes a mass spectrometer downstream from the reactor to measure evolved gases (minus water). The details of the system have been published elsewhere (Scheffe et al., 2011; McDaniel et al., 2013). Briefly, approximately 100 mg of each of the powder samples are placed on a zirconia platform forming a loosely-packed shallow bed, and the reactor is heated to an oxidation temperature (T_{ox}) of either 850°C or 1,000°C

---

[1] It is possible to run the reduction and oxidation segments non-sequentially, with a cool down in between, but the oxidation will then occur at a less than optimal temperature, complicating the analysis. This also requires that the reduced state be thermally quenched in the low p_{O2} environment. A slow cooling rate allows the sample to getter oxygen from the gas environment, creating additional analysis complications.

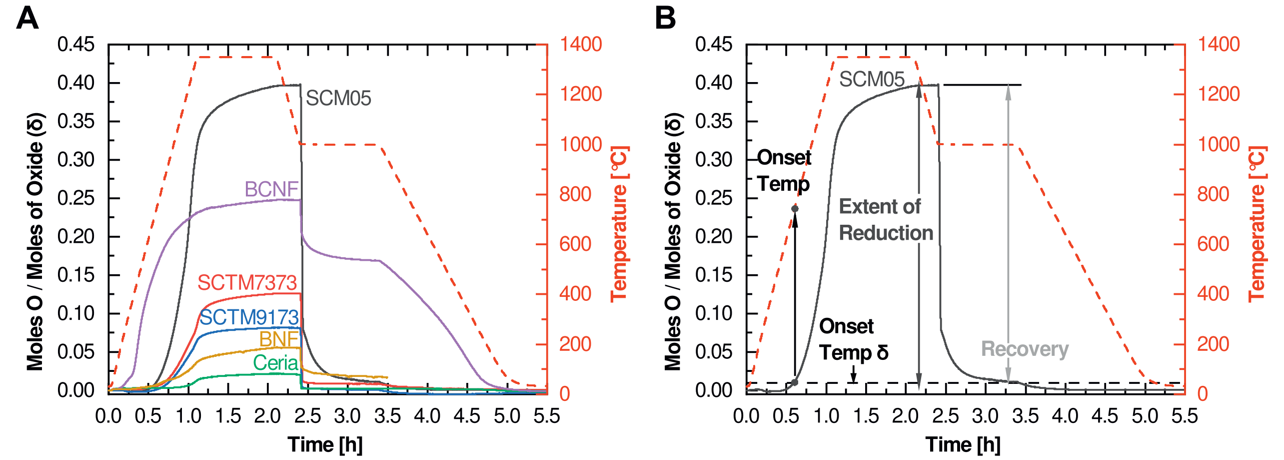

FIGURE 1 | (A) TPTR results for the six compositions of interest. **(B)** Visual descriptions of the three figures of merit for SCM05.

under UHP Ar atmosphere. Samples are heated by the laser at a controlled rate of 10°C/s from T_{ox} to a reduction temperature (T_{red}) of either 1,350°C or 1,400°C, where they are held for 330 s. Upon turning off the laser, the samples cool to T_{ox} in a matter of seconds, minimizing the potential for reoxidation with any trace amount of O_2 still in the chamber. 40 vol% water vapor in Ar gas flow is introduced to the system to initiate reoxidation. Reoxidation is conducted for 1,200 s. The total amount of H_2 produced is calculated by integrating the baseline-corrected mass spectrometer signal over the entire gas evolution envelope. Two additional redox cycles are then executed without a complete reoxidation in air.

RESULTS AND DISCUSSION

The TPTR results for the six compositions in this study are shown in **Figure 1**. The original mass traces were converted and normalized to δ using **Eq. 1**:

$$\delta = -\left(\frac{\Delta m}{\mathrm{M_O}}\right)\left(\frac{\mathrm{M_{oxide}}}{m_{\mathrm{oxide}}}\right) \equiv \frac{\text{Moles O}}{\text{Moles Oxide}} \tag{1}$$

where Δm is the mass change, m_{oxide} is the initial mass of sample oxide, and $\mathrm{M_{oxide}}$ and $\mathrm{M_O}$ are the molar mass of the oxide and atomic oxygen, respectively. The sign is reversed so that positive values signify increases in δ. Other normalizations can be used, as discussed later. Rather than relying on qualitative evaluation to make determinations on STCH suitability, we advocate quantitative analysis of the TPTR results using three calculable figures of merit. An in-depth example illustrating the calculation and interpretation of these three figures of merit is provided in following sections.

Figures of Merit

Onset Temperature

The first proposed metric is the reduction onset temperature. The onset temperature is a construction borrowed from other thermal analysis techniques that investigate thermally activated reactions and processes. However, since reduction is a continuous thermal process (there is no sharp and distinct temperature onset for reduction in contrast to melting or solid-state phase changes), we consider here a modified application of the concept. Rather than attempting to determine the temperature at which the first measurable reduction occurs, we suggest using the temperature at which the extent of reduction reaches 0.01 (**Figure 2A**), or in cases where the room temperature non-stoichiometry is non-zero, when the thermal reduction component reaches 0.01. The onset temperature is closely correlated with the enthalpy of reduction (related to the formation enthalpy of oxygen vacancies), so higher reduction enthalpies should correspond to higher onset temperatures.

For the compositions investigated here, only two had an onset temperature below 800°C (BCNF and SCM05). Most high-potential water splitting materials exhibit reduction onset temperatures of at least 800°C, although as will be seen later there are examples of active water-splitting materials with reduction onset temperatures as low as 625°C. Thus, the reduction onset temperature metric cannot be used in isolation to evaluate water splitting potential. At the other end of the spectrum, ceria's onset temperature of 1,300°C is consistent with its nonviability for cycles designed around lower reduction temperatures. Favorable reduction onset temperatures between 800 and 1,000°C are observed for the remaining three compositions (SCTM7373, SCTM9173, and BNF).

Extent of Reduction

The second proposed figure of merit focuses on the total extent of reduction at the temperature of interest (in the investigations illustrated here, that is a T_{red} of 1,350°C). It is best evaluated at the end of the high temperature reduction soak (**Figure 2B**). This metric is more straightforward and intuitive than reduction onset temperature. It captures the degree of non-stoichiometry achieved for a given material at the given T_{red}. If evaluated as a function of soak-time, it can also provide some insight into the kinetics of the reduction process, although due to the many

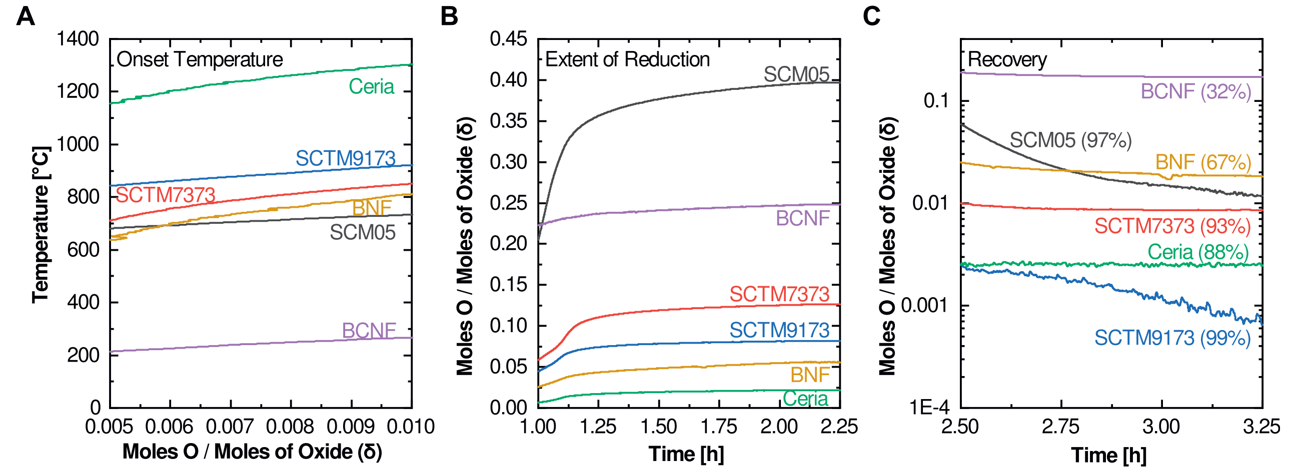

FIGURE 2 | Highlight plots of the relevant experimental data regions for the three figures of merit: **(A)** Onset Temperature, **(B)** Extent of Reduction, and **(C)** Recovery (calculated percentage of reoxidation at 1,000°C is also listed).

variables that influence kinetics, both from a material and experimental standpoint, kinetics is not considered in this screening method. In most cases, the optimal target for this metric is rapid equilibration to a moderate level of reduction. Higher levels of reduction typically signify that the material is too easily reduced and thus it is unlikely to reoxidize under water-splitting conditions. Low extents of reduction mean that the per-cycle hydrogen yield is likely to be too low for viability. This is examined in more detail later.

Ceria and BNF have extent of reduction values that are likely too low for viable water splitting potential, while the extent of reduction value for SCM05 is likely too high. Although BCNF has an attractive extent of reduction, its extremely low reduction onset temperature suggests that it is not a viable candidate. This again leaves the SCTM compositions as the most favorable candidates.

Recovery

The final figure of merit concerns the reoxidation behavior. Because reoxidation occurs in air rather than steam in this protocol, the reoxidation metric does not provide direct insight into the oxidation behavior of a material under actual water-splitting conditions. The potential to split water is best evaluated using the first two metrics, which more closely correspond to the thermodynamic potential for water splitting. Thus, this reoxidation metric, which we term “recovery”, is instead best used to provide insight into the cyclability and stability of a candidate material. Like extent of reduction, this metric is best evaluated after the high-temperature reoxidation soak (**Figure 2C**) and can either be evaluated as the δ value or as a percentage of the extent of reduction. A perfect result is a return to the zero δ or zero Δδ condition (or 100% recovery). In some cases, this value will be either greater or less than the extent of reduction, in which case a secondary metric at room temperature can be informational. If the mass returns to the initial value only upon fully cooling to room temperature, this implies that full reoxidation cannot occur at T_{ox} even with air as an oxidant; reoxidation in steam will therefore likely be greatly limited, and thus per cycle hydrogen production will be low or non-existent. If the material does not fully reoxidize even after reaching room temperature, the material is likely either unstable or has undergone an irreversible phase change. This is seen in the case of $BaCe_{0.25}Mn_{0.75}O_3$ (BCM) (**Figure 3**): an initial phase change leads to an incomplete reoxidation during the first measurement cycle, however, subsequent cycles do not show the same behavior as the material retains its new phase and the redox behavior stabilizes.

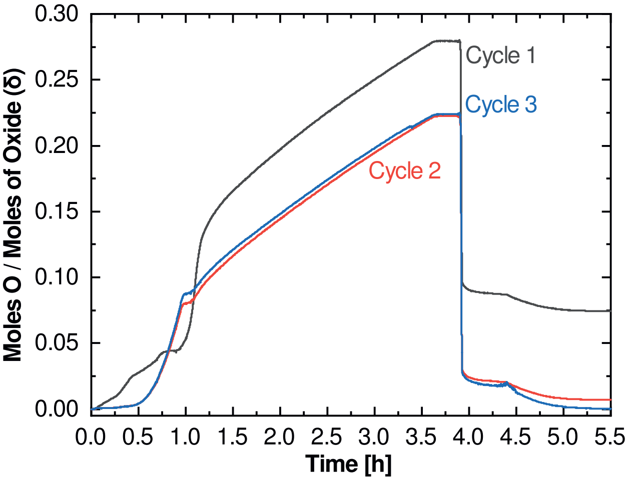

FIGURE 3 | Cycles of TPTR in BCM (Barcellos et al., 2018). adapted and used by permission of The Royal Society of Chemistry.

Considering the 6 materials tested here, BCNF shows poor recovery with a final value of ~0.18. When compared against its extent of reduction value of ~0.25, this gives a relative recovery of only 32%, strongly reinforcing the conclusion that BCNF is a nonviable candidate for STCH application. Similarly, the 67% recovery metric determined for BNF, when taken in concert with its low extent of reduction, suggests it is also not likely to be a

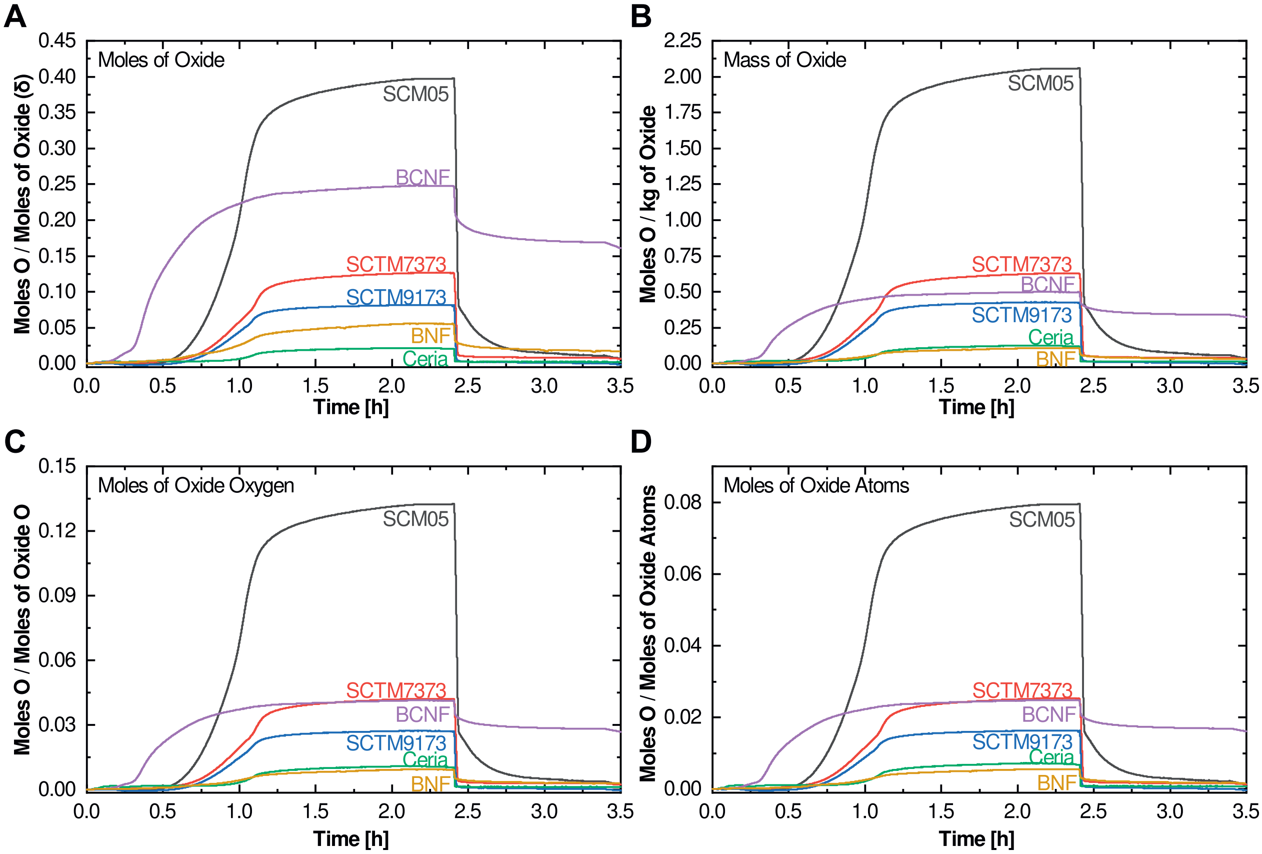

FIGURE 4 | Plots of four different normalization of the TGA data from the TPTR experiments: namely normalization by **(A)** moles of oxide, **(B)** mass of oxide, **(C)** moles of oxide oxygen, and **(D)** moles of oxide atoms.

promising water splitting candidate. In contrast, SCTM9173 nearly reaches 100% recovery, suggesting that it is therefore very likely to split water and maintain stability during cycling. Finally, SCM05 and SCTM7373 yield recovery values of 98 and 93%, suggesting that they also show promising cyclability and may provide sufficient reoxidation potential under water splitting conditions for continued consideration. Ceria's seemingly low 88% recovery is more a function of the low extent of reduction and resulting measurement uncertainty. The final δ of 0.002 is low enough to be essentially zero and can be considered 100% recovery.

Examining Alternative Normalizations

The TPTR trace analyses discussed so far are based on a normalization of the moles of oxygen released per mole of sample oxide. This is convenient since it is equivalent to δ, but there are potential issues with this normalization approach. Built into this normalization is a bias against compositions with less oxygen per formula unit (e.g., ceria's two oxygens vs. BCNF's six). Alternative options for normalization can shift the results of the figures of merit (mostly extent of reduction, the others are largely unaffected), potentially enabling a more representative analysis. **Figure 4** compares four different normalization options; namely normalization by (A) moles of oxide, (B) mass of oxide, (C) moles of oxide oxygen, and (D) moles of oxide atoms. Oxide mass normalization (**Figure 4B**) leads to dramatic shifts in the BNF and BCNF traces, while the others are only modestly affected. The shifts between **Figures 4A,B** are simply due to the way the chemical formulae for the double perovskites are written (or how the unit cell is defined) and do not reflect any fundamental changes in materials behavior. For mass-based normalization, there will also be a bias towards lighter elements, although this does not appear to be a large driver in STCH viability. It is possible to remove both the formula and mass bias by normalizing with a metric that better captures the relative oxygen content of each material. One possibility is to normalize by the number of moles of oxygen in the oxide. This normalizes differences between simple oxides like ceria and complex oxides like BCNF and BNF. As shown in **Figure 4C**, this normalization procedure results in additional shifts for BCNF and BNF. Most of the other compositions remain unchanged since they are simple perovskites. Finally, as shown in **Figure 4D**, the normalization can be taken one step further so that all the atoms in the oxide, rather than just the oxygen atoms are used in the normalization. This makes a small difference for the simple fluoride ceria, but most other compositions remain unaffected compared to normalization by the oxygen-atoms only.

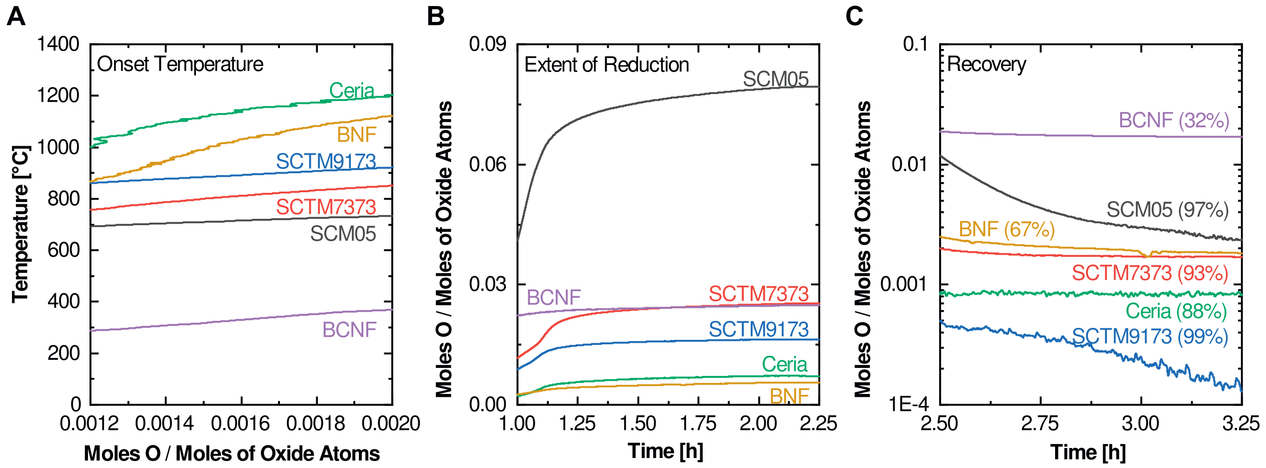

FIGURE 5 | Highlight plots of the relevant experimental data regions for the three figures of merit after re-normalization using moles of oxide atoms: **(A)** Onset temperature, **(B)** Extent of reduction, and **(C)** Recovery (calculated percentage of reoxidation at 1,000°C is also listed).

Importantly, however, the total number of atoms has a strong influence on the heat capacity of a material, which unlike mass alone, is strongly correlated with STCH efficiency. For that reason, total atoms is increasingly viewed as the preferred normalization for hydrogen productivity, so we propose employing this normalization option (i.e., **Figure 4D**) for TPTR analysis as well.

Revisiting the figures of merit to account for the moles of oxide atoms normalization approach (**Figure 5**) shows that, with the exception of BNF, the order for onset temperature and recovery for the six oxides examined here do not change relative to the original normalization approach (although as expected, the actual magnitudes have changed such that target ranges need to be revised). The exception is the large increase in onset temperature for BNF. This is most likely an artifact of the dramatic change in slope of the low temperature portion of the curve between the two normalizations. BCNF and BNF show dramatic changes in the extent of reduction using the moles of oxide atoms normalization approach; under this normalization method, BCNF is seen to be a more attractive candidate than previously viewed, although its other figures of merit remain poor. Even with the modified normalization, BNF does not appear to be viable for STCH application.

Correlation With Water-Splitting Performance

Five of the new compositions were sent to Sandia National Lab for water-splitting experiments using their SFR (SCM05 was estimated from data for higher ceria contents published in Bergeson-Keller et al.). By comparing the TPTR screening results to the SFR water splitting results, we identified target ranges for the three figures of merit that result in water splitting activity. **Figure 6** plots a wide variety of compositions, both those obtained directly from this study as well as results from other relevant published materials, using the first two figures of merit as the coordinate axes (**Figure 6A** uses the simple normalization while **Figure 6B** uses the number of oxide atoms normalization). **Table 1** summarizes all included materials and their hydrogen yields.

The results show that low onset temperatures and high extents of reduction are indeed strongly associated with little or no water splitting. While there doesn't appear to be a strong correlation between the hydrogen yields and position on either axis, there is nevertheless a clear clustering of the viable water-splitting materials. The cluster is tighter in **Figure 6A**, however the normalization in **Figure 6B** better predicts that BNF will behave like ceria. The shaded regions in **Figure 6** encompass most of the materials that successfully split water, and thus can be used to establish target ranges for reduction onset temperature and extent of reduction.

What is not captured in this representation is how the production will change under more challenging oxidation conditions. As discussed elsewhere (Bayon et al., 2022; Li et al., 2022), there is a problem with most perovskite compositions as an excessive quantity of steam is needed to produce significant hydrogen. In most cases, steam-to-hydrogen ratios in excess of 500:1 are necessary for compositions like SLMA to split at all. This inefficiency has hindered the adoption of perovskites as viable STCH materials. Testing under ratios lower than pure steam has only been carried out for select materials in this study and a few others. As the results show in **Table 1**, only ceria and BCM continue to split water near the levels achieved under pure steam, all other drop to less than 32%. Interestingly, ceria and BCM lie at different ends of the target window. BCM may be an outlier, however, since most analysis strongly correlates higher reduction enthalpy values to improved performance under low steam-to-hydrogen ratio conditions (Muhich et al., 2018), which is also related to onset temperatures and extents of reduction closer to ceria than BCM (lower right corner of **Figure 6**).

Limitations and Pitfalls of TPTR

While TPTR is especially useful as a rapid screening method, it is not recommended as a replacement for actual thermochemical

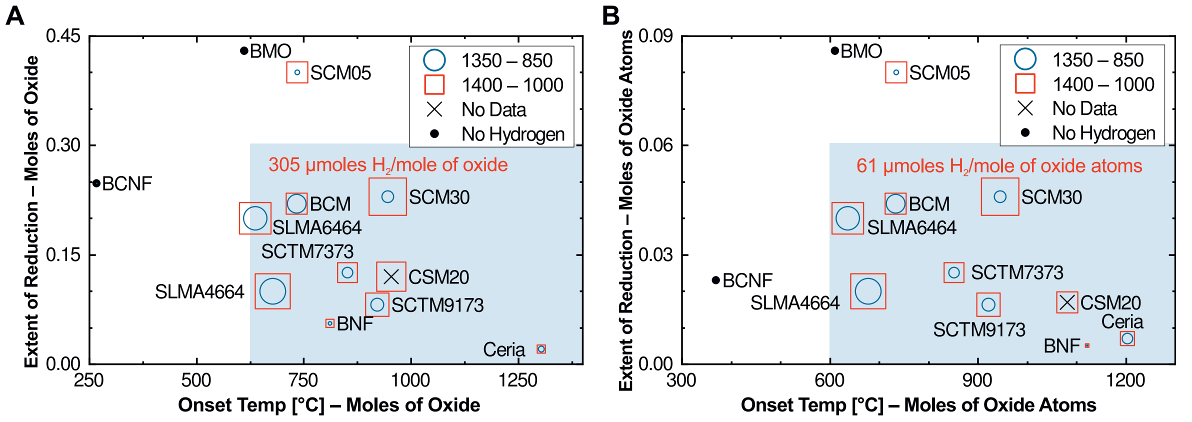

FIGURE 6 | Comparison of water-splitting hydrogen yields for new compositions, along with other published results from same facility, using both normalizations; **(A)** moles of oxide, and **(B)** moles of oxide atoms. Symbol sizes represent the magnitude of hydrogen produced during actual water-splitting for two different redox temperature pairs. The maximum production, SCM30 under the higher temperature conditions, is listed on the plot for scale. Shading indicates the target window for onset temperature and extent of reduction (McDaniel et al., 2013; Barcellos et al., 2018; Barcellos et al., 2019; Bergeson-Keller et al., 2022).

TABLE 1 | Summary of hydrogen yields from water-splitting experiments.

	µmoles H_2 per Mole of Oxide		µmoles H_2 per Mole of Oxide Atoms		% Of Max H_2 Production at H_2O:H_2 Ratio of 1,333:1
	1,350–850	1,400–1,000	1,350–850	1,400–1,000	
Ceria	51	71	17	24	100[c]
SCM05[b]	40[a]	175[a]	8[a]	35[a]	—
SCTM9173	102	193	20.4	38.6	25
SCTM7373	83	166	16.6	33.2	—
BNF	32.4	78.4	3.2	7.8	32
BCNF	8.82	6.19	0.88	0.62	—
$Sr_{0.7}Ce_{0.3}MnO_{3-\delta}$ (SCM30)[b]	91	305	18.2	61	—
$BaMnO_{3-\delta}$ (BMO)[c]	0	0	0	0	—
$BaCe_{0.25}Mn_{0.75}O_{3-\delta}$ (BCM)[c]	140	181	28	36.2	71[c]
$Ce_{0.2}Sr_{1.8}MnO_{4-\delta}$ (CSM20)[d]	—	247	—	35	26
$Sr_{0.6}La_{0.4}Mn_{0.6}Al_{0.4}O_{3-\delta}$ (SLMA6464)[e]	175	263	35	53	—
$Sr_{0.4}La_{0.6}Mn_{0.4}Al_{0.6}O_{3-\delta}$ (SLMA4664)[e]	194	292	38	58.4	26[c]

[a] *Estimated.*
[b] *(Bergeson-Keller, Sanders, and O'Hayre 2022).*
[c] *(Barcellos et al., 2018).*
[d] *(Barcellos et al., 2019).*
[e] *(McDaniel et al., 2013).*

testing and/or thermodynamic studies. As stated previously, actual water-splitting capability correlates well with the TPTR predictions, but variations do occur, and two materials with similar TPTR results may nevertheless show significant differences in thermochemical activity and hydrogen production. We partly ascribe such discrepancies to a major limitation of TPTR: kinetic behavior is not fully captured. This is especially true for oxidation, where the use of air can mask problems in oxidation kinetics due to the larger required driving force and differing reaction mechanism(s) for reoxidation by water-splitting vs. simple reoxidation in air. Poor reduction kinetics can also mask true extent of reduction results. Another related limitation is that a full thermodynamic picture is not developed by the single set of conditions present in TPTR. Such testing is not meant to tease apart the enthalpic and entropic contributions for a given material, but rather give an indication as to whether such exploration is warranted.

Another limitation is that the TPTR screening test is most relevant to short, non-isothermal cycles. Materials designed for isothermal cycling or that rely on full phase changes would likely perform very poorly under these screening conditions. However, the basic premise of the TPTR screening procedure could be adapted by changing the experimental conditions to mimic isothermal redox cycling or use longer soak times to examine phase-change materials; it is possible that useful analogous figures of merit can be established for such scenarios.

Finally, one of the largest pitfalls of TPTR analysis, and non-stoichiometry analysis in general, is the complexity posed by multi-phase samples. If the sample of interest is not a single phase or undergoes decomposition into one or more new phases during the TPTR test, this can complicate or completely invalidate the screening results. The analysis is based on the implicit assumption that the entire sample behaves as a single redox-active phase. If a sample instead consists of an unknown mix of phases, each of which presents a different redox behavior, then the results require careful scrutiny. For example, if the redox active phase is a minority phase diluted by non-active secondary phases, the TPTR results will be skewed, especially the extent of reduction, which will be greatly underestimated. This may give false positives for compositions that would reduce too much if phase-pure or false negatives if the extent of reduction appears to be very low because only a small amount of redox active phase is present.

Equivalent Methods Using Other Experimental Techniques

A number of other experimental techniques can and have been used to produce similar evaluations of candidate STCH materials without resorting to direct water splitting tests. One alternative is to use a small plug flow reactor, preferably with a rapid heating furnace. Since the mass cannot be tracked in this case, the evolved gas is instead monitored to evaluate the amount of oxygen evolved during reduction and consumed during oxidation. This technique works best for evaluating the reduction process since the resulting sharp oxygen release signal peaks produced during reduction are easier to analyze than the low-signal sigmoidal curves produced by oxygen uptake during reoxidation. With additional complexity, a small solar simulator can be used to achieve similar reduction measurements (Charvin et al., 2007). While these and other techniques are capable of making analogous measurements of redox activity, our view is that they are generally more complex and/or require more specialized equipment than that needed for TPTR. Additionally, these alternative techniques often require far larger sample amounts than the <100 mg needed for TG screening.

CONCLUSION

Temperature-programmed thermal reduction (TPTR) provides a simple TGA-based single-run experiment that measures the redox behavior of a specimen under thermal reduction and reoxidation conditions relevant to STCH. As such, it provides valuable information that can be used to rapidly screen candidate STCH materials without the complexity associated with directly measuring water splitting performance. In this work, several unreported STCH candidates were screened using the TPTR technique, and their water-splitting potential was analyzed on the basis of three figures of merit: reduction onset temperature, extent of reduction, and reoxidation recovery. Target ranges for STCH viability were established by comparing the figures of merit to the actual measured water splitting behavior for a wide variety of materials. We hope that this demonstration motivates the community to consider TPTR as a standardized protocol for the exploration of new and promising STCH candidate oxide materials. For such consideration, a proposed protocol is given in the **Supplementary Material S1**.

DATA AVAILABILITY STATEMENT

The datasets presented in this study can be found in online repositories. The names of the repository/repositories and accession number(s) can be found below: https://datahub.h2awsm.org/.

AUTHOR CONTRIBUTIONS

MS contributed to design of the study and the development of the protocol and performed the bulk of experiments, as well as authored the manuscript. AB-K assisted with experiments and wrote sections of the manuscript. EC assisted with the protocol document. RO provided oversight and critical revisions. All authors contributed to manuscript revision, read, and approved the submitted version.

FUNDING

This material is based upon work supported by the US. Department of Energy's Office of Energy Efficiency and Renewable Energy (EERE) under the Hydrogen and Fuel Cell Technologies Office, Award Number DE-EE0008087 and as a part of HydroGEN Energy Materials Network (EMN) consortium. Sandia National Laboratories is a multi-mission laboratory managed and operated by National Technology and Engineering Solutions of Sandia, LLC, a wholly owned subsidiary of Honeywell International, Inc., for the US. Department of Energy's National Nuclear Security Administration under contract DE-NA0003525. The views expressed in the article do not necessarily represent the views of the DOE or the US. Government.

ACKNOWLEDGMENTS

The authors would like to thank everyone in the STCH community that has organized, assisted in running, and participated over the past 4 years in the HydroGen/AWSM Benchmarking and Protocols Workshops.

SUPPLEMENTARY MATERIAL

The Supplementary Material for this article can be found online at: https://www.frontiersin.org/articles/10.3389/fenrg.2022.856943/full#supplementary-material

REFERENCES

Abanades, S., Charvin, P., Flamant, G., and Neveu, P. (2006). Screening of Water-Splitting Thermochemical Cycles Potentially Attractive for Hydrogen Production by Concentrated Solar Energy. *Energy* 31 (14), 2805–2822. doi:10.1016/j.energy.2005.11.002

Barcellos, D. R., Sanders, M. D., Tong, J., McDaniel, A. H., and O'Hayre, R. P. (2018). BaCe0.25Mn0.75O3−δ-a Promising Perovskite-type Oxide for Solar Thermochemical Hydrogen Production. *Energ. Environ. Sci.* 11 (11), 3256–3265. doi:10.1039/C8EE01989D

Barcellos, D. R., Coury, F. G., Emery, A., Sanders, M., Tong, J., McDaniel, A., et al. (2019). Phase Identification of the Layered Perovskite CexSr2-xMnO4 and Application for Solar Thermochemical Water Splitting. *Inorg. Chem.* 58 (12), 7705–7714. doi:10.1021/acs.inorgchem.8b03487

Bartel, C. J., Rumptz, J. R., Weimer, A. W., Holder, A. M., and Musgrave, C. B. (2019). High-Throughput Equilibrium Analysis of Active Materials for Solar Thermochemical Ammonia Synthesis. *ACS Appl. Mater. Inter.* 11 (28), 24850–24858. doi:10.1021/acsami.9b01242

Bayon, A., de la Calle, A., GhoseGhose, K. K., Page, A., and McNaughton, R. (2020). Experimental, Computational and Thermodynamic Studies in Perovskites Metal Oxides for Thermochemical Fuel Production: A Review. *Int. J. Hydrogen Energ.* 45 (23), 12653–12679. doi:10.1016/j.ijhydene.2020.02.126

Bayon, A., de la Calle, A., Stechel, E. B., and Muhich, C. (2022). Operational Limits of Redox Metal Oxides Performing Thermochemical Water Splitting. *Energy Tech* 10 (1), 2100222. doi:10.1002/ente.202100222

Bergeson-Keller, A. M., Sanders, M. D., O'Hayre, R. P., and O'Hayre, R. P. (2022). Reduction Thermodynamics of Sr1− XCeXMnO3 and CeXSr2− XMnO4 Perovskites for Solar Thermochemical Hydrogen Production. *Energ. Tech* 10 (1), 2100515. doi:10.1002/ente.202100515

Charvin, P., Abanades, S., Flamant, G., and Lemort, F. (2007). Two-step Water Splitting Thermochemical Cycle Based on Iron Oxide Redox Pair for Solar Hydrogen Production. *Energy* 32 (7), 1124–1133. doi:10.1016/j.energy.2006.07.023

Cheng, W.-H., de la Calle, A., Atwater, H. A., Stechel, E. B., and Xiang, C. (2021). Hydrogen from Sunlight and Water: A Side-By-Side Comparison between Photoelectrochemical and Solar Thermochemical Water-Splitting. *ACS Energ. Lett.* 6 (9), 3096–3113. doi:10.1021/acsenergylett.1c00758

Chueh, W. C., Falter, C., Abbott, M., Scipio, D., Furler, P., Haile, S. M., et al. (2010). High-Flux Solar-Driven Thermochemical Dissociation of CO_2 and H_2O Using Nonstoichiometric Ceria. *Science* 330 (6012), 1797–1801. doi:10.1126/science.1197834

Emery, A. A., Saal, J. E., Kirklin, S., Hegde, V. I., and Wolverton, C. (2016). High-Throughput Computational Screening of Perovskites for Thermochemical Water Splitting Applications. *Chem. Mater.* 28 (16), 5621–5634. doi:10.1021/acs.chemmater.6b01182

Hurst, N. W., Gentry, S. J., Jones, A., and McNicol, B. D. (1982). Temperature Programmed Reduction. *Catal. Rev.* 24 (2), 233–309. doi:10.1080/03602458208079654

Jones, A. (1986). *Temperature-Programmed Reduction for Solid Materials Characterization*, New York: M. Dekker.

Li, S., Wheeler, V. M., Kumar, A., Venkataraman, M. B., Muhich, C. L., Hao, Y., et al. (2022). Thermodynamic Guiding Principles for Designing Nonstoichiometric Redox Materials for Solar Thermochemical Fuel Production: Ceria, Perovskites, and beyond. *Energ. Tech* 10 (1), 2000925. doi:10.1002/ente.202000925

Lu, Y., Zhu, L., Agrafiotis, C., Vieten, J., Roeb, M., and Sattler, C. (2019). Solar Fuels Production: Two-step Thermochemical Cycles with Cerium-Based Oxides. *Prog. Energ. Combust. Sci.* 75, 100785. doi:10.1016/j.pecs.2019.100785

McDaniel, A. H., Miller, E. C., Arifin, D., Ambrosini, A., Coker, E. N., O'Hayre, R., et al. (2013). Sr- and Mn-Doped LaAlO3−δ for Solar Thermochemical H2 and CO Production. *Energy Environ. Sci.* 6 (8), 2424–2428. doi:10.1039/C3EE41372A

Muhich, C. L., Blaser, S., Hoes, M. C., and Steinfeld, A. (2018). Comparing the Solar-To-Fuel Energy Conversion Efficiency of Ceria and Perovskite Based Thermochemical Redox Cycles for Splitting H_2O and CO_2. *Int. J. Hydrogen Energ.* 43 (41), 18814–18831. doi:10.1016/j.ijhydene.2018.08.137

Nair, M. M., and Abanades, S. (2018). Experimental Screening of Perovskite Oxides as Efficient Redox Materials for Solar Thermochemical CO_2 Conversion. *Sustain. Energ. Fuels* 2 (4), 843–854. doi:10.1039/C7SE00516D

Qian, X., He, J., Mastronardo, E., Baldassarri, B., Wolverton, C., Haile, S. M., et al. (2020). Favorable Redox Thermodynamics of SrTi0.5Mn0.5O3−δ in Solar Thermochemical Water Splitting. *Chem. Mater.* 32, 9335–9346. doi:10.1021/acs.chemmater.0c03278

Qian, X., He, J., Mastronardo, E., Baldassarri, B., Yuan, W., Wolverton, C., et al. (2021). Outstanding Properties and Performance of CaTi0.5Mn0.5O3-δ for Solar-Driven Thermochemical Hydrogen Production. *Matter* 4 (2), 688–708. doi:10.1016/j.matt.2020.11.016

Sai Gautam, G., Stechel, E. B., and Carter, E. A. (2020). Exploring Ca-Ce-M-O (M = 3d Transition Metal) Oxide Perovskites for Solar Thermochemical Applications. *Chem. Mater.* 32 (23), 9964–9982. doi:10.1021/acs.chemmater.0c02912

Scheffe, J. R., and Steinfeld, A. (2014). Oxygen Exchange Materials for Solar Thermochemical Splitting of H_2O and CO_2: a Review. *Mater. Today* 17 (7), 341–348. doi:10.1016/j.mattod.2014.04.025

Scheffe, J. R., Allendorf, M. D., Coker, E. N., Jacobs, B. W., McDaniel, A. H., and Weimer, A. W. (2011). Hydrogen Production via Chemical Looping Redox Cycles Using Atomic Layer Deposition-Synthesized Iron Oxide and Cobalt Ferrites. *Chem. Mater.* 23 (8), 2030–2038. doi:10.1021/cm103622e

Shang, M., Tong, J., and O'Hayre, R. (2013). A Novel Wet-Chemistry Method for the Synthesis of Multicomponent Nanoparticles: A Case Study of BaCe0.7Zr0.1Y0.1Yb0.1O3−δ. *Mater. Lett.* 92, 382–385. doi:10.1016/j.matlet.2012.11.038

Steinfeld, A. (2005). Solar Thermochemical Production of Hydrogen-Aa Review. *Solar Energy* 78 (5), 603–615. doi:10.1016/j.solener.2003.12.012

Vieten, J., Bulfin, B., Huck, P., Horton, M., Guban, D., Zhu, L., et al. (2019). Materials Design of Perovskite Solid Solutions for Thermochemical Applications. *Energ. Environ. Sci.* 12 (4), 1369–1384. doi:10.1039/C9EE00085B

Voorhoeve, R. J. H., Trimble, L. E., and Khattak, C. P. (1974). Exploration of Perovskite-like Catalysts: Ba2CoWO6 and Ba2FeNbO6 in NO Reduction and CO Oxidation. *Mater. Res. Bull.* 9 (5), 655–666. doi:10.1016/0025-5408(74)90136-6

Wang, Z., Roberts, R. R., Naterer, G. F., and Gabriel, K. S. (2012). Comparison of Thermochemical, Electrolytic, Photoelectrolytic and Photochemical Solar-To-Hydrogen Production Technologies. *Int. J. Hydrogen Energ.* 37 (21), 16287–16301. doi:10.1016/j.ijhydene.2012.03.057

Zhang, G., Sun, S., Jiang, W., Miao, X., Zhao, Z., Zhang, X., et al. (2017). A Novel Perovskite SrTiO3-Ba2FeNbO6Solid Solution for Visible Light Photocatalytic Hydrogen Production. *Adv. Energ. Mater.* 7 (2), 1600932. doi:10.1002/aenm.201600932

Conflict of Interest: The authors declare that the research was conducted in the absence of any commercial or financial relationships that could be construed as a potential conflict of interest.

The handling editor ES declared a past collaboration with the author(s) EC.

frontiers | Frontiers in Energy Research

METHODS
published: 25 April 2022
doi: 10.3389/fenrg.2022.817981

Metal-Supported Solid Oxide Electrolysis Cell Test Standard Operating Procedure

*Fengyu Shen, Martha M. Welander and Michael C. Tucker**

Energy Storage Group, Energy Storage and Distributed Resources Division, Lawrence Berkeley National Laboratory, Berkeley, CA, United States

This procedure describes the setup and testing protocol for metal-supported solid oxide electrolysis cell (MS-SOEC) button cell performance evaluation. It defines a standard testing protocol, describes materials selection, and identifies common pitfalls for testing MS-SOEC button cells.

Keywords: Soec, metal-supported, standard operating procedure, glass seal, ceramic paste

Edited by:
Marcelo Carmo,
Nel, Norway

Reviewed by:
Aniruddha Pramod Kulkarni,
Commonwealth Scientific and Industrial Research Organisation (CSIRO), Australia
Dong Ding,
Idaho National Laboratory (DOE), United States

***Correspondence:**
Michael C. Tucker
mctucker@lbl.gov

Specialty section:
This article was submitted to Process and Energy Systems Engineering, a section of the journal Frontiers in Energy Research

Received: *18 November 2021*
Accepted: *05 April 2022*
Published: *25 April 2022*

Citation:
Shen F, Welander MM and Tucker MC (2022) Metal-Supported Solid Oxide Electrolysis Cell Test Standard Operating Procedure. Front. Energy Res. 10:817981. doi: 10.3389/fenrg.2022.817981

INTRODUCTION

This procedure describes the setup and testing of metal-supported solid oxide electrolysis cell (MS-SOEC) button cells. Many features are quite similar to the procedure for testing electrode-supported or electrolyte-supported SOECs. There are several key differences for MS-SOECs, however. The operating and sealing temperature limits are lower, as MS-SOECs with stainless steel supports should not be exposed to oxidizing conditions at temperatures that promote rapid chromia scale growth. The operating temperature is typically lower than 750°C for long term stability, and the maximum sealing temperature is around 850°C. For symmetric-architecture MS-SOECs with porous metal supports on both sides, the sealing surface is the thin face of the dense electrolyte on the edge of the cell. This makes compression seals difficult to implement, so glass paste or ceramic adhesive seals are preferred. Electrical leads can be directly spot-welded to the metal support, eliminating the challenges associated with applying paste-and-mesh current collectors.

Several groups globally have reported MS-SOEC steam electrolysis testing efforts, and the results were reviewed recently (Tucker, 2020). For oxide-conducting MS-SOECs, cells were operated in the temperature range 600–800°C with steam content ranging from 30 to 90%. Proton-conducting MS-SOECs were typically operated around 600°C, with some as low as 400°C. A range of test rig designs, materials, and sealing strategies were implemented. For example, a ceramic rig with Pt mesh current collectors and gold/glass sealing was used to test an oxide-conducting cell prepared by plasma spraying the electrolyte onto a stainless steel substrate (Schiller et al., 2009). A stainless steel rig with Pt mesh current collectors welded to the cell and glass sealing was used to test an oxide-conducting cell prepared by co-sintering and catalyst infiltration (Wang et al., 2019; Shen et al., 2020). A commercial Probostat test rig with Pt mesh and Pt paste current collector and compressed mica seal was used to test a proton-conducting cell prepared by pulsed laser deposition (Stange et al., 2017). In many cases the details of the test rig, sealing material, and test protocol were not reported.

AbbreviationsAcronyms: ASC/ESC, anode-supported cell or electrolyte-supported cell; ASR, area-specific resistance; CTE, coefficient of thermal expansion; DI, deionized (water); MS-SOEC, metal-supported solid oxide electrolysis cell; OCV, open-circuit voltage; SOEC, solid oxide electrolysis cell; SOFC, solid oxide fuel cell; SCCM, standard cubic centimeters per minute.

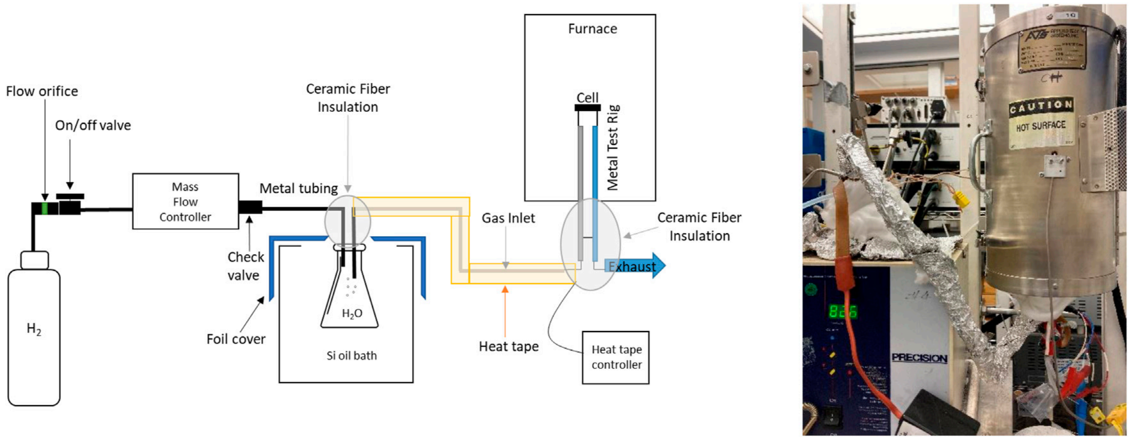

FIGURE 1 | Schematic and photograph of a MS-SOEC test setup with a heated bubbler as the humidification system.

The objectives of this procedure are to define a standard testing protocol, describe materials selection, and identify common pitfalls for testing MS-SOEC button cells. This procedure contains preparation and operation details specific to MS-SOECs, a discussion of seal and test rig materials, alternative sealing and start-up protocols for a metal test rig with glass seal or alumina test rig with ceramic adhesive seal, and a discussion of the consequences of off-normal operation.

PROTOCOL SCOPE

Scope and Applicability

This procedure applies to sealing and operation of MS-SOEC button cells. Procedures for larger cells mounted with flowfields, manifolds, or interconnects can be adapted from this procedure but are not explicitly described. The procedure does not cover cell fabrication, rig design details, steam generator or humidifier designs, detailed electrochemical diagnostic, and operational techniques, or post-mortem analysis, many of which are covered in detail elsewhere in this issue. The step-by-step procedure was developed during the authors' research on symmetric cells with oxide-conducting electrolyte and porous stainless steel supports on both sides. Variations in the procedure for other electrolyte and support materials or cell architectures may be necessary.

Summary of Method

The protocol provides for reproducible operation of MS-SOEC button cells at a variety of operating conditions. A pre-fabricated metal-supported solid oxide electrolysis cell is connected to a platinum or nickel mesh with conductive wire leads on the steam electrode side. Then the cell is sealed on a test rig (typically with glass paste or ceramic adhesive). Hydrogen is humidified to a specific steam content and delivered to the test rig via a heated tube. The MS-SOEC is then operated. A schematic setup with heated bubbler for controlling the steam:hydrogen ratio is shown in **Figure 1**.

Personnel Qualifications/Responsibilities

Users must be trained on the safe handling and use of hydrogen, high-temperature furnaces, pressurized gas systems, and electrical systems. Users also need basic knowledge of electrochemistry and understanding of electrochemical characterization methods prior to implementing the procedure. Additional training or certification is required before modifying the setup or equipment, for example the Qualified Electrical Worker training.

Health and Safety Warning

H_2 is flammable and explosive, with flammability occurring between the limits of 4.0 and 75.0% based on the volume of hydrogen in air at 1 atm. H_2 cylinders should be secured away from the testing furnace or any other heat source. Metal tubing (not plastic) should be used for H_2 and all tubing and connections should be leak-checked before normal operation. The testing furnace should be located in a fume hood or other ventilated area for increased safety in the case of a hydrogen leak. It is preferred to have a hydrogen gas sensor mounted in the lab area. Other hazards include: glassware which may become pressurized, electrical energy, hot steam, and hot surfaces. Follow guidelines of the research institute, fire marshal, and other regulatory bodies.

Equipment and Supplies

Examples of useful equipment and supplies are listed in **Table 1**. Many alternatives exist, but these items have been used successfully by the authors. Required equipment includes a furnace, electrochemical potentiostat, mass flow controller, humidification system, and gas delivery system for hydrogen. Optional equipment includes a gas delivery system for air, humidity meter (for example EE23, E + E Elektronik Ges.m.b.H, Germany) suitable for high absolute humidity, hydrogen sensor, and fume hood.

Options for the hydrogen humidification system include a heated bubbler, reaction of mixed oxygen, and excess hydrogen streams inside the test rig, a controlled evaporation mixer,

TABLE 1 | List of suitable supplies and test stand equipment.

Item	Supplier	Part number or model	Notes
Supplies			
Seal—glass powder	Schott	GM31107	Demonstrated for >1000 h operation
Seal—vehicle for glass	Fuel Cell Materials	311237 VEH	Good viscosity for syringe application of paste
Seal—ceramic paste	Aremco	Ceramabond 552	Contains some alkali elements
Pt mesh	Johnson Matthey	11714, 52 mesh, 0.1 mm diam	Flexible, but strong enough for spot welding
Ni mesh	Alfa aesar	44128, 100 mesh, 0.1 mm diam	Flexible, but strong enough for spot welding
Test stand			
Mass flow controller	Alicat	MC-500SCCM-D/5M	Built-in controller and display
Oil bath	Polyscience	WBE02	Fits 500 ml glass jar
Silicone oil	Alfa aesar	A12728	Rated –40–200°C
Ported cap	Ace glass	7632-02 for GL-45 glass bottle	Keep out of silicone oil, which degrades cap strength
Heat tape	Briskheat	BS0101060LG	Wraps easily around 1/4″ stainless steel gas tubing
Heat tape controller	Digi-sense	TC1500	Safer and more precise control than on/off time controllers
Heat tape over-temp. shutoff	Briskheat	HL120KA-C	Prevents over-heating of gas line
Insulation—alumina mat	Zircar	D9201	High purity, rated to 1650°C
Test furnace	Applied test systems	3210 split tube furnace	NRTL-listed, rated to 1000°C
Potentiostat	Biologic	VMP-300	External boosters available for wide range of current

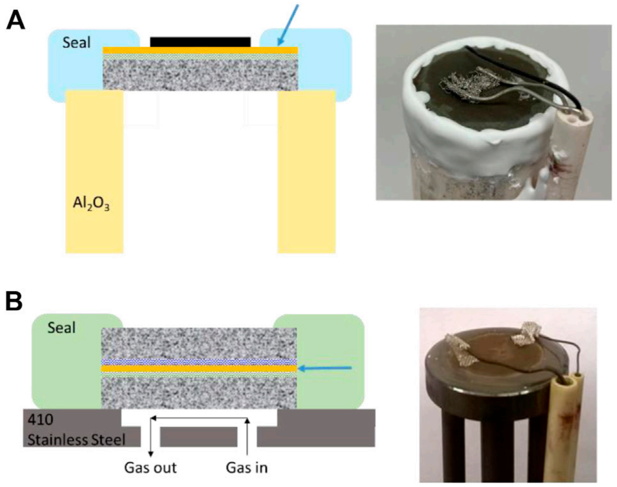

FIGURE 2 | Schematic and photographs of MS-SOECs sealed onto test rigs. Electrical lead wires and gas tubing are omitted from the schematic for clarity. The arrows point to the critical sealing surface where the seal material (light blue or light green) contacts the dense electrolyte layer (orange). **(A)** MS-SOEC with a metal support on one side only, and exposed electrolyte on the perimeter of the top surface, sealed to an alumina tube test rig using ceramic adhesive. **(B)** Symmetric-architecture MS-SOEC mounted with glass seal on a test rig machined from 410 stainless steel. Note that the sealing surface is much smaller for **(B)**.

vaporization chamber with low-flow liquid pump for water delivery, a pressurized vaporization chamber with restricted flow orifice, and a steam generator. Due to the low flowrates associated with button cell operation, the first two options are the most suitable, whereas the other options are preferred for large cells or stacks. Downstream of the hydrogen/steam mixing unit (for example a heated bubbler), all tubing and connections must be heated to above the dewpoint of mixture to eliminate condensation of liquid water. A temperature of ~120°C is recommended. This can be accomplished with heat-traced lines or heating tapes wrapped around the lines. Junctions between lines and other fittings are common cold spots, and special attention must be paid to insulating or actively heating them.

Required materials include hydrogen, DI water, and a seal material. Optional materials include compressed air and an ink vehicle for glass powder such as terpineol.

The ubiquitous alumina tube test rig design used in research laboratories worldwide for SOFC/SOEC button cell testing can also be used for MS-SOEC testing, **Figure 2A** (Pomfret et al., 2008; Wu et al., 2017; Shen and Lu, 2018; Cui et al., 2021). A ceramic adhesive or sealing glass that wets and bonds to both the button cell and the test rig is required. Alumina paste (Ceramabond 552, Aremco) or glass powder (GL-1709, Mo-Sci) are acceptable (Tucker, 2017; Wu et al., 2017). The alumina tube and MS-SOEC have significantly different coefficients of thermal expansion (CTE), and the resulting stress typically cracks the seal during cooling down from operating temperature to room temperature. This precludes repeated or rapid thermal cycling, which is an important feature to demonstrate for MS-SOECs. A metal test rig with well-matched CTE enables thermal cycling. Stainless steel alloy 410 is a suitable material for the test rig. Various glasses will wet and bond with the metal test rig and MS-SOEC, including GM31107 (Schott) and V1515 (3M) (Tucker, 2017; Deka et al., 2019). Both have CTE that is well matched with the metal components, enabling rapid thermal cycling. Seal materials that contain K or Na can accelerate Cr poisoning of the SOEC anode by enhancing Cr evaporation from nearby stainless steel components (Cruse et al., 2007; Tucker et al., 2017). This is especially a concern for MS-SOEC architectures that have a porous Cr-containing alloy support, such as stainless steel, in the anode (oxygen) side, **Figure 2B**. Cermabond 552 contains Na, so is best used for short-term performance studies only. Alkali-free glasses, such as GM31107 are preferred for long-term durability studies.

PROCEDURE

Step-by-Step Procedure

Step by Step Procedure—metal rig and glass seal

1) Check the test rig for any damage. Polish the surface which will be in contact with the cell with sandpaper.
2) Prepare glass seal slurry: A typical example is 12 g Schott GM31107 glass powder and 3 g terpineol ink vehicle mixed by a centrifugal mixer (Thinky, Japan). A typical amount of slurry used is 60 mg per cm of cell perimeter length.
3) Connect the steam electrode to a Pt or nickel mesh by spot welding. The mesh is spot welded to metal wire leads for electrical connection to the potentiostat.
4) Center the cell on the test rig and load glass paste on the edge of the cell with a syringe. It is critical to ensure the seal material contacts the thin electrolyte edge, as this is the sealing surface, see **Figure 2B**. Typical thermal treatment: 90°C/0.2 h (10°C/min), 200°C/0 h (2°C/min), 700°C/1 h (10°C/min), cool down to room temperature (10°C/min).
5) Connect the air electrode to a Pt or Au mesh by spot welding. Similar to the steam electrode side, the mesh is spot welded to metal wire leads for electrical connection.
6) Apply a second layer of glass slurry if needed to cover defects in the first layer and fire it with the same procedure.
7) Connect the conductive metal wires to the potentiostat and monitor the OCV change. The OCV should be close to 0 V.
8) Check the water bubbler and H_2 tubing. Make sure all connections are tight and there is no leakage.
9) Flush the water bubbler with H_2 to remove the oxygen inside.
10) Flush the test rig with nitrogen before connecting it to the H_2 tube. The OCV is around 0.1 V with nitrogen.
11) Connect H_2 tube to the test rig. The OCV should increase to >1.1 V. Typical H_2 flow is 150 SCCM for 3% H_2O/97% H_2 and 75 SCCM for 50% H_2O/50% H_2. Keep an eye on the water level in the bubbler during testing and refill it if the water is depleted.
12) Set the temperature (81.7°C for 50% H_2O/50% H_2) of the silicone oil bath with the DI water bubbler inside. Wrap the metal tube connecting the bubbler to the test rig with a heating belt. Set the temperature of the heating belt to be 40 °C higher than the oil bath (around 120°C). It should be noted to avoid wrapping the heat tape on itself or it could be burned.
13) Wait for equilibrium of the bubbler temperature; it could take up to 2 h.
14) Conduct electrochemical tests, such as LSV, EIS at OCV, durability with constant voltage or current. For LSV, scan the voltage from 0 V (*vs.* Eoc) to 1.5 V (*vs.* Ref) with the speed of 10 mV/s. For EIS at OCV, scan the frequency from 200 kHz to 100 mHz with amplitude of 5 mV. For the durability test, apply a constant voltage (like 1.3 V *vs.* Ref) or a constant current (like 2.5 A, which is equal to 0.5 A/cm^2 for a 5 cm^2 cell).

Step by Step Procedure—alumina rig and ceramic adhesive seal

1) Secure fuel electrode electrical leads by spot welding with Pt or Ni mesh.
2) Mix the alumina paste (Ceramabond 552, Aremco) well and apply a thin layer of paste to the top surface of the alumina test rig tube.
3) Working quickly (to avoid dry paste), center the SOEC button cell on the test rig with the steam electrode and wires facing down and press down gently to secure to the alumina paste. Allow to dry for ~1 h.
4) Apply another layer of the alumina paste to the perimeter of the SOEC taking care to thoroughly seal the dense electrolyte on the edge of the cell. A typical amount of paste is 100 mg per cm of cell perimeter length. Allow to dry for ~1 h.
5) Apply a third layer of paste to drape over the edge of the cell. Allow to dry for ~1 h and repeat.
6) Spot weld the electrical leads to the oxygen electrode (facing up) using Pt or Au mesh.
7) Curing the alumina paste can be done in the same furnace used for testing. Typical thermal treatment includes: 93°C/2 h (10°C/min), 260°C/2 h (2°C/min), and 700°C/hold (10°C/min). Thermal treatment can be done under flowing H_2 starting at room temperature. This is in contrast to the glass seal, where the cell and seal is heated in air then hydrogen is introduced at the operating temperature.
8) Check tubing and connections for leaks, and flush the system with nitrogen prior to the flow of H_2.
9) When the cell is at desired operating temperature, connect metal wires to the potentiostat and monitor OCV. The OCV should be > 1.1 V.
10) For operation with 50%H_2O/50%H_2 conditions see steps 12–13 above.
11) Wait for the temperature of the water bubbler to reach equilibrium and conduct the electrochemical test (see step14 above).

When the test is done and the furnace has cooled down to room temperature, disassemble the cell from the rig. For glass seal, one way to detach the cell from the test rig is using a diamond saw to cut off a small seam on the interface of the cell edge and the glass seal, and then peel off the cell with a tweezer. Ceramic adhesive seals often are cracked after cooling down, and can be removed by grinding with an abrasive wheel or by impacting with a small hammer. Measure the active area of the cell for use in calculating the current density, hydrogen production rate, or other area-based metrics. For a cell with metal support on one side only, the active area is generally defined by the smaller electrode (top electrode in **Figure 2A**). For a symmetric-architecture cell with metal supports on both sides, the active area is defined by the portion of the cell that is not covered by seal material.

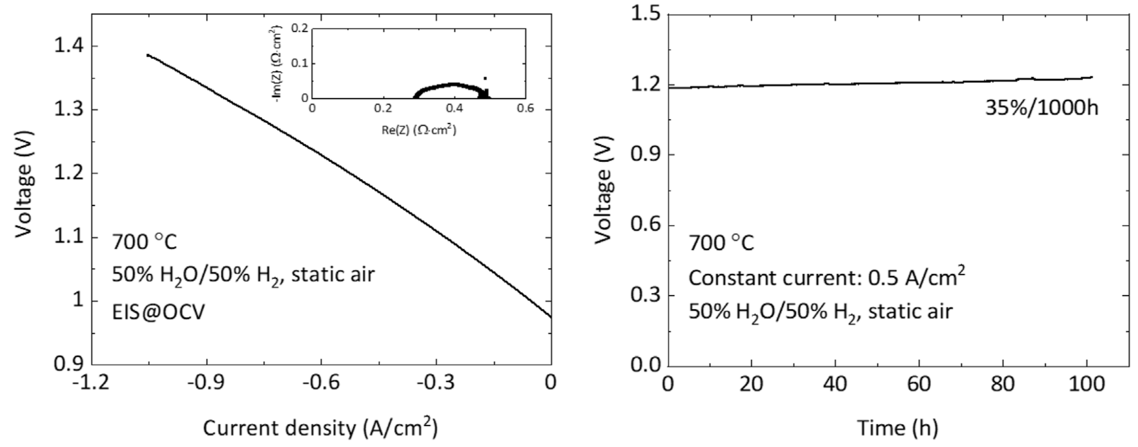

FIGURE 3 | An example of graphical data reporting. **(A)** I-V plot with EIS at OCV (~0.97 V); **(B)** Durability.

The procedure for metal-supported proton-conducting electrolysis cells is similar to that described above except for the gas compositions. Generally, dry hydrogen or nitrogen is used as the sweep gas on the cathode and steam/air or steam/oxygen on the anode side.

Possible improvements include adding flowing air to sweep oxygen produced at the anode. It is recommended to intermittently monitor OCV when undertaking long-term tests, to assess electrolyte or seal damage that could result in gas leakage. When performing electrolysis operation, a drop in OCV due to leakage or increased steam content appears as a false improvement in performance (increased current at fixed voltage, or decreased voltage at fixed current). While 50% H_2O/50% H_2 and 700°C is the standard operating point, it is useful to characterize the cell performance over a wide range of steam: hydrogen ratio and operating temperature. In addition, limiting the voltage to <1.8 V is important for the constant current mode, as the voltage could spike due to off-normal operation, such as heating tape failure, water depletion in the bubbler, and so on. The high voltage would delaminate the cell, leading to test failure.

Sample Preparation and Analysis

It is desirable to monitor and analyze the composition of the inlet and outlet gases, especially the hydrogen content, to enable a mass balance on the cell operation. Suitable methods include humidity meter, gas chromatography, flame detection, and others. Implementation is outside the scope of this procedure.

Data Collection, Analysis, and Results

After acquiring raw data, the current, power, hydrogen production rate, ohmic and polarization impedances, and other area-dependent metrics must be normalized by the active area of the cell. All figures should have the initial OCV, steam:hydrogen ratio, temperature, and constant current density or constant voltage clearly stated in the figure or in the figure caption. The polarization curve should be reported with voltage on the *y*-axis and current density on the *x*-axis with negative current density for electrolysis mode. The electrochemical impedance spectrum should be reported with square axes using the same number spacing on both axes to preserve the shape of the spectrum. Durability should be reported as voltage or current density vs. time, with calculated ASR optionally shown on a second *y*-axis. Degradation rates should be reported as %/1000 h (or % kh^{-1}). An example of the data reporting is shown in **Figure 3**.

QUALITY CONTROL AND QUALITY ASSURANCE

Instrument or Method Calibration and Standardization

Calibrate the electrochemical work station, thermocouple readouts, and flow meters periodically using the manufacturer recommended procedure. Repeat experiments with multiple cells to confirm the quality of the data. Maintaining the steam: hydrogen ratio at the intended level is critically important, as it impacts the OCV and polarization behavior of the cell. Using a thermocouple, calibrate the temperature controller for the heated bubbler by measuring the difference between the set point value and the temperatures in the water and at the outlet of the bubbler. Do the same for the heating tape or heat tracing on the gas delivery tubing and fittings, for which the temperature should be at least 20°C higher than the dew point of the flowing gas to avoid cold spots and condensation. Confirm the steam:hydrogen ratio at the junction between the test rig and gas delivery tubing, using a humidity meter with the sensor heated to above the dew point. Sealant loading on the cell edge changes the active area of the cell in contact with the supplied gases, and the small area of the cell covered by sealant do not participate in the electrochemical reactions. It is recommended to keep the same loading area to enhance cell performance repeatability.

Durability tests are prone to be interrupted by water bubbler refilling. When the water is colder immediately after refilling, the partial pressure of steam supplied to the cell is lower. For fixed current, this causes an increase in operating voltage and possibly mass transport limitation. If the cell voltage spikes too high, the cell could be damaged permanently. To avoid this, pause the cell operation when refilling the bubbler and restart after the water warms up and the OCV stabilizes, which could take around 1 h.

Cautions, Common Issues, and Interferences

To avoid an explosive mixture entering the hot zone, flush the bubbler with H_2 and flush the test rig with nitrogen to remove oxygen inside before connecting the gas delivery system to the test rig. To avoid shattering the glass humidification bubbler jar in the event of over-pressure, install a pressure release valve (<10 psi) upstream of the bubbler.

Use a four-probe test system to compensate for resistance in the conductive wires, by attaching one voltage lead and one current lead to each electrode. The current lead must be thick enough to pass the total cell current without overheating. Pt wire of at least 0.75 mm diameter is recommended. Thin wire can become hot at high current, posing a safety risk, and also limiting the lifetime of the wire.

The metal test rig must not be in contact with electrical ground or electrified components of the system. A common issue is that the metal test rig comes into contact with a metal tube, metal clamp, etc. Because the metal test rig is also in contact with the cell, the potential of the cell will not be “floating”, and the potentiostat will pass current to the contacted metal as well as the cell. This often appears as unstable OCV, noisy data, or a large drop in voltage between OCV and the first data point when doing a current-voltage polarization scan. This issue can be avoided by insulating nearby metal components, and installing a short PTFE or alumina tube between the test rig and the metal gas delivery tubing to electrically isolate the test rig from the gas delivery system.

Maintaining the intended steam:hydrogen ratio throughout the system can be challenging. If the OCV is higher than 0.97 V with 50% H_2O/50% H_2, the moisture concentration could be lower than the intended 50%. This may be due to the bubbler or tubing temperature being lower than 81.7°C, and the user must search for cold spots in the gas delivery system. If the exhaust gas line coming from the test rig out of the furnace is colder than the dew point at that location, liquid water will condense. The droplets of water can block the exhaust flow, or be pushed out as liquid slugs by the exhaust gas. This causes small changes in pressure and flowrate which can appear as noise in the current or voltage data. Refilling the humidification bubbler with water generally changes the temperature of the bubbler, and therefore the steam:hydrogen ratio. One way to minimize the impact is to add the fresh cold water slowly through a tube inserted to the bottom of the bubbler. This minimizes the change in temperature of the top of the water column, which is in direct contact with the flowing gas and therefore controls the dewpoint of the gas. Pre-heating the water before adding it to the bubbler is also useful. If addition of cold water to the bubbler causes a drop in steam content, and the cell is held at constant current, then the cell voltage can briefly rise until the water warms up. If the voltage is above a certain threshold, it can permanently damage the cell. We observe that the cell voltage must be below ~1.85 V to avoid permanent damage.

Stainless steel supports are sensitive to oxidation, which is highly temperature-dependent (Karczewski et al., 2019; Reisert et al., 2020). If there is a pinhole in the electrolyte or seal, it may cause local heating due to hydrogen burning. This heating can cause rapid breakaway oxidation of the support and the resulting local volume change can cause cracking of the electrolyte or delamination (Dogdibegovic et al., 2019). The crack promotes further burning and heating, quickly leading to cell failure. A telltale sign of this phenomenon is rapid decay of OCV, and brown/red iron oxide visible on the failed cell. Cells should be leak-tested before long-term operation begins. If the OCV is much lower than 1.1 V with 3% H_2O/97% H_2, the cell or seal could be leaking.

DATA AVAILABILITY STATEMENT

The original contributions presented in the study are included in the article/**Supplementary Material**, further inquiries can be directed to the corresponding author.

AUTHOR CONTRIBUTIONS

FS, MW, and MT contributed to protocol development, writing, and editing. MT contributed to funding acquisition.

FUNDING

This material is based upon work supported by the United States Department of Energy’s Office of Energy Efficiency and Renewable Energy (EERE) under the Hydrogen and Fuel Cell Technologies Office (HFTO) HydroGEN program. This work was funded in part by the United States Department of Energy under contract no. DE-AC02-05CH11231.

ACKNOWLEDGMENTS

The authors thank Ruofan Wang for establishing the initial MS-SOEC test setup on which this work is based. The views and opinions of the authors expressed herein do not necessarily state or reflect those of the United States Government or any agency thereof. Neither the United States Government nor any agency thereof, nor any of their employees, makes any warranty, expressed or implied, or assumes any legal liability or responsibility for the accuracy, completeness, or usefulness of any information, apparatus, product, or process disclosed, or represents that its use would not infringe privately owned rights.

SUPPLEMENTARY MATERIAL

The Supplementary Material for this article can be found online at: https://www.frontiersin.org/articles/10.3389/fenrg.2022.817981/full#supplementary-material

REFERENCES

Cruse, T. A., Ingram, B. J., Liu, D.-J., and Krumpelt, M. (2007). Chromium Reactions and Transport in Solid Oxide Fuel Cells. *ECS Trans.* 5, 335–346. doi:10.1149/1.2729015

Cui, C., Wang, Y., Tong, Y., Wang, S., Chen, C., and Zhan, Z. (2021). Syngas Production through CH4-Assisted Co-electrolysis of H2O and CO2 in La0.8Sr0.2Cr0.5Fe0.5O3-δ-Zr0.84Y0.16O2-δ Electrode-Supported Solid Oxide Electrolysis Cells. *Int. J. Hydrogen Energ.* 46, 20305–20312. doi:10.1016/j.ijhydene.2021.03.177

Deka, D. J., Gunduz, S., Kim, J., Fitzgerald, T., Shi, Y., Co, A. C., et al. (2019). Hydrogen Production from Water in a Solid Oxide Electrolysis Cell: Effect of Ni Doping on Lanthanum Strontium Ferrite Perovskite Cathodes. *Ind. Eng. Chem. Res.* 58, 22497–22505. doi:10.1021/acs.iecr.9b03731

Dogdibegovic, E., Wang, R., Lau, G. Y., Karimaghaloo, A., Lee, M. H., and Tucker, M. C. (2019). Progress in Durability of Metal-Supported Solid Oxide Fuel Cells with Infiltrated Electrodes. *J. Power Sourc.* 437, 226935. doi:10.1016/j.jpowsour.2019.226935

Karczewski, J., Brylewski, T., Miruszewski, T., Andersen, K. B., Jasinski, P. Z., and Molin, S. (2019). High-temperature Kinetics Study of 430L Steel Powder Oxidized in Air at 600-850 °C. *Corrosion Sci.* 149, 100–107. doi:10.1016/j.corsci.2019.01.005

Pomfret, M. B., Marda, J., Jackson, G. S., Eichhorn, B. W., Dean, A. M., and Walker, R. A. (2008). Hydrocarbon Fuels in Solid Oxide Fuel Cells: *In Situ* Raman Studies of Graphite Formation and Oxidation. *J. Phys. Chem. C* 112, 5232–5240. doi:10.1021/jp711312p

Reisert, M., Berova, V., Aphale, A., Singh, P., and Tucker, M. C. (2020). Oxidation of Porous Stainless Steel Supports for Metal-Supported Solid Oxide Fuel Cells. *Int. J. Hydrogen Energ.* 45 (55), 30882–30897. Submitted. doi:10.1016/j.ijhydene.2020.08.015

Schiller, G., Ansar, A., Lang, M., and Patz, O. (2009). High Temperature Water Electrolysis Using Metal Supported Solid Oxide Electrolyser Cells (SOEC). *J. Appl. Electrochem.* 39, 293–301. doi:10.1007/s10800-008-9672-6

Shen, F., and Lu, K. (2018). Comparison of Different Perovskite Cathodes in Solid Oxide Fuel Cells. *Fuel Cells* 18, 457–465. doi:10.1002/fuce.201800044

Shen, F., Wang, R., and Tucker, M. C. (2020). Long Term Durability Test and post Mortem for Metal-Supported Solid Oxide Electrolysis Cells. *J. Power Sourc.* 474, 228618. doi:10.1016/j.jpowsour.2020.228618

Stange, M., Stefan, E., Denonville, C., Larring, Y., Rørvik, P. M., and Haugsrud, R. (2017). Development of Novel Metal-Supported Proton Ceramic Electrolyser Cell with Thin Film BZY15-Ni Electrode and BZY15 Electrolyte. *Int. J. Hydrogen Energ.* 42, 13454–13462. doi:10.1016/j.ijhydene.2017.03.028

Tucker, M. C., Carreon, B., Charyasatit, J., Langston, K., Taylor, C., Manjarrez, J., et al. (2017). Playing with Fire: Commercialization of a Metal-Supported SOFC Product for Use in Charcoal Cookstoves for the Developing World. *ECS Trans.* 78, 229–236. doi:10.1149/07801.0229ecst

Tucker, M. C. (2017). Durability of Symmetric-Structured Metal-Supported Solid Oxide Fuel Cells. *J. Power Sourc.* 369, 6–12. doi:10.1016/j.jpowsour.2017.09.075

Tucker, M. C. (2020). Progress in Metal-Supported Solid Oxide Electrolysis Cells: A Review. *Int. J. Hydrogen Energ.* 45, 24203–24218. doi:10.1016/j.ijhydene.2020.06.300

Wang, R., Dogdibegovic, E., Lau, G. Y., and Tucker, M. C. (2019). Metal-Supported Solid Oxide Electrolysis Cell with Significantly Enhanced Catalysis. *Energy Technol.* 7, 1801154. doi:10.1002/ente.201801154

Wu, W., Ding, D., and He, T. (2017). Development of High Performance Intermediate Temperature Proton-Conducting Solid Oxide Electrolysis Cells. *ECS Trans.* 80, 167–173. doi:10.1149/08009.0167ecst

Conflict of Interest: The authors declare that the research was conducted in the absence of any commercial or financial relationships that could be construed as a potential conflict of interest.

frontiers | Frontiers in Energy Research

METHODS
published: 03 May 2022
doi: 10.3389/fenrg.2022.887893

Standard Operating Protocol for Ion-Exchange Capacity of Anion Exchange Membranes

Lan Wang[1], Santiago Rojas-Carbonell[1], Keda Hu[1], Brian P. Setzler[2], Andrew R. Motz[3], Matthew E. Ueckermann[2] and Yushan Yan[1,2]*

[1]Versogen, Wilmington, DE, United States, [2]Center for Catalytic Science and Technology, Department of Chemical and Biomolecular Engineering, University of Delaware, Newark, DE, United States, [3]Nel Hydrogen, Wallingford, CT, United States

Ion-exchange capacity (IEC) is the measure of a material's capability to displace ions formerly incorporated within its structure. IEC is a key feature of anion-exchange membranes (AEM), as it determines the AEM's ability to conduct the ions required to sustain the electrochemical reactions where they are utilized. As an intrinsic property, measuring the IEC accurately is essential to study AEMs and understand their performance within devices. In this method article, a facile and accurate standard operating procedure (SOP) to measure the IEC of AEMs is proposed. When compared to conventional acid-base back-titration or Mohr titration, the proposed method combines the fast reaction between silver and halide ions and the accuracy of the potentiometric titration, providing a convenient and precise protocol for researchers in the field.

Keywords: SOP, AEM, IEC, protocol, ion exchange, membrane

Edited by:
Olga A. Marina,
Pacific Northwest National Laboratory (DOE), United States

Reviewed by:
Christopher George Arges,
Louisiana State University, United States
Enrico Negro,
University of Padua, Italy

****Correspondence:***
Yushan Yan
Yushan@Versogen.com

Specialty section:
This article was submitted to Process and Energy Systems Engineering,
a section of the journal Frontiers in Energy Research

Received: *02 March 2022*
Accepted: *28 March 2022*
Published: *03 May 2022*

Citation:
Wang L, Rojas-Carbonell S, Hu K, Setzler BP, Motz AR, Ueckermann ME and Yan Y (2022) Standard Operating Protocol for Ion-Exchange Capacity of Anion Exchange Membranes. Front. Energy Res. 10:887893. doi: 10.3389/fenrg.2022.887893

1 INTRODUCTION

Ion-exchange capacity (IEC) is a key material property of anion-exchange membranes (AEM). The IEC value is a measure of the concentration of ion-conducting functional groups as milliequivalent per gram of the AEM and generally has a proportional relationship with many other AEM properties such as anion conductivity, swelling ratio, water uptake, and water/gas permeance. Coupled with other characterization techniques, changes in the IEC can provide insights on active sites—associated with durability of anion conductivity—cation degradation (NMR), carboxylic acid formation (NMR), hydroxyl group formation (NMR), and undesired ion contamination (XRF). This information provides critical insights towards the efficient design and diagnostic of the AEM utilized in electrochemical systems and provides guidance to researchers on chemical structure design, morphology control, applications, and device troubleshooting. Therefore, a standard operating procedure (SOP) to accurately measure IEC on AEMs is essential.

Conventional methods such as acid-base back-titration (Si et al., 2014a; Si et al., 2014b; Mohanty et al., 2015; Liu et al., 2018; You et al., 2018; Han et al., 2019; Yang et al., 2019; You et al., 2019; Zhu et al., 2019) and Mohr titration (Mohanty et al., 2015; Vandiver et al., 2016; Liu and Kohl, 2018; Allushi et al., 2019; Divekar et al., 2019; Mandal et al., 2019; Pham et al., 2019; Ziv et al., 2019; Buggy et al., 2020; Mondal et al., 2020; Yang et al., 2020) are widely applied in AEM research. The acid-base back-titration utilizes the molar difference between the basic titrant and the acid analyte when testing an OH^- form AEM to calculate the sample IEC value. The endpoint is determined with a phenolphthalein indicator. The Mohr titration is based on the fast reaction of a silver ion titrant and halide analyte, with potassium chromate (K_2CrO_4) as colorimetric indicator. Both methods have the advantages of widely accessible supplies and short learning curves. However, the acid-base back-titration requires precise

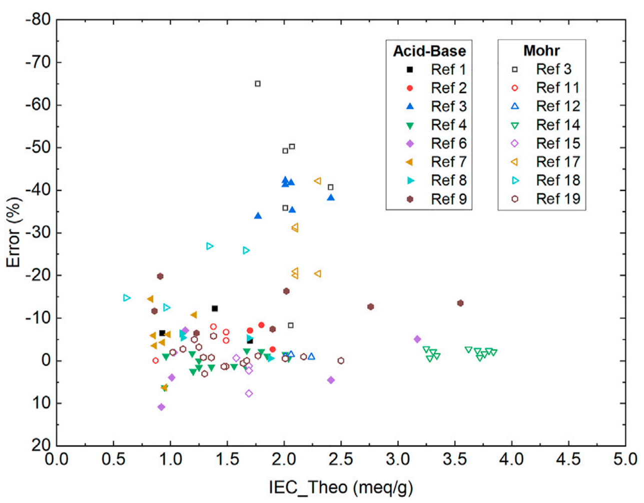

FIGURE 1 | Summary of Errors versus Theoretical IEC values from typical aggregated from the AEMs reported (Si et al., 2014a; Si et al., 2014b; Mohanty et al., 2015; Vandiver et al., 2016; Liu et al., 2018; Liu and Kohl, 2018; You et al., 2018; Allushi et al., 2019; Divekar et al., 2019; Han et al., 2019; Mandal et al., 2019; Pham et al., 2019; Yang et al., 2019; You et al., 2019; Zhu et al., 2019; Ziv et al., 2019; Buggy et al., 2020; Mondal et al., 2020; Yang et al., 2020). The error was calculated as (IEC_Meseaured - IEC_Theoretical)/(IEC_Theoretical) × 100%.

measurement of the concentration and volume for both the titrant and analyte. The Mohr titration, on the other hand, requires multiple ion-exchanges with sodium nitrate ($NaNO_3$) and transfers of the rinsate for analyte preparation. Additionally, for both methods, the titration endpoint is determined by the color change of the indicators, which is prone to operator errors. These factors often introduce artificial errors and lead to erroneously measured IEC values, sometimes being as high as -65% error versus theoretical value (**Figure 1**). Here we focus on comparing the new method with acid-base back-titration and Mohr titration due to their domination in recent AEM publications. Other colorimetric titrations such as Volhard titration reported by Ramani and coworkers are valuable progress in the AEM field (Arges et al., 2012). However, they are not widely used in the AEM field and thus they are not included in this discussion.

Herein, we propose a facile and precise method to measure the IEC of an AEM sample by utilizing the fast reaction of the silver ion with bromide coupled with the high accuracy of the potentiometric titration for endpoint determination. The proposed method encompasses four steps: 1. Ion-exchange to Br^- form; 2. Dry weight measurement; 3. Sample pretreatment; and 4. Potentiometric titration. No liquid transfer, manual titration, or indicators are involved in the procedure. Lithium triflate (LiOTf) is added to the analyte to drive the ion-exchange to completion—getting all the bromide ions to the analyte—and the auto titrator equipped with the silver selective electrode is used to measure the endpoint with high accuracy. Sample dry weight is the only input data obtained manually. The new method overcomes the errors that were introduced in the conventional methods due to incomplete ion-exchange, long procedure, manual titration, and difficulties in determining the titration endpoint.

2 PROTOCOL SCOPE

2.1 Scope and Applicability

The purpose of this SOP is to describe the method for measuring the IEC of an AEM. The membrane sample must have a mass greater than 50 mg.

2.2 Summary of Method

An AEM sample (50–100 mg) in hydroxide, bicarbonate, chloride, or bromide form is exchanged to the bromide form by soaking in a solution (15–40 ml) composed of 4 M KBr and 0.02 M KOH. After each exchange, the sample is rinsed in DI water (50–100 ml). This procedure is repeated three times. The same procedure can be applied to AEM samples in any mixed form of hydroxide, carbonate, and/or bicarbonate as will occur when hydroxide form samples are exposed to air. If the sample is in an unknown or any other anion form, such as iodide, it is recommended to repeat the ion-exchange procedure 10 times. It is optional to perform extra ion-exchange with bromide form samples but recommended to prevent undesired anion contamination. A small amount of KOH is added to ensure that any primary, secondary, and tertiary amines (including any other types of acid acceptors such as imidazole, tertiary phosphine, and pyridine) in the sample are not protonated and do not contribute to the measured IEC. Based on the relative affinity of bromide and hydroxide ions, the error caused by the exchange of hydroxide for bromide in the membrane is estimated to be less than 0.1%. The membrane is then rinsed with DI water until the conductivity of the rinsate is within 10% of that of DI water. The dry weight of the membrane sample is obtained. Then, the AEM sample is exchanged with LiOTf (lithium triflate) by mixing an equal weight of LiOTf salt and 150 ml of DI water with the sample. About 1 ml of 2% HNO_3 is added to adjust the pH to ca. 3–4. The Hanna HI901 automatic titrator is used for titration with a 0.02N $AgNO_3$ standard solution. A silver/sulfide combination ion-selective electrode (HI 4115) is used to monitor the titration.

2.3 Personnel Qualifications/Responsibilities

Operators should have basic laboratory knowledge on titration processes and should be trained on the operation of the Hanna HI901 potentiostatic titrator and accompanying software before performing this experiment.

2.4 Health and Safety Warning

All solutions should be handled with care, using appropriate PPE. The operator should review the safety data sheets for the chemicals involved, especially the ones of nitric acid and lithium triflate. The membrane should never be handled without gloves, as the chloride ions in the sweat can interfere with the measurement. Additionally, the silver nitrate standard solution should be kept away from light, as it will hydrolyze and affect the measurements. Discard if you see brown deposits of silver oxide.

2.5 Equipment and Supplies

Potassium bromide (KBr), deionized (DI) water, 0.02 M silver nitrate standard solution ($AgNO_3$, 0.02 M), lithium triflate (LiOTf), nitric acid (HNO_3), potassium hydroxide (KOH), Hanna HI901, and sensor HI 4115.

2.6 Nomenclature and Definitions

Ion-exchange capacity (IEC); anion-exchange membrane (AEM),
Potassium bromide (KBr);
Deionized (DI);
Silver nitrate ($AgNO_3$), lithium triflate (LiOTf), potassium hydroxide (KOH);
Nitric acid (HNO_3).

2.7 Recommended Reading

Kenkel, J. (2003). *Analytical Chemistry for Technicians*. 1 (3 ed.). CRC Press. pp. 108–109.

Yoder, L. (1919). "Adaptation of the Mohr Volumetric Method to General Determinations of Chlorine". *Industrial and Engineering Chemistry*. 11 (8): 755.

Hulanicki, A. Głąb, S. (2013) *Encyclopedia of Analytical Science*. (2 ed.). Elsevier. pp. 114–121.

3 PROCEDURE

3.1 Step-by-Step Procedure

3.1.1 Ion-Exchange to Br^- Form

- The AEM sample (50 ± 10 mg is recommended), originally in bicarbonate form, for example, is exchanged to the bromide form by soaking in ~15 ml 4 M KBr and 0.02 M KOH solution in a 20 ml glass vial then rinsing with ~50 ml of DI water for 30 min for each soaking. This is completed on a shaker table at room temperature and repeated three times with fresh solutions. For anion-exchange resins or thicker AEM (≥100 μm), longer soaking time (3 h), vigorous shaking, elevated temperature (50°C), and extra exchange times (10 times) are recommended to prevent incomplete ion-exchange. When testing thick resins, an initial baseline should be established by testing ion exchange over 3, 9, and 24 h and measuring the IEC. If different IEC values are measured, the ion exchange time will need to be increased until no difference is measured. Increments of 12 h can be used after the 24 h mark is reached. Grade II or ASTM Type II DI water (conductivity ≤1 μS/cm) is required in all the processes.
- The membrane is then rinsed with DI water and completely immersed in ~50 ml DI water at room temperature for 30 min while placing it again on a shaker table. This is repeated at least three times with fresh DI water until the conductivity of the rinsate is comparable to DI water (within 10%).

3.1.2 Dry Weight Measurement

- The membrane sample is dried overnight at 80°C on a glass vial using a convection oven. The dry mass of the membrane sample is obtained using an analytical balance with a resolution of 0.1 mg. 50 mg sample weight is recommended. The weight measurement should be made promptly after removing the sample from the oven, as the membrane will absorb water from the atmosphere. The membrane does not need to be kept dry after weight measurement.
- Alternatively, the bromide form membrane can be also dried in a sealed vial with an inlet/outlet of dry nitrogen flow overnight at room temperature. After removing the nitrogen flow and resealing, the vial with the sample inside it was transferred to the analytical balance. The sample dry weight measurement should be completed promptly within 5 min.

3.1.3 Sample Pre-Treatment

- A Hanna HI901 charged with a 0.02N $AgNO_3$ solution is used to titrate the sample. The $AgNO_3$ solution must be kept in a dark or amber bottle. Verify the expiration date of this analytical standard.
- The sensor HI 4115 must be charged with enough 1 M KNO_3 so that the electrode solution is above the ceramic junction. In the case of a low electrode solution, 1M KNO_3 standard solution should be purchased and filled.
- The Burette tip of Hanna HI901 must be primed through dispensing increasingly smaller amounts of titrant into the waste solution until it can reliably dispense the smallest solution increment.
- The AEM sample is exchanged with LiOTf by mixing ~50 mg of dry LiOTf salt and ~150 ml of DI water in a 250 ml beaker with 1,000 RPM agitation at room temperature for 30 min. Adjust the beaker position to prevent any splash, which will cause a lower IEC value. The sample cup must be stirred while titrating. The HI901 has a built-in impeller, but for small-volume sample cups, a magnetic stir bar can be used. LiOTf should be stored before and after use in a desiccator due to its hygroscopic nature.
- Add about 1 ml of 2% HNO_3 to tune the pH to ca. 3–4 required to ensure silver ions are completely immersed in the solution. Adjust the beaker position and solution level with DI water so that all the electrodes are fully immersed.

3.1.4 Potentiometric Titration

- Select the IEC titration program on the auto-titrator. The mass of the AEM sample is entered into the software and the titration begins with 0.05 ml of 0.02 N $AgNO_3$ per increment.
- The solution is continuously stirred and automatically titrated with sensor HI 4115 recording the potential of the silver ion-selective electrode, which is determined by the solubility product of silver bromide and the remaining free bromide concentration.
- IEC, potential, and volume dispensed results are displayed.

- Sample cup is removed and stir bar is rinsed with DI water. Sensor HI 4115 should also be cleaned by dabbing with a Kimwipe that has been wetted with DI water.

3.2 Sample Preparation and Analysis

A sample of 50 ± 10 mg should be anion exchanged with KBr, washed with DI water, dried overnight, and weighed carefully.

Bromide Exchange	**20 ml Glass Scintillation Vial, 4 M KBr +0.02 M KOH Solution**
DI water washing	20 ml glass scintillation vial, DI water
Sample	50 mg sample recommended
Ion exchange	50 mg LiOTf
Sample Cup	250 ml glass beaker
Sensor	HI 4115 (included with the Hanna HI901 analyzer)
Sensor solution	1M KNO_3 solution
Titrant	0.02N $AgNO_3$ solution, ~ 5 ml

3.3 Sample Handling and Preservation

Before and after the experiment, AEM samples should be stored in clean sample containers (e.g. Petri dish).

3.4 Computer Hardware and Software

Origin or an equivalent program can be used to find the maximum of the first derivative of the measured Ag ISE potential over volume. Data files can be moved to the computer from the Hanna HI901 using a thumb drive.

3.5 Data Collection, Analysis, and Records Management

Sample ID, polymer dry weight, number of ion-exchange repeats, calculation of IEC, measured IEC, and theoretical IEC (if applicable) should be recorded elsewhere both electronically and in a lab notebook by the user.

4 RESULTS

The measured IEC value in bromide form will be displayed on the auto titrator screen at the end of the titration. Calculations of IEC are performed by finding the maximum of the first derivative of the measured Ag ISE potential over volume (**Figure 2**). This gives the equivalence point of the titration. The IEC value can be calculated with **Eq. 1**.

The IEC in bromide form is determined as follows (meq/g):

$$\mathrm{IEC_{Br}} = \frac{\mathrm{V_{AgNO3}} \times \mathrm{C_{AgNO3}}}{\mathrm{m_{dry}}} = \frac{2.410\,(mL) \times 0.02\,(meq/mL)}{0.0244\,(g)} = 1.97\,(meq/g) \tag{1}$$

where $\mathrm{V_{AgNO3}}$ is the titrated volume of $AgNO_3$ titrant (ml); $\mathrm{C_{AgNO3}}$ is the normality of $AgNO_3$ (mmol/mL or meq/mL); and $\mathrm{m_{dry}}$ is the weight of dry AEM sample (g).

The measured IEC value (1.97 meq/g) of the AEM sample (i.e. PAP-TP-85) is very close to the theoretical value of 1.94 meq/g in Br^- form with only a 2% error (Wang et al., 2019).

Converting the IEC into other forms can be calculated with **Eq. 2**. Take AEM, $(A)_m(B)_n$, for example.

$$\mathrm{IEC_X} = \mathrm{IEC_{Br}} \times \frac{m\mathrm{FW_A} + n\mathrm{FW_B} + m\mathrm{FW_{Br}}}{m\mathrm{FW_A} + n\mathrm{FW_B} + m\mathrm{FW_X}} \tag{2}$$

where $\mathrm{FW_A}$ and $\mathrm{FW_B}$ are the formula weights of monomer units A and B without anions (g/mol); $\mathrm{FW_{Br}}$ and $\mathrm{FW_X}$ are the formula weight of anions (g/mol, e.g. $X = OH^-$, Cl^-); and m and n are the monomer ratio (%) on the polymer structure.

5 QUALITY CONTROL AND QUALITY ASSURANCE

5.1 Instrument or Method Calibration and Standardization

Hanna HI901 calibration check should be performed before experiments. This calibration is performed by dispensing bromide standard solution into a sample cup at a known volume (e.g., 2 ml, 10 ml), and running the IEC test. The IEC test results should show the consumption matches the volume dispensed and the IEC should match the bromide standard concentration within 2%. Additionally, the IEC of each AEM should be measured in triplicate for verification, as well as having a sample weight of ~50 mg to minimize error.

5.2 Cautions

Clean equipment after each use. Solutions used are not generally corrosive to the system, but they should still be removed immediately after an experiment for best practices. Keep silver nitrate in an amber bottle, as it is light-sensitive. Keep lithium

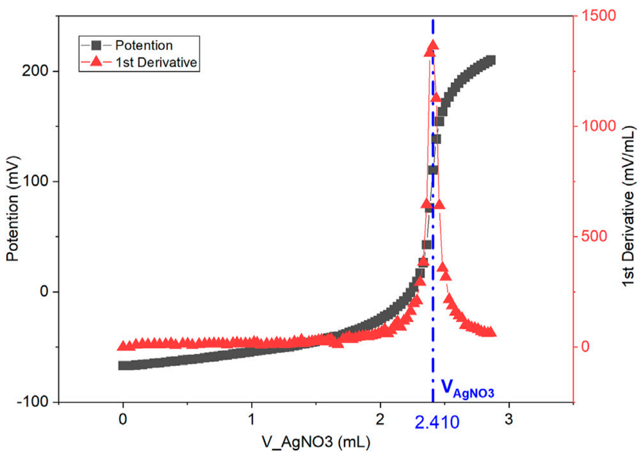

FIGURE 2 | Titration curve of Ag ISE potential (mV) over $AgNO_3$ titrant volume (ml) is denoted as black squares. First derivative of potential over volume, mV/mL vs. mL is denoted as red triangles. The maximum at V_{AgNO3} (2.410 ml) is the titration endpoint. AEM sample dry weight is measured as m_{dry} = 24.4 mg.

triflate in a dry environment and well-sealed as it is hygroscopic. The titration needs to be conducted in slightly acid conditions to avoid the formation of silver oxides. Never touch the membrane with bare hands, as it will lead to interfering ions.

5.3 Common Issues

- Membrane dry weight is too low (less than 50 mg).
- Ion-exchange solution is not refreshed after each exchange.
- The conductivity/salt content of DI water rinsate is not measured.
- Sample is not fully dried before weighing.
- Weight measurement is not conducted in a dry environment.
- Sample is not measured timely after moving out of the oven/dryer.
- Sample has static electricity (very common in a dry environment).
- Auto titrator is not calibrated before titration.
- Burette and pipe are not primed.
- Splash from vigorous stirring.
- End tips of electrodes are not fully immersed in the analyte.
- The electrode standard solution is low.

5.4 Interferences

- Incomplete ion exchange—May lead to lower IEC value when nonhalide anions are left in the AEM sample.
- Insufficient DI water rinse—Leads to higher IEC value when extra Br^- is left in AEM sample.
- Inaccurate membrane weight—Leads to lower IEC value due to falsely high membrane weight with extra water.
- Degraded $AgNO_3$ standard solution—Leads to higher IEC value due to extra volume needed with lower Ag^- concentration. $AgNO_3$ decomposes when exposed to light.
- Faulty sensor—Unable to determine the titration endpoint due to malfunctional sensor.
- Unprimed burette—Leads to lower IEC value due to air trapped inside the burette or pumping line.
- Violent stirring—Leads to lower IEC value due to analyte loss from splash.
- Poor lab hygiene—Leads to lower IEC value from $AgNO_3$ residue or higher IEC value from Br-residue due to lack of clean up after experiments. Contact of the membrane with bare hands introduces chloride ions from the sweat.

5.5 Troubleshooting

Lower measured IEC value than theoretical.

- Instrument calibration.
- Clean impeller, burette, and electrodes with DI water.
- Increase exchange repeats in the "ion-exchange to Br-form" step.
- Prolong drying time and weigh dry membrane promptly after removing from the dry environment.
- Use an anti-static gun such as Zerostat when measuring membrane dry weight.
- Prime burette to remove air bubbles.
- Increase minimum dispensing amount until the burette can reliably dispense the smallest solution increment.
- Adjust analyte level so that impeller and electrodes are fully immersed.

5.5.1 Higher Measured IEC Value Than Theoretical

- Instrument calibration.
- Clean impeller, burette, and electrodes with DI water.
- Increase DI water rinse repeats and verify rinsate conductivity.
- Verify the normality of the standard $AgNO_3$ solution. Replace with a fresh standard solution if the $AgNO_3$ degraded.

5.5.2 Multiple Equivalent Points on the Titration Curve

- Increase exchange repeats to 15 or even 20 times in the "ion-exchange to Br-form" step.
- Check LiOTf and HNO_3 solutions for halide contamination by titration of diluted samples of each.

5.5.3 Unable to Obtain Titration Curve

- Charge the sensor HI 4115 with enough 1M KNO_3 so that the electrode solution is above the ceramic junction.
- Adjust analyte level so that the impeller and electrodes are fully immersed.
- Replace sensors if necessary.

5.6 Error Analysis

Inevitably, most four-place analytical balances are accurate to ±0.0001 g. Therefore, for the sample of 24.4 mg dry weight, in an ideal case, it consists of a relative error of 0.4% (= 0.1/24.4 mg × 100%) from weight measurement. The purchased 0.02 N silver nitrate standard solution (Hanna HI70448) does not list the concentration error which is also usually too small to take into consideration. We can assume that there is no concentration error of fresh standard 0.02N $AgNO_3$ solution. Despite the fast reaction of silver with halide and the high sensitivity of electrodes, the endpoint volume of $AgNO_3$ may deviate from the true volume by one minimum dispensing amount which is 0.02 ml in this case. The relative error from titration is calculated as 0.8% (= 0.02/2.41 ml × 100 %).

Based on **Eq. 1**, the relative error of IEC shall be calculated with **Eq. 3**.

$$e_{\%,\,IEC} = \sqrt{\left(e_{\%,\,V}\right)^2 + \left(e_{\%,m}\right)^2} = \sqrt{(0.8\%)^2 + (0.4\%)^2} = 0.9\% \quad (3)$$

where $e_{\%,IEC}$ is the relative error of IEC, $e_{\%,V}$ is the relative error of endpoint volume, and $e_{\%,m}$ is the relative error of sample dry weight.

In the case study, a relatively light sample (<25 mg) was selected to showcase the accuracy of the proposed method. The $e_{\%,V}$ and $e_{\%,m}$ will decrease to half if the recommended sample dry weight (50 mg) is applied and the $e_{\%,IEC}$ will be as low as 0.4%. To minimize the relative error, a proper sample dry weight and multiple weight measurements are recommended.

6 DISCUSSION

The results show the significant improvement of the Silver–Halide potentiometric method over the other two conventional colorimetric methods. The acid-base back-titration has the advantage of simplicity. However, the requirements of standard solutions for both acid and base, as well as the colorimetric endpoint determination, inevitably introduce more artificial errors. Mohr titration, on the other hand, suffers from the poor sensitivity of potassium chromate indicator.

Additionally, the auto-metering capability of the auto-titrator notably decreases the concerns of operator error, as manual operations are significantly minimized. The improvement in simplicity and accuracy is due to the fast reaction of silver-bromide, sensitive reading of electrode, precise metering of auto-titrator, and well-designed procedure.

Finally, it is worth noting that after addressing the titration endpoint issue, the measurement of sample dry weight becomes the major source of errors. Even with just a few water molecules coordinated to each cation group, errors of 2%–5% are easily introduced. Compared to other anion forms, bromide from AEM is usually less hygroscopic. Thus, it loses water faster and absorbs water slower. When weighing is conducted correctly according to the Step-by-Step Procedure, the operator can obtain accurate sample dry weight easily.

In summary, a facile and accurate standard operating procedure (SOP) for measuring the IEC of AEM samples is described. The switch from using two standard solutions in acid-base back-titration to using a single $AgNO_3$ standard solution in the Silver–Halide system greatly simplifies the sample preparation process. The implementation of the potentiometric method with silver selective electrode overcomes the difficulties of determining the titration endpoint, which exists in the Mohr titration where the colorimetric indicator is applied.

DATA AVAILABILITY STATEMENT

The original contributions presented in the study are included in the article/Supplementary Material, further inquiries can be directed to the corresponding authors.

AUTHOR CONTRIBUTIONS

LW developed the standard operating protocol. SR-C and KH set up the apparatus and performed measurements of ion-exchange capacity. BS and AM provided guidance on electrochemistry. MU performed sample preparation. LW, SR-C, KH, and YY conceived the ideas and wrote the manuscript with support from other coauthros.

FUNDING

The information, data, or work presented herein was funded in part by the Advanced Research Projects Agency-Energy (ARPA-E), U.S. Department of Energy, under Award Number DE-AR0000771 and DE-AR0001149. The views and opinions of authors expressed herein do not necessarily state or reflect those of the United States Government or any agency thereof.

REFERENCES

Allushi, A., Pham, T. H., Olsson, J. S., and Jannasch, P. (2019). Ether-free Polyfluorenes Tethered with Quinuclidinium Cations as Hydroxide Exchange Membranes. *J. Mater. Chem. A.* 7 (47), 27164–27174. doi:10.1039/c9ta09213g

Arges, C. G., Parrondo, J., Johnson, G., Nadhan, A., and Ramani, V. (2012). Assessing the Influence of Different Cation Chemistries on Ionic Conductivity and Alkaline Stability of Anion Exchange Membranes. *J. Mater. Chem.* 22 (9), 3733. doi:10.1039/c2jm14898f

Buggy, N. C., Du, Y., Kuo, M.-C., Ahrens, K. A., Wilkinson, J. S., Seifert, S., et al. (2020). A Polyethylene-Based Triblock Copolymer Anion Exchange Membrane with High Conductivity and Practical Mechanical Properties. *ACS Appl. Polym. Mater.* 2 (3), 1294–1303. doi:10.1021/acsapm.9b01182

Divekar, A. G., Kuo, M. C., Park, A. M., Motz, A. R., Page-Belknap, Z. S., Owczarczyk, Z., et al. (2019). The Impact of Alkyl Tri-methyl Ammonium Side Chains on Perfluorinated Ionic Membranes for Electrochemical Applications. *J. Polym. Sci. Part. B: Polym. Phys.* 57 (11), 700–712. doi:10.1002/polb.24825

Han, J., Peng, Y., Lin, B., Zhu, Y., Ren, Z., Xiao, L., et al. (2019). Hydrophobic Side-Chain Attached Polyarylether-Based Anion Exchange Membranes with Enhanced Alkaline Stability. *ACS Appl. Energ. Mater.* 2 (11), 8052–8059. doi:10.1021/acsaem.9b01553

Liu, L., Chu, X., Liao, J., Huang, Y., Li, Y., Ge, Z., et al. (2018). Tuning the Properties of Poly(2,6-Dimethyl-1,4-Phenylene Oxide) Anion Exchange Membranes and Their Performance in H2/O2 Fuel Cells. *Energy Environ. Sci.* 11 (2), 435–446. doi:10.1039/c7ee02468a

Liu, L., and Kohl, P. A. (2018). Anion Conducting Multiblock Copolymers with Different Tethered Cations. *J. Polym. Sci. Part. A: Polym. Chem.* 56 (13), 1395–1403. doi:10.1002/pola.29020

Mandal, M., Huang, G., Hassan, N. U., Peng, X., Gu, T., Brooks-Starks, A. H., et al. (2019). The Importance of Water Transport in High Conductivity and High-Power Alkaline Fuel Cells. *J. Electrochem. Soc.* 167 (5), 054501. doi:10.1149/2.0022005jes

Mohanty, A. D., Ryu, C. Y., Kim, Y. S., and Bae, C. (2015). Stable Elastomeric Anion Exchange Membranes Based on Quaternary Ammonium-Tethered Polystyrene-B-Poly(ethylene-Co-Butylene)-B-Polystyrene Triblock Copolymers. *Macromolecules* 48 (19), 7085–7095. doi:10.1021/acs.macromol.5b01382

Mondal, A. N., Hou, J., He, Y., Wu, L., Ge, L., and Xu, T. (2020). Preparation of Click-Driven Cross-Linked Anion Exchange Membranes with Low Water Uptake. *Particuology* 48, 65–73. doi:10.1016/j.partic.2018.08.012

Pham, T. H., Olsson, J. S., and Jannasch, P. (2019). Effects of the N-Alicyclic Cation and Backbone Structures on the Performance of Poly(terphenyl)-Based Hydroxide Exchange Membranes. *J. Mater. Chem. A.* 7 (26), 15895–15906. doi:10.1039/c9ta05531b

Si, Z., Qiu, L., Dong, H., Gu, F., Li, Y., and Yan, F. (2014). Effects of Substituents and Substitution Positions on Alkaline Stability of Imidazolium Cations and Their Corresponding Anion-Exchange Membranes. *ACS Appl. Mater. Inter.* 6 (6), 4346–4355. doi:10.1021/am500022c

Si, Z., Sun, Z., Gu, F., Qiu, L., and Yan, F. (2014). Alkaline Stable Imidazolium-Based Ionomers Containing Poly(arylene Ether Sulfone) Side Chains for Alkaline Anion Exchange Membranes. *J. Mater. Chem. A.* 2 (12), 4413–4421. doi:10.1039/c3ta15178f

Vandiver, M. A., Caire, B. R., Pandey, T. P., Li, Y., Seifert, S., Kusoglu, A., et al. (2016). Effect of Hydration on the Mechanical Properties and Ion Conduction in a Polyethylene-B-Poly(vinylbenzyl Trimethylammonium) Anion Exchange Membrane. *J. Membr. Sci.* 497, 67–76. doi:10.1016/j.memsci.2015.09.034

Wang, J., Zhao, Y., Setzler, B. P., Rojas-Carbonell, S., Ben Yehuda, C., Amel, A., et al. (2019). Poly(aryl Piperidinium) Membranes and Ionomers for Hydroxide Exchange Membrane Fuel Cells. *Nat. Energ.* 4 (5), 392–398. doi:10.1038/s41560-019-0372-8

Yang, C., Liu, L., Huang, Y., Dong, J., and Li, N. (2019). Anion-conductive Poly(2,6-Dimethyl-1,4-Phenylene Oxide) Grafted with Tailored Polystyrene Chains for Alkaline Fuel Cells. *J. Membr. Sci.* 573, 247–256. doi:10.1016/j.memsci.2018.12.013

Yang, K., Chu, X., Zhang, X., Li, X., Zheng, J., Li, S., et al. (2020). The Effect of Polymer Backbones and Cation Functional Groups on Properties of Anion Exchange Membranes for Fuel Cells. *J. Membr. Sci.* 603, 118025. doi:10.1016/j.memsci.2020.118025

You, W., Hugar, K. M., and Coates, G. W. (2018). Synthesis of Alkaline Anion Exchange Membranes with Chemically Stable Imidazolium Cations: Unexpected Cross-Linked Macrocycles from Ring-Fused ROMP Monomers. *Macromolecules* 51 (8), 3212–3218. doi:10.1021/acs.macromol.8b00209

You, W., Padgett, E., MacMillan, S. N., Muller, D. A., and Coates, G. W. (2019). Highly Conductive and Chemically Stable Alkaline Anion Exchange Membranes via ROMP of Trans -cyclooctene Derivatives. *Proc. Natl. Acad. Sci. U.S.A.* 116 (20), 9729–9734. doi:10.1073/pnas.1900988116

Zhu, L., Yu, X., Peng, X., Zimudzi, T. J., Saikia, N., Kwasny, M. T., et al. (2019). Poly(olefin)-Based Anion Exchange Membranes Prepared Using Ziegler-Natta Polymerization. *Macromolecules* 52 (11), 4030–4041. doi:10.1021/acs.macromol.8b02756

Ziv, N., Mondal, A. N., Weissbach, T., Holdcroft, S., and Dekel, D. R. (2019). Effect of CO2 on the Properties of Anion Exchange Membranes for Fuel Cell Applications. *J. Membr. Sci.* 586, 140–150. doi:10.1016/j.memsci.2019.05.053

Conflict of Interest: LW, SR-C, KH, and YY were employed by Versogen; AM is employed by Nel Hydrogen.

The remaining authors declare that the research was conducted in the absence of any commercial or financial relationships that could be construed as a potential conflict of interest.

frontiers | Frontiers in Energy Research

METHODS
published: 10 May 2022
doi: 10.3389/fenrg.2022.840140

Long-Term Stability Metrics of Photoelectrochemical Water Splitting

*Srinivas Vanka[1], Guosong Zeng[2,3], Todd G. Deutsch[4], Francesca Maria Toma[3] and Zetian Mi[1]**

[1]Department of Electrical Engineering and Computer Science, University of Michigan, Ann Arbor, MI, United States, [2]Department of Mechanical and Energy Engineering, Southern University of Science and Technology, Shenzhen, China, [3]Lawrence Berkeley National Laboratory, Chemical Sciences Division, Berkeley, CA, United States, [4]National Renewable Energy Laboratory, Chemistry and Nanoscience Center, Golden, CO, United States

Photoelectrochemical (PEC) water splitting, one of the most promising technologies for clean hydrogen generation, has drawn considerable attention over the past few decades. Achieving simultaneous highly efficient and stable unassisted PEC water splitting has been the “holy grail” in clean and renewable fuel generation. State-of-the-art photoelectrodes have shown relatively high efficiencies (~10–20%). Still, their stability is limited due to photoelectrode chemical instability, electrolyte resistance, mass transfer issues, and an often unoptimized experimental setup. In this work, we present a framework and a set of protocols for conducting long-term stability experiments and further provide details on several critical factors such as light source calibration, choosing the right counter electrode, the configuration of the PEC cell, and photoelectrode sample preparation.

Keywords: photoelectrochemical, solar water splitting, hydrogen, stability, photoelectrode

OPEN ACCESS

Edited by:
Chengxiang Xiang,
California Institute of Technology,
United States

Reviewed by:
Raman Vedarajan,
International Advanced Research Centre for Powder Metallurgy and New Materials, India
Valentine Ivanov Vullev,
University of California, Riverside,
United States

****Correspondence:***
Zetian Mi
ztmi@umich.edu

Specialty section:
This article was submitted to Process and Energy Systems Engineering,
a section of the journal
Frontiers in Energy Research

Received: *20 December 2021*
Accepted: *01 April 2022*
Published: *10 May 2022*

Citation:
Vanka S, Zeng G, Deutsch TG, Toma FM and Mi Z (2022) Long-Term Stability Metrics of Photoelectrochemical Water Splitting. Front. Energy Res. 10:840140. doi: 10.3389/fenrg.2022.840140

INTRODUCTION

An essential requirement for large-scale commercialization of PEC water splitting is the device’s durability against harsh electrolytes and under dark and different illumination intensities (Nandjou and Haussener, 2017; Kaneko et al., 2018). Due to the intermittency of solar radiation, the degradation of PEC devices is more accelerated than photovoltaic-electrolyzer devices (Shaner et al., 2016). Most of the high-efficiency semiconductors for PEC like Si (King et al., 2017; Ros et al., 2017) and III-V (Britto et al., 2016) are easily prone to chemical corrosion in the electrolyte (even under dark conditions). Si is easily oxidized to SiO_2 in an aqueous solution (see **Eq. 1**) and forms a passivation layer on the Si surface, leading to a reduction (Kainthla et al., 1986).

$$Si + 2OH^- + 4H_2O \rightarrow Si(OH)_2^{2+} + 2H_2 + 4OH^- \quad (1)$$

III-V compounds, like GaAs, also go through corrosion reactions (see **Eq. 2**) due to either accumulation of a large surface hole concentration in the dark or light illumination, generating holes at the surface (Lewerenz, 2014). However, p-type III-arsenide semiconductors have shown remarkable stability under conditions where an As^0 enriched surface provides passivation against corrosion (Young et al., 2016).

$$GaAs + 6h^+ + H_2O + aq \rightarrow Ga_{aq}^{3+} + 2AsO_2^- + 4H^+ \quad (2)$$

It was observed that N-terminated III-nitride nanostructures show virtually no chemical or photoelectrochemical corrosions when in contact with different electrolytes (Kibria et al., 2016; AlOtaibi et al., 2013; Vanka et al., 2018; Varadhan et al., 2017). Recent studies further revealed that

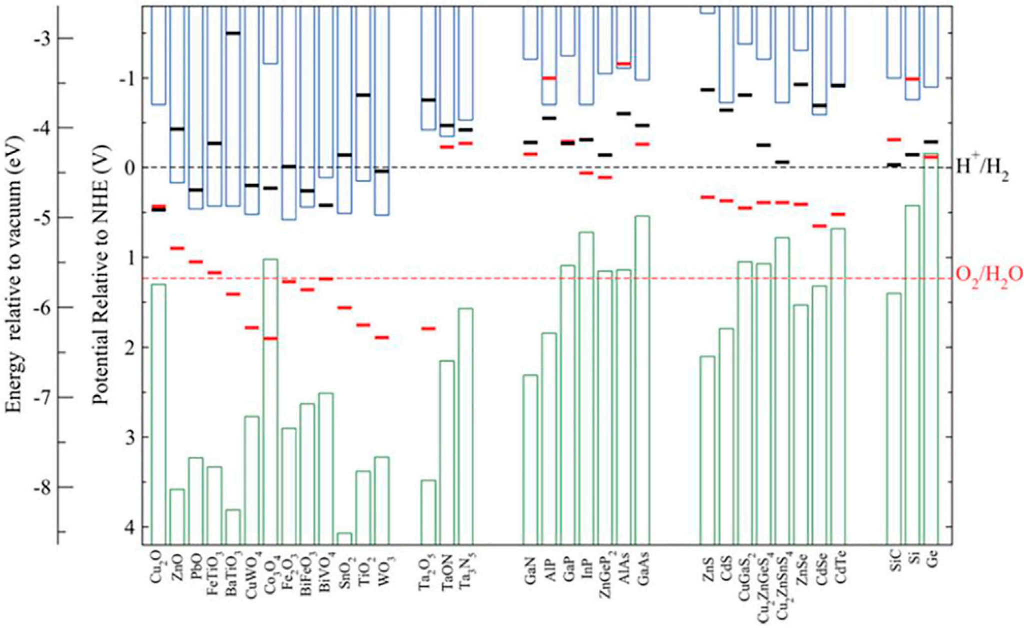

FIGURE 1 | Calculated ϕ^e_{corr} (black bars) and ϕ^h_{corr} (red bars) relative to NHE and vacuum level for various semiconductor photoelectrodes pH = 0 solutions, ambient temperature 298.15 K, and pressure 1 bar. The blue and green bars represent ϕ_{CB} and ϕ_{VB}, respectively. The black and red dotted lines are the $E_{cathodic}$ and E_{anodic}, respectively. Reprinted (adapted) with permission from Chen and Wang (2012). Copyright 2012 American Chemical Society.

the surfaces of such III-nitride nanostructures could be transformed to oxynitride, which leads to improved PEC performance, instead of degradation, under both one-sun and concentrated sunlight illumination (Zeng et al., 2021). Mi et al. reported one of the longest stability (>3,000 h) using an N-terminated multifunctional GaN nanowire protection scheme on Si photocathode (Vanka et al., 2019) and demonstrated durability under accelerated testing conditions (Zeng et al., 2021). Furthermore, Mi et al. demonstrated high stability of >100 h under a two-electrode experimental setup by utilizing single (STH ~3%) (Wang et al., 2019) and double junction (STH ~10%) (Vanka et al., 2020) InGaN/Si photocathodes. The underlying thermodynamic and kinetics of N-terminated (In)GaN nanostructures have been investigated in previous publications (Vanka et al., 2018; Zeng et al., 2021; Vanka et al., 2019; Vanka et al., 2020; He et al., 2019). The basic stability criteria for conduction band minimum (ϕ_{CB}) and valence band maximum (ϕ_{VB}) of a photoelectrode include: ϕ_{CB} below ϕ^e_{corr} and ϕ_{VB} above ϕ^h_{corr} (Chen and Wang, 2012), where ϕ^e_{corr} is energy level for cathodic corrosion reaction of semiconductor and ϕ^h_{corr} is energy level for anodic corrosion reaction of semiconductor (Chen and Wang, 2012). If ϕ^e_{corr} and ϕ^h_{corr} fall within the energy bandgap, then the material tends to become corroded or etched under PEC conditions. Furthermore, to avoid the competition of cathodic and anodic photocorrosion with the hydrogen evolution reaction (HER) and oxygen evolution reaction (OER), respectively, the photoelectrode must satisfy the criteria: ϕ^e_{corr} above $E_{cathodic}$ (0 V *vs.* NHE (Chen and Wang, 2012)) and ϕ^h_{corr} below E_{anodic} [−1.23 V *vs.* NHE (Chen and Wang, 2012)]. None of the semiconductor materials shown in **Figure 1** (Chen and Wang, 2012) satisfy both thermodynamic conditions of stability. In addition to these considerations, excess charge carriers in the photoaborber (mainly metal oxides) will lead to lattice distortions and form localized polarons (Di Valentin and Selloni, 2011; Janotti et al., 2014; Butler et al., 2016). These polarons can inhibit the charge transfer kinetics and affect the interface catalysis process. Thus, electron-hole pair recombination via polarons may hamper the stability of the photoelectrode. Although theoretically PEC water splitting requires 1.23 V, depending on the type of the photoelectrode, co-catalysts, and electrolyte, overpotentials for both hydrogen and oxygen evolution vary, and the redox potential lies typically in the range of 1.4–1.9 V (Chen et al., 2011; Shaner et al., 2016). Application of co-catalysts (e.g., Pt) on the photoelectrode surface provides kinetic protection by directing photogenerated charge carriers towards the favored water-splitting half reactions instead of corrosion reactions (Nandjou and Haussener, 2017). Therefore, the primary role of co-catalysts is to reduce the redox overpotential, facilitate the mass transfer, and efficient charge carrier extraction (Chen et al., 2011; Kaneko et al., 2018).

Over the years, various protection schemes have been employed to enhance the stability of both photocathode and photoanode. The first approach (see **Figure 2A**) uses relatively thick metal oxide such as TiO_2 (Ros et al., 2017; Yin et al., 2018), Al_2O_3 (Fan et al., 2015), or IrO_x (Mei et al., 2014) as passivation layers for photocathode and photoanode. Even though the stability performance has improved substantially (Ros et al., 2017; Yin et al., 2018), the major issue is photocurrent loss due to poor charge carrier transfer kinetics and light absorption (Kaneko et al., 2018). In addition, these protective

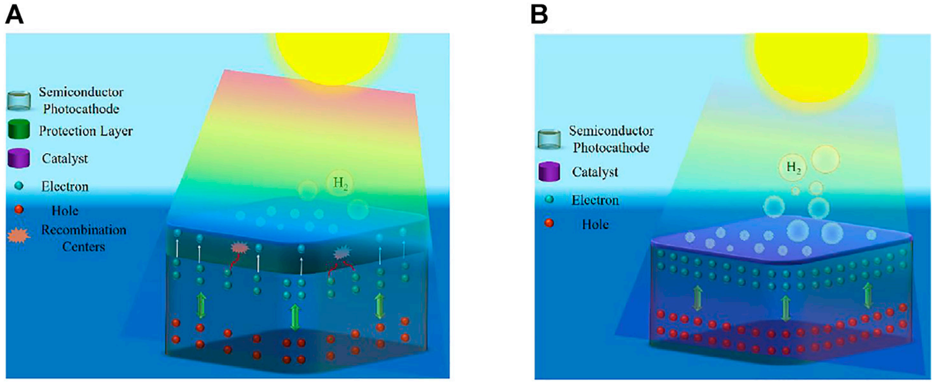

FIGURE 2 | (A) Schematic showing the conventional thick protective layer with a catalyst on top of the light absorber. **(B)** Schematic showing the photoelectrode with catalyst layer as a protective layer. Reprinted (adapted) with permission from Vanka et al. (2019). Copyright 2019 Royal Society of Chemistry.

layers suffer from the presence of pinholes and often involve the use of additional deposition methods, such as ALD. Henceforth, during stability testing, these pinholes may act as catalytic degradation sites, which eventually leads to exposure of the photoelectrode to the electrolyte solution (Ros et al., 2017; Ben-Naim et al., 2020). Moon et al. observed in their stability experiments a decrease in photocurrent density and photovoltage for TiO_2 protected III-V triple-junction solar cell photocathode (Moon et al., 2020). This performance degradation is due to the pinholes within the TiO_2 layer, which erodes the top junction by allowing acidic electrolyte solution to dissolve the top junction and ultimately lead to delamination (Moon et al., 2020). The second approach (see **Figure 2B**) is to couple photoelectrode with a highly active catalyst, simultaneously improving stability and maintaining excellent reaction kinetics by efficiently extracting the photogenerated charge carriers (Nandjou and Haussener, 2017). One of the best stabilities achieved for a photocathode (~60 days) with a relatively low photocurrent was reported by (King et al., 2017) using MoS_2 on Si. Furthermore, high two-electrode stability for GaInAsP/GaAs with MoS_2 protection under 2.6 suns illumination was reported recently (Ben-Naim et al., 2020). Interface losses and device complexity limit the performance of these devices. Although Si photoanode with $NiCrO_x/TiO_2$ protection (Shaner et al., 2015) showed high stability of ~2,200 h, the photocurrent density is low, and the applied bias is greater than 1.23 V *vs.* NHE. Furthermore, hematite (α-Fe_2O_3) and bismuth vanadate ($BiVO_4$) showed considerable stability (Dias et al., 2016; Kuang et al., 2016). The highest stability for nanostructured $BiVO_4$ photoanode is >1,000 h using *in-situ* on-demand NiFe catalyst regeneration (Kuang et al., 2016). The primary issue with the metal-oxides is their low efficiencies because of the limitations in bulk transport of charge carriers and their wide bandgaps (Bae et al., 2017). Another exciting set of stable water splitting electrodes, which have gained attraction over the past decade, is self-healing/self-repairing catalysts. These (photo)electrodes/catalysts (Kanan and Nocera, 2008; Lutterman et al., 2009; Najafpour et al., 2015; Costentin and Nocera, 2017; Feng et al., 2021; Zeng et al., 2021) with the capacity to renew themselves during the water-splitting reaction require special protocols to evaluate the origins of their stability (Zeng et al., 2021). These protocols are beyond the scope of this work.

An important factor in the stability measurements is the configuration of the PEC cell. As discussed earlier, most of the photoelectrodes are relatively stable in a three-electrode configuration (Vanka et al., 2019), but few devices can reach 100 h under a two-electrode (zero-bias) PEC configuration (Ben-Naim et al., 2020; Vanka et al., 2020). Three-electrode PEC configuration accounts for only the stability of the working photoelectrode ignoring the performance of the counter electrode and the overall PEC system stability (Chen et al., 2011). On the other hand, the two-electrode PEC configuration gives the actual efficiency and durability under a realistic operating environment of the entire PEC cell, including both the working electrode and counter electrode (Hodes, 2012). Thus, it is crucial to perform the stability tests for the photoelectrodes in a two-electrode configuration under AM1.5G one-sun illumination to understand the real stability of the device. While this work focuses on continuous illumination over long durations, understanding PEC system durability under intermittent illumination is also essential for moving this technology from the bench to the field. Henceforth, it is pertinent to develop standard benchmarking stability protocols for the two and three-electrode configurations to permit researchers to evaluate the stability performance of the photoelectrodes against state-of-the-art devices and thereby accelerate the progress of PEC technology for large-scale deployment.

PROCEDURES

Summary of Method

The stability experiments are essential to gain insights into the lifetime of the material. These experiments are conducted by recording the photocurrent against time under continuously applied bias in a two- or three-electrode configuration (Chen et al., 2011). As discussed earlier (see **Figure 1**), for most materials

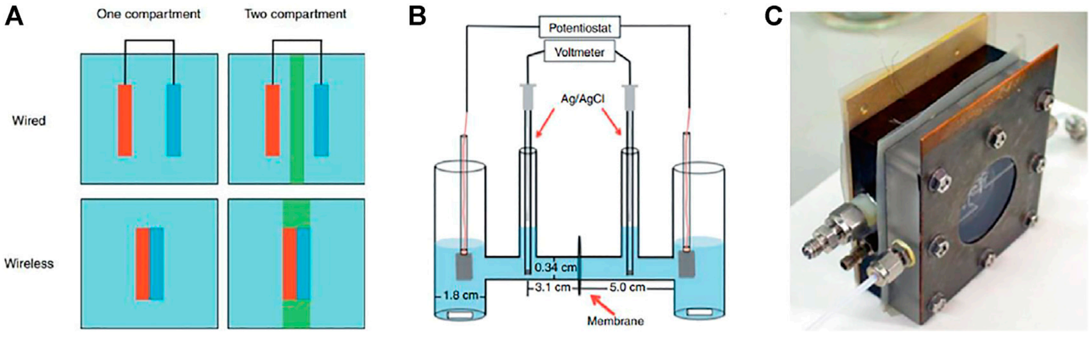

FIGURE 3 | (A) Schematic illustration of wired and wireless configurations in one- and two-compartment PEC cells. Reprinted from Bosserez et al. (2015). Copyright 2012 EDP Sciences. **(B)** H-type glass chamber for PEC H_2 and O_2 evolution.Reprinted (adapted) with permission from Hernández-Pagán et al. (2012). Copyright 2012 Royal Society of Chemistry. **(C)** Dual compartment PEC cell with SEA, in-, and outlet connection. Reprinted from Bosserez et al. (2015). Copyright 2012 EDP Sciences.

without protection schemes photocorrosion is thermodynamically favorable compared to HER or OER in an aqueous environment under illumination. The main cause is the accumulation of excess photogenerated charge carriers (holes or electrons), leading to side reactions (such as self-reduction or oxidation) (Su et al., 2017). Therefore, during stability experiments, it is recommended to quantify the evolved H_2 and O_2 to determine FE and STH (Chen et al., 2011). Photocorrosion is indicated by the degradation of photocurrent and/or LSV characteristics (such as onset potential, saturation photocurrent, and fill-factor) with time (Yang et al., 2019). The stability (or CA) experiments are conducted until the failure point, i.e., when the device photocurrent shows a significant drop at a given voltage. As shown in the flowchart (see **Figure 3**). The stability evaluation of the photoelectrode starts with either CV or LSV scans. These scans reveal whether the photoelectrode has favorable characteristics such as good photocurrent onset voltage, high photocurrent density, and high STH. After determining the photoelectrode photocurrent density *vs.* voltage (J-V) characteristics, the device's CA response is measured in an aqueous electrolyte under AM1.5G one sun or concentrated sunlight illumination with no bias (0 V *vs.* counter electrode) in a two-electrode configuration. The J-V characteristics of the photoelectrode are periodically recorded during the stability experiments to evaluate whether the sample has degraded (reduction in photocurrent density or onset potential). Once the device reaches its catastrophic failure point, physical failure modes observed microscopically, and spectroscopic analysis of chemical transformations can be coupled with electrochemical procedures to inform the degradation mechanism.

Spectroscopy and electron microscopy provide further insight into the failure mechanism *via* structural analysis. Using these techniques, we can effectively compare the chemical transformation of the surface morphology before and after the photoelectrochemical reaction, while such chemical transformation either leads to catastrophic degradation or self-healing/self-improving (Kanan and Nocera, 2008; Malara et al., 2016; Toma et al., 2016; Zeng et al., 2021). Either way, the knowledge we obtain through structural analysis will provide feedback for further optimization of our device. Toma et al. (2016) employed EC-AFM to monitor the corrosion of $BiVO_4$ and provide mechanistic insights into the chemical and photochemical instability of this material, which can be used to guide approaches for further improvement of $BiVO_4$ photoanode. On the other hand, self-improving *via* chemical transformation can also be revealed by structural analysis. Zeng et al. (2021) reported that GaN can achieve self-improvement during HER by forming an ultrathin layer of gallium oxynitride, which led to lower overpotential, and higher charge transfer efficiency, and improved durability.

Equipment and Supplies

Electrochemical potentiostat- This is the essential equipment required to conduct J-V, Mott-Schottky, OCP, and CA experiments.

GC- A GC analyzer is required to detect hydrogen and oxygen gas products during PEC reactions. This equipment is also used to determine FE (Chen et al., 2011) and H_2 gas evolution rates.

ICP-MS- ICP-MS is essential to determine any dissolved photoelectrode material, co-catalysts, and other metals/non-metals in electrolyte solution during the reaction (Deutsch et al., 2006).

SEM- This is one of the most used techniques to determine the morphological changes before and after stability experiments, with resolutions in the range of a few nanometers to sub-micrometer scale.

STEM- STEM is essential in analyzing nanometer, or atomic-scale feature sizes by using annular dark-field imaging, spectroscopic mapping by EDX, or EELS.

AFM- AFM scans provide nanometer resolution images of the top surface. For 2D films, AFM is sufficient to understand the surface degradation after stability experiments. However, for 1D nanostructures, this technique may be somewhat limited. Therefore, it is preferred to use SEM or STEM for 1D photoelectrodes. As mentioned earlier, *in-situ* AFM measurements such as EC-AFM and PC-AFM are instrumental in determining the nanoscale origin of photocurrent (Eichhorn et al., 2018; Nellist et al., 2018; Zeng et al., 2021).

XPS- This technique helps identify the elements, chemical states, and electronic structure of the photoelectrode material.

XRD- XRD scans provide critical information for structural changes of the photoelectrode materials, such as crystal structures, phases, defects, and strain distribution. Therefore, any changes in crystallinity of the material revealed by XRD scans can provide critical information regarding photocorrosion on the surfaces.

Reagents- Alkaline solution (potassium hydroxide, etc.), acid solution (sulfuric acid, etc.), and deionized water.

The essential protocols, based on the authors' practical experience (Vanka et al., 2019; Zeng et al., 2021), needed for performing long term stability tests for >1,000 h are:

1. PEC cell design: The major parameters impacting the PEC cell performance include electrolyte solution/volume and the ionic path length (Hernández-Pagán et al., 2012). The PEC cells (or reactors) can be classified based on compartmentalization. As shown in **Figure 3A**, both wired and wireless electrode assembly configurations can be implemented in PEC cells comprising either a single or double compartment (Bosserez et al., 2015). A major limitation of single compartment PEC cells (see **Figure 3A**) is that evolving H_2 and O_2 gases are mixed in the same chamber, which leads to recombination reactions. These unwanted chemical reactions can be avoided by producing H_2 and O_2 in separate compartments using an H-cell (see **Figure 3B**). An important issue with unsealed PEC cells is the presence of atmospheric oxygen, which often produces deleterious effects on the water-splitting experiments (Hagfeldt et al., 1995). Using a dual compartment cell (see **Figure 3C**) with SEA helps seal off the sample from the environment and thus prevents air from entering the cell (Bosserez et al., 2015). In addition, this cell (see **Figure 3C**) has in- and outlet connections for feeding electrolyte solution and product collection, respectively. It is also essential to design proper compression cells to minimize bubbling and/or electrolyte resistance (Vanka et al., 2019). Furthermore, it is highly desirable that the cells have various aperture openings to properly test samples of different sizes.
2. Back contacts: Dissolution of epoxy accelerates photoelectrode degradation (Bae et al., 2019; Vanka et al., 2019), and dissolved silver may lead to dubious results in surface-sensitive XPS/ICP-MS analysis. Thus, it is essential to eliminate epoxy and silver paste by designing the compression cell with a metal pad, which allows the front side of the sample to be exposed to the electrolyte with the backside of the sample making electrical contact with the metal pad.
3. Electrolyte: In many cases, PEC experiments are conducted in near-neutral pH electrolyte solutions because of safety concerns and exacerbation of pinholes issues in the protection layers (as discussed earlier) under extremely acidic or alkaline electrolyte solutions (which are used in commercial electrolyzers) (Obata et al., 2020). However, the major disadvantage of using such pH-neutral conditions is the low concentration of H^+/OH^- in the electrolyte solutions. At such low concentrations, the reactants are rapidly consumed during CA experiments, and their refurbishment from the other electrolyte regions is hampered by mass transport limitations (Shinagawa and Takanabe, 2015a). This concentration imbalance leads to extra overpotentials in addition to kinetic overpotentials from catalysts (Shinagawa and Takanabe, 2015b; Ahmet et al., 2019). Furthermore, in an H-cell (see **Figure 3B**) with no buffer in the electrolyte solution, the generation of H_2 and O_2 gases in separate compartments leads to elevated and reduced pH, respectively. The local pH shift in the electrolyte solution during PCET reactions near the photoelectrode surface is a critical in factor determining its stability and efficiency. To mitigate this issue, buffer ions are added to the electrolyte

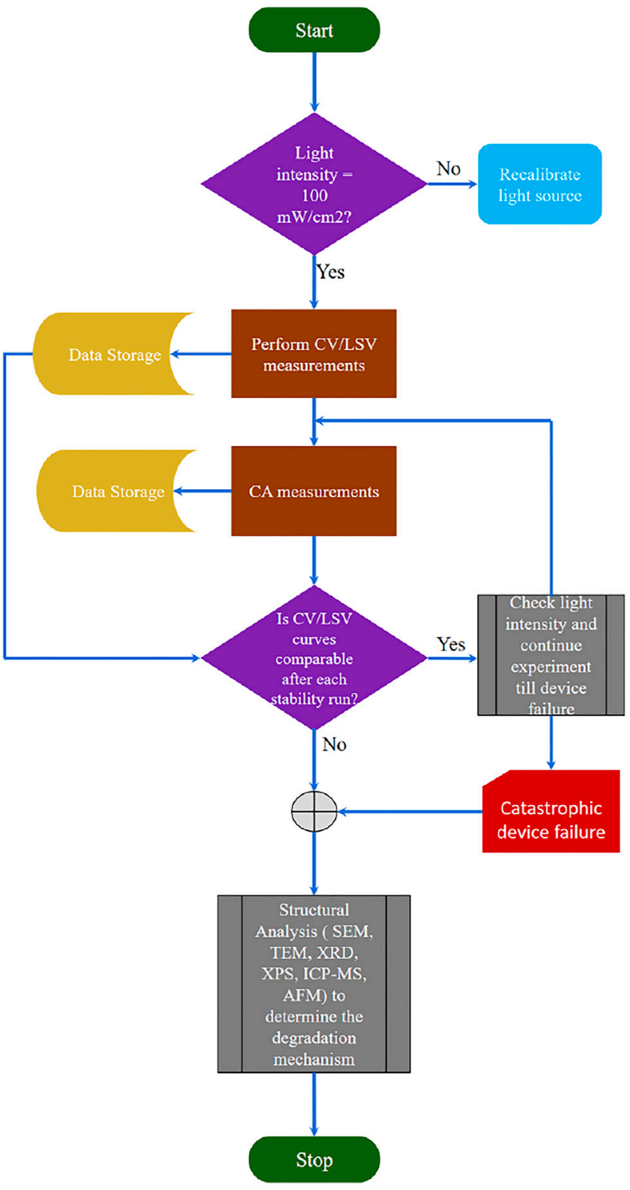

FIGURE 4 | Flowchart illustrating the steps for performing long-term stability experiments.

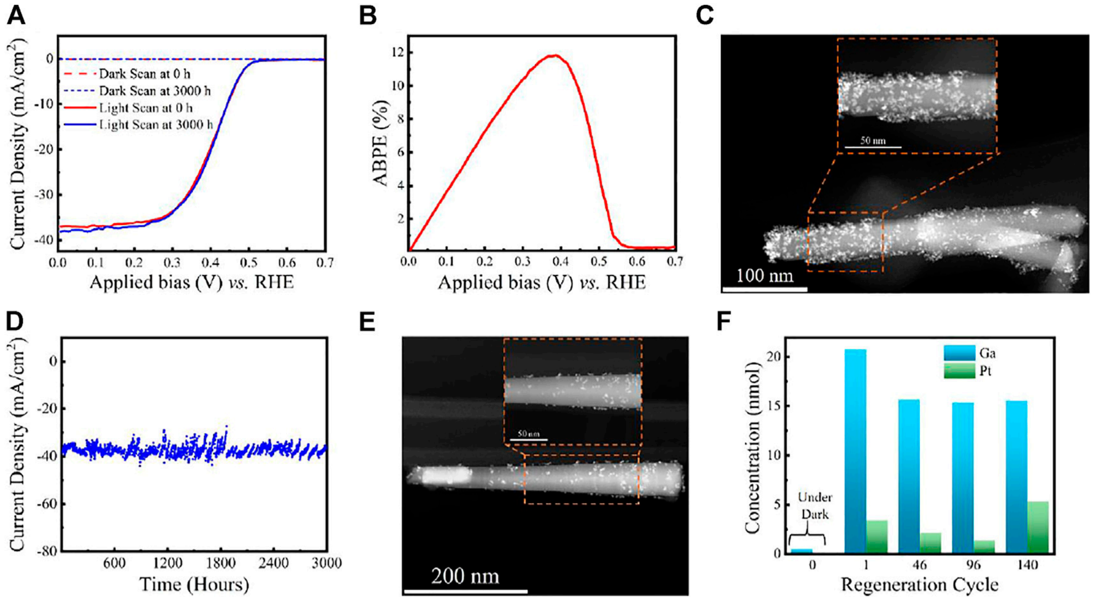

FIGURE 5 | (A) LSV comparison of GaN/Si photocathode before and after 3,000 h stability experiments. **(B)** ABPE of Pt decorated GaN/Si photocathode before stability experiments in 0.5 M H_2SO_4 under AM 1.5G one-sun illumination. **(C)** STEM image of Pt decorated GaN nanowire before stability experiment. **(D)** Ultra-long term stability experiments using GaN/Si photocathode under continuous AM 1.5G one-sun illumination. **(E)** STEM image of Pt decorated GaN nanowire after 3,000 h stability experiments. **(F)** ICP-MS measurements of liquid samples at different runs during the experiment. Reprinted (adapted) with permission from Vanka et al. (2019). Copyright 2019 Royal Society of Chemistry.

solution. However, it is hard to eliminate the local pH gradient as the diffusion coefficients of buffer ions are smaller compared to those of H^+/OH^- ions (Shinagawa and Takanabe, 2016; Ahmet et al., 2019).

4. Counter electrode: The counter electrode plays a vital role in determining the stability of the entire PEC cell (Hodes, 2012). Some counter electrodes dissolve in the electrolyte during the reaction and can be plated on the photoelectrode, complicating PEC analysis (Choi et al., 2014). Thus, choosing stable counter electrodes and constructing a PEC compression cell with a membrane is important to prevent unwanted metal deposition on the photoelectrode surface.

Instrument or Method Calibration and Standardization

Light source intensity: The light source needs to be regularly recalibrated to maintain 100 mW/cm^2 power density throughout the stability test (Chen et al., 2011), especially if it is not continuously measured over time.

Electrochemical potentiostat: It is quintessential to calibrate these instruments by following the vendor's recommendations correctly to obtain reliable and consistent results.

Example of Pt-Decorated GaN/Si Photocathode Stability

Here we explain the three-electrode stability measurements of N-terminated GaN/Si photocathode considering the protocols mentioned earlier.

Step 1: From **Figure 4**, the first basic step is to calibrate the light source to 100 mW/cm^2. Mi et al. used Si (bandgap ~1.1 eV) reference cell to calibrate their light source for GaN/Si photocathode (Vanka et al., 2018).

Step 2: From **Figures 5A,B**, LSV scans show photocurrent onset voltage ~0.56 V *vs.* NHE, high saturation photocurrent density ~37 mA/cm^2 and ABPE ~11.9% (at 0.37 V *vs.* NHE) (Vanka et al., 2018; Vanka et al., 2019). As discussed earlier and shown in **Figure 4**, using the best sample for stability experiments in terms of high ABPE and excellent LSV characteristics is essential. The morphology of the 1D nanowires with co-catalyst nanoparticles is determined using STEM and SEM techniques (Vanka et al., 2018; Vanka et al., 2019). However, as discussed earlier, the AFM technique may be challenging for analyzing 1D nanowires and catalyst nanoparticles. **Figure 5C** shows the STEM image of the Pt decorated GaN/Si photocathode before CA experiments.

Step 3: For the GaN/Si photocathode samples having ABPE >10%, CA experiments are performed in a three-electrode PEC configuration at 0 V *vs.* NHE in 0.5 M H_2SO_4 under AM 1.5G one sun (Vanka et al., 2018; Vanka et al., 2019). Zeng et al. demonstrated that the photocurrent density of GaN/Si photocathode does not degrade under concentrated sunlight (~3 suns) illumination for 150 h (Zeng et al., 2021).

Step 4: LSV scans are measured after every run (each run is about 22–24 h duration). As shown in **Figure 4**, these scans need to be compared with the J-V characteristics before starting the stability experiments to determine whether to proceed further with the CA stability experiments or not (Vanka et al., 2019).

Step 5: The GaN/Si photocathode showed a decrement in photocurrent density, and J-V characteristics changed dramatically after 113 h (Vanka et al., 2018). By performing the structural analysis (STEM and SEM), the root cause of this degradation was attributed to the loss of Pt co-catalyst nanoparticles on the GaN nanowire surface (Vanka et al., 2018). Thus, to maintain the J-V and CA characteristics of GaN/Si photocathode over long periods of stability testing, it is pertinent to regenerate the co-catalyst regularly.

Step 6: Using a new sample (with the same J-V characteristics mentioned in step 2), the experiment is repeated from step 1. In this run, catalyst regeneration is implemented after approximately every 24 h to achieve long-term stability of >3,000 h (Vanka et al., 2019) (see **Figure 5D**) with no degradation in J-V performance after the experiments (see **Figure 5A**).

Step 7: The ultra-long stability (CA) experiments for GaN/Si photocathode are stopped after 3,000 h. From **Figure 5E**, STEM analysis reveals no apparent degradation in GaN nanowire dimensions and fewer Pt co-catalyst nanoparticles on the GaN surface than in **Figure 5C** (Vanka et al., 2019). Furthermore, ICP-MS (**Figure 5F**) shows that GaN remains stable throughout the CA experiments. Thus, the structural analysis and theoretical studies reveal that the stability of Pt decorated GaN/Si photocathode is limited by Pt nanoparticles rather than GaN/Si light absorber (Vanka et al., 2018; Vanka et al., 2019; Zeng et al., 2021).

CONCLUSION

This work provides an overview of the stability requirements of a photoelectrode and the pertinent need to develop standard protocols for long-term stability measurements in a two-electrode and three-electrode configuration. We have illustrated a framework to evaluate the stability of photoelectrode with an optimized experimental setup based on light source calibration, counter electrode optimization, PEC chamber, and sample preparation. The GaN/Si photoelectrode example showed how these protocols lead to proper stability measurements of the device and further improve the performance by understanding the degradation mechanism. We believe that for future stability studies, these benchmarking protocols can serve as valuable guidelines in accelerating the search for new photoelectrodes which can cut the "Gordian knot" of simultaneously achieving ultra-high stability (>10,000 h) and high efficiency (>15%).

DATA AVAILABILITY STATEMENT

Publicly available datasets were analyzed in this study. This data can be found here: https://pubs.rsc.org/en/content/articlelanding/2019/ta/c9ta09926c#!divAbstract.

AUTHOR CONTRIBUTIONS

SV and ZM conceived the study and wrote the manuscript. GZ, TD, and FT assisted in writing the article.

ACKNOWLEDGMENTS

The authors gratefully acknowledge research support from the HydroGEN Advanced Water Splitting Materials Consortium, established as part of the Energy Materials Network under the U. S. Department of Energy, under Contract Number DE-EE0008086 for the University of Michigan. This work was authored in part by the National Renewable Energy Laboratory, operated by Alliance for Sustainable Energy, LLC, for the U.S. Department of Energy under Contract Number DE-AC36-08GO28308. The U.S. Government retains and the publisher, by accepting the article for publication, acknowledges that the U.S. Government retains a nonexclusive, paid-up, irrevocable, worldwide license to publish or reproduce the published form of this work, or allow others to do so, for the U.S. Government purposes.

REFERENCES

Ahmet, I. Y., Ma, Y., Jang, J.-W., Henschel, T., Stannowski, B., Lopes, T., et al. (2019). Demonstration of a 50 Cm2 BiVO4 Tandem Photoelectrochemical-Photovoltaic Water Splitting Device. *Sustain. Energ. Fuels* 3 (9), 2366–2379. doi:10.1039/c9se00246d

AlOtaibi, B., Nguyen, H. P. T., Zhao, S., Kibria, M. G., Fan, S., and Mi, Z. (2013). Highly Stable Photoelectrochemical Water Splitting and Hydrogen Generation Using a Double-Band InGaN/GaN Core/Shell Nanowire Photoanode. *Nano Lett.* 13 (9), 4356–4361. doi:10.1021/nl402156e

Bae, D., Seger, B., Hansen, O., Vesborg, P. C. K., and Chorkendorff, I. (2019). Durability Testing of Photoelectrochemical Hydrogen Production under Day/Night Light Cycled Conditions. *Chemelectrochem* 6 (1), 106–109. doi:10.1002/celc.201800918

Bae, D., Seger, B., Vesborg, P. C. K., Hansen, O., and Chorkendorff, I. (2017). Strategies for Stable Water Splitting via Protected Photoelectrodes. *Chem. Soc. Rev.* 46 (7), 1933–1954. doi:10.1039/c6cs00918b

Ben-Naim, M., Britto, R. J., Aldridge, C. W., Mow, R., Steiner, M. A., Nielander, A. C., et al. (2020). Addressing the Stability Gap in Photoelectrochemistry: Molybdenum Disulfide Protective Catalysts for Tandem III-V Unassisted Solar Water Splitting. *ACS Energ. Lett.* 5 (8), 2631–2640. doi:10.1021/acsenergylett.0c01132

Bosserez, T., Rongé, J., van Humbeeck, J., Haussener, S., and Martens, J. (2015). Design of Compact Photoelectrochemical Cells for Water Splitting. *Oil Gas Sci. Technol. - Rev. IFP Energies Nouvelles* 70 (5), 877–889. doi:10.2516/ogst/2015015

Britto, R. J., Benck, J. D., Young, J. L., Hahn, C., Deutsch, T. G., and Jaramillo, T. F. (2016). Molybdenum Disulfide as a Protection Layer and Catalyst for Gallium Indium Phosphide Solar Water Splitting Photocathodes. *J. Phys. Chem. Lett.* 7 (11), 2044–2049. doi:10.1021/acs.jpclett.6b00563

Butler, K. T., Dringoli, B. J., Zhou, L., Rao, P. M., Walsh, A., and Titova, L. V. (2016). Ultrafast Carrier Dynamics in BiVO4 Thin Film Photoanode Material: Interplay between Free Carriers, Trapped Carriers and Low-Frequency Lattice Vibrations. *J. Mater. Chem. A.* 4 (47), 18516–18523. doi:10.1039/c6ta07177e

Chen, S., and Wang, L.-W. (2012). Thermodynamic Oxidation and Reduction Potentials of Photocatalytic Semiconductors in Aqueous Solution. *Chem. Mater.* 24 (18), 3659–3666. doi:10.1021/cm302533s

Chen, Z., Jaramillo, T. F., Deutsch, T. G., Kleiman-Shwarsctein, A., Forman, A. J., Gaillard, N., et al. (2011). Accelerating Materials Development for Photoelectrochemical Hydrogen Production: Standards for Methods, Definitions, and Reporting Protocols. *J. Mater. Res.* 25 (01), 3–16. doi:10.1557/jmr.2010.0020

Choi, M. J., Jung, J.-Y., Park, M.-J., Song, J.-W., Lee, J.-H., and Bang, J. H. (2014). Long-term Durable Silicon Photocathode Protected by a Thin Al2O3/SiOx Layer for Photoelectrochemical Hydrogen Evolution. *J. Mater. Chem. A.* 2 (9), 2928. doi:10.1039/c3ta14443g

Costentin, C., and Nocera, D. G. (2017). Self-healing Catalysis in Water. *Proc. Natl. Acad. Sci. U.S.A.* 114 (51), 13380–13384. doi:10.1073/pnas.1711836114

Deutsch, T. G., Koval, C. A., and Turner, J. A. (2006). III−V Nitride Epilayers for Photoelectrochemical Water Splitting: GaPN and GaAsPN. *J. Phys. Chem. B* 110 (50), 25297–25307. doi:10.1021/jp0652805

Di Valentin, C., and Selloni, A. (2011). Bulk and Surface Polarons in Photoexcited Anatase TiO2. *J. Phys. Chem. Lett.* 2 (17), 2223–2228. doi:10.1021/jz2009874

Dias, P., Vilanova, A., Lopes, T., Andrade, L., and Mendes, A. (2016). Extremely Stable Bare Hematite Photoanode for Solar Water Splitting. *Nano Energy* 23, 70–79. doi:10.1016/j.nanoen.2016.03.008

Eichhorn, J., Kastl, C., Cooper, J. K., Ziegler, D., Schwartzberg, A. M., Sharp, I. D., et al. (2018). Nanoscale Imaging of Charge Carrier Transport in Water Splitting Photoanodes. *Nat. Commun.* 9 (1), 2597. doi:10.1038/s41467-018-04856-8

Fan, R., Dong, W., Fang, L., Zheng, F., Su, X., Zou, S., et al. (2015). Stable and Efficient Multi-Crystalline N+p Silicon Photocathode for H2 Production with Pyramid-like Surface Nanostructure and Thin Al2O3 Protective Layer. *Appl. Phys. Lett.* 106 (1), 013902. doi:10.1063/1.4905511

Feng, C., Wang, F., Liu, Z., Nakabayashi, M., Xiao, Y., Zeng, Q., et al. (2021). A Self-Healing Catalyst for Electrocatalytic and Photoelectrochemical Oxygen Evolution in Highly Alkaline Conditions. *Nat. Commun.* 12 (1), 5980. doi:10.1038/s41467-021-26281-0

Hagfeldt, A., Lindström, H., Södergren, S., and Lindquist, S.-E. (1995). Photoelectrochemical Studies of Colloidal TiO_2 Films: The Effect of Oxygen Studied by Photocurrent Transients. *J. Electroanalytical Chem.* 381 (1), 39–46. doi:10.1016/0022-0728(94)03622-a

He, Y., Vanka, S., Gao, T., He, D., Espano, J., Zhao, Y., et al. (2019). Dependence of Interface Energetics and Kinetics on Catalyst Loading in a Photoelectrochemical System. *Nano Res.* 12, 2378–2384. doi:10.1007/s12274-019-2346-3

Hernández-Pagán, E. A., Vargas-Barbosa, N. M., Wang, T., Zhao, Y., Smotkin, E. S., and Mallouk, T. E. (2012). Resistance and Polarization Losses in Aqueous Buffer–Membrane Electrolytes for Water-Splitting Photoelectrochemical Cells. *Energ. Environ. Sci.* 5 (6), 7582. doi:10.1039/C2EE03422K

Hodes, G. (2012). Photoelectrochemical Cell Measurements: Getting the Basics Right. *J. Phys. Chem. Lett.* 3 (9), 1208–1213. doi:10.1021/jz300220b

Janotti, A., Varley, J. B., Choi, M., and Van de Walle, C. G. (2014). Vacancies and Small Polarons in $SrTiO_3$. *Phys. Rev. B* 90 (8), 085202. doi:10.1103/physrevb.90.085202

Kainthla, R. C., Zelenay, B., and Bockris, J. O. M. (1986). Protection of n-Si Photoanode against Photocorrosion in Photoelectrochemical Cell for Water Electrolysis. *J. Electrochem. Soc.* 133 (2), 248–253. doi:10.1149/1.2108556

Kanan, M. W., and Nocera, D. G. (2008). *In Situ* Formation of an Oxygen-Evolving Catalyst in Neutral Water Containing Phosphate and Co 2+. *Science* 321 (5892), 1072–1075. doi:10.1126/science.1162018

Kaneko, H., Minegishi, T., and Domen, K. (2018). Recent Progress in the Surface Modification of Photoelectrodes toward Efficient and Stable Overall Water Splitting. *Chem. Eur. J.* 24 (22), 5697–5706. doi:10.1002/chem.201703104

Kibria, M. G., Qiao, R., Yang, W., Boukahil, I., Kong, X., Chowdhury, F. A., et al. (2016). Atomic-Scale Origin of Long-Term Stability and High Performance Ofp-GaN Nanowire Arrays for Photocatalytic Overall Pure Water Splitting. *Adv. Mater.* 28 (38), 8388–8397. doi:10.1002/adma.201602274

King, L. A., Hellstern, T. R., Park, J., Sinclair, R., and Jaramillo, T. F. (2017). Highly Stable Molybdenum Disulfide Protected Silicon Photocathodes for Photoelectrochemical Water Splitting. *ACS Appl. Mater. Inter.* 9 (42), 36792–36798. doi:10.1021/acsami.7b10749

Kuang, Y., Jia, Q., Ma, G., Hisatomi, T., Minegishi, T., Nishiyama, H., et al. (2016). Ultrastable Low-Bias Water Splitting Photoanodes via Photocorrosion Inhibition and *In Situ* Catalyst Regeneration. *Nat. Energ.* 2 (1), 16191. doi:10.1038/nenergy.2016.191

Lewerenz, H. J. (2014). Semiconductor Surface Transformations for Photoelectrochemical Energy Conversion. *J. Electrochem. Soc.* 161 (13), H3117–H3129. doi:10.1149/2.0211413jes

Lutterman, D. A., Surendranath, Y., and Nocera, D. G. (2009). A Self-Healing Oxygen-Evolving Catalyst. *J. Am. Chem. Soc.* 131 (11), 3838–3839. doi:10.1021/ja900023k

Malara, F., Fabbri, F., Marelli, M., and Naldoni, A. (2016). Controlling the Surface Energetics and Kinetics of Hematite Photoanodes through Few Atomic Layers of NiOx. *ACS Catal.* 6 (6), 3619–3628. doi:10.1021/acscatal.6b00569

Mei, B., Seger, B., Pedersen, T., Malizia, M., Hansen, O., Chorkendorff, I., et al. (2014). Protection of P+-N-Si Photoanodes by Sputter-Deposited Ir/IrOx Thin Films. *J. Phys. Chem. Lett.* 5 (11), 1948–1952. doi:10.1021/jz500865g

Moon, C., Seger, B., Vesborg, P. C. K., Hansen, O., and Chorkendorff, I. (2020). Wireless Photoelectrochemical Water Splitting Using Triple-Junction Solar Cell Protected by TiO2. *Cel Rep. Phys. Sci.* 1 (12), 100261. doi:10.1016/j.xcrp.2020.100261

Najafpour, M. M., Fekete, M., Sedigh, D. J., Aro, E.-M., Carpentier, R., Eaton-Rye, J. J., et al. (2015). Damage Management in Water-Oxidizing Catalysts: From Photosystem II to Nanosized Metal Oxides. *ACS Catal.* 5 (3), 1499–1512. doi:10.1021/cs5015157

Nandjou, F., and Haussener, S. (2017). Degradation in Photoelectrochemical Devices: Review with an Illustrative Case Study. *J. Phys. D: Appl. Phys.* 50 (12), 124002. doi:10.1088/1361-6463/aa5b11

Nellist, M. R., Qiu, J., Laskowski, F. A. L., Toma, F. M., and Boettcher, S. W. (2018). Potential-Sensing Electrochemical AFM Shows CoPi as a Hole Collector and Oxygen Evolution Catalyst on BiVO4 Water-Splitting Photoanodes. *ACS Energ. Lett.* 3 (9), 2286–2291. doi:10.1021/acsenergylett.8b01150

Obata, K., van de Krol, R., Schwarze, M., Schomäcker, R., and Abdi, F. F. (2020). *In Situ* observation of pH Change during Water Splitting in Neutral pH Conditions: Impact of Natural Convection Driven by Buoyancy Effects. *Energy Environ. Sci.* 13 (12), 5104–5116. doi:10.1039/d0ee01760d

Ros, C., Andreu, T., Hernandez-Alonso, M. D., Penelas-Perez, G., Arbiol, J., and Morante, J. R. (2017). Charge Transfer Characterization of ALD-Grown TiO_2 Protective Layers in Silicon Photocathodes. *ACS Appl. Mater. Inter.* 9 (21), 17932–17941. doi:10.1021/acsami.7b02996

Shaner, M. R., Atwater, H. A., Lewis, N. S., and McFarland, E. W. (2016). A Comparative Technoeconomic Analysis of Renewable Hydrogen Production Using Solar Energy. *Energ. Environ. Sci.* 9 (7), 2354–2371. doi:10.1039/c5ee02573g

Shaner, M. R., Hu, S., Sun, K., and Lewis, N. S. (2015). Stabilization of Si Microwire Arrays for Solar-Driven H2O Oxidation to O2(g) in 1.0 M KOH(aq) Using Conformal Coatings of Amorphous TiO2. *Energ. Environ. Sci.* 8 (1), 203–207. doi:10.1039/c4ee03012e

Shinagawa, T., and Takanabe, K. (2015). Electrocatalytic Hydrogen Evolution under Densely Buffered Neutral pH Conditions. *J. Phys. Chem. C* 119 (35), 20453–20458. doi:10.1021/acs.jpcc.5b05295

Shinagawa, T., and Takanabe, K. (2016). Electrolyte Engineering toward Efficient Hydrogen Production Electrocatalysis with Oxygen-Crossover Regulation under Densely Buffered Near-Neutral pH Conditions. *J. Phys. Chem. C* 120 (3), 1785–1794. doi:10.1021/acs.jpcc.5b12137

Shinagawa, T., and Takanabe, K. (2015). Identification of Intrinsic Catalytic Activity for Electrochemical Reduction of Water Molecules to Generate Hydrogen. *Phys. Chem. Chem. Phys.* 17 (23), 15111–15114. doi:10.1039/c5cp02330k

Su, J., Wei, Y., and Vayssieres, L. (2017). Stability and Performance of Sulfide-, Nitride-, and Phosphide-Based Electrodes for Photocatalytic Solar Water Splitting. *J. Phys. Chem. Lett.* 8 (20), 5228–5238. doi:10.1021/acs.jpclett.7b00772

Toma, F. M., Cooper, J. K., Kunzelmann, V., McDowell, M. T., Yu, J., Larson, D. M., et al. (2016). Mechanistic Insights into Chemical and Photochemical Transformations of Bismuth Vanadate Photoanodes. *Nat. Commun.* 7, 12012. doi:10.1038/ncomms12012

Vanka, S., Arca, E., Cheng, S., Sun, K., Botton, G. A., Teeter, G., et al. (2018). High Efficiency Si Photocathode Protected by Multifunctional GaN Nanostructures. *Nano Lett.* 18 (10), 6530–6537. doi:10.1021/acs.nanolett.8b03087

Vanka, S., Sun, K., Zeng, G., Pham, T. A., Toma, F. M., Ogitsu, T., et al. (2019). Long-term Stability Studies of a Semiconductor Photoelectrode in Three-

Electrode Configuration. *J. Mater. Chem. A.* 7, 27612–27619. doi:10.1039/c9ta09926c

Vanka, S., Zhou, B., Awni, R. A., Song, Z., Chowdhury, F. A., Liu, X., et al. (2020). InGaN/Si Double-Junction Photocathode for Unassisted Solar Water Splitting. *ACS Energ. Lett.* 5 (12), 3741–3751. doi:10.1021/acsenergylett.0c01583

Varadhan, P., Fu, H.-C., Priante, D., Retamal, J. R. D., Zhao, C., Ebaid, M., et al. (2017). Surface Passivation of GaN Nanowires for Enhanced Photoelectrochemical Water-Splitting. *Nano Lett.* 17 (3), 1520–1528. doi:10.1021/acs.nanolett.6b04559

Wang, Y., Wu, Y., Schwartz, J., Sung, S. H., Hovden, R., and Mi, Z. (2019). A Single-Junction Cathodic Approach for Stable Unassisted Solar Water Splitting. *Joule* 3 (10), 2444–2456. doi:10.1016/j.joule.2019.07.022

Yang, W., Prabhakar, R. R., Tan, J., Tilley, S. D., and Moon, J. (2019). Strategies for Enhancing the Photocurrent, Photovoltage, and Stability of Photoelectrodes for Photoelectrochemical Water Splitting. *Chem. Soc. Rev.* 48 (19), 4979–5015. doi:10.1039/c8cs00997j

Yin, Z., Fan, R., Huang, G., and Shen, M. (2018). 11.5% Efficiency of TiO2 Protected and Pt Catalyzed N+np+-Si Photocathodes for Photoelectrochemical Water Splitting: Manipulating the Pt Distribution and Pt/Si Contact. *Chem. Commun.* 54 (5), 543–546. doi:10.1039/c7cc08409a

Young, J. L., Steirer, K. X., Dzara, M. J., Turner, J. A., and Deutsch, T. G. (2016). Remarkable Stability of Unmodified GaAs Photocathodes during Hydrogen Evolution in Acidic Electrolyte. *J. Mater. Chem. A.* 4 (8), 2831–2836. doi:10.1039/c5ta07648j

Zeng, G., Pham, T. A., Vanka, S., Liu, G., Song, C., Cooper, J. K., et al. (2021). Development of a Photoelectrochemically Self-Improving Si/GaN Photocathode for Efficient and Durable H2 Production. *Nat. Mater.* 20, 1130–1135. doi:10.1038/s41563-021-00965-w

Author Disclaimer: The views expressed in the article do not necessarily represent the views of the DOE or the U.S. Government.

Conflict of Interest: Some IP related to this work has been licensed to NS Nanotech, Inc. and NX Fuels, Inc. (dba Carbon Fuels), which were co-founded by ZM. The University of Michigan and Mi have a financial interest in NS Nanotech and NX Fuels.

The remaining authors declare that the research was conducted in the absence of any commercial or financial relationships that could be construed as a potential conflict of interest.

NOMENCLATURE

ABPE applied bias photon-to-current efficiency

AFM atomic force microscopy

ALD atomic layer deposition

CV cyclic voltammetry

EC-AFM electrochemical AFM

EDX energy-dispersive X-ray spectroscopy

EELS electron energy loss spectroscopy

FE faradaic efficiency

GC gas chromatography

ICP-MS inductively coupled plasma mass spectrometry

LSV linear scan voltammetry

OCP open circuit potential

PC-AFM- photoconductive AFM

PCET proton-coupled electron transfer

SEA separator-electrode assemblies

SEM scanning electron microscopy

STEM scanning transmission electron microscopy

STH solar-to-hydrogen efficiency

XPS x-ray photoelectron spectroscopy

XRD x-ray diffraction

frontiers | Frontiers in Energy Research

METHODS
published: 26 May 2022
doi: 10.3389/fenrg.2022.871604

Protocol for Screening Water Oxidation or Reduction Electrocatalyst Activity in a Three-Electrode Cell for Alkaline Exchange Membrane Electrolysis

*Erin Brahm Creel[1], Xiang Lyu[1], Geoff McCool[2], Ryan J. Ouimet[3] and Alexey Serov[1]**

[1]*Electrification and Energy Infrastructures Division, Oak Ridge National Laboratory, Oak Ridge, TN, United States,* [2]*Pajarito Powder, LLC (PPC), Albuquerque, NM, United States,* [3]*Nel Hydrogen, Wallingford, CT, United States*

Accurate and reproducible screening of the electrocatalytic activity of novel materials for Oxygen Evolution Reaction (OER) and Hydrogen Evolution Reaction (HER) requires establishing an easily adoptable harmonized testing protocol. Herein, we describe a robust, instrumentation-independent testing technique utilizing a three-electrode cell with a fully immersed working electrode. Compared to rotating disk electrode (RDE) techniques, this protocol produces current densities close to those obtained in real electrolyzers and eliminates the usage of the expensive RDE apparatus.

Keywords: oxygen evolution reaction, hydrogen evolution reaction, electrochemistry, electrolysis, water splitting

Edited by:
Olga A. Marina,
Pacific Northwest National Laboratory (DOE), United States

Reviewed by:
Mike Lyons,
Trinity College Dublin, Ireland
Mikkel Kraglund,
Technical University of Denmark, Denmark

****Correspondence:***
Alexey Serov
serova@ornl.gov

Specialty section:
This article was submitted to Process and Energy Systems Engineering, a section of the journal Frontiers in Energy Research

Received: *08 February 2022*
Accepted: *12 May 2022*
Published: *26 May 2022*

Citation:
Creel EB, Lyu X, McCool G, Ouimet RJ and Serov A (2022) Protocol for Screening Water Oxidation or Reduction Electrocatalyst Activity in a Three-Electrode Cell for Alkaline Exchange Membrane Electrolysis. Front. Energy Res. 10:871604. doi: 10.3389/fenrg.2022.871604

INTRODUCTION

The number of novel electrocatalysts for low-temperature water electrolysis is dramatically increasing annually. Having a tremendous amount of OER/HER performance data associated with various catalyst formulations makes comparison of their activity extremely complicated and convoluted. It is well known that most activity data is obtained under different conditions, usually based on legacy parameters used within each individual research groups to compare data with a previous dataset.

This situation makes establishing baseline state-of-the-art (SoA) electrocatalysts complex, impedes the selection of future material development for low-temperature water electrolysis, and overall slows down progress in the field of green hydrogen production.

We note that the electrochemical activity of electrocatalysts is evaluated primarily in RDE experiments (McCrory et al., 2013), which may not be the best comparison for electrolysis, especially for OER (Hartig-Weiss et al., 2020). The low loading of Platinum Group Metal (PGM)-free oxides on the RDE (typically 0.2–0.6 mg cm^{-2}) makes the evaluation of these catalysts complicated, as these oxides usually have very low electrical conductivity and thus low activity at low loading. The electrochemical activity of low-conductivity catalysts in Gas Diffusion Electrodes (GDEs) or Catalyst Coated Membranes (CCMs) at loadings of 2–8 mg cm^{-2} will be substantially different than that in a conventional RDE (Kroschel et al., 2019). Additionally, the substrate for catalyst loading in the RDE instrument is very small (usually <0.5 cm^2), which is hundreds of times below in the electrode geometric surface area in real electrolyzers. The smooth, nonporous (typically glassy carbon) catalyst support in an RDE is substantially different from the textured, high-porosity GDEs in an electrolyzer. Finally, the RDE is an expensive instrument, and not accessible widely.

A static electrode can be used to compare the electrochemical activity of catalysts without the need for an RDE (Du et al., 2014). Herein, we describe a robust, instrumentation-independent testing technique utilizing a three-electrode cell with a fully immersed working electrode. The protocol's advantages compared to RDE testing include the ability to test low-conductivity catalysts at higher loading and thus increased current densities, eliminating the usage of expensive RDE equipment, and easier bubble management in OER, more versatility in substrate. This protocol with fully immersed working electrode allows for rapid catalyst screening in conditions that are closer to those in an electrolyzer than the conditions in an RDE.

PROTOCOL SCOPE

Scope and Applicability

This protocol describes a standard method for screening HER/OER electrocatalysts using fully immersed electrodes covered with an aqueous electrolyte. The methods described here are optimized for use in room temperature alkaline solutions with a high loading of electrocatalyst (up to 4 mg cm^{-2}) and can be used for both PGM and PGM-free catalysts.

Summary of Method

This protocol allows the user to quickly and easily measure an electrocatalyst's HER/OER activity. The electrochemical performance datasets from electrocatalysts characterized using these methods can be directly compared. This protocol enables rapid screening of newly developed electrocatalyst materials before incorporating them into a full electrolyzer membrane electrode assembly (MEA). In this protocol, users will perform linear sweep voltammetry (LSV) and bulk electrolysis via chronoamperometry (CA) in a standard three-electrode electrochemical cell with an aqueous electrolyte.

Personnel Qualifications/Responsibilities

Following proper safety training on the electrical equipment used in this protocol, these experiments can be done by technicians, undergraduate students, graduate students, postdoctoral researchers, or other scientists.

Health and Safety Warning

Do not touch the electrochemical cell, wires, or potentiostat while the experiment is in progress (active potentiostat) to prevent electrical shock. Be aware of all hazards listed in the safety data sheet (SDS) for the electrolyte used in the electrochemical cell.

Equipment and Supplies

To complete the procedure properly, researchers need a potentiostat, electrolyte, and electrodes. A standard potentiostat with 5 V and 5 A capability is sufficient for this protocol. The electrolyte consists of de-ionized (DI) water and an electrolyte salt. The electrolyte salt—commonly potassium hydroxide (KOH)—should be at least 95% purity. Typical electrolyte concentrations are 0.1–1 M. Here, we use different KOH concentrations (0.1, 0.5, and 1 M) as an example. The electrolyte needs to be sparged through with an inert gas such as argon to remove any dissolved reactive gases.

For the three-electrode measurement described here, a working, counter, and reference electrode are needed. The working electrode is the electrode of interest; typically, the catalyst of interest is deposited on a conductive substrate with low electrochemical activity such as stainless-steel mesh, glassy carbon, or carbon paper. A platinum (Pt) wire or sheet of at least 99% purity should be used as the counter electrode if the working electrode contains PGMs. If the working electrode is PGM-free, a graphite rod should be used as the counter electrode. Finally, a standard reference electrode is needed. A mercury/mercury oxide (Hg/HgO) reference is recommended for basic solutions. Optionally, researchers can use a multimeter and a second reference electrode of the same type as the first to check the stability and accuracy of the reference electrode that will be used in the electrochemical cell. This second electrode should be unused other than for periodic checks against the reference electrode used in testing and should be stored properly per the manufacturer's directions.

Recommended Reading

For general electrochemical theory, we recommend reading the following textbook chapters: 1) the introduction and chapters on potential sweep and bulk electrolysis methods in Bard, A. J.; Faulkner, L. R. Electrochemical Methods: Fundamentals and Applications, second ed.; John Wiley and Sons, Inc, New York, 2001. and 2) the introduction and chapter on reference electrodes in Newman, J.; Thomas-Alyea, K. E. Electrochemical Systems, third ed.; Wiley: Hoboken, NJ, 2004.

PROCEDURE

Step-by-Step Procedure

Prepare the three-electrode cell and perform electrochemical measurements on the working electrode according to the steps below.

1) Prepare electrolyte solution with different KOH concentrations (0.1, 0.5, and 1 M). The volume of electrolyte prepared should be enough to fill the beaker or specialized electrochemical cell.
2) Rinse the electrochemical cell, electrodes, and inert gas feed tube with DI water.
3) Add electrolyte solution to the electrochemical cell.
4) Sparge the electrolyte with inert gas for at least ten minutes before starting an electrochemical experiment and continue to bubble gas through the electrolyte during electrochemical measurements.
5) Measure and record the temperature of the electrolyte.
6) Add electrodes to the cell and connect them to the appropriate leads on the potentiostat. Use the HER or OER catalyst of interest as the working electrode (WE), a counter electrode (CE), and a reference electrode (RE). Make sure that none of the electrodes are in contact with each other

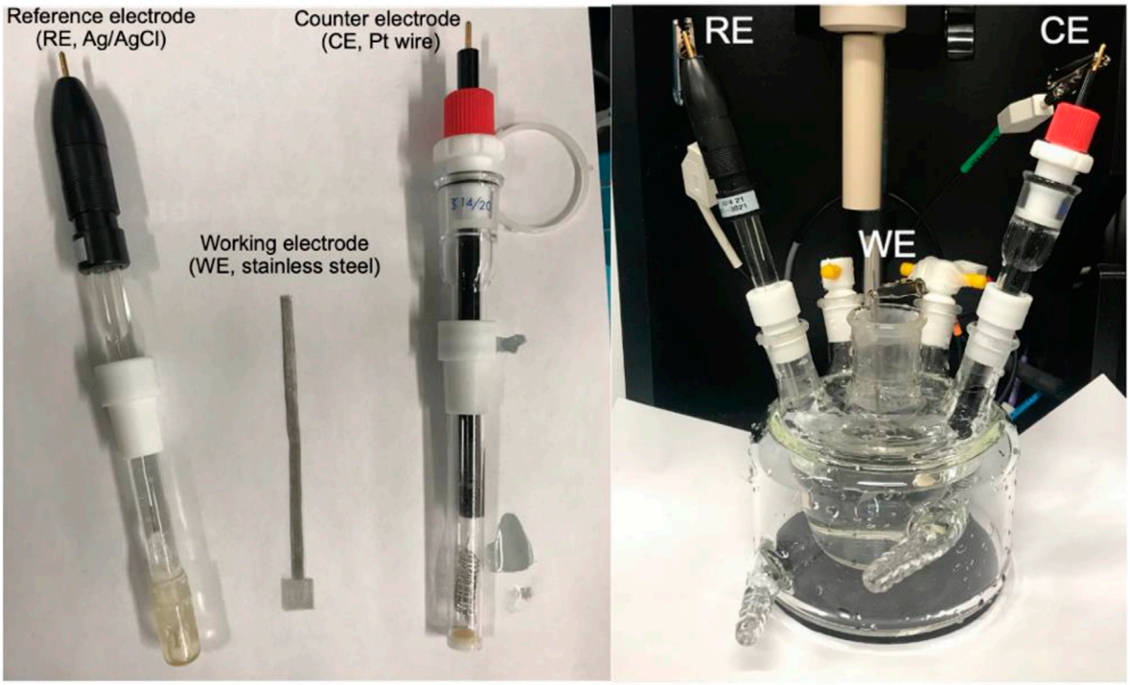

FIGURE 1 | Picture of WE, CE, and RE, and the corresponding connections in a cell.

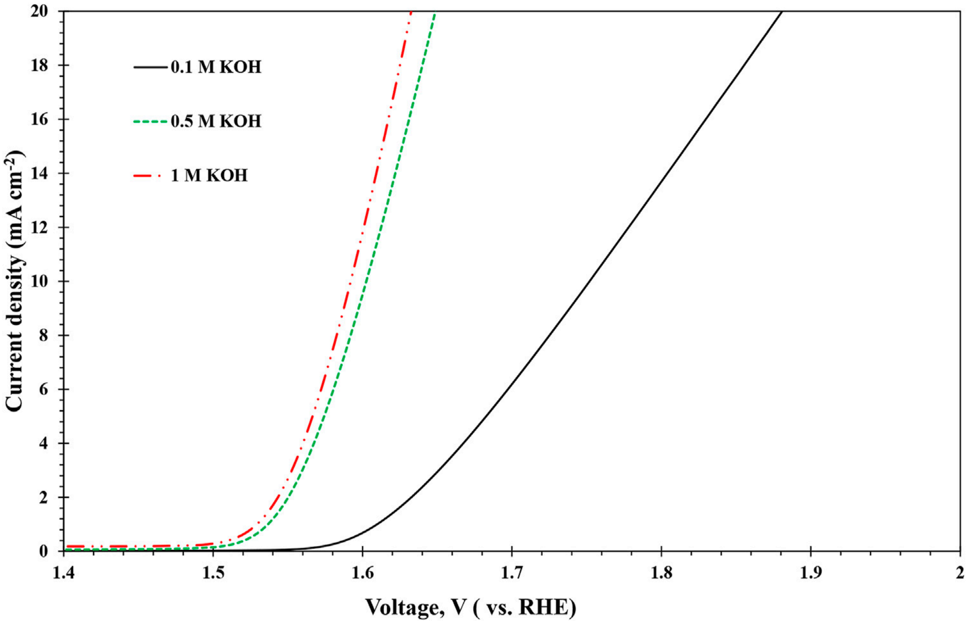

FIGURE 2 | The performance of stainless-steel WE for OER in different concentrations of KOH electrolytes.

above or in the electrolyte. Make sure that none of the alligator clips used to connect the electrodes to the potentiostat are in contact with the electrolyte or each other, and that the electrode wires and alligator clips do not show any signs of corrosion or mechanical failure. Cell components and the final cell assembly are shown in **Figure 1**. Measure the geometric area of the working electrode that is exposed to the electrolyte (1 cm × 1 cm is recommended).

7) Condition the catalyst for electrochemical testing.

8) A) For OER catalysts, e an LSV between 1.4 and 2.2 V vs. reversible hydrogen electrode (RHE) at 10 mV/s.**Figure 2** shows an example for OER with stainless-steel mesh WE, Pt wire CE, and Ag/AgCl RE in different concentrations of KOH electrolytes. B) For HER catalysts, perform an LSV between 0 and −0.5 V vs. RHE at 10 mV s^{-1}. Measure the resistance between the WE and the RE by impedance spectroscopy between 100 kHz and 0.1 Hz. The obtained resistance from the lowest *x*-intercept in a Nyquist plot is used for IR correction.
9) Measure and determine the electrochemically active surface area (ECSA) of the immersion WE using double-layer capacitance (McCrory et al., 2013; Shao et al., 2013; Cossar et al., 2020).
10) Perform bulk electrolysis using CA. Hold at 0 A for 3 s for the induction period followed by 20 mA for 1 h for the electrolysis period. End with 0 A for 1 s in the relaxation period.

Sample Preparation and Analysis

Working electrodes with the catalyst of interest can be prepared in a variety of ways. Here, we discuss the preparation of a working electrode using a stainless-steel mesh as a support for the catalyst of interest. Put a stainless-steel mesh into pure ethanol and sonicate in an ultrasonic bath for 10 min. Dry in air for 15 min. Measure the mass of the mesh. Deposit desired amount of catalyst ink (typically consisting of a catalyst and a polymer binder) on the surface of the mesh using a commercial airbrush or other method. (Ensure deposition methods used are repeatable among samples). Dry at 50°C for 25 min. Measure the mass of the coated electrode to ensure the correct loading of electrocatalyst (e.g., 1, 2, or 3 mg cm^{-2}). Stainless steel can be electrochemically activated to form NiFe-hydroxides on the surface; thus, a control experiment with the uncoated stainless steel is required.

Sample Handling and Preservation

Rinse electrodes and electrochemical cell in DI water and allow to air dry after electrochemical testing.

Computer Hardware and Software

A standard laptop or desktop with corresponding potentiostat connection (available in USB and wireless connections as of 2021) is required to operate the potentiostat record electrochemical data. Software to operate the potentiostat is supplied with the instrument from the manufacturer (e.g., Biologic, Pine Instruments, Gamry, or other vendors).

Data Collection, Analysis, and Records Management

Divide the current measured during the experiments by the ECSA of the working electrode exposed to the electrolyte to calculate current density. Collected polarization curves from LSV measurements can be used to determine either the current density at a given potential or the potential at an operational current density (e.g., 0.2 A/cm^2 @ 1.8 V vs. RHE).

RESULTS

Results from this protocol include LSV (current density plotted against potential) and chronoamperograms (current density plotted against time). In order for data to be compared reliably with results from other publications, it is important to include the composition, pH, temperature, and concentration of electrolyte and to reference the voltage reported to a particular standard reference electrode. To compare results from different reference electrodes, consult a conversion table. The Tafel slope of the catalyst can be obtained from LSV data (Hu et al., 2019; YANG et al., 2021). Additionally, the effect of IR correction can be critical in low concentration electrolytes. The stainless steel mesh is used to connect the active area of the WE and the clip from the equipment, and the ECSA of the immersion area (active area of the electrode) is determined to make sure that the active area is constant among different experiments. The current density needs to be normalized if the ECSA is not constant.

QUALITY CONTROL AND QUALITY ASSURANCE

Electrochemical testing must be repeated for each working electrode type at least once for a total of two measurements. If the difference in current density is more than 10%, repeat the measurements for a third trial to achieve data consistency.

Instrument or Method Calibration and Standardization

Reference electrodes are used because they have a stable and known potential. However, the potential of the reference electrode can drift due to improper reference electrode storage or long duration usage in an electrolyte different from the reference electrode storage solution. Ensure that the reference electrode is in working order by checking it against a fresh, unused reference electrode or by preparing a hydrogen reference electrode.

1) Fresh reference method: Immerse the reference electrode and another fresh, unused reference electrode of the same type into an unused electrolyte solution. Use a multimeter to measure the potential between the electrical leads on the two reference electrodes. The magnitude of the difference should be < 5 mV for the reference to pass the calibration check.
2) Hydrogen electrode method: Assemble a 3-electrode cell with a platinum working electrode, any compatible counter electrode, the desired reference electrode, and an acidic electrolyte with a 1 M proton concentration [(H^+)]. Run a CV in which the current switches from cathodic to anodic (or vice versa), adjusting the voltage extrema until this condition is met. The potential corresponding to 0 current should be ± 5 mV from the theoretical potential of the reference electrode versus the standard hydrogen electrode (SHE).

Cautions

Do not allow any electrodes or exposed wires to touch while an electrochemical measurement is running. Always store reference electrodes in the standard solution appropriate for the reference type. Do not allow reference electrode to dry out.

Common Issues

Always follow the manufacturer's guidance on electrolyte compatibility with the desired reference electrode. Reference electrodes should always be stored in the manufacturer-recommended storage solution and never be allowed to dry out. A dry reference electrode can lead to crystallization of salts in the porous frit, clogging the pores and changing the potential of the reference electrode.

Be sure to convert the current reported by the potentiostat software to current density so that results from differently sized electrodes can be compared. Only the portion of the electrodes that are submerged in electrolyte are electrochemically active, so only the submerged area of the working electrode should be used to calculate current density. Reporting the catalyst areal loading (mass of catalyst per electrode area) allows researchers to account for differences in catalyst activity resulting from different loadings.

Check the potentiostat manual and software settings to be sure the correct cables are used to connect each of the three electrodes to the potentiostat.

Troubleshooting

The main issues with the three-electrode method are related to poor electrical contact between wires connected from the potentiostat to the working electrode, reference electrode, and counter electrode and the connection from the potentiostat to the computer. These should be checked before starting the experiment. Open circuit voltages are typically less than 10 mV but greater than 2 mV.

Error Analysis

Potentiostats arrive pre-calibrated from the manufacturer, but many are supplied with a dummy cell to use in checking the potentiostat function. Repeated experiments with fresh working electrode and electrolyte should be used to determine repeatability and standard deviation.

DISCUSSION

Any analytical methods applied to the data generated by the protocol must be referenced or described. Results must be replicable.

DATA AVAILABILITY STATEMENT

The original contributions presented in the study are included in the article/supplementary material, further inquiries can be directed to the corresponding author.

AUTHOR CONTRIBUTIONS

AS, XL, and GM—protocol design, experimentation EC and RO—data analysis, protocol discussion AS, XL, EC, RO, and GM—manuscript preparation

ACKNOWLEDGMENTS

The authors EC, XL, and AS acknowledge funding support from DOE H2NEW consortium and DOE DE-EE0008081 "High Efficiency PEM Water Electrolysis Enabled by Advanced Catalysts, Membranes, and Processes" project. GM acknowledged funding support from DE-AR0000688 project. RO acknowledges funding support from DOE-DE-EE0008092 "Benchmarking Advanced Water Splitting Technologies: Best Practices in Materials Characterization" project.

REFERENCES

Cossar, E., Houache, M. S. E., Zhang, Z., and Baranova, E. A. (2020). Comparison of Electrochemical Active Surface Area Methods for Various Nickel Nanostructures. *J. Electroanal. Chem.* 870, 114246. doi:10.1016/j.jelechem.2020.114246

Du, C., Tan, Q., Yin, G., and Zhang, J. (2014). "Rotating Disk Electrode Method," in *Rotating Electrode Methods and Oxygen Reduction Electrocatalysts* (Elsevier), 171–198. doi:10.1016/b978-0-444-63278-4.00005-7

Hartig-Weiss, A., Tovini, M. F., Gasteiger, H. A., and El-Sayed, H. A. (2020). OER Catalyst Durability Tests Using the Rotating Disk Electrode Technique: the Reason Why This Leads to Erroneous Conclusions. *ACS Appl. Energy Mat.* 3, 10323–10327. doi:10.1021/acsaem.0c01944

Hu, X., Tian, X., Lin, Y.-W., and Wang, Z. (2019). Nickel Foam and Stainless Steel Mesh as Electrocatalysts for Hydrogen Evolution Reaction, Oxygen Evolution Reaction and Overall Water Splitting in Alkaline Media. *RSC Adv.* 9, 31563–31571. doi:10.1039/c9ra07258f

Kroschel, M., Bonakdarpour, A., Kwan, J. T. H., Strasser, P., and Wilkinson, D. P. (2019). Analysis of Oxygen Evolving Catalyst Coated Membranes with Different Current Collectors Using a New Modified Rotating Disk Electrode Technique. *Electrochimica Acta* 317, 722–736. doi:10.1016/j.electacta.2019.05.011

McCrory, C. C. L., Jung, S., Peters, J. C., and Jaramillo, T. F. (2013). Benchmarking Heterogeneous Electrocatalysts for the Oxygen Evolution Reaction. *J. Am. Chem. Soc.* 135, 16977–16987. doi:10.1021/ja407115p

Shao, M., Odell, J. H., Choi, S.-I., and Xia, Y. (2013). Electrochemical Surface Area Measurements of Platinum- and Palladium-Based Nanoparticles. *Electrochem. Commun.* 31, 46–48. doi:10.1016/j.elecom.2013.03.011

Yang, X.-m., Li, Z.-p., Qin, J., Wu, M.-x., Liu, J.-l., Guo, Y., et al. (2021). Preparation of Ni-Fe Alloy Foam for Oxygen Evolution Reaction. *J. Fuel Chem. Technol.* 49, 827–834. doi:10.1016/s1872-5813(21)60084-1

Author Disclaimer: This manuscript has been authored by UT-Battelle, LLC, under contract DE-AC05-00OR22725 with the US Department of Energy (DOE). The US government retains and the publisher, by accepting the article for

publication, acknowledges that the US government retains a nonexclusive, paid-up, irrevocable, worldwide license to publish or reproduce the published form of this manuscript, or allow others to do so, for US government purposes. DOE will provide public access to these results of federally sponsored research in accordance with the DOE Public Access Plan (http://energy.gov/downloads/doe-public-access-plan).

Conflict of Interest: Author GM is employed by Pajarito Powder, LLC. Author RO is employed by Nel Hydrogen.

The remaining authors declare that the research was conducted in the absence of any commercial or financial relationships that could be construed as a potential conflict of interest.

NOMENCLATURE

Abbreviations

Units of measurement:

A ampere
cm^2 centimeter squared
mg milligram
mV millivolt
s second
V volt

Acronyms:

CA chronoamperometry
CE counter electrode
CV cyclic voltammetry
DI de-ionized
ECSA electrochemically active surface area
HER hydrogen evolution reaction
Hg/HgO mercury: mercury oxide
KOH potassium hydroxide
LSV linear sweep voltammetry
MEA membrane electrode assembly
OER oxygen evolution reaction
OCP open circuit potential
PGM platinum group metal
Pt platinum
RDE rotating disk electrode
RE reference electrode
RHE reversible hydrogen electrode
SDS safety data sheet
SHE tandard hydrogen electrode
SoA state-of-the-art
WE working electrode

Frontiers in Energy Research

METHODS
published: 31 May 2022
doi: 10.3389/fenrg.2022.911077

Measurement of Resistance, Porosity, and Water Contact Angle of Porous Transport Layers for Low-Temperature Electrolysis Technologies

Ryan J. Ouimet[1]*, *James L. Young*[2], *Tobias Schuler*[2], *Guido Bender*[2], *George M. Roberts*[1] *and Katherine E. Ayers*[1]

[1]*Nel Hydrogen, Wallingford, CT, United States,* [2]*National Renewable Energy Laboratory, Golden, CO, United States*

The porous transport layer is an important component of low-temperature electrolysis devices, such as proton exchange membrane water electrolyzers or anion exchange membrane water electrolyzers. PTLs have significant influence on the cell performance as their bulk resistance can impact the ohmic resistance, their contact resistance can impact electrode performance, and their structure can impact the liquid flow to the cell, which could cause mass-transport losses. In order to improve cell performance, optimization of the PTL is critical. Standardized protocols should be utilized to adequately compare PTLs being developed from different institutions. This method will detail a standardized protocol for measuring the resistance of the PTL using a four-wire setup and will also detail a process for measuring the porosity and water contact angle of the PTL using capillary flow porometry.

Keywords: contact angle, porosity, porous transport layer, resistance, proton exchange membrane based water electrolysis

Edited by:
Olga A Marina,
Pacific Northwest National Laboratory (DOE), United States

Reviewed by:
Aniruddha Pramod Kulkarni,
Cavendish Renewable Technology, Australia
Tatyana V. Reshetenko,
University of Hawaii at Manoa, United States

Correspondence:
Ryan J. Ouimet
rouimet@nelhydrogen.com

Specialty section:
This article was submitted to Process and Energy Systems Engineering, a section of the journal Frontiers in Energy Research

Received: *01 April 2022*
Accepted: *13 May 2022*
Published: *31 May 2022*

Citation:
Ouimet RJ, Young JL, Schuler T, Bender G, Roberts GM and Ayers KE (2022) Measurement of Resistance, Porosity, and Water Contact Angle of Porous Transport Layers for Low-Temperature Electrolysis Technologies. Front. Energy Res. 10:911077. doi: 10.3389/fenrg.2022.911077

1 INTRODUCTION

Porous transport layers (PTLs) perform many important functions for low-temperature electrolysis technologies. PTLs distribute water to the entire active area of the cell, assist with the removal of product gases and heat away from the cell, apply even force across the active area, and act as a current collector (Majasan, et al., 2018). As a result of these functions, the PTL plays a role in the mass transport overpotentials and ohmic overpotentials that occur within proton exchange membrane water electrolyzers (PEMWEs) and anion exchange membrane water electrolyzers (AEMWEs).

Ohmic overpotentials have an increasingly detrimental effect on PEMWE cell performance as the current density is increased. The ohmic resistance associated with this overpotential is caused by ionic transport through the membrane, contact resistances, and bulk electrical resistances. While research has been ongoing to examine methods to reduce membrane thickness as a mechanism for reducing ohmic resistance, there has been little focus on studying the effect of contact resistance of cell components on ohmic resistance. Research by Liu et al. has examined the effect of reducing the ohmic resistance by sputter coating Ir onto a Ti PTL and observed an 81 mV performance improvement at 2 A cm^{-2} (Liu et al. 2018). In addition, research by Majasan et al. examined the effect of PTL porosity on cell performance and determined that reduction of mean PTL pore diameter led to less ohmic resistance at all measured current densities leading to the conclusion that contact resistance is a relevant factor in cell performance (Majasan, et al., 2018).

Mass transport overpotential is primarily caused by a lack of water interacting with the anode catalyst as well as the ineffective removal of product gases away from the catalyst surface. When operating at higher currents, more water is required and more gas is produced, which causes increased mass transport resistance and begins to limit efficient water splitting at those high current densities. In addition to porosity, it has been determined that the wettability of the PTL is important for understanding the two-phase flow through a PTL and its impact on mass transport resistance (Bromberger, et al., 2018). The wettability can be determined through the measurement of the contact angle of the internal pores of the PTL as proposed by Bromberger et al. by using capillary flow porometry.

Despite the importance of PTLs on the performance of low-temperature water electrolyzers, there has been significantly less research to study and optimize these components compared to similar studies on gas diffusion layers used for fuel cells (Ayers, et al., 2019). To advance and optimize PTLs for water electrolysis applications, additional studies and standardized methodologies are required. The method proposed here will provide researchers with a standardized protocol to examine the resistance, porosity, and water contact angle of PTLs to be used in low-temperature water electrolyzers. Using a four-wire resistance measurement method, researchers can examine how to further reduce ohmic losses related to the resistance of the PTLs. In addition, this protocol will utilize capillary flow porometry as a standardized method for measuring the porosity of the PTL.

2 PROTOCOL SCOPE

2.1 Scope and Applicability

The purpose of this procedure is to determine the electrical bulk resistance of the porous transport layer (PTL) as well as the pore size distribution (PSD), mean flow pore diameter, and water contact angle of the PTL. This protocol assumes that the PTL being tested has uniform thickness and is defect-free.

2.2 Summary of Method

This protocol will utilize a potentiostat with four-wire measurements to determine the bulk resistance of the PTL. Following the resistance measurement, capillary flow porometry (CFP) will be performed on the PTL which will provide information on the porosity of the PTL. When using a wetting liquid with a low contact angle (such as POREFIL™ or Porofil™), the CFP will show the smallest pore, largest pore, and the mean flow pore of the PTL. When comparing CFP data from the low contact angle measurement to CFP data taken with deionized water as the wetting liquid, calculations can be made to determine the internal contact angle of the deionized water on the PTL.

2.3 Personnel Qualifications/Responsibilities

Users should have basic laboratory knowledge and experience. Users should be trained to use all equipment listed in **Section 2.5**. Users have the responsibility of ensuring that they have read through all pertinent SDS related to this protocol.

2.4 Health and Safety Warning

It is important to be aware of all hazards and thoroughly read through all safety data sheets (SDS) associated with this protocol. When performing the resistance measurement, a current will be momentarily passed through the test setup. Ensure that the area is dry and free of any shock hazards. Additionally, during the resistance test, the sample will be under compressive load (~7 bar). Be aware that the lab press used during that test is a pinch hazard.

2.5 Equipment and Supplies

Resistance Measurements: Potentiostat arranged for four-wire resistance measurements or an accurate power supply (such as a Bio-Logic SP-300 potentiostat or a California Instruments AST1501 power supply), carbon gas diffusion layers, 2 pieces of gold-coated copper with tabs where the potentiostat leads can be attached, laboratory press, voltmeter for calibration (such as Keithley 2000).

Water Property Tests: Capillary flow porometer (such as POROMETER POROLUX™ 1,000, Anton Paar Porometer 3G, or similar), POREFIL™ or similar wetting fluid, deionized water.

2.6 Nomenclature and Definitions

Alkaline exchange membrane water electrolysis (AEMWE); capillary flow porometry (CFP); proton exchange membrane water electrolysis (PEMWE); pore size distribution (PSD); porous transport layer (PTL); safety data sheet (SDS).

2.7 Recommended Reading

In addition to the papers listed in the reference, the following journal articles are recommended for further understanding the concepts listed in this methods article as well as how these PTL properties impact cell performance:

- Gigac, Juraj, Monika Stankovska, and Maria Fiserova. 2017. “Comparison of Capillary Flow Porometry and Mercury Intrusion Porosimetry in Determination Pore Size Distribution of Papers.” *Wood Research* 587–596.
- Grigoriev, S.A., P. Millet, S.A. Volobuev, and V.N. Fateev. 2009. “Optimization of porous current collectors for PEM water electrolyzers.” *International Journal of Hydrogen Energy* 4,968–4,973.
- Ito, Hiroshi, Tetsuhiko Maeda, Akihiro Nakano, Atsushi Kato, and Tetsuya Yoshida. 2012. “Influence of pore structural properties of current collectors on the performance of proton exchange membrane electrolyzer.” *Electrochimica Acta* 242–248.
- Lickert, Thomas, Maximilian L. Kiermaier, Kolja Bromberger, Jagdishkumar Ghinaiya, Sebastian Metz,

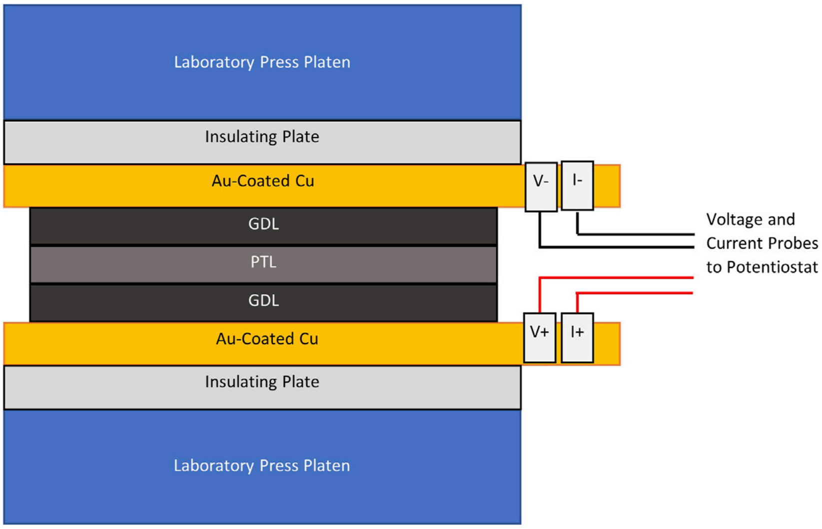

FIGURE 1 | Test setup for the PTL resistance measurement.

Arne Fallisch, and Tom Smolinka. 2020. "On the influence of the anodic porous transport layer on PEM electrolysis performance at high current densities." *International Journal of Hydrogen Energy* 6,047–6,058.

3 PROCEDURE

3.1 Step-By-Step Procedure

3.1.1 Resistance Measurements

1. Clean the as-received PTL prior to testing. One example of an acceptable cleaning procedure would be to first soak the PTL in isopropyl alcohol for 5 min. Rinse the PTL with a bottle of deionized water and then place the PTL in a beaker of boiling deionized water for 5 min. Remove the PTL and place it on a clean surface in an oven set to 75°C for 15 min to evaporate any remaining water.
2. Cut a piece of cleaned PTL to a dimension of 55 mm × 55 mm by using a cutting method that ensures a flat PTL sample such as a steel rule die, laser cutting, or shears. Ensure that the sample is flat, clean, and without defects.
3. Place the cleaned PTL between two pieces of carbon GDL material.
4. Place the GDL|PTL|GDL between two pieces of highly conductive metal, such as gold electroplated on copper or gold sputtered on copper. The Au-coated Cu should be of the same size or slightly larger than the PTL sample. Ensure that the Au-coated Cu pieces are not in physical contact of each other. One side of each Au-coated Cu plate should have an insulating layer applied. Ensure that the insulating layer is facing away from the GDL|PTL|GDL sample. If there is no insulating layer on the Au-coated Cu, electrically insulating plates must be placed between each Au-coated Cu plate and the laboratory press.
5. Place the Au-coated Cu|GDL|PTL|GDL|Au-coated Cu setup into a laboratory press so that the setup is centered in the press. The setup should be similar to what is shown in **Figure 1**.
6. Press the sample to 7 bar.
7. Once the sample is affixed in the press hardware, connect the positive voltage and current leads of the potentiostat to one of the Au-coated Cu plates and the negative voltage and current leads to the other Au-coated Cu plate. If the Au-coated Cu plates do not extend beyond the size of the press platens as shown in **Figure 1**, adjust the configuration by adding an additional current collector between the Au-coated Cu plates and insulating plates so that it is possible to ensure tight connection between the potentiostat and the test hardware. Take note of any modified setup.
8. Once at the proper pressure, use the potentiostat to apply a 0.5 A current across the sample and record the voltage. Increase the current in 0.5 A increments so that a total of 10 measurements are collected between 0.5 and 5 A.
9. Plot the voltage versus the current and obtain the slope of the linear regression of the collected data. The slope of the line will be the resistance of the PTL.
10. Repeat steps 8 and 9 an additional two times minimum to ensure the precision of the PTL resistance values obtained in step 9.
11. Once complete, remove the PTL and reassemble the Au-coated Cu|GDL|GDL|Au-coated Cu test setup.
12. Repeat the test again by pressing the test setup to 7 bar. Apply a 1 A current across the test setup and record the voltage. Increase the current in 0.5 A increments so that a total of 10 measurements are collected between 0.5 and 5 A.
13. Plot the voltage versus the current and obtain the slope of the linear regression of the collected data. The slope of the line will be the background test setup resistance.

14. Repeat steps 12 and 13 an additional two times minimum to ensure the precision of the background test setup resistance values obtained in step 13.
15. Subtract the average test setup resistance obtained in step 13 from the average of the overall resistance measured in step 9 to determine the bulk resistance of the PTL.

3.1.2 Porosity and Water Contact Angle Measurements

1. Following the resistance measurements, cut out a piece of the PTL to a diameter of 50 mm.
2. Weigh the mass of the dry PTL sample
3. Place the dry PTL sample into the sample holder of the capillary flow porometer, place an o-ring over the edge of the sample, and tighten the sample holder until it is closed.
4. Run the porometer with the pressure kept constant for 20 s at each point to obtain stable data.
5. Following the collection of the dry curve data, immerse the PTL sample into a wetting liquid with a high wettability (ex. POREFIL™) so that the PTL sample is completely wet
6. Place the wet PTL sample into the sample holder of the capillary flow porometer, place an o-ring over the edge of the sample, and tighten the sample holder until it is closed.
7. Run the porometer with the pressure kept constant for 20 s at each point to obtain stable data
8. Following the collection of the wet curve data, in order to obtain the contact angle of water on the PTL surface, immerse the PTL sample into water in an ultrasonication bath. Sonicate the sample for 10 min or until the PTL is completely wet.
9. Place the wet PTL sample into the sample holder of the capillary flow porometer, place an o-ring over the edge of the sample, and tighten the sample holder until it is closed.
10. Run the porometer with the pressure kept constant for 20 s at each point to obtain stable data
11. Following the collection of the wet curve data, run the porometer again with the dry sample to obtain the dry curve.

3.2 Sample Preparation and Analysis

The PTL sample should be prepped to 55 mm × 55 mm prior to the resistance measurement. Once cut, the sample should be flat and free of cracks or defects. Similarly, the sample should be cut to be a round disk with a 50 mm diameter prior to the CFP measurements. The sample should be flat and free of cracks or defects after the cutting step.

3.3 Sample Handling and Preservation

After cleaning and prior to testing, the samples should be kept in a sterile container to ensure that no dust or foreign object debris contaminates the pores of the PTL. Handle with clean gloves to prevent contamination of the PTL.

3.4 Computer Hardware and Software

Software for the potentiostat should be provided by the potentiostat manufacturer. Software for the CFP hardware should be provided by the CFP manufacturer.

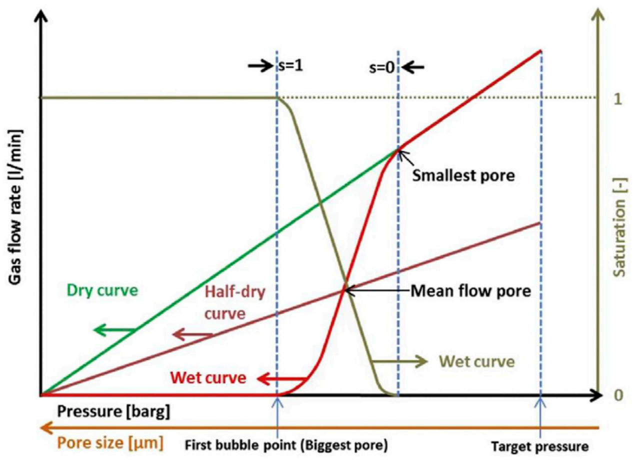

FIGURE 2 | An example of a wet curve, dry curve, and half-dry curve obtained by capillary flow porometry. Reproduced with permission from Bromberger et al.

3.5 Data Collection, Analysis, and Records Management

Record PTL dimensions prior to testing. During the resistance testing, record the potentiostat current and voltage readings. During the CFP tests, record the weight of the PTL before and after testing. Be sure to have all data recorded in a lab notebook and/or electronically.

4 RESULTS

For the PTL resistance measurements, the resistance would be calculated using Ohm's law. With the current, I, set on the potentiostat, and the voltage, V, measured on the potentiostat, the resistance, R, can be calculated as:

$$R_{setup+PTL} = \frac{V}{I}. \tag{1}$$

Using Ohm's law and the data collected in the resistance measurement protocol, a plot can be generated with the voltage on the y-axis and the current on the x-axis. The slope of the linear regression will be the combined resistance of the PTL and the test setup. In order to extract the PTL resistance, the resistance of the test setup without the PTL sample must also be measured using the same method. Once the resistance of the test setup with the PTL, $R_{setup+PTL}$, is known along with the resistance of just the test setup, R_{setup}, then the PTL bulk resistance can be calculated as:

$$R_{PTL} = R_{setup+PTL} - R_{setup}. \tag{2}$$

The CFP data should be plotted with the gas flow rate vs pressure as shown in **Figure 2** from Bromberger et al. (Bromberger, et al., 2018) Three curves should be plotted: the wet curve, dry curve, and half-dry curve. While the wet curve and dry curve is plotted from data collected by the CFP, the half-dry curve is typically calculated and plotted by the CFP software. The half-dry curve is calculated as being equal to one half of the gas flow rate of the dry curve at a given pressure. When examining the plot, the intersection of the dry curve and wet curve indicates the smallest pore in the PTL. The first bubble point on the wet curve indicates the largest pore in the PTL. The intersection of the wet curve and the half-dry curve is the mean flow pore of the PTL.

The pore diameter as a given pressure can be determined by:

$$d = \frac{4B\gamma \cos\theta}{p}. \tag{3}$$

In this equation, d is the characteristic pore size (in m), B is the capillary constant, γ is the surface tension (in N/m), θ is the contact angle of the wetting liquid (in degrees), and p is the pressure (in Pa).

To calculate the contact angle of the water on the surface of the PTL, a specific pore diameter is examined and the equation above can be compared between the POROFIL™ CFP data and the water CFP data as:

$$\frac{\gamma_w \cos\theta_w}{p_w} = \frac{\gamma_p \cos\theta_p}{p_p}, \tag{4}$$

where the w subscript is related to the water data while the p subscript is related to the POROFIL™ data. With $\theta_p = 0°$, the equation above can be rewritten as:

$$\theta_w = \cos^{-1}\left(\frac{\gamma_p p_p}{\gamma_w p_w}\right). \tag{5}$$

5 QUALITY CONTROL AND QUALITY ASSURANCE SECTION

The potentiostat and the CFP hardware should be calibrated annually according to the manufacturers' specified calibration standards and procedures. All data should be properly and securely logged to ensure repeatability and consistency among tests.

5.1 Instrument or Method Calibration and Standardization

When operating the potentiostat for the resistance measurements, it is recommended to use a voltmeter that has been calibrated to 10^{-4} V or better to ensure that the voltage being measured between the sense leads is accurate. Additionally, the resistance of the GDL material should be obtained prior to measuring the resistance of the PTL sample. If the resistance of the GDL is not negligible, it should be subtracted from the PTL resistance measurements to have a more accurate PTL resistance value. The CFP should be calibrated against a standard material annually. Check with the porometer manufacturer for recommended calibration standards and procedures.

5.2 Cautions

When handling the PTL, be sure to keep the PTL clean and avoid contamination. The introduction of foreign object debris to the PTL may result in higher resistance and could negatively impact the water properties of the PTL. Also, be sure not to introduce any bends or cracks into the PTL as that may also result in higher resistance.

5.3 Common Issues

While performing the experiments listed above, there are a few areas where common issues may occur. All PTL samples, as well as other materials used in this study, should be cleaned. If there are any contaminants on the Au-coated Cu plate, GDL, or PTL during the resistance measurements, the contaminant could cause the measured ohmic resistance to be higher than anticipated. When pressing the Au-coated Cu|GDL|PTL|GDL| Au-coated Cu, be sure to limit the applied force to within ±5% error. Research by Vikram et al. shows the impact of compression pressure on measured resistance and demonstrates how important it is to be as close as possible to the targeted compression pressure listed in the procedure (Vikram, et al., 2016).

During the porosity and water contact angle measurements, it is important to ensure that the sample is completely dry before testing and that there are no contaminants on the scale prior to weighing the PTL sample. It may be helpful to wipe the surface of the scale with acetone to ensure the scale is clean prior to weighing the sample. Lastly, when the PTL is to be submerged and wet with water prior to capillary flow porometry testing, be aware that it is difficult to ensure that the sample is completely wet as water may have difficulty wetting interior pores of the PTL. Use ultrasonication or any additional precautions to ensure that the sample is properly wetted prior to the capillary flow porometry measurements.

5.4 Interferences

The instrumentation used for this protocol should be calibrated prior to testing to ensure the accuracy of these tests. If pores are not completely wetted prior to CFP experiments, data may be inaccurate or incomplete.

5.5 Troubleshooting

To ensure the accuracy of the potentiostat during the resistance measurements, a calibrated multimeter can be used to measure the voltage across the sample which can be compared to the potentiostat measurements. If the voltage readings are different, additional troubleshooting of the potentiostat may be required to ensure accuracy.

5.6 Error Analysis

When collecting resistance measurements, it is recommended to obtain multiple measurements at the same location to ensure the accuracy and repeatability of the measurement. Following the data collection, the measured resistance should be reported as an average of all collected measurements at that point (σ) and the standard deviation (σ) should follow to show the error in the obtained measurements. For this analysis, a minimum of 3 repeat measurements should be taken to ensure the precision of the results.

When collecting the capillary flow porometry data, error should be based upon the instrument error obtained during calibration. Multiple tests should be performed to ensure that the porosity results are repeatable and precise.

6 DISCUSSION

Resistance data collected with this protocol should be replicable and comparable to other similar data in literature. If the method is being used to examine the effect of PTL porosity on the resistance, the resistance should be plotted versus the porosity and that data should be compared to other existing literature to ensure accuracy or novelty of the obtained results. Similarly, if the method is being used to examine the effect of the compression pressure acting on the PTL, a plot of the resistance vs compression pressure should be plotted and compared to similar literature, such as Vikram et al.

When collecting the capillary flow porometry data, the obtained dry, wet, and half-wet curves should be plotted vs the applied pressure of the porometer. This data can then be analyzed as described in the Results section and compared to literature sources, such as Bromberger et al. Using the porosity data obtained by the CFP measurements, the data can then be compared to literature sources for similar PTL materials to ensure the accuracy of the obtained data.

DATA AVAILABILITY STATEMENT

The original contributions presented in the study are included in the article/supplementary material, further inquiries can be directed to the corresponding author.

AUTHOR CONTRIBUTIONS

RO wrote the first draft of the manuscript. RO, JY, TS, GB, and KA all contributed to the manuscript revision. GR and KA supervised and assisted with the manuscript development.

FUNDING

This work was funded by the United States Department of Energy under the program “Benchmarking Advanced Water Splitting Technologies: Best Practices in Materials Characterization” (Award #: DE-EE0008092).

ACKNOWLEDGMENTS

The authors would like to acknowledge the U.S. Department of Energy and the funding support from project DOE-DE-EE0008092, “Benchmarking Advanced Water Splitting Technologies: Best Practices in Materials Characterization”.

REFERENCES

Ayers, K., Danilovic, N., Ouimet, R., Carmo, M., Pivovar, B., and Bornstein, M. (2019). Perspectives on Low-Temperature Electrolysis and Potential for Renewable Hydrogen at Scale. *Annu. Rev. Chem. Biomol. Eng.* 10, 219–239. doi:10.1146/annurev-chembioeng-060718-030241

Bromberger, K., Ghinaiya, J., Lickert, T., Fallisch, A., and Smolinka, T. (2018). Hydraulic *Ex Situ* Through-Plane Characterization of Porous Transport Layers in PEM Water Electrolysis Cells. *Int. J. Hydrogen Energy* 43, 2556–2569. doi:10.1016/j.ijhydene.2017.12.042

Liu, C., Carmo, M., Bender, G., Everwand, A., Lickert, T., Young, J. L., et al. (2018). Performance Enhancement of PEM Electrolyzers through Iridium-Coated Titanium Porous Transport Layers. *Electrochem. Commun.* 97, 96–99. doi:10.1016/j.elecom.2018.10.021

Majasan, J. O., Iacoviello, F., Shearing, P. R., and Brett, D. J. (2018). Effect of Microstructure of Porous Transport Layer on Performance in Polymer Electrolyte Membrane Water Electrolyser. *Energy Procedia* 151, 111–119. doi:10.1016/j.egypro.2018.09.035

Vikram, A., Chowdhury, P. R., Phillips, R. K., and Hoofar, M. (2016). Measurement of effective bulk and contact resistance of gas diffusion layer under inhomogeneous compression - Part I: Electrical conductivity. *Journal of Power Sources* 320, 274–285. doi:10.1016/j.powsour.2016.04.110

Conflict of Interest: Authors RO, GR and KA were employed by Nel Hydrogen.

The remaining authors declare that the research was conducted in the absence of any commercial or financial relationships that could be construed as a potential conflict of interest.

frontiers | Frontiers in Energy Research

METHODS
published: 28 June 2022
doi: 10.3389/fenrg.2022.867783

Conductivity and Transference Number Determination Protocols for Solid Oxide Cell Materials

John S. Hardy[1]*, Aniruddha P. Kulkarni[2], Jeffry W. Stevenson[1] and Olga A. Marina[1]

[1]Pacific Northwest National Laboratory, Battelle Memorial Institute, Electrochemical Materials and Devices Team, Energy and Environment Directorate, Richland, WA, United States, [2]Department of Chemical and Biological Engineering, Monash University, Clayton South, VIC, Australia

To standardize materials and component characterization for next generation hydrogen production and energy generation solid oxide cell (SOC) technologies, test protocols are being established to facilitate comparison across the numerous laboratories and research institutions where SOC development for application in solid oxide fuel cells (SOFCs) and solid oxide electrolyzes cells (SOEC) is conducted. This paper proposes guiding protocols for fundamental electrical properties characterization of SOC materials, including temperature- and oxygen partial pressure (pO_2)-dependent conductivity measurements, and use of the electromotive force for determining the transference numbers, or contributions of each charge carrier (i.e., ions and electrons), to the total conductivity. The protocol for Archimedes density measurements is also provided as an integral technique to both of these methods.

Keywords: conductivity, solid oxide cell, transference number, ionic, electronic, electrode, electrolyte, interconnect

Edited by:
Muhammad Wakil Shahzad,
Northumbria University,
United Kingdom

Reviewed by:
Muhammad Ahmad Jamil,
Northumbria University,
United Kingdom
Chi Zhang,
Wuyi University, China
Fahad Noor,
University of Engineering and Technology, Lahore, Pakistan

***Correspondence:**
John S. Hardy
john.hardy@pnnl.gov

Specialty section:
This article was submitted to Process and Energy Systems Engineering,
a section of the journal Frontiers in Energy Research

Received: *01 February 2022*
Accepted: *25 May 2022*
Published: *28 June 2022*

Citation:
Hardy JS, Kulkarni AP, Stevenson JW and Marina OA (2022) Conductivity and Transference Number Determination Protocols for Solid Oxide Cell Materials.
Front. Energy Res. 10:867783.
doi: 10.3389/fenrg.2022.867783

1 INTRODUCTION

Solid-state electrochemistry is a continually evolving area of science and technology, with researchers and developers from numerous universities, laboratories, and industries globally carrying out measurements to characterize various materials and processes. As a result, there is a vast variety of experimental protocols, sample preparation methods, test fixtures, and instruments. The Energy Materials Network (ENM) consortium is attempting to bring together researchers and experts from academia, national labs, and industry across the globe to review test procedures and agree on and establish a testing protocol for various routine measurements. This manuscript is part of a series of guidelines and protocols prepared by a cohort of researchers brought together at the HydroGEN Advanced Water Splitting Technology Pathways Benchmarking and Protocols Workshop organized by ENM over the last few years. The aim here is to provide a technical guideline that may better compare the published results where possible and provide much-needed operating procedures for new entrants and students in the field. It is acknowledged that the proposed method may need to be modified to suit particular laboratory equipment and would evolve with the development of new methods and new instruments. However, we believe protocol will be helpful as a starting point to develop globally unified testing approaches. The objective here is not to provide specific experimental results but to share a step-by-step procedure for the techniques discussed in this paper.

Electrical conductivity measurements are essential for characterization of SOC component materials. Electrical charge transport in solid oxide materials involves conduction via ions, electrons, and holes as governed by defect chemistry. The total conductivity (σ_{total}) is expressed as

$$\sigma_{total} = \sigma_{ion} + \sigma_{electronic} \quad (1)$$

and is usually measured using four-probe conductivity measurements, a technique extensively applied to electronic ceramics and electrochemical materials, including SOC cathodes and electrolytes (Badwal et al., 1991; Vladislav, 2009; Jo et al., 2021).

The operating environment, pressure, and temperature affect conductivity mechanisms and dictate dominant conducting species. The theoretical foundations of defect chemistry of solid-state electrochemical systems and the thermodynamics of electronic and ionic charge carriers are presented in the literature (Geller, 1977; Tuller and Balkanski, 2012). The charge carrier contributions govern the suitability of materials for application in SOCs. Thus, once total electrical conductivity is known, it is essential to determine the contribution of each charge carrier (ions, electrons, and holes).

In SOC electrolytes, ionic conductivity should be dominant with minimal electronic conduction to maximize Faradic efficiency. For electrode materials, mixed ionic electronic conduction is desired to extend the electrochemical reaction zone beyond the electrode/electrolyte interface. Furthermore, mixed conductivity in barrier layers or functional interfaces can also significantly affect cell performance (Matsuzaki and Yasuda, 2002). Therefore, accurate ionic and electronic conductivity assessments are essential for SOC development. Common methods for determining ionic transference and separating ionic and electronic conductivity include Wagner-Hebb Polarization (blocking electrodes) (Riess, 1992), electromotive force (EMF) measurement (Norby, 1988), four-probe conductivity measured with varying pO_2, and ion permeation measurements.

Selecting methods for deconvoluting ionic and electronic conductivity depends upon the intended use of the materials. For electrolytes, where dominant conductivity should be ionic, the EMF method can determine the transference number and has been used to characterize electrolytes like doped ceria (Ananthapadmanabhan et al., 1990; Kang et al., 2006; Fagg et al., 2009). The EMF method has also been extensively used to measure transference numbers in proton conducting ceramics (Norby, 1988). The method is prone to errors when electronic conductivity is comparable to or higher than ionic conductivity and when interfacial resistance is significant (Liu and Hu, 1996). In SOC electrodes, electronic conductivity is dominant. Thus, for separating their ionic and electronic conductivities, four-probe methods with varying pO_2 are more suitable (Yoon et al., 2009; Yang et al., 2013).

Electrochemical characterization of ceramics is complex and specimen preparation, size, equipment, and environmental condition can affect the measurements. Moreover, experimental procedures often cannot be reported in full detail due to manuscript constraints. Thus, this protocol provides detailed procedures for four-probe conductivity and EMF methods as applied to SOCs.

2 PROTOCOL SCOPE

2.1 Scope and Applicability

Conductivity is measured as a function of temperature and under controlled pO_2 or gas compositions of interest and provides the overall conductivity, ionic and electronic together. Separating oxygen ionic and electronic contributions is based upon the relationship between the concentrations of charge carriers (ions, electrons or holes) and pO_2 around the specimen. The method applies to measurement of oxygen conductivity based upon certain assumptions described in the Results section.

For more accurate separation of ionic and electronic conductivity in oxygen ionic conductors, additional measurements using the EMF method can more directly determine the transference numbers of contributing charge carriers. Different partial pressures of the gases of interest (e.g., oxygen, hydrogen, or steam) are maintained over the two sides of a solid oxide membrane (typically a disc). As an approximation, the ionic transference number (T_i) corresponds to the ratio between the open circuit voltage (OCV) and the theoretical Nernst voltage (Norby, 1988 and Jasna, 2011). Impedance measurements provide a correction for polarization resistance effects on the measured OCV which causes errors in the determination of T_i (Jasna, 2011). Results from different partial pressure combinations can be averaged to obtain T_i. The emf method is limited to materials with sufficient T_i that electronic conductivity does not prevent a measurable OCV.

For accurate conductivity and transference number measurements, both methods require bulk density measurements. Thus, a density measurement protocol will also be provided. In SOC development, sintered density measurements also provide useful information regarding the suitability of a given processing or fabrication approach to achieve the density/porosity required for a given material application.

2.2 Summary of Method

Four-point conductivity. Four platinum paste electrodes are applied to a bar-shaped specimen with ≥95% relative density. Silver is generally avoided due to its tendency for electromigration, which can artificially inflate the measured conductivity. Platinum wires are connected to the electrodes and the sample is placed in a furnace with a calibrated zirconia oxygen sensor. A gas mixer supplies gas mixtures, such as CO/CO_2 or Ar/O_2, to accurately control the pO_2. Other gas mixtures, including $H_2/Ar/N_2/H_2O$, can be used to discriminate proton conduction. Another convenient buffer gas system, H_2/CO_2, does not require handling CO or controlling H_2O vapor. Four-point conductivity measurements are performed as a function of oxygen, hydrogen, or steam partial pressure and/or temperature.

EMF method. A sintered disc is prepared with circular screenprinted Pt electrodes on each side. Here again, silver should be avoided due to electromigration. Generally, a single screenprinted layer thickness is sufficient for the electrode. The two electrodes are hermetically isolated from each other using glass, gold or ceramic seals in a test fixture, such as a SOC button cell test fixture. A precision gas mixer supplies gas mixtures to control the partial pressures of gases on the electrodes. The voltage (EMF) across the sample is measured over a range of partial pressures and temperatures to determine ionic transference number using a high precision multi-meter. The background voltage is measured without a chemical gradient. Impedance is measured using a frequency analyzer and potentiostat. Transference numbers are calculated from the measured emf values based on the Nernst equation with corrections for polarization resistance dictated by impedance results.

Density measurement. For bulk specimens, the Archimedes (or saturated-suspended weight) method generally provides the most accurate results, particularly for irregularly shaped specimens.

2.3 Personnel Qualifications/Responsibilities

Ceramic processing, dry-pressing, high-temperature sintering, and use of electrical devices (e.g., direct current (DC) power supply and multi-meter), and gas safety training are required.

2.4 Health and Safety Warning

Only trained persons should operate equipment, fabricate and prepare specimens, and handle chemicals. Safety measures for hazards and risks associated with powders and solvents, electrical equipment, hot surfaces, and flammable and asphyxiant gases are mandatory. Refer to safe working instructions, personal protective equipment guidelines, Safety Data Sheets (SDS), and best health, safety, and environment (HSE) practices in your lab.

Special safety precautions must be observed as CO is a toxic gas (hazardous chemical) and inhalation of only 4,000 ppm in air could prove fatal in less than one hour. Reference the SDS prior to use.

Check all sensors for current calibration. Gas safety interlocks must be fully operational. Check light emitting diode (LED) and other indicators on the gas safety panel before use (refer to manual).

2.5 Equipment and Supplies

- Platinum wire (typical diameter ~0.25 mm)
- >95% dense bar specimen; typical dimensions are 2–5 mm × 4–5 mm × 40 mm.
- Platinum or gold ink/paste
- Diamond saw
- Small paint brush
- Needle nose pliers
- Micrometer calipers
- Tube furnace
- High purity gas source
- High impedance precision digital multi-meter or potentiostat
- Sintered disc specimen (1 mm thick, 18–27 mm diameter)
- Button cell test fixture
- Sealing material (Gold, ceramic or glass)
- Gas mixer (*MIX-2000 Digital or in-house equivalent*)
- A pair of hydrogen/oxygen sensors
- Bronkhorst Steam generator-gas mixer or separate humidifier
- Frequency analyzer or electrochemical analyzer capable of electrochemical impedance spectroscopy (EIS) measurements
- High temperature 4-point conductivity test fixture
- Mass balance
- Liquid of known density
- Apparatus for determining the apparent mass of a specimen suspended in liquid (density kits are available for most mass balances)

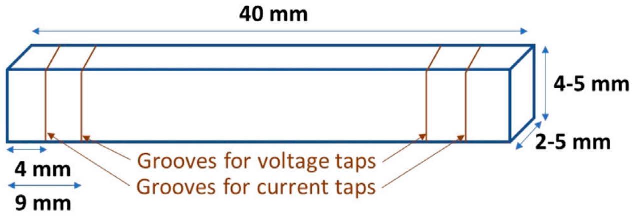

FIGURE 1 | Schematic of four probe conductivity bar.

2.6 Nomenclature and Definitions

AC	alternating current
DC	direct current
DMM	digital multimeter
EIS	electrochemical impedance spectroscopy
EMF	electromotive force
HSE	health, safety, and environment
LED	light emitting diode
OCV	open circuit voltage
OEM	original equipment manufacturer
pH_2O	water partial pressure
pO_2	oxygen partial pressure
SOC	solid oxide cell
SOEC	olid oxide electrolysis cell
SOFC	solid oxide fuel cell
SOP	standard operating procedure
XRD	x-ray diffraction
YSZ	yttria-stabilized zirconia

3 PROCEDURE

3.1 Step-By-Step Procedure

3.1.1 Four-point Conductivity

1) Perform density measurement on the sample using the Archimedes' method described below. Relative density ≥95% is expected.
2) With a diamond saw, cut thin notches around the bar ~4 and 9 mm from each lengthwise end (see **Figure 1**). The distance

between the inner notches should be ≥4 times the larger perpendicular (cross-sectional) dimension. The notches should be shallow, only deep enough to keep the wire in the groove from sliding.

3) Using a small paint brush, paint a small band of platinum ink (Engelhard 6082 or equivalent) in the notches. The nominal band thickness is 0.5 mm. Silica-free masking tape may be used to control the thickness.
4) Wrap platinum wire around the platinum bands in the notches and twist to tighten them down with needle nose pliers, taking care not to break the wire.
5) Heat the assembly to 900°C for 30 min in synthetic air to sinter the Pt ink.
6) After cooling, check that the wires are still tight and gently retighten if needed.
7) Use micrometer calipers to measure the width and thickness of the sample bar and distance between the innermost platinum wires.
8) Electrically connect the Pt wires to the potentiostat with the innermost wires connected to voltage leads and the outer wires to current leads. This can be done by spot welding.
9) Place the bar in the furnace with the thermocouple near its center.
10) Alternatively to the steps above, commercial fixtures (e.g., *Probostat™—NORECS*) are also available. Follow the manufacturer's instructions for attaching the specimen.

Furnace and potentiostat control software can automate the following:

11) Heat to the desired measurement temperature.
12) Introduce the desired gas atmosphere (if other than air). When gas composition [e.g., pO_2 or water partial pressure (pH_2O)]is varied, allow a suitable purge time of at least 30 min for equilibration of each gas. Suitable gas sensors can be used where applicable. For example, pO_2 could be monitored using a calibrated oxygen sensor or steam could be monitored using an appropriate dew point sensor.
13) Set the potentiostat to a constant current of between 0.5 and 10 mA and measure the voltage, then the same current in the opposite direction (negative value) and measure the voltage. Allowing the measured voltage to stabilize is a good way to confirm equilibration.
14) Repeat steps 12–13 for each gas composition of interest. Do not exceed the range of gas compositions within which the specimen is stable (i.e., avoid sample decomposition.) Measurements should be performed in doublets (i.e., while changing partial pressures in one direction, then while going back in the reverse direction) to observe any hysteresis.
15) Heat to the next temperature of interest and repeat steps 12–14.

3.1.2 Emf Method for Transference Numbers

1) Screen print Pt or Au electrodes (8–15 mm dia) onto both sides of the dense sample disc, using Pt or Au ink (e.g., Engelhard 6082), and fire at 800°C for 1 h.
2) An in-house made or commercial button cell test fixture can be used. It should have springloaded Pt meshes on the electrodes for firm connections. Alternatively, leads can be welded to Au or Pt mesh previously attached to the electrodes with sintered Au or Pt paste. Connect the leads to the frequency analyzer and potentiostat for voltage and EIS measurements.
3) Check the apparatus for mechanical integrity of the alumina tube and test fixture and for thermocouple positioning.
4) Use glass, ceramic, or gold for cell sealing. Follow the appropriate seal application procedures and heating/cooling cycles. (See **Appendix** for the typical cycles for each seal type.) To avoid contamination, use synthetic air as a purge gas during seal formation.
5) Connect oxygen sensors at the outlet of both chambers to measure pO_2. Ideally these sensors would be located near the electrodes, however, such placement is difficult in typical button cell fixtures.
6) After sealing, ramp at 3°C/min to the test temperature, where at least 30 min should be allowed to equilibrate.
7) N_2 or another inert gas should be used to flush air out prior to introducing hydrogen in step 8.
8) Introduce hydrogen to one side of the sealed cell using a constant flow rate (e.g., 20 ml/min) to pressure test the seal. After closing the exhaust, drop the hydrogen flow rate to zero. After 30 min, OCV should reach above 1.1 V. The pressure test and OCV will confirm seal formation.
9) With a quality seal, flush both chambers with the same gas mixture. For example, for proton transference number determination, both chambers can be flushed with 45% H_2/50% Ar/5% H_2O. The mixture can be generated using gas mixers and a *Bronkhorst* steam generator or humidifier with a heated gas line. Allow 30 min for equilibration. Typical flow rates are 20 ml/min (For oxygen transport number determination, different gas mixtures can be used). Confirm the partial pressures in each chamber using gas sensors at the outlets.
10) After 30 min, the OCV should ideally be zero. Note any deviation from zero voltage. This compensation voltage should be subtracted from subsequent voltage measurements.
11) Vary the partial pressure in one chamber, keeping the other chamber constant.
12) Record the voltage after at least 30 min at each partial pressure (or until the voltage stabilizes).
13) Collect an EIS spectrum covering a range of frequencies that captures the high and low frequency *x*-axis intercepts in a Nyquist plot, reflective of the ohmic and total resistances of the specimen.
14) Repeat steps 12–13 for at least 4 to 5 different partial pressures.
15) Repeat steps 9–14 for at least 3 different temperatures.
16) Log the data using a Labview interface connected to flow meters, gas sensors, and digital multimeter (DMM), or simply record in a lab book.

3.1.3 Archimedes Density Measurement

1) Measure the dry weight of the specimen (W_d) using a balance.
2) Measure the saturated weight (W_{sat}) after fully saturating the specimen with a liquid of known density (e.g., water, alcohol, or kerosene). To expedite filling the open pores, place the container holding the immersed sample inside a vacuum chamber and apply a vacuum until the sample no longer outgasses. Remove surface liquid prior to measuring the saturated weight. If volatile liquid is used (e.g., ethanol), conduct the measurement fairly quickly after removal from the bath to avoid evaporation.
3) Measure the weight suspended in the liquid (W_{susp}). Commercial "density kits" are available for standard balances to conveniently allow suspended weight measurements.
4) Record the Liquid Temperature

3.2 Sample Preparation and Analysis

Four-probe conductivity samples are typically ≥95% dense 2–5 mm × 4–5 mm × 40 mm rectangular bars with square, flat faces.

Electrolyte discs for the emf method can be prepared by die pressing electrolyte powder into circular discs and sintering to at least 95% relative density, as determined by the Archimedes method. The suggested disc diameter is 18–27 mm, depending on test fixture requirements. Tapecasting or other alternative processes can also be used to fabricate the discs.

Sample bars and discs are best pressed from fine powders that can be obtained from the vendor in the desired particle size or attrition milled from a coarser powder. Generally, powders with an average particle size of less than 5 microns should be used. Prior to introducing the powder into the die, the die should be lubicated by applying a thin layer of zinc stearate solution or oleic acid to the inner walls. After the desired pressure is achieved, the pressure should be held for a few seconds followed by a slow release of the pressure. Both lubrication and gradual pressure release will help avoid springback which can cause the pressed part to crack or fracture. During sintering and subsequent heating of the samples, heating rates should be limited to less than 10°C/min to avoid damage resulting from thermal shock.

Specimens for Archimedes density should be clean and dry.

3.3 Computer Hardware and Software

Data is acquired using an electrochemical workstation, the software interface for the DMM and current source, and/or Labview. Most modern potentiostats have original equipment manufacturer (OEM) software for data monitoring, control, and collection.

3.4 Data Collection, Analysis, and Records Management

Back up data as a text file and in software readable format. Process conditions, dates, and times should be noted. Readouts from gas flow meters and furnace temperature controllers can be integrated into electrochemical measurements using LabVIEW software or an Excel macro.

4 RESULTS

Four-point conductivity. Conductivity (σ) is calculated from current (I), voltage (V), and bar dimensions including cross-sectional area (A) and distance between inner/voltage wire contacts (d) according to:

$$\sigma = \frac{dI}{AV} \tag{2}$$

Plot the results as Log conductivity vs. P_{O2}: For a typical ionic conductor, the electronic conductivity is proportional to $P_{O2.}$ Using defect chemistry, the ionic and electronic conductivity can be separated, and the transference number determined (Kosacki and Tuller, 1995; Riess, 2003). A typical response from a proton conducting oxide measured over a range of temperatures and pO_2 is shown in **Figure 2**.

The method relies on certain assumptions to "separate" ionic and electronic conductivity:

1. The entire specimen responds to changes in the environment.
2. No significant voltage is generated at bar interface.

For more accurate separation, the electromotive force (EMF) method or blocking electrode method (Hebb-Webner) is recommended.

Emf method. For each measurement condition, the ionic transference number, T_i, is calculated using:

$$T_i = 1 - \frac{R_o}{R_t}\left(1 - \frac{E_{oc}}{E_N}\right) \tag{3}$$

where R_o and R_t are the ohmic and total resistance from EIS, respectively, E_{oc} is the open circuit voltage or emf, and E_N is the theoretical Nernst voltage calculated based on a knowledge of the chemical gradients introduced across the cell and electrochemical principles.

Archimedes density. The bulk density, p, (typically expressed in g/cc, although any units may be used if applied consistently) is calculated using:

$$p = \frac{(W_d)(p_f)}{W_{sat} - W_{susp}} \tag{4}$$

where W_d, W_{sat}, and W_{susp} were defined previously, and p_f is the liquid density at the measured temperature.

Sintered densities are frequently expressed as relative density, p_r, obtained simply by dividing the bulk density by the theoretical (i.e., pore-free) density of the material, p_t:

$$p_r = \frac{p}{p_t} \tag{5}$$

The fractional porosity in the specimen is expressed as (1-p_r). The theoretical density is obtained from appropriate tables or x-ray diffraction (XRD) analyses.

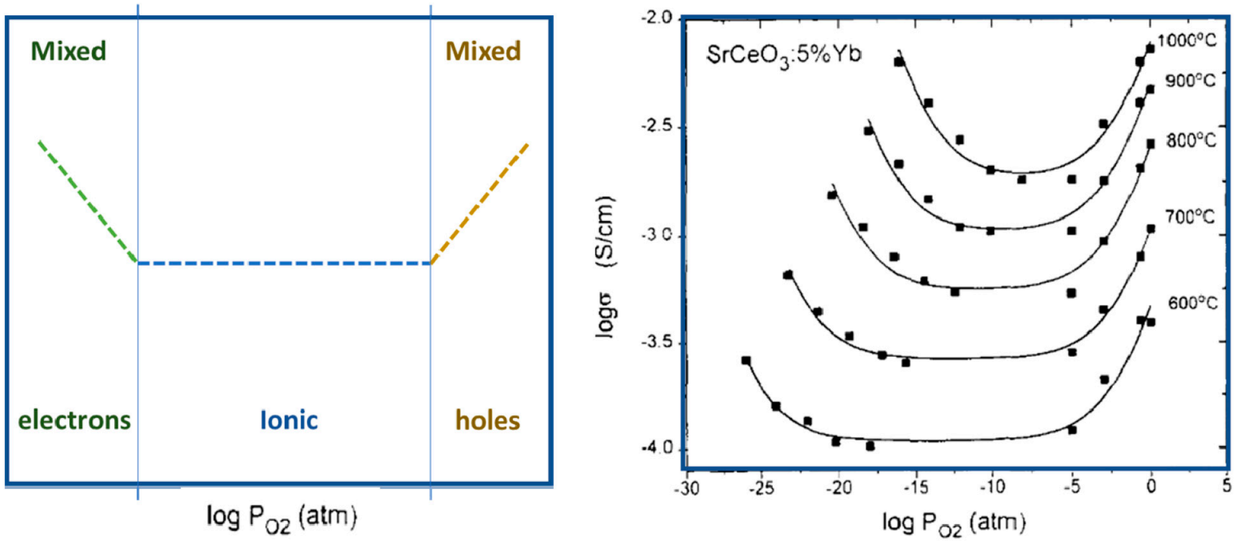

FIGURE 2 | Schematic of Conductivity behavior as function of pO_2 (LHS), Experimental Data from reference (RHS) showing electrical conductivity of SrCeO:5%Yb vs. pO_2. (*Figure adapted from Reference 16 with permission from Elsevier*).

5 QUALITY CONTROL AND QUALITY ASSURANCE

Repeated experiments should be performed and statistical methods employed to confirm the data quality and consistency.

5.1 Instrument or Method Calibration and Standardization

Oxygen (or other gas) sensors must be calibrated over the expected range of partial pressures in a separate experiment to determine sensor drift and deviation. Where air is to be used, substitute synthetic air to avoid contaminants.

Calibrate electrochemical equipment using manufacturer provided test circuits.

Periodically test thermocouples and flow meters using manufacturer recommended procedures.

Follow all instrument standard operating procedures (SOPs) and/or calibration procedures.

5.2 Cautions

Check test rigs for mechanical integrity of ceramic tubes and test fixtures, and for thermocouple positioning. Check the seals by pressure testing at 0.5 bar with nitrogen.

Insulating material can be used to avoid short circuiting the Pt lead wires.

Observe special gas safety precautions as CO is a toxic gas (hazardous chemical).

Other precautions: Hot surfaces, flammable/asphyxiant gases, hazardous chemicals.

5.3 Common Issues

Unusual resistance is often attributable to common problems such as poor contacts, a broken sample or wire, or short circuiting.

5.4 Interferences

Electromagnetic interference associated with the main power supply, induction due to lead wires and furnace windings, and/or the Seebeck effect should be compensated using a "dummy cell". The dummy cell could be a platinum foil or single crystal yttria-stabilized zirconia (YSZ) with sputtered Pt electrodes.

5.5 Troubleshooting

For unusual results, check the gas flows and system temperature, and reset the electrochemical data acquisition system.

If a seal leak is suspected after step 8 of the emf method, repeat the *in-situ* sealing heat treatment cycle in step 4.

5.6 Error Analysis

See Reference (Singh, 2013) for error sources relating to 4-point measurements.

6 LESSONS LEARNED

1. For four-probe conductivity measurements, machining the bar and its grooves can break the specimens, especially electrode materials or non-zirconia electrolytes. Thus, specimen preparation can be a materials-intensive process if new materials synthesized at lab scales are evaluated.
2. For EMF measurements, hermetic sealing is critical. Pre-mixed sealants like Ceramabond should be well-mixed before use to avoid solids settling. The shelf life of pre-mixed sealants is limited and hermetic sealing is unlikely after their expiration.
3. For EMF measurements, use of house air may lead to erroneous EMFs, hence certified synthetic air must be used.

DATA AVAILABILITY STATEMENT

The original contributions presented in the study are included in the article/supplementary material, further inquiries can be directed to the corresponding author.

REFERENCES

Ananthapadmanabhan, P. V., Venkatramani, N., Rohatgi, V. K., Momin, A. C., and Venkateswarlu, K. S. (1990). Structure and Ionic Conductivity of Solid Solutions in the System 0·9{(ZrO2)1−x-(CeO2)x}-0·1(Y2O3). *J. Eur. Ceram. Soc.* 6 (2), 111–117. doi:10.1016/0955-2219(90)90044-g

Badwal, S. P. S., Ciacchi, F. T., and Ho, D. V. (1991). A Fully Automated Four-Probe d.C. Conductivity Technique for Investigating Solid Electrolytes. *J. Appl. Electrochem.* 21, 721–728. doi:10.1007/bf01034052

Fagg, D. P., Pérez-Coll, D., Núñez, P., Frade, J. R., Shaula, A. L., Yaremchenko, A. A., et al. (2009). Ceria Based Mixed Conductors with Adjusted Electronic Conductivity in the Bulk And/or along Grain Boundaries. *Solid State Ion.* 180 (11–13), 896–899.

Geller, S. (1977). *Solid Electrolytes Topics in Applied Physics*. Berlin Heidelberg New York: Springer-Verlag.

Jasna, J. (2011). *Proton Conductive Ceramic Materials for an Intermediate Temperature Proton Exchange Fuel Cell*. Ph.D. Thesis. United Kingdom: The University Of British Columbia.

Jo, K., Ha, J., Ryu, J., Lee, E., and Lee, H. (2021). DC 4-Point Measurement for Total Electrical Conductivity of SOFC Cathode Material. *Appl. Sci.* 11 (11), 4963. doi:10.3390/app11114963

Kang, C. H. Y., Kusaba, H., Yahiro, H., Sasaki, K., and Teraoka, Y. (2006). Preparation, Characterization and Electrical Property of Mn-Doped Ceria-Based Oxides. *Solid State Ion.* 177 (19–25), 1799–1802. doi:10.1016/j.ssi.2006.04.016

Kosacki, I., and Tuller, H. L. (1995). Mixed Conductivity in $SrCe_{0.95}Yb_{0.05}O_3$ Protonic Conductors. *Solid State Ion.* 80 (3–4), 223–229. doi:10.1016/0167-2738(95)00142-s

Liu, M., and Hu, H. (1996). Effect of Interfacial Resistance on Determination of Transport Properties of Mixed-Conducting Electrolytes. *J. Electrochem. Soc.* 143, L109–L112. doi:10.1149/1.1836892

Matsuzaki, Y., and Yasuda, I. (2002). Electrochemical Properties of Reduced-Temperature SOFCs with Mixed Ionic-Electronic Conductors in Electrodes And/or Interlayers. *Solid State Ionics* 152-153, 463–468. doi:10.1016/s0167-2738(02)00373-9

Norby, T. (1988). EMF Method Determination of Conductivity Contributions from Protons and Other Foreign Ions in Oxides. *Solid State Ionics* 28-30, 1586–1591. doi:10.1016/0167-2738(88)90424-9

AUTHOR CONTRIBUTIONS

OM directed the effort. JH and AK collaborated to write the 4-point conductivity protocol. AK wrote the EMF method protocol. JS wrote the Archimedes density protocol. JH compiled the writings into a single manuscript.

Riess, Ilan. (1992). Four Point Hebb-Wagner Polarization Method for Determining the Electronic Conductivity in Mixed Ionic-Electronic Conductors. *Solid State Ion.* 51 (3–4), 219–229. doi:10.1016/0167-2738(92)90204-3

Riess, I. (2003). Mixed Ionic–Electronic Conductors—Material Properties and Applications. *Solid State Ion.* 157 (1–4), 1–17. doi:10.1016/s0167-2738(02)00182-0

Singh, Y. (2013). Electrical Resistivity Measurements: a Review. *Int. J. Mod. Phys. Conf. Ser.* 22, 745–756. doi:10.1142/s2010194513010970

Tuller, H. L., and Balkanski, M. (2012). *Science and Technology of Fast Ion Conductors*. Berlin: Springer Science & Business Media.

V. K. Vladislav (Editor) (2009). *Solid State Electrochemistry I: Fundamentals, Materials and Their Applications* (WILEY-VCH Verlag GmbH & Co. KGaA).

Yang, N., Meng, X., Meng, B., Tan, X., Ma, Z.-F., and Sunarso, J. (2013). Effect of Preparation Methods on the Properties of Ni-YSZ Cermets for SOFC Anodes. *ECS Trans.* 45, 267–277. doi:10.1149/04529.0267ecst

Yoon, K. J., Zink, P. A., Gopalan, S., Pal, U. B., and Pederson, L. R. (2009). Defect Chemistry and Electrical Properties of (La[sub 0.8]Ca[sub 0.2])[sub 0.95]FeO[sub 3−δ]. *J. Electrochem. Soc.* 156, B795–B800. doi:10.1149/1.3123284

Conflict of Interest: The authors declare that the research was conducted in the absence of any commercial or financial relationships that could be construed as a potential conflict of interest.

APPENDIX

Sealing procedure for glass and gold seals are as follows:

1. For glass sealing: seals may be formed *in-situ* or pre-formed externally:
    1) For *in-situ* glass sealing, a glass ring or a paste of Schott G018-311 or a similar glass may be used. Such seals are commercially available from Schott. A typical heating cycle is: 100°C/0.5 h (5°C/min), 180°C/0.2 h (3°C/min), 720°C/1 h (10°C/min) used to reach the operating temperature of the cells. During sealing, use either air or argon for purging the fixture. If sealing paste is desired, a glass powder may be mixed with organic binder (e.g., Ferro Corporation/Schott).
    2) For pre-formed glass sealing: The glass seal is applied using glass powder slurry prepared with commercial materials such as Schott GM31107 glass powder mixed with organic binder (typically 4:1 wt%) and annealed to obtain a gas tight seal (refer to instructions provided by Schott for pre-formed seals).
2. Alternatively, a ceramic sealant such as Ceramabond® (Aremco) can be used, and the procedure provided by the manufacturer should be followed for pre-formed ceramic sealing.
3. Gold paste or gold rings can be used for sealing, which involves heating the cell close to the melting temperature of gold (1,050°C) using a 2°C/min ramp rate, holding at 1,050°C for 20 min, and cooling to operating temperature (2°C/min). The ramp rates and hold time are indicative and may change with fixture design and gas flow rates.

Frontiers in Energy Research

METHODS
published: 13 July 2022
doi: 10.3389/fenrg.2022.945654

Gas Permeability Test Protocol for Ion-Exchange Membranes

*Eun Joo Park**, *Siddharth Komini Babu and Yu Seung Kim*

MPA-11: Materials Synthesis and Integrated Devices, Los Alamos National Laboratory, Los Alamos, NM, United States

The membrane-based electrolysis of water is a growing topic of interest due to the advantages of employing membranes in hydrogen production efficiency and system safety over the traditional alkaline water electrolysis. Ion-exchange membranes with low gas permeability are highly desirable for stable and safe operation of membrane-based water-splitting technologies, hence gas permeability through ion-exchange membranes needs to be properly assessed with standardized methods. We addressed three methods to measure gas permeability of ion-exchange membranes, a pressure permeation cell, chronoamperometry microelectrodes, and *in situ* testing of the membrane electrode assembly, and provide a guideline for choosing the appropriate method for the targeted operating conditions of the water electrolyzers.

Keywords: water electrolysis, gas permeability, hydrogen permeability, oxygen permeability, proton exchange membrane, anion exchange membrane

Edited by:
Marcelo Carmo,
Nel, Norway

Reviewed by:
John S. Hardy,
Pacific Northwest National Laboratory (DOE), United States
Raman Vedarajan,
International Advanced Research Centre for Powder Metallurgy and New Materials, India

****Correspondence:***
Eun Joo Park
epark@lanl.gov

Specialty section:
This article was submitted to Hydrogen Storage and Production, a section of the journal Frontiers in Energy Research

Received: *16 May 2022*
Accepted: *21 June 2022*
Published: *13 July 2022*

Citation:
Park EJ, Komini Babu S and Kim YS (2022) Gas Permeability Test Protocol for Ion-Exchange Membranes. Front. Energy Res. 10:945654. doi: 10.3389/fenrg.2022.945654

INTRODUCTION

Electrochemical splitting of water to generate green hydrogen as an energy carrier is a promising method for sustainable fuel production. Compared to the traditional alkaline electrolyzer that uses aqueous alkaline electrolytes confined in a porous diaphragm, solid electrolyte water electrolyzers use ion-conducting membranes serving both as electrolytes and as a gas separator. This zero-gap design using non-porous membranes has distinct advantages in terms of efficiency, safety, and durability: low internal resistance, high hydrogen production rate, high-pressure operation, and the ability to prevent intermixing of the gaseous products.

The proton exchange membrane (PEM) water electrolyzer splits water at the anode into oxygen and protons, then the proton migrates through the PEM to the cathode where hydrogen is evolved. On the other hand, the anion exchange membrane (AEM) water electrolyzer splits water at the cathode into hydrogen and hydroxide ions, and the latter migrates through the AEM, liberating oxygen at the anode. Both membrane-based water electrolyzer systems allow the operation of the cell under differential pressure to produce high-pressure hydrogen and atmospheric pressure oxygen to minimize the need for additional mechanical compression for hydrogen use or storage (Motz et al., 2021). Preventing physical crossover of the gaseous products of electrolysis is of particular interest due to the flammable nature of hydrogen and possible formation of an explosive mixture of hydrogen and oxygen (Grigoriev et al., 2009; Xiang et al., 2016). In addition, interdiffusion of reactant gases may cause the formation of aggressive radical species such as peroxide, leading the chemical degradation of the ion-exchange membranes, especially perfluorosulfonic acid-based PEMs. Therefore, a proper measurement of the gas permeation rate across the membrane is necessary in the context of efficiency, safety, and durability of water electrolyzer systems.

In this protocol, three methods used for the measurement of gas permeability through an ion-exchange membrane are summarized and described in a procedure to help to establish a guideline for the ion-exchange membrane–based water-splitting technology community.

PROTOCOL SCOPE

Scope and Applicability

- This protocol is designated to develop standard procedures for the measurement of gas permeability of an ion-exchange membrane, including PEM and AEM. Hydrogen and oxygen would be the gases of the interest for the purpose.

Summary of Method

- The gas permeation rate can be measured using (A) a pressure permeation cell, (B) chronoamperometry with microelectrodes, or (C) *in situ* testing of the membrane electrode assembly (MEA). A pressure permeation cell is used with controlled humidified gas flow and gas chromatography (GC) or mass spectrometry. For the chronoamperometric technique, a microelectrode is used for hydrogen permeability, and the oxygen permeability can be calculated from the voltammetric limiting currents. *In situ* testing uses MEA configurations for fuel cell testing for hydrogen or oxygen permeability measurement, quantifying the limiting current of the electrochemical reaction through the membrane.

Personnel Qualifications/Responsibilities

- The user should be properly trained in hydrogen safety and pressure safety prior to the permeability measurement. The user should be properly trained to safely operate the instruments and able to perform the analysis to collect data used for permeability coefficient calculation.

Health and Safety Warning

- The user should be wearing appropriate personal protective equipment, including protective eyewear, gloves, and laboratory coats, in the laboratory at the time when the measurement procedure is followed. The use of compressed gases in laboratory settings need to be permitted prior to protocol implementation.

Equipment and Supplies

The following equipment and supplies are needed for each measurement:

A) Pressure Permeation Cell
  - For the measurement at low pressure, a conventional diffusion cell could be used. For high-pressure testing, an electrolyzer cell rated to a pressure greater than the highest pressure is required for the measurement, that is, EH-50 from Greenlight (rated to 50 bar).
  - A porous transport layer (PTL) and gas diffusion layer (GDL) will play an important role in H_2 permeation as they will affect the compression of the membrane. Use a Ti sinter or Ti felt for the anode PTL, that is, 2GDL10-0.25 Bekaert, and Ti PTL or carbon GDL for the cathode GDL, that is, MGL370, AvCarb.
  - A measure of 1–2 mil (1 mil = 0.001 inches or 25.4 μm) of PTFE for the sub-gasket.
  - An instrument to monitor the gas product, that is, gas chromatography (GC).

B) Microelectrode Chronoamperometry
  - Pt microdisk working electrode.
  - Pt counter electrode and Pt dynamic hydrogen electrode.
  - A controlled humidity chamber for control over gas, pressure, humidity, and temperature.
  - A potentiostat, that is, EG&G PAR Model 283.
  - Syringe filters (PTFE, 0.2 or 0.45 μm).
  - A measure of 0.1 M of H_2SO_4 or 0.1 M of NaOH aqueous solution.

C) *In Situ* Measurement in MEA
  - A standard single-cell hardware (one example is shown in **Figure 1**).
  - GDL.
  - A fuel cell station, that is, Scribner 850e.
  - An electrochemical interface potentiostat, that is, Solartron 1287.

PROCEDURE

Step-By-Step Procedure

A) Pressure Permeation Cell (Broka and Ekdunge, 1997; Bernt et al., 2020)
  1. Prepare a flat, dry membrane piece with a known thickness (wet) and a matching hardware plate (greater than the active area, e.g., 100 cm^2 plate for 50 cm^2 active area) to provide a good seal for the hardware. Any wrinkles in the membrane may lead to gas leak and hardware not being able to achieve the desired pressures.
  2. Assemble an electrolyzer cell–like standard operation with the exception of no catalyst layer on electrodes and utilizing a PTL without Pt coating (**Figure 1**), where each plate is connected to a gas inlet and outlet. Adding a sub-gasket between the PTL and the membrane is recommended to avoid PTL edges causing pinholes in the membrane. For instance, for the PTL area of 50 cm^2; the sub-gasket masks the active area up to 49 cm^2.
  3. Before starting the experiment, check the pressure to ensure proper sealing of the hardware at high pressure. Flow N_2 on both the anode and cathode side at a fixed flow rate (<300 sccm) through a mass flow controller similar to the actual experiment. Gradually increase the pressure on the cathode side to the highest operating pressure while the anode side is at 1 atm. If the anode side is not able to reach the highest pressure, then repeat the cell assembly with a new membrane. For low-pressure testing, the cathode pressure should be 5 atm, and for high pressure, the cathode pressure should be 30 atm.
  4. After the pressure check, flow H_2 to the cathode side and a carrier gas to the anode side at a fixed flow rate (<300 sccm). Flow water at 2 $ml\ min^{-1}\ cm^{-2}$ through a pump on the anode side to provide sufficient hydration to the membrane. The carrier gas can be either N_2 or O_2 depending on the membrane; if the membrane contains gas recombination catalyst, the carrier gas should be O_2 otherwise N_2 could be used. Set partial pressure of the

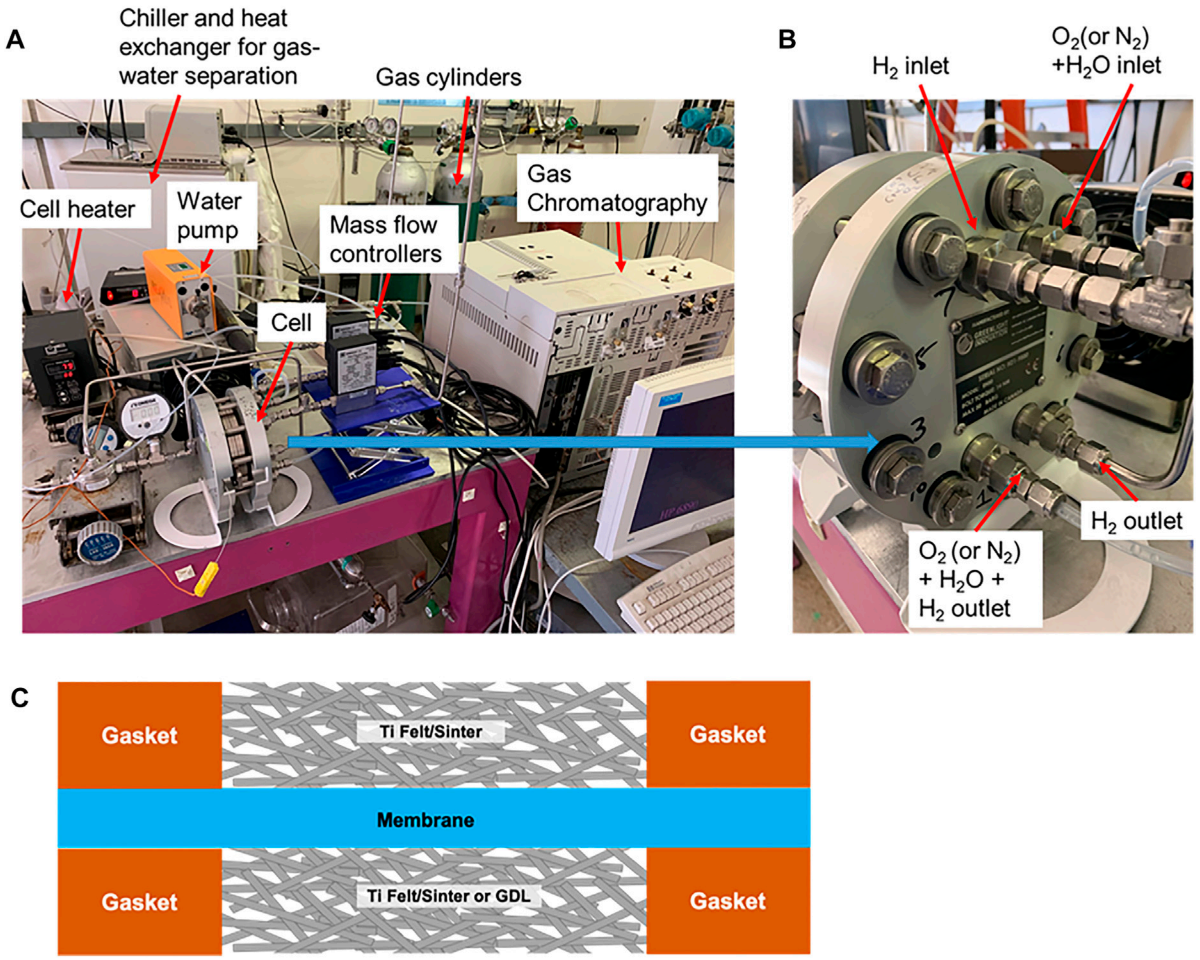

FIGURE 1 | (A) Experiment set up for *ex situ* gas permeation measurement using a pressure permeation cell, **(B)** closed-up view of the cell with gas inlet and outlets, and **(C)** cell assembly diagram.

H_2 and carrier gas at 1 atm accounting for the saturation pressure of water at the operating temperature (50–80°C).

5. The exhaust of the anode should be connected to a gas–water separator or chiller to remove the water from the gas.
6. If O_2 is used as carrier gas, an inert gas (N_2) should be introduced at a known flow rate after the anode exhaust and before the gas–water separator. When the carrier gas is O_2, gas dilution with N_2 is added, to prevent the exhaust gas from the gas–water separator from reaching flammable concentration levels of H_2. For safety, it is advised to maintain the H_2 concentration in the exhaust stream to less than 1% using dilution. This step is not required if N_2 is used as a carrier gas.
7. The gaseous exhaust from the gas–water separator could be connected directly to the analyzer (GC).
8. After the desired pressure is set on the anode and cathode, let the cell stabilize for about 30 min before taking measurement in GC. Repeat the measurement until a stable concentration reading is reached, that is, at least five measurements.
9. Take measurements of the H_2 concentration in the carrier gas at different partial pressures of H_2 up to the operating conditions or system limitation.
10. If N_2 dilution is utilized, ensure to correct the H_2 concentration for the dilution with the N_2 flow rate used.

B) Chronoamperometric Technique Using Microelectrodes (Beattie et al., 1999; Gode et al., 2002; Astill et al., 2009; Chlistunoff, 2014; Yim et al., 2015)

1. Dissolve an ion-exchange membrane in a solvent to prepare a 5 wt% ionomer solution. Filter through the solution with a syringe filter (PTFE, 0.2 or 0.45 μm) to remove any dust particle.
2. Drop-cast a thin layer of the solution on the Pt microdisk electrode.
3. Connect the microelectrode to the other sides of the glass body of the electrode by an ion conductive ribbon, for example, Nafion™ for PEM or quaternized Diels–Alder polyphenylene (Hibbs, 2013) for AEM, which acts as an electrolytic bridge between the external reference and working electrode (**Figure 2A**).

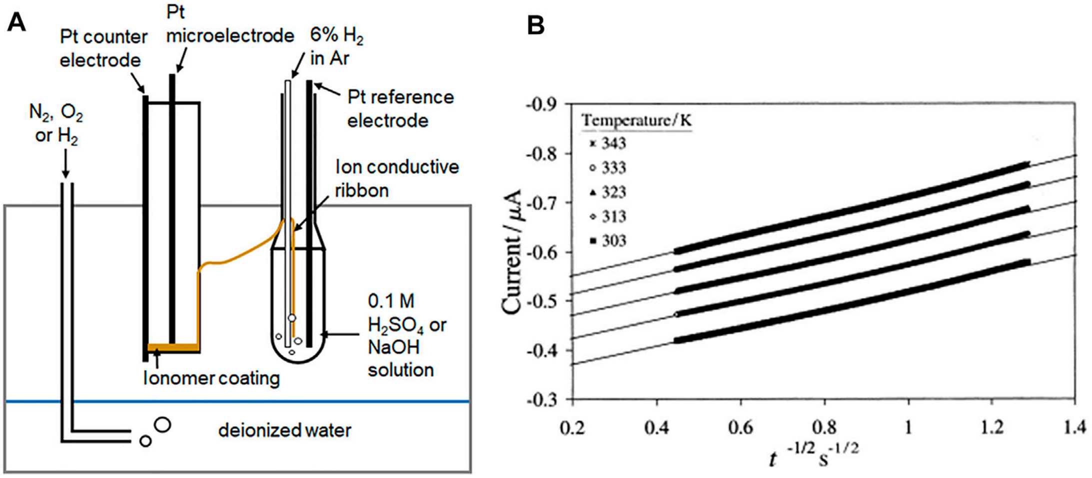

FIGURE 2 | (A) Representative microelectrode set up and **(B)** example of *I* versus $t^{-1/2}$ plots for O_2 reduction at a Pt | BAM® 407 membrane interface (Beattie et al., 1999. Copyright 1999 Elsevier Science S.A.).

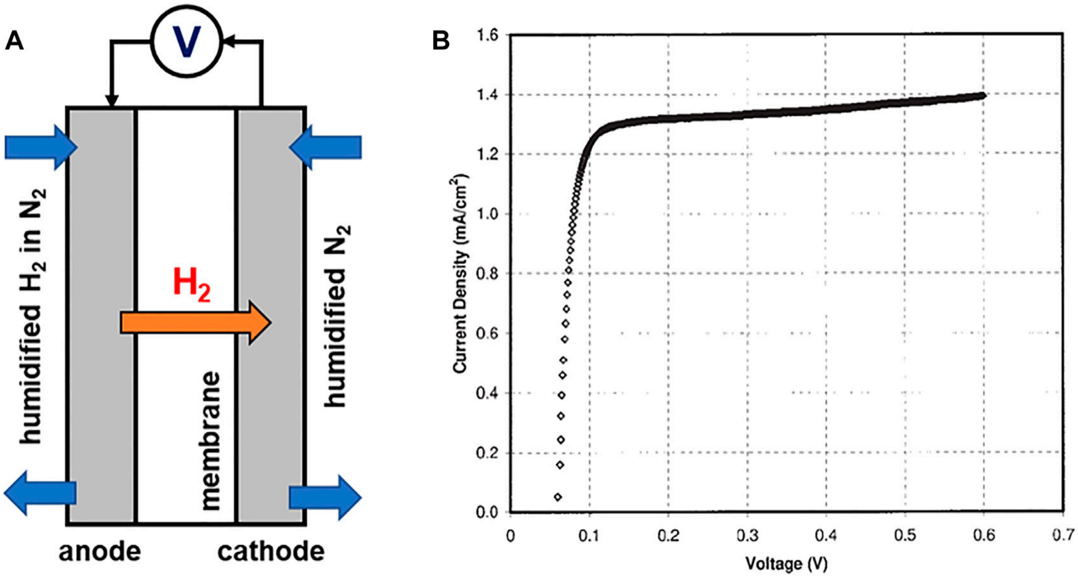

FIGURE 3 | Representative experimental set up for **(A)** *in situ* MEA measurement for hydrogen permeation and **(B)** example of linear sweep voltammogram to measure the hydrogen crossover current density (Kocha et al., 2006. Copyright 1999–2022 John Wiley & Sons, Inc.).

4. Connect the microelectrode to the hydrogen reference electrode (6% H_2 in Ar | Pt | 0.1 M H_2SO_4 or NaOH) and place it in a controlled humidity chamber.
5. Before the experiments, cycle the electrode potential at 50 mV s^{-1} between 0 and +1.4 V using a potentiostat until a stable voltammogram is obtained. In order to provide a consistent electrode pretreatment and a clean Pt surface for every experiment, keep the microelectrode for 10 s at 1.4 V before applying a cathodic potential step or voltammetric scan.
6. Hold the potential of the microelectrode at 1.2 V for 20 s, and then proceed to 0.4 V where O_2 reduction is diffusion controlled for 5 s.

C) *In Situ* Measurement in MEA (Kocha et al., 2006)

1. Prepare a flat, dry membrane piece with a known thickness (wet) and a matching hardware plate.
2. Assemble a standard fuel cell MEA with GDLs. Flow humidified H_2 (4% in N_2) on the anode side of the electrochemical cell, which acts as the reference and counter electrode. Flow humidified nitrogen to the cathode at 300 sccm (**Figure 3A**).

3. Apply voltage with a potentiostat and measure the resulting currents from 0 to 0.6 V with 1 mV s^{-1} scan rate. H_2 that crosses over to the other side of the membrane gets oxidized at the cathode by the application of a voltage.
4. Obtain the H_2 oxidation current density generated from the voltammogram by the y-axis intercept of a linear fit between 0.25 and 0.35 V (**Figure 3B**).
5. For oxygen permeability measurement (Baik et al., 2013; Zhang et al., 2013), flow humidified O_2 to the anode instead of H_2 in N_2. Apply voltage with a potentiostat and measure the resulting currents from 0.4 to 1.1 V in increments of 0.1 V. Obtain the O_2 crossover limiting current between 0.8 and 1.1 V.

Data Collection and Analysis

All raw experimental data should be recorded in a laboratory notebook with the date of measurement. Any observation during the measurement and analysis should be also noted for future references.

A) Pressure Permeation Cell

Calculate the corresponding permeation rate of hydrogen, p (mol cm^{-1} s^{-1}), using the following equation:

$$P = 22.4 \cdot x_{H2} \cdot \frac{Q}{1000} \frac{\delta}{A},$$

where 22.4 is the conversion factor (1 mol = 22.4 L at standard temperature and pressure), x_{H2} is the hydrogen concentration in the carrier gas (mol L^{-1}), Q is the flow rate of the carrier gas (sccm, kmol s^{-1}), δ is the membrane thickness (wet, cm), and A is the permeating area of the MEA (cm^2).

B) Chronoamperometric Technique

Chronoamperometric determination of diffusion coefficient (D_b, cm^2 s^{-1}) and solubility (C_b, mol cm^{-3}) of hydrogen or oxygen in the membrane can be determined from the linear regression analysis of the experimental slope and intercept (int) of I vs. $t^{-1/2}$ plots (**Figure 2B**).

$$D_b = \frac{r^2 (int)^2}{\pi (slope)^2}, \qquad C_b = \frac{(slope)^2}{\pi n F r^3 (int)},$$

where r is the radius of the microdisc electrode (cm), n is the number of electrons, F is the Faraday constant (96,485 s A mol^{-1}), and n is the number of electrons (mol).

D_b and C_b are used to calculate gas permeability ($p=D_bC_b$, mol cm^{-1} s^{-1}) of the membrane.

C) *In Situ* Measurement in MEA

The hydrogen permeation rate, p (mol cm^{-1} s^{-1}), of the membrane can be expressed as:

$$P = \frac{i_{H2}}{nF} \frac{th}{p_{H2}},$$

where i_{H2} is the crossover current density of hydrogen (A cm^{-2}), p_{H2} is the feed partial pressure of hydrogen (mol^{-1}), th is the wet thickness the membrane (cm), F is the Faraday constant (96,485 s A mol^{-1}), and n is the number of electrons (mol).

QUALITY CONTROL AND QUALITY ASSURANCE

Instrument or Method Calibration and Standardization

- It is recommended to start the measurement with the commercially available membranes with the reported hydrogen and oxygen permeation rate in the literature (Nafion 112, Nafion 117 (Sakai et al., 1985; Beattie et al., 1999; Kim and Lee, 2015) or commercially available AEMs (Henkensmeier et al., 2021)) as a reference point.

- The GC for the pressure permeation cell needs to be properly calibrated with the gas standards prior to the analysis.

Cautions

- Special cautions needed during the measurement include avoiding inhalation of vapor or mist, ensuring adequate ventilation of the space, and removing all sources of ignition, heat, open flames, and sparks. No smoking or electrostatic charge is allowed. An oxygen cylinder has to be separated from hydrogen or combustible materials. All gas cylinders must be kept tightly closed in a dry, well-ventilated place.

- When using a membrane with gas recombination layers and O_2 is used as a carrier gas, it is necessary to monitor the H_2 content in O_2 with a combustible gas detection system.

Interferences

- The pressure effect on the gas permeation rate is significant to the measurement. The gas permeation rates measured under pressurized conditions, such as pressure cells and microelectrodes with pressurized gases, are higher than those measured by non-pressurized techniques. For the systems operating under pressurized conditions, it is appropriate to measure the gas permeation rate under a similar pressure condition. Other non-pressurized methods such as diffusion cells and microelectrodes without pressurized gases can be used for general screening or comparing the gas permeation rate of different ion-exchange membranes.

- Gas permeability strongly depends on the hydration level of membranes. The membrane needs to be in the fully hydrated state for the measurement, and insufficient hydration to the membrane can result in a low permeation measurement.

- Gas permeability as membrane properties is measured in pure water. In a practical system, AEM water electrolyzers often circulate alkaline solution, for example, NaOH, KOH, or K_2CO_3 solution (0.1–2 M) (Kraglund et al., 2016), and a high concentration of the solution may significantly impact the gas permeability by lowering diffusivity.

DISCUSSION

This protocol describes three methods that can be used to measure gas permeability across membranes of interest. All three methods can be applied to measure hydrogen permeability. Oxygen permeability can be measured by either microelectrodes or *in situ* measurement in MEA, yet, it is of less concern than hydrogen crossover due its production at ambient pressure and the lower permeation rate of oxygen than that of hydrogen (Sakai et al., 1985).

For a membrane used in high differential pressure operations or a membrane with recombination layers, a pressure permeation cell would be suitable. Microelectrode chronoamperometry would be favored when the membrane is available in an ionomer solution. Using MEA configuration would be preferred when hardware for the fuel cell testing set up is available. Running different methods on the same membrane sample would result in similar gas permeabilities (Kim and Lee, 2015). It is recommended to identify the operating conditions of water electrolyzers to select the appropriate gas permeation measurement methods for the membranes.

DATA AVAILABILITY STATEMENT

The original contributions presented in the study are included in the article; further inquiries can be directed to the corresponding author.

AUTHOR CONTRIBUTIONS

EP and YK wrote the first draft of the manuscript. SK provided the setup and procedure for pressure permeation measurement. EP revised the manuscript with help from SK and YK.

ACKNOWLEDGMENTS

We thank Kathy Ayers and Diana De Porcellinis for providing helpful comments. The authors gratefully acknowledge research support from the HydroGEN Advanced Water Splitting Materials Consortium, established as part of the Energy Materials Network under the U.S. Department of Energy, Office of Energy Efficiency and Renewable Energy, Fuel Cell Technologies Office (Program Manager: D. Peterson). Los Alamos National Laboratory is operated by Triad National Security, LLC under U.S. Department of Energy under contract no. 89233218CNA000001.

REFERENCES

Astill, T., Xie, Z., Shi, Z., Navessin, T., and Holdcroft, S. (2009). Factors Influencing Electrochemical Properties and Performance of Hydrocarbon-Based Electrolyte PEMFC Catalyst Layers. *J. Electrochem. Soc.* 156 (4), B499. doi:10.1149/1.3082119

Baik, K. D., Hong, B. K., and Kim, M. S. (2013). Novel Technique for Measuring Oxygen Crossover through the Membrane in Polymer Electrolyte Membrane Fuel Cells. *Int. J. hydrogen energy* 38 (21), 8927–8933. doi:10.1016/j.ijhydene.2013.04.142

Beattie, P. D., Basura, V. I., and Holdcroft, S. (1999). Temperature and Pressure Dependence of O2 Reduction at Pt|Nafion 117 and Pt|BAM 407 Interfaces. *J. Electroanal. Chem.* 468 (2), 180–192. doi:10.1016/s0022-0728(99)00164-3

Bernt, M., Schröter, J., Möckl, M., and Gasteiger, H. A. (2020). Analysis of Gas Permeation Phenomena in a PEM Water Electrolyzer Operated at High Pressure and High Current Density. *J. Electrochem. Soc.* 167 (12), 124502. doi:10.1149/1945-7111/abaa68

Broka, K., and Ekdunge, P. (1997). Oxygen and Hydrogen Permeation Properties and Water Uptake of Nafion® 117 Membrane and Recast Film for PEM Fuel Cell. *J. Appl. Electrochem.* 27 (2), 117–123. doi:10.1023/a:1018469520562

Chlistunoff, J. (2014). Oxygen Permeability of Cast Ionomer Films from Chronoamperometry on Microelectrodes. *J. Power Sources* 245, 203–207. doi:10.1016/j.jpowsour.2013.06.128

Gode, P., Lindbergh, G., and Sundholm, G. (2002). *In-situ* Measurements of Gas Permeability in Fuel Cell Membranes Using a Cylindrical Microelectrode. *J. Electroanal. Chem.* 518 (2), 115–122. doi:10.1016/s0022-0728(01)00698-2

Grigoriev, S. A., Millet, P., Korobtsev, S. V., Porembskiy, V. I., Pepic, M., Etievant, C., et al. (2009). Hydrogen Safety Aspects Related to High-Pressure Polymer Electrolyte Membrane Water Electrolysis. *Int. J. Hydrogen Energy* 34 (14), 5986–5991. doi:10.1016/j.ijhydene.2009.01.047

Henkensmeier, D., Najibah, M., Harms, C., Žitka, J., Hnát, J., and Bouzek, K. (2021). Overview: State-Of-The Art Commercial Membranes for Anion Exchange Membrane Water Electrolysis. *J. Electrochem. Energy Convers. Storage* 18 (2). doi:10.1115/1.4047963

Hibbs, M. R. (2013). Alkaline Stability of Poly(phenylene)-Based Anion Exchange Membranes with Various Cations. *J. Polym. Sci. Part B Polym. Phys.* 51 (24), 1736–1742. doi:10.1002/polb.23149

Kim, Y. S., and Lee, K.-S. (2015). Fuel Cell Membrane Characterizations. *Polym. Rev.* 55 (2), 330–370. doi:10.1080/15583724.2015.1011275

Kocha, S. S., Deliang Yang, J., and Yi, J. S. (2006). Characterization of Gas Crossover and its Implications in PEM Fuel Cells. *AIChE J.* 52 (5), 1916–1925. doi:10.1002/aic.10780

Kraglund, M. R., Aili, D., Jankova, K., Christensen, E., Li, Q., and Jensen, J. O. (2016). Zero-gap Alkaline Water Electrolysis Using Ion-Solvating Polymer Electrolyte Membranes at Reduced KOH Concentrations. *J. Electrochem. Soc.* 163 (11), F3125–F3131. doi:10.1149/2.0161611jes

Motz, A. R., Li, D., Keane, A., Manriquez, L. D., Park, E. J., Maurya, S., et al. (2021). Performance and Durability of Anion Exchange Membrane Water Electrolyzers Using Down-Selected Polymer Electrolytes. *J. Mat. Chem. A* 9 (39), 22670–22683. doi:10.1039/d1ta06869e

Sakai, T., Takenaka, H., Wakabayashi, N., Kawami, Y., and Torikai, E. (1985). Gas Permeation Properties of Solid Polymer Electrolyte (SPE) Membranes. *J. Electrochem. Soc.* 132 (6), 1328–1332. doi:10.1149/1.2114111

Xiang, C., Papadantonakis, K. M., and Lewis, N. S. (2016). Principles and Implementations of Electrolysis Systems for Water Splitting. *Mat. Horiz.* 3 (3), 169–173. doi:10.1039/c6mh00016a

Yim, S.-D., Chung, H. T., Chlistunoff, J., Kim, D.-S., Fujimoto, C., Yang, T.-H., et al. (2015). A Microelectrode Study of Interfacial Reactions at the Platinum-Alkaline Polymer Interface. *J. Electrochem. Soc.* 162 (6), F499–F506. doi:10.1149/2.0151506jes

Zhang, J., Gasteiger, H. A., and Gu, W. (2013). Electrochemical Measurement of the Oxygen Permeation Rate through Polymer Electrolyte Membranes. *J. Electrochem. Soc.* 160 (6), F616–F622. doi:10.1149/2.081306jes

Conflict of Interest: The authors declare that the research was conducted in the absence of any commercial or financial relationships that could be construed as a potential conflict of interest.

NOMENCLATURE

Abbreviations

AEM anion exchange membrane.

GC gas chromatography.

GDL gas diffusion layer.

MEA membrane electrode assembly.

PEM proton exchange membrane.

Pt platinum.

PTFE polytetrafluoroethylene.

PTL porous transport layer.

frontiers | Frontiers in Energy Research

TYPE Methods
PUBLISHED 19 August 2022
DOI 10.3389/fenrg.2022.908672

OPEN ACCESS

EDITED BY
Brendan Bulfin,
ETH Zürich, Switzerland

REVIEWED BY
Andries Kruger,
Schaeffler, Germany
Hiroshi Ito,
National Institute of Advanced Industrial Science and Technology (AIST), Japan

*CORRESPONDENCE
Jennifer R. Glenn,
jglenn@nelhydrogen.com

SPECIALTY SECTION
This article was submitted to Process and Energy Systems Engineering, a section of the journal Frontiers in Energy Research

RECEIVED 30 March 2022
ACCEPTED 20 July 2022
PUBLISHED 19 August 2022

CITATION
Glenn JR, Lindquist GA, Roberts GM, Boettcher SW and Ayers KE (2022), Standard operating procedure for post-operation component disassembly and observation of benchtop water electrolyzer testing.
Front. Energy Res. 10:908672.
doi: 10.3389/fenrg.2022.908672

Standard operating procedure for post-operation component disassembly and observation of benchtop water electrolyzer testing

Jennifer R. Glenn[1]*, Grace A. Lindquist[2], George M. Roberts[1], Shannon W. Boettcher[2] and Katherine E. Ayers[1]

[1]Nel Hydrogen, Wallingford, CT, United States, [2]Department of Chemistry and Biochemistry, University of Oregon, Eugene, OR, United States

Post-operation component disassembly and observation of electrolyzer parts is useful in understanding the interactions of the components and the electrochemical environment beyond the systems electrochemical output. We report a standard protocol for post-operation component disassembly and observation, including directions for cell-component preservation, preliminary visual inspection of cell components, and a guide for the advanced inspection of specific components with suggestions for further analysis if necessary. The procedures outlined here allow for a standardized method that can be used and compared between different laboratories and for literature comparison to experimental results.

KEYWORDS

teardown analysis, electrolyzer, membrane, gas diffusion layer, porous transport layer, electrode

1 Introduction

Water electrolysis for green hydrogen production is expected to scale substantially in the coming decade as the global renewable energy economy develops (Pivovar et al., 2018). While multiple established water electrolysis technologies exist at various stages of commercialization and scale (Ayers et al., 2019), component-specific development is still needed to improve performance and decrease capital and operating expenses. Many components used in electrolysis are adapted from other systems, for example fuel cells, and thus may not be the ideal design for an electrolyzer environment where water and gas transport needs differ

---

Abbreviations: PEM, Proton Exchange Membrane; AEM, Anode Exchange Membrane; CCM, Catalyst Coated Membrane; GDL, Gas Diffusion Layer; GDE, Gas Diffusion Electrode; PTL, Porous Transport Layer; PTE, Porous Transport Electrode; SEM, Scanning Electron Microscopy; EDS, Energy Dispersive Spectroscopy; XRF, X-ray Fluorescence Spectroscopy; TOC, Total Organic Carbon; ICP, Inductively Coupled Plasma; NVR, Non-Volatile Reactants.

dramatically. With increased interest in electrolyzers, research efforts toward electrolyzer-specific components have increased. These specialized components have enabled improved efficiency, longer system lifetimes and lower costs.

Multiple protocols specific to low-temperature electrolysis systems have been published. However, these are specific to individual components, such as catalysts (Alia and Denilovic, 2022; Creel et al., 2022), porous transport layers (PTLs) (Quimet et al., 2022), or membranes (Arges et al., 2022; Wang et al., 2022). Once a material passes this initial screening, the next step is to understand the operational performance in a full cell. Interactions between different components may alter performance or introduce additional stresses not observed *ex-situ*.

Limited information can be obtained from electrochemical analysis of full-cell electrolysis systems, as cells are complex and all components contribute to the total observed current-voltage response. Thus, post-operation analysis of test stacks and cells reveal additional information regarding how each component is contributing to cell performance. The concept of post-operation component disassembly and observation is not new, however the best practices for doing so reproducibly, in-house and across laboratories, is lacking. This article provides a standard protocol for post-operation component disassembly and observation of electrolyzer cells that were tested at a small scale, benchtop size and for short durations of less than 8 h. The protocol is applicable to both proton exchange membrane (PEM) and anion exchange membrane (AEM) systems and will cover cell/component preservation and storage, a workflow for the preliminary visual inspection of components, and advanced component specific analysis with recommendations for further analysis. As the primary analysis in this protocol is visual, the indications of degradation that are key to determining failures or the necessity for further analysis include changes in physical appearance such as color changes or tactile texture differences, delamination of electrodes from components, holes or cracking of components, etc. Guidance regarding how to present the data so that it is replicable and comparable between laboratories is also discussed.

2 Protocol scope

2.1 Scope and applicability

This procedure is intended to provide guidelines and best practices for diagnosing component failure in operated low-temperature electrolyzer cells for both PEM and AEM systems. The components covered in this protocol are present in both PEM and AEM systems and are typically made of the same or similar materials, apart from the membranes. While the membranes differ in composition, the analysis process is similar enough to be compared here. Instructions for disassembling cell hardware, labeling and preserving cell components, and diagnostic test methods for these components are discussed. This procedure is primarily designed for a bench-top, short-duration, single-cell water electrolyzer system, but it is possible to adapt the procedure for other cell hardware and multi-cell stacks.

2.2 Summary of method

This protocol describes the component disassembly, preservation, and *ex-situ* testing of the following electrolyzer components: membrane/catalyst coated membrane (CCM), carbon gas diffusion layer (GDL), porous transport layer (PTL), gaskets, and the bipolar/cell plate. The component disassembly and initial observation procedure will cover the disassembly of the cell, marking all relevant inlets/outlets to preserve the orientation of components within the cell, preparation of components for *ex-situ* testing when necessary, and suggestions for further *ex-situ* analysis.

2.3 Personnel qualifications/responsibilities

All personnel must be trained to handle chemicals and to mitigate chemical hazards. Training and familiarity with the test stand equipment and cell components is necessary for all personnel.

2.4 Health and safety warming

2.4.1 Chemical hazards

Standard personal protective equipment, including safety glasses, lab coat and gloves, must be worn at all times. Ensure that all gas cylinders used in the experiments are properly secured and regulated. Ensure that any gas venting lines are located in a well-ventilated area such as a hood. If the experiment used nanoparticles, take additional appropriate precautions as nanoparticles are frequently found to be more reactive than their parent compound.

2.4.2 Electrical hazards

Before disassembling the cell, check that the power source is turned off and disconnected, and that the cell is discharged to prevent personal injury and the potential to short the cell during disassembly.

2.4.3 Heat hazard

Allow the cell stack to cool before handling to prevent injury due to contact with hot cell components, metal cell components are excellent conductors of heat.

2.4.4 Sharp edges

Wear latex or nitrile gloves at all times to protect against any sharp edges of stack components.

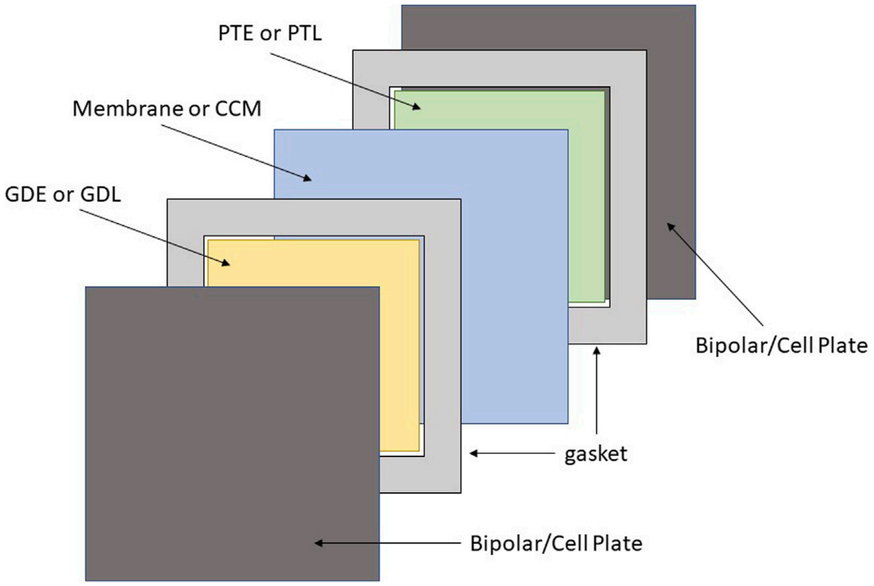

FIGURE 1
Illustration of the cell components including bipolar/cell plate, gaskets, GDE or GDL, Membrane or CCM, and the PTE or PTL displayed in dark grey, light grey, yellow, blue and green respectively.

2.5 Equipment and supplies

The supplies listed below are suggested tools for this component disassembly and initial observation test protocols; depending on the testing, additional equipment and supplies may be necessary:

Storage container suitable for containing liquids
Deionized (DI) water compliant with ASTM Standard D 1193-99e1 Type 1 or 2
Latex or nitrile gloves
Stainless steel or plastic spatula
Light table
Benchtop optical microscope with a recommended resolution of at least ×10
Camera

3 Procedure

3.1 Entire cell preservation procedure

This procedure is typically used to preserve cells during the extraction process when immediate examination of the components is not possible.

1) Remove all components from the test setup without separating components. One repeat unit consisting of each of the components will be referred to as a cell from this point forward. For the purpose of this protocol, a cell contains gasketing, gas diffusion layer, membrane, porous transport layer and bipolar/cell plate. An illustration of the cell components is displayed in Figure 1. If there are any visible changes during operation that may be disrupted when submerging in water, make a note and consider photographing the cell.
2) Place the entire cell in a watertight container with sufficient DI water to keep the CCM hydrated.
a) Note: The components may shift from their original position over time depending on the type of container used. If this is of concern, mark the components (such as with a dull pencil) to indicate orientation.

3.2 Preliminary visual inspection of cell components

Note: Always wear latex or nitrile gloves when handling cell components to prevent contamination.

1) Remove all components from the test hardware as one cell (one repeating unit) if cells have not already been preserved (Section 3.1). It is easier to separate parts outside of the test hardware.
2) Place cell components on a clean surface, where they will not be exposed to other chemicals or contaminants.

3) Disassemble each cell component in order of their stack up in the cell starting at your preferred side of the cell. When removing each part gently mark the orientation of the parts by a distinguishing factor of the cell (ex. Voltage tab, flow direction, etc.) using a dull graphite pencil or an ink marker. A spatula can be utilized to help separate cell components; however, care must be taken to not inflict damage on the cell components during this initial evaluation. Note any damage that occurs from the cell disassembly.
   a) Note: For wet materials a dull graphite pencil is recommended for marking as it will not bleed like an ink pen would; however, the mark will wear off over time if exposed to excessive rubbing or water flow. Use a dull pencil to prevent puncturing any delicate cell components. If the component is dry and will not be stored in a wet environment, an ink marker is also appropriate.
   b) Note: Unless intending to complete water content sampling on the membrane, keep the membrane hydrated with DI water during this process.
4) Visually inspect any cell components for differences relative to new unoperated cell hardware. Some differences may be expected due to operation, which would be indicated from historical data. One example of this is impressions on gasket materials made from neighboring cell components. Historical data is useful in these cases to determine if this is a “normal” operational difference or a larger/unusual difference that would indicate a failure. Using the same example of impression in a gasket material, this could mean that the impression is greater than usual, a different shape, resulting in tears that are not typically observed, etc.
   a) Note: Collecting images of difference is a good way to compare to historical data and useful in reporting damage. It is recommended that new components are also analyzed as part of this historical data for comparison. All images should contain a scale bar of some form for reference. (i.e., scale bar provided by imaging source, ruler or comparison to an object of known size such as monetary coins which have standardized dimensions).
5) If inspection of parts ends after visual inspection, reassemble cell components in original order and orientation, and store in watertight container with DI water to keep the membrane hydrated. If it is more appropriate to store the components separately, ensure that the membrane is stored in an airtight container with DI water and the components that do not require hydration are stored so that they remain clean and free of additional contamination.

3.3 Component-specific analysis

This protocol applies to the teardown of two configurations: GDL-CCM-PTL and GDE-PEM or AEM -PTE.

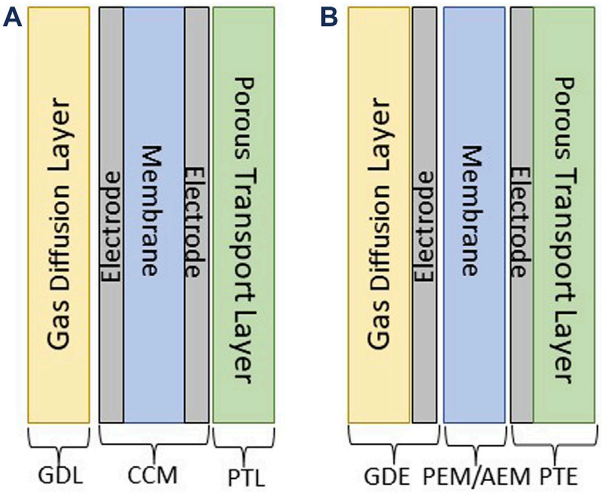

FIGURE 2
Illustration of **(A)** GDL-CCM-PTL and **(B)** GDE-PEM/AEM-PTE configurations respectively.

1) GDL-CCM-PTL: Gas Diffusion Layer – Catalyst Coated Membrane – Porous Transport Layer (catalyst is on the membrane, Figure 2A)
2) GDE—PEM/AEM—PTE: Gas Diffusion Electrode – Proton Exchange Membrane or Anion Exchange Membrane – Porous Transport Electrode (catalyst layer is on the gas diffusion layer and porous transport layer, Figure 2B)

3.3.1 Membrane/electrode

1) Mark PEM/AEM or CCM with a graphite pencil or ink marker (discussion in Section 3.2 sub-bullet 3) to indicate the orientation within the cell.
2) Visually inspect PEM/AEM or CCM for discoloration and, in the case of an CCM, electrode dissolution. If present, additional testing may be required suggestions for which are made in Section 3.4.
3) Visually and tactilely inspect membrane for unusual wrinkling. This potentially indicates under or over hydration of the membrane and/or a possible water flow issue.
4) Place PEM/AEM or CCM on a light table. If light shows through the electrode, an electrode void or pinhole in the membrane may be present. For PEM/AEM without an electrode (e.g. the catalyst layers were applied to the GDL and PTL), a pinhole may be more difficult to identify as there will not be as significant of a color difference.
5) To differentiate between an electrode void and a pinhole, inspect the membrane under an optical microscope.
6) If an electrode void is not present and a pinhole is suspected but not visually identifiable under an optical microscope, blot the membrane surface dry, and put DI

FIGURE 3
An extreme example of a hole present in a membrane post-operation. Reproduced with permission from Millet et al. (2012).

water under the membrane in the suspected area. If a pinhole is present DI water will pass through the hole to the membrane surface.

a) Note: This technique does not always work if the pinhole is too small. One strategy to find such a pinhole is to pressurize one side of the membrane while covering the other side with DI water. If there is a small pinhole bubbles will appear in the water at the location of the pinhole. This can help identify an area of interest, which can then be examined closer.

7) If a pinhole is identified, a cross section of the area of interest can be taken and observed under a higher resolution microscopy instrument to confirm the pinhole along with its size and possibly its source.

a) Figure 3 illustrates an example of a large hole present in an CCM (Millet et al., 2012). This is an extreme example, and many pinholes are much smaller.

3.3.2 Gas diffusion layer and porous transport layer

1) Mark carbon gas diffusion layer and/or metal porous transport layer with a graphite pencil or ink marker (see discussion in Section 3.2 sub-bullet 3) to indicate orientation within the cell.
2) Visually inspect the GDL or PTL for damage or transfer of electrode material either onto the GDL/PTL from the CCM or from the GDE/PTE to the membrane if the electrode was applied directly to the GDL/PTL.
3) Inspect any areas of interest under an optical microscope or a high-resolution microscopy instrument if appropriate.

3.3.3 Gaskets

1) Mark gasket(s) with a graphite pencil or ink marker (see discussion in Section 3.2 sub-bullet 3) to indicate orientation within the cell.
2) Visually and tactilely inspect gasket for any discoloration, increased indentations, wrinkles, tears or stretching.

a) Potential reasons for discoloration include material transfer from another cell component, contamination, or a temperature event.

b) Increased indentations, wrinkling, tears or stretching can be a result of a pressure event or unevenly applied load.

3.3.4 Bipolar/cell plate

1) Mark bipolar/cell plate with a graphite pencil or ink marker (see discussion in Section 3.2 sub-bullet 3) to indicate orientation within the cell if the plate does not already have an orientation-defining feature.
2) Visually and tactilely inspect bipolar/cell plate for any discoloration, new or different indentations, cracking, etc.

a) Potential reasons for discoloration include material transfer from another cell component, oxidation of the plate depending on the material it is composed of, or a temperature event.

b) New or different indentations and cracking may indicate that a pressure event occurred or that an uneven load was applied to the cell.

c) Figure 4 depicts discoloration of a bipolar/cell plate due to corrosion (Feng et al., 2017).

d) Figure 5 demonstrates an extreme example of damage caused by a thermal event (Millet et al., 2012).

3.4 Suggestions for advanced characterization

After visual inspection and proper documentation, additional testing and characterization may be warranted. These tests will be cell-specific and should be conducted only if necessary at the discretion of the analyzer. The additional testing and characterization discussed here are suggestions by the authors and as such are not intended to be an inclusive list of potential testing and will not cover the procedures for each characterization method in exhaustive detail.

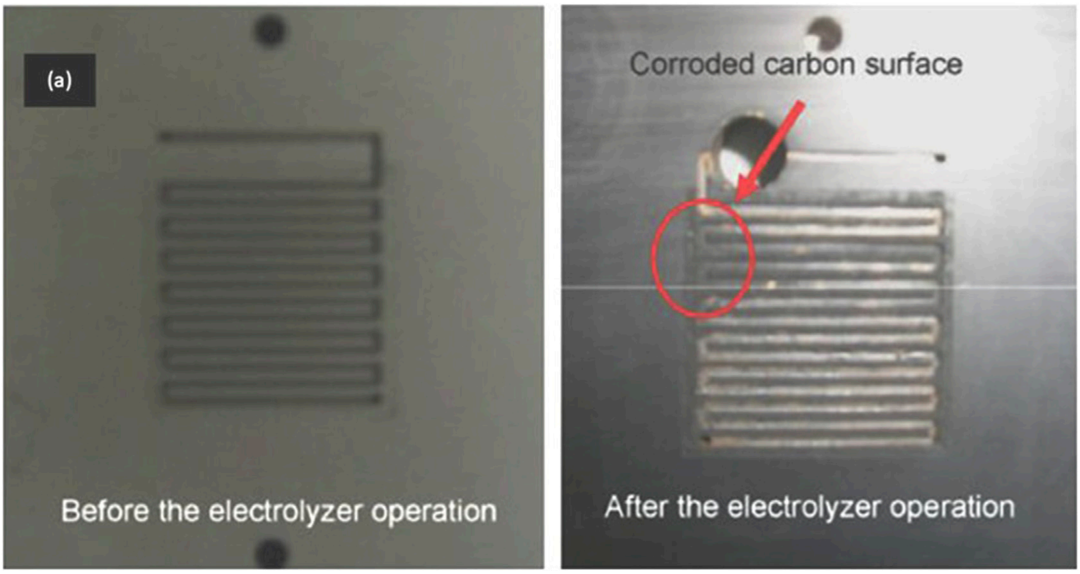

FIGURE 4
Example of a bipolar/cell plate that has incurred corrosive damage after electrolyzer operation (right) as compared to the bipolar/cell plate before electrolyzer operation (left). Reproduced with permission from Feng et al. (2017).

FIGURE 5
Bipolar/cell plate that has been damaged by a thermal event. Reproduced with permission from Millet et al. (2012).

3.4.1 Water sampling

Water sampling is useful if contamination or low water quality are known or suspected. This testing may include tests such as total organic carbon (TOC), inductively coupled plasma (ICP) metals scans, nonvolatile reactants (NVR), etc. (Watts et al., 1982; Meyer, 1987; Bisutti et al., 2004) For TOC and ICP testing SEM 5310 B, C and D and EPA 200.7 are recommended respectively. NVR is a test involving the evaporation of the water and measurement of the residue; however, the complete procedure is outside the scope of this protocol. General instructions for water sample collection will be provided below.

1) Collect water samples from the water reservoir if the water in the system recirculates or the water outlet of the stack if it does not recirculate. It may also be advisable to collect water samples pre-circulation in systems that recirculate water or the water inlet for the stack for non-recirculating systems if a blank measurement is desired.
a) Note: Some testing may require special sampling containers to take accurate measurements. For example, water samples for TOC analysis must be stored in a container that will not leach organic carbons into the water sample prior to testing. Additionally, biological sampling may be time sensitive. Check all analysis protocols for specific sampling requirements prior to collecting samples.
2) Prepare water samples appropriately for the chosen analysis technique.

a) If contaminants are suspected in extremely small quantities, it may be necessary to concentrate the sample prior to analysis. If the sample is concentrated, this must be reported with the data to accurately assess the contaminant level.

Note: Some contaminants of concern and common to electrolyzers include iron, cobalt, chromium, zinc, chlorine, and sodium. However, this is not an exhaustive list. When considering potential contaminants, it is helpful to create a list of material compositions for the components as well as the materials used in the test setup.

3.4.2 Component-specific: membrane/ electrode

1) Discoloration: In case of component discoloration further investigation may be warranted, such as SEM coupled with EDS or XRF (this will only identify elements with fluorescent properties) to determine if the discoloration is due to contaminants or elemental transfer from another cell component.
b) Note: For AEM cells if any further testing requires the membrane be dried, the membrane must be ion exchanged out of the OH^- counter-ion form. During drying, the nucleophilicity of OH^- increases and may cause chemical degradation of the polymer. To ion-exchange, follow manufacturer recommendations for OH^- operation but instead replace the hydroxide solution with the same concentration chloride solution. For example, if a manufacturer recommends soaking in 1 M KOH for 24 h, soak the membrane in 1 M NaCl for the same amount of time prior to drying.
2) Electrode Dissolution: The degree of electrode dissolution can be determined with a calcination test, provided the initial loading was known. (Kuntze, 2009). This test is destructive.
3) Small Features: SEM can also be used to observe smaller features on the surface of the PEM/AEM or CCM and to view the PEM/AEM or CCM in cross-section if it is suspected that a defect penetrates the sample. Note that this testing would be destructive unless the full sample is small enough to fit in the SEM. Depending on the material of the PEM/AEM or CCM, a gold or conductive carbon coating might be advisable as organic materials are less stable under the electron beam required for this analysis.
a) Figure 6 is an example of how a cross-section of an CCM observed with SEM can help identify delamination of the catalyst (Feng et al., 2017).
b) Figure 7 demonstrates how SEM can be used to observe topographical features on a PEM/AEM or CCM and how cross-section can be used to determine how/if a feature affects the layers of the PEM/AEM/CCM (LaConti et al., 2006).

3.4.3 Component-specific: gas diffusion layer and porous transport layer

1) Coating Retention: If a coating was applied to either the carbon gas diffusion layer or the porous transport layer, assess the retention of that layer through imaging techniques or thickness measurements.
a) A few examples of ways to do thickness measurements include: XRF elemental thickness if your instrument has this function and the coating is a fluorescent material, measurement with a micrometer that has an appropriate measurement range for the expected coating thickness, cross-sectional measurements of coatings via SEM (cracking samples with liquid nitrogen is recommended to reduce the chance of compression of the coating from cutting), optical profilometry or X-ray photoelectron spectroscopy.
b) An example of using SEM for cross-sectional measurements of coating thickness is displayed in Figure 8 (Frensch et al., 2019).
2) Material Density: The relative density of the material and/or coating can be determined through flow-through testing or bubble-point testing. Use an applicable standard for comparison of the results.
a) Flow Through Testing—While attached to a vacuum set-up, time how long it takes for a set amount of water to pass through the GDL or PTL with or without electrodes applied.
b) Bubble Point Testing—Pressurize one side of the GDL or PTL while covering the other side with an appropriate solvent (i.e., DI water or isopropanol). The pressure at which bubbles start to appear is considered the initial bubble point, and when the bubbling resembles a rolling boil the full bubble point has been reached.

4 Instrument, methods, and results reporting formats

Throughout this protocol numerous experimental methods and analytical instrumentation have been called out as suggested analysis routes for further/additional investigation. If further/additional investigation is necessary and the suggested techniques or others are utilized, use appropriate instrument or methods calibration and standards for the technique as outlined by instrument procedures, additional standard operating procedures or any industrial standards that are being followed. Historical data should be cataloged for comparison, for how the cell components are expected to look before and after operation and what the test results are for a known good test. For example, if an ICP metals scan is being collected for a water sample of stack/cell that is suspected to have contamination, it would be beneficial to have historical data of the ICP metals for a water sample of a stack/cells that have not

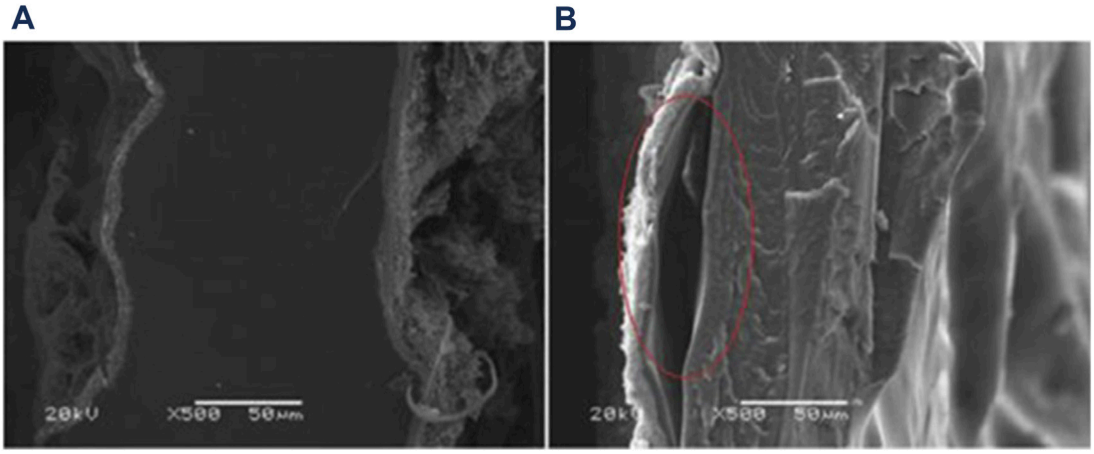

FIGURE 6
SEM micrographs of cross-sections of **(A)** CCM with a well adhered electrode layer and **(B)** an electrode layer that is starting to delaminate. Reproduced with permission from Feng et al. (2017).

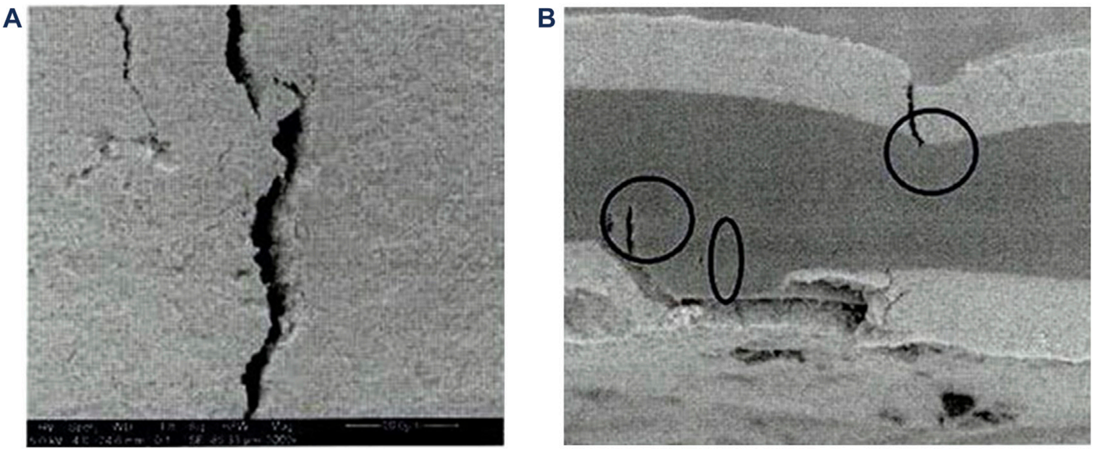

FIGURE 7
Morphology of an CCM investigated using SEM to observe the surface topography. **(A)** The surface of the CCM displaying a crack in the electrode layer. **(B)** A cross-sectional micrograph displaying how the electrode cracking is penetrating the CCM and the beginning of a pinhole/tearing of the membrane. Reproduced with permission from LaConti et al. (2022).

been operated and a stack/cells that are known to not contain any contaminants so that the level of contamination can be compared to what is "normal" for the system.

When reporting the results of any post-operation component analysis, it is important to report the data in a reliable, reproducible manner. It is essential due to the qualitative nature of the analysis to report how the analysis was done and provide as much information as possible. This can be done by providing the experimental details of how data is collected and/or by pointing to standard analysis protocols that were followed. Also state any standard materials that were used for comparison, either as technique/instrument standards or a comparison to the standard "normal" for the specific system. If providing such standards is prohibited by the need to protect proprietary information, the authors suggest providing a statement such as the following "These results have been compared to proprietary internal standards/results and were determined/observed to . . .." and add an appropriate comparison of the results. Include references to the instrumentation and the setting used for any advanced analysis in addition to the technique standards for ease of reproducibility by others. Sample size information should be provided or the data normalized by reporting values per active area (or component area) whenever

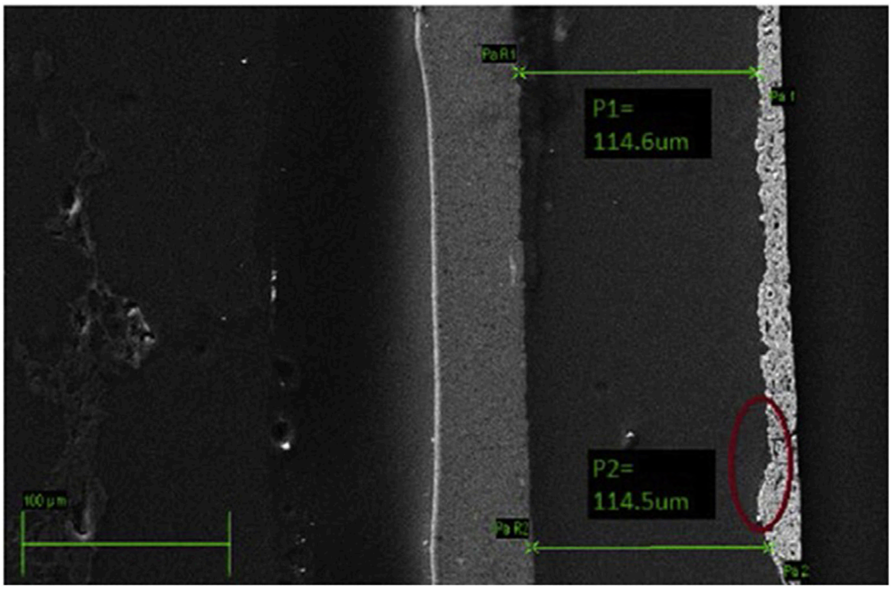

FIGURE 8
SEM micrograph exemplifying how cross-sectioning of samples can be used to measure component thicknesses. This example is of an CCM, but the technique can be extended to GDEs and PTEs as well. Reproduced with permission from Frensch et al. (2019).

possible so that comparison may be made between samples of different platform size. Some examples of this would include stating the overall stack voltage is for a cell stack of *x* number of cells, the NVR as grams/sample area, ICP results as mg/L, etc. By including the information discussed above there will be more transparency regarding how the results were collected, their significance, and how the results compare to other experimental results not only within one's own laboratory but between laboratories leading to better understandings and comparability of data.

4.1 Reminders to prevent common issues

Wear latex or nitrile gloves while handling all cell components to prevent transfer of any potential contaminants to the cell components, especially if the components will be analyzed for chemical contamination. Change gloves between any other tasks involving substances incompatible with the cell (e.g. oils, lubricants, etc.) and working with cell parts. It may also be necessary to change gloves more frequently if cell components have the potential to contaminate one another, one example of which would be if handling the different electrodes is suspected to leave residue on the gloves resulting in transfer to the other electrode during handling.

When collecting samples, in particular water samples, ensure that the sampling method/sample containers are compatible with the analysis technique (e.g., plastic versus glass, use of preservatives, filling process, etc.).

Some forms of analysis will negate the testing of others; ensure that your test plan takes this into consideration. For example, it is suggested to do all non-destructive testing first as destructive testing may not allow for further testing of the material in part or as a whole.

Data availability statement

The original contributions presented in the study are included in the article/supplementary material, further inquiries can be directed to the corresponding author.

Author contributions

JG wrote the body of the article and GL wrote the introduction. GL and SB edited the article and proofed the sections regarding AEM electrolysis. GR and KA edited the article and proofed the sections regarding PEM electrolysis.

Funding

The authors would like to acknowledge the U.S. Department of Energy and the funding support from project DOE-DE-EE0008092, “Benchmarking Advanced Water Splitting Technologies: Best Practices in Materials Characterization”.

Conflict of interest

The authors declare that the research was conducted in the absence of pany commercial or financial relationships that could be construed as a potential conflict of interest.

The handling editor BB is currently organizing a Research Topic with the author(s) KA.

Publisher's note

References

Alia, S. M., and Denilovic, N., "Rotating disk electrode standardization and best practices in acidic oxygen evolution for low temperature electrolysis", *Front. Energy Res.*, 2022, Provisionally Accepted. doi:10.3389/feng.2022.857663

Arges, C. G., Ramani, V., Wang, Z., and Ouimet, R. J. (2022). Assessing the oxidative stability of anion exchange membranes in oxygen saturated aqueous alkaline solutions. *Front. Energy Res.* 10, 871851. doi:10.3389/fenrg.2022.871851

Ayers, K., Danilovic, N., Oiumet, R., Carmo, M., Pivovar, B., and Bornstein, M., "Perspectives on low-temperature electrolysis and potential for renewable hydrogen at scale", *Annu. Rev. Chem. Biomol. Eng.*, 2019, 10, 219–239. doi:10.1146/annurev-chembioeng-060718-030241

Bisutti, I., Hilke, I., and Raessler, M. (2004). Determination of total organic carbon – An overview of current methods. *TrAC Trends Anal. Chem.* 23, 716–726. doi:10.1016/j.trac.2004.09.003

Creel, E. B., Lyu, X., McCool, G., Quimet, R. J., and Serov, A. (2022). Protocol for screening water oxidation or reduction electrocatalyst activity in a three-electrode cell for alkaline exchange membrane electrolysis. *Front. Energy Res.* 10, 871604. doi:10.3389/fenrg.2022.871604

Feng, Q., Yuan, X.-Z., Liu, G., Wei, B., Zhang, Z., Li, H., et al. (2017). A review of proton exchange membrane water electrolysis on degradation mechanisms and mitigation strategies. *J. Power Sources* 366, 33–55. doi:10.1016/j.jpowsour.2017.09.006

Frensch, S. H., Fouda-Onana, F., Serre, G., Thoby, D., Araya, S. S., and Kær, S. K. (2019). Influence of the operation mode on PEM water electrolysis degradation. *Int. J. Hydrogen Energy* 44, 29889–29898. doi:10.1016/j.ijhydene.2019.09.169

Kuntze, R. (2009). Calcination processes. *Gypsum:Connecting Sci. Technol.*, 37–60. doi:10.1520/MNL11585M

LaConti, A. B., Liu, H., Mittelsteadt, C., and McDonald, R. C. (2006). Polymer electrolyte membrane degradation mechanisms in fuel cells – findings over the past 30 years and comparison with electrolyzers. *ECS Trans.* 1, 199–219. doi:10.1149/1.2214554

Meyer, G. A. (1987). ICP: Still the panacea for trace metal analysis? *Anal. Chem.* 59 (23), 1345A–1354A. doi:10.1021/ac00150a001

Millet, P., Ranjbari, A., de Guglielmo, F., Grigoriev, S. A., and Auprêtre, F. (2012). Cell failure mechanisms in PEM water electrolyzers. *Int. J. Hydrogen Energy* 37, 17478–17487. doi:10.1016/j.ijhydene.2012.06.017

Pivovar, B., Rustagi, N., and Satyapal, S. (2018). Hydrogen at scale (H2 @ scale): Key to a clean, economic, and sustainable energy system. *Electrochem. Soc. Interface* 27, 47–52. doi:10.1149/2.F04181if

Quimet, R. J., Young, J. L., Schuler, T., Bender, G., Roberts, G. M., and Ayers, K. E. (2022). Measurement of resistance, porosity, and water contact angle of porous transport layers for low-temperature electrolysis technologies. *Front. Energy Res.* 10, 911077. doi:10.3389/fenrg.2022.911077

Wang, L., Rojas-Carbonell, S., Hu, K., Setzler, B. P., Motz, A. R., Ueckermann, M. E., et al. (2022). Standard operating protocol for ion-exchange capacity of anion exchange membranes. *Front. Energy Res.* 10, 887893. doi:10.3389/fenrg.2022.887893

Watts, C. D., Crathorne, B., Fielding, M., and Killops, S. D. (1982). Nonvolatile organic compounds in treated waters. *Environ. Health Perspect.* 46, 87–99. doi:10.1289/ehp.824687

frontiers | Frontiers in Energy Research

TYPE Methods
PUBLISHED 02 September 2022
DOI 10.3389/fenrg.2022.963777

OPEN ACCESS

EDITED BY
Roel Van de Krol,
Helmholtz Association of German Research Centers (HZ), Germany

REVIEWED BY
Bin Chen,
Shenzhen University, China
Faran Razi,
University of British Columbia—Okanagan Campus, Canada

*CORRESPONDENCE
Kevin Huang,
HUANG46@cec.sc.edu

SPECIALTY SECTION
This article was submitted to Hydrogen Storage and Production, a section of the journal Frontiers in Energy Research

RECEIVED 07 June 2022
ACCEPTED 28 July 2022
PUBLISHED 02 September 2022

CITATION
Zhang Y, Xu N, Tang Q, Gibbons W and Huang K (2022), Evaluation of steam supply performance: Steamer vs. bubbler.
Front. Energy Res. 10:963777.
doi: 10.3389/fenrg.2022.963777

Evaluation of steam supply performance: Steamer vs. bubbler

Yongliang Zhang[1], Nansheng Xu[1], Qiming Tang[1], William Gibbons[2] and Kevin Huang[1]*

[1]Department of Mechanical Engineering, University of South Carolina, Columbia, SC, United States, [2]Hydrogen and Fuel Cell Technologies Office, United States Department of Energy, Washington, DC, MD, United States

Water/steam electrolysis is a key enabling technology for clean, low-carbon and sustainable production of hydrogen and will play a crucial role in future hydrogen economy. For high temperature solid oxide electrolytic cells, steam is the chemical feedstock. A stable and accurate supply of steam to solid oxide electrolytic cells is of vital importance to smooth production of hydrogen. In this study, we compare steam supply performance of two commonly used steam generators: steamer and bubbler. Our results show that bubbler with proper volume and fritted inlet gas tubing can provide more stable and accurate steam supply than steamer for laboratory use. We also provide the explanation for the unstable steam supply observed in steamer. Overall, we conclude that bubbler is generally a better choice for small-scale laboratory use (e.g., ≤50% H_2O, ≤100 sccm carrier gas flow) to produce stable and accurate steam and steamer might be a better choice for higher steam contents and flow rates (e.g., >60% H_2O and >200) encountered in large-scale testing and/or aggressive high steam conditions.

KEYWORDS

water feed rate, fritted head, bubbler volume, steam content, solid oxide electrolytic cell

Introduction

Producing hydrogen from water/steam is considered as a key enabling technology to realize a sustainable clean and low-carbon future (Buttler and Spliethoff, 2018; Glenk and Reichelstein, 2019; Staffell et al., 2019). There are three types of water/steam electrolyzers categorized on the types of electrolytes used: alkaline solutions (Zeng and Zhang, 2010), proton exchange membranes (PEMs) (Carmo et al., 2013) anion exchange membranes (AEMs) (Vincent and Bessarabov, 2018) and solid oxides (SOs) (Hauch et al., 2020), among which solid oxide electrolyzers are operated at elevated temperatures with unique thermodynamic and kinetic advantages to achieve high H_2 production rate at high electrical efficiency (Buttler and Spliethoff, 2018; Hauch et al., 2020). The current effort on solid oxide electrolysis cells (SOECs) development is primarily focused on improving the durability of H_2 production at the highest possible hydrogen production rate and electrical efficiency.

Steam supply is an important component of SOEC systems. A stable and accurate supply of steam can ensure smooth operation of electrolyzers, precise determination of electrolysis performance (e.g., Faradaic efficiency) and identification of the root causes of any cell anomalies. Currently, three types of steam generators have been devised to provide steam for SOECs: 1) bubbler (O'Brien et al., 2007; Zhang et al., 2013; Schefold et al., 2017), 2) steamer (Kim-Lohsoontorn and Bae, 2011; Shen et al., 2022; Zhang et al., 2022), and 3) hydrogen-burner (Hauch et al., 2005). The bubbler is the most popular design, by which a carrier gas is passed through and exits with saturated steam. The bubble design is simple, easy to operate and often used for low-flow-rate steam supply. Therefore, it is widely adopted in laboratory-scale testing, not larger-scale testing. In the steamer design, a precise amount of liquid water per unit time is injected by a syringe pump into a superheated confined space where liquid water is instantaneously vaporized into steam; the latter is then mixed with the carrier gas in the downstream before feeding into the electrolyzer. This design is often used for bench-scale testing, where medium-scale steam flow rates are encountered (Yamada et al., 2006; Fujiwara et al., 2008). Hydrogen-burner design operates on the principle that excess hydrogen is burned in a pure oxygen environment to produce the desirable hydrogen/steam mixture for electrolysis (Hochmuth, 1978; Hauch et al., 2005; Alabbadi, 2012). By controlling the ratio of hydrogen/oxygen, different ratios of hydrogen/steam can be created. This design produces stable steam supply in precision flow rates, but requires special design of reactor (or microreactor) and additional safety considerations. Therefore, it is only suited for large-scale SOECs requiring high steam flow rates and high safety standard.

There are commercial steam generators on today's market. However, nearly all of them are designed for high steam-flow-rate applications. Direct use of these commercial steam generators in small-scale laboratory testing would compromise the accuracy of steam supply. For example, Scribner 850 stand-along humidifier has a range of 0–5 slpm with ±0.25% accuracy, which translates to ±12.5 sccm uncertainty in steam flow rate. This level of uncertainty is well within the range of steam flow rate used by laboratory-scale electrolyzers. On the other hand, studies on the design and performance of steam generators are also rather rare in the literature. The present study is aimed to develop a technical solution for laboratory-scale steam electrolyzers by conducting a comparative study of the steam generation performance between bubbler and steamer. To ensure the accuracy and responsiveness of the results, we used an online mass spectrometer (MS) to constantly monitor steam concentration variations during testing. The stability and accuracy of the obtained steam content are closely compared between bubbler and steamer. The accuracy of the steam content is also verified by Nernst equation in a practical solid oxide cell (SOC).

Experimental procedure

Bubbler and steamer setup

For this study, we have designed two steam-generators: steamer and bubbler; their actual pictures along with schematic internal structures are shown in Figure 1. Figure 1A shows the steamer system, mainly consisting of a syringe pump (SyringeONE Programmable syringe pump) controlling the DI water feed rate in the range of 0.452 μL/h (1 cc syringe) to 1,451 ml/h (60 cc syringe) and an in-house evaporator. For the evaporator, a stainless-steel tubing with a diameter of 1/8″ and a length of 25′ was wound tightly around a heating rod (Metric Cartridge Heaters, McMaster-Carr). At the end of ϕ1/8″ tubing, for the purpose of easy steam expansion, thus providing stable steam flow, another ϕ1/4″ tubing in a length of 6′ wound around another heating rod is connected. The above assembly is finally inserted along with a thermocouple into an aluminum tubing (ϕ2″) filling with ceramic fiber insulation. The two heaters are controlled by two independent Variac transformers set at 30V, which results in ~180°C. The steam line is then mixed with the carrier gas through a "T" connector and led to the analytical instrument (MS). All gas lines are wrapped with heating tape and insulation material and controlled at 120°C with a temperature controller (TC-508, VivTek Instruments).

For the bubbler system, Figure 1B, it consists of a cylindrical aluminum tank in diameter of 3″ and height of 9″ wound by a heating tape (Tubing Heaters, McMaster-Carr), and a thick layer of ceramic fiber thermal insulation. The temperature of the bubbler is provided by the heating tape and controlled by a temperature controller (TC-508, VivTek Instruments). The carrier gas is led through a tube with a fritted end (a metal sponge) into the bubbler set at a desirable temperature and expected to be saturated with the amount of steam determined by the bubbler temperature. Table 1 lists some typical vapor pressures of water vs. temperatures. To study the effect of the bubble volume and fritted bubble head on the steam concentration, we made two bubblers: one with a volume of 1.25 L without the fritted end and another one with a volume of 3.0 L with the fritted end, for comparison.

Steam content and fuel cell measurements

The steamer and the bubbler were evaluated by a mass spectrometer (MS, Pfeiffer Omnistar 100), see Figure 2. The

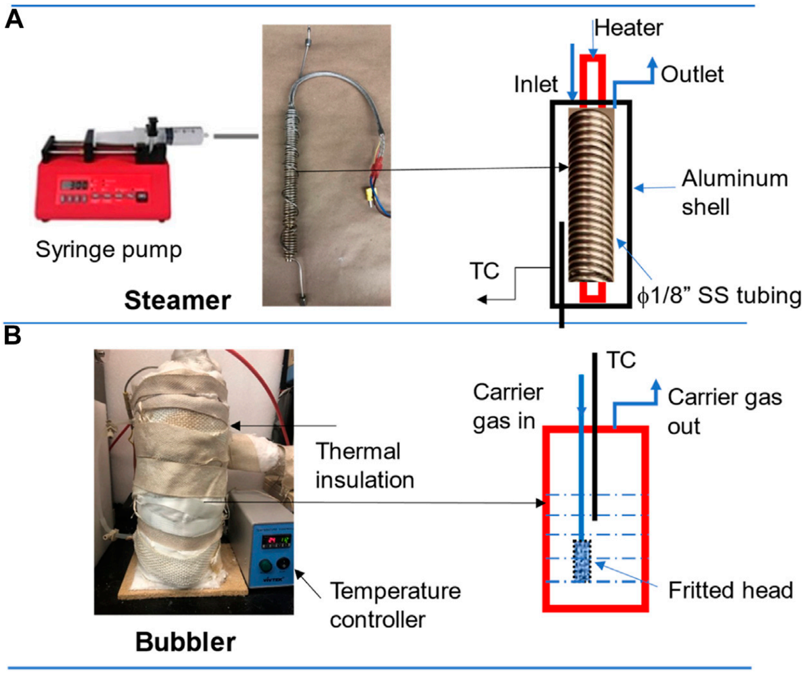

FIGURE 1
System setup of **(A)** steamer and **(B)** bubbler.

TABLE 1 Typical vapor pressure of water versus temperature (Lide, 2004).

Temperature/°C	p/kPa	Temperature/°C	p/kPa
25	3.169	73	35.448
47	10.62	76	40.205
55	15.75	79	45.487
61	20.873	82	51.342
65	25.022	86	60.119
70	31.176	90	70.117

argon with a flow rate of 60 ml/min was used as the carrier gas for the measurement and was controlled by a mass flow controller (Alicat Scientific MFC Series). For the steamer, the generated steam was mixed with the carrier gas in a buffer vessel (200 ml, maintained at 200°C) through a "T" connector, where the steam content was controlled by the feeding rate of the syringe pump. For the bubbler, the carrier gas was fed directly into the water tank and the steam content was controlled by the bubbler temperature. The mixed gas was also led into a buffer vessel (1 L volume) for a better mixing before measurement. In all the measurements, the gas pipelines after the steamer/bubbler were made of stainless-steel tubing and maintained at 120°C all the time using the heating tape and ceramic fiber thermal insulation.

To independently verify the steam content measured by the MS, we also used a SOC to measure open circuit voltage (OCV), by which it was compared with the theoretical Nernst potential using H_2/H_2O ratio measured from the MS.

The SOC used for this study is consisted of a Ni/ScSZ (Sc-stabilized ZrO_2) hydrogen electrode (HE)-supported ScSZ electrolyte cell with a GDC ($Gd_{0.1}Ce_{0.9}O_2$) barrier layer and $SrCo_{0.9}Ta_{0.1}O_{3-\delta}$ (SCT) oxygen electrode (OE). The overall testing system is shown in Figure 2. Silver wire/mesh together with gold paste were used as the current collector for OE, and Pt wire/Ni mesh with NiO paste was used as the current collector for HE. The cell was first glass sealed to an alumina tube and then heated to 700°C. The HE was first reduced by a 3% H_2O-H_2 at a flow rate of 50 ml min^{-1}. The OCV of the cell was then measured at the same H_2 flow rate but with different H_2O contents: 3, 10, 20, 30, 40 and 50% H_2O; the latter steam contents were created by either syringe-pump's push rate in the steamer design or tank temperature of the bubbler design. At each steam content, OCV was measured continuously for 24-hour to check the stability of the steam supply. We have also measured the short-term electrolysis stability of the cell under 40%H_2O-H_2 using an electrochemical workstation (Solartron 1470E/FRA1255 Multi-Channel System).

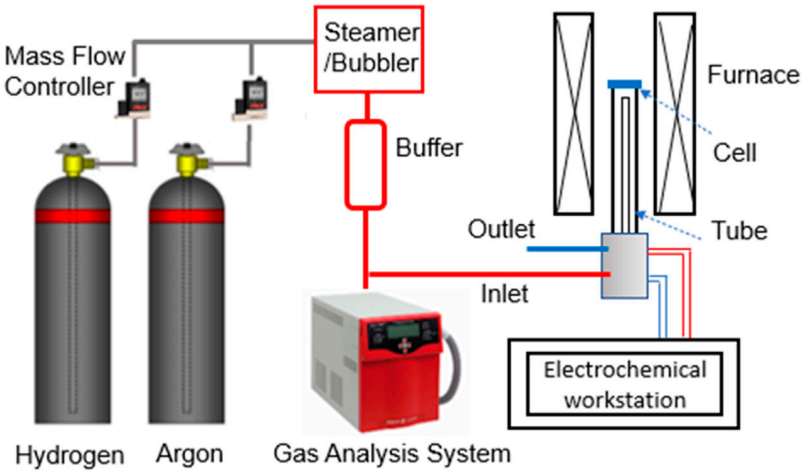

FIGURE 2
System setup for steam content and fuel cell measurement.

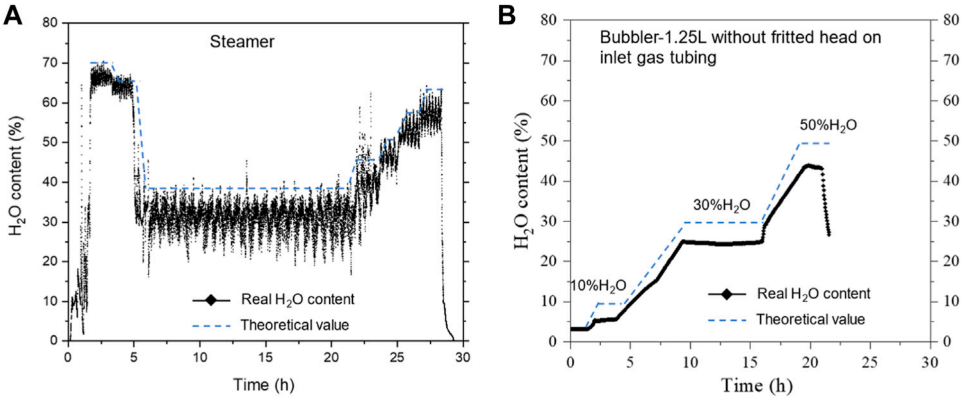

FIGURE 3
Comparison of steam contents from the homemade **(A)** steamer and **(B)** bubbler. Carrier gas flow rate: 60 sccm Ar.

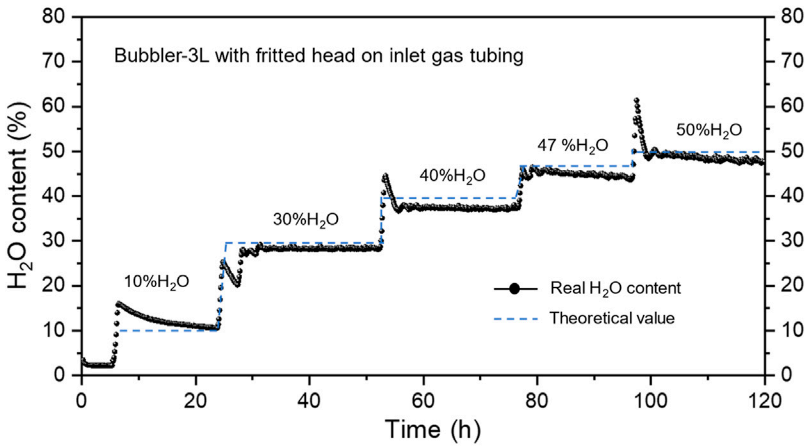

FIGURE 4
Steam content at different temperatures of a 3 L bubbler with fritted head of gas inlet tubing. Carrier gas flow rate: 60 sccm Ar.

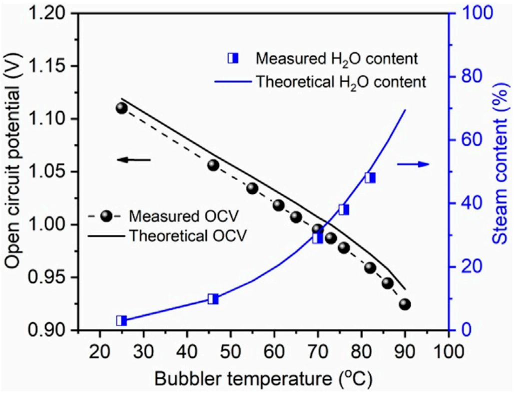

FIGURE 5
Comparison of OCV and steam content between measured and calculated values.

Results and discussion

Comparison of steam contents by different steam generating devices

We first measured and compared the steam contents vs. device temperature for in-house steamer and Bubbler-1.25 L with an inlet gas tubing without fritted end; Figure 3 shows the results. For the steamer, oscillations occurred throughout the measurements at all H_2O contents studied. We believe that it was due to the noncontinuous (stepwise) water feed by the syringe pump, particularly at low feed rate (low steam content). This explanation is supported by the fact that at a higher steam content (higher feed rate), the oscillations become less pronounced. Therefore, it is reasonable to predict that a better precision pump will produce more stable steam flow. Nevertheless, the average steam content for the steam seems to match with the desired value. On the other hand, a longer tube may also help provide steam stability. For Bubbler-1.25 L without inlet gas tubing fritted head, the steam content is stable during the test and no fluctuation was observed. However, roughly 5~8% lower steam content than the set values is consistently observed. We believe this is likely due to the insufficient mixing of carrier gas and the steam caused by un-fritted inlet gas tubing head.

Based on the above observation, we then changed the bubbler by increasing the total volume of the bubble from 1.25 to 3.0 L and added a fritted head to the inlet gas tubing. The testing results are shown in Figure 4. It is clear that the steam content is stable at all levels during the test; no sign of oscillations is seen. Moreover, the difference of H_2O content between the set and measured values is within 0~2%,

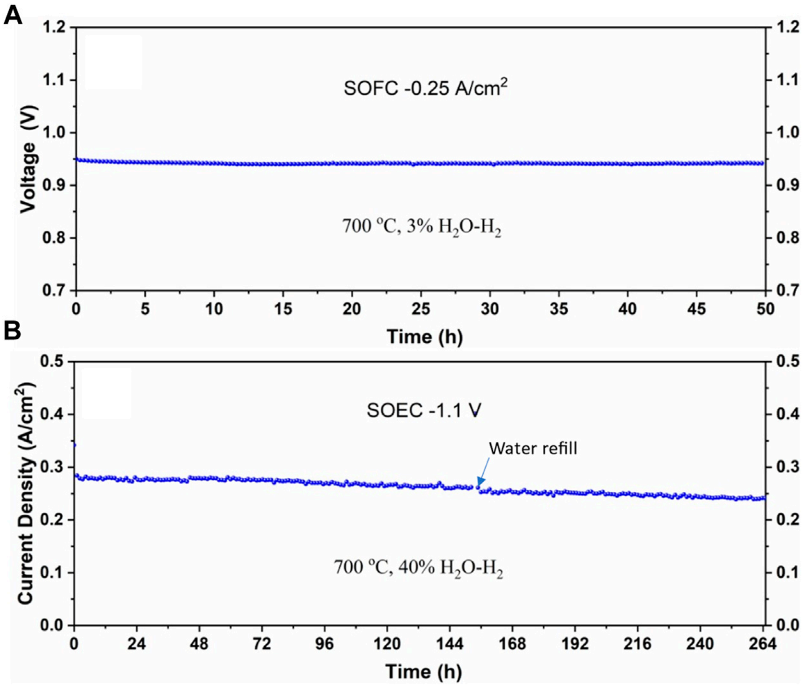

FIGURE 6
The stability of the cell under **(A)** low-steam SOFC and **(B)** high-steam SOEC modes at 700°C.

TABLE 2 Steam generators anomalies and corresponding correction actions.

Steam generator	Observed anomaly	Correction step
Bubbler	H_2O content lower than the set value	• Use fritted head in inlet gas tubing • Increasing bubbler volume
	H_2O content oscillations	• Check heat tracing line temperature, especially at corner locations • Increase the line temperature to above 120°C if needed
Steamer/syringe pump	H_2O content oscillations	• Increase total carrier gas flow rate to allow higher steam flow rate • Verify operation using syringes with different diameters (larger/smaller) to rule out pulsation from pump motor stop/start • Use a high precision pump
	H_2O content lower than the set value	• Calibrate the water feed rate of the pump

demonstrating the improvement by the change of bubbler volume and inlet tubing. On the other hand, it is found that the steam content tends to drift with time, particularly at higher steam contents. This can be attributed to the partial steam condensation somewhere such as dead corners inside the bubbler as well as gradually lowered water level inside the bubbler. Thus, a larger volume is always preferrable for the bubbler to operate longer time without interruption such as water refill. In addition, the steam content variations at each temperature transition are likely caused by the bubbler temperature variations, which can be mitigated by re-tuning the temperature controller.

Tesing bubbler performance in a solid oxide cell

To further verify the accuracy of the steam content generated by the 3.0 L bubbler, we used a solid oxide cell and measured its OCV as a function of H_2/H_2O ratio. From the measured steam contents, we first used Nernst equation to calculate the theoretical OCV; the comparison between the measured and calculated ones is shown in Figure 5. It is evident that the two data sets are reasonably close. Alternately, we also used the measured OCV to back calculate the steam content. Figure 5 again shows excellent agreement between the two. We, therefore, conclude that the bubbler is suited for providing accurate steam content for laboratory-scale solid oxide cell testing.

To demonstrate the steam stability in real cells, we tested SOFC operation at a low steam content for 50 h and SOEC operation at a high steam content for 264 h at 700°C; the results are shown in Figure 6. Evidently, there is no oscillation in either case, further proving the suitability of the bubbler we have designed for the laboratory-scale testing.

Throughout this study, we have gained some experience on designing and testing bubblers and steamers. Here we would like to share our candidate views on how to correct common abnormalities of steam generators; they are summarized in Table 2.

Conclusion

In summary, we have demonstrated in this study that bubbler can provide a more stable steam supply than steamer at low steam flow rates, exhibiting less oscillations and accurate steam content up to 50% H_2O. The main reason for the unstable steam generation by the steamer is likely due to the noncontinuous or stepwise water feed by the syringe pump, particularly at low water feed rates. At higher steam concentrations (or water feed rates), particularly at >60% H_2O, where the accuracy of water feed of the pump is improved, steamer design may be better suited than bubbler. However, the energy consumption of steamers might be higher than bubblers since the former requires more energy to produce superheated steam (e.g., >150°C) than heating bubbler at less than 100°C. We also recommend the use of fritted inlet gas tubing to maximize the steam saturation of the carrier gas and larger volume to avoid interruptions by the frequent water refilling. Overall, bubbler is a better choice for laboratory-scale SOEC testing when low steam flow rates are encountered.

Data availability statement

The raw data supporting the conclusion of this article will be made available by the authors, without undue reservation.

Author contributions

YZ: Conducting experiments NX: Steamer setup QT: MS setup WG: design and results discussion KH: Supervision and manuscript writing.

Acknowledgments

This material is based upon work supported by the U.S. Department of Energy's Office of Energy Efficiency and Renewable Energy (EERE) under the Fuel Cell Technologies Office (FCTO) under Award Number DE-EE-0008842. We would also like to thank National Science Foundation for the financial support under award number 1801284.

Conflict of interest

The authors declare that the research was conducted in the absence of any commercial or financial relationships that could be construed as a potential conflict of interest.

Publisher's note

References

Alabbadi, S. A. (2012). Hydrogen oxygen steam generator integrating with renewable energy resource for electricity generation. *Energy Procedia* 29, 12–20. doi:10.1016/j.egypro.2012.09.003

Buttler, A., and Spliethoff, H. (2018). Current status of water electrolysis for energy storage, grid balancing and sector coupling via power-to-gas and power-to-liquids: A review. *Renew. Sustain. Energy Rev.* 82, 2440–2454. doi:10.1016/j.rser.2017.09.003

Carmo, M., Fritz, D. L., Mergel, J., and Stolten, D. (2013). A comprehensive review on PEM water electrolysis. *Int. J. hydrogen energy* 38, 4901–4934. doi:10.1016/j.ijhydene.2013.01.151

Fujiwara, S., Kasai, S., Yamauchi, H., Yamada, K., Makino, S., Matsunaga, K., et al. (2008). Hydrogen production by high temperature electrolysis with nuclear reactor. *Prog. Nucl. Energy* 50, 422–426. doi:10.1016/j.pnucene.2007.11.025

Glenk, G., and Reichelstein, S. (2019). Economics of converting renewable power to hydrogen. *Nat. Energy* 4, 216–222. doi:10.1038/s41560-019-0326-1

Hauch, A., Jensen, S., Menon, M., and Mogensen, M. (2005). "Stability of solid oxide electrolyser cells," in *Risø international energy conference*, 23–25.

Hauch, A., Küngas, R., Blennow, P., Hansen, A. B., Hansen, J. B., Mathiesen, B. V., et al. (2020). Recent advances in solid oxide cell technology for electrolysis. *Science* 370, eaba6118. doi:10.1126/science.aba6118

Hochmuth, F. W. (1978). *Burning hydrogen and oxygen to superheat steam*. Hudson, Canada: Google Patents.

Kim-Lohsoontorn, P., and Bae, J. (2011). Electrochemical performance of solid oxide electrolysis cell electrodes under high-temperature coelectrolysis of steam and carbon dioxide. *J. Power Sources* 196, 7161–7168. doi:10.1016/j.jpowsour.2010.09.018

Lide, D. R. (2004). *CRC handbook of chemistry and physics*. Boca Raton, FL: CRC Press.

O'Brien, J. E., Stoots, C. M., Herring, J. S., and Hartvigsen, J. J. (2007). Performance of planar high-temperature electrolysis stacks for hydrogen production from nuclear energy. *Nucl. Technol.* 158, 118–131. doi:10.13182/nt07-a3830

Schefold, J., Brisse, A., and Poepke, H. (2017). 23, 000 h steam electrolysis with an electrolyte supported solid oxide cell. *Int. J. Hydrogen Energy* 42, 13415–13426. doi:10.1016/j.ijhydene.2017.01.072

Shen, F., Welander, M. M., and Tucker, M. C. (2022). Metal-supported solid oxide electrolysis cell test standard operating procedure. *Front. Energy Res.* 10, 500. doi:10.3389/fenrg.2022.817981

Staffell, I., Scamman, D., Abad, A. V., Balcombe, P., Dodds, P. E., Ekins, P., et al. (2019). The role of hydrogen and fuel cells in the global energy system. *Energy Environ. Sci.* 12, 463–491. doi:10.1039/c8ee01157e

Vincent, I., and Bessarabov, D. (2018). Low cost hydrogen production by anion exchange membrane electrolysis: A review. *Renew. Sustain. Energy Rev.* 81, 1690–1704. doi:10.1016/j.rser.2017.05.258

Yamada, K., Makino, S., Ono, K., Matsunaga, K., Yoshino, M., Ogawa, T., et al. (2006). *High temperature electrolysis for hydrogen production using solid oxide electrolyte tubular cells assembly unit*. San Francisco, CA: AIChE Annual Meeting.

Zeng, K., and Zhang, D. (2010). Recent progress in alkaline water electrolysis for hydrogen production and applications. *Prog. Energy Combust. Sci.* 36, 307–326. doi:10.1016/j.pecs.2009.11.002

Zhang, X., O'Brien, J. E., O'Brien, R. C., Hartvigsen, J. J., Tao, G., and Housley, G. K. (2013). Improved durability of SOEC stacks for high temperature electrolysis. *Int. J. Hydrogen Energy* 38, 20–28. doi:10.1016/j.ijhydene.2012.09.176

Zhang, Y., Xu, N., Tang, Q., and Huang, K. (2022). Intermediate temperature solid oxide cell with a barrier layer free oxygen electrode and phase inversion derived hydrogen electrode. *J. Electrochem. Soc.* 169, 034516. doi:10.1149/1945-7111/ac565a

frontiers | Frontiers in Energy Research

METHODS
published: 09 September 2022
doi: 10.3389/fenrg.2022.857663

Rotating Disk Electrode Standardization and Best Practices in Acidic Oxygen Evolution for Low-Temperature Electrolysis

***Shaun M. Alia*[1]* and *Nemanja Danilovic*[2]**

[1]Chemistry and Nanoscience Center, National Renewable Energy Laboratory, Golden, CO, United States, [2]Lawrence Berkeley National Laboratory, Energy Storage and Distributed Resources Division, Berkeley, CA, United States

Efforts in oxygen evolution catalyst development have significantly increased and often use rotating disk electrode half-cells to evaluate intrinsic kinetics and screen materials for short-term durability. Standardizing rotating disk electrode test protocols is critical to experimental accuracy, to realistically assess their potential impact at a device level and to assess how different catalyst approaches and concepts are prioritized. The goal of this study is to provide standardized test protocols and suggest best practices to help reduce variability in *ex situ* materials characterization in the broader community. Specifically, these protocols focus on test cleanliness and materials choices, including how electrodes are prepared and tested, and the impact on activity observations.

Keywords: electrolysis, rotating disk electrode, oxygen evolution, catalysis, acidic systems

Edited by:
Roel Van de Krol,
Helmholtz Association of German Research Centers (HZ), Germany

Reviewed by:
Diogo M. F. Santos,
University of Lisbon, Portugal
Branimir Nikola Grgur,
University of Belgrade, Serbia

****Correspondence:***
Shaun M. Alia
shaun.alia@nrel.gov

Specialty section:
This article was submitted to Process and Energy Systems Engineering,
a section of the journal Frontiers in Energy Research

Received: *18 January 2022*
Accepted: *18 April 2022*
Published: *09 September 2022*

Citation:
Alia SM and Danilovic N (2022) Rotating Disk Electrode Standardization and Best Practices in Acidic Oxygen Evolution for Low-Temperature Electrolysis. Front. Energy Res. 10:857663. doi: 10.3389/fenrg.2022.857663

1 INTRODUCTION

While hydrogen historically has had a limited market in energy storage and conversion, electricity cost reductions have enabled growth opportunities. Further cost reductions in electrochemical water splitting, however, are needed to be cost-competitive with other technologies. While advanced manufacturing accounts for a large portion of that reduction, catalyst development has been extensively pursued to address iridium scarcity and the performance, durability, and cost of proton exchange membrane-based systems (Pivovar et al., 2018; Ayers et al., 2019; IRENA, 2020; Alia, 2021).

Most catalyst development efforts use rotating disk electrode (RDE) testing to focus on intrinsic capabilities and to avoid the complications of materials integration and cell-level testing. There is wide variability, however, in RDE baseline activity (several orders of magnitude) and stability metrics that complicate catalyst development (Alia and Anderson, 2019). This article provides standardized protocols and best practices for screening acidic oxygen evolution (OER) materials in RDE, discusses sources for discrepancies, and provides troubleshooting recommendations. This effort focuses on the impact of electrode coating and test choices on activity/stability evaluations and leverages previous studies in RDE activity/stability testing (Alia et al., 2016a; Yu et al., 2018; Alia and Anderson, 2019; Rakousky et al., 2019), surface area quantification (Zhao et al., 2015; Alia et al., 2016b), and cell-level testing comparisons (Alia et al., 2019).

2 PROTOCOL SCOPE

2.1 Scope and Applicability

This protocol standardizes RDE testing for OER catalysts intended for use in proton exchange membrane-based electrolyzers. It includes procedures related to activity, stability, and surface area determinations for acidic OER catalysts.

2.2 Summary of Method

The protocol describes the preparation and execution of RDE experiments as follows:

- Preparation of the catalyst ink.
- Coating the catalyst film onto an electrode.
- Setup of the electrochemical cell and its components.
- Execution of RDE tests.

2.3 Personnel Qualifications/ Responsibilities

- All personnel should be trained to handle chemicals and mitigate chemical hazards.

2.4 Health and Safety Warming

- Chemical Hazards–This test protocol uses concentrated acids for the preparation of the electrolyte and the cleaning of the glassware. Follow SDS safety precautions when handling concentrated perchloric acid or sulfuric acid solutions. All concentrated acids should be handled in a fume hood. Standard personal protective equipment, including safety glasses and gloves (acid-compatible), must be worn. Ensure that gas cylinders are properly secured and regulated.
- Rotation Hazard–The RDE working shaft rotates during testing.

2.5 Equipment and Supplies

- Personal Protective Equipment
  - Safety glasses
  - Gloves
  - Lab coat
- Glassware
  - Beakers, volumetric flask (50 ml, 1 L)
  - 20-ml vials
  - RDE electrochemical cell
  - Optional: Luggin capillary, counter bridge/junction
- Equipment
  - Electrode rotator (Pine Research: AFMSRCE)
  - RDE tip (Pine Research: AFE5TQ050)
  - RDE working electrode—gold disk (Pine Research: AFED050P040AU)
  - Reference electrode (reversible hydrogen preferred)
  - Wire and mesh counter electrode (gold preferred)
  - Bath, horn sonicator
- Chemicals
  - Perchloric acid (70%, Veritas® Double Distilled, GFS Chemicals: 230)
  - Sulfuric acid
  - Inert gas, nitrogen, or argon
  - Deionized water (Milli-Q Millipore quality minimum standard)
  - Isopropanol (certified ACS)
  - Nafion® dispersion, 1100 EW at 5 wt%
  - Iridium oxide (Alfa Aesar 43396)
  - ALNOCHROMIX™ solution (Alconox Inc.)

2.5.1 Nomenclature and Definitions

- RDE: rotating disk electrode
- OER: oxygen evolution reaction

2.6 Recommended Reading

- S.M. Alia, G.C. Anderson, *Journal of The Electrochemical Society*, 166, F282 (2019).

3 PROCEDURE

3.1 Step-by-Step Procedure

- Preparing, polishing, and assembling the RDE Tip. Fixed gold working electrodes are preferred.
  1. For standard cleaning, affix a microfiber polishing cloth to a polisher or a flat, stationary surface. Place a small amount of 0.05 μm polishing slurry onto the microfiber cloth. In a figure-8 pattern, polish the gold disk for about 4 min. Rinse the disk thoroughly with deionized water when polishing is completed. Sonicate in deionized water for 3 × 3 minutes, replacing the deionized water between each step to ensure the removal of leftover alumina polishing paste.
  2. Repeatedly wipe electrode surface with a water-soaked Kimwipe, followed by a 2-propanol, then water-soaked Kimwipe.
- Preparation and application of the catalyst ink
  1. Using a small, clean spatula, measure 3.5 mg of iridium oxide into a clean the vial. Cap the vial to prevent contamination.
  2. Using a pipette, dispense a total of 7.6 ml of deionized water into the vial. After replacing the tip, use the pipette to dispense a total of 2.4 ml of 2-propanol into the vial.
  3. Ice ink for 5 min before adding ionomer. Use a clean 10–100 μl micropipette to dispense 20 μl of Nafion® dispersion (1100 EW at 5 wt%) into the catalyst ink. Tightly cap the vial. NOTE: Depending on the type of material, the Nafion content may have to be altered for optimal activity.
  4. Sonicate the ink for 20 min. Validate dispersion of the ink by observing if there is catalyst settling. One example protocol is the following:
     - Sonicate the catalyst ink for 30 s in a horn sonicator, followed by 20 min in a bath sonicator.

    - NOTE: Use an ice bath to prevent heating of the ink. Not icing the ink can have a significant impact on the dispersion quality, how the ink dries, and the resulting activity (Alia and Anderson, 2019).
  5. Place the RDE tip and rod into the rotator upside down so that the ink can be drop cast on the RDE tip.
  6. Once sonicated, use the micropipette to dispense a 10 µl drop of catalyst ink onto the gold disk of the working electrode rotating at 100 rpm. Turn up the rotator slowly from 100 to 700 rpm. Wait until dry (20 min) before turning off the rotation.
    - NOTE: To avoid spillage anchor elbows on a stationary surface and ensure that the rotator/shaft is not damaged (rotation on-axis). The drop of catalyst ink should not contain bubbles, should dry on the surface of the gold disk, and should not contact the PTFE shroud. After drying, the coating should be uniform (without a coffee ring). If any of these issues are observed, repolish the electrode and repeat.

- Glassware cleaning. Should be used for all glassware used at any point in RDE preparation or testing.
  1. Soak all glassware in concentrated sulfuric acid, then ALNOCHROMIX™ overnight.
  2. Immerse the electrochemical cell and components (stoppers, cleaned counter electrode, cleaned reference electrode if hydrogen) in deionized water and boil the water.
  3. Remove the water, refill, and repeat the procedure 8 times.
  4. Following the conclusion of each test, store glassware in a cleaned beaker filled with deionized water. Periodically reclean beaker/cell.
- 0.1 M Perchloric Acid Electrolyte. Recommend completing in a washdown fume hood.
  1. Fill a clean 1-L volumetric flask 2/3 full with deionized water.
  2. Weigh 14.39 g of concentrated perchloric acid into a clean beaker and add the perchloric acid into the volumetric flask.
  3. Rinse the beaker that contained the perchloric acid multiple times with deionized water and pour the diluted perchloric acid into the volumetric flask until the solution is near to the 1 L mark. Slowly fill the volumetric flask to the 1 L mark.
  4. Mix the flask to ensure that the electrolyte solution is homogeneously mixed.
- RDE Cell Setup. For temperature control during testing, jacketed cells could be used if cleanliness can be maintained.
  1. Rinse the electrochemical cell at least twice with the prepared perchloric acid electrolyte.
  2. Fill the electrochemical cell with a measured volume of electrolyte solution so that the reference electrode, gas bubbler, and counter electrode are all submerged in the electrolyte solution and not in contact with each other. The working electrode should be submerged, but below the electrode/rotator junction to prevent contact corrosion, contamination, and resistance accumulation. If there are any unused ports on the electrochemical cell, cover the ports with cleaned glass. Record volume of solution for effluent analysis purposes.
  3. Assemble cell components.
    - High surface area counter electrode (mesh spot welded to wire) is preferred to minimize counter contributions to electrochemical measurements, including counter/working plating.
    - CAUTION: The high purity gold counter electrode is fragile.
    - Gold counter electrodes are preferred since upon dissolution, they will not improve OER activity or add contaminants (Alia and Pivovar, 2018).
  4. If using a non-hydrogen reference electrode, calibrate the reference. Hydrogen reference electrodes are preferred to prevent contamination and data inaccuracies due to miscalibration and potential drift during testing (Garsany et al., 2010). For non-hydrogen references, sulfates (mercurous sulfate) are preferred to chloride (silver chloride, calomel) due to individual contaminant effects.
    - Use the RDE setup (cleaned glassware, 0.1 M perchloric acid electrolyte) just prior to electrochemical testing.
    - Saturate the electrolyte with hydrogen and use a polycrystalline platinum electrode as the working.
    - Complete 10 cyclic voltammograms in the potential range −0.1–1 V versus a reversible hydrogen electrode (approximate from past calibrations) at 100 mV s^{-1}, then one cathodic linear sweep voltammogram at 10 mV s^{-1} in the same potential range.
    - Use the hydrogen oxidation/evolution intercept as the reference to hydrogen calibration.
  5. Connect an inert gas (nitrogen/argon) cylinder with the gas bubbler. Slowly increase the regulator pressure from the cylinder until gas begins bubbling in the electrochemical cell. The gas should purge through the electrochemical cell for at least 15 min prior to beginning electrochemical measurements. A bubbler/scrubber is also preferred to remove line contaminants prior to the gas entering the electrochemical cell.
  6. Using the potentiostat, attach the appropriate cables to the working electrode port, reference electrode, and counter electrode.
- Electrochemical Testing. Electrochemical measurements may begin once the electrochemical cell has been purged with inert gas, the RDE components are immersed in the electrolyte, and the potentiostat is on and connected to the RDE setup.
  1. OER activity measurements
    - If potentiostat allows, immerse the RDE working electrode at 1.2 V (vs. RHE). Otherwise, immerse under closed or open circuit voltage conditions.
    - Condition for 50 cycles, 1.2–1.8 V vs. RHE at 100 mV s^{-1} and 2,500 rpm.
    - Remove the working electrode, rinse with water, and allow to dry to remove bubbles that formed on the electrode surface or within the catalyst layer. Re-immerse the working electrode into the electrolyte for the activity evaluation.

- Reduce the scan rate to 20 mV s^{-1} to collect activity data. Scan from 1.2 to a variable upper potential limit.
- NOTE: It is preferable to correct for internal resistance (current interrupt) in the program file and not during data analysis to minimize inaccuracies. The upper potential can vary, and the intent is to balance the current range (fixed when correcting for internal resistance) and to capture the entire kinetic region (moderate current range) while minimizing noise (low current range). The potential of comparison (1.5–2 V) may also need to change based on catalyst loading and intrinsic activity. Tafel plots should be consulted to ensure that activities were compared at a potential where the observed current was within the kinetic region and not biased by capacitance or transport.

2. Cyclic voltammogram measurements.
   - Potential cycle 0–1.5 V vs. RHE at 100 mV s^{-1} for five cycles or until the current response becomes stable. Limit excessive cycling at the low potential to minimize the impact of near-surface reduction on OER activity/stability.
   - Record voltammograms 0–1.5 V vs. RHE at 20 mV s^{-1} and 10 mV s^{-1} for three cycles.
   - Complete surface area determinations if equipment and safety considerations allow (Zhao et al., 2015; Alia et al., 2016b).
3. Stability testing. The purpose of this test is to assess the short-term stability of the electrocatalyst (test results should not be used to predict long-term durability). Rotate the working electrode at 2,500 rpm, or the highest rotation speed allowed to limit the impact of transport.
   - Stability testing is marginally relevant for device-level testing. Longer-term testing at high potential is preferred if inferring electrolysis-relevant durability. Test the stability of the catalyst at 2 V vs. RHE for 13.5 h (Alia and Anderson, 2019).
   - NOTE: Longer durations and high potentials are preferred in RDE durability testing. If these conditions (2 V for 13.5 h) cannot be completed due to poor catalyst stability, short-term stability testing (example 1.55 V for 1 h) can be used to assess whether a catalyst is suitable for device-level performance testing.
   - Following the conclusion of the stability test, withdraw the RDE working electrode, rinse it with water, and allow it to dry to remove bubbles that formed on the electrode surface or within the catalyst layer. Pipette 10 ml of the solution into a centrifuge tube for analysis with inductively coupled plasma mass spectrometry (ICP-MS). Replicates and repeated tests are encouraged.
   - Discard electrolyte, rinse electrochemical cell (water, then fresh perchloric acid electrolyte), and fill with perchloric acid electrolyte. Re-immerse the working electrode into the electrolyte for the activity evaluation and cyclic voltammograms after the stability test (repeat procedures in steps 1 and 2).
   - NOTE: For catalyst stability, report dissolution data (ICP-MS) and OER activity following the potential hold. It is not preferable to report the raw current decrease during the potential hold due to the significant impact of transport on electrode activity over time, which is not a relevant loss mechanism. Potential holds are preferred for stability tests, since potential drives catalyst dissolution; RDE current holds can result in large differences in potential exposure that narrow in device-level testing (catalyst integration and site access differences, use of a membrane); RDE transport losses can increase potential and catalyst dissolution in a way that is not device relevant; and at particularly low current density, RDE may not be reflective of device-level operation or catalyst layer stresses (Alia et al., 2019; Alia, 2021; Alia et al., 2021).

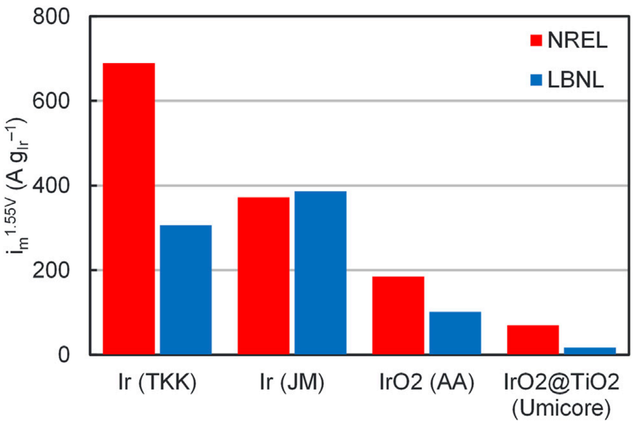

FIGURE 1 | Catalyst OER mass activities at 1.55 V for NREL (red) and LBNL (blue), comparing TKK, JM, AA, Umicore catalysts. Data adapted from (Alia et al., 2016a; Alia and Anderson, 2019).

3.2 Sample Handling and Preservation

- If significant time passes between the working electrode coating drying and the start of testing, cover the working electrode to ensure that nothing touches the thin film prior to or during testing.
- If there is a brief amount of time between the drying of the film and the start of the testing, place a small drop of deionized water or electrolyte solution on the thin film to prevent contamination from the air.
- If there are any open ports to the electrochemical cell, cover with a cleaned, glass stopper. Ensure that the electrolyte does not touch any foreign material.
- Following the conclusion of each test, ensure that all glassware is stored in a cleaned glass beaker filled with deionized water. Cover the beaker with a cleaned watch glass to prevent contamination and limit evaporation. The beaker and cell must be recleaned periodically.
- When checking for the presence of catalyst material in the electrolyte (catalyst degradation), stir the electrolyte to ensure mixing, then carefully pour or pipette 10 ml of the

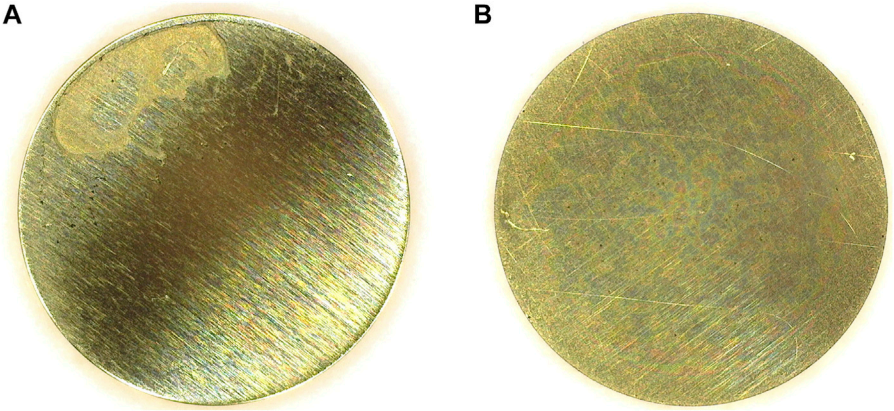

FIGURE 2 | Working electrodes coated with AA iridium to a loading of 17.8 μg_{Ir} cm^{-2}, **(A)** without and **(B)** with electrode rotation (Alia and Anderson, 2019). © The Electrochemical Society. Reproduced by permission of IOP Publishing. All rights reserved.

solution into an aliquoting vessel for ICP-MS. Record the volume/mass of cells with and without electrolytes at the starting point of the test.

3.3 Computer Hardware and Software

- The potentiostat software will be required to perform the electrochemical tests and may be able to assist in data analysis. This software may be hardware specific and not standardized for this protocol.

4 RESULTS

Comparisons of OER activities between NREL and LBNL are included in **Figure 1**. This comparison was completed on four different catalysts–iridium from Tanaka Kikinzoku Kogyo (TKK, product number US171109), iridium from Johnson Matthey (JM, product number C2026/160000), iridium oxide from Alfa Aesar (AA, product number 43396), and iridium oxide supported on titania from Umicore (0821/01-D5). While similar activities were found at 1.55 V vs. RHE for JM iridium, significant differences were observed for the other catalysts (2.3x TKK, 1.8x AA, 4.2x Umicore) and continued efforts are needed to close these gaps. These differences, however, tend to be smaller than for the broader community (Alia and Anderson, 2019).

Several differences in material, ink, and test conditions were noted that may have contributed to activity differences. First, the catalyst tested by NREL/LBNL were from different batches/lot numbers, and time elapsed between when these materials were purchased. Catalyst differences over time and between batches can have a significant effect on activity and have been observed in several instances. For the TKK catalyst, the higher NREL activity may have been due to higher metal content and a more complete oxide was generally found in later batches (Alia and Anderson, 2019). Second, differences in how electrodes were cleaned and coated were found. This included electrode polishing (automated polisher/manual), ink icing (iced/not), and sonication (bath/horn and duration). Third, differences were also found in how electrodes were tested, including the experimental setup (cell design, glassware manufacturer and purity, hydrogen/chloride reference electrode, Luggin capillary) and whether or not working electrodes were rinsed and dried between conditioning and activity testing to minimize transport concerns.

Specific considerations and concerns are also included to address potential deviations that focus on the electrode coating process and test methodology. A demonstration of a preferred and not preferred working electrode coating is included in **Figure 2**, after having been coated with AA iridium to loading of 17.8 μg_{Ir} cm^{-2}. In this particular instance, differences were based on whether the electrode was rotated during the coating/drying process. In general, however, significant ink or coating inadequacies tend to present visually on the working electrode surface. For the ink, these nonidealities include low ionomer content, unoptimized solvent ratios, less sonication, not thoroughly iced inks, and catalyst settling; for coating, these include coating/drying without rotation and electrodes that have been roughened or inadequately resurfaced.

In activity determinations, chronoamperometry and voltammograms can be valid provided that the comparisons are made in the kinetic region. Voltammograms include the capacitive region and force the user to make evaluations at moderate potential/current density to avoid the capacitance or incorporate capacitance in kinetic comparisons. Chronoamperometry experiments remove the capacitive region, but also dramatically increase transport losses at moderate potential/current density due to the increased experiment duration allowing for higher gas generation rates (**Figure 3**) (Alia and Anderson, 2019). The increase in transport loss lowers the potential window for kinetic comparisons and puts higher-performing catalysts at a disadvantage due to the higher gas generation rate. Chronoamperometry experiments thereby force the user to make evaluations at low potential/current density to avoid or minimize transport. Linear sweep voltammograms at 20 mV s^{-1} are preferred to avoid capacitance (faster scan rates), avoid transport (slower scan rates, chronoamperometry), and expand the kinetically-valid

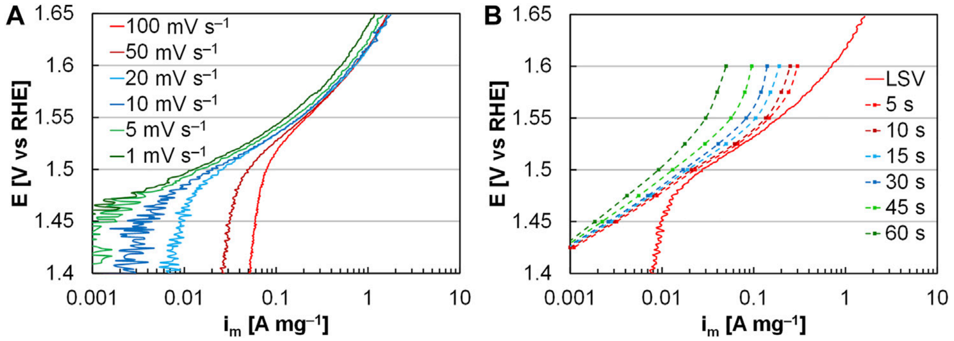

FIGURE 3 | (A) Linear sweep voltammograms at varying scan rates. **(B)** Successive chronoamperometry tests, varied by duration, compared to a linear sweep voltammogram at 20 mV s^{-1}. Electrodes were coated with AA iridium to a loading of 17.8 μg_{Ir} cm^{-2} (Alia and Anderson, 2019). © The Electrochemical Society. Reproduced by permission of IOP Publishing. All rights reserved.

potential window to moderate current density (measurement accuracy).

5 QUALITY CONTROL AND QUALITY ASSURANCE

5.1 Instrument or Method Calibration and Standardization

Two aspects of RDE testing require calibration and standardization: the electrochemical test setup, including glassware cleanliness, and electrode choice and placement; working electrode preparation, including the catalyst evaluated, electrode/substrate polishing, ink formulation, and electrode coating. These aspects can be verified and standardized through:

- Verify cell cleanliness with activity evaluations of a polycrystalline iridium disk (OER) or a polycrystalline platinum disk (oxygen reduction) (Shinozaki et al., 2015; Alia et al., 2016a). Verifying activity is preferred due to the higher sensitivity over evaluating cyclic voltammograms for specific adsorbates.
- Verify catalyst, ink, and coating process with evaluations of baseline materials (Alia and Anderson, 2019).

5.2 Cautions

Contamination is a significant source of activity error. Ensure that all cleaning procedures have been followed prior to testing.

5.3 Common Issues

Cleanliness, and the degree to which it is required, is a common issue in suboptimal performance. Cleaning procedures (acid exposure, water boiling) is needed for not only the electrochemical cell but anything that comes into contact with it. This includes other cell components (stoppers, counter electrode), glassware used for storage and to prepare the electrolyte, and glassware used for inks. Care should be taken to not introduce contaminants through contact (skin, countertop), storage, or working electrode polishing.

5.4 Interferences

There is a potential for signal noise to interfere with the electrochemical measurements. Grounding and proper current ranges need to be used to minimize signal noise.

5.5 Troubleshooting

Differences in the setup orientation, cleanliness, ink optimization, and test parameters can all impact activity values and published baselines can be used as comparison points (Alia et al., 2016a; Yu et al., 2018; Alia and Anderson, 2019; Rakousky et al., 2019). Testing of both nanoparticle catalysts and a polycrystalline iridium disk can be used to troubleshoot sub-optimal activity and the source of deficiencies. The disproportionately lower polycrystalline activity would suggest issues with cleaning protocols; disproportionately lower nanoparticle activity would suggest issues with catalyst ink or working electrode coating.

5.6 Error Analysis

Error analysis is critical in separating causes of suboptimal activity. Use a polycrystalline iridium electrode to separate errors due to the cell setup (cleanliness and configuration) and the catalyst/working electrode fabrication process.

6 DISCUSSION

Materials and test choices are critical in minimizing differences in baseline activity.

In materials choices, the electrodes and their composition have impact on activity observations. While non-hydrogen reference electrodes are a cost-effective solution, the inaccuracy makes standardization more difficult. While the use of platinum hydrogen evolution/oxidation can minimize those inaccuracies (compared to a multimeter), regular calibration is needed as the value drifts (typically a few millivolts per day) and before/after each electrode set is preferred. The use of non-hydrogen references may also introduce contaminants (chloride, sulfate), and more frequent cell cleaning is needed to minimize the impact. Gold is also typically used as the working electrode substrate and the counter electrode, to improve stability at high potential (working) while minimizing contaminant effects (carbon counter) and a plating benefit (Pourbaix, 1974; Alia and Pivovar, 2018). A gold working substrate, however, can oxidize and electronically isolate portions of the catalyst layer; dissolution can also delaminate the catalyst layer. Electrode polishing (as smooth as possible) and ink/coating process optimization are necessary to minimize substrate/electrolyte contact and substrate contributions to catalyst durability measurements, along with limiting the operating potential and avoiding internal resistance corrections (Alia and Anderson, 2019). Gold as a substrate also impacts surface area measurements, and duplicate experiments with glassy carbon electrodes may be necessary for surface area validation (Alia et al., 2016b). Although the counter electrode choice is less critical in OER due to the operating potential, gold may be necessary under circumstances where a negative current is applied to condition the working electrode (Alia and Pivovar, 2018).

In test choices, conditioning protocols vary dramatically and are often shorter or to lower potential than those presented here. Minimal to no conditioning may be necessary to preserve faceting or to minimize the impact of electrochemical testing. Longer protocols however are generally needed to marginally project device-level kinetics and should be included with statements on the far-reaching impact of a specific materials approach (Alia et al., 2019). Transport in RDE also has a significant effect on activity and stability assessments, due to the convective working electrode rotation (as opposed to a flowing electrolyte) and orientation (level, face-down). In activity testing, care needs to be taken to avoid incorporating transport into assessments and including site-level gas trapping and bulk bubble formation. When using longer conditioning protocols, electrodes need to be rinsed and dried prior to activity assessments due to the role bubble formation plays in blocking catalyst sites. In stability testing, the unprocessed performance decrease should not be reported as material stability since the RDE transport does not correspond to a relevant loss mechanism and reporting of the dissolution rate and activity after testing (with rinsing, drying) is preferred. Transport, however, still alters these measurements through bubble formation lessening site access and other experimental approaches (flow cell) may be better suited to evaluate material stability in a less qualitative way.

DATA AVAILABILITY STATEMENT

The original contributions presented in the study are included in the article/Supplementary Material, further inquiries can be directed to the corresponding author.

AUTHOR CONTRIBUTIONS

All authors listed have made a substantial, direct, and intellectual contribution to the work and approved it for publication.

FUNDING

This work was authored by the National Renewable Energy Laboratory, operated by Alliance for Sustainable Energy, LLC, for the U.S. Department of Energy (DOE) under Contract No. DE-AC36-08GO28308, and Lawrence Berkeley National Laboratory under Contract Number DE-AC02-05CH11231. Funding was provided by U.S. Department of Energy Office of Energy Efficiency and Renewable Energy, Hydrogen and Fuel Cell Technologies Office.

REFERENCES

Alia, S. M., and Anderson, G. C. (2019). Iridium Oxygen Evolution Activity and Durability Baselines in Rotating Disk Electrode Half-Cells. *J. Electrochem. Soc.* 166, F282–F294. doi:10.1149/2.0731904jes

Alia, S. M. (2021). Current Research in Low Temperature Proton Exchange Membrane-Based Electrolysis and a Necessary Shift in Focus. *Curr. Opin. Chem. Eng.* 33, 100703. doi:10.1016/j.coche.2021.100703

Alia, S. M., Ha, M.-A., Anderson, G. C., Ngo, C., Pylypenko, S., and Larsen, R. E. (2019). The Roles of Oxide Growth and Sub-surface Facets in Oxygen Evolution Activity of Iridium and its Impact on Electrolysis. *J. Electrochem. Soc.* 166, F1243–F1252. doi:10.1149/2.0771915jes

Alia, S. M., Hurst, K. E., Kocha, S. S., and Pivovar, B. S. (2016). Mercury Underpotential Deposition to Determine Iridium and Iridium Oxide Electrochemical Surface Areas. *J. Electrochem. Soc.* 163, F3051–F3056. doi:10.1149/2.0071611jes

Alia, S. M., Manco, J., Anderson, G. C., Hurst, K. E., and Capuano, C. B. (2021). The Effect of Material Properties on Oxygen Evolution Activity and Assessing Half-Cell Screening as a Predictive Tool in Electrolysis. *J. Electrochem. Soc.* 168, 104503. doi:10.1149/1945-7111/ac28c5

Alia, S. M., and Pivovar, B. S. (2018). Evaluating Hydrogen Evolution and Oxidation in Alkaline Media to Establish Baselines. *J. Electrochem. Soc.* 165, F441–F455. doi:10.1149/2.0361807jes

Alia, S. M., Rasimick, B., Ngo, C., Neyerlin, K. C., Kocha, S. S., Pylypenko, S., et al. (2016). Activity and Durability of Iridium Nanoparticles in the Oxygen Evolution Reaction. *J. Electrochem. Soc.* 163, F3105–F3112. doi:10.1149/2.0151611jes

Ayers, K., Danilovic, N., Ouimet, R., Carmo, M., Pivovar, B., and Bornstein, M. (2019). Perspectives on Low-Temperature Electrolysis and Potential for Renewable Hydrogen at Scale. *Annu. Rev. Chem. Biomol. Eng.* 10, 219–239. doi:10.1146/annurev-chembioeng-060718-030241

Garsany, Y., Baturina, O. A., Swider-Lyons, K. E., and Kocha, S. S. (2010). Experimental Methods for Quantifying the Activity of Platinum Electrocatalysts for the Oxygen Reduction Reaction. *Anal. Chem.* 82, 6321–6328. doi:10.1021/ac100306c

IRENA (2020). *Green Hydrogen Cost Reduction: Scaling up Electrolysers to Meet the 1.5°C Climate Goal*. Abu Dhabi: International Renewable Energy Agency.

Pivovar, B., Rustagi, N., and Satyapal, S. (2018). Hydrogen at Scale (H 2 @Scale): Key to a Clean, Economic, and Sustainable Energy System. *Electrochem. Soc. Interface* 27, 47–52. doi:10.1149/2.f04181if

Pourbaix, M. (1974). *Atlas of Electrochemical Equilibria in Aqueous Solutions*. Houston, Texas: National Association of Corrosion Engineers.

Rakousky, C., Shviro, M., Carmo, M., and Stolten, D. (2019). Iridium Nanoparticles for the Oxygen Evolution Reaction: Correlation of Structure and Activity of Benchmark Catalyst Systems. *Electrochimica Acta* 302, 472–477. doi:10.1016/j.electacta.2018.11.141

Shinozaki, K., Zack, J. W., Richards, R. M., Pivovar, B. S., and Kocha, S. S. (2015). Oxygen Reduction Reaction Measurements on Platinum Electrocatalysts

Utilizing Rotating Disk Electrode Technique. *J. Electrochem. Soc.* 162, F1144–F1158. doi:10.1149/2.1071509jes

Yu, H., Danilovic, N., Wang, Y., Willis, W., Poozhikunnath, A., Bonville, L., et al. (2018). Nano-size IrOx Catalyst of High Activity and Stability in PEM Water Electrolyzer with Ultra-low Iridium Loading. *Appl. Catal. B Environ.* 239, 133–146. doi:10.1016/j.apcatb.2018.07.064

Zhao, S., Yu, H., Maric, R., Danilovic, N., Capuano, C. B., Ayers, K. E., et al. (2015). Calculating the Electrochemically Active Surface Area of Iridium Oxide in Operating Proton Exchange Membrane Electrolyzers. *J. Electrochem. Soc.* 162, F1292–F1298. doi:10.1149/2.0211512jes

Author Disclaimer: The views expressed in the article do not necessarily represent the views of the DOE or the U.S. government. The U.S. government retains and the publisher, by accepting the article for publication, acknowledges that the U.S. government retains a nonexclusive, paid-up, irrevocable, worldwide license to publish or reproduce the published form of this work, or allow others to do so, for U.S. government purposes.

Conflict of Interest: The authors declare that the research was conducted in the absence of any commercial or financial relationships that could be construed as a potential conflict of interest.

Frontiers in Energy Research

TYPE Methods
PUBLISHED 14 September 2022
DOI 10.3389/fenrg.2022.1001684

EDITED BY
Abdolali K. Sadaghiani,
Sabancı University, Turkey

REVIEWED BY
Alp Yurum,
Sabancı University, Turkey
Xinjian Shi,
Henan University, China

*CORRESPONDENCE
Chengxiang Xiang,
cxx@caltech.edu

SPECIALTY SECTION
This article was submitted to Process and Energy Systems Engineering, a section of the journal Frontiers in Energy Research

RECEIVED 23 July 2022
ACCEPTED 12 August 2022
PUBLISHED 14 September 2022

CITATION
Lucas É, Han L, Sullivan I, Atwater HA and Xiang C (2022), Measurement of ion transport properties in ion exchange membranes for photoelectrochemical water splitting.
Front. Energy Res. 10:1001684.
doi: 10.3389/fenrg.2022.1001684

Measurement of ion transport properties in ion exchange membranes for photoelectrochemical water splitting

Éowyn Lucas, Lihao Han, Ian Sullivan, Harry A. Atwater and Chengxiang Xiang*

Department of Engineering and Applied Science, California Institute of Technology, Pasadena, CA, United States

Photoelectrochemical (PEC) water-splitting systems have the unique ability to produce renewable hydrogen directly from sunlight, independent of the electrical grid. These systems are therefore appealing technological options for resilient long-term energy storage. Ion selective membranes, such as monopolar and bipolar membranes, are a vital component of PEC water-splitting systems. These membranes allow for ionic conduction between the cathode and anode chambers, separation of products, and improved catalyst environments for reactions. In order to measure key properties and to study the performance of these ion exchange membranes, it is imperative to develop a robust testing protocol that can be used across the field. This paper introduces two standard electrochemical cells designed to directly measure ion transport properties in monopolar and bipolar membranes. The first electrochemical cell uses commercially available Pt disk electrodes to preform electrochemical impedance spectroscopy (EIS) and reliably measure through-plane conductivity of monopolar membranes. The second electrochemical cell uses four-point measurements with Luggin capillaries and a series of membrane configurations to perform current density-voltage and Faradaic efficiency (FE) measurements for water dissociation (WD) reactions on bipolar membranes. The cell designs and techniques laid out below allow for accurate measurement of ion transport parameters in ion exchange membranes, direct comparison of membranes being developed across the field, and in turn, greater advancements in ion exchange membranes and PEC water-splitting systems.

KEYWORDS

ion tranport, ion exchange membrane, monopolar membrane, bipolar membrane, cation exchange membrane (CEM), anion exchange membrane (AEM), photoelectrocemical (PEC), photoelectrochemical water spitting

1 Introduction

As our world shifts towards a renewable energy future, it is imperative to develop new technological solutions across many industrial sectors (i.e., energy, transportation, chemical production, etc.). One such technology is photoelectrochemical (PEC) water splitting systems, which allow for renewable production of hydrogen (H_2) using solar irradiation as the primary source of energy. Hydrogen is an important commodity chemical used for power generation, transportation, ammonia and methanol production, petroleum refining and many other industrial applications (Abergel et al., 2021). In 2020, the global demand for H_2 was 90 Mt, with approximately 80% of this hydrogen produced through the reforming of fossil fuels, a process which produces CO_2 as a byproduct and was responsible for 2.5% of global energy and industry CO_2 emissions (Abergel et al., 2021). Hydrogen is now considered to be a centerpiece for renewable fuel production and decarbonization of multiple sectors in our society, therefor, the demand for renewable hydrogen has increased rapidly in recent years. PEC water splitting systems provide a clean alternative in which renewable sunlight powers the electrochemical separation of water into H_2 and O_2 (Walter et al., 2010; Nocera, 2012; Cox et al., 2014; Xiang et al., 2016; Spitler et al., 2020; Cheng et al., 2021; Hamdani and Bhaskarwar, 2021; Segev et al., 2022). With electrolysis currently making up only 0.03% of the global H_2 production, these technologies have significant room for growth (Abergel et al., 2021).

Lowering cell voltage and improving product separation are essential elements in developing efficient, robust and safe PEC water-splitting systems. For practical deployment of large-scale PEC water-splitting systems, a robust method that can prevent diffusive and convective crossover of H_2 and O_2 is critically important to ensure the system stays below the flammability limit of 4% H_2 in O_2 mixture in a dynamic operation (Russel, 2011; Roger et al., 2017; Ardo et al., 2018). The low operating current densities of PEC water splitting systems relative to water electrolysis systems have more stringent requirements for product separations (Berger et al., 2014). Ion exchange membranes with the proper thickness and permeability can provide product separation and minimize crossovers (Haussener et al., 2012; Ardo et al., 2018; Cheng et al., 2021; Welch et al., 2021). This separation barrier, however, must be ionically conductive, as to maintain charge balance across the cell. It is also crucial to improve the efficiency and economic feasibility of PEC systems by lowering the overall cell voltage. The use of membranes in the system for product separation adds to the overall cell voltage, therefore, increasing the conductivity of these membranes is key to their development (Haussener et al., 2012; Fountaine et al., 2016; Ardo et al., 2018). As described further below, the use of ion exchange membranes can also lead to improved catalyst environments, further reducing the cell voltage and creating ideal environments for Earth abundant catalysts for both the oxygen evolution reaction (OER) and the hydrogen evolution reaction (HER) (Haussener et al., 2012; McDonald et al., 2014; Vermaas et al., 2015; Chabi et al., 2017; Oener et al., 2020, 2021; Thiele et al., 2020).

Ion exchange membranes consist of polymers containing ionizable functional groups that allow for the selective transport of cations in cation exchange membranes (CEMs) and anions in anion exchange membranes (AEMs) (Xu, 2005; Ran et al., 2017; Luo et al., 2018). Monopolar membranes (CEMs or AEMs) are used in PEC systems to carry ionic currents from one electrochemical cell chamber to another and prevent H_2 and O_2 crossovers (Haussener et al., 2012; Ardo et al., 2018; Spitler et al., 2020; Cheng et al., 2021; Welch et al., 2021). Bipolar membranes (BPM) consist of a cation exchange layer (CEL) laminated to an anion exchange layer (AEL), usually with a water dissociation (WD) catalyst at the junction between the CEL and AEL. Under reverse bias, enhanced WD due to the presence of a catalyst and a large electric field occurs at the junction between the CEL and AEL. H^+ ions then travel selectively through the CEL, while OH^- ions travel selectively through the AEL, creating separate acidic and basic streams on either side of the BPM (Xu, 2005; Ran et al., 2017; Giesbrecht and Freund, 2020). When implemented into PEC systems, BPMs allow for sustained large pH gradients (0–14) between the cathode and anode chamber. The pH of the catholyte and anolyte can therefore be independently optimized for Earth abundant catalysts for HER, which is kinetically more feasible under acidic conditions, and OER, which is kinetically more feasible under alkaline conditions (Haussener et al., 2012; McDonald et al., 2014; Vargas-Barbosa et al., 2014; Vermaas et al., 2015; Luo et al., 2016a; Vermaas and Smith, 2018; Bui et al., 2020; Giesbrecht and Freund, 2020; Oener et al., 2020, 2021; Yan and Mallouk, 2021).

For continued advancement of ion exchange membranes, it is important to develop consistent benchmarking protocols to measure ion transport properties in these CEMs, AEMs, and BPMs. We describe the development of electrochemical cells and measurement techniques that directly probe ion transport in ion exchange membranes *via* electrochemical impedance spectroscopy (EIS), current density-voltage measurements, and Faradaic efficiency (FE) measurements for WD reactions. One of the most important parameters of ion exchange membranes in PEC water-splitting applications is the through-plane conductivity (Fountaine et al., 2016; Xiang et al., 2016; Ran et al., 2017; Luo et al., 2018). To reliably measure the through-plane conductivity in these membranes, a custom cell was designed and fabricated, in which the membrane is pressed between two Pt disk electrodes and electrochemical impedance spectroscopy (EIS) was performed (Figure 1A). Although some important information can also be drawn from EIS of BPMs, (Wilhelm et al., 2001; Blommaert et al., 2019; Chen et al., 2020) the more important and fundamental parameters for understanding ion transport through a BPM and water dissociation efficiency at the BPM junction are voltage drop

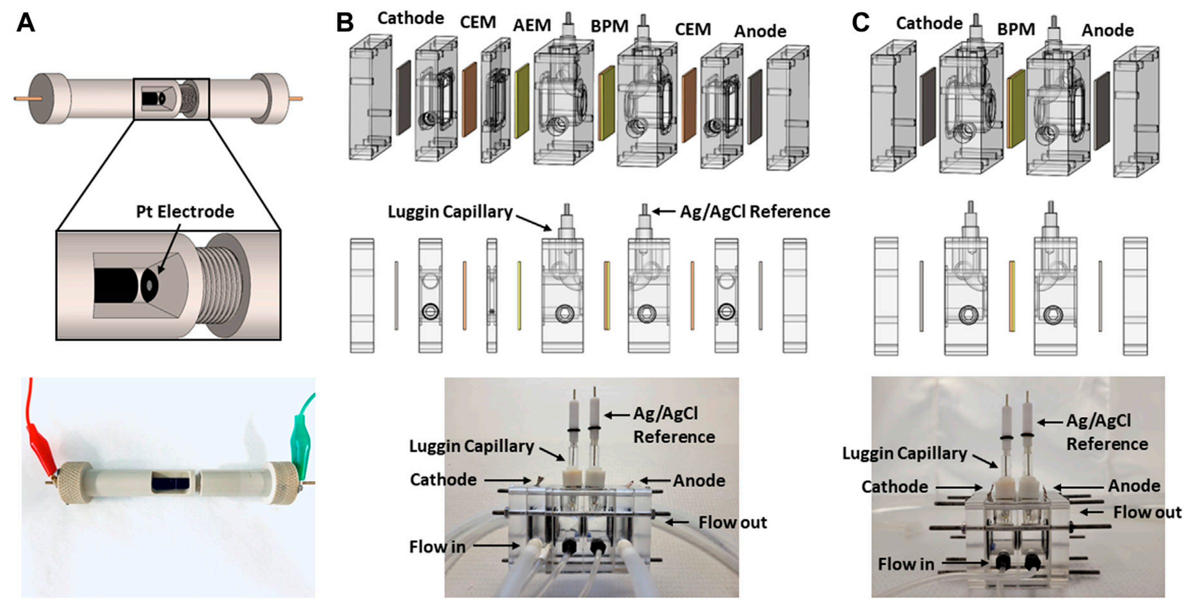

FIGURE 1
Custom cell for EIS measurements **(A)** and custom electrodialysis flow cell for testing BPMs **(B,C)**. **(B)** shows five chamber configuration and **(C)** showed two chamber configuration.

across the BPM and FE for H^+ and OH^- production (Wilhelm et al., 2002; Chabi et al., 2017; Shen et al., 2017; Vermaas and Smith, 2018; Chen et al., 2020; Blommaert et al., 2021). To most effectively measure these parameters, a custom electrodialysis flow cell with embedded Luggin capillaries was developed (Figures 1B,C). Both the EIS and the electrodialysis custom cells described in this paper are designed to overcome losses due to electrolyte resistance, which is the main limitation of many testing methods. Beyond providing a testing environment for developing a deeper understanding of ion transport in ion exchange membranes, consistently using these types of systems and following the protocols laid out in this paper will allow for the direct comparison of membranes across many devices in the PEC community and in turn further advancements in the field.

2 Procedure and methods

2.1 Step-by-step procedure

Prior to testing, all membranes are stored in a clean, dry environment to prevent warping and degradation. Once ready for testing, membranes are pretreated according to their product instructions and stored in DI water or relevant electrolyte for exchange to the desired transport ion (i.e., H^+, OH^-, Na^+, Cl^-, etc.). Pretreatment procedures depend on the type of membrane being investigated and are discussed further in Section 2.1.1. When working with ion exchange membranes it is important to note that they are delicate and easy to damage while handling. To avoid damage, handle gently and avoid contact with sharp objects. Damaged membranes can lead to invalid results due to leakage through pinholes or tears.

2.1.1 Step-by-step procedure for electrochemical impedance spectroscopy measurements of cation exchange membranes and anion exchange membranes

To measure the conductivity of CEMs and AEMs, a rapid electrochemical impedance spectroscopy (EIS) through-plane conductivity measurement and analysis technique was developed, in which two Pt disk electrodes (2 mm in diameter) were aligned with each other and pressed against the membrane materials during the measurements. A custom measurement tool (Figure 1A) was developed that allows for the controlled tightening of the Pt disk electrodes to minimize any contact resistance between the metal/membrane interface, as well as losses due to electrolyte resistance present in most electrochemical cells. Please reach out to point of contact to obtain CAD files for this custom EIS measurement cell.

In preparation for testing, CEM samples are preheated in a 70°C degree water bath for ~30 min, and soaked in the desired electrolyte (i.e., acid for H^+ conductivity measurement, or NaCl for Na^+ conductivity measurement) for at least 24 h. AEM samples are prepared in the same way and soaked in a relevant electrolyte (i.e., base for OH^- conductivity measurement, or NaCl for Cl^- conductivity measurement) for at least 24 h. The membranes are then cut into a strip large enough to completely cover the 2 mm diameter Pt electrode area when being installed in the custom cell. The pretreated and cut membrane is then installed in the slot of the cell, and the cell is tightened until the membrane contacts both Pt electrodes.

Once the membrane is loaded in the cell, the electrodes are connected to a potentiostat using two-electrode EIS measurements. A typical frequency range between 100 kHz and 1 MHz and an AC amplitude of 10 mV are applied during the EIS measurements to obtain the high frequency characteristics of the ion exchange membranes. For membrane conductivity >1 $mS{\cdot}cm^{-1}$, the high frequency response shows a linear response in the Nyquist plot (Bard and Faulkner, 2011). A Debye circuit model is used to evaluate the through-plane conductivity of the membrane (Bard and Faulkner, 2011). This method allows for rapid evaluation of ion conductivity of the synthesized membrane. The Z_{real} value is the membrane resistance (R_b) when $-Z_{imag} = 0$ ohm in the Nyquist plot figure. Conductivity can be determined from this bulk resistance using Eq. 1, where σ is conductivity, L is the distance between the contacting electrodes, and A is the area of the membrane. See results in Section 4.1 for an example of the technique and data fitting.

$$\sigma = \frac{L}{R_b A} \tag{1}$$

2.1.2 Step-by-step procedure for voltage and faradaic efficiency measurements of bipolar membranes

To benchmark BPMs by measuring voltage drop and FE for generation of H^+ and OH^- *via* WD reaction, a custom electrochemical flow cell with embedded Luggin capillaries was developed (Figures 1B,C). Please reach out to point of contact to obtain CAD files for this custom electrochemical cell. The Luggin capillaries in the cell allow for the minimization of losses due to iR drop in the electrolyte and the multiple chambers and flow system allow for direct monitoring of the pH on either side of the BPM. The five-chamber cell depicted in Figure 1B is the ideal configuration if pH and FE measurements are desired. In this configuration, since the ions in the center chamber are contained by the outer AEM and CEMs, H^+ and OH^- produced *via* WD can be directly measured using titration or a pH meter. These calculations are discussed later in the paper. In the two-chamber configuration, depicted in Figure 1C, for every H^+/OH^- made from WD, an H^+/OH^- is consumed at its respective electrode. Therefore, although direct measurements of co-ion crossover such as ICP analysis can be performed (Luo et al., 2016b), this configuration is not ideal for measuring pH and FE. This two-chamber configuration, however, is designed for maintaining a steady-state pH differential between the catholyte and anolyte, therefore, studying how HER and OER perform with specific catalysts in acidic and basic environments, respectively (Sun et al., 2016; Zhou et al., 2016).

As with monopolar membranes, bipolar membranes are pretreated for best results when testing. For the case of BPMs, the CEM and AEM are pretreated before constructing the full membrane. CEMs and AEMs are pretreated as described in Section 2.1.1. Fully constructed BPMs are stored in DI water or relevant electrolyte. These pretreated and wetted BPMs are then ready for testing in the custom electrodialysis cell.

The electrodialysis cell consists of multiple layers, shown in Figures 1B,C. The following steps should be taken to construct either cell configuration. Copper tape is applied as leads on the anode and cathode. Both electrodes, as well as pretreated BPM, CEMs, and AEM are stacked into the custom electrodialysis cell, as indicated in Figures 1B,C. The cell is then screwed together until hand tight, to prevent leaking. Ag/AgCl reference electrodes are placed in the Luggin capillaries and potentiostat leads are attached to the two reference electrodes, anode, and cathode in a four-point measurement configuration. Finally, the tubing is attached to pumps and the following flow configuration is set up. 1 M Na_2SO_4, NaOH, or KOH is flowed through the outer electrode chamber chambers in the five-chamber configuration, 0.5 M NaCl is flowed through the chambers on either side of the BPM in both cell configurations (e.g., the acid chamber and base chamber), and 3 M NaCl is flowed through between the AEM and CEM chamber (e.g., the dilute chamber) in the five-cell configuration. For the electrode chambers, the electrolyte is fed from one chamber directly into the next and then recirculated using a flow rate on the order of 10–20 ml/min. Instead of the water-splitting reaction at the electrodes, redox couples, such as ferro/ferricyanide can also be used for electrode reactions (Digdaya et al., 2020). The 3 M NaCl is recirculated through the dilute chamber, also using a similar or faster flow rate, as to not deplete all of the ions in solution and to maintain the conductivity of the solution. In the acid and base chambers, 0.5 M NaCl flows through both chambers individually, without recirculating. A pump with accurate flow rate (usually on the order of 0.1–1 ml/min) control is used for the chambers on either side of the BPM, so that FE can be calculated as explained later in this section.

Once the cell is constructed, chronopotentiometry measurements are taken by applying a specific current across the anode and cathode and measuring the voltage between the two reference electrodes. Measurements are often started at 0 A and increased step-wise from there. For each step, the current is held at a constant value until a steady voltage is reached (~10–30 min). This voltage is then recorded and current density-voltage plots are constructed from this data.

Also of importance in understanding the performance of a BPM is the pH obtained on either side of the BPM, which allows for calculation of the Faradaic efficiency (FE) of H^+ and OH^- produced. FE of H^+ and OH^- generation and transport through the BPM is dependent on current density, due to co-ion crossover being more dominate at lower current densities, before WD takes over. To obtain FE for a given BPM, the BPM is pretreated and cell constructed as described above. A selected current is then applied across the cell and 0.5 M NaCl is flowed through the chambers on either side of the BPM at a specified flow rate (chosen based on the desired final pH value). The cell is allowed 10–30 min for the voltage to stabilize and then a few mL of the out flow from the chambers on either side of the BPM (acidic stream and basic stream) is collected. It is best to collect multiple samples over time to determine any error present in measurements and note if the pH is shifting with time. Once the acid and base stream samples are collected, the best method to determine the H^+/OH^- concentration, and in turn the pH, is titration of a known buffer. A pH probe can also be used, however, these probes tend to lose accuracy at extreme pH values, whereas titrations will remain accurate at all pH values. For the FE values shown in the results of this paper, a pH probe was used for measurements at low currents (≤ 10 mA) and titration was performed for measurements at high currents (>10 mA).

Titrations are performed by titrating the unknown acid or base sample into a known buffer. For the results presented in this paper, a phosphate buffer with a pK_a of 7.21 was made using KH_2PO_4 and K_2HPO_4. The corresponding buffer reactions are given in Eq. 2 (acid) and Eq. 3 (base). When making the buffer solution, all salts were dried before being weighed and the molarity is determined based on the pH values to be measured. For each titration, a specific amount of buffer is measured into a beaker with a stir bar and placed on a stir plate. A pH probe is then submerged in the buffer and an auto log of the pH over time is started. The acid or base sample with unknown concentration is then slowly added to the buffer using a pump with an accurate flow rate. The titration is monitored by watching the change in pH and observing when the equivalence point occurs. Once the titration is complete, pH vs. time is plotted and the derivative is taken to determine at what time the equivalence point occurs. The amount of time to the equivalence point along with the flow rate is used to determine the volume of unknown sample added to the buffer. If access is available, an automatic titration system can also be used. Once the equivalence point and volume of sample added are determined, Eqs 4–6 along with the molar mass of the phosphate salts are then used to calculate the H^+/OH^- concentration.

$$HPO_4^{2-} + H_3O^+ \rightarrow H_2PO_4^- + H_2O \tag{2}$$

$$HPO_4^- + OH^- \rightarrow HPO_4^{2-} + H_2O \tag{3}$$

$$pH = pK_a + \log\left(\frac{[HPO_4^{2-}]}{[H_2PO_4^-]}\right)(Henderson\text{–}Hasselbalch\ equation) \tag{4}$$

$$[H^+]_{experimental} = \frac{moles\ HPO_4^{2-}}{Liters\ unknown\ acidic\ sample} \tag{5}$$

$$[OH^-]_{experimental} = \frac{moles\ H_2PO_4^-}{Liters\ unknown\ basic\ sample} \tag{6}$$

Once the pH, H^+, or OH^- values have been determined, *via* titration or a pH probe, Eqs 7–18 can be used to calculate FE (Digdaya et al., 2020).

$$G_{H^+} = \frac{I_{applied}}{nF} \tag{7}$$

$$[H^+]_{added} = \frac{G_{H^+}}{Q_{0.5\,M\,NaCl}} \tag{8}$$

$$[H^+]_{present} = 10^{-6.85} \tag{9}$$

$$[H^+]_{theoretical} = [H^+]_{added} + [H^+]_{present} \tag{10}$$

$$[H^+]_{experimental} = 10^{-pH_{acidic}} \tag{11}$$

$$FE_{[H^+]} = \frac{[H^+]_{experimental}}{[H^+]_{theoretical}} \tag{12}$$

$$G_{OH^-} = \frac{I_{applied}}{nF} \tag{13}$$

$$[OH^-]_{added} = \frac{G_{OH^-}}{Q_{ow}} \tag{14}$$

$$[OH^-]_{present} = \frac{10^{-13.71}}{10^{-6.85}} \tag{15}$$

$$[OH^-]_{theoretical} = [OH^-]_{added} + [OH^-]_{present} \tag{16}$$

$$[OH^+]_{experimental} = 10^{-(13.71 - pH_{basic})} \tag{17}$$

$$FE_{[OH^-]} = \frac{[OH^-]_{experimental}}{[OH^-]_{theoretical}} \tag{18}$$

In the above equations, G_{H^+} and G_{OH^-} (mol/s) are the generation rates of H^+ and OH^- ions, $I_{applied}$ (A) is the total applied current, n is the number of electron per generation of one H^+ and one OH^- (in a single stack cell, $n = 1$), F is the Faraday constant (96,485.3329 s·A/mol), $[H^+]_{added}$ and $[OH^-]_{added}$ (mol/L) are the concentration of H^+ and OH^- ions theoretically added due to water dissociation for a given current and flow rate, and $Q_{0.5\,M\,NaCl}$ (L/s) is the flow rate of 0.5 M NaCl through the cell. The total theoretical concentrations of H^+ ($[H^+]_{theoretical}$) and OH^- ($[OH^-]_{theoretical}$), if all electrons are going toward water dissociation, is then calculated as $[H^+]_{added}$ plus the H^+ concentration already present ($[H^+]_{present}$) in the 0.5 M NaCl solution or as $[OH^-]_{added}$ plus the OH^- concentration already present ($[OH^-]_{present}$) in the 0.5 M NaCl solution, respectively. The addition of salt ions to water causes the pK_w and, therefore, the neutral pH to shift. According to Liberti, Liberti and Light (1962), for 0.5 M NaCl the pK_w is calculated to be 13.71 and the neutral pH is 6.85. This is reflected in the calculation of $[H^+]_{present}$ and $[OH^-]_{present}$. The Faradaic efficiencies of H^+ and OH^- are then given by $FE_{[H^+]}$ and $FE_{[OH^-]}$, respectively.

2.2 Data collection, analysis, and records management

2.2.1 Data collection, analysis, and record management of electrochemical impedance spectroscopy measurements for cation exchange membranes and anion exchange membranes

All data was collected through Gamry Instruments Framework software and analyzed using OriginLab. Example plots made in OriginLab can be seen in Figure 2 in Section 4.1. A standard naming system for each sample should be developed and the following information should be recorded for each saved file: date, sample name, electrolyte type and concentration, and sample thickness. Determined resistances should then be recorded for each sample, from which conductivity can be calculated.

2.2.2 Data collection, analysis, and record management of voltage and faradaic efficiency measurements for bipolar membranes

All data was collected through EC-lab software and analyzed using OriginLab. Example plots made in OriginLab are shown in Figure 3 in Section 4.2. A standard naming system should also be developed for all samples in these experiments and the following information should be recorded for each saved file: date, sample name, electrolyte type and concentration, and flow rate. Applied currents and measured voltages are then recorded as well as titration and pH measurements. This is the raw data that can then be used for current-voltage and FE plot.

2.3 Equipment and supplies

2.3.1 Electrochemical impedance spectroscopy cell materials/chemicals

Membranes (CEM, AEM). Chemicals for pretreating membranes (HCl, KOH, NaCl, etc.). DI water.

2.3.2 Hardware for electrochemical impedance spectroscopy cell

Customized pressing cell resistant to the electrolyte (PEEK). Potentiostat with capability of EIS measurement (e.g., Gamry Reference 620 potentiostat). Electrical lead cables 2 working electrodes with 2 mm in diameter Pt coated in the center of the tip (CHI102P by CH Instruments Inc.).

2.3.3 Software for electrochemical impedance spectroscopy cell

Potentiostat software (e.g., Gamry Instruments Framework). Bode plot, Nyquist plot, and Debye model fitting software (e.g., Gamry Echem Analyst). Data analysis and figure plotting software (e.g., Microsoft Office, OriginLab).

2.3.4 Electrodialysis cell materials/chemicals

Membranes (CEM, AEM, BPM). Chemicals for pretreating membranes (HCl, KOH, NaCl, etc.). Electrolyte in the desired concentration (e.g., 0.5 M H_2SO_4, 0.5 M NaCl, 3 M NaCl). DI water.

2.3.5 Hardware for electrodialysis cell

Customized electrodialysis cell resistant to the electrolyte (Acrylic). Customized Luggin capillaries (custom made in glass shop). Potentiostat with the capabilities of four-point chronopotentiometry measurement (e.g., Biologic Potentiostat). Electrical lead cables Pt coated Ti foil for anode and cathode.

2.3.6 Software for electrodialysis cell

Potentiostat software (e.g., EC-lab). Data analysis and figure plotting software (e.g., Microsoft Office, OriginLab).

2.3.7 Materials for measuring [H^+] and [OH^-]

pH meter (Hanna instruments desktop pH meter). pH meter calibration solutions. Software for logging pH over time (Hanna desktop pH meter software). Pump that allows for accurate set flow rate (syringe pump or peristaltic pump). Stir plate/stir bar. Phosphate salts (KH_2PO_4 and K_2HPO_4). DI water.

2.4 Units, nomenclature, and definitions

mA/cm^2—standard units for current density. V—standard for voltage. M—standard for concentration (mol/L). FE—Faradaic efficiency, percent of current (e-) going toward producing desired product. BPM—Bipolar membrane. CEM/CEL—Cation exchange membrane/cation exchange layer. AEM/AEL—Anion exchange membrane/anion exchange layer.

3 Quality control and quality assurance

3.1 Calibration and standardization

3.1.1 Calibration and standardization of electrochemical impedance spectroscopy measurements for cation exchange membranes and anion exchange membranes

Common and well-studied membranes, such as Nafion, should be used as standards in the EIS cell. The same procedures laid out in Section 2.1 can be used to test these standard membranes. Specifications about the conductivity of these standard membranes are typically given by the company from which they were purchased. Conductivities obtained using the EIS cell should be comparable to the conductivities given by the membrane companies. If this is the case, these standards can then be used to compare against new membranes being tested in the EIS cell. Results for Nafion 117 (Fuel Cell Store) testing in the custom EIS cell are also given in Section 4.1 and can be used as a standard for calibrating new systems.

3.1.2 Calibration and standardization of voltage and faradaic efficiency measurements for bipolar membranes

Commercial BPMs, such as the Fumasep FBM (Fumasep BPM, Fuel Cell Store), should be used as a standard in the custom electrodialysis cell. Chronopotentiometry and pH measurements can be taken as described in Section 3.2 for the Fumasep BPM. Examples of the expected resulting current voltage and faradaic efficiency plots are shown in Figure 3. If results match these plots, then the cell is working correctly and can be used to test and compare new membranes.

For pH measurements and titrations, the pH probe should be calibrated daily, using standard buffer solutions. The pump for titrations should also be calibrated to determine an accurate flow rate.

3.2 Common issues and troubleshooting

When troubleshooting membrane systems, the first step is to test a standard commercial membrane, such as the ones described in Section 3.1.1 and Section 3.1.2. This will help to determine if the error is coming from the testing environment or the membrane itself. If the data collected from the standard membrane looks accurate compared to other published results, then likely the issue is with the new membrane being tested. In this case, try making a new sample and seeing if the error occurs again.

3.2.1 Common issues and troubleshooting of electrochemical impedance spectroscopy measurements for cation exchange membranes and anion exchange membranes specifics

It is important to make sure that membranes remain fully wetted through testing and cover the entire electrode surface. To avoid dehydration of the membrane, they should be stored in solution until just before testing and tested immediately after loading into the EIS cell. It is also important to avoid over tightening the custom EIS cell, as this can lead to inaccurate results due to compression of the membrane. The cell should be tightened until the Pt electrodes are contacting the membrane on either side, but no farther. If improbable results are obtained, try rewetting the membrane and loading it back into the cell.

3.2.2 Common issues and troubleshooting of voltage and faradaic efficiency measurements for bipolar membranes

When assembling the electrodialysis cell and initially filling the chambers with electrolyte, it is important to make sure that no bubbles are trapped on the surface of the BPM or at the tip of the reference electrodes within the Luggin capillaries. Trapped bubbles in these locations can lead to increased voltage values that are not representative of the actual voltage across the BPM. If bubbles are seen at the surface of the BPM, tilt and shake the cell until the bubbles are removed. A pipette with electrolyte solution can also be used to push bubbles out of the capillaries and away from the BPM surface.

The Ag/AgCl reference electrodes contain porous frits which are immersed in electrolyte and can be prone to leaking and voltage drifting. It is important to frequently test these reference electrodes against a standard reference electrode (for instance, the standard hydrogen electrode, SHE). Faulty reference electrodes can significantly alter the voltage measured across the BPM, giving inaccurate results.

It is also important to note that even though the Luggin capillaries reduce much of the losses due to iR drop in the electrolyte, some loss will remain. For the best results using Luggin capillaries, it is recommended that the tip of the Luggin capillary is placed no closer than a distance of 2d, where d is the diameter of the Luggin tip, from the surface of the BPM (Biani, 2003). The Luggins should also be placed toward the top of the BPM active area to block as little of the surface as possible. These placement requirements will help avoid interference of the Luggin capillaries with the electric field at the surface of the BPM.

4 Results and discussion

4.1 Electrochemical impedance spectroscopy measurements for cation exchange membranes and anion exchange membranes results and discussion

As previously discussed, measurements performed in an electrochemical cell usually include un-compensated resistance due to the electrolyte surrounding a membrane. The measurement errors would be significant when the conductivity and the thickness of the electrolyte layers are comparable to membranes. Figure 2A shows a current voltage plot of a Nafion 117 CEM tested using Luggin capillaries in the electrodialysis cell pictured in Figure 1B. The linear fit shown by the line in gray follows Ohm’s Law (V = IR) and can therefore, ideally be used to calculate the conductivity of the monopolar membrane. However, even with the use of Luggin capillaries, when testing a monopolar membrane in a liquid electrolyte

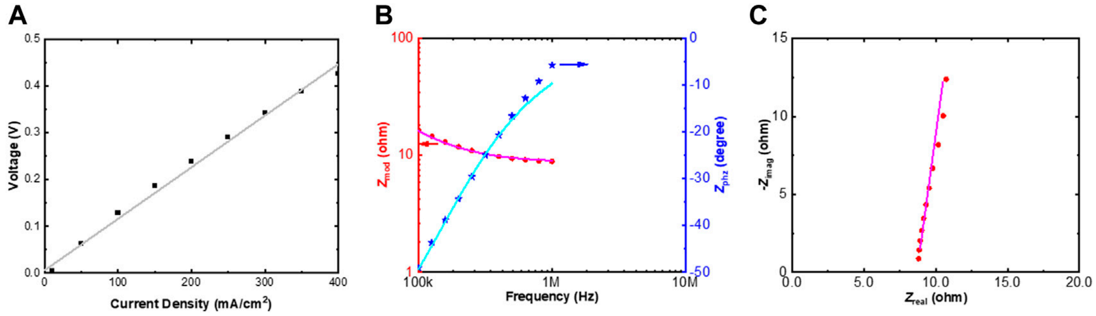

FIGURE 2
Current-voltage plot, with linear fit, for Nafion 117 (cation exchange membrane), using electrodialysis flow cell **(A)**. Bode plot **(B)** and Nyquist plot **(C)** with a Debye model fit for Nafion N117 in 0.5 M H_2SO_4.

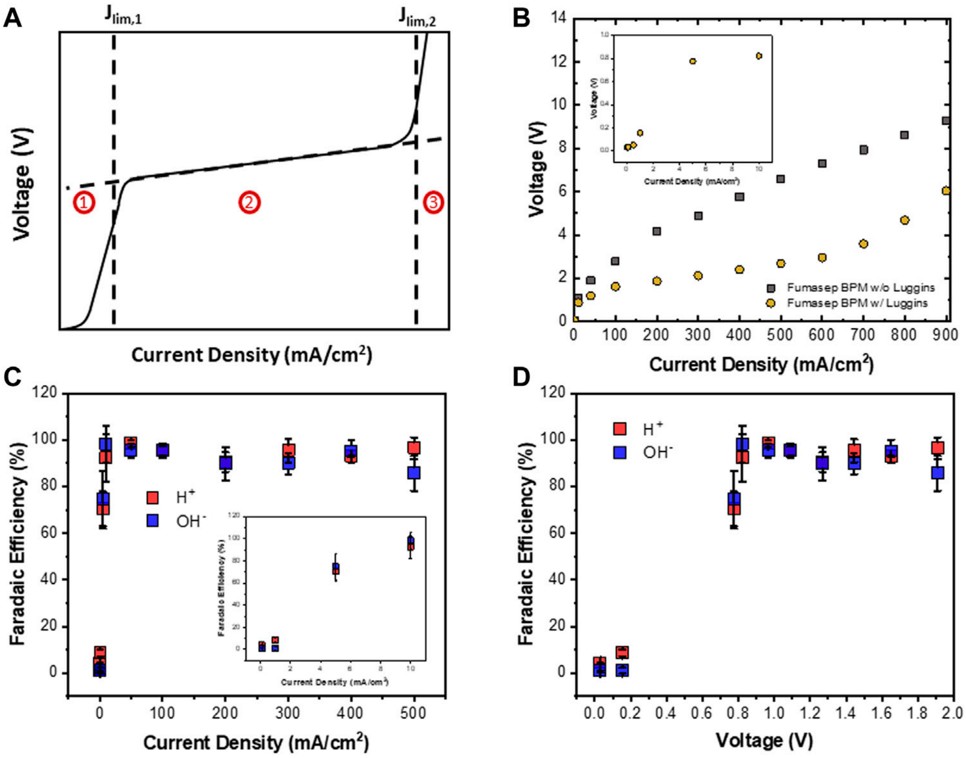

FIGURE 3
Typical current voltage profile for a bipolar membrane under reverse bias **(A)**. Current-voltage **(B)**, Faradaic efficiency of H^+ and OH^- vs. current density **(C)**, and Faradaic efficiency of H^+ and OH^- vs. voltage **(D)** plots for a commercial Fumasep bipolar membrane tested in custom electrodialysis flow cell (flow rate: 1 ml/min).

environment, the electrolyte resistance dominates and the measured conductivity is much lower than the intrinsic membrane conductivity. For example, when calculated from the slope in Figure 2A, a much lower conductivity of 16.6 $mS{\cdot}cm^{-1}$ was obtained due to the contribution from the un-compensated solution resistance. As a result, a custom EIS cell shown in Figure 1A was designed specifically to determine the conductivity of monopolar membranes without solution resistance losses. Figures 2B,C show the Bode plot and Nyquist plot results of the Nafion N117 CEM measured by the EIS technique in the custom cell and then fitted by the Debye electrochemical model within the high frequency range (typically between 100 kHz and 1 MHz). The pink curve in Figure 2C crosses the -Z_{imag} = 0 ohm at Z_{real} = 8.683 ohm, meaning that the through-plane resistance of the Nafion N117 CEM is 8.683 ohm. After being normalized by the thickness, L (183 µm), and the cross-sectional area, A (), the through-plane conductivity σ of 67.09 mS·cm^{-1} was obtained. This conductivity value, unlike the one measured using Luggin capillaries in the electrodialysis cell, is more accurate and within the expect range for fully wetter Nafion 117 at room temperature (Wang et al., 2011; Thompson, 2014; Nafion N115, N117, N1110: Ion Exchange Materials, 2019).

Ideally, CEMs and AEMs can be developed with high conductivities such that they can be added to PEC water splitting cells to manage product separation without significantly increasing the voltage due to resistance in the cell. Conductivity measurements obtained through the methods exemplified here can be used to directly compare the efficiencies of membrane being studied for PEC systems.

4.2 Voltage and faradaic efficiency measurements for bipolar membranes results and discussion

A typical current density-voltage curve for a BPM contains three regions, as depicted in Figure 3A. In region 1, where the applied current is low, water dissociating is not yet prominent and co-ion crossover dominates. At the first limiting current ($J_{lim,1}$), H$^+$ and OH$^-$ migration begins to dominate as the co-ions are flushed out of the membrane and WD at the junction occurs more rapidly. Eventually, migration of H+ and OH- is the prevailing source of current, leading to the plateau in region 2. Here, the current density-voltage relationship becomes ohmic and the small increase in voltage is due purely to the membrane resistance and residual resistance from the electrolyte. As the membrane is taken to higher currents, however, a second limiting current ($J_{lim,2}$) is observed. $J_{lim,2}$ occurs due to water transport limitations in the membrane. At this point, the rate of water transport through the CEL and AEL can no longer keep up with the rate of water dissociation at the junction, therefor, a sigmoidal increase in voltage is observed (region 3) (Strathmann et al., 1997; Krol et al., 1998; Blommaert et al., 2019; Giesbrecht and Freund, 2020; Hohenadel et al., 2021; Pärnamäe et al., 2021).

Observing where each of these regions occur for newly developed membranes will allow for deeper understanding of membrane performance and help advance BPM technologies. The value of $J_{lim,1}$ is an indication of the perspectivity (ability of the CEL to selectively transport cations and the AEL to selectively transport cations) of the CEL and AEL (Giesbrecht and Freund, 2020; Pärnamäe et al., 2021). Lower voltages and a more gradual slope in region 2 indicate more efficient water dissociation at the BPM junction and less resistance in the membrane, respectively. Lastly, the value of $J_{lim,2}$ can be used to determine the onset of water transport limitations.

Figure 3B shows a typical current density-voltage plot for a commercial Fumasep BPM. The importance of using Luggin capillaries was evidenced by comparing the two curves in Figure 3B. When Luggin capillaries were not employed, the voltages at higher current densities were much larger due to iR losses in the electrolyte (Vargas-Barbosa et al., 2014; Chen et al., 2020). When Luggin capillaries were used, the voltage was lowered significantly (Figure 3B). Although there may still be small iR losses due to the un-compensated solution resistance in these measurements, the polarization curves obtained with Luggin capillaries are much more indicative of the actual voltage across the BPM and allows for clear visualization of the three regimes laid out in Figure 3A. For the Fumasep BPM, $J_{lim,1}$ occurs at ~5 mA/cm^2 and $J_{lim,2}$ occurs at ~500 mA/cm^2. In these experiments, a sigmoidal curve is not observed at $J_{lim,2}$. This is due to the experimental design, in which the voltage measurement is taken after the current is held for 20 min. This does not allow time for the membrane junction to fully dry out and, therefore, the voltage is not yet at steady state. If demonstration of the sigmoidal curve is desired, these higher currents should be held for longer until steady state voltage is reached.

Figures 3C,D show the FE of H$^+$/OH$^-$ vs. current density and voltage, respectively. At low current densities, the FE for both H$^+$ and OH$^-$ is low, indicating that co-ion crossovers accounted for a significant portion of the measured current. In this region, the voltages are relatively low, as an insignificant amount of H$^+$ and OH$^-$ is being transported thought the membrane. At current densities ≥10 mA/cm^2, however, the FE for both H$^+$ and OH$^-$ improved significantly and the measured current was dominated by the generation of H$^+$ and OH$^-$ from water dissociation. An increase in voltage is also observed as WD begins. FE measurements provide greater insight into the amount of current being used toward co-ion crossover and leakage vs. transport of H$^+$ and OH$^-$ from WD. Using these standard measurements will allow for the comparison of ion transport selectivity in new BPMs and in turn the efficiency of these new BPMs toward creating acidic and basic environments for HER and OER, respectively.

5 Conclusion

Understanding ion transport in monopolar and bipolar membranes is key for improving their performance in PEC water splitting systems, allowing for lower cell voltages, improved product isolations, and superior environments for Earth abundant HER and OER catalysts. This protocol paper describes two custom electrochemical cells designed for measuring ion transport in and performance of ion exchange membranes: an EIS cell perfected for determining conductivity of CEMs and AEMs and an electrochemical flow cell with Luggin capillaries for measuring voltage and FE of BPMs. The former is designed such that a membrane can be sandwiched directly between two Pt electrodes and the conductivity can be determined without the interference of electrolyte resistance. The latter is designed such that a direct measurement of voltage across the BPM can be obtained through reference electrodes placed in the Luggin capillaries, without iR drops due to the surrounding electrolyte. Two different designs, five-chamber and two-chamber, allow for ideal environments for measuring pH/FE and OER/HER performance in a bipolar membrane enhances water splitting cell, respectively. These direct measurements of voltage and FE are vital for understanding WD efficiency and co-ion crossover/leakage within a BPM. Applied across the field, these developments in testing systems and protocol will lead to easy comparison and advances in ion exchange membrane technology for PEC water splitting systems.

Data availability statement

The raw data supporting the conclusion of this article will be made available by the authors, without undue reservation.

Author contributions

ÉL: Designed the electrochemical cell for measuring ion transport in bipolar membranes described in this work. She took all measurments associated with this system. She was also the main author of the manuscript text and developed all final figures. LH: Designed the electrochemical cell for EIS measurements. He collected all data related to this system and contributed to the figures and writing of these sections of the manuscript. IS: Contributed significantly to the development of the titration system described in the test, as well as adding important edits and contributions to the manuscript text. HA: Advised EL in the development of the electrochemical testing systems and data collection/analysis. CX: Advised ÉL, LH, and IS in the development of the electrochemical testing systems and data collection/analysis and added significant revisions to the manuscript text.

Acknowledgments

The authors acknowledge the support from of the United States Department of Energy, Energy Efficiency and Renewable Energy (EERE) under contract number DE-EE0008092, and United States Department of Energy, Advanced Research Projects Agency–Energy (ARPA-e) under contract number DE-AR0001407.

Conflict of interest

The authors declare that the research was conducted in the absence of any commercial or financial relationships that could be construed as a potential conflict of interest.

Publisher’s note

References

Abergel, T., Armijo, J., Bains, P., Bennett, S., Berghout, N., Bibra, E. M., et al. (2021). *Global hydrogen review*. Paris, France: International Energy Agency (IEA)

Ardo, S., Rivas, D. F., Modestino, M. A., Greiving, V. S., Abdi, F. F., Llado, E. A., et al. (2018). Pathways to electrochemical solar-hydrogen technologies. *Energy Environ. Sci.* 11, 2768–2783. doi:10.1039/c7ee03639f

Bard, A., and Faulkner, L. (2011). *Electrochemical methods: Fundamentals and applications*. 2nd Edition. New York: Wiley.

Berger, A., Segalman, R. A., and Newman, J. (2014). Material requirements for membrane separators in a water-splitting photoelectrochemical cell. *Energy Environ. Sci.* 7, 1468–1476. doi:10.1039/c3ee43807d

Biani, P. Z. C. N. F. F. de (2003). *Inorganic electrochemistry: Theory, practice and application*. Cambridge: RSC Publishing.

Blommaert, M. A., Aili, D., Tufa, R. A., Li, Q., Smith, W. A., and Vermaas, D. A. (2021). Insights and challenges for applying bipolar membranes in advanced electrochemical energy systems. *ACS Energy Lett.* 6, 2539–2548. doi:10.1021/acsenergylett.1c00618

Blommaert, M. A., Vermaas, D. A., Izelaar, B., In’T Veen, B., and Smith, W. A. (2019). Electrochemical impedance spectroscopy as a performance indicator of water dissociation in bipolar membranes. *J. Mat. Chem. A* 7, 19060–19069. doi:10.1039/c9ta04592a

Bui, J. C., Digdaya, I., Xiang, C., Bell, A. T., and Weber, A. Z. (2020). Understanding multi-ion transport mechanisms in bipolar membranes. *ACS Appl. Mat. Interfaces* 12, 52509–52526. doi:10.1021/acsami.0c12686

Chabi, S., Wright, A. G., Holdcroft, S., and Freund, M. S. (2017). Transparent bipolar membrane for water splitting applications. *ACS Appl. Mat. Interfaces* 9, 26749–26755. doi:10.1021/acsami.7b04402

Chen, Y., Wrubel, J. A., Klein, W. E., Kabir, S., Smith, W. A., Neyerlin, K. C., et al. (2020). High-performance bipolar membrane development for improved water dissociation. *ACS Appl. Polym. Mat.* 2, 4559–4569. doi:10.1021/acsapm.0c00653

Cheng, W., Calle, A., Atwater, H. A., Stechel, E. B., and Xiang, C. (2021). Hydrogen from sunlight and water: A side- by-side comparison between photoelectrochemical and solar thermochemical water-splitting. *ACS Energy Lett.* 6, 3096–3113. doi:10.1021/acsenergylett.1c00758

Cox, C. R., Lee, J. Z., Nocera, D. G., and Buonassisi, T. (2014). Ten-percent solar-to-fuel conversion with nonprecious materials. *Proc. Natl. Acad. Sci. U. S. A.* 111, 14057–14061. doi:10.1073/pnas.1414290111

Digdaya, I. A., Sullivan, I., Lin, M., Han, L., Cheng, W. H., Atwater, H. A., et al. (2020). A direct coupled electrochemical system for capture and conversion of CO2 from oceanwater. *Nat. Commun.* 11, 4412–4510. doi:10.1038/s41467-020-18232-y

Fountaine, K. T., Lewerenz, H. J., and Atwater, H. A. (2016). Efficiency limits for photoelectrochemical water-splitting. *Nat. Commun.* 7, 13706. doi:10.1038/ncomms13706

Giesbrecht, P. K., and Freund, M. S. (2020). Recent advances in bipolar membrane design and applications. *Chem. Mat.* 32, 8060–8090. doi:10.1021/acs.chemmater.0c02829

Hamdani, I. R., and Bhaskarwar, A. N. (2021). Recent progress in material selection and device designs for photoelectrochemical water-splitting. *Renew. Sustain. Energy Rev.* 138, 110503. doi:10.1016/j.rser.2020.110503

Haussener, S., Xiang, C., Spurgeon, J. M., Ardo, S., Lewis, N. S., and Weber, A. Z. (2012). Modeling, simulation, and design criteria for photoelectrochemical water-splitting systems. *Energy Environ. Sci.* 5, 9922–9935. doi:10.1039/c2ee23187e

Hohenadel, A., Gangrade, A. S., and Holdcroft, S. (2021). Spectroelectrochemical detection of water dissociation in bipolar membranes. *ACS Appl. Mat. Interfaces* 13, 46125–46133. doi:10.1021/acsami.1c12544

Nafion N115, N117, N1110: Ion Exchange Materials Nafion N115, N117, N1110: Ion exchange materials (2019). Available at: www.fuelcellstore.com.

Krol, J. J., Jansink, M., Wessling, M., and Strathmann, H. (1998). Behaviour of bipolar membranes at high current density water diffusion limitation. *Sep. Purif. Technol.* 14, 41–52. doi:10.1016/S1383-5866(98)00058-6

Liberti, A., and Light, T. S. (1962). Potentiometric determination of kw with the glass electrode. *J. Chem. Educ.* 39, 236–239. doi:10.1021/ed039p236

Luo, J., Vermaas, D. A., Bi, D., Hagfeldt, A., Smith, W. A., and Grätzel, M. (2016a). Bipolar membrane-assisted solar water splitting in optimal pH. *Adv. Energy Mat.* 6, 1600100–1600107. doi:10.1002/aenm.201600100

Luo, J., Vermaas, D. A., Bi, D., Hagfeldt, A., Smith, W. A., and Grätzel, M. (2016b). Bipolar membrane-assisted solar water splitting in optimal pH. *Adv. Energy Mat.* 6, 1600100. doi:10.1002/aenm.201600100

Luo, T., Abdu, S., and Wessling, M. (2018). Selectivity of ion exchange membranes: A review. *J. Memb. Sci.* 555, 429–454. doi:10.1016/j.memsci.2018.03.051

McDonald, M. B., Ardo, S., Lewis, N. S., and Freund, M. S. (2014). Use of bipolar membranes for maintaining steady-state pH gradients in membrane-supported, solar-driven water splitting. *ChemSusChem* 7, 3021–3027. doi:10.1002/cssc.201402288

Nocera, D. G. (2012). The artificial leaf. *Acc. Chem. Res.* 45, 767–776. doi:10.1021/ar2003013

Oener, S. Z., Foster, M. J., and Boettcher, S. W. (2020). Accelerating water dissociation in bipolar membranes and for electrocatalysis. *Sci. (80-.)* 369, 1099–1103. doi:10.1126/science.aaz1487

Oener, S. Z., Twight, L. P., Lindquist, G. A., and Boettcher, S. W. (2021). Thin cation-exchange layers enable high-current-density bipolar membrane electrolyzers via improved water transport. *ACS Energy Lett.* 6, 1–8. doi:10.1021/acsenergylett.0c02078

Pärnamäe, R., Mareev, S., Nikonenko, V., Melnikov, S., Sheldeshov, N., Zabolotskii, V., et al. (2021). Bipolar membranes: A review on principles, latest developments, and applications. *J. Memb. Sci.* 617, 118538–118625. doi:10.1016/j.memsci.2020.118538

Ran, J., Wu, L., He, Y., Yang, Z., Wang, Y., Jiang, C., et al. (2017). Ion exchange membranes : New developments and applications. *J. Memb. Sci.* 522, 267–291. doi:10.1016/j.memsci.2016.09.033

Roger, I., Shipman, M. A., and Symes, M. D. (2017). Earth-abundant catalysts for electrochemical and photoelectrochemical water splitting. *Nat. Rev. Chem.* 1, 0003. doi:10.1038/s41570-016-0003

Russel, R. (2011). Explosive lessons in hydrogen safety. *Ask. Mag.*, 46–50. doi:10.1049/cce:19980202

Segev, G., Kibsgaard, J., Hahn, C., Xu, Z. J., Cheng, W.-H., Xiang, C, et al. (2022). The 2022 solar fuels roadmap. *J. Phys. D. Appl. Phys.* 55, 323003. doi:10.1088/1361-6463/ac6f97

Shen, C., Wycisk, R., and Pintauro, P. N. (2017). High performance electrospun bipolar membrane with a 3D junction. *Energy Environ. Sci.* 10, 1435–1442. doi:10.1039/c7ee00345e

Spitler, M. T., Modestino, M. A., Deutsch, T. G., Xiang, C. X., Durrant, J. R., Esposito, D. V., et al. (2020). Practical challenges in the development of photoelectrochemical solar fuels production. *Sustain. Energy Fuels* 4, 985–995. doi:10.1039/c9se00869a

Strathmann, H., Krol, J. J., Rapp, H. J., and Eigenberger, G. (1997). Limiting current density and water dissociation in bipolar membranes. *J. Memb. Sci.* 125, 123–142. doi:10.1016/S0376-7388(96)00185-8

Sun, K., Liu, R., Chen, Y., Verlage, E., Lewis, N. S., and Xiang, C. (2016). A stabilized, intrinsically safe, 10% efficient, solar-driven water-splitting cell incorporating earth-abundant electrocatalysts with steady-state pH gradients and product separation enabled by a bipolar membrane. *Adv. Energy Mat.* 6, 1600379–1600387. doi:10.1002/aenm.201600379

Thiele, S., Mayerhöfer, B., McLaughlin, D., Böhm, T., Hegelheimer, M., and Seeberger, D. (2020). Bipolar membrane electrode assemblies for water electrolysis. *ACS Appl. Energy Mat.* 3, 9635–9644. doi:10.1021/acsaem.0c01127

Thompson, E. L. (2014). *Behavior of proton exchange membrane fuel cells at sub-freezing temperatures*. New York: University of Rochester.

Vargas-Barbosa, N. M., Geise, G. M., Hickner, M. A., and Mallouk, T. E. (2014). Assessing the utility of bipolar membranes for use in photoelectrochemical water-splitting cells. *ChemSusChem* 7, 3017–3020. doi:10.1002/cssc.201402535

Vermaas, D. A., Sassenburg, M., and Smith, W. A. (2015). Photo-assisted water splitting with bipolar membrane induced pH gradients for practical solar fuel devices. *J. Mat. Chem. A* 3, 19556–19562. doi:10.1039/c5ta06315a

Vermaas, D. A., and Smith, W. A. (2018). *Advances in photoelectrochemical water splitting: Theory, experiment and systems analysis*. London: Royal Society of Chemistry. doi:10.1039/9781782629863-00208

Walter, M. G., Warren, E. L., McKone, J. R., Boettcher, S. W., Mi, Q., Santori, E. A., et al. (2010). Solar water splitting cells. *Chem. Rev.* 110, 6446–6473. doi:10.1021/cr1002326

Wang, C., Li, N., Shin, D. W., Lee, S. Y., Kang, N. R., Lee, Y. M., et al. (2011). Fluorene-based poly(arylene ether sulfone)s containing clustered flexible pendant sulfonic acids as proton exchange membranes. *Macromolecules* 44, 7296–7306. doi:10.1021/ma2015968

Welch, Alex J., Digdya, Ibadillah A., Kent, Ron, Paul, Ghougassian, Atwater, Harry A., and Xiang, Chengxiang (2021). Comparative technoeconomic analysis of renewable generation of methane using sunlight, water, and carbon dioxide. *ACS Energy Lett.* 6, 1540–1549. doi:10.1021/acsenergylett.1c00174

Wilhelm, F. G., Van Der Vegt, N. F. A., Strathmann, H., and Wessling, M. (2002). Comparison of bipolar membranes by means of chronopotentiometry. *J. Memb. Sci.* 199, 177–190. doi:10.1016/S0376-7388(01)00696-2

Wilhelm, F. G., Van der Vegt, N. F. A., Wessling, M., and Strathmann, H. (2001). Chronopotentiometry for the advanced current-voltage characterisation of bipolar membranes. *J. Electroanal. Chem. (Lausanne).* 502, 152–166. doi:10.1016/S0022-0728(01)00348-5

Xiang, C., Weber, A. Z., Ardo, S., Berger, A., Chen, Y. K., Coridan, R., et al. (2016). Modeling, simulation, and implementation of solar-driven water-splitting devices. *Angew. Chem. Int. Ed.* 55, 12974–12988. doi:10.1002/anie.201510463

Xu, T. (2005). Ion exchange membranes: State of their development and perspective. *J. Memb. Sci.* 263, 1–29. doi:10.1016/j.memsci.2005.05.002

Yan, Z., and Mallouk, T. E. (2021). Bipolar membranes for ion management in (Photo)Electrochemical energy conversion. *Acc. Mat. Res.* 2, 1156–1166. doi:10.1021/accountsmr.1c00113

Zhou, X., Liu, R., Sun, K., Chen, Y., Verlage, E., Francis, S. A., et al. (2016). Solar-Driven reduction of 1 atm of CO2 to formate at 10% energy-conversion efficiency by use of a TiO2-protected III-V tandem photoanode in conjunction with a bipolar membrane and a Pd/C cathode. *ACS Energy Lett.* 1, 764–770. doi:10.1021/acsenergylett.6b00317

frontiers | Frontiers in Energy Research

METHODS
published: 27 October 2022
doi: 10.3389/fenrg.2022.884364

Best Practices in PEC Water Splitting: How to Reliably Measure Solar-to-Hydrogen Efficiency of Photoelectrodes

Olivia J. Alley[1], *Keenan Wyatt*[2], *Myles A. Steiner*[2], *Guiji Liu*[1], *Tobias Kistler*[1,3], *Guosong Zeng*[1,4], *David M. Larson*[1], *Jason K. Cooper*[1], *James L. Young*[2], *Todd G. Deutsch*[2]* and *Francesca M. Toma*[1]*

[1]Lawrence Berkeley National Laboratory, Chemical Sciences Division, Berkeley, CA, United States, [2]National Renewable Energy Laboratory, Chemistry and Nanoscience Center, Golden, CO, United States, [3]Walter Schottky Institute and Physics Department, Technische Universität München, Garching, Germany, [4]Department of Mechanical and Energy Engineering, College of Engineering, Southern University of Science and Technology, Shenzhen, China

Edited by:
Chengxiang Xiang,
California Institute of Technology,
United States

Reviewed by:
Yun Hau Ng,
City University of Hong Kong, Hong Kong SAR, China
Fatwa Abdi,
Helmholtz Association of German Research Centers (HZ), Germany
Shaohua Shen,
Xi'an Jiaotong University, China

***Correspondence:**
Todd G. Deutsch
todd.deutsch@nrel.gov
Francesca M. Toma
fmtoma@lbl.gov

Specialty section:
This article was submitted to Process and Energy Systems Engineering,
a section of the journal Frontiers in Energy Research

Received: 26 February 2022
Accepted: 27 April 2022
Published: 27 October 2022

Citation:
Alley OJ, Wyatt K, Steiner MA, Liu G, Kistler T, Zeng G, Larson DM, Cooper JK, Young JL, Deutsch TG and Toma FM (2022) Best Practices in PEC Water Splitting: How to Reliably Measure Solar-to-Hydrogen Efficiency of Photoelectrodes.
Front. Energy Res. 10:884364.
doi: 10.3389/fenrg.2022.884364

Photoelectrochemical (PEC) water splitting, which utilizes sunlight and water to produce hydrogen fuel, is potentially one of the most sustainable routes to clean energy. One challenge to success is that, to date, similar materials and devices measured in different labs or by different operators lead to quantitatively different results, due to the lack of accepted standard operating procedures and established protocols for PEC efficiency testing. With the aim of disseminating good practices within the PEC community, we provide a vetted protocol that describes how to prepare integrated components and accurately measure their solar-to-hydrogen (STH) efficiency (η_{STH}). This protocol provides details on electrode fabrication, η_{STH} test device assembly, light source calibration, hydrogen evolution measurement, and initial material qualification by photocurrent measurements under monochromatic and broadband illumination. Common pitfalls in translating experimental results from any lab to an accurate STH efficiency under an AM1.5G reference spectrum are discussed. A III–V tandem photocathode is used to exemplify the process, though with small modifications, the protocol can be applied to photoanodes as well. Dissemination of PEC best practices will help those approaching the field and provide guidance for comparing the results obtained at different lab sites by different groups.

Keywords: solar-to-hydrogen conversion efficiency, photoelectrochemical, incident photon-to-current efficiency, III–V tandem solar cells, faradaic efficiency, light source calibration, water splitting

INTRODUCTION

Purpose of This Protocol

This protocol aims to provide guidance on the best practices for benchmarking the solar-to-hydrogen (STH) efficiency of photoelectrochemical (PEC) materials. STH efficiency is a key metric for judging the quality of new PEC materials and their feasibility for implementation in practical water-splitting devices. Direct measurement of hydrogen generated by the PEC material is required for an accurate characterization of STH efficiency. Some materials developed for water splitting may have low photocurrents, require an applied voltage to produce hydrogen, or have a lifetime too short to measure generated hydrogen. They still can be characterized by other metrics such as photocurrent density and device lifetime, but in that case STH efficiency values cannot be extrapolated from the measured current density, nor compared with others. In addition to communicating the need for this direct measurement, it is hoped that improved uniformity of experimental practices for performing this key measurement will facilitate the development of new materials.

The STH efficiency (η_{STH}) is calculated as follows:

$$\eta_{STH} = \frac{j_{sc}\left(\frac{mA}{cm^2}\right) * 1.23\ V * \eta_F}{P_{total}\left(\frac{mW}{cm^2}\right)}. \tag{1}$$

Therefore, accurate calculation of η_{STH} relies on an accurate measurement of j_{sc} (photocurrent density at short circuit) and η_F (the system Faradaic efficiency), and calibration of P_{total} (the power density of the light source illuminating the sample). In **Eq. 1**, 1.23 V is the potential difference necessary to generate H_2 and O_2 under standard conditions (25°C). η_F can be defined as the quantity of hydrogen produced for a given current supplied

$$\eta_{F,\ H2} = \frac{(H_2\ \text{produced})}{(\text{measured current})} = \frac{\left(\frac{mol}{s} H_2 * \frac{2e^-}{H_2} * F\left(\frac{C}{mol}\right)\right)}{I\ (A)}. \tag{2}$$

The accurate measurement of P_{total}, H_2 produced, measured current, and measured current density requires attention to equipment calibration and sample preparation. These topics will be discussed in the remainder of this protocol. In addition, we will present the best practices for measuring and reporting the broadband and monochromatic photocurrent response of a material, considering spatial variability and reproducibility of the material fabrication, and the effect of the measurements on the material. Finally, durability measurements, combined with η_{STH} calculations to determine device lifetime, will be briefly discussed. Previously published guidelines for efficiency determination and reporting for PEC devices are presented in Chen et al. (2011) and in more detail in Chen et al. (2013).

PEC Experimental Design and Data Reporting

Prior to η_{STH} measurements, initial material characterization should be done by measuring the photocurrent of a representative sample of the synthesized PEC material under broadband and monochromatic light, to determine the reproducibility and variability of photocurrent. The order of broadband and monochromatic measurements on the photoelectrode pieces should be randomized to detect if one measurement affects the other. For example, if a representative sample of 10 is selected for each material, the monochromatic response is measured first in 5 of the 10, and the broadband response is measured first in the other 5. If a systematic discrepancy is seen between the two datasets, troubleshooting is warranted to decrease corrosion caused by the measurement. If no discrepancy is seen, the statistical robustness of the results will be strengthened.

As another consideration for experimental design, the variability of performance of a new PEC material—within each batch and between synthetic batches—should be reported. Many complex solar absorbers representing the top tier of the current PEC performance show varied performance between synthetic batches, so it remains important for the field to report not only the best result but also the average and range of measured efficiencies for a series of nominally identical syntheses. Many synthetic methods also display variability within the area of one growth/deposition. For example, there is often variation in layer thickness/quality between the center and the edge of the substrate for growth methods such as metalorganic vapor-phase epitaxy (MOVPE) and electrodeposition, as well as deposition from solution by spin coating. Physical vapor deposition and sputtering can also result in non-uniformities across the width of the substrate. Therefore, the sample selected from each batch should be selected to be truly representative of the spatial variability present for a given fabrication method.

Outliers should be removed from the dataset only in extreme cases. For instance, if the edge pieces for a wafer grown by MOVPE are systematically worse than the center pieces, they can be habitually discarded and not tested. While, in this protocol, we have looked at a specific synthetic methodology (MOVPE), considerations with respect to the utilized synthetic routes should be considered when defining outliers. For example, heterogeneities on samples can originate during sputtering deposition and electrodeposition or by deposition of pre-synthesized powders. In all these cases, our recommendation is to perform a combination of characterizations of photophysical, chemical, and photoelectrochemical properties on different sample regions. In addition, some surface modifications treat an entire undivided wafer (e.g., sputtering) while others, such as electrodeposition, are typically done on individual electrodes. In both cases, multiple electrodes from nominally identical treatments should be measured, compared, and reported. This approach should help in the outliers' determination and may provide feedback on improving the deposition/fabrication of the photoelectrodes.

It is also important to mention that choosing the appropriate electrolyte, with respect to pH, requires consideration of the kinetic influence on performance and the chemistry of decomposition reactions on durability. In order to achieve maximum efficiency, a photocathode should be operated in an acidic electrolyte where the hydrogen evolution reaction (HER) is favored. Conversely, a photoanode should be operated in basic solution, where the oxygen evolution reaction (OER) is most kinetically favored. The choice of electrolyte pH for best overall performance is more nuanced. Some research groups have achieved higher durability in neutral, buffered electrolytes. However, these results come at the expense of a diminished efficiency due to kinetic factors, increased solution resistance, and the buildup of a pH gradient with time (Xu et al., 2021). Therefore, we recommend using an electrolyte that balances all of the above considerations and reporting the justification for its selection. If different electrolytes are used, for example, acid for photocathode efficiency and neutral for durability

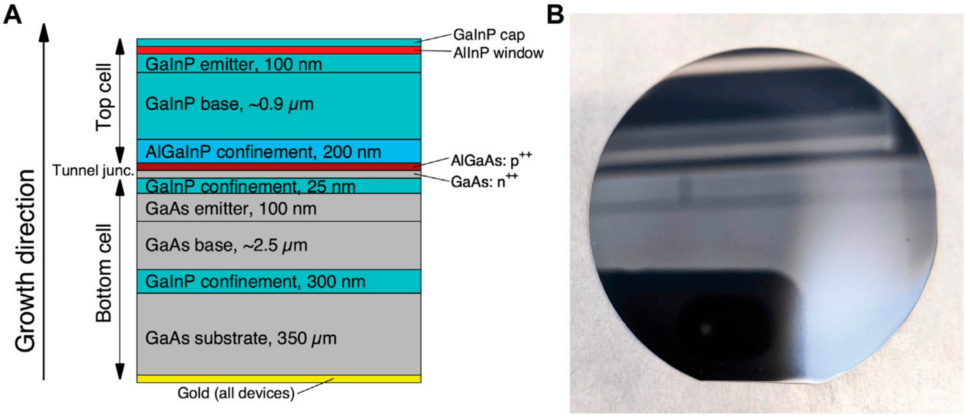

FIGURE 1 | Tandem photoabsorber architecture. **(A)** The vertical structure of layers in the III–V tandem photocathode characterized in this document. **(B)** A 2″ wafer of **(A)**, GaInP top surface.

measurements, those details should be explicitly reported, as well included as part of the discussion of results.

Overview of the Remainder of the Document

With a focus on the characterization and η_{STH} benchmarking of a new photocathode material, this protocol is based on established best practices developed at LBNL (Lawrence Berkeley National Laboratory) and NREL (National Renewable Energy Laboratory) (Chen et al., 2011; Steiner et al., 2012; Chen et al., 2013; Döscher et al., 2016; Young et al., 2017). First, the fabrication of photoelectrodes to probe the performance and statistics of a new PEC material is shown, followed by broadband and monochromatic photocurrent testing of each electrode and suggestions to probe material durability. In this context, we also describe the calibration of light sources. Finally, methods for consistently testing η_F and η_{STH} will be provided, along with examples of their measurement. The testing vessel used herein for measuring η_F and η_{STH} is a sealed compression cell that accommodates a 1 cm^2 photoelectrode, and its assembly will also be described. Finally, there will be a brief discussion of durability testing, which allows tracking η_{STH} over time.

III–V Tandem Photoabsorber Example

To describe the steps of this protocol, we will use, as a model example, a III–V tandem photocathode material with GaInP and GaAs junctions that have band gaps of ~1.8 eV (GaInP) and ~1.4 eV (GaAs). In a cell with sufficient ionic conductivity and appropriate hydrogen and oxygen evolution catalysts, this material can evolve hydrogen under 1-sun illumination without externally applied bias. The structure of the photocathode is shown in **Figure 1**, with similar tandem photocathode materials having been previously reported (Döscher et al., 2016; Young et al., 2017). Note that the metallic back contact was deposited after growth.

PEC ELECTRODE FABRICATION AND INTEGRATED TESTING VESSEL

This section discusses the fabrication details of photoelectrodes for material characterization and assembly of the integrated testing vessel for η_F measurements. We provide detailed information about the material we tested to show a prototypical example for a procedure that can be adaptable and amenable to many different material systems.

Radial Strip Photoelectrodes: Fabrication and Area Determination

For PEC materials grown on wafers by MOVPE, as the III–V tandem photocathode was, the full diameter of the wafer should be characterized to probe the spatial variation in the material growth quality between the edge and center. Here, we take a 5 mm wide strip from the center of the 2″ wafer, as shown in **Figures 2A,B**, and divide it into ten 5 × 5 mm squares. After obtaining the 5 × 5 mm squares, the next step in the photoelectrode fabrication is mounting each square on a glass handle for ease of PEC testing. For PEC materials deposited by other methods and on other substrates, a representative sample should be tested by considering the variations introduced by processing methodologies.

Experimental Setup

The following components are needed for the fabrication of photoelectrodes:

1. Photoelectrode material or tandem junction with or without suitable catalyst deposited.
2. 1″ × 3″ glass microscope slides.
3. Diamond scribe.
4. Glass running pliers.
5. ¼″ copper tape (or other conductive tape).

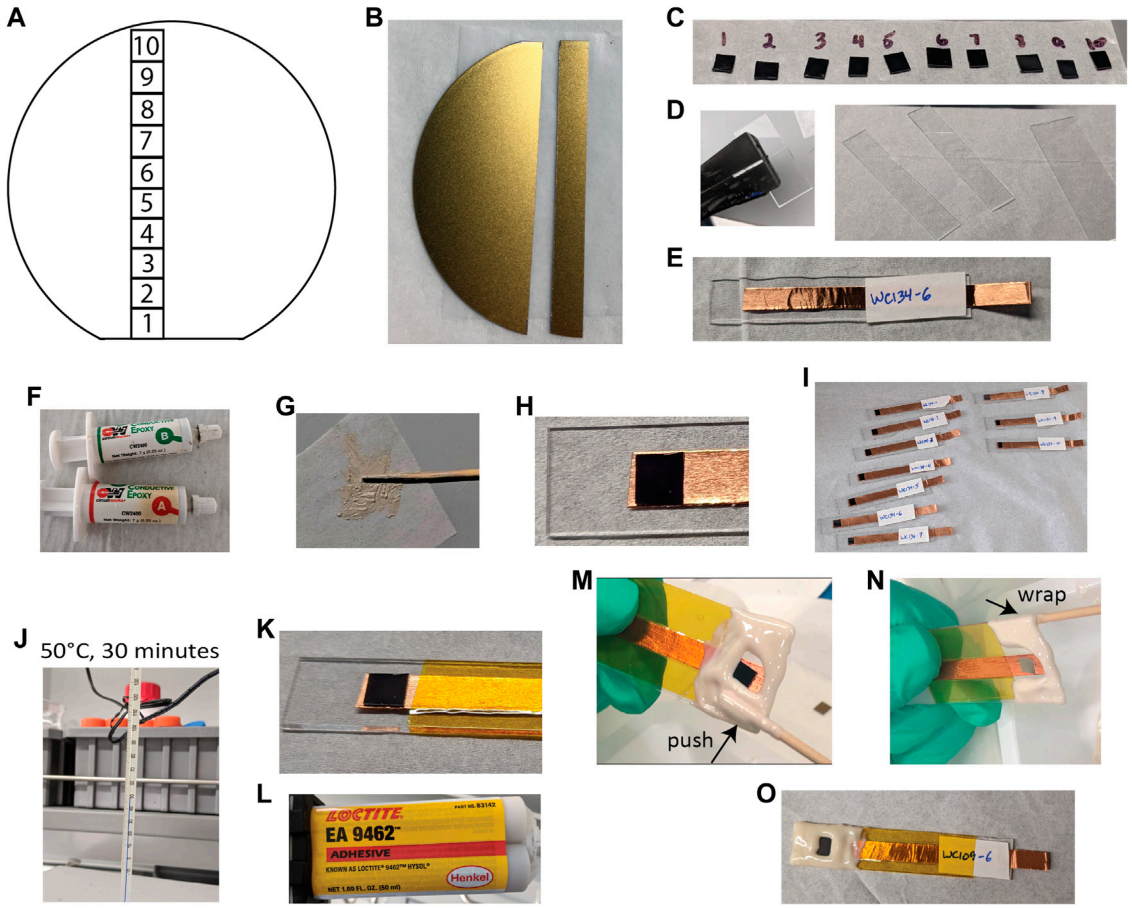

FIGURE 2 | Photoelectrode preparation. **(A)** Schematic of a 2″ wafer showing ten 5 × 5 mm squares in a radial strip. **(B)** A 5 mm strip cleaved from a GaInP/GaAs wafer, showing back ohmic contact. **(C)** 5 × 5 mm squares from the wafer. **(D)** Running pliers and prepared glass slide handles. **(E)** Copper tape and label applied to one handle. **(F)** CircuitWorks CW2400 silver epoxy. **(G)** Prepared silver epoxy. **(H)** 5 mm square adhered to copper tape with a small amount of silver epoxy. **(I)** Ten electrodes prepared for curing. **(J)** Electrodes are cured at 50°C for 30 min. **(K)** Kapton tape added to cover most of the exposed tape. **(L)** Loctite EA 9462 epoxy. **(M,N)** Defining surface area and sealing photoelectrode edges. **(O)** Completed electrodes after 24 h of curing EA 9462 epoxy.

6. For materials without an existing ohmic back contact: indium-gallium (InGa) eutectic (e.g., from Thermo Scientific or Millipore Sigma) and InGa-dedicated diamond scribe.
7. Silver epoxy (CircuitWorks CW2400).
8. ½″ or 1″ Kapton tape.
9. Non-conductive epoxy (opaque, e.g., Loctite Hysol EA 9462, or transparent, e.g., Epo-Tek 302-3M) that is compatible with the electrolyte planned.
10. Plastic-tipped tweezers to avoid metal contamination.
11. 50°C oven for curing.
12. Computer hardware and software for area determination including a flatbed scanner (resolution at least 1200 dpi) and a computer with free ImageJ software installed.

Photoelectrode Fabrication Procedure

The workflow for the photoelectrode fabrication is summarized in **Figure 2** and described as follows:

1. Cut 5 mm squares of the PEC material. If starting with a crystalline wafer, one option is to place it facedown on a scratch-free surface such as lens paper and then isolate a 5 mm strip by lightly scoring a line down the back with a diamond scribe, guided by a glass slide or cover slip. Then, grip the edge on either side of the line with forceps or gloved fingers, and gently flex away from the score until it breaks. For many wafers, a tick mark at the edge is sufficient rather than a full score—the required method for neatly dicing the material under study should be tested on a small piece first. For glass or FTO/ITO substrate, dice in the same way as for glass slides (see below), being mindful to not cause damage to the deposited material. **Figure 2C** shows 5 mm squares cut from a radial strip of a GaInP/GaAs wafer.
2. Prepare the glass handles for the electrodes (**Figure 2D**). The handle width depends on the particular testing vessel planned for the PEC measurements–if there is 1″ or ½″ opening. For a ½″ wide handle, score a glass slide lengthwise once only, with firm pressure, using a diamond scribe and ruler, and break

along the score with running pliers. For a 1″ wide handle, use an entire glass slide for each electrode.

3. Cut a piece of copper tape slightly longer than the microscope slide, then remove the paper backing, apply lengthwise to the middle of the glass, and stop around 5–10 mm short of one end. Fold the other end over to provide a connection for an alligator clip (**Figure 2E**). Repeat to prepare handles for as many electrodes as desired. Label each electrode with a unique identifier.
4. If the back of the material does not have an integrated ohmic contact and forms a native oxide layer (e.g., a Si substrate), apply a small amount of InGa eutectic, then scratch lightly with the InGa-dedicated diamond scribe, and remove the native oxide layer while spreading the eutectic to form an ohmic contact. This can result in a better electrical contact than scratching through the oxide first, followed by InGa application, because SiO_2 and other native oxides begin to reform quickly after exposure to air.
5. To connect the ohmic contact to the copper tape, mix a small amount of two-part silver epoxy, such as CW2400, on a piece of weighing paper using a wooden applicator (**Figures 2F,G**). Apply a minimal amount to the copper tape near the end, and place the 5 mm square ohmic contact down onto the silver epoxy, leveling by pressing the corners with plastic-tipped tweezers (**Figure 2H**). *Caution: if too much silver epoxy is applied, leading to it contacting the edges of the sample, a short may occur, or the components of the silver epoxy may create additional features in the current density-voltage (J-V) curves. Apply only as much as needed to adhere to the sample. If the epoxy is observed to ooze up the edges of the sample after it is pressed down, too much has been added.*
6. Place samples in an oven to cure (50°C for 30 min, when using CW2400) (**Figure 2J**).
7. After the silver epoxy is cured, remove the electrodes from the oven and apply Kapton tape to tightly cover most of the copper tape (**Figure 2K**). Covering more of the tape here decreases the amount of epoxy needed in the next step.
8. Use the non-conductive epoxy to seal the remainder of the copper tape and the electrode edges from the electrolyte. Mix Loctite Hysol EA 9462 (**Figure 2L**) or another inert epoxy in a weigh boat or the other suitable surface with a separate wooden applicator (not the same one used for the silver epoxy to avoid inadvertent contamination with conductive particles), and spread the mixed epoxy to cover the edges of the photoelectrode. Roll the applicator, push a thick ridge of epoxy slightly over the photoelectrode edges to create a good surface area definition (**Figure 2M**), and wrap the epoxy slightly around the edges of the glass handle to create a good seal (**Figure 2N**). *While defining the surface area, leave as large an exposed surface area as possible while still sealing the edges from electrolyte exposure.* A well-defined edge is particularly important if the epoxy around the electrode surface is nominally opaque yet appears transparent when applied in a thin layer. Transparency at the edges will lead to area underestimation of the surface area that is exposed to light and, therefore, overestimation of current density. (For the purposes of this protocol, we neglect the imperfect transparency of "transparent epoxy" at short wavelengths.)
9. Allow Loctite 9462 epoxy to cure at room temperature overnight or allow other epoxy to cure as stated. A better quality of cured epoxy may be obtained for 9462 if done at room temperature rather than elevated temperature.

Illuminated Area Measurement

The electrode area exposed to electrolyte and/or illumination is directly proportional to the magnitude of the photocurrent. Therefore, it is important to accurately and consistently measure the exposed surface area of each electrode prior to commencing PEC measurements.

Once the epoxy is cured, the exposed geometric surface area must be measured, with the process summarized in **Figure 3**. A flatbed scanner is recommended for this purpose because it is accurate and typically readily available. Other imaging techniques, as long as they provide high resolution and are accurate, can be used to determine the area. One example is a camera with a macro lens, immobilized and calibrated at a set distance from the test surface and with corrections for lens distortion (Dunbar et al., 2015). Note: If instead of a nominally opaque epoxy, a transparent epoxy such as Epo-Tek 302-3M is used to seal the photoelectrode, the entire 5 mm square area will be used to calculate the current density. However, the surface should still be scanned to measure the 5 mm square area accurately.

1. Place the electrode on the flatbed scanner, so the electrode surface is held parallel to the scanner glass, and scan in grayscale with at least 1200 dpi resolution. Save as a .tif file. Lower resolution scans should not be used for measuring the surface area because they can introduce errors by the pixilation of the boundary between the electrode surface and the epoxy surface.
2. From the resolution of the scan, calculate the number of pixels/cm^2 as (dpi/2.54)^2. For example, for 2400 dpi, the conversion is 892802 pixels/cm^2.
3. Install free ImageJ software if not already installed. Load the scanned .tif file into ImageJ, and then select a region around the electrode surface with the rectangle tool and crop the image (Ctrl + Shift + X) (**Figure 3A**).
4. Find the surface of the electrode bordered by epoxy. Select Image > Adjust > Threshold (Ctrl + Shift + T), and move the bottom slider such that the red region covers the electrode area, leaving the area covered with epoxy gray. Click "Apply" (**Figure 3B**).
5. Select the electrode area with the magic wand tool and then Edit > Fill, and Edit > Clear Outside (**Figure 3C**).
6. Count the pixels using the histogram tool: Select Analyze > Histogram (Ctrl + H), observe if the electrode area corresponds to 0 or 255 on the grayscale, and then click "List" to get a count of the number of black and white pixels (**Figure 3D**). Divide the pixel count of the electrode surface area by the pixels/cm^2 from the scanner resolution to get the electrode surface area in square centimeters (**Figure 3E**). Alternatively, select Analyze > Measure to obtain the pixel count.

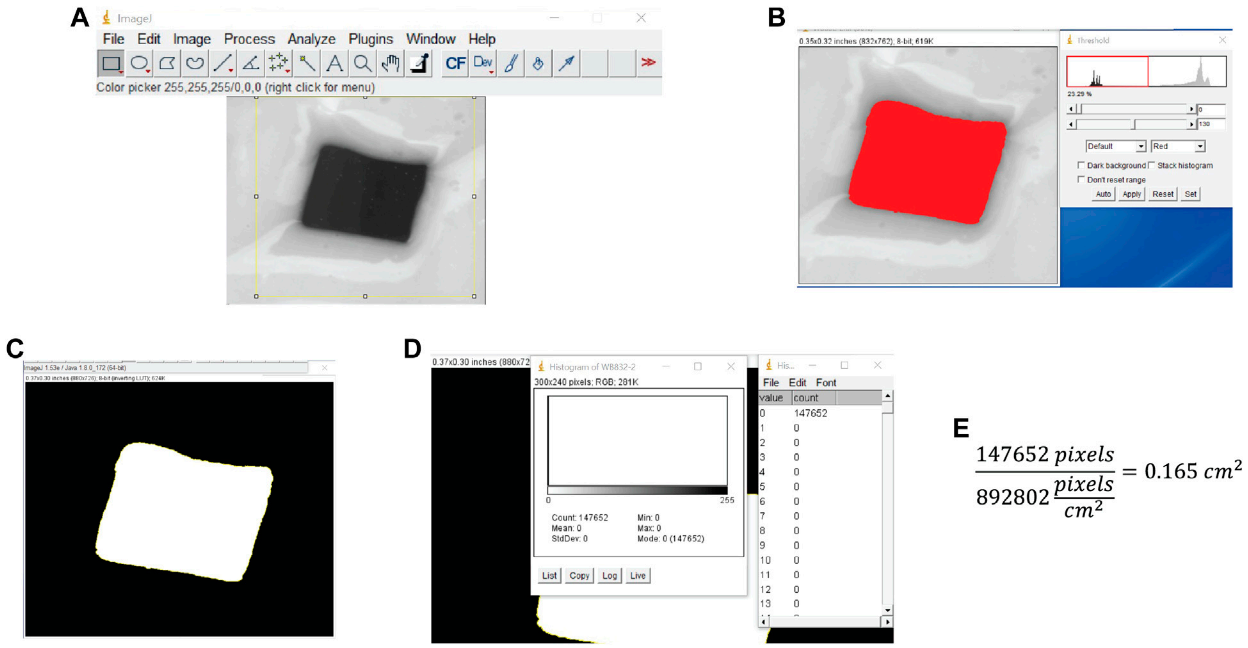

Color picker 255,255,255/0,0,0 (right click for menu)

0.35x0.32 inches (832x762); 8-bit; 619K

23.29 %

0

130

0.37x0.30 inches (880x72

300x240 pixels; RGB; 281K

0 255

Count: 147652
Mean: 0
StdDev: 0

Min: 0
Max: 0
Mode: 0 (147652)

value	count
0	147652
1	0
2	0
3	0
4	0
5	0
6	0
7	0
8	0
9	0
10	0
11	0
12	0
13	0

$$\frac{147652\ pixels}{892802\,\frac{pixels}{cm^2}} = 0.165\ cm^2$$

FIGURE 3 | Test electrode area determination. **(A)** Image is cropped to isolate the electrode surface. **(B)** The threshold is set by adjusting the slider to fill the entire electrode area while excluding surrounding epoxy. **(C)** The area is selected and filled to get a black and white image. **(D)** The number of pixels in the electrode surface area is determined using the histogram. **(E)** The surface area is computed by dividing the number of pixels in the surface area by the scan resolution in pixels/cm^2.

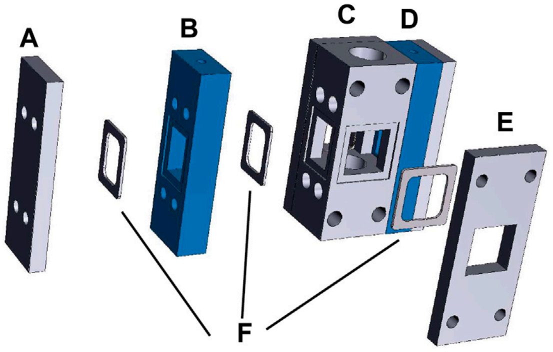

FIGURE 4 | Testing vessel design. **(A)** Compression plate for anode compartment 1. **(B)** Anode compartment 1. **(C)** Cathode compartment. **(D)** Assembled anode compartment 2. **(E)** Compression plate for cathode compartment. **(F)** Gaskets and O-rings to form gas- and liquid-tight seals.

To quantify the PEC properties of each electrode, skip to the section on PEC measurements. To perform testing vessel assembly for η_{STH} measurement of a 1 cm^2 sample, continue with Photoelectrode Integration section.

Photoelectrode Integration Into η_{STH} Testing Vessel

In order to measure the η_{STH} for a photocathode, the hydrogen produced must be accurately quantified while simultaneously measuring the photocurrent. To quantify the evolved hydrogen, gas chromatography (GC) should be used. To prevent leakage of H_2 and O_2 after their generation and separation, a well-sealed testing vessel is needed, which incorporates the photocathode (working electrode, or WE), counter electrode (CE), and a membrane separating the anode and cathode chambers. A reference electrode (RE) can be used for measuring η_F of a catalyst but should not be used in measuring or reporting η_F or η_{STH} of an integrated photocathode. In a PEC device deployed in the field, the anode and cathode compartments will be separated by a proton exchange membrane (PEM) or anion exchange membrane (AEM), depending on the pH of the electrolyte, to allow the collection of H_2 and O_2 without risking their loss or reaction through recombination. Because the membrane will have a potential drop across it, the presence of a membrane will change the output characteristics compared to a PEC cell with no membrane, and higher potentials may be needed for the integrated cell when a membrane is used. Therefore, the membrane separating the compartments is an integral part of accurately measuring η_{STH}, and the testing vessel used must accommodate it.

In this protocol, we use a testing vessel that accommodates a 1 cm^2 surface area photocathode and dual anode chambers, with the anodes oriented at 90° angles to the photocathode (**Figure 4**). Dual anodes and the 90° orientation between the photocathode and each anode are chosen to minimize asymmetric corrosion of the photocathode during a stability test. Compared to the 5 mm squares used in the previous section, the larger surface area used for this demonstrates the practical application of the PEC materials and demands

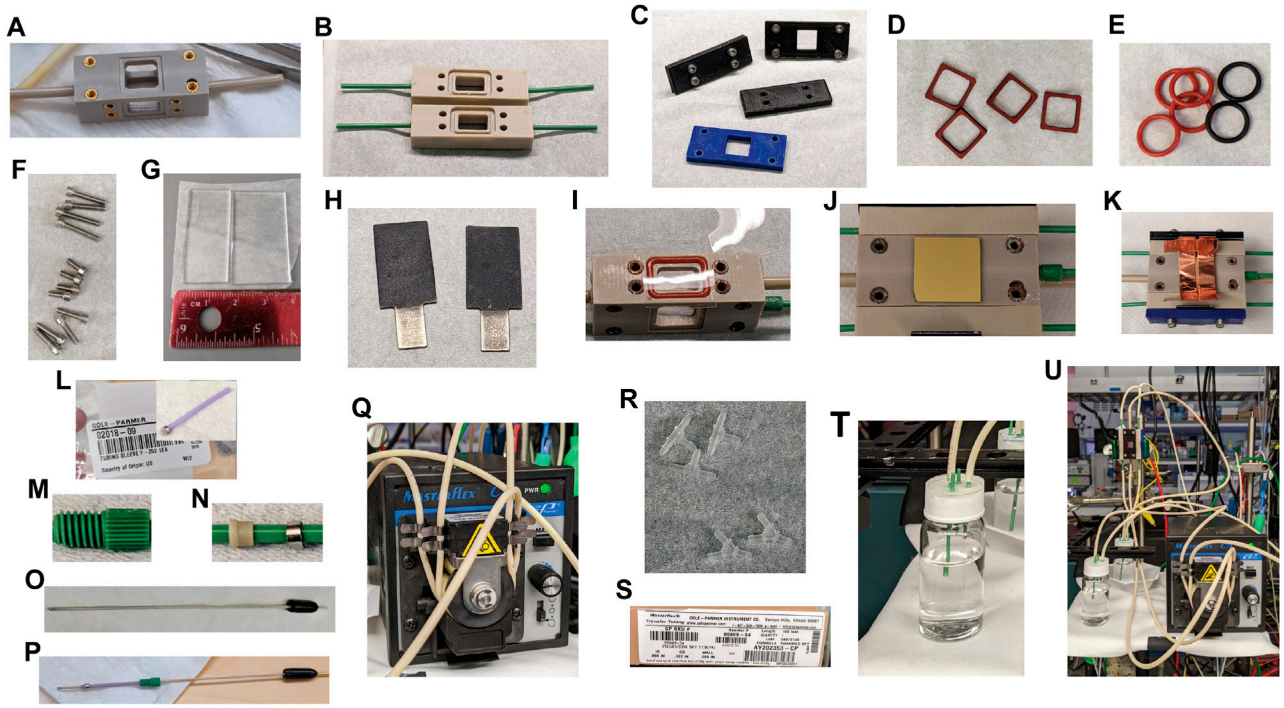

FIGURE 5 | Components of the testing vessel. **(A)** PEEK cathode compartment. **(B)** PEEK anode compartments. **(C)** 3D-printed PLA compression plates. **(D)** Laser-cut silicone gaskets. **(E)** Size 013 silicone and Viton O-rings. **(F)** 2–56 stainless steel screws. **(G)** Quartz glass window. **(H)** Iridium oxide anodes with integrated electrical connection. **(I)** Nafion 115 cut to fit. **(J)** 1.1 cm square photocathode with a back ohmic contact. **(K)** An electrical connection, like copper tape, to the photocathode. **(L)** F-252 tubing sleeve for the reference electrode. **(M)** IDEX M-644-03X flangeless nut. **(N)** IDEX M-650X ferrules. **(O)** LF-1 Ag/AgCl reference electrode. **(P)** Complete reference electrode assembly. **(Q)** Masterflex peristaltic pump. **(R)** 1/16″ PVDF barbed “Y” or “T” fittings. **(S)** 1.42 mm ID PharMed BPT tubing. **(T)** Electrolyte reservoirs. **(U)** Assembled cell, pump, and reservoirs.

a higher quality standard for photocathode synthesis. An ion exchange membrane is placed between the anode and cathode compartments to separate products, and the testing vessel is amenable to the front or back illumination of the photoelectrode. During PEC measurements, the electrolyte flows through the anode and cathode chambers and transports products out for quantification by the GC. The testing vessel can also be used for a 1 cm^2 photoanode and dual cathodes.

The milling machine, laser cutter, and 3D printer files for building the testing vessel are available on request.

Experimental Setup

The following components are required to assemble the testing vessel (**Figures 5A–P**):

1. The main body of cathode and anode compartments milled from polyether ether ketone (PEEK) plastic, assembled with threaded fittings and with glued (Epo-Tek 302-3M) PEEK tubing.
2. 3D-printed polylactic acid (PLA) compression plates for anodes, window, and cathode.
3. Silicone or Viton gaskets for sealing the photocathode and window.
4. Silicone or Viton O-rings for sealing between the anode, anode compartment, and membrane, and Nafion or other PEM.
5. 2–56 stainless steel screws for installing printed compression plates and hex wrench for assembly. Varying lengths needed depending on electrode and window thicknesses.
6. Fused silica or quartz window for front illumination, around 1.5 × 1.5 cm.
7. Two counter anodes with integrated electrical connections, no more than 1.2 cm wide, and two rectangles of Nafion approximately 0.5 × 1.2 cm.
8. Photocathode with ohmic contact and electrical connection, cut into 1.1 × 1.1 cm for a 1 cm^2 surface area that will be exposed to the electrolyte.
9. Reference electrode (Innovative Instruments 1 mm OD Ag/AgCl Ref Electrode) for three-electrode measurements or a sham RE made from sealed 1/16″ PEEK tubing if RE will not be needed.
10. Fittings for RE or sham RE assembly:
    a. IDEX M-650X Ferrules,
    b. IDEX M-644-03X flangeless nut,
    c. F-252 tubing sleeve for reference electrode (0.042″ ID × 1/16″ OD, for 1 mm OD tubing).

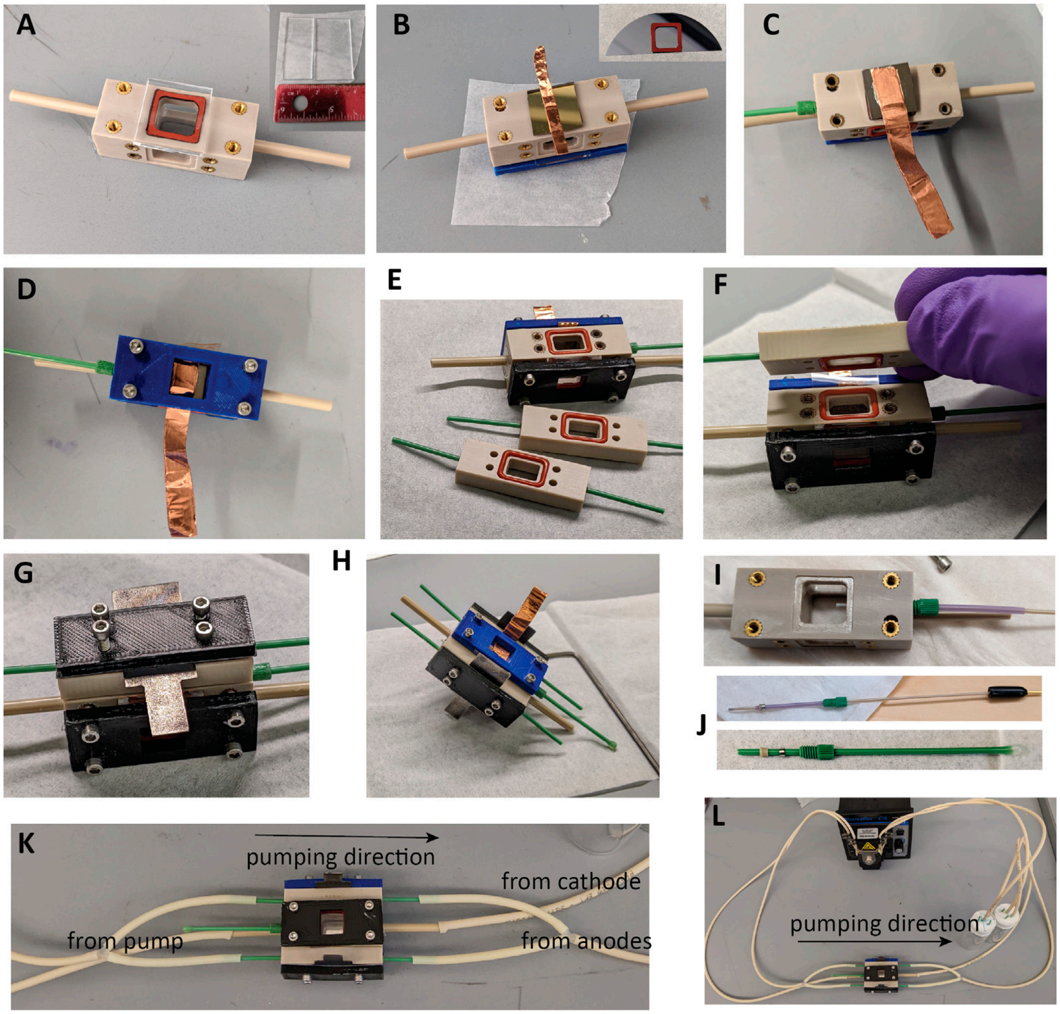

FIGURE 6 | Assembly of the testing vessel. **(A)** Placing window. **(B)** Placing a placing a photoelectrode with integrated ohmic contact and folded copper tape for the connector. **(C)** Photoelectrode with ohmic contact added using InGa eutectic, silver epoxy, and copper tape. **(D)** Compression plate added to WE. **(E)** O-rings added to anode chambers. **(F)** Nafion added. **(G)** Anode chamber added. **(H)** Assembled with one anode compartment. **(I)** Depth for reference electrode in the cell. **(J)** RE and sham assembly. **(K)** Tubing connections and flow direction. **(L)** Pump, testing vessel, and reservoirs.

The following fluidics components are required for electrolyte circulation through the testing vessel during measurement (**Figures 5Q–T**):

1. A two-channel peristaltic pump (e.g., Masterflex from Cole Parmer), which provides the desired flow rate, approximately 5–10 ml/min.
2. Tubing: PharMed BPT, 1.42 mm ID, ColeParmer #95809-34.
3. 1/16″ polyvinylidene fluoride (PVDF) barbed “Y” or “T” fittings.
4. Anolyte and catholyte reservoirs. For this example, 2 × 20 ml glass scintillation vials were assembled with four pieces of 1/16″ PEEK tubing sealed into the caps with epoxy. One piece of tubing should extend into the vial far enough to draw up electrolyte from the bottom, while the other three should be short enough to not contact electrolyte when the measurement is running. An air-tight epoxy seal can be obtained by running a lip of tape around each cap to make a well, adding the four tubing pieces, then filling the well ~1 mm deep with epoxy and allowing it to cure. One possible epoxy for this purpose is Epo-Tek 302-3M, used here. The “epoxy well” method of producing a thick epoxy layer produces a durable seal around the PEEK tubing, particularly when using corrosive electrolytes. An O-ring of appropriate size and material inside the cap is also required for an air-tight seal. One completed reservoir is shown in **Figure 5T**.

Parts should be cleaned before use: laser-cut gaskets should be sonicated in 10% nitric acid or soap and water prior to use. The leak-free reference electrode LF-1 should be stored assembled with the end submerged in 50 mM H_2SO_4. The quartz window should be cleaned with ethanol and dried with N_2. The Nafion PEM can be used dry (as-received) or soaked in electrolyte before assembly, with more difficult assembly with a soaked membrane but potentially also with quicker equilibration of the membrane and PEC cell through pre-hydration of the membrane.

Testing Vessel Assembly Procedure

The procedure is summarized in **Figure 6**:

1. Cut a piece of quartz glass or fused silica to 1.5 × 1.5 cm using the diamond scribe and running pliers. Place one of the square gaskets in the cell body on the side further from the RE inlet, and add the window (**Figure 6A**). Fix the front plate over a window with four screws, selecting screws long enough that there is even pressure on all sides, but avoiding bottoming out the screws, which may pull out threaded inserts and prevent sealing.
2. Using a diamond scribe dice the photocathode to ~1.1 × ~1.1 cm to fit the WE gasket (**Figure 6B**, inset).
3. If not already present, ohmic contact to the back should be made using the InGa eutectic alloy. Basically, for the material without preexisting ohmic contact, the steps discussed above for a photocathode without ohmic contact should be followed. The best process for the particular material should be determined by the experimenter. Care should be taken throughout this process to not generate uneven surfaces that will result in asymmetric pressures upon installation of the compression plate.
4. For photoelectrodes with an integrated ohmic contact as used here, InGa is not needed, and contact can be made by placing doubled conductive tape or other strong, pliable conductor on the back of the photoelectrode as in **Figure 6B** and holding it in place with the compression plate.
5. Place the second square gasket on the opposite side of the cell body, and add the prepared photocathode, followed by the second compression plate, arranging the electrical connector so it can be accessed from the long or short edge as desired. Add four screws of an appropriate length and tighten until just secured (**Figure 6D**). Overtightening the front and back plates can make them bend, eventually leading to electrolyte leaks, cracking a fragile sample, or pulling the threaded inserts out of the PEEK body.
6. Install O-rings in all six grooves of the anode compartments (**Figure 6E**). Viton O-rings can be used in contact with the counter electrode if transferring marks from silicone to the surface of the electrode is a concern. Use tweezers to add a piece of Nafion to one side (**Figure 6F**) and sandwich the Nafion with an anode compartment (**Figure 6G**). Add one anode and a compression plate with four long screws, and tighten the first anode compartment down (**Figure 6H**). To fully seat the O-rings and attain a good seal, tighten the screws until no gaps are visible between the main PEEK body and the PEEK anode compartment. Repeat to add the second anode.
7. Remove the RE assembly from the storage solution and screw it in firmly, or if not using a RE, the mockup/sham RE can be left installed between uses. Install the RE so that the tip extends into the chamber, as in **Figure 6I**. To prepare the RE or mockup for the first time, assemble components as illustrated in **Figure 6J** and screw them firmly into the RE port to set the ferrule and attain a permanent seal.
8. Attach tubing and a peristaltic pump between the cell and the electrolyte reservoirs and check for fluid leaks. See **Figure 6K** for suggested connections. The two CE chambers should be joined with Y- or T-connectors, or else three pump channels could be used. It is recommended that the cell be tested for electrolyte leaks with deionized water prior to adding an electrolyte to the reservoirs.

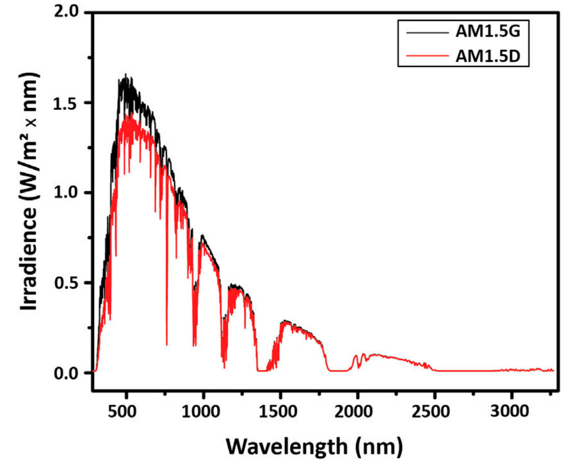

FIGURE 7 | Terrestrial spectral irradiance. Available at https://www.nrel.gov/grid/solar-resource/spectra-am1.5.html.

The use of this testing vessel for η_F and η_{STH} determination will be discussed below.

PEC MEASUREMENTS

Light Source Calibration

Broadband measurements used to measure the saturation current level, onset potential, and STH efficiency are done under illumination by a solar simulator that mimics natural sunlight. The individual solar simulator to be used should be calibrated against the known spectrum of the sun prior to broadband current density-voltage (J-V) or η_{STH} measurements. The absorption losses due to the absorption of quartz windows and water electrolytes are negligible for most photoelectrodes. However, absorption in water becomes important for $\lambda > 1000$ nm for water film thicknesses of a typical PEC testing vessel (~1 cm) and has to be accounted for smaller band gap absorbers and tandem absorber configurations (Döscher et al., 2014; Cendula et al., 2018; Moon et al., 2020). However, a PEC device in the field would experience similar UV/IR losses. Therefore, the reference spectrum and intensity should be calibrated at the front surface of the vessel to avoid errors that lead to artificially inflated performance values (Young et al., 2017). Additionally,

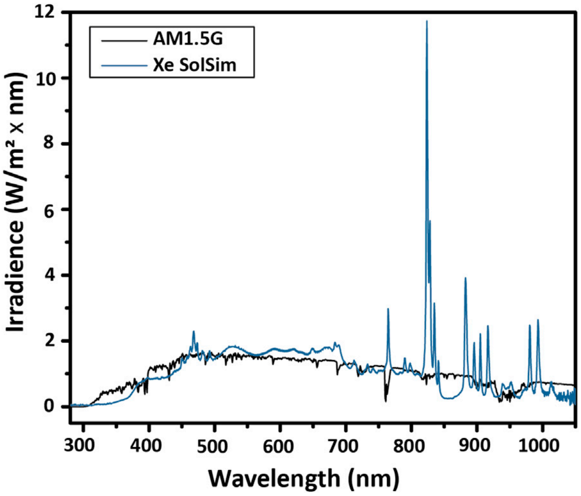

FIGURE 8 | Spectral mismatch. The spectral shape of the lamp (Xe SolSim) differs from that of the reference spectrum, particularly due to the strong emission lines of Xe lamps around 800 nm. For accurate calibration, either a band gap-matched, calibrated reference cell or a spectral mismatch calculation is required.

careful calibration is needed for monochromatic light sources to accurately measure quantum efficiencies.

The output of the sun is attenuated by the atmosphere to varying degrees depending on the latitude on earth, because of the different angles of the incidence of sunlight. The angle of incidence governs the air mass (AM) that the light has to travel through. The standardized solar spectrum used for testing is the AM1.5 spectrum, illustrated in **Figure 7**. It is used as the reference spectrum for terrestrial solar testing because it corresponds to the sunlight reaching the ground through the average air mass above global mid-latitude locations. The AM1.5G (global) spectrum has a total irradiance of 1000 W/m^2 and includes both direct and diffuse radiation, where diffuse radiation encompasses reflected and scattered light and is roughly 10% of the AM1.5G irradiance. The AM1.5D (direct) spectrum does not provide the diffuse component, only the direct component, and has a total irradiance of about 900 W/m^2. Because AM1.5G is more representative of real-world conditions, it is the standard for most terrestrial solar applications.

Broadband Solar Simulator Calibration

Solar simulators vary in their ability to replicate the AM1.5G spectrum, and in general, their intensity may be adjusted to provide the correct total irradiance to the test device. The intensity adjustment can be done using a calibrated reference cell, ideally one with a band gap equal to that of the test cell. The reference cell used here consists of a Si photovoltaic cell with a calibrated short-circuit current value of 27.2 mA under the AM1.5G spectrum. The reference cell is calibrated separately (often by an external standards laboratory) to give the short-circuit current under a particular reference spectrum at a well-defined total irradiance.

The reference cell (RC) is placed at a set distance from the simulator, and its short-circuit current ($I_{sim,RC}$) is measured. Then, the irradiance falling on the reference cell is adjusted until the output current equals the calibration value. The irradiance is adjusted by moving the reference cell closer to or farther from the solar simulator. While the total irradiance can also be adjusted by varying the power going to the lamp, changing the current can change the spectral output of the lamp, so this is not recommended. The adjustment is complete when the measured short-circuit current from the reference cell equals the calibrated short-circuit current under the reference spectrum $I_{sim,RC}$:

$$I_{sim,RC} = I_{ref,RC} = 27.2\,mA.$$

For this to be accurate, the band gap of the reference cell should match the band gap of the limiting junction of the photoabsorber under study. A Si reference cell will permit calibration for a Si photoabsorber, or another material with an equal band gap, to a reasonably high accuracy. However, a given photoabsorber that is studied may not have a band-gap-matched reference cell. In this situation, a reference cell of a different band gap may be used, with additional measurements made to compensate for the mismatch and accurately calibrate the solar simulator to deliver 1-sun illumination to the test cell.

Here, a Si reference cell with a band gap of 1.1 eV (1127 nm) is used to calibrate the total intensity of a xenon arc solar simulator to measure a GaInP test cell with a band gap of 1.8 eV (689 nm). In order to illustrate the issue that the mismatched band gaps can create, the spectrum of the lamp compared with the AM1.5G spectrum is shown in **Figure 8**. The total irradiance delivered to the Si reference cell corresponds to the integral from 1127 to 280 nm, and the total irradiance delivered to a GaInP test cell corresponds to the integral from 689 to 280 nm.

Because of the strong emission lines from Xe lamps above 800 nm, by setting the intensity of the lamp using a Si reference cell such that there is the correct total irradiance below 1127 nm, the total irradiance for GaInP is too low. This means that if the total irradiance is calibrated without adjusting for the spectral mismatch, the photocurrent of the GaInP cell under reference conditions will be underestimated.

The solar simulator output is adjusted using a spectral mismatch factor M to address this issue (derivation in (Osterwald, 1986)):

$$\mathrm{I_{sim,RC}} = \frac{\mathrm{I_{ref,RC}}}{\mathrm{M}}. \tag{3}$$

To calculate M, the spectrum of the solar simulator $\mathrm{E_{sim}}$, the reference spectrum $\mathrm{E_{ref}}$, and the spectral response of the reference and test cells, $\mathrm{S_{ref}}$ and $\mathrm{S_{test}}$, must be known. The spectrum of the solar simulator can be found using an irradiance calibrated spectrometer, while the AM1.5G reference spectrum is widely available, for instance, from https://www.nrel.gov/grid/solar-resource/spectra-am1.5.html.

Spectral response is determined by measuring the quantum efficiency (QE) of the test and reference cells, which will be discussed more in later sections.

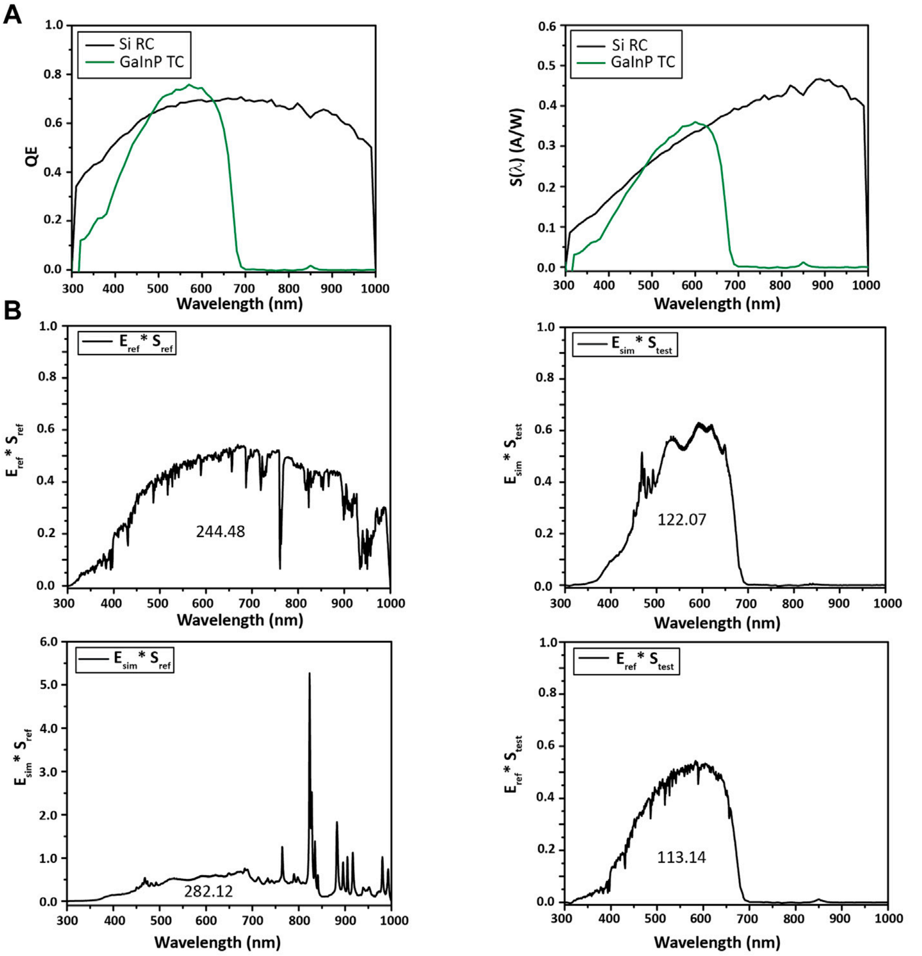

C

$$M = \frac{\int_{300}^{1000} E_{ref}(\lambda) * S_{ref}(\lambda)\, d\lambda}{\int_{300}^{1000} E_{sim}(\lambda) * S_{ref}(\lambda)\, d\lambda} * \frac{\int_{300}^{1000} E_{sim}(\lambda) * S_{test}(\lambda) d\lambda}{\int_{300}^{1000} E_{ref}(\lambda) * S_{test}(\lambda) d\lambda} = \left(\frac{244.48}{282.12}\right) * \left(\frac{122.07}{113.14}\right) = 0.94$$

FIGURE 9 | Calculating M for a Si reference cell (RC) and a GaInP test cell (TC). **(A)** Quantum efficiency and spectral response S(λ) from 300 to 1,000 nm. **(B)** Each product plotted against wavelength for calculating M, with the integral noted under the curve. **(C)** M is calculated to be 0.94 for this system, indicating the test cell should be moved closer to the solar simulator (vide infra). Specifically, the mismatch factor can be calculated with **Eq. 4**.

$$M = \frac{\int_a^b E_{ref}(\lambda) * S_{ref}(\lambda) d\lambda}{\int_a^b E_{sim}(\lambda) * S_{ref}(\lambda)\, d\lambda} * \frac{\int_a^b E_{sim}(\lambda) * S_{test}(\lambda) d\lambda}{\int_a^b E_{ref}(\lambda) * S_{test}(\lambda) d\lambda}. \tag{4}$$

The spectral response S(λ) is calculated from the QE by correcting for the relative energy of photons with different wavelengths:

$$S(\lambda)\left(\frac{A}{W}\right) = \frac{q\lambda}{hc} * QE(\lambda)\left(\frac{electrons}{photon}\right) = \frac{QE(\lambda) * \lambda(nm)}{1239.8}. \tag{5}$$

The quantum efficiency and spectral response of the reference and test cells are shown in **Figures 9A,B** for this example. In **Figure 9A**, the Si and GaInP test cells absorb light between the UV limit and their respective band gaps.

The spectral mismatch calculation is shown in **Figure 9C**. Numerical integration is done over the combined set of all wavelengths, with missing values filled in for each measurement by linear interpolation.

The details of the numerical methods during data collection and calculation can significantly affect the accuracy and precision of the calculated result. Because the various spectra were likely acquired at different sets of discrete wavelengths, it is necessary to interpolate the datasets to a common wavelength set for subsequent calculations. The best practice is to generate a single set of wavelengths that includes all of the various measurement wavelengths and then interpolate each spectrum to that common set. This scheme thereby preserves all of the original measurement information. The next-best option is to use the most granular of the individual datasets as the common wavelength set. For example, if the AM1.5G reference spectrum is measured every 0.5 nm but the spectral response is measured only every 10 nm, interpolate the spectral response data to the reference spectra wavelengths to generate the additional values.

In one suggested method for accomplishing this in an automated fashion, each spectrum can be imported into a Pandas dataframe in Python, followed by concatenation of the spectral response, solar simulator spectrum, and AM1.5G spectrum dataframes, and sorting by the wavelength column, for example:

```
df_all_list = [df_SR, df_sol_sim, df_am1pt5]
df_all = pd.concat(df_all_list, ignore_index = True)
df_all.sort_values(by = “nm”, ascending = True, inplace =
True)
```

Linear interpolation may then be done (a simple method uses Excel), followed by numerical integration and calculation of M.

Once the mismatch parameter is obtained, the absolute irradiance of the solar simulator can be set using the reference cell to complete calibration.

$$I_{sim,RC} = \frac{I_{ref,RC}}{M} = \frac{27.2\,mA}{0.94} = 28.9\,mA. \tag{6}$$

Additional information on this calculation, modifying the solar simulator spectrum by adding light emitting diodes (LEDs) to increase the intensity at specific wavelengths, and application to multijunction cells can be found in the literature (Osterwald, 1986; Moriarty et al., 2012). Note that the spectral mismatch M should be considered a correction factor rather than a random error. Failing to account for the mismatch systematically reduces the accuracy of the measurement by changing the irradiance. It does not simply increase the uncertainty of the measurement. A full treatment of the problems associated with large values of M is beyond the scope of this protocol.

For a multijunction material consisting of components with different light absorption properties, it may be difficult to set the absolute irradiance to satisfy all constituent cells with a given solar simulator. In general, one needs adjustable LEDs or narrow-band light sources and separate reference cells for each junction in the multijunction cell. If those features are not available, the irradiance should be set to provide 1 sun to the current-limiting junction, which can usually be determined from the QE or incident photon to current efficiency (IPCE) (below). This should be noted in the publication. In the example here, GaInP is the current-limiting junction, so the light source calibration was done to deliver 1 sun to that junction. It is also a good idea to estimate the irradiance to the other junctions using the spectral mismatch procedure described above to make sure that the assumed non-limiting junctions are, in fact, not limiting.

Monochromatic Light Source Calibration

Measuring QE for the reference and test cell in the previous section requires a monochromatic light source, typically consisting of a white light source combined with a monochromator. For determining QE, the photocurrent is measured as the wavelength is scanned; then, the photocurrent at each wavelength is normalized by the monochromatic light output. The light output is measured at each session using a photodiode (PD) of a known (calibrated) QE. Photodiodes with measured, NIST-traceable QE can be obtained from Thorlabs (e.g., ThorLabs FDS1010-CAL) or other vendors, or any other stable photodiodes can be calibrated using a spectrometer. The calibration data of the photodiodes are typically collected at short circuit, and they should be measured at short circuit here as well. The band gap of the PD has to be equal to or lower than the band gap of the investigated material.

The simplest method to find the monochromatic light power is to use a photodiode with an up-to-date factory calibration of spectral responsivity. Herein, a ThorLabs FDS1010-CAL photodiode was used to determine the output of the monochromator by measuring the photocurrent output at each wavelength and dividing by the value of the spectral responsivity at that wavelength (**Figure 10A**).

To calibrate a photodiode which was not factory calibrated, the monochromator power can be measured with a spectrometer; then, the responsivity plot can be generated from the ratio—at each wavelength—between the photodiode current and the measured power. In **Figure 10B**, the measured spectrum of each monochromatic wavelength of interest (300–1010 nm, in increments of 10 nm) is shown overlaid. The spectra were measured with an OceanOptics HR+C2276 spectrometer with a cosine corrector. The total optical power at each wavelength of the monochromator is found by integrating each spectrum. After the power spectrum is obtained, it can be used to calculate the responsivity curve of the photodiode that will be used during IPCE. Note a slight difference in scale between the measured and calculated monochromator power due to a different spot size used for the two photodiode measurements. However, the spot size will not affect the IPCE measurement because an underfill spot (only a fraction of the active area is illuminated) is used on the photodiode and sample at each measurement.

Monochromatic Photocurrent Measurement *via* Incident Photon-to-Current Efficiency

The photocurrent under a monochromatic light source is used to determine the spectral response of a PEC cell. QE—the efficiency with which photons are absorbed and converted into mobile electrons (i.e., current)—is a key measurement for PEC materials, just as it is important for characterizing photovoltaic (PV) materials. QE is also needed to calculate the spectral mismatch factor for light source calibration as in the previous section. For PEC, QE is measured by IPCE, where the photocurrent, as a function of wavelength, is determined for the photoelectrode. The wavelength of a monochromator is scanned while the short-circuit current is recorded, and the current is normalized to the light flux from the monochromatic source.

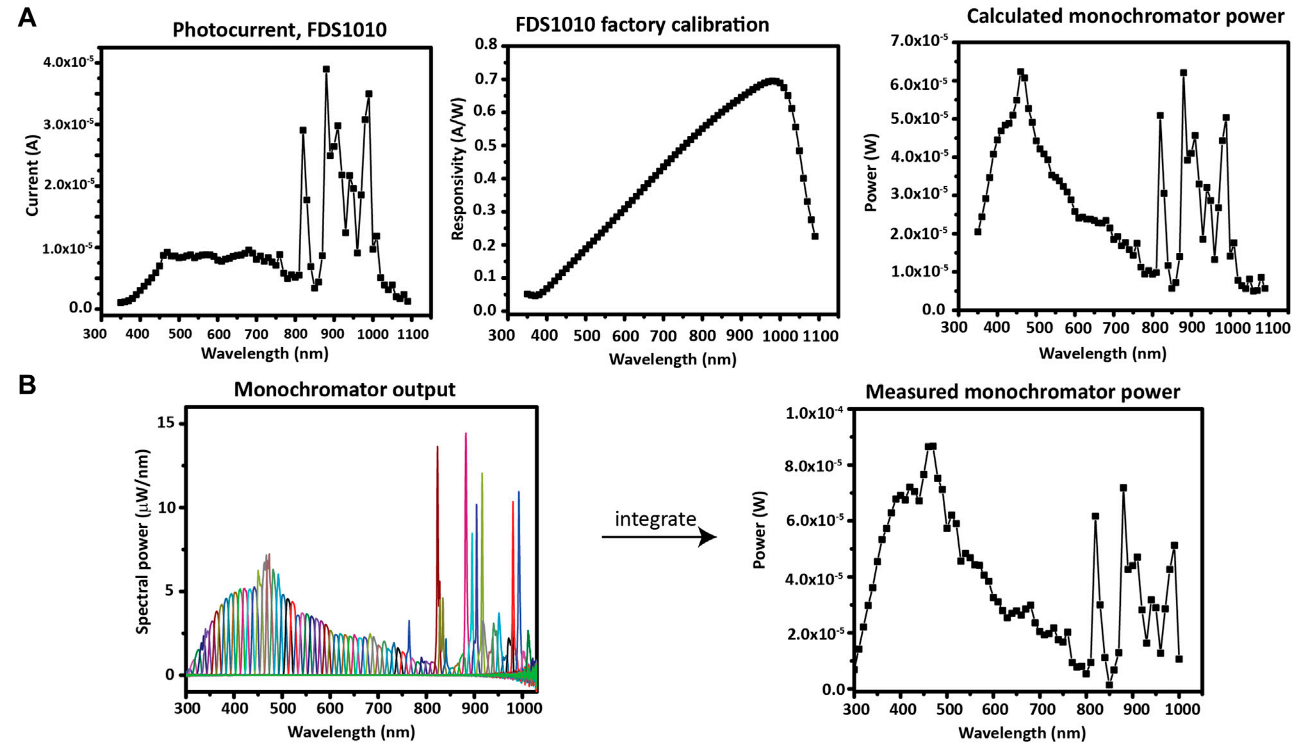

FIGURE 10 | Photodiode application and calibration. **(A)** Using a calibrated photodiode to measure monochromator output. **(B)** Measuring the monochromator output with a spectrometer in order to calibrate a photodiode.

The IPCE shows values between 0 and 1 in the region of the spectrum where the photoabsorber is sensitive. IPCE is generally a direct current measurement, in contrast to the QE measurement of solar cells, which is typically an alternating current measurement done with chopped monochromatic light and a lock-in amplifier.

Experimental Setup

Equipment:

1. Photoelectrodes prepared as above from 5 mm square samples.
2. Potentiostat.
3. IPCE testing vessel, that is, an electrochemical cell with optical glass/other optically transparent windows.
4. Counter electrode.
5. Reference electrode (if a bias must be applied to split water).
6. Broadband light source, monochromator, and second-order/order-sorting filters.
7. Bias light source(s), for example, high-power LEDs.
8. Calibrated photodiode.
9. Measurement automation, for example LabVIEW, to control the monochromator and potentiostat throughout the wavelength sweep, and control the shutter for measuring dark and light current.

Two examples of IPCE setups are shown in **Figure 11**, with components labeled, but other arrangements are possible.

Because the photocurrents measured during IPCE are relatively small, a dark box/enclosure must be used to enclose the entire optical path to eliminate interference from stray light.

Different experimental setups with respect to the electrical and light bias applied should be used depending on the type of the analyzed photocathode.

In all cases, the monochromatic light should fall fully within the photoelectrode active surface area and the active surface area of the calibrated photodiode. This is referred to below as forming an “underfill spot” on the photoelectrode/photodiode and is required to obtain meaningful results from an IPCE measurement.

For photocathodes that spontaneously split water, a two-electrode setup is used, with 0 V bias applied between the WE and CE. The CE should be a high-quality OER catalyst such as IrO_x. Report the CE and any other conditions used along with the IPCE.

For photocathodes that do not spontaneously split water, in order to apply a controlled bias during the measurement to attain water splitting, a three-electrode setup is used. The required bias is applied between the WE and RE as the wavelength is scanned and the photocurrent monitored. It is good practice to report these conditions along with the IPCE results.

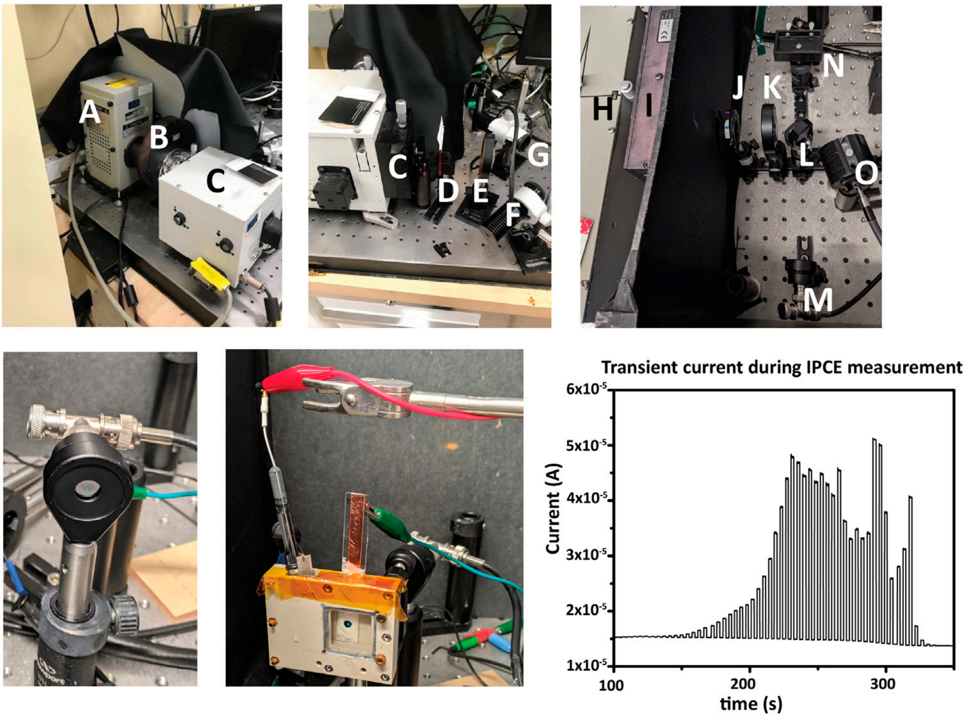

FIGURE 11 | IPCE measurement. Top row, two examples of instrumentational setup. **(A)** a Xe arc lamp, **(B)** computer-controlled shutter for generating light/dark conditions, **(C**,**H)** monochromators, **(D**,**I)** second-order filter(s) **(E**,**K)** lenses to focus monochromatic light to an underfilled spot on the sample, **(F**,**O)** high-power LEDs for applying bias light, and **(G**,**N)** the sample locations. Also shown is the option of using a mirror **(L)** to alternate directing the monochromatic light from the PD **(M)** and the sample **(N)**. An iris **(J)** can restrict or increase the total light intensity if needed. A dark box or enclosure surrounding the light path from the monochromator aperture to the sample is required to eliminate stray light from the measurement. Bottom row: at the start of each IPCE measurement, the photodiode current is measured to determine monochromator spectral output for the underfill spot. The underfilled spot is then aligned to the photoelectrode in the electrochemical cell, and bias lights and any electrical bias are set. Chronoamperometry is then measured simultaneously with the wavelength scan. Light and dark measurements can be shown during acquisition in the form of a transient photocurrent graph.

In addition to an electrical bias, a light bias is often used, for instance, through illuminating the sample with a high-power LED.

For single-junction photoelectrodes, a white light bias is often needed. A high-power LED such as a 1,000 mA Mightex fiber-coupled LED light source, outputting up to around 10 mW of illumination, can be used. A bias light is needed because the flux from the monochromator is typically much lower than that of an AM1.5G source in a given wavelength range, and additional illumination is needed to increase the signal/noise ratio of the photocurrent and fill trap states that would otherwise interfere with the measurement by artificially inflating the onset potential. The power of the bias light is set so that the photocurrent with the bias light, plus any electrical bias, is around 37% of the saturation photocurrent for the device (Chen et al., 2013), with adjustments made as needed after initial data are acquired.

For tandem or multijunction photoelectrodes, the total device photocurrent is that of the current-limiting junction (we neglect luminescent coupling effects here (Steiner et al., 2012). Thus, to measure the IPCE of each junction individually, the other junction is illuminated with a bias light of an appropriate wavelength. The intensity of the bias light is set high enough to saturate the second cell and make the first the current-limiting junction (and vice versa) so that the measured current from the PEC cell will correspond only to the photocurrent of the investigated junction. For the GaInP/GaAs tandem junction photoelectrode discussed in this study, a 470 nm LED bias light is used to saturate the GaInP cell while measuring IPCE of the GaAs subcell, and an 850 nm LED bias light is used to saturate the GaAs cell while measuring the IPCE of GaInP.

The flux of the LED should typically be several times that of the flux from the monochromatic source to ensure that the measured subcell is current-limiting at all wavelengths. To prevent issues resulting from this, the experimenter should make sure no features from the monochromator are observed in the IPCE measurement. For example, a Xe-based monochromatic light source will have several very large emission peaks in the IR. If corresponding features are observed in the IPCE measurement of the GaAs subcell of GaInP/GaAs, the bias light intensity to the GaInP subcell is not sufficiently high. Another way to assure high enough bias light intensity is with a calibrated photodiode or irradiance

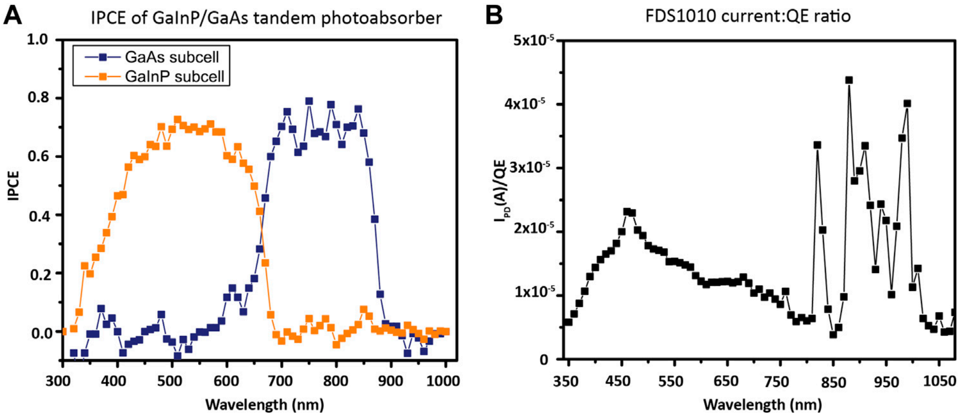

FIGURE 12 | IPCE calculation. **(A)** Two-electrode, 0 V bias, IPCE of GaInP/GaAs photocathode, acquired with 1 mW bias light illuminating the junction not being measured. **(B)** Calibrated photodiode photocurrent:QE ratio. Because the calibration of FDS1010 is done from 350 to 1050 nm, the *x*-axis between the two samples differs slightly.

calibrated spectrometer. For example, the 470 nm LED was set to 0.3 A to attain power from the LED of 1 mW after it was determined that the monochromator had around 400 µW reaching the GaInP cell.

For the GaInP/GaAs tandem photocathode, with a 1.8 eV/689 nm GaInP top junction and 1.4 eV/886 nm GaAs bottom junction, water is split at 0 V applied bias under an AM1.5G illumination source, so no electrical bias is used. As a multijunction photocathode, in order to measure the IPCE of the top GaInP cell, the bottom cell is illuminated with a high-power 850 nm LED while the monochromatic response of the cell as a whole is scanned. The infrared light causes excitation of the smaller band gap GaAs only, rendering the larger band gap GaInP current-limiting. To measure the IPCE of the bottom GaAs cell, the top cell is illuminated with a high-power 470 nm LED while the short-circuit current of the cell is measured (Young et al., 2017). The measured IPCE for this photocathode from 300 to 1000 nm is shown in **Figure 12A**.

A range of different electrochemical cell architectures can be used as a testing vessel for measuring IPCE, so long as an optically transparent window is present. Compression cells allow for easy sample mounting and make it possible to expose an identical surface area for each sample. On the other hand, as shown in **Figure 11**, a cuvette cell allows for rapid WE exchange and typically more flexibility in WE dimensions and in the used type of CE and/or RE. Here, we used a cuvette cell for characterization.

The IPCE spot size is also important. An underfill spot, where the monochromatic light spot is fully contained in the photodiode and WE surface area, is used for IPCE measurements. This means total irradiance is used in determining IPCE rather than spectral power density over the spot area. This is done to remove errors resulting from the relative concentration of the monochromatic spot in the PEC cell compared to the photodiode. Because all solar simulators have a diverging beam and J-V measurements are generally conducted with illumination overfilling the active area, the light is concentrated when passing through the air/glass/electrolyte interfaces of PEC cells (Döscher et al., 2016). This error is generally 10% or more for top-of-the-line commercial solar simulators but also depends on sample area and light pathlength through the electrolyte. Because the amount of concentration in the PEC cell compared to the photodiode (which has no electrolyte-caused concentration of light) is unknown, using an overfill spot will introduce a potentially large error into the experiment and should be avoided. Thus, IPCE measurements are performed with a spot size smaller than the active area of the sample (i.e., underfill illumination, with examples seen on both the photodiode and the WE in **Figure 11**) to serve as a validation measurement that is active-area independent and absent of the PEC cell concentration error. Focusing the light to an underfill spot for both the sample and the calibration photodiode also simplifies the calculation of IPCE, which would otherwise require measurement of the illuminated region of the sample and the photodiode.

Procedure

Because the output of the monochromator will vary as the lamp ages, the light output must be measured with the photodiode at a minimum at the start of each IPCE session, following lamp warmup. Most lamps require about 20 min of operation before the time-stable output is achieved, so this should be done before beginning measurements.

1. Turn on the lamp 20+ min before starting a measurement.
2. As lamp warms up, set up the PEC cell with the WE, CE, and optionally RE in the IPCE testing vessel. Confirm that the WE surface is fully immersed in the electrolyte solution.
3. The monochromator spot can also be aligned during the warm-up period. Set the monochromator to 550 nm, and focus the light to make an underfilled spot (light falls fully within the active area) on the photodiode (PD). Then, replace the PD with the assembled PEC cell, and adjust the location of the electrodes and cell so that the monochromatic light forms an underfill spot on the center of the WE. If needed, adjust the lens, iris, and/or mirror locations, distances, and angles to

obtain a focused underfill spot on both the PD and WE when one is simply switched for the other without adjusting optical angles. It is important not to inadvertently alter the light path between the PD measurement and the sample measurements.

4. Select a wavelength range over which to measure based on the expected band gap(s). A shutter should be employed to permit measuring light and dark current at each wavelength.
   - Non-ideal photoelectrodes that exhibit transient, capacitive current should allow sufficient time at each wavelength for the photocurrent to stabilize. Otherwise, the IPCE data will be inflated. Typical stabilization times can be several seconds or longer and chopping frequencies of 1 Hz or faster generally lead to error—hence a shutter is preferred to a chopper as the switching frequencies should be set to 0.2 Hz or slower to allow any capacitive currents to settle out.
5. To identify the suitable potential for IPCE measurements, for photoelectrodes that do not split water at zero bias, broadband J-V and/or chronoamperometry (CA) measurements should be carried out in a three-electrode setup. Generally, the bias may be selected based on the desired current density.
   - A direct translation between performance under 1-sun broadband and that of IPCE measurements is generally not expected. Because IPCE is measured at low light flux (uA), the kinetic overpotentials are lower than under broadband illumination (mA) and thus, this loss channel may not be accounted for in the IPCE measurement. For this reason, the integrated IPCE measurement should be considered the best-case, upper limit of photocurrent under broadband illumination.
6. Using the calibrated photodiode, measure the short-circuit current at each wavelength in the desired range with the chosen step size (typically 5–10 nm, but restricted by the peak width of the monochromatic light at each wavelength). During this measurement, the positioning should ensure that all of the monochromatic light is focused within the photodiode active area, and the photodiode should not be placed in a filled/empty beaker or any other "simulated" PEC condition. Dark current should be avoided or subtracted out using dark current measurements.
7. Following photodiode measurement, direct the monochromatic beam to an underfill spot on the photoelectrode in the PEC cell, turn on the bias light if needed, start the zero-bias or applied-bias CA measurement, and begin the monochromatic light sweep.
   - An example of an automation sequence that may be done in LabVIEW or other available software: the monochromator moves to a new wavelength, the shutter opens, potentiostat continuously records current, photocurrent is allowed to stabilize, a period of data points after stabilization is averaged, the shutter closes, potentiostat continues to record current, the current is allowed to stabilize, and a period of dark current data points after stabilization is averaged. If automation is not possible with available equipment, stepping the monochromator in a single step from a long wavelength corresponding to sub-band-gap photon energies to a short wavelength characterized by above-band-gap photon energy at the start of the sweep will create an instantaneous capacitance current that can be read in the measured current to identify the time at which the sweep began.

Other experimental considerations are presented below.

Luminescent coupling of multi-junction cells, where radiative recombination of carriers in one junction generates additional photocurrent in a neighboring junction, can lead to non-linear response as a function of the broadband light intensity. To determine if there is concern that this is a factor for the multijunction cell used, we can perform measurements at several bias light intensities for junctions other than the top junction and assess the linearity of response (Steiner and Geisz, 2012).

If reaction kinetics are limiting, a comparison of measurements with and without a facile redox couple could be used. If a redox couple is used that has absorption features overlapping with those of the measured photoelectrode, the electrolyte solution should be prepared with a low enough concentration of the redox couple to ensure that parasitic light absorption by the couple is minimized. Alternately, the absorption coefficients of the redox couple, combined with the known path length of the cell, can be used to correct the irradiance of the incident light to account for absorption by the redox couple. The presence of a redox couple should be reported along with the data.

Calculating IPCE

The QE of the calibrated photodiode is easily determined from its spectral responsivity (with an example of the factory calibration shown in the center panel of **Figure 10A**). From the QE of the photodiode (QE_{PD}) and the photocurrents of the photodiode and the photoelectrode (I_{PD} and I_{PEC}, respectively), the photoelectrode sample IPCE (QE_{PEC}) can be calculated by setting equal the ratios of the photocurrent/QE:

$$\frac{I_{PEC}}{QE_{PEC}} = \frac{I_{PD}}{QE_{PD}}. \quad (7)$$

Therefore, at each wavelength, IPCE should be calculated as I_{PEC} divided by I_{PD}/QE_{PD} (**Figure 12**). Prior to this calculation, the measured dark current should be subtracted from the measured current under illumination to obtain the photocurrent for each wavelength.

Broadband Photocurrent Measurement

The broadband photocurrent is measured under a solar simulator spanning all the wavelengths present in the AM1.5G spectrum. The photocurrent is a function not only of the photoelectrode but also of the specifics of the PEC cell setup, including the presence of a membrane and the electrolyte, and whether it is a two- or three-electrode configuration. In the case of a two-electrode configuration, the properties of the counter electrode are important. Therefore, each of these details should be reported precisely in publications and kept constant between

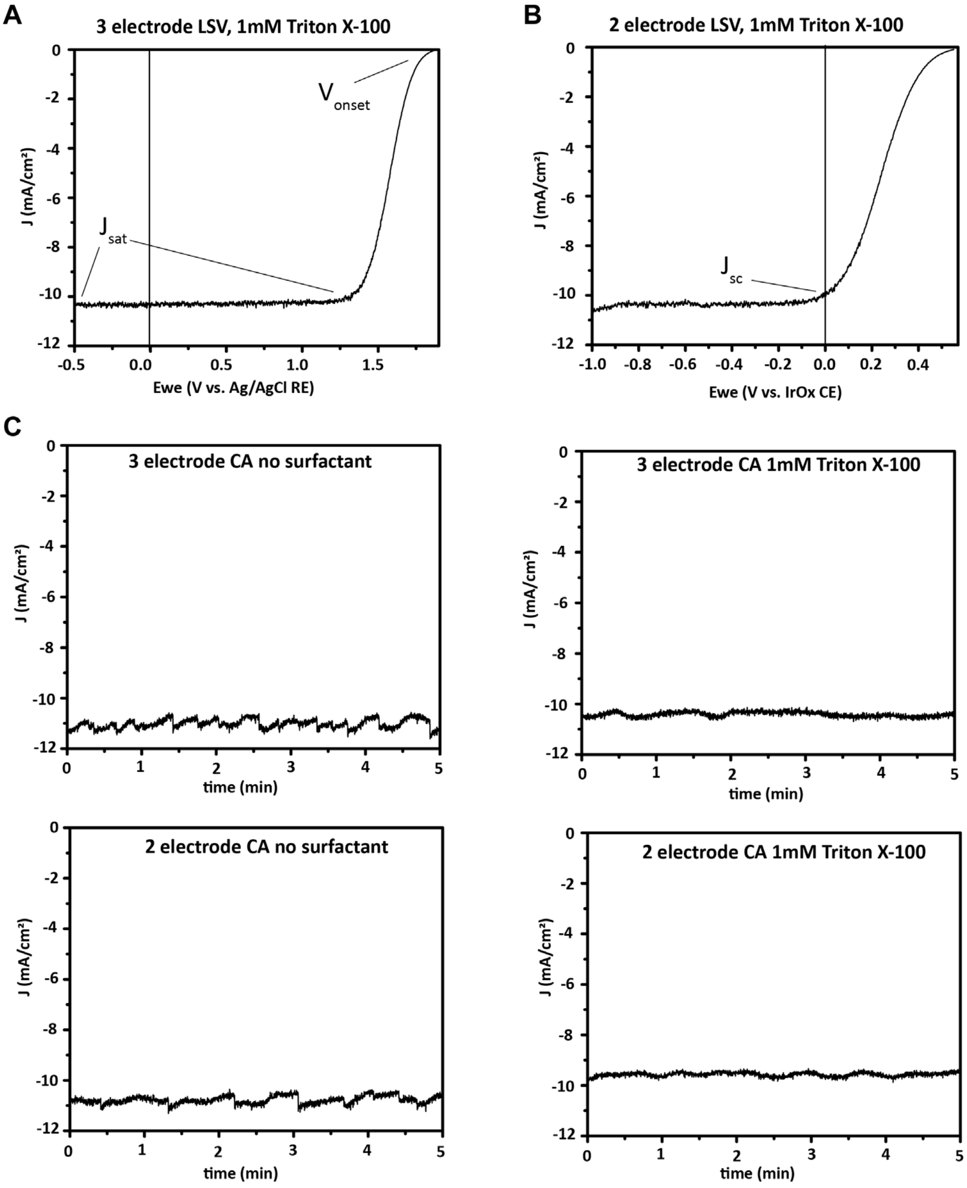

FIGURE 13 | Broadband PEC characterization. **(A)**, three-electrode and **(B)**, two-electrode linear sweep voltammetry (LSV or J-V) showing onset potential, saturation current density, and short-circuit current density for a III–V photoelectrode, in 0.5 M H_2SO_4 with 1 mM Triton X-100 surfactant. **(C)**, Photocurrent at 1-sun illumination and 0 V applied potential for a III–V photoelectrode. A comparison is made between two- and three-electrode bias free water splitting, and another between electrolyte with and without 1 mM Triton X-100 as surfactant effects on bias free water splitting. The electrode is seen to have similar currents in two- and three-electrode formats, with less variation in current over time when surfactant was used in the electrolyte. Surfactants such as Triton X-100 decrease the size of hydrogen bubbles formed, which prevents formation of large bubbles blocking portions of the photoelectrode. However, surfactant may decrease the average current, as seen here, while providing less variation over time by eliminating large bubbles.

measurements of a particular photoelectrode material. In addition, testing vessels for PEC water splitting may have various shapes and configurations that can affect the iR drop in the photoelectrochemical system. High concentrations of the electrolyte can help mitigate this issue.

Two broadband measurements will be discussed here. First, linear sweep voltammetry (LSV) can measure current J-V characteristics of the photoelectrode under the calibrated broadband source and provide photocurrent onset potential and current density at the desired operating potential. Second, the photocurrent can be measured over a period of time, designed to mimic operational conditions to track stability (chronoamperometry). The J-V characteristics of the cell prior to, during, and following the stability test can be used to understand changes in the performance of the photoelectrode and cell over time. Additionally, the measurement of the potential required to maintain a constant current (chronopotentiometry) can also provide information on the stability of the photoelectrode. Photoelectrode corrosion products can be tracked by inductively coupled plasma mass spectrometry (ICP-MS) of the used electrolyte and X-ray photoelectron spectroscopy (XPS) of the photoelectrode following completion of the durability test, although describing these measurements is outside the scope of this work.

LSV is used to measure the J-V characteristics of a PEC cell. The saturation current density, expressed in mA per cm^2 of electrode surface area, is a key metric for determining η_{STH} of a material. Onset potential determines if a PEC cell will generate enough photovoltage to operate bias-free. **Figures 13A,B** show a characteristic J-V curve when applying a bias negative of the onset of photocurrent in two- and three-electrode configurations.

CA is used to determine photoelectrode stability. In CA, the operation potential of the cell—0 V for a bias-free water-splitting material in a two-electrode configuration, or a non-zero applied potential in a three-electrode configuration if a bias is needed—is applied and the current is measured as a function of time under illumination. Alternatively, with chronopotentiometry (CP), a specific current density is maintained in the cell by altering the potential applied, and the applied potential is tracked. CA is often chosen for measuring the stability of photoelectrodes. In contrast, CP may be chosen to monitor the stability of stand-alone catalyst layers to determine how long the current density of interest can be driven through them before they fail. Prior to CP or CA, LSV is done and the operating point is selected (0 V in the case of the example here, as shown by the J_{sc} point in **Figure 13B**).

Following the stability test (1, 10, or 100 h, etc.), another LSV is done to monitor degradation in performance. During longer stability tests, it is common to stop the CP or CA periodically, for instance, every hour, and collect additional LSV so that changes in the J-V characteristics can be recorded over time. For example, recently, the J-V characteristics of a GaN/Si photocathode were tracked every 1–2 h over a 10 h CA measurement, and it was seen that the largest change in onset potential occurred during the first hour (Zeng et al., 2021).

Figure 13 illustrates the difference that surfactant in the electrolyte makes in the current profile of a CA measurement with 0 V applied bias. A surfactant lowers surface tension and encourages the formation of small bubbles, which are easily released from the photocathode surface. Large bubbles that form without a surfactant block part of the photocathode surface from light and electrolyte. This effect reduces the current until the bubble releases from the surface and generates a periodic fluctuation of the photocurrent.

Both two- and three-electrode measurements are useful for broadband measurements of a new PEC material.

In a three-electrode measurement, a known potential is applied between the WE and RE, and the properties of the WE are determined. In this measurement, the potential is dropped solely between the RE and the WE, and the potential of the RE remains essentially constant under small applied potentials. Therefore, sensitive measurement of the properties of the working photoelectrode in the specific cell and electrolyte can be made. In this case, the potential required to drive the hydrogen evolution reaction for a given photocathode can be determined independently of the CE reactions.

In a two-electrode measurement, on the contrary, the potential is applied between the WE and CE, and because the counter electrode has an unknown and undefined potential in the system, the onset potential measured in a two-electrode setup is the potential required for that system, with no independent values calculable for the photocathode specifically. Because of this difference, two-electrode properties such as η_{STH} of an integrated photoelectrode cannot be extrapolated from data collected in a three-electrode setup. In contrast, materials that do not split water at zero bias may still be quantified as to the amount of hydrogen produced. A three-electrode setup is used for this case, and a potential is applied between the RE and WE to provide the voltage needed for water splitting. However, these conditions must be reported, and the values obtained cannot be compared with two-electrode short-circuit water-splitting efficiencies since that attempts to replicate conditions that will be suitable to use in the field.

Two-electrode measurements are vital for demonstrating bias-free water splitting and quantifying η_{STH} because they mimic the real-world conditions of a PEC water-splitting device with only sunlight as an input. For example, **Figure 13** shows the two-electrode J-V and durability measurements for a GaInP/GaAs photocathode and an IrO_x anode. The J-V measurement illustrates that the material will perform bias-free water splitting, while the CA shows a slow decrease in photocurrent over the first hour of bias-free water splitting.

Experimental Setup

Equipment and supplies for broadband measurements:

1. Photoelectrode(s) as the working electrode.
2. Potentiostat.
3. Testing vessel (can be the same used for IPCE).
4. Counter electrode.
5. Reference electrode.
6. Broadband light source.

The PEC cell should be set up the same way as IPCE, except that a reference electrode is needed to obtain three-electrode measurements, irrespective of if the photocathode splits water at 0 V applied bias. Three-electrode measurements allow the characterization of the new PEC material alone, independent of the CE, and can be informative for material development.

Procedure

J-V analysis:

1. Prior to a measurement, warm up the lamp for 20+ min with the shutter closed. During that time, set up the PEC cell in a three-electrode format (WE, CE, and RE, each clipped to the appropriate potentiostat lead). The WE should be fully immersed, and at least, an equal area of the CE should also be immersed in the electrolyte.
2. Set the potentiostat to perform LSV in the region of interest. For cathodic currents for HER, with the

photocathode as the WE, the potential should scan from negative values to the open-circuit voltage (V_{oc}). If anodic currents are known to damage the photocathode, it is important to stop the scan before the current crosses the x-axis (i.e., becomes positive) and to scan from negative values toward V_{oc}, which prevents a small anodic current from being drawn through variation of the V_{oc} between the initial measurement and the start of the LSV scan. Input the surface area of the WE measured previously into the potentiostat software. The scan rate should be set to no more than 10–20 mV/s to avoid non-Faradaic current contributions that artificially inflate measured current values. The potential range and scan rate should both be reported when publishing.

3. With the shutter still closed, perform an LSV scan in the dark to confirm there is minimal dark current. Then, open the shutter and collect an illuminated LSV scan. Alternatively, a single scan where the light is chopped every other 100 mV can collect dark and illuminated responses in a single run, but illumination should not be blocked within a few 100 mV of V_{oc}.
4. Unclip the potentiostat lead from the RE in the PEC cell, and clip it onto the CE to short the potentiostat RE and CE leads. Run a two-electrode LSV.
5. Finally, replace the RE lead and run a second three-electrode LSV. This can later be used for a comparison with the first scan.
6. Repeat the 3-2-3 series of measurements with additional photoelectrodes.

Stability:

1. Prior to a stability test, measure dark and light LSV in the same format (two- *vs*. three-electrode) as is planned for the stability test.
2. Set up the potentiostat for CA with a constant voltage (can be 0 V) applied. It can also be set up to periodically measure LSV, for example, alternating 1 h of CA with an LSV measurement. One important consideration is the total length of the file—if many hours or days of data will be collected, it is best to collect a data point only once per second or once per 5 s. Otherwise, it is possible to produce unmanageably large files.
3. Run the CA.

Data

In the software of your choice, divide the current from the potentiostat in mA by the measured area in cm^2 before plotting LSV, CA, or CP. See above for surface area measurement. Some potentiostat software may permit exporting data in terms of current density if the surface area is entered into the experimental parameters, and most software will show a plot of current density as the experiment is running if the surface area has been entered as a parameter.

Record the saturation current density and the onset potential for each LSV. We find that the definition of onset potential for a photoelectrochemical reaction may have different descriptions across the field (Zou and Zhang, 2015). It is sometimes defined by the potential at which the current density reaches a certain value, for instance, 1–10 mA/cm^2, or as the potential at the intersection of a line fit to the squared photocurrent in the region near the onset potential of the LSV with the voltage axis (Chen et al., 2013). When reporting results, state clearly how the onset potential is defined for your system, along with reporting its values.

Measurement of Faradaic Efficiency and Solar-to-Hydrogen Efficiency

The Faradaic efficiency η_F, is the efficiency with which electrical current is converted into hydrogen and oxygen in an electrochemical cell; see **Eq. 8**. Hydrogen consumes two electrons per molecule H_2 produced, while oxygen produces four electrons per O_2 molecule produced.

$$\eta_{F,\,H2} = \frac{(H_2\text{produced})}{(\text{measured current})} = \frac{\left(\frac{\text{mol}}{\text{s}} H_2 * \frac{2e^-}{H_2} * F\left(\frac{\text{C}}{\text{mol}}\right)\right)}{\text{I (A)}}$$

$$\eta_{F,\,O2} = \frac{(O_2\text{produced})}{(\text{measured current})} = \frac{\left(\frac{\text{mol}}{\text{s}} O_2 * \frac{4e^-}{O_2} * F\left(\frac{\text{C}}{\text{mol}}\right)\right)}{\text{I (A)}}\ . \quad (8)$$

This is equivalent to the fraction of current measured in the PEC circuit consumed in the water reduction and oxidation half-reactions, not considering product losses. A less than 100% η_F indicates competing electrochemical reactions, recombination of products prior to collection, loss of products prior to measurement, and/or membrane crossover in the testing vessel.

STH efficiency or η_{STH} is the efficiency with which incident sunlight is turned into hydrogen (and oxygen).

η_{STH} can be calculated by first measuring η_F and then using **Eq. 1** (repeated) here:

$$\eta_{STH} = \frac{j_{sc}\left(\frac{mA}{cm^2}\right) * 1.23V * \eta_F}{P_{total}\left(\frac{mW}{cm^2}\right)}.$$

In this equation, J_{sc} is the short-circuit current density from a two-electrode measurement (not from a three-electrode measurement). The amount of H_2 produced is best measured with a GC, though volumetric methods (i.e., the Hofmann apparatus used by Chen et al. (2011)) can also be used if corrected using the vapor pressure of water at the collection temperature. While the evolved gas can be quantified by GC either by periodically sampling with a syringe or using a continuous purge of carrier gas, the latter method is preferred because sampling with a syringe may be subjected to sample contamination with air (Wang et al., 2021). Therefore, a closed electrolyte loop and a closed carrier gas channel loop through the electrolyte reservoir's head space is used in this protocol as a demonstration.

For determining η_F, a two-electrode CA at 0 V WE/CE bias under 1-sun illumination is run, and the amount of H_2 produced is measured. The sealed compression cell presented above can be used as the testing vessel for this purpose, as done here for GaInP/GaAs. For materials that do not split water at zero bias, a three-

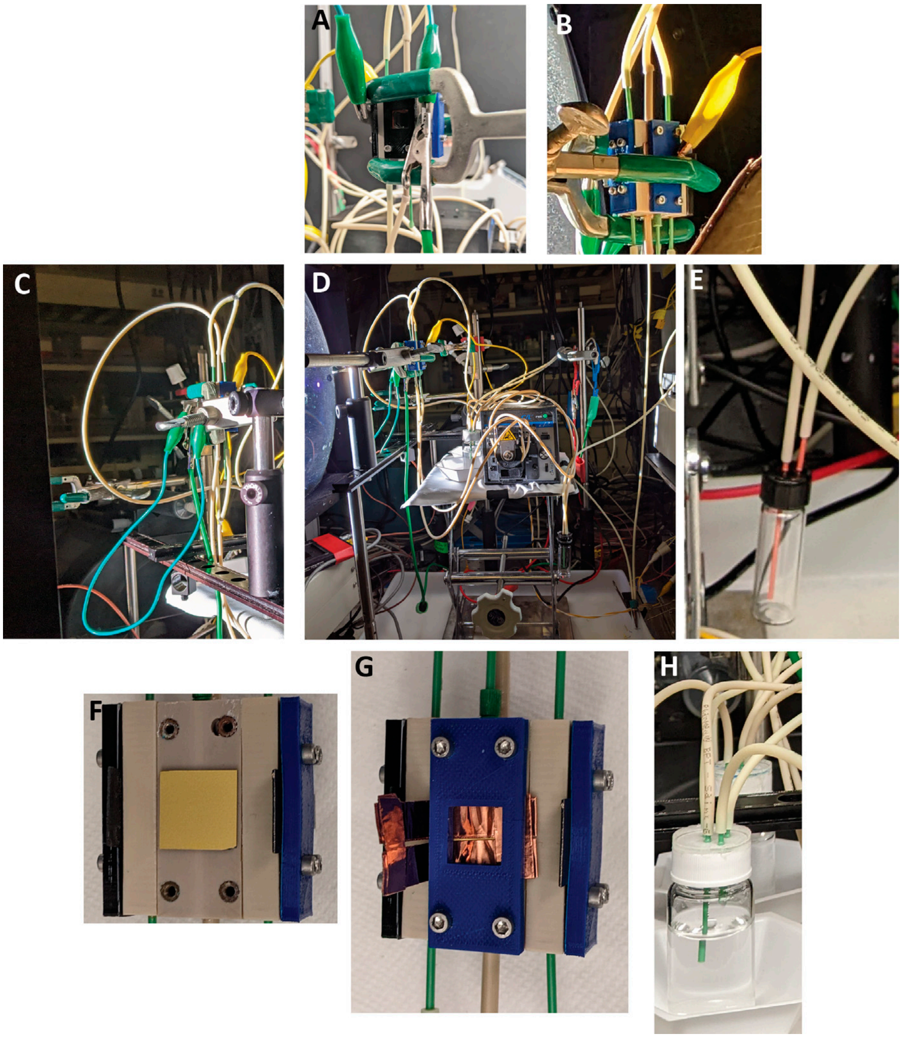

FIGURE 14 | Schematic of η_F measurement. **(A)** Anode connections to potentiostat. **(B)** Photocathode connection to potentiostat. **(C)** Testing vessel clamped at a distance of 1-sun from the solar simulator. **(D)** Test vessel setup: solar simulator on left, electrolyte pump, and reservoirs in the center, and GC traps leading to the GC on the right. **(E)** A liquid trap placed between the electrolyte reservoir head space and the GC to prevent liquid from being drawn into the GC. **(F)** Photocathode. **(G)** Electrical connection for photocathode and compression plate. **(H)** Two electrolyte reservoirs with carrier gas inlets and outlets connected to the GC traps, in addition to the electrolyte circulation inlet and outlet.

electrode CA can be done with a voltage applied between the WE and RE, but this alternative setup must be clearly stated in reporting results, and the results cannot be extrapolated to indicate η_{STH} of the photoelectrode.

Experimental Setup

Required equipment:

1. Sealed compression cell described above.
2. Gas-tight electrolyte reservoirs and tubing connections.
3. Gas-tight traps to prevent liquid from entering the GC.
4. WE and CE of appropriate form factors for compression cell.
5. Reference electrode (if a bias must be applied to split water).
6. GC.
7. Broadband light source.
8. Computer hardware and software such that timestamps can be synchronized between CA and GC output data to correlate changes in products with changes in current. The log files of mass flow meters may be used to quantify product streams for accurate η_F/η_{STH} calculation.

The specifics of GC operation will differ depending on the system, and we provide here an overview of the process of η_F measurement using an Agilent GC. Adjustments should be made based on the equipment available. **Figure 14** details the experimental setup used here with the above equipment.

An inert gas, N_2 or Ar, is used as a carrier gas flowing through the head space of both electrolyte reservoirs. It is beneficial to measure both H_2 and O_2 production to confirm no leaks in the system (see data analysis section) and detect possible corrosion reactions (Kistler et al., 2019). Therefore, the head space of both anolyte and catholyte reservoirs should be sampled. The carrier gas flow rate should be chosen accordingly to place the concentration of H_2 and O_2 within the calibration range of the GC and speed up the equilibration of the system and GC readings. Greater flow rates have the benefit of resulting in quicker measurement of the generated H_2 because it is pushed faster from the reservoir head space to the GC. However, a too high flow rate will decrease the signal-to-noise ratio of the GC peaks. In extreme cases, it can also dilute the H_2 beyond the limit of detection of the GC, so some experimentation may be required to find the optimal flow rate. Faster equilibration may be obtained by first flushing the electrolyte reservoir headspaces with carrier gas for 20 min before beginning the experiment. The choice of the carrier gas can be determined by the location of the N_2 peak in the particular GC spectrum. If it overlaps with the peak of interest, Ar can be used instead.

Prior to measurement, the GC should be calibrated by delivering a series of known concentrations of H_2 and O_2 using calibrated flow controllers/meters, ideally at the flow rate used in the η_F measurement.

Warm up the calibrated solar simulator for 20+ min before taking any measurements. The flow rates of carrier gas are ideally controlled programmatically, for example, by LabVIEW.

1. Testing vessel setup:
   a. Assemble the compression cell, including WE, CE, and optional RE, and attach anode and cathode chambers to the electrolyte reservoirs with tubing. Circulate the electrolyte with a previously calibrated peristaltic pump. The flow rate used for the examples here is 10 ml/min.
      i. Clamp the cell such that the photoelectrode is in the plane of the 1-sun calibration for the solar simulator.
2. Mass flow controller (MFC) setup:
   a. Typically, the inlet of the carrier gas will be controlled by one MFC, and a mass flow meter (MFM) will measure the flow rate at the outlet of the GC column. Confirm that the correct gas (N_2 or Ar) is selected on each MFC and MFM.
   b. Set the flow rate of the carrier gas to 1 SCCM (standard cubic centimeter per minute) to prevent liquid from the reservoir that is pushed up into the MFC. Attach the tubing from each of the two GC inlets to the outlet of an air-tight trap, and then attach the trap inlets to the anolyte and catholyte reservoirs. The traps are required to prevent the electrolyte from entering the GC. The volume in the trap should be minimized to decrease the dead volume between the reservoirs and the GC, which will decrease the time to the equilibrium of H_2 and O_2 peaks. However, during longer tests, the volume in the trap should still be sufficient to protect the GC.
3. GC setup:
   a. Load a sequence that samples from the H_2 and O_2 reservoirs, either simultaneously or alternately. The sequence should repeat for a minimum of 2 h the first time a photoelectrode is measured, so equilibration time and stability can be assessed. Depending on the column, measurements are taken approximately every 10 min. With the Agilent GC used here, one is taken every 7.5 min. Specifics will be determined by the GC used.
4. Potentiostat setup:
   a. Connect the WE and CE (and RE if used) of the PEC cell to the appropriate leads to the potentiostat. If doing a two-electrode measurement with no RE, short the potentiostat RE and CE leads.
   b. Input the appropriate surface area (1 cm^2 for the testing vessel used here) as the area of the WE, and set the desired potentials for LSV. The potentials required may be higher than those observed during broadband PEC measurements due to the dimensions of the compression cell and the presence of a membrane between the WE and CE chambers.
   c. Collect a dark current LSV, then open the shutter to the solar simulator, and collect an illuminated LSV.
   d. Select the potential or current to run the CP or CA. For a short-circuit photoabsorber measurement of η_F and η_{STH}, run CA and set the potential in the potentiostat software at 0 V between the WE and the CE. If measuring catalyst η_F with no photoabsorber, run CP at the desired current density (e.g., 10 mA/cm^2) instead.

Procedure

Control sample measurement:

Prior to measuring η_{STH} from a test sample, the testing vessel and the airtight seal of the setup should be validated by performing two-electrode electrolysis of water with good HER and OER electrodes (such as Pt and IrO_x) in an acidic electrolyte such as 0.5 M H_2SO_4. The H_2 and O_2 generated should be quantified by GC over a period of at least a few hours to confirm that near 100% η_F is measured. Note: Tilt the cell to a 45° angle during operation to improve bubble clearance and FE measurement if the FE measured here is below 95%.

Test sample measurement:

1. Increase the flow rates for carrier gas to the desired set point, and confirm that the pressure holds within the system by checking the measured mass flow rates at the outlet are equal to those at the inlet.
2. Begin the GC sequence, and monitor the O_2 peak until it stabilizes. This indicates that the remaining oxygen in the system has been flushed out.
3. Once the GC measures a stable baseline, start the CA measurement and open the shutter to the light source.
4. Monitor peak heights in the GCs and confirm they increase from baseline and become stable if the measured photocurrent is stable. Run until sufficient data are collected or the photocurrent from the sample dies off, recording the flow rate at the GC outlet mass flow meters prior to each injection.
5. Export data from the potentiostat, GC, and mass flow meters for analysis.

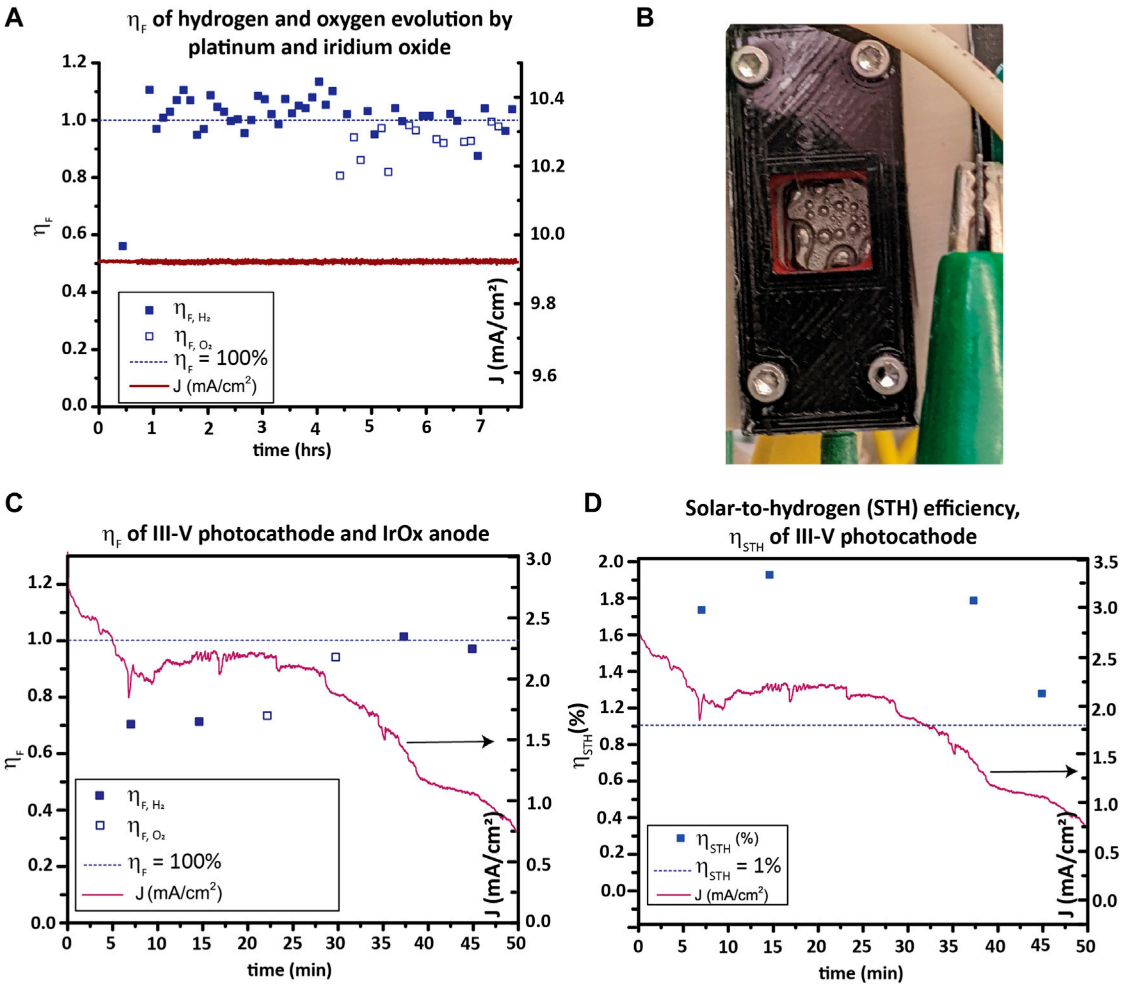

FIGURE 15 | η_F and η_{STH}. **(A)** Hydrogen and oxygen evolution faradaic efficiency (η_F) of a Pt WE and IrO_x CE in 0.5 M H_2SO_4 over 7 h. Average measured η_F is 103% +/− 5% for HER and 93% +/− 6% for OER, with likely sources of loss being minor system leaks and minor crossover and recombination. **(B)** Hydrogen evolution from a Pt foil electrode in the test vessel during the η_F measurement in **(A)**. **(C)** H_2 and O_2 η_F of a GaInP/GaAs photocathode and IrO_x anode in a two-electrode CA measurement. **(D)** η_{STH} calculated from **(C)**.

Calculations

Peak areas are converted into mol/s product generated. The measured photocurrent is aligned with the peaks by matching potentiostat and GC timestamps.

1. Convert peak areas to mol/s:
   a. Find the concentration (in ppm) for each peak using the GC calibration for H_2.
   b. Calculate mol/s H_2 produced for each peak by multiplying the measured concentration with the mass flow rate at the GC outlet converted to mol/s.
2. Calculate η_F from the mol/s H_2 produced and the measured current.
3. Line up the calculated η_F with the CA data for H_2 and O_2.
4. From η_F, calculate η_{STH} as discussed above. P_{total} is taken as the total irradiance of the AM1.5G reference spectrum of 100 mW/cm^2.
5. In the present example, the initial Pt/IrO_x electrolysis benchmark in a two-electrode configuration, 20 mA/cm^2 CP, displays η_F of around 100% for H_2 and O_2, indicating that the system has minimal product losses (see **Figure 15A**). After benchmarking with Pt/IrO_x, the η_F of GaInP/GaAs was measured in the same testing vessel, ranging between 70% and 100%. Due to the short lifetime of the photocathode, only a limited number of measurements could be taken before the current density dropped off (**Figure 15C**). The η_{STH} calculated is shown in **Figure 15D**. While the photocurrent and hydrogen production from the sample dies off in under an hour, η_{STH} is shown to be 1.2%–1.9% for the tandem photocathode over that time.

Membrane Crossover Quantification

While proton exchange membranes such as Nafion selectively transport protons while excluding anionic species, they have some permeability to gases. The permeation of H_2 from the cathode chamber to the anode chamber through the membrane (i.e., membrane crossover) is estimated by quantifying the H_2

Acronym	Stands for	Definition/comments
AEM	Anion exchange membrane	Membrane which selectively conducts anions such as hydroxide
AM1.5G	Global standard spectrum air mass (AM) 1.5	Global standard spectrum
AM1.5D	Direct standard spectrum air mass (AM) 1.5	Direct standard spectrum
CA	Chronoamperometry	Measurement of photocurrent over time used to measure the durability of a photoelectrode
CE	Counter electrode	Auxiliary electrodes in two- or three-electrode setup
QE	Quantum efficiency	Measurement of photogenerated electron/hole collection as photocurrent
η_F	Faradaic efficiency	Measured efficiency of electrical current to product generation (H_2 or O_2)
HER	Hydrogen evolution reaction	Cathode reaction in the PEC water-splitting device
GC	Gas chromatograph	Used to quantify hydrogen and oxygen production
ICP-MS	Inductively coupled plasma mass spectrometry	Method for analyzing trace metals in the electrolyte following a stability
IPCE	Incident photon-to-current efficiency	QE measurement of a photoelectrochemical material
J-V	Current density/voltage measurement	Measurement of photocurrent density over a range of applied voltages
GC	Linear sweep voltammetry	Shows saturation current, maximum power point, and onset potential
LED	Light-emitting diode	Used to even out solar simulator spectra
MFC	Mass flow controller	Sets the volumetric flow rate of inert gas
MOVPE	Metalorganic vapor-phase epitaxy	Use for controlled growth of high quality photoabsorbers
OER	Oxygen evolution reaction	Anode reaction in the a PEC water-splitting device
PEM	Proton exchange membrane	Membrane which selectively conducts cations such as protons
PD	Photodiode	Used in IPCE calibration
PEEK	Polyether ether ketone	Machinable polymer with good thermal and chemical properties
PLA	Polylactic acid	One type of 3D printing filament
PVDF	Polyvinylidene fluoride	Inert polymer used for barbed tubing connectors
PEC	Photoelectrochemical	Solar-to-fuel conversion carriers performed by an integrated photoelectrode
PV	Photovoltaic	Solar-to-electric conversion technology
RE	Reference electrode	Electrodes for potential reference in three-electrode setup
RC	Reference cell	Solar cell with calibrated photocurrent at 1 sun illumination
η_{STH}	Solar-to-hydrogen efficiency	Efficiency of hydrogen produced by sunlight on a PEC water splitting cell
SR	Spectral response	Current under illumination in A/W across a range of wavelengths
TC	Test cell	Photoabsorber of interest
WE	Working electrode	Electrode of interest in two- or three-electrode
XPS	X-ray photoelectron spectroscopy	Used to assess changes to the chemical makeup or oxidation state of WE or CE surface

detected in the anode outlet with GC. This provides a lower bound to the crossover because H_2/O_2 recombination may occur when mixed in the anolyte, which may lead to underestimation of crossover. Because crossover decreases η_{STH} of a photocathode, anything observed should be reported along with η_{STH}.

Durability Characterization

Durability testing can be done simultaneously with η_{STH} measurement to obtain the total H_2 evolved over the device lifetime and the rate changes of H_2 evolution with time. For the development of materials that are viable for deployment in bias-free solar water-splitting devices that can compete with hydrocarbon-based hydrogen generation, it is thought that a lifetime of over 30,000 h on the sun will be required (Nandjou and Haussener, 2017). Given that today many devices do not survive for 100 h, it is clear that measuring and improving durability is important.

DEFINITIONS AND ACRONYMS FOR PEC WATER SPLITTING

This section presents the acronyms used in PEC water splitting to ensure that the literature is consistent between research groups.

Current sign: the convention in the PEC field is for cathodic currents, with electrons flowing into the electrolyte from the photoelectrode, to be designated as negative. Anodic currents are designated as positive.

DATA AVAILABILITY STATEMENT

The raw data supporting the conclusions of this article will be made available by the authors without undue reservation and at HydroGEN Data Hub (http://datahub.h2awsm.org/).

AUTHOR CONTRIBUTIONS

All the authors contributed to and read the final version of the manuscript.

ACKNOWLEDGMENTS

The authors gratefully acknowledge research support from the HydroGEN Advanced Water Splitting Materials Consortium, established as part of the Energy Materials Network under the U.S. Department of Energy, Office of Energy Efficiency and Renewable Energy, Hydrogen and Fuel Cell Technologies Office. This work was authored in part by the National Renewable Energy Laboratory, operated by Alliance for Sustainable Energy, LLC, for the U.S. Department of Energy under Contract Number DE-AC36-08GO28308 for National Renewable Energy Lab and under Contract no. DE-AC02-05CH11231 for Lawrence Berkeley National Laboratory. The views expressed in the article do not necessarily represent the views of the DOE or the U.S. Government. By accepting the article for publication, the publisher acknowledges that the U.S. Government retains a nonexclusive, paid-up, irrevocable, worldwide license to publish or reproduce the published form of this work or allow others to do so for the U.S. Government purposes. The authors thank Peter Agbo for the insightful discussions.

REFERENCES

Cendula, P., Steier, L., Losio, P. A., Grätzel, M., and Schumacher, J. O. (2018). Analysis of Optical Losses in a Photoelectrochemical Cell: A Tool for Precise Absorptance Estimation. *Adv. Funct. Mat.* 28 (1), 1702768. doi:10.1002/adfm.201702768

Chen, Z., Dinh, H. N., and Miller, E. (2013). *Photoelectrochemical Water Splitting*. Springer.

Chen, Z., Jaramillo, T. F., Deutsch, T. G., Kleiman-Shwarsctein, A., Forman, A. J., Gaillard, N., et al. (2011). Accelerating Materials Development for Photoelectrochemical Hydrogen Production: Standards for Methods, Definitions, and Reporting Protocols. *J. Mat. Res.* 25 (1), 3–16. doi:10.1557/jmr.2010.0020

Döscher, H., Geisz, J. F., Deutsch, T. G., and Turner, J. A. (2014). Sunlight Absorption in Water – Efficiency and Design Implications for Photoelectrochemical Devices. *Energy & Environ. Sci.* 7 (9), 2951–2956.

Döscher, H., Young, J. L., Geisz, J. F., Turner, J. A., and Deutsch, T. G. (2016). Solar-to-hydrogen Efficiency: Shining Light on Photoelectrochemical Device Performance. *Energy & Environ. Sci.* 9 (1), 74–80.

Dunbar, R. B., Barbe, A., and Fell, C. J. (2015). An Optical Imaging Method for High-Accuracy Solar Cell Area Measurement. *IEEE J. Photovoltaics* 5 (5), 1422–1427. doi:10.1109/jphotov.2015.2457297

Kistler, T. A., Danilovic, N., and Agbo, P. (2019). Editors' Choice-A Monolithic Photoelectrochemical Device Evolving Hydrogen in Pure Water. *J. Electrochem. Soc.* 166 (13), H656–H661. doi:10.1149/2.1151913jes

Moon, C., Seger, B., Vesborg, P. C. K., Hansen, O., and Chorkendorff, I. (2020). Wireless Photoelectrochemical Water Splitting Using Triple-Junction Solar Cell Protected by TiO2. *Cell Rep. Phys. Sci.* 1 (12), 100261. doi:10.1016/j.xcrp.2020.100261

Moriarty, T., Jablonski, J., and Emery, K. (2012). *Algorithm for Building a Spectrum for NREL's One-Sun Multi-Source Simulator, 001291-001295*. Golden, CO, United States: National Renewable Energy Lab.

Nandjou, F., and Haussener, S. (2017). Degradation in Photoelectrochemical Devices: Review with an Illustrative Case Study. *J. Phys. D. Appl. Phys.* 50 (12), 124002. doi:10.1088/1361-6463/aa5b11

Osterwald, C. R. (1986). Translation of Device Performance Measurements to Reference Conditions. *Sol. Cells* 18 (3), 269–279. doi:10.1016/0379-6787(86)90126-2

Steiner, M. A., and Geisz, J. F. (2012). Non-linear Luminescent Coupling in Series-Connected Multijunction Solar Cells. *Appl. Phys. Lett.* 100 (25), 251106. doi:10.1063/1.4729827

Steiner, M. A., Kurtz, S. R., Geisz, J. F., Mcmahon, W. E., and Olson, J. M. (2012). Using Phase Effects to Understand Measurements of the Quantum Efficiency and Related Luminescent Coupling in a Multijunction Solar Cell. *IEEE J. Photovoltaics* 2 (4), 424–433. doi:10.1109/jphotov.2012.2206566

Wang, Z., Hisatomi, T., Li, R., Sayama, K., Liu, G., Domen, K., et al. (2021). Efficiency Accreditation and Testing Protocols for Particulate Photocatalysts toward Solar Fuel Production. *Joule* 5 (2), 344–359. doi:10.1016/j.joule.2021.01.001

Xu, Y., Wang, C., Huang, Y., and Fu, J. (2021). Recent Advances in Electrocatalysts for Neutral and Large-Current-Density Water Electrolysis. *Nano Energy* 80, 105545. doi:10.1016/j.nanoen.2020.105545

Young, J. L., Steiner, M. A., Döscher, H., France, R. M., Turner, J. A., and Deutsch, T. G. (2017). Direct Solar-To-Hydrogen Conversion via Inverted Metamorphic Multi-Junction Semiconductor Architectures. *Nat. Energy* 2 (4), 17028. doi:10.1038/nenergy.2017.28

Zeng, G., Pham, T. A., Vanka, S., Liu, G., Song, C., Cooper, J. K., et al. (2021). Development of a Photoelectrochemically Self-Improving Si/GaN Photocathode for Efficient and Durable H2 Production. *Nat. Mat.* 20 (8), 1130–1135. doi:10.1038/s41563-021-00965-w

Zou, X., and Zhang, Y. (2015). Noble Metal-free Hydrogen Evolution Catalysts for Water Splitting. *Chem. Soc. Rev.* 44 (15), 5148–5180. doi:10.1039/c4cs00448e

Conflict of Interest: The authors declare that the research was conducted in the absence of any commercial or financial relationships that could be construed as a potential conflict of interest.

The handling editor CX declared a past co-authorship with the author TD.

frontiers | Frontiers in Energy Research

TYPE Methods
PUBLISHED 01 December 2022
DOI 10.3389/fenrg.2022.931364

OPEN ACCESS

EDITED BY
Brendan Bulfin,
ETH Zürich, Switzerland

REVIEWED BY
Francesca Maria Toma,
Berkeley Lab (DOE), United States
Roel Van de Krol,
Helmholtz Center Berlin for Materials and Energy, Helmholtz Association of German Research Centers (HZ), Germany

*CORRESPONDENCE
Sarah Shulda,
Sarah.Shulda@nrel.gov

SPECIALTY SECTION
This article was submitted to Process and Energy Systems Engineering, a section of the journal Frontiers in Energy Research

RECEIVED 28 April 2022
ACCEPTED 26 October 2022
PUBLISHED 01 December 2022

CITATION
Shulda S, Bell RT, Strange NA, Metzroth L, Heinselman KN, Sainio S, Roychoudhury S, Prendergast D, McDaniel AH and Ginley DS (2022), Synchrotron-based techniques for characterizing STCH water-splitting materials.
Front. Energy Res. 10:931364.
doi: 10.3389/fenrg.2022.931364

Synchrotron-based techniques for characterizing STCH water-splitting materials

Sarah Shulda[1]*, Robert T. Bell[1], Nicholas A. Strange[2], Lucy Metzroth[1], Karen N. Heinselman[1], Sami Sainio[2,3], Subhayan Roychoudhury[4], David Prendergast[4], Anthony H. McDaniel[5] and David S. Ginley[1]

[1]National Renewable Energy Laboratory, Golden, CO, United States, [2]Stanford Synchrotron Radiation Lightsource, SLAC National Accelerator Laboratory, Menlo Park, CA, United States, [3]Microelectronics Research Unit, Faculty of Information Technology and Electrical Engineering, University of Oulu, Oulu, Finland, [4]Molecular Foundry, Lawrence Berkeley National Laboratory, Berkeley, CA, United States, [5]Sandia National Laboratory, Livermore, CA, United States

Understanding the role of oxygen vacancy–induced atomic and electronic structural changes to complex metal oxides during water-splitting processes is paramount to advancing the field of solar thermochemical hydrogen production (STCH). The formulation and confirmation of a mechanism for these types of chemical reactions necessitate a multifaceted experimental approach, featuring advanced structural characterization methods. Synchrotron X-ray techniques are essential to the rapidly advancing field of STCH in part due to properties such as high brilliance, high coherence, and variable energy that provide sensitivity, resolution, and rapid data acquisition times required for the characterization of complex metal oxides during water-splitting cycles. X-ray diffraction (XRD) is commonly used for determining the structures and phase purity of new materials synthesized by solid-state techniques and monitoring the structural integrity of oxides during water-splitting processes (e.g., oxygen vacancy–induced lattice expansion). X-ray absorption spectroscopy (XAS) is an element-specific technique and is sensitive to local atomic and electronic changes encountered around metal coordination centers during redox. While *in operando* measurements are desirable, the experimental conditions required for such measurements (high temperatures, controlled oxygen partial pressures, and H_2O) practically necessitate *in situ* measurements that do not meet all operating conditions or *ex situ* measurements. Here, we highlight the application of synchrotron X-ray scattering and spectroscopic techniques using both *in situ* and *ex situ* measurements, emphasizing the advantages and limitations of each method as they relate to water-splitting processes. The best practices are discussed for preparing quenched states of reduction and performing synchrotron measurements, which focus on XRD and XAS at soft (e.g., oxygen K-edge, transition metal L-edges, and lanthanide M-edges) and hard (e.g., transition metal K-edges and lanthanide L-edges) X-ray energies. The X-ray absorption spectra of these complex oxides are a convolution of multiple contributions with accurate interpretation being contingent on computational methods. The state-of-the-art methods are discussed that enable peak positions and intensities to be related to material electronic and structural properties. Through careful experimental design, these studies can elucidate complex structure−property relationships as they pertain to nonstoichiometric water splitting. A survey of modern approaches for the evaluation of water-splitting materials at synchrotron sources under various experimental conditions is provided, and available software for data analysis is discussed.

KEYWORDS

XAS, XRD, STCH, complex oxides, redox chemistry, thermochemical water splitting

1 Introduction

Solar thermochemical hydrogen production, termed STCH, is an emerging process for thermochemical water-splitting technologies with little or no greenhouse gas emissions (Steinfeld, 2005; Rao and Dey, 2017; Lu et al., 2019). Out of the numerous STCH cycles described in the literature (Steinfeld, 2005; Perret, 2011; Muhich et al., 2015; Rao and Dey, 2017; Lu et al., 2019), the two-step redox-active metal oxide cycle is one of the more promising candidate approaches. The fundamental basis for the oxide cycle is simple—a metal oxide is reduced at a high temperature to create oxygen vacancies that are subsequently filled when the defected material is exposed to steam, splitting the H_2O molecule, generating H_2, and completing the cycle (Figure 1). Efficacious STCH water splitting necessitates a metal oxide that can undergo reduction *via* non-stoichiometry at sufficiently low temperatures, demonstrate fast reoxidation kinetics with H_2 present in the steam feed, and exhibit structural stability over the course of up to hundreds of thousands of redox cycles. Identifying an oxide material with the necessary chemical properties for robust water splitting has thus far eluded researchers and is a key challenge that must be overcome for STCH to be considered a viable technology for large-scale hydrogen production. The development of novel STCH materials is contingent on unraveling the relationship between a material's structural and

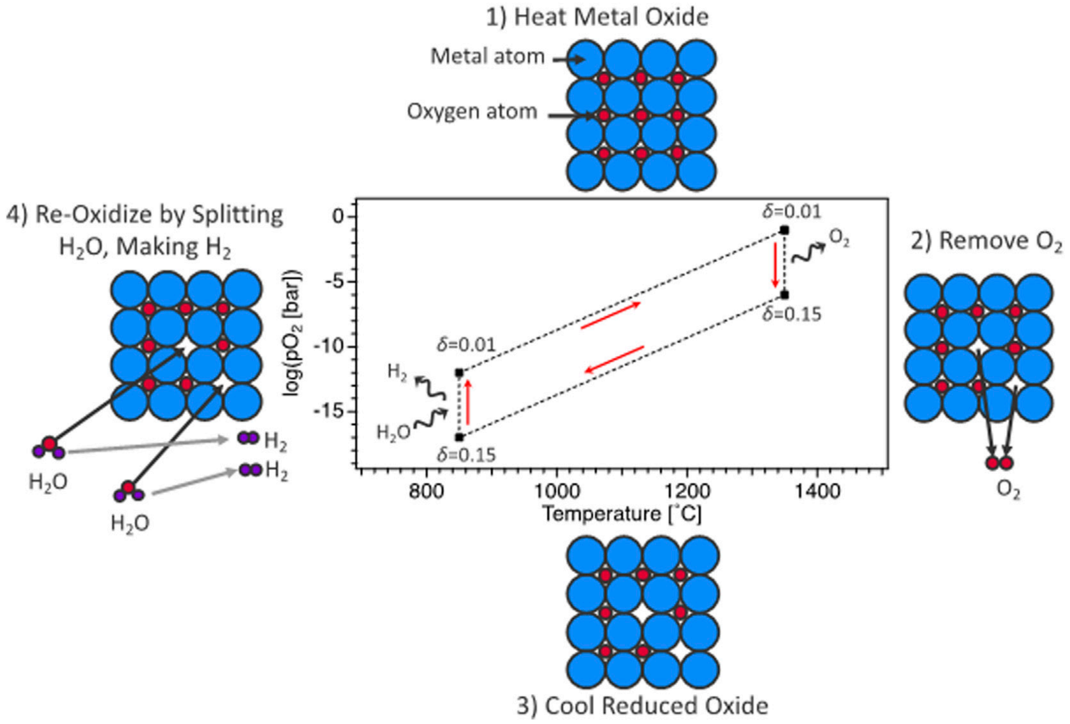

FIGURE 1
Representation of oxygen-vacancy STCH cycle divided into four thermochemical steps: 1) heating of metal oxide at constant (low) vacancy concentration, 2) high-temperature reduction resulting in oxygen vacancy creation, 3) cooling of metal oxide at constant (high) vacancy concentration, and 4) steam reaction where STCH material vacancy concentration decreases (reoxidization) and H_2O is reduced to H_2.

electronic response to the enthalpy and entropy of vacancy formation, requiring empirical and modeling efforts working in tandem (Zinkevich et al., 2006; Lany, 2008; Deml et al., 2014; Hao et al., 2014; Bork et al., 2015; Deml et al., 2015; Muhich et al., 2015; Zhang et al., 2015; Emery et al., 2016; Tsvetkov et al., 2016; Naghavi et al., 2017; Sai Gautam et al., 2020).

Currently, ceria is the benchmark material for two-step metal-oxide–based STCH (Hao et al., 2014; Rothensteiner et al., 2015; Tanwar et al., 2016; Lu et al., 2019). Ceria demonstrates phase stability in the reduced state (Zinkevich et al., 2006; Chueh et al., 2012; Hao et al., 2014; Rothensteiner et al., 2015; Naghavi et al., 2017; Lu et al., 2019), fast reoxidation kinetics (McDaniel et al., 2013; Hao et al., 2014; Ackermann et al., 2015), and importantly, a high tolerance to hydrogen in the steam stream during reoxidation (Chueh et al., 2012; Hao et al., 2014; Barcellos et al., 2018). Unfortunately, temperatures in excess of 1,500°C are required to reduce ceria appreciably, limiting practical viability (Barcellos et al., 2018; Cheng et al., 2021). Increasingly, researchers are turning their attention away from simple oxide materials to more complex material systems, which include redox-active nonstoichiometric oxides such as $Sr_xLa_{1-x}Mn_yAl_{1-y}O_{3-\delta}$ (SLMA) (McDaniel et al., 2013; Suntivich et al., 2014) and $BaCe_{0.25}Mn_{0.75}O_{3-\delta}$ (BCM) (Barcellos et al., 2018). Here, δ is used to indicate the deviation in oxygen stoichiometry from the fully oxidized state. However, there are multiple ways to define or discuss δ such as normalizations by formula units of oxygen, cations, or volume (e.g., concentration and vacancies·cm^{-3}). The perovskite-based oxides have demonstrated significant promise through an increased per-cycle yield at lower temperatures, governed by changes in oxygen vacancy concentration between the reduced and reoxidized states ($\Delta\delta$), at given H_2 to H_2O ratios. Continued progress in STCH materials' development requires a more complete understanding of the water-splitting mechanism. The impact of oxygen vacancies on the structural response of materials can be subtle and is often difficult to observe with conventional laboratory instruments, thus requiring synchrotron radiation–enabled techniques such as X-ray diffraction (XRD) for precise determination of complex structures and element-specific localized electronic responses to redox through X-ray absorption spectroscopy (XAS).

Typical changes in oxygen vacancy concentration, $\Delta\delta$, during redox cycling between reduced and reoxidized states are in the order of $\Delta\delta \geq 0.1$ mol O mol^{-1} cation. The high brilliance of photons and broad range of energies accessible at a synchrotron X-ray source furnish exceptional signal-to-noise ratio for probing structural and electronic changes arising from the small concentration of oxygen defects and enable measurements under *in situ* or *in operando* experimental conditions that align with realistic STCH operating parameters. Herein, *in operando* refers to an experiment carried out under conditions that fully align with all conditions of a representative redox water-splitting cycle (i.e., an experiment to study reoxidation behavior at realistically high temperatures and representative steam:H_2 ratio), while *in situ* refers to an experiment in which a single condition, or subset of conditions, is being probed (i.e., an experiment at elevated temperature but under ultrahigh vacuum). However, although possible, the full range of operating conditions of STCH materials are for the most part prohibitively difficult to reach for fully *in operando* experiments and challenging at best with typical *in situ* experimental apparatuses, with temperatures ranging from 700°C to 1,600°C, and oxygen partial pressures ranging from (pO_2) = 1 bar to $\leq 1 \times 10^{-20}$ bar. While certain ambitious *in situ* experiments can capture subranges of the full operating range of STCH materials and are sometimes necessary for unraveling structural behavior at high temperatures, careful sample preparation and experimental design allow *ex situ* experiments to reveal a wealth of structural and electronic responses of materials to reduction.

Developing next-generation STCH materials will be dependent on understanding the structural and electronic changes that enable reversible oxygen defect formation in complex metal oxides. The high brilliance and variable energy of synchrotron sources provide the resolution and sensitivity necessary for probing the impact of a relatively small percentage of oxygen defects in a bulk material, unobtainable with conventional laboratory-scale techniques. This informs an increasingly useful computational model of these high defect oxides. Despite this, the use of synchrotron characterization has been limited in the STCH field. Herein, we strive to inform researchers of the mechanistic insight that synchrotron experiments can provide into STCH material behavior and provide the best practices for carrying out experiments and interpreting the resultant data. First, we demonstrate a methodology of quenching complex metal oxides in known reduced states such that oxygen vacancies are preserved upon cooling to room temperature. Quenching of samples into a range of known reduced states is achieved using a combination of variable oxygen partial pressures and determination of mass loss during quenching using thermogravimetric analysis (TGA) to determine, and ultimately control, the extent of reduction. The ability to quench oxygen deficient states enables the *ex situ* probing of a material's structural and electronic response to reduction. We therefore describe the applicability of XAS and XRD techniques for characterizing STCH materials which includes the information that each technique provides, best practices for carrying out the experiments, and advanced data analysis methods for interpreting complex data. Finally, recently developed tools for *in situ* characterization of water-splitting materials under STCH operating parameters are summarized.

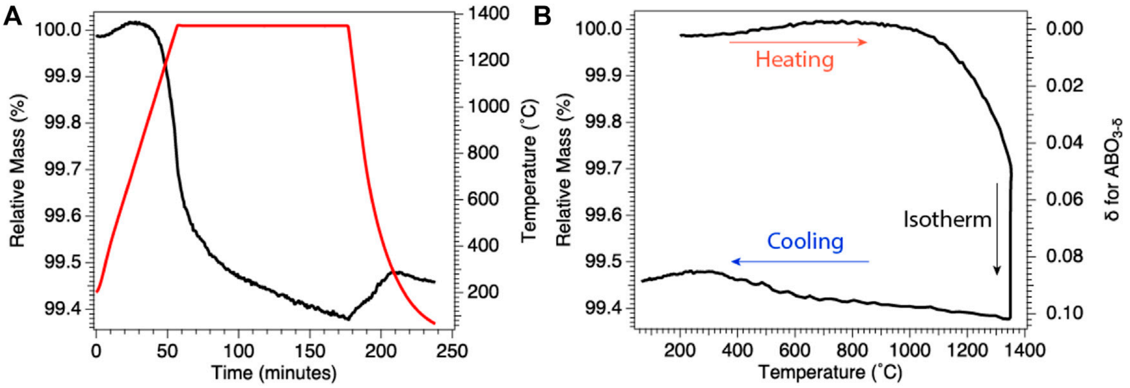

FIGURE 2
Results of representative BCM thermogravimetric analysis under reducing conditions. **(A)** Change in relative mass (black), instantaneous mass/initial mass, with temperature (red), demonstrating mass loss during 1,350˚C isothermal reduction. **(B)** Relative mass from **(A)** plotted as a function of temperature (left axis) and with relative mass transformed into oxygen off-stoichiometry, δ (inverted right axis), for BCM. Results demonstrate quenching of a known reduced state for subsequent *ex situ* investigations.

2 Preparation of controllably reduced samples for *ex situ* experiments

Although *in operando* or *in situ* experiments are ideal, the conditions required for STCH cycling are typically prohibitive and well-designed *ex situ* experiments can provide valuable insights. In this section, we detail the best practices for quenching in defects for *ex situ* characterization.

Generating fully oxidized materials for *ex situ* studies is relatively straightforward. Fully oxidized samples may be prepared by heating and cooling in atmosphere or at 1 bar O_2. Even under 1 bar of O_2, most samples develop small levels of oxygen vacancy concentration at or near the surface during cooling, with the depth-dependent concentration depending on bulk diffusivity, surface reaction kinetics, and morphology of samples. However, for fully oxidized samples, the difference in oxygen vacancy concentration between the near surface and bulk should be small when compared with the oxygen vacancy concentration between operational reduced and reoxidized states. In other words, care should be taken to not overanalyze small differences between fully oxidized samples, but when comparing fully oxidized and reduced samples, the results should be relatively insensitive to the exact mechanism of creating the fully oxidized samples.

By contrast, making representative reduced STCH samples for *ex situ* testing requires careful preparation. Essentially, almost all reduced STCH samples are metastable at room temperature in atmosphere. Only the slow kinetics of surface reoxidation and bulk oxygen diffusion prevent reduced samples from reoxidizing in air. At low temperatures, bulk oxygen diffusion in oxide ceramics is anticipated to be much slower than surface reactions, that is, some surface reoxidation is possible in the top couple of nanometers while the bulk is expected to remain in a reduced state (Li et al., 2021). Therefore, the samples are reduced under controlled reducing conditions and are then "quenched" to room temperature where slow kinetics traps the desired reduced states.

One method for determining the amount of reduction quenched into the *ex situ* sample is to use thermogravimetric analysis (thermogravimetric analysis) either to quench reduced samples or replicate as precisely as possible the cooling rates, temperatures, and pO_2 values used for sample reduction. In Figure 2, we give an example plot of thermogravimetric analysis data taken during isobaric (fixed pO_2) cooling from high temperature for preparation of reduced samples of $BaCe_{0.25}Mn_{0.75}O_3$ (BCM) for *ex situ* studies. In thermogravimetric analysis, the change in oxygen vacancy concentration can be seen as (and calculated from) the loss of sample mass during the experiment, with reduction appearing as mass loss and reoxidation as mass gain. Using the thermogravimetric analysis data, the reduction state trapped at room temperature can be quantified. Similarly, if bulk samples are prepared in a furnace, the pO_2 and cooling rate can be duplicated using thermogravimetric analysis to approximate the *ex situ* sample reduction.

Achieving the desired degree of reduction in quenched samples requires controlling the temperature and pO_2. Ideally, pO_2 and temperature are chosen to align with a condition of interest. However, if the equipment used for reducing samples cannot meet the conditions of interest, alternate temperatures and pO_2 can be used to reduce samples to equivalent extents. Environments with the same pO_2 are more reducing at high temperatures than at low temperatures, and similarly, environments with the same temperature are more reducing at lower pO_2 than higher pO_2. The pO_2 range of interest can span over 20 orders of magnitude, and pO_2 is often very difficult to control precisely over this full range due to the presence of trace leaks and virtual sources of O_2 in many vacuum systems. Options for controlling pO_2 include using blends of gas with known fractions of pO_2.

Samples must also equilibrate at the reducing conditions, and equilibration times differ dramatically between bulk, nanoparticle, and thin film samples. One ideal way to measure equilibration times is to examine bulk samples using thermogravimetric analysis (TGA) under reducing environments and determine the length of time necessary for the mass loss to reach an asymptote that aligns with the *in operando* condition that the *ex situ* experiment is attempting to mimic (for example, if 1% of the oxygen is removed during reduction in a water-splitting cycle of interest, then the sample being prepared for *ex situ* analysis should also be monitored such that 1% of the oxygen is removed). Monitoring for asymptotic mass loss is important to prevent samples from developing steep reduction gradients that can be unrepresentative when later probed with surface-sensitive measurements.

Controlling the cooling rate is an equally important consideration when preparing *ex situ* reduced oxides. Under isobaric pO_2 conditions, the samples tend to reoxidize during cooling. The maximum rate of reoxidation that will occur during cooling depends on a sample's reoxidation kinetics (at a given temperature) and the difference between the current and equilibrium oxygen vacancy concentrations and availability of oxygen. In general, the faster the sample is cooled, the more closely the extent of reduction will be preserved from high temperature into the quenched sample.

A number of precautions should be taken when performing measurements on and analyzing the data from *ex situ* reduced samples. The formation of surface layers of carbonate, hydroxyl, or other non-oxide coatings is possible and potentially more likely in reduced samples due to the reactivity of oxygen vacancies. Special care should be taken when using structural characterization techniques that are selective to only the sample surface. Another important consideration is that the effects of oxygen vacancy concentration on atomic and electronic structures can exhibit temperature dependence. For example, the concentration of oxygen vacancies causes concentration-dependent structural distortions, often referred to as chemical expansion, where crystal lattices tend to expand when oxygen vacancies are present. This chemical expansion is temperature dependent, so the difference in lattice parameters between reduced and reoxidized samples will depend on the temperature (Marrocchelli et al., 2012). Likewise, the location of oxygen vacancies in the crystal lattice may differ between high and low temperatures, with an increased probability of vacancies occurring at higher energy sites at high temperatures due to contributions from configurational entropy and k_BT terms. While the examination of samples *ex situ* can be *representative* of materials under operating conditions, the aforementioned warnings stress the importance of not assuming an identical behavior between the quenched oxides and samples maintained under operating conditions. The following two sections focus specifically on XAS and XRD techniques for characterizing quenched samples.

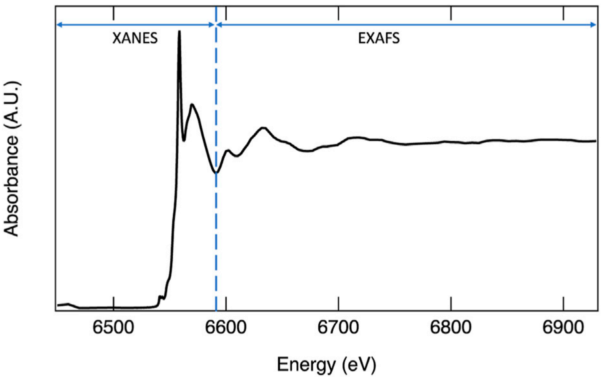

FIGURE 3
X-ray absorption spectrum of Mn K-edge with XANES and EXAFS regions identified.

3 X-ray absorption spectroscopy for solar thermochemical hydrogen production material characterization

X-ray absorption spectroscopy (XAS) is a powerful technique for characterizing STCH materials. XAS provides invaluable insights into the oxygen binding environment and quantification of cation oxidation states, enabling the redox-active elements to be identified and unraveling more complex phenomena, such as those where the cations reduce further in multi-cation systems with more than one redox-active element. Comparing the oxidation binding environments and cation oxidation states of STCH materials before and after, or during, reduction can provide significant insights into water-splitting mechanisms. Here, we provide a brief introduction to the fundamentals underlying XAS (Section 3.1) and how XAS is applicable for characterizing STCH materials specifically (Section 3.2), and finally, introducing advanced data analysis methods for interpreting the complex spectra (Section 3.3).

3.1 Brief introduction to X-ray absorption spectroscopy

X-ray absorption spectroscopy probes the excitation of electrons from core orbitals to unoccupied or partially occupied orbitals, or to the continuum. Incident photons generated by a synchrotron source over a range of well-defined energies interact with a material, and X-ray

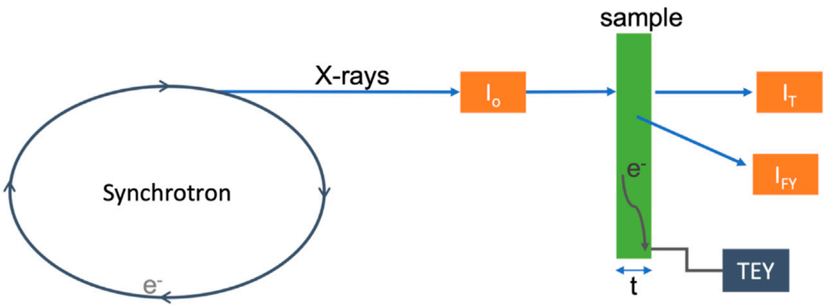

FIGURE 4
Simplified schematic of an XAS experiment, with the sample in green. The orange boxes represent detectors, where I_o measures the incident photons, I_T measures the transmitted photons, and I_F measures the fluoresced photons. The arrow with e^- indicates electrons at the sample surface from excitation measured *via* electron yield experiments, indicated by the gray box labeled TEY.

absorption (I/I_o) at each energy step is measured. Sharp increases in absorption occur at *edges* where the incident X-ray energy corresponds to the energy necessary for ejecting a core electron to a partially filled or unoccupied orbital. The term XANES, or X-ray absorption near edge structure, refers to the portion of the spectrum containing the edge step, a loosely defined region just before the edge termed the pre-edge, and the region up to approximately 50 eV after the edge (Figure 3). The XANES region can provide quantitative information on the oxidation state, extent of hybridization, and insights into coordination geometry. At higher energies, the core electron is ejected to the continuum with kinetic energy dependent on the energy of the incident photon. To understand the higher energy region, referred to as the extended X-ray absorption fine structure (EXAFS), the wave nature of an electron must be considered. The ejected electron can interact with electrons from neighboring atoms causing it to backscatter. The outgoing wave can interfere with the backscattered wave either constructively or destructively. At incident photon energies resulting in constructive interference, the probability of absorption increases, while destructive interference results in a decreased probability of adsorption (Calvin, 2013). Thus, the EXAFS region often exhibits periodic oscillations (Figure 3). The Fourier transform of this region can be modeled to provide the identity of neighboring atoms and quantitative information such as coordination number and bond distances. One significant advantage of XAS is that the technique is suitable for both crystalline and amorphous materials. For more detailed information on XANES and EXAFS analyses, interested readers are referred to the following sources: Stöhr (1992), Bunker (2010), Calvin (2013), and Frati et al. (2020).

Most XAS data are collected using transmission mode, total electron yield (TEY), or fluorescence yield (FY), as represented in Figure 4. All three of these techniques measure the absorption of X-ray photons as a function of energy. More specifically, they are a measure of the absorption coefficient as a function of energy, as defined in Eq. 1.

$$I = I_o e^{-\mu(E)t}, \tag{1}$$

where I_o is the intensity of the incident photons, I is the intensity of the photons after the beam passes through the sample (unabsorbed photons), μ is the absorption coefficient (linear attenuation coefficient), and t is the thickness of the material. In the transmission mode, the linear attenuation of X-rays [$\mu(E)t = \ln(I_o/I)$] is measured directly by monitoring the intensity of photons before (I_o) and after (I) the sample is positioned, often using ionization chambers. Due to the strong attenuation of soft X-rays by many materials, transmission experiments are typically carried out only with hard energy X-rays capable of penetrating the sample. FY detection is an alternative technique for measuring X-ray absorption, whereby a fluorescent photon is emitted during the relaxation of an electron from a higher energy state to the core hole formed by the initial X-ray absorption event. The intensity of fluorescent photons is proportional to the fraction of the incident photons absorbed $\mu(E) \propto I_f/I_o$, where I_f is the intensity of fluoresced electrons. Electron yield methods for XAS detection rely on the measurement of electrical current generated from electrons excited from core levels during absorption, where the current is proportional to the fraction of incident X-rays absorbed. These techniques are particularly advantageous at soft X-ray energies where methods based on photon emission struggle due to low escape depths. Additional measurement techniques include partial fluorescent and photoemission-based methods. For additional information on all of the aforementioned techniques and the best practices for collecting high-quality data with each method, readers are directed to the books 'XAFS for Everyone' by Scott Calvin (Calvin, 2013) and 'Introduction to XAFS: A Practical Guide to X-ray Absorption Fine Structure Spectroscopy' by Grant Bunker (Bunker, 2010).

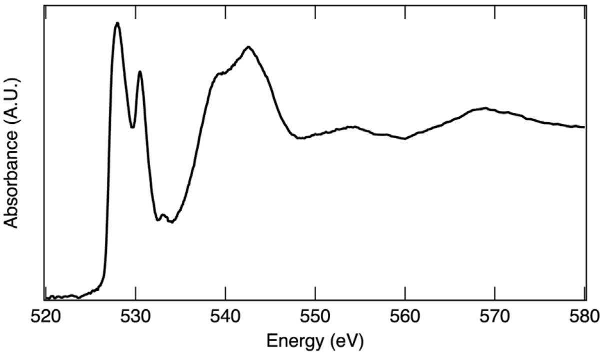

FIGURE 5
X-ray absorption spectrum of MnO_2 at the O K-edge.

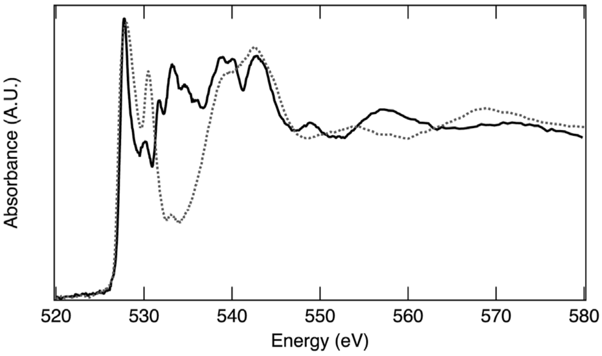

FIGURE 6
X-ray absorption spectra of reoxidized BCM (solid line) and MnO_2 (dashed line) at the O K-edge.

3.2 Application of X-ray absorption spectroscopy to solar thermochemical hydrogen production materials

In an XAS experiment, the energy of the absorption event is dependent on both the element and the specific electronic transition probed. The ability to observe an electronic transition is governed by the electric dipole selection rules (e.g., single electron, $\Delta\ell \pm 1)^{31}$, thus transitions from 1s to 2p orbitals and 2p to 3d orbitals result in high absorption intensity. The full range of X-ray energies available at a synchrotron X-ray source enables absorption measurements on most of the elements across the periodic table, which include low Z elements such as oxygen, making XAS a powerful tool for investigating material structures, chemical properties, and electronic behaviors of STCH materials. The oxygen 1s electron binding energy is 543.1 eV, relative to the vacuum level (Thompson et al., 2009). XAS at the oxygen K-edge excites 1s electrons to 2p orbitals and is essentially a measure of empty 2p states, providing a wealth of information on oxygen–metal hybridization. As an example, the oxygen K-edge spectrum of MnO_2 is provided in Figure 5 and is representative of the oxygen in 3d transition metal oxides where hybridization occurs between the oxygen 2p and transition metal 3d orbitals. The lower energy peaks between approximately 525 eV and 535 eV are within the pre-edge region and correspond to O 2p states hybridized with Mn 3d, with the doublet arising from crystal field splitting. The first peak with maximum intensity at 528 eV arises from the spin down t_{2g} and spin up e_g, which are too close in energy to separately resolve, while the second peak, 2.4 eV higher in energy, is related to the spin down e_g. The broader peaks at higher energy are O 2p with Mn 4s and 4p character. The area under the curve related to O 2p with transition metal 3d character is quantitatively correlated to the extent of oxygen–transition metal hybridization (Suntivich et al., 2014). Figure 6 overlays the oxygen K-edge spectrum of MnO_2 with the BCM water-splitting material. Significant differences in the pre-edge region are readily observable arising from the different oxygen binding environments, which include covalency and electronic configuration. Transition metal oxides play a prominent role in materials being pursued for STCH applications. XAS provides a means to compare the oxygen binding environments between materials, and more importantly, between a single material in reduced and reoxidized states necessary for providing insights into water-splitting mechanisms.

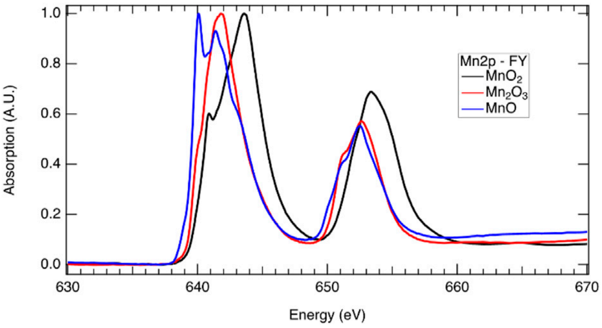

FIGURE 7
X-ray absorption spectra at the Mn 2p edge demonstrating the shift in energy associated with oxidation state which includes a sample that is predominately Mn^{2+} from MnO (blue), Mn^{3+} from Mn_2O_3, and Mn^{4+} from MnO_2 (black). The L_3 edge is at approximately 640 eV, while the L_2 edge is at approximately 652 eV (see above for discussion on the L_2 and L_3 edges). Multiple peaks are present for all three samples in the L_3 and L_2 edges, indicating that the samples are not pure and have some contribution from other Mn oxidation states.

Reduction of a redox-active cation is integral to the two-step metal-oxide STCH cycle. Lower energy X-rays (termed *soft* X-rays when <1 keV and *tender* X-rays when between 1 and

5 keV) probe lower energy electron transitions in metals and transition metals, while higher energy X-rays (>5 keV termed *hard* X-rays) probe higher energy transitions. For example, at the Mn L-edge, 2p electrons are excited to unoccupied or partially occupied 3d states with soft X-rays, whereas at the higher energy K-edge, 1s electrons are excited to 2p states with hard X-rays. The L-edge is split into two states due to spin orbital coupling, resulting in two separate peaks in the L-edge spectrum. The lower energy L_3 edge involves transitions from the $2p_{3/2}$, while the higher energy L_2 edge involves transitions from the $2p_{1/2}$ with 3/2 and 1/2, referencing the total angular momentum quantum number, $J = l + s$ (Figure 7). The L- and K-edges shift to lower energies with reduction as a consequence of greater nuclear shielding by the surrounding electron cloud. Thus, XAS at both the L- and K-edges provide a means to determine which cations are redox active and the extent of reduction in the mixed cation systems, enabling elucidation of the redox behavior in STCH materials (Figure 7). It should be noted that despite probing transitions to the 3d orbitals (which are hybridized with the oxygen 2p orbital), the L-edge does not necessarily provide information on oxygen–metal hybridization. For example, with 3d transition metals, the local effects such as the 2p spin orbital coupling and 2p–3d electron interaction contribute strongly to the L-edge spectrum shape such that, unlike the oxygen 1s, it is not a measure of unoccupied states (Frati et al., 2020). In addition to oxidation state information from the XANES region of metals and transition metals, detailed analysis of the EXAFS region can provide structural information such as identification of neighboring atoms and bond distances. This method is particularly useful for weakly crystalline or amorphous materials where XRD provides little assistance.

When choosing an XAS measurement technique, it is imperative that the experimentalist be cognizant of limitations and potential pitfalls. TEY probes only the first few nanometers of the sample (de Groot and Kotani, 2008) and is therefore a surface-sensitive technique, the results from which may not be representative of the bulk material. FY probes the bulk of the sample material from the first hundreds of nanometers to several micrometers depending on the incident energy and sample composition, making it an effective method for studying bulk changes in STCH materials. However, FY is not without its limitations. In thick samples where the element of interest is concentrated, as is the case with metal oxide powders, self-absorption is a prevalent issue. In fluorescence yield, at an absorption edge, the penetration depth of the incident photons decreases such that they interact with fewer atoms and the relationship between the florescence signal and absorption is no longer linear resulting in artifacts being introduced into the spectral intensity and shape (Bunker, 2010). At energies above the edge, when the element being probed is concentrated, it becomes more likely that the incident photons will be absorbed regardless of the energy suppressing the EXAFS oscillations (Calvin, 2013). There are experimental techniques to reduce or eliminate self-adsorption, such as working with thinner samples and changing the angle of the incident energy or detector angle, as well as data analysis methods that correct for self-absorption, details of which can be found elsewhere (Bunker, 2010; Calvin, 2013). Often, it is possible to collect TEY and FY data simultaneously. Although small differences between the two methods may be expected, significant differences in relative peak intensities is a strong indication that self-absorption is an issue, an example of which is provided in Figure 8. It is recommended that both TEY and FY be collected, when possible, for STCH materials.

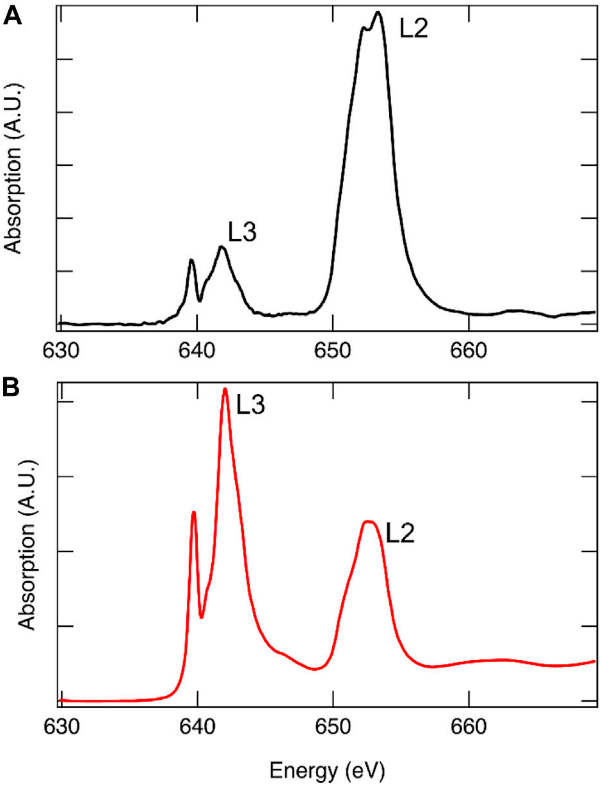

FIGURE 8
Mn L-edge of $12R\text{-}Ba_4Ce_1Mn_3O_{12}$ collected using FY[**(A)**, black] and TEY [**(B)**, red]. Due to spin–orbit coupling, the L-edge is comprised of two edges, with the lower energy edge arising from $J = (1 + s) = 3/2$ transitions termed L_3 and the higher energy from $J = (1 - s) = 1/2$ transitions termed L_2. From degeneracy of the states, it is expected that the L3:L2 intensity ratio is approximately 2:1. Self-absorption is readily apparent in the FY spectrum where the relative intensities are not correct.

3.3 Data analysis

The oscillations of the EXAFS region are a well-understood phenomenon that can be accurately modeled as a function of wavenumber with the EXAFS equation (Eq. 2)[27].

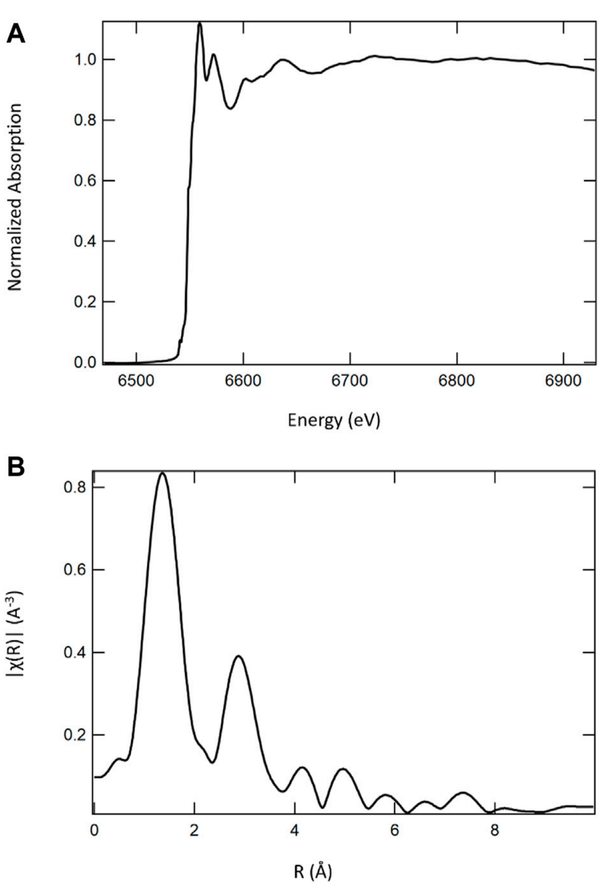

FIGURE 9
Mn K-edge X-ray absorption spectrum **(A)** of a calcium cerium–manganese oxide STCH material and its corresponding Fourier transform **(B)**. It is the Fourier transform that would be fit with the EXAFS equation to determine nearest neighbors, bond distances, and coordination numbers.

$$\chi(k) = S_o^2 \sum_i N_i \frac{f_i(k)}{kD_i^2} e^{-\frac{2D_i}{\lambda(k)}} e^{-2k^2\sigma_i^2} \sin(2kD_i + \delta(k)). \qquad (2)$$

The EXAFS equation is a sum of all paths between the absorbing atom and the scattering atoms, termed scattering paths, or *i* in the equation. For examples, when Ce is the absorbing element in CeO_2, the predominant path contributing to the first peak in the Fourier transform would be the path between Ce and its nearest oxygen neighbors. S_o is an amplitude reduction factor that accounts for the experimental Fourier transform amplitude being less than that predicted with the EXAFS equation, *N* is the degeneracy of the scattering path, *D* is the half path length or distance between the absorbing and scattering atom, σ^2 is a measure in the variance of the half path length, *k* is wavenumber, *f* is related to the probability of scattering, and δ is a phase shift that acts as a correction for assuming the electron maintains a constant wavenumber throughout the round trip (the wavenumber varies due to its interaction with the absorbing and scattering atoms' potential wells). After some data processing (such as normalization to the incident energy, removing the background contribution, and converting from energy to wavenumber), the Fourier transform of the EXAFS region can be fit using the EXAFS equation, where *N*, *D*, and σ^2 are the fit parameters. *δ(k)* and *f(k)* are atomic number dependent and are typically calculated within the fitting software. S_o is chemically transferable and often determined *via* running a standard with known structure, therefore with known *D* and *N*, making S_o readily determined from running a fit on a standard where the coordination number is known for each path. Figure 9 provides an example of an X-ray absorption spectrum at the Mn K-edge of an STCH material and its corresponding Fourier transform of the EXAFS region. From fitting the EXAFS, neighboring species can be identified with bond distances and coordination number quantitatively determined (Alia et al., 2017). For example, in Figure 9, the first peak in the Fourier transform corresponds to the Mn-O paths, thus fitting the first peak would provide the average number of oxygen atoms neighboring each manganese and the average bond distance. Depending on the quality and extent of the EXAFS data collected, the fit can incorporate atoms beyond the nearest neighbors to the absorbing element. There are excellent software packages available free to the research community for data processing and fitting that include detailed tutorials and other resources with extensive information on the best practices for data analysis that target both the novice and experienced experimentalists (Ravel et al., 2005; Webb, 2005).

The EXAFS equation is not applicable to the XANES region of the spectra. Analysis of the XANES region is typically more qualitative, although some quantitative information is retrievable. If multiple molecular species are present in a sample, the observed spectrum becomes a linear combination of contributions from the different species. As such, a linear combination fit to the experimental XANES spectrum can often provide the relative weight fractions of the constituents. Particularly applicable to studying STCH materials, oxidation states can also be quantitatively determined. At higher oxidation states, there is less electron shielding of the positively charged atomic nucleus and a greater energy is required to eject a core electron, moving the edge position to higher energy. When using the edge shift to determine the oxidation state, it is important to ensure that the shift is not an artifact of a change in the experimental configuration, such as a shift in the monochromator angle. It is usually possible to collect XAS data on a known reference material simultaneously with data collected on the sample. The spectrum from the reference material provides a reference spectrum for each sample measured. Each sample spectrum is then essentially tied to its corresponding reference spectrum so that by aligning the reference spectra and shifting the sample spectra equivalently, robust alignment is possible and shifts in edge energy can be associated with differences in the oxidation state.

As described above, pre-edge features in the XANES region are often attributable to more complex material properties and behavior, such as transition metal–oxygen hybridization and electronic configuration, both important for relating the STCH material structure to performance. However, the extraction of physical meaning from the pre-edge region requires correlating the peaks in a XANES spectrum to the specific molecular orbitals into which an excited core electron transitions, often necessitating a computational approach. The density functional theory (DFT) is a valuable tool for unraveling complex contributions to X-ray absorption spectra. Like the Schrodinger wave equation that other quantum chemical methods rely on, the DFT is rooted in an electronic structure (Hohenberg and Kohn, 1964). However, instead of attempting to solve the wave equation, DFT uses exchange–correlation energy functional to define a system's electronic density. These functionals are a mathematical description of how electrons interact with each other. This key element of DFT is how one can approach an interacting problem (solving the wave equation) by mapping it exactly to an easier-to-solve noninteracting problem (electron density) (Burke, 2007). From the electron density, it is then possible to determine the ground state electronic structure of the system from which materials' physical properties arise. Calculated vibrational force constants provide insights into chemical bonding or behavior with other species (i.e., electrical polarizability and relative energies in chemical reactions). In relation to spectroscopic properties one can also find excitation energies to the *n*th excited state and the probabilities of their occurrence, also known as the density of states (DOS) (Kohn et al., 1996). As XAS is essentially a measure of partially occupied or unoccupied states available for an electron transition, DFT is a useful tool for associating X-ray absorption spectra peaks to specific core level electron transitions to unoccupied molecular orbitals. In other words, calculating the DOS identifies the unoccupied orbitals to which the core electrons can transition. However, the substantial difference in resolution between theory and experiment can readily lead to erroneous assignments; for example, from the DFT, it is known that the two lowest unoccupied states in MnO_2 are the t_{2g} spin-down and e_g spin-up, but these do not correspond to the first two peaks in the X-ray absorption spectrum (Figure 5) as the energy states are only separated by a few tenths of an electron volt and cannot be resolved using XAS. The first peak represents a combination of these two electronic transitions. Although computationally more intensive, simulating the X-ray absorption spectrum, as detailed below, can be critical to resolving multiple contributions to complex spectra for robust peak identifications, such as those resulting from hybridized states. In addition, when a simulated spectrum matches the experimental spectrum, it can be assumed that the DFT structural model that was used to simulate the XANES spectrum is accurate and the subsequent computational analyses are more likely to be reliable. The following two subsections provide further details on the DFT, and calculations are used to simulate XANES spectra.

3.3.1 Density functional theory

The density functional theory (DFT), which has consistently been the leading workhorse in electronic structure calculations with applications across a wide variety of systems and phenomena (Becke, 2014; Tozer and Peach, 2014; Jones, 2015; Besley, 2021), can be extremely useful in prediction, verification, and analysis of the experimental results in STCH research. The DFT is rooted in the two Hohenberg–Kohn theorems (Hohenberg and Kohn, 1964) which state that for any system of interacting electrons: 1) the external potential is uniquely determined by the ground state electron density, and 2) this density and the associated energy can be found variationally by minimizing the total energy as a function of the density. In practice, the DFT is used mostly within the Kohn–Sham (KS) (Kohn and Sham, 1965) framework, which seeks a fictitious noninteracting system of electrons whose densities equal that of the interacting system. Such a system is under the influence of the multiplicative KS potential: $v_{KS} = v_{ext} + v_H + v_{XC}$, where v_{ext} is the external potential on the interacting system, v_H is the classical Hartree potential corresponding to the electron density, and v_{XC} is the exchange–correlation (XC) potential, which accounts for the quantum mechanical exchange interaction and the effects of correlation that arise from the interaction between individual electron pairs beyond a mean-field treatment. The exact form of v_{XC} is as yet unknown and depending on the problem at hand, various approximations (Kohn and Sham, 1965; Becke, 1988; Lee et al., 1988; Perdew et al., 1996a; Rappoport et al., 2011) are used for this term. Additionally, for the sake of computational efficiency, many DFT calculations (especially those that use plane waves as the basis function) replace the collective effect of the core electrons with a pseudopotential (Hellmann, 1935; Schwerdtfeger, 2011) term dependent on the atomic species.

Even though KS-DFT does not guarantee an equivalence (Kohn et al., 1996) [the highest occupied level is an exception (Janak, 1978; Perdew et al., 1982; Perdew and Levy, 1997)] between the single-particle wave functions/energies of the KS system and those associated with the addition or removal of electrons in the real system, such an equivalence is often observed in many systems to an appreciable extent, although this can be subject to the use of exchange–correlation functionals pertaining to the generalized KS framework (Seidl et al., 1996; Kümmel and Kronik, 2008; Perdew et al., 2017). Therefore, the KS energies and wave functions are routinely used as approximate quasiparticle (Onida et al., 2002) counterparts in several contexts (e.g., band structure plots). However, it must be noted that commonly used (semi-)local XC potentials, within the local density approximation (LDA) (Kohn and Sham, 1965) or the generalized gradient approximation (GGA) (Perdew et al., 1996a; Perdew et al., 1996b), tend to delocalize the electron density unphysically (Mori-Sánchez et al., 2008) due to inherent *self-interaction errors* (Perdew, 1985), whereby each electron interacts spuriously with itself *via* the mean-field of all electrons. For STCH materials, the description of the electrons in the localized *d* and *f* orbitals of the transition metal/rare earth atoms can be heavily affected by such an error. Therefore, v_{KS} is usually supplemented with an additional orbital-dependent, nonlocal Hubbard correction (Himmetoglu et al., 2014) term that with a user-specified Hubbard parameter U [often obtained empirically (Wang et al., 2006)] enforces electron localization by penalizing fractional occupation in some predefined atomic *d* and/or *f* orbitals. Inclusion of a fraction of nonlocal exact exchange in v_{KS} (analogous to the Hartree–Fock calculations) can also counteract the self-interaction error, although typically at a much higher computational expense.

Regarding STCH research, the DFT can play a crucial role in complementing XRD experiments for structural analysis and XAS experiments for the analysis of electronic structure. The former is typically accomplished with the help of a calculation of geometry relaxation, which entails computing the net force on each ion as the gradient of the total energy and optimizing the structure until the force drops below a certain threshold. Additionally, the thermal motion of the ions can be simulated with the help of molecular dynamics (MD) (Car and Parrinello, 1985; Iftimie et al., 2005) or calculation of phonon (Giannozzi et al., 1991; Parlinski et al., 2005) modes. DFT-based computational tools are also routinely used in prediction and analysis of various spectroscopic experiments. KS-DFT is found to be particularly adept at simulating the K-edge absorption spectra (such as the oxygen K-edge) since multiplet effects typically play a minor role in such excitations and consequently, the corresponding many-body state can be approximated as a single-reference system (de Groot and Kotani, 2008), consistent with the existing common approximations to the exchange–correlation functional within the DFT.

3.3.2 Simulation of X-ray absorption spectra

Within the framework of KS-DFT, one tries to simulate the X-ray absorption spectrum by using Fermi's golden rule #2 to compute the absorption probability:

$$W(\omega) \propto \omega \sum\nolimits_f \left|\langle \Psi_f | \hat{T} | \Psi_i \rangle\right|^2 \delta\left(E_f - E_i - \hbar\omega\right), \tag{3}$$

where ω is the angular frequency of the absorbed photon, $\hat{T}$ is the transition operator, $|\Psi_i\rangle$ ($|\Psi_f\rangle$) is the initial (final) state associated with the X-ray absorption process, and E_i (E_f) is the energy thereof. In the large-wavelength limit, $\hat{T}$ can be expressed as the dipole operator $\boldsymbol{e} \cdot \hat{\boldsymbol{R}}$, where $\boldsymbol{e}$ is a unit vector along the polarization direction and $\hat{\boldsymbol{R}}$ is the many-body position operator.

In practice, the absorption cross-section probability is found with the help of two separate KS self-consistent field (SCF) calculations: 1) a ground state SCF calculation for simulating the initial state and 2) another DFT calculation run on a positively charged system in which the core of the excited atom is represented by a modified pseudopotential mimicking a full core-hole (FCH) [alternatively, this calculation can be run with a neutral cell producing the excited-electron core-hole (XCH) state]. The latter calculation, referred to as the FCH state calculation hereafter, is used for extracting information on the final core-excited states. In the so-called single-particle treatment, the dipole matrix element is approximated as

$$\langle \Psi_f | \boldsymbol{e}.\hat{\boldsymbol{R}} | \Psi_i \rangle \approx S \langle \tilde{\phi}_c | \boldsymbol{e}.\hat{\boldsymbol{r}} | \phi_{core} \rangle, \tag{4}$$

where $\hat{\boldsymbol{r}}$ is the one-body position operator, ϕ_{core} denotes a core orbital, and $\tilde{\phi}_c$, which is the orbital of the excited electron after the absorption, is an unoccupied (conduction) KS orbital of the FCH state. The recently developed many-body X-ray absorption spectroscopy (MBXAS) method (Liang et al., 2017; Liang and Prendergast, 2018; Liang and Prendergast, 2019) seeks to improve upon the single-particle treatment by approximating the many-body state $|\Psi_f\rangle$ ($|\Psi_i\rangle$) by a Slater determinant (SD) constructed by populating the relevant KS orbitals obtained from the FCH (ground) state calculation. Note that each possible final state will have a different set of occupied orbitals, and then, with some algebra, the transition matrix element reduces to

$$\langle \Psi_f | \boldsymbol{e}.\hat{\boldsymbol{R}} | \Psi_i \rangle = \sum_{c}^{empty} \langle \Psi_f | \Psi_i^c \rangle \langle \phi_c | \boldsymbol{e}.\hat{\boldsymbol{r}} | \phi_{core} \rangle, \tag{5}$$

where the sum is over all the unoccupied orbitals ϕ_c of the ground state system and $|\Psi_i^c\rangle$, which is a neutral core-excited state with an excited electron in the orbital ϕ_c, is represented (non–self-consistently) by an SD composed of the ground state–occupied valence KS orbitals in combination with ϕ_c. The term $\langle \Psi_f | \Psi_i^c \rangle$, which is an inner product between two Slater determinants built from orbitals of two different SCF calculations (i.e., FCH and ground state calculation), can be reexpressed as the complex conjugate of a determinant composed of the overlap matrix elements between the FCH and ground state orbitals. Thus, in a nutshell, MBXAS expresses each transition matrix element as a weighted sum of single-particle transitions $\langle \phi_c | \boldsymbol{e}.\hat{\boldsymbol{r}} | \phi_{core} \rangle$ with the weighing factor given by the projection of the corresponding SD expressed in terms of the ground state orbitals onto an SD representing the actual final state of interest. It is important to note here that the abovementioned simulation methods, which use the KS eigenvalues/eigenfunctions in their pristine form, present a computationally cheaper and faster alternative to the techniques (Vinson et al., 2011; Gilmore et al., 2015; Vorwerk et al., 2019) rooted in many-body perturbation theory (Shirley, 1998; Rohlfing and Louie, 2000). They are particularly useful and efficient for systems with large unit cells (such as materials with defects) or for systems where the effect of finite-temperature lattice dynamics needs to be incorporated *via* molecular dynamics (Prendergast and Galli, 2006; Pascal et al., 2014; Roychoudhury et al., 2021a).

Using pseudopotentials (i.e., instead of including the core electrons explicitly) necessitates the use of an overall empirical shift to align to experimental energy scales. In addition, we must also account for the so-called chemical shifts associated with different chemical or coordination environments of the same excited element, for example, at symmetry inequivalent atomic sites in a given crystal or in entirely different materials. The use of two different sets of pseudopotentials for the ground and excited state calculations prevents us from relying on the raw total energy differences to align spectral contributions of inequivalent atoms. The relative excitation energies for distinct atomic sites are determined with respect to a common theoretical reference, the isolated atom (England et al., 2011; Jiang et al., 2013; Roychoudhury et al., 2021b). To this end, for excitation of atom X, the term $(E_f - E_i)$ in Eq. 3 is replaced by an effective formation energy difference,

$$\Delta E_F = \left[E_f - e'_X\right] - \left[E_{GS} - e_X\right], \tag{6}$$

where $e_X\,(e'_X)$ denotes the total energy of the isolated, neutral atom X using the pseudopotential employed in the ground state (FCH) calculation. The total energy E_f of any final state can now be estimated as

$$E_f = E_{XCH} + \left(\sum_i \tilde{\varepsilon}_i - \sum_j \tilde{\varepsilon}_j\right), \tag{7}$$

where $\tilde{\varepsilon}$ denotes a Kohn–Sham orbital eigenenergy of the core hole–excited self-consistent field. The index i runs over all orbitals that are occupied in the final state of interest (f) but unoccupied in the so-called excited-electron core-hole (XCH) state (Prendergast and Galli, 2006), which is the core-excited state with the lowest energy. Conversely, the index j runs over all orbitals that are unoccupied in the final state f but occupied in the XCH state. The total energy E_{XCH} of the XCH state can be found from a separate DFT SCF calculation on the neutral system employing the pseudopotentials used in the FCH calculation. In the simplest case involving the creation of only a single electron–hole pair upon X-ray absorption [denoted as $f^{(1)}$ in Liang and Prendergast (2018)], the realignment of the final state energies is accomplished with a simpler expression (since there is only one term in each sum above) for a system with N valence electrons and a final excited state with a hole in the core orbital and an electron in orbital $f > N$:

$$E_f = E_{XCH} + \left(\tilde{\varepsilon}_f - \tilde{\varepsilon}_{N+1}\right). \tag{8}$$

This alignment scheme is crucial not only for comparing the onset energy of the spectra of different materials but also for simulating the accurate line shape of the resultant spectrum for a material in which the excited atomic species occupy multiple inequivalent sites. In particular, the aforementioned formalism has proven to be highly effective in simulating the O K-edge spectra, both in terms of line shape and onset energy, of transition metal oxides (Roychoudhury et al., 2021b).

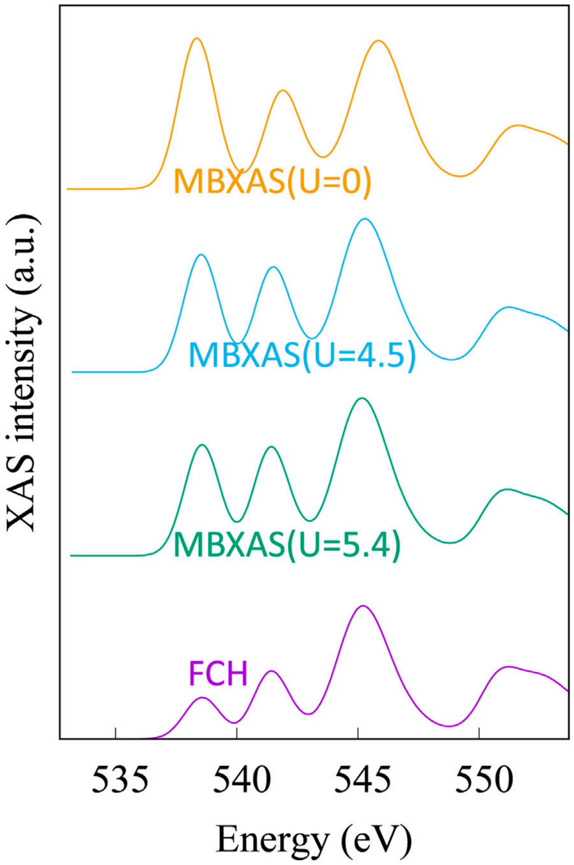

FIGURE 10
Simulated XAS plots for oxygen K-edge of CeO_2. In the “FCH” plot, the dipole matrix element is obtained with the single-particle treatment presented in Eq. 4. This plot is obtained from KS-DFT calculations using a Hubbard parameter of U = 5.4 eV. The three MBXAS plots, which correspond to different values of Hubbard U (namely, 5.4, 4.5, and 0 eV), use the many-body expression of Eq. 5 to calculate the dipole term.

Figure 10 shows the simulated O K-edge X-ray absorption spectra of CeO_2 (ceria) using the single-particle treatment (Eq. 4) and the MBXAS method (Eq. 5), with the latter being calculated separately using three different values of Hubbard U. It must be noted that even though Ce^{4+} is in a $4f_0$ configuration in ceria, it is still important to use a Hubbard correction for the f electrons due to the hybridized nature of the electronic orbitals. Hubbard parameters ranging from U = 4.5 eV to U = 6 eV have been suggested (Fabris et al., 2005; Da Silva et al., 2007; Loschen et al., 2007; Ismail et al., 2011; Grieshammer et al., 2014; Grieshammer, 2018) in the existing

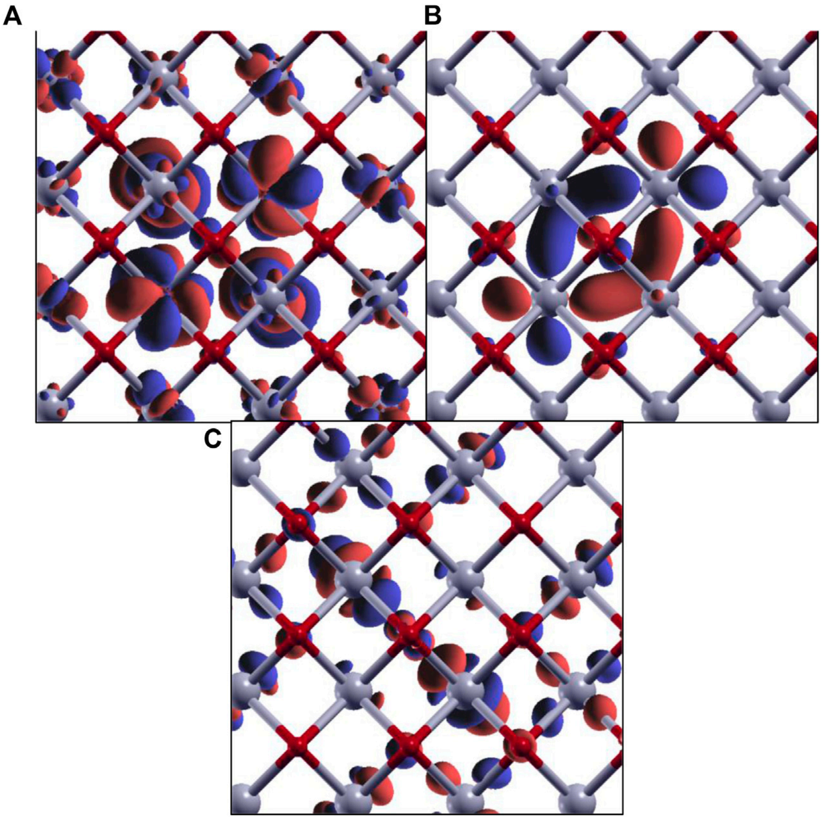

FIGURE 11
Isovalue plots of KS orbitals of the core-excited state with significant contribution in the first **(A)**, second **(B)**, and third **(C)** peaks in the O *K*-edge MBXAS plot, as shown in Figure 10 (green line). The red and gray spheres represent oxygen and cerium atoms, respectively. Note that these are all hybrid orbitals containing O *p* and Ce *d*/*f* characters, with different degrees of hybridization.

literature. Comparison of the top three spectra in Figure 10 can attest to the importance of Hubbard U in XAS simulation of STCH materials. The two plots at the bottom of Figure 10, both of which are obtained using the same Hubbard parameter (U = 5.4 eV), show a severe underestimation of the pre-peak height in the single-particle FCH treatment when compared to the MBXAS spectrum, which is in good agreement with the experimental results (Aguiar et al., 2010). This underestimation is reported for oxides of a large number of transition metals and can be explained with the help of a simple tight-binding model (Liang and Prendergast, 2018). Thus, MBXAS, which can be seen to rectify the relative peak heights, is a particularly useful tool for research on STCH materials, which are typically transition metal/rare-earth oxides. Finally, we note that DFT-based simulations provide valuable information regarding the nature and constitution of the single-particle orbitals of the excited electrons. As representative examples, in Figure 11, we show the isovalue plots of three KS orbitals, transitions to which contribute appreciably to the first three peaks in the MBXAS spectrum shown with the green curve in Figure 10.

4 X-ray diffraction for solar thermochemical hydrogen production material characterization

XRD with a synchrotron X-ray source provides sensitivity and resolution unachievable with conventional laboratory-source diffractometers. Synchrotron XRD enables complex crystal structures to be solved (and resolved), subtle changes in the structure (such as strain or changes in bond distances) to be detected, and low-concentration impurity phases to be identified and quantified, features critical to unraveling STCH material behavior. The following provides a brief description of the fundamentals underlying XRD (Section 4.1) and its applicability for characterizing STCH materials (Section 4.2).

4.1 Brief introduction to X-ray diffraction

X-ray diffraction (XRD) is a scattering-based technique suitable for investigating the identity and arrangement of atoms within a given lattice. Here, an elementary background on the theory behind X-ray diffraction will be presented such that the reader is made familiar with how a diffraction experiment can aid the structural characterization and development of STCH materials.

Photon scattering is encountered when the wavelength of radiation is comparable to interatomic spacing. For incident photons having wave vector, **k**, scattering from two positions separated by **r** into scattered photons with wave vector, **k'**, the difference in the path length between the scattered wave vectors must be equal to $(\mathbf{k}—\mathbf{k'}) \cdot \mathbf{r} = \mathbf{Q}\,\mathbf{r}$, i.e., the normal projection of **r** onto **Q**. For elastic scattering, the phase difference between the incident and scattered waves must be equal to $2\pi/\lambda$ times the path difference in order for the photon to constructively interfere with the wave scattered from the adjacent atom. The Laue equations are formed when this one-dimensional example is further expanded into three dimensions. The intensity of scattering from a lattice of ordered atoms is defined by the crystal structure factor:

$$F(\mathbf{Q}) = \sum\nolimits_{\mathbf{r}_j} f_j(\mathbf{Q}) e^{i\mathbf{Q}\cdot\mathbf{r}_j} \sum\nolimits_{\mathbf{R}_n} e^{i\mathbf{Q}\cdot\mathbf{R}_n}. \tag{9}$$

The value of F(**Q**) is nonzero when **Q** coincides with a reciprocal lattice vector. $f_j(\mathbf{Q})$ in the first summation of the expression above defines the atomic form factor, which is a measure of the X-ray "scattering efficiency" for a given atom. Since photons scatter *via* interactions with electrons, the form factor naturally increases monotonically as a function of atomic number, Z. The first summation in Eq. 9 describes scattering from atomic sites within a given unit cell, where *j* is the number of distinct atoms within the unit cell. The second summation extends the scattering contribution to the lattice sum and together these summations make up the crystal structure factor (Als-Nielsen and McMorrow, 2011).

4.2 Application of X-ray diffraction to solar thermochemical hydrogen production materials

As it pertains to STCH processes, *ex situ* XRD measurements provide the ability to solve the crystal structures of new candidate STCH compounds, demonstrate phase purities of as-synthesized and redox-cycled materials, and determine/differentiate lattice changes associated with thermal expansion and oxygen non-stoichiometry in the reduced state (Metcalfe et al., 2019). These properties are critical for evaluating the performance of a new candidate STCH material by identifying/separating contributions from the known impurity compounds/phases. *In situ* XRD measurements (e.g., high temperature and controlled gaseous environments) provide a valuable route for deriving relationships between atmospheric redox conditions and material structure (i.e., structure–property relationships) (Metcalfe et al., 2019; Mastronardo et al., 2020). The advantage of XRD with a synchrotron source is exemplified by Bell et al. (2022), where impurity phases at less than 0.4 weight percent were identified within the high-purity STCH material BCM, as well as by Strange et al. (2022), where a novel BCM polytype was identified and found to form under high-temperature reducing conditions. The results described in both studies would have not been observed with conventional laboratory-source XRD. The high brilliance offered by a synchrotron X-ray source also enables kinetic studies where structural changes can be monitored as fast as 1 kHz with hybrid photon counting detectors.

Using the most basic definition of a structural refinement, the atomic identities and positions are determined from experimental diffraction patterns in order to describe the crystal structure. Since the atomic form factor exhibits a dependence on atomic number, X-rays are relatively insensitive to oxygen atoms, especially when present in a lattice of elements with high Z (e.g., period 6 and 7 elements), which is the case for the top contending STCH materials. This limitation can be overcome with neutron diffraction, where the coherent scattering cross sections are independent of Z, and scattering from oxygen is appreciably relative to the cations. Additionally, in XRD, atoms with similar atomic numbers are not readily distinguished in a structural refinement since differences in form factor contributions are relatively low. To overcome this limitation, resonant X-ray diffraction is more suitable, whereby the diffraction intensities are recorded as the energy scanned over an atom's absorption edge. The relative changes in diffraction intensities then allow for differentiation of site occupancies.

The two most common XRD measurement geometries are Debye–Scherrer (transmission) and Bragg–Brentano (reflection), both exhibiting advantages and disadvantages. Transmission measurements require small sample volumes and are often performed in capillaries that offer a uniform cylindrical geometry with respect to the scattering angle. Sample absorption is of particular concern in transmission geometry, but a correction to the observed diffraction intensities as a function of the scattering angle can be made with *a priori* knowledge of μ t (where μ is the linear attenuation coefficient and t is the sample thickness) and an estimated particle packing fraction. The primary advantage of transmission geometry is the ability to perform measurements in extreme environments (e.g., high/low temperatures and pressures and controlled atmospheres) with low attenuation from the sample cell (typically thin-walled borosilicate glass, quartz, or sapphire). Reflection geometries overcome the absorption problem but present additional complications. When performing *in situ* measurements with a heating stage, the poor thermal conductivity of STCH materials (e.g., thermally insulating ceramics) results in a severe temperature gradient between the heating element and radiated sample volume, particularly when the sample is in the form of a pressed puck. Powders measured in reflection geometry must be uniformly deposited using a suitable nonreactive solvent in order to prevent movement of the sample during gas flow. Using this approach, there are also potential complications with sample roughness, i.e., the change in apparent density as a function of powder depth. Alternatively, a thin film may be used, but there are uncertainties regarding the structure and STCH performance of thin films when compared to their bulk counterparts. In reflection geometries, since the heating element and sample are likely to expand as a function of increasing temperature, an external calibration should be performed such that the degree of expansion is known (and reproducible) and a manual correction of offset sample position can be applied to the data. Knowledge of the temperature-dependent sample displacement is especially important when differentiating the relative contributions of thermal *vs* chemical expansion of an oxide during STCH.

5 Survey of solar thermochemical hydrogen production applicable *in situ* tools

While laboratory *in situ* measurements of STCH materials are widely performed (such as thermogravimetric analysis mass spectrometry of the effluent gas to correlate mass loss or gain to the species lost), *in situ* measurements *via* X-ray methods at a synchrotron are much less common. For redox-active materials used in water-splitting processes, the temperatures required for reduction typically exceed 1,000°C and require fine control over pO_2. Some of the primary challenges associated with *in situ* measurements are access of photons at necessary energies to the sample (typically achieved through the choice of the window/capillary material), and a well-controlled sample environment exhibiting uniform temperature under simultaneous gas flow with a known composition. Heating samples to over 1,000°C is particularly challenging due to instrumental and material-based limitations. Conduction heating is highly inefficient for X-ray cells, which cannot be completely enclosed by heating elements and insulation. On the materials side, the number of mechanically stable and inert compounds, which are still permeable to X-rays, is very limited (Rothensteiner et al., 2015). Furthermore, the interpretation of structural data can be especially difficult at high temperatures where lattice motions distort the time-averaged depiction of the crystal structure. However, there are notable successes in the literature where synchrotron experiments have been carried out under realistic operating conditions, or a subset thereof, which are summarized below.

Among the studies that have used *in situ* synchrotron X-ray measurements for thermochemical cycling conditions, the most common techniques used are XPS, XAS, and XRD. Thermochemical energy storage materials have been investigated at temperatures under 1,000°C for materials systems such as Mg-H-F (Tortoza et al., 2018) for using H_2 as a hydrogen storage material, $SrFeCuO_3$ (Vieten et al., 2019) for oxygen storage and air separation, and reactive carbon composites such as $BaCO_3$ (Møller et al., 2020) and $CaMg(CO_3)_2$ (Humphries et al., 2019). These studies often use a quartz capillary tube with thin walls to hold the sample, allowing a controlled gas flow across the sample during transmission XRD, X-ray photoemission spectroscopy (XPS), and/or XAS measurements.

For ceria-based materials, which in some cases contain other elements such as Hf or Zr, the cerium K-edge has been measured under realistic thermochemical conditions, with the reduction occurring at 1,500°C and reoxidation at 800°C in the presence of steam or CO_2 (Rothensteiner et al., 2015; Rothensteiner et al., 2016; Rothensteiner et al., 2017). These studies use synchrotron X-rays to ultimately perform XAS, XRD, and simultaneous mass spectrometry (MS) in transmission geometry to measure full thermochemical cycles, ramping up to 1,500°C in Ar for reduction of the ceria, and cooling to 800°C before introducing CO_2 or steam for reoxidation. The heating source used was an infrared focusing furnace to heat an alumina inner tube while maintaining a cooler environment for the outer quartz tube leading to the gas outlet and MS (Rothensteiner et al., 2017). Additional studies have also been done using XANES under conditions up to 1,100°C with exposure to ambient air, vacuum, and hydrogen to examine surface concentration of Ce^{3+} in ceria–zirconia catalyst materials (Yuan et al., 2020).

6 Conclusion

Developing a robust redox-active metal oxide that performs well under reasonable operating conditions is key for realizing STCH as a commercially viable process for clean hydrogen generation. Progress in material development is contingent on developing structure–property relationships, which requires a mechanistic understanding of reactions, material stability, and failure routes. Synchrotron radiation is a powerful tool for characterizing STCH materials. X-ray absorption spectroscopy identifies those cations that are redox active and the extent to which they are reduced under quenched conditions. By probing the oxygen K-edge, XAS provides quantitative information on the extent of metal–oxygen hybridization and qualitative information on how the oxygen electronic environment responds to defects and reoxidation. X-ray diffraction provides the ability to solve the crystal structure of new materials and quantify purity, as well as identify secondary phases and determine how the crystal structure responds to oxygen defects during a redox cycle. The high-energy X-rays generated by a synchrotron source opens up opportunities for *in situ* experiments unobtainable with laboratory-scale techniques. While it would be impossible to cover all the information and details necessary to design and carry out the various synchrotron experiments, the goal herein has been to make interested readers aware of what can be learned from the various techniques relevant to STCH materials and provide a wealth of resources that can be further consulted.

Data availability statement

The original contributions presented in the study are included in the article/Supplementary Material; further inquiries can be directed to the corresponding author.

Author contributions

All authors listed have made a substantial, direct, and intellectual contribution to the work and approved it for publication.

Funding

Funding was provided by the HydroGEN Advanced Water Splitting Materials Consortium, established as part of the Energy Materials Network under the United States Department of Energy, Office of Energy Efficiency and Renewable Energy, Hydrogen and Fuel Cell Technologies Office, under Award Number DE-EE0008087. Computational work (SR and DP) was carried out using supercomputing resources of the National Energy Research Scientific Computing Center (NERSC). The work by SR and DP at the Molecular Foundry was supported by the Office of Science, Office of Basic Energy Sciences, of the United States Department of Energy under Contract No. DEAC02-05CH11231. The use of the Stanford Synchrotron Radiation Lightsource, SLAC National Accelerator Laboratory, is supported by the United States Department of Energy, Office of Science, Office of Basic Energy Sciences under Contract No. DE-AC02-76SF00515. SS acknowledges funding from theWalter Ahlstróm Foundation. SS has received funding from the European Union's Horizon 2020 research and innovation program under the Marie Skłodowska-Curie grant agreement No 841621.

Licenses and permissions

This work was authored in part by the National Renewable Energy Laboratory, operated by Alliance for Sustainable Energy, LLC, for the United States Department of Energy (DOE) under Contract No. DE-AC36-08GO28308. The United States Government retains the publisher, by accepting the article for publication, acknowledges that the United States Government retains a non-exclusive, paid-up, irrevocable, and worldwide license to publish or reproduce the published form of this work, or allow others to do so, for United States Government purposes.

Conflict of interest

SS, RB, LM, KH and DG are employees of Alliance for Sustainable Energy, LLC. AM is employee of Sandia National Laboratories.

The remaining authors declare that the research was conducted in the absence of any commercial or financial relationships that could be construed as a potential conflict of interest.

Publisher's note

Author disclaimer

The views expressed in the article do not necessarily represent the views of the DOE or the United States Government.

Supplementary material

The Supplementary Material for this article can be found online at: https://www.frontiersin.org/articles/10.3389/fenrg.2022.931364/full#supplementary-material.

References

Ackermann, S., Sauvin, L., Castiglioni, R., Rupp, J. L., Scheffe, J. R., and Steinfeld, A. (2015). Kinetics of CO2 reduction over nonstoichiometric ceria. *J. Phys. Chem. C* 119 (29), 16452–16461. doi:10.1021/acs.jpcc.5b03464

Aguiar, J., Grönbech-Jensen, N., Perlov, A., Milman, V., Gao, S., Pickard, C., et al. (2010). Electronic structure of oxide fuels from experiment and first principles calculations. *J. Phys. Conf. Ser.* 241, 012062. doi:10.1088/1742-6596/241/1/012062

Alia, S., Ngo, C., Shulda, S., Dameron, A., Weker, J., Neyerlin, K., et al. (2017). Exceptional oxygen reduction reaction activity and durability of platinum–nickel nanowires through synthesis and post-treatment optimization. *ACS Omega* 2, 1408–1418. doi:10.1021/acsomega.7b00054

Als-Nielsen, J., and McMorrow, D. (2011). *Elements of modern X-ray physics*. Second Edition. Chichester, West Sussex, PO19 8SQ, United Kingdom: John Wiley & Sons, Ltd: The Atrium, Southern Gate.

Barcellos, R. D., Sanders, M. D., Tong, J., McDaniel, A. H., and O'Hayre, R. P. (2018). BaCe0.25Mn0.75O3−δ—A promising perovskite-type oxide for solar thermochemical hydrogen production. *Energy Environ. Sci.* 11 (11), 3256–3265. doi:10.1039/c8ee01989d

Becke, A. D. (1988). Density-functional exchange-energy approximation with correct asymptotic behavior. *Phys. Rev. A . Coll. Park.* 38 (6), 3098–3100. doi:10.1103/physreva.38.3098

Becke, A. D. (2014). Perspective: Fifty years of density-functional theory in chemical physics. *J. Chem. Phys.* 140 (18), 18A301. doi:10.1063/1.4869598

Bell, R., Strange, N., Plattenberger, D., Shulda, S., Park, J., Ambrosini, A., et al. (2022). *Synthesis of high-purity BaCe0.25Mn0.75O3; an improved material for thermochemical water splitting.* Acta Crystallographica Section B. doi:10.1107/S2052520622010393

Besley, N. A. (2021). Modeling of the spectroscopy of core electrons with density functional theory. *WIREs Comput. Mol. Sci.* 11 (6), e1527. doi:10.1002/wcms.1527

Bork, A. H., Kubicek, M., Struzik, M., and Rupp, J. L. M. (2015). Perovskite La0.6Sr0.4Cr1−xCoxO3−δ solid solutions for solar-thermochemical fuel production: Strategies to lower the operation temperature. *J. Mat. Chem. A Mat.* 3 (30), 15546–15557. doi:10.1039/c5ta02519b

Bunker, G. (2010). *Introduction to XAFS: A practical guide to X-ray absorption fine structure spectroscopy*. Cambridge: Cambridge University Press.

Burke, K. (2007). *The ABC of DFT*. Irvine, CA: Department of Chemistry, University of CA.

Calvin, S. (2013). *XAFS for Everyone*. 1 ed. Boca Raton: CRC Press, 457.

Car, R., and Parrinello, M. (1985). Unified approach for molecular dynamics and density-functional theory. *Phys. Rev. Lett.* 55 (22), 2471–2474. doi:10.1103/physrevlett.55.2471

Cheng, W.-H., de la Calle, A., Atwater, H. A., Stechel, E. B., and Xiang, C. (2021). Hydrogen from sunlight and water: A side-by-side comparison between photoelectrochemical and solar thermochemical water-splitting. *ACS Energy Lett.* 6 (9), 3096–3113. doi:10.1021/acsenergylett.1c00758

Chueh, W. C., McDaniel, A. H., Grass, M. E., Hao, Y., Jabeen, N., Liu, Z., et al. (2012). Highly enhanced concentration and stability of reactive Ce3+ on doped CeO2 surface revealed in operando. *Chem. Mat.* 24 (10), 1876–1882. doi:10.1021/cm300574v

Da Silva, J. L. F., Ganduglia-Pirovano, M. V., Sauer, J., Bayer, V., and Kresse, G. (2007). Hybrid functionals applied to rare-Earth oxides: The example of ceria. *Phys. Rev. B* 75 (4), 045121. doi:10.1103/physrevb.75.045121

de Groot, F., and Kotani, A. (2008). *Core level spectroscopy of solids*. 1 ed. Boca Raton: CRC Press.

Deml, A. M., Holder, A. M., O'Hayre, R. P., Musgrave, C. B., and Stevanovic, V. (2015). Intrinsic material properties dictating oxygen vacancy formation energetics in metal oxides. *J. Phys. Chem. Lett.* 6 (10), 1948–1953. doi:10.1021/acs.jpclett.5b00710

Deml, A. M., Stevanović, V., Muhich, C. L., Musgrave, C. B., and O'Hayre, R. (2014). Oxide enthalpy of formation and band gap energy as accurate descriptors of oxygen vacancy formation energetics. *Energy Environ. Sci.* 7 (6), 1996. doi:10.1039/c3ee43874k

Emery, A. A., Saal, J. E., Kirklin, S., Hegde, V. I., and Wolverton, C. (2016). High-throughput computational screening of perovskites for thermochemical water splitting applications. *Chem. Mat.* 28 (16), 5621–5634. doi:10.1021/acs.chemmater.6b01182

England, A. H., Duffin, A. M., Schwartz, C. P., Uejio, J. S., Prendergast, D., and Saykally, R. J. (2011). On the hydration and hydrolysis of carbon dioxide. *Chem. Phys. Lett.* 514 (4), 187–195. doi:10.1016/j.cplett.2011.08.063

Fabris, S., de Gironcoli, S., Baroni, S., Vicario, G., and Balducci, G. (2005). Taming multiple valency with density functionals: A case study of defective ceria. *Phys. Rev. B* 71 (4), 041102. doi:10.1103/physrevb.71.041102

Frati, F., Hunault, M. O. J. Y., and Groot, F. M. F. d. (2020). Oxygen K-edge X-ray absorption spectra. *Chem. Rev.* 120 (9), 4056–4110. doi:10.1021/acs.chemrev.9b00439

Giannozzi, P., de Gironcoli, S., Pavone, P., and Baroni, S. (1991). *Ab initio* calculation of phonon dispersions in semiconductors. *Phys. Rev. B* 43 (9), 7231–7242. doi:10.1103/physrevb.43.7231

Gilmore, K., Vinson, J., Shirley, E. L., Prendergast, D., Pemmaraju, C. D., Kas, J. J., et al. (2015). Efficient implementation of core-excitation Bethe–Salpeter equation calculations. *Comput. Phys. Commun.* 197, 109–117. doi:10.1016/j.cpc.2015.08.014

Grieshammer, S., Grope, B. O. H., Koettgen, J., and Martin, M. (2014). A combined DFT + U and Monte Carlo study on rare Earth doped ceria. *Phys. Chem. Chem. Phys.* 16 (21), 9974–9986. doi:10.1039/c3cp54811b

Grieshammer, S. (2018). Influence of the lattice constant on defects in cerium oxide. *Phys. Chem. Chem. Phys.* 20 (30), 19792–19799. doi:10.1039/c8cp03677b

Hao, Y., Yang, C.-K., and Haile, S. M. (2014). Ceria–zirconia solid solutions (Ce$_{1−<i>x</i>}$Zr$_{<i>x</i>}$O$_{2−δ}$, $x \le 0.2$) for solar thermochemical water splitting: A thermodynamic study. *Chem. Mat.* 26 (20), 6073–6082. doi:10.1021/cm503131p

Hellmann, H. (1935). A new approximation method in the problem of many electrons. *J. Chem. Phys.* 3 (1), 61. doi:10.1063/1.1749559

Himmetoglu, B., Floris, A., de Gironcoli, S., and Cococcioni, M. (2014). Hubbard-corrected DFT energy functionals: The LDA+U description of correlated systems. *Int. J. Quantum Chem.* 114 (1), 14–49. doi:10.1002/qua.24521

Hohenberg, P., and Kohn, W. (1964). Inhomogeneous electron gas. *Phys. Rev.* 136 (3B), B864–B871. doi:10.1103/physrev.136.b864

Humphries, T. D., Møller, K. T., Rickard, W. D. A., Sofianos, M. V., Liu, S., Buckley, C. E., et al. (2019). Dolomite: A low cost thermochemical energy storage material. *J. Mat. Chem. A Mat.* 7 (3), 1206–1215. doi:10.1039/c8ta07254j

Iftimie, R., Minary, P., and Tuckerman, M. E. (2005). *Ab initio* molecular dynamics: Concepts, recent developments, and future trends. *Proc. Natl. Acad. Sci. U. S. A.* 102 (19), 6654–6659. doi:10.1073/pnas.0500193102

Ismail, A., Hooper, J., Giorgi, J. B., and Woo, T. K. (2011). A DFT+U study of defect association and oxygen migration in samarium-doped ceria. *Phys. Chem. Chem. Phys.* 13 (13), 6116–6124. doi:10.1039/c0cp02062a

Janak, J. F. (1978). Proof that∂E∂ni=εin density-functional theory. *Phys. Rev. B* 18 (12), 7165–7168. doi:10.1103/physrevb.18.7165

Jiang, P., Prendergast, D., Borondics, F., Porsgaard, S., Giovanetti, L., Pach, E., et al. (2013). Experimental and theoretical investigation of the electronic structure of Cu2O and CuO thin films on Cu(110) using x-ray photoelectron and absorption spectroscopy. *J. Chem. Phys.* 138 (2), 024704. doi:10.1063/1.4773583

Jones, R. O. (2015). Density functional theory: Its origins, rise to prominence, and future. *Rev. Mod. Phys.* 87 (3), 897–923. doi:10.1103/revmodphys.87.897

Kohn, W., Becke, A. D., and Parr, R. G. (1996). Density functional theory of electronic structure. *J. Phys. Chem.* 100 (31), 12974–12980. doi:10.1021/jp960669l

Kohn, W., and Sham, L. J. (1965). Self-consistent equations including exchange and correlation effects. *Phys. Rev.* 140 (4A), A1133–A1138. doi:10.1103/physrev.140.a1133

Kümmel, S., and Kronik, L. (2008). Orbital-dependent density functionals: Theory and applications. *Rev. Mod. Phys.* 80 (1), 3–60. doi:10.1103/revmodphys.80.3

Lany, S. (2008). Semiconductor thermochemistry in density functional calculations. *Phys. Rev. B* 78 (24), 245207. doi:10.1103/physrevb.78.245207

Lee, C., Yang, W., and Parr, R. G. (1988). Development of the Colle-Salvetti correlation-energy formula into a functional of the electron density. *Phys. Rev. B* 37 (2), 785–789. doi:10.1103/physrevb.37.785

Li, X., Kuang, X., and Sun, J. (2021). Rare Earth elements based oxide ion conductors. *Inorg. Chem. Front.* 8 (5), 1374–1398. doi:10.1039/d0qi00848f

Liang, Y., and Prendergast, D. (2018). Quantum many-body effects in x-ray spectra efficiently computed using a basic graph algorithm. *Phys. Rev. B* 97 (20), 205127. doi:10.1103/physrevb.97.205127

Liang, Y., and Prendergast, D. (2019). Taming convergence in the determinant approach for x-ray excitation spectra. *Phys. Rev. B* 100 (7), 075121. doi:10.1103/physrevb.100.075121

Liang, Y., Vinson, J., Pemmaraju, S., Drisdell, W. S., Shirley, E. L., and Prendergast, D. (2017). Accurate X-ray spectral predictions: An advanced self-consistent-field approach inspired by many-body perturbation theory. *Phys. Rev. Lett.* 118 (9), 096402. doi:10.1103/physrevlett.118.096402

Loschen, C., Carrasco, J., Neyman, K. M., and Illas, F. (2007). Erratum: First-principles LDA+U and GGA+U study of cerium oxides: Dependence on the effective U parameter [Phys. Rev. B**75**, 035115 (2007)]. *Phys. Rev. B* 75 (3), 199906. doi:10.1103/physrevb.84.199906

Lu, Y., Zhu, L., Agrafiotis, C., Vieten, J., Roeb, M., and Sattler, C. (2019). Solar fuels production: Two-step thermochemical cycles with cerium-based oxides. *Prog. Energy Combust. Sci.* 75, 100785. doi:10.1016/j.pecs.2019.100785

Marrocchelli, D., Bishop, S. R., Tuller, H. L., and Yildiz, B. (2012). Understanding chemical expansion in non-stoichiometric oxides: Ceria and zirconia case studies. *Adv. Funct. Mat.* 22 (9), 1958–1965. doi:10.1002/adfm.201102648

Mastronardo, E., Qian, X., Coronado, J. M., and Haile, S. M. (2020). The favourable thermodynamic properties of Fe-doped CaMnO3 for thermochemical heat storage. *J. Mat. Chem. A Mat.* 8 (17), 8503–8517. doi:10.1039/d0ta02031a

McDaniel, A. H., Miller, E. C., Arifin, D., Ambrosini, A., Coker, E. N., O'Hayre, R., et al. (2013). Sr- and Mn-doped LaAlO3−δ for solar thermochemical H2 and CO production. *Energy Environ. Sci.* 6 (8), 2424. doi:10.1039/c3ee41372a

Metcalfe, I. S., Ray, B., Dejoie, C., Hu, W., de Leeuwe, C., Dueso, C., et al. (2019). Overcoming chemical equilibrium limitations using a thermodynamically reversible chemical reactor. *Nat. Chem.* 11 (7), 638–643. doi:10.1038/s41557-019-0273-2

Møller, K. T., Williamson, K., Buckley, C. E., and Paskevicius, M. (2020). Thermochemical energy storage properties of a barium based reactive carbonate composite. *J. Mat. Chem. A Mat.* 8 (21), 10935–10942. doi:10.1039/d0ta03671d

Mori-Sánchez, P., Cohen, A. J., and Yang, W. (2008). Localization and delocalization errors in density functional theory and implications for band-gap prediction. *Phys. Rev. Lett.* 100 (14), 146401. doi:10.1103/physrevlett.100.146401

Muhich, C. L., Ehrhart, B. D., Witte, V. A., Miller, S. L., Coker, E. N., Musgrave, C. B., et al. (2015). Predicting the solar thermochemical water splitting ability and reaction mechanism of metal oxides: A case study of the hercynite family of water splitting cycles. *Energy Environ. Sci.* 8 (12), 3687–3699. doi:10.1039/c5ee01979f

Naghavi, S. S., Emery, A. A., Hansen, H. A., Zhou, F., Ozolins, V., and Wolverton, C. (2017). Giant onsite electronic entropy enhances the performance of ceria for water splitting. *Nat. Commun.* 8 (1), 285. doi:10.1038/s41467-017-00381-2

Onida, G., Reining, L., and Rubio, A. (2002). Electronic excitations: Density-functional versus many-body green's-function approaches. *Rev. Mod. Phys.* 74 (2), 601–659. doi:10.1103/revmodphys.74.601

Parlinski, K. (2005). "Lattice dynamics: Vibrational modes," in *Encyclopedia of condensed matter physics*. Editors F. Bassani, G. L. Liedl, and P. Wyder (Oxford: Elsevier), 98–102.

Pascal, T. A., Boesenberg, U., Kostecki, R., Richardson, T. J., Weng, T.-C., Sokaras, D., et al. (2014). Finite temperature effects on the X-ray absorption spectra of lithium compounds: First-principles interpretation of X-ray Raman measurements. *J. Chem. Phys.* 140 (3), 034107. doi:10.1063/1.4856835

Perdew, J. P., Burke, K., and Ernzerhof, M. (1996). Generalized gradient approximation made simple. *Phys. Rev. Lett.* 77 (18), 3865–3868. doi:10.1103/physrevlett.77.3865

Perdew, J. P., Burke, K., and Wang, Y. (1996). Generalized gradient approximation for the exchange-correlation hole of a many-electron system. *Phys. Rev. B* 54 (23), 16533–16539. doi:10.1103/physrevb.54.16533

Perdew, J. P. (1985). Density functional theory and the band gap problem. *Int. J. Quantum Chem.* 28 (S19), 497–523. doi:10.1002/qua.560280846

Perdew, J. P., and Levy, M. (1997). Comment on "Significance of the highest occupied Kohn-Sham eigenvalue". *Phys. Rev. B* 56 (24), 16021–16028. doi:10.1103/physrevb.56.16021

Perdew, J. P., Parr, R. G., Levy, M., and Balduz, J. L. (1982). Density-functional theory for fractional particle number: Derivative discontinuities of the energy. *Phys. Rev. Lett.* 49 (23), 1691–1694. doi:10.1103/physrevlett.49.1691

Perdew, J. P., Yang, W., Burke, K., Yang, Z., Gross, E. K. U., Scheffler, M., et al. (2017). Understanding band gaps of solids in generalized Kohn–Sham theory. *Proc. Natl. Acad. Sci. U. S. A.* 114 (11), 2801–2806. doi:10.1073/pnas.1621352114

Perret, R. (2011). *Solar thermochemical hydrogen production research (STCH): Thermochemical cycles selection and investment priority*. New Mexico, United States: Sandia National Laboratories.

Prendergast, D., and Galli, G. (2006). X-ray absorption spectra of water from first principles calculations. *Phys. Rev. Lett.* 96 (21), 215502. doi:10.1103/physrevlett.96.215502

Rao, C. N. R., and Dey, S. (2017). Solar thermochemical splitting of water to generate hydrogen. *Proc. Natl. Acad. Sci. U. S. A.* 114 (51), 13385–13393. doi:10.1073/pnas.1700104114

Rappoport, D., Crawford, N. R. M., Furche, F., and Burke, K. (2011). "Approximate density functionals: Which should I choose?," in *Encyclopedia of inorganic and bioinorganic Chemistry* (New Jersey, United States: Wiley Online Library).

Ravel, B., Newville, M., and Athena, A. R. T. E. M. I. S. (2005). *ATHENA*, *artemis*, *hephaestus*: Data analysis for X-ray absorption spectroscopy using *IFEFFIT*. *J. Synchrotron Radiat.* 12 (4), 537–541. doi:10.1107/s0909049505012719

Rohlfing, M., and Louie, S. G. (2000). Electron-hole excitations and optical spectra from first principles. *Phys. Rev. B* 62 (8), 4927–4944. doi:10.1103/physrevb.62.4927

Rothensteiner, M., Bonk, A., Vogt, U. F., Emerich, H., and van Bokhoven, J. A. (2016). Structural changes in Ce0.5Zr0.5O2−δ under temperature-swing and isothermal solar thermochemical looping conditions determined by *in situ* Ce K and Zr K edge X-ray absorption spectroscopy. *J. Phys. Chem. C* 120 (26), 13931–13941. doi:10.1021/acs.jpcc.6b03367

Rothensteiner, M., Jenni, J., Emerich, H., Bonk, A., Vogt, U. F., and van Bokhoven, J. A. (2017). *In situ* flow cell for combined X-ray absorption spectroscopy, X-ray diffraction, and mass spectrometry at high photon energies under solar thermochemical looping conditions. *Rev. Sci. Instrum.* 88 (8), 083116. doi:10.1063/1.4994890

Rothensteiner, M., Sala, S., Bonk, A., Vogt, U., Emerich, H., and van Bokhoven, J. A. (2015). Ce K edge XAS of ceria-based redox materials under realistic conditions for the two-step solar thermochemical dissociation of water and/or CO2. *Phys. Chem. Chem. Phys.* 17 (40), 26988–26996. doi:10.1039/c5cp03179f

Roychoudhury, S., Qiao, R., Zhuo, Z., Li, Q., Lyu, Y., Kim, J.-H., et al. (2021). Deciphering the oxygen absorption pre-edge: A caveat on its application for probing oxygen redox reactions in batteries. *Energy Environ. Mat.* 4 (2), 246–254. doi:10.1002/eem2.12119

Roychoudhury, S., Zhuo, Z., Qiao, R., Wan, L., Liang, Y., Pan, F., et al. (2021). Controlled experiments and optimized theory of absorption spectra of Li metal and salts. *ACS Appl. Mat. Interfaces* 13 (38), 45488–45495. doi:10.1021/acsami.1c11970

Sai Gautam, G., Stechel, E. B., and Carter, E. A. (2020). Exploring Ca–Ce–M–O (M = 3d transition metal) oxide perovskites for solar thermochemical applications. *Chem. Mat.* 32, 9964–9982. doi:10.1021/acs.chemmater.0c02912

Schwerdtfeger, P. (2011). The pseudopotential approximation in electronic structure theory. *ChemPhysChem* 12 (17), 3143–3155. doi:10.1002/cphc.201100387

Seidl, A., Görling, A., Vogl, P., Majewski, J. A., and Levy, M. (1996). Generalized Kohn-Sham schemes and the band-gap problem. *Phys. Rev. B* 53 (7), 3764–3774. doi:10.1103/physrevb.53.3764

Shirley, E. L. (1998). *Ab initio* inclusion of electron-hole attraction: Application to X-ray absorption and resonant inelastic X-ray scattering. *Phys. Rev. Lett.* 80 (4), 794–797. doi:10.1103/physrevlett.80.794

Steinfeld, A. (2005). Solar thermochemical production of hydrogen––a review. *Sol. Energy* 78 (5), 603–615. doi:10.1016/j.solener.2003.12.012

Stöhr, J. (1992). *NEXAFS spectroscopy*. 1 ed. Germany: Springer-Verlag Berlin Heidelberg, 404.

Strange, N. A., Park, J. E., Goyal, A., Bell, R. T., Trindell, J. A., Sugar, J. D., et al. (2022). formation of 6H-Ba3Ce0.75Mn2.25O9 during thermochemical reduction of 12R-Ba4CeMn3O12: Identification of a polytype in the Ba(Ce, Mn)O3 family. *Inorg. Chem.* 61 (16), 6128–6137. doi:10.1021/acs.inorgchem.2c00282

Suntivich, J., Hong, W. T., Lee, Y.-L., Rondinelli, J. M., Yang, W., Goodenough, J. B., et al. (2014). Estimating hybridization of transition metal and oxygen states in perovskites from O K-edge X-ray absorption spectroscopy. *J. Phys. Chem. C* 118, 1856–1863. doi:10.1021/jp410644j

Tanwar, K., Jaiswal, N., Kumar, D., and Parkash, O. (2016). Synthesis & characterization of Dy and Ca Co-doped ceria based solid electrolytes for IT-SOFCs. *J. Alloys Compd.* 684, 683–690. doi:10.1016/j.jallcom.2016.05.223

Thompson, A., Attwood, D., Gullikson, E., Howells, M., Kim, K.-J., Kirz, J., et al. (2009). *X-ray data booklet*. 3 ed. Berkeley, CA: Lawernce Berkeley National Laboratory.

Tortoza, M. S., Humphries, T. D., Sheppard, D. A., Paskevicius, M., Rowles, M. R., Sofianos, M. V., et al. (2018). Thermodynamics and performance of the Mg–H–F system for thermochemical energy storage applications. *Phys. Chem. Chem. Phys.* 20 (4), 2274–2283. doi:10.1039/c7cp07433f

Tozer, D. J., and Peach, M. J. G. (2014). Density functional theory and its applications. *Phys. Chem. Chem. Phys.* 16 (28), 14333. doi:10.1039/c4cp90074j

Tsvetkov, N., Lu, Q., Sun, L., Crumlin, E. J., and Yildiz, B. (2016). Improved chemical and electrochemical stability of perovskite oxides with less reducible cations at the surface. *Nat. Mat.* 15 (9), 1010–1016. doi:10.1038/nmat4659

Vieten, J., Bulfin, B., Starr, D. E., Hariki, A., de Groot, F. M. F., Azarpira, A., et al. (2019). Redox behavior of solid solutions in the SrFe1-xCuxO3-δ system for application in thermochemical oxygen storage and air separation. *Energy Technol.* 7 (1), 131–139. doi:10.1002/ente.201800554

Vinson, J., Rehr, J. J., Kas, J. J., and Shirley, E. L. (2011). Bethe-Salpeter equation calculations of core excitation spectra. *Phys. Rev. B* 83 (11), 115106. doi:10.1103/physrevb.83.115106

Vorwerk, C., Aurich, B., Cocchi, C., and Draxl, C. (2019). Bethe–salpeter equation for absorption and scattering spectroscopy: Implementation in the exciting code. *Electron. Struct.* 1 (3), 037001. doi:10.1088/2516-1075/ab3123

Wang, L., Maxisch, T., and Ceder, G. (2006). Oxidation energies of transition metal oxides within theGGA+Uframework. *Phys. Rev. B* 73 (19), 195107. doi:10.1103/physrevb.73.195107

Webb, S. M. (2005). Sixpack: A graphical user interface for XAS analysis using ifeffit. *Phys. Scr.*, 1011. doi:10.1238/physica.topical.115a01011

Yuan, W., Ma, Q., Liang, Y., Sun, C., Narayanachari, K. V. L. V., Bedzyk, M. J., et al. (2020). Unexpected trends in the enhanced Ce3+ surface concentration in ceria–zirconia catalyst materials. *J. Mat. Chem. A Mat.* 8 (19), 9850–9858. doi:10.1039/d0ta02762f

Zhang, S., Han, N., and Tan, X. (2015). Density functional theory calculations of atomic, electronic and thermodynamic properties of cubic LaCoO3 and La1−xSrxCoO3surfaces. *RSC Adv.* 5 (1), 760–769. doi:10.1039/c4ra12563k

Zinkevich, M., Djurovic, D., and Aldinger, F., Thermodynamic modelling of the cerium–oxygen system☆. *Solid State Ionics* 2006, 177 (11-12), 989–1001. doi:10.1016/j.ssi.2006.02.044

frontiers | Frontiers in Energy Research

TYPE Methods
PUBLISHED 05 December 2022
DOI 10.3389/fenrg.2022.945788

OPEN ACCESS

EDITED BY
Vânia Oliveira,
Faculty of Engineering, University of Porto, Portugal

REVIEWED BY
Kevin Huang,
University of South Carolina, United States
Miguel A Laguna-Bercero,
University of Zaragoza, Spain

*CORRESPONDENCE
Yeong-Shyung Chou,
yeong-shyung.chou@pnnl.gov

SPECIALTY SECTION
This article was submitted to Fuel Cells, Electrolyzers and Membrane Reactors, a section of the journal Frontiers in Energy Research

RECEIVED 16 May 2022
ACCEPTED 24 August 2022
PUBLISHED 05 December 2022

CITATION
Chou Y-S, Hardy J and Marina OA (2022), Leak test for solid oxide fuel cells and solid oxide electrolysis cells. *Front. Energy Res.* 10:945788.
doi: 10.3389/fenrg.2022.945788

Leak test for solid oxide fuel cells and solid oxide electrolysis cells

Yeong-Shyung Chou*, John Hardy and Olga A. Marina

Pacific Northwest National Laboratory, Energy and Environment Division, Richland, WA, United States

A simple, fast, and economical alcohol penetration method for assessing the solid oxide cell to metal window frame seal in a typical planar design is presented. An alcohol such as ethanol or isopropanol is placed into the cavity of a cell sealed to the window frame. Within 3–5 min, one can determine if the glass seal is hermetic by visual observation along the seal edges on the side of the sealed frame. Cross bubbling and open circuit voltage methods for determining whether the seal failed or cracked at high temperature after final stack firing are also discussed.

KEYWORDS

SOFC and SOEC, leak test, seal quality, cell wetting by alcohol, OCV, method

Introduction

Emerging SOFC and SOEC technologies require hermetic seals between the cell and the window frame plates or other manifold configurations. Otherwise, leaks will result in direct mixing of fuel and oxidants at elevated temperatures, greatly reducing the cell/stack electrochemical performance and potentially leading to total cell failure or fire in extreme cases. To separate fuels such as hydrogen from oxidants such as air, these seals are typically composed of borosilicate glasses (Gunawan et al., 2021; Singh and Walia, 2021) which are fired at elevated temperatures according to a specified temperature profile based on the thermal and physical properties of each individual sealing glass. Other sealing technologies such as brazing and compressive mica seals have also been investigated (Weil et al., 2003; Simner and Stevenson, 2001; Chou et al., 2002; Fergus, 2005; Lessing, 2007). However, with few exceptions, brazing is generally conducted in reducing environment which is not cost competitive and can destabilize air electrode materials (Weil et al., 2003; Fergus, 2005; Lessing, 2007). Compressive mica seals, on the other hand, require an external loading mechanism and are not completely hermetic (Simner and Stevenson, 2001; Chou et al., 2002; Sang et al., 2008). As a result, glass seals continue to be the leading technology for SOFC/SOEC applications. Glass seals, in general, are thermally stable in oxidizing and reducing environments, tailorable in composition to match thermal expansion, have reasonable mechanical strength and good wetting on oxide surfaces, are electrically insulating, and have low volatility. However, long-term (e.g., >5000 h) issues such as interfacial stability, microstructural evolution, and volatile species in reducing and humid conditions remain unknown. The sealing glass will melt and wet the faying surfaces of the cell and window frame plate to form the desired hermetic seal. Often this sealing process is conducted separately from the final stack assembly, where many tens of leak-tested cell-to-window frame plates are assembled with appropriate

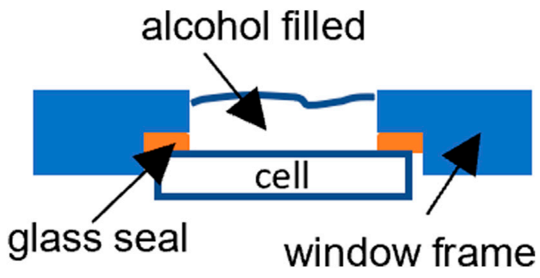

FIGURE 1
Schematic drawing showing the leak test of a planar cell glass sealed onto a metal window frame.

contact materials and metallic interconnect plates to form the stack. This is because a glass seal leak will not self-heal. When glass materials are used, they undergo a crystallization process from their initial vitreous state to form a microstructure with substantial crystalline phases. This causes the sealing glasses to behave more like typical brittle ceramics in that any pre-existing cracks (and leaks) will continue to propagate rather than fuse together and shrink. In addition, any leak will serve as a local hot spot from the direct exothermic reaction of fuel and air causing local overheating, and eventually, total stack failure. Therefore, one needs to verify that the cell to window frame plate seal is fully hermetic before assembling the cell/stack from both an economic and fire safety point of view.

To date, no standard leak test of SOFC/SOEC cells has been recognized by industry. There are a few limited reports addressing leak testing in the literature (Chou et al., 2002; Chou et al., 2007; Sang et al., 2008); however, they are all focused primarily on compressive mica seals for perimeter seals rather than cell to window frame seals where compressive stresses can be applied to the stronger metal parts (Chou et al., 2002), instead of the weak porous ceramic cell, which is typically only around 0.5 mm thick with 30–50% porosity. These test methods typically use a pressure sensor to monitor the pressure change within a known volume over time and can be adapted for either room temperature or high temperature testing. One can introduce a small positive pressure and measure the pressure change over time to calculate the leak rate in sccm/cm (standard cubic centimeters of gas per minute per centimeter of seal length). One can use this method to leak test the cell-to-window-frame seal. However, it is time consuming and can be confounded if the seal between the required leak test fixture and the window frame plate around the perimeter cannot be guaranteed to be completely hermetic. In a room temperature test, one can use typical grease to create this seal; however, the window frame plates (especially for larger cells of 4 inches or more in length) are often slightly warped after sealing at elevated temperatures, making it difficult to form a hermetic seal. Applying a compressive load to the frame may potentially damage the weak glass seal and lead to seal or cell fracture. In addition, one also has to carefully establish baseline measurements at ambient temperatures.

Summary of method

This method describes a simple, fast, non-destructive, and yet reliable way to identify leaks in the cell assembly. The procedure is based on applying an alcohol such as isopropanol or ethanol to the cell surface for a few minutes and observing whether the alcohol penetrates to the opposite side. The concept is also applicable to tubular cells where ceramic tubes are sealed to the manifold plate; however, the procedure may require minor modifications to accommodate specific tubular designs. For high temperature leak testing of single cells and short stacks, two methods are proposed: the cross-bubbling and OCV techniques. The cross-bubbling technique is used for cells before the hydrogen electrode is reduced so that air can be used in both channels (i.e., anode and cathode). By flowing air through only the anode or the cathode channel, one can determine whether a leak exists by observing whether bubbling occurs in the opposite channel's bubbler. The leak could also be identified after cell reduction by measuring the OCV at a known oxygen partial pressure gradient and cell temperature and comparing the measured OCV with the theoretical value predicted by the Nernst equation. If the difference is larger than 20 mV, then there is likely a leak.

Personnel qualifications/responsibilities

Only trained personnel should operate the test equipment. Appropriate safety measures for remediation of hazards and risks associated with powders and solvents, electrical equipment, hot surfaces on the furnace, and flammable gases (hydrogen) should be taken. Refer to safe working instructions, personal protective equipment guidelines and compliance requirements in your lab.

For high temperature leak tests using the OCV technique, a basic knowledge of how to calculate the theoretical OCV using the Nernst equation with a known oxygen partial pressure gradient and cell temperature is needed. Operators must complete proper training on how to operate the cell at elevated temperatures, including the safe use and handling of flammable gases and the emergency shut down procedures, according to company and state regulations, where applicable.

Equipment and supplies

A general grade of ethanol or isopropanol is sufficient, no need for high purity. A flat plate glass (larger than the window frame plate) is needed so that the sealed cell to window frame plate can be placed flat on spacers on top of the glass plate. For

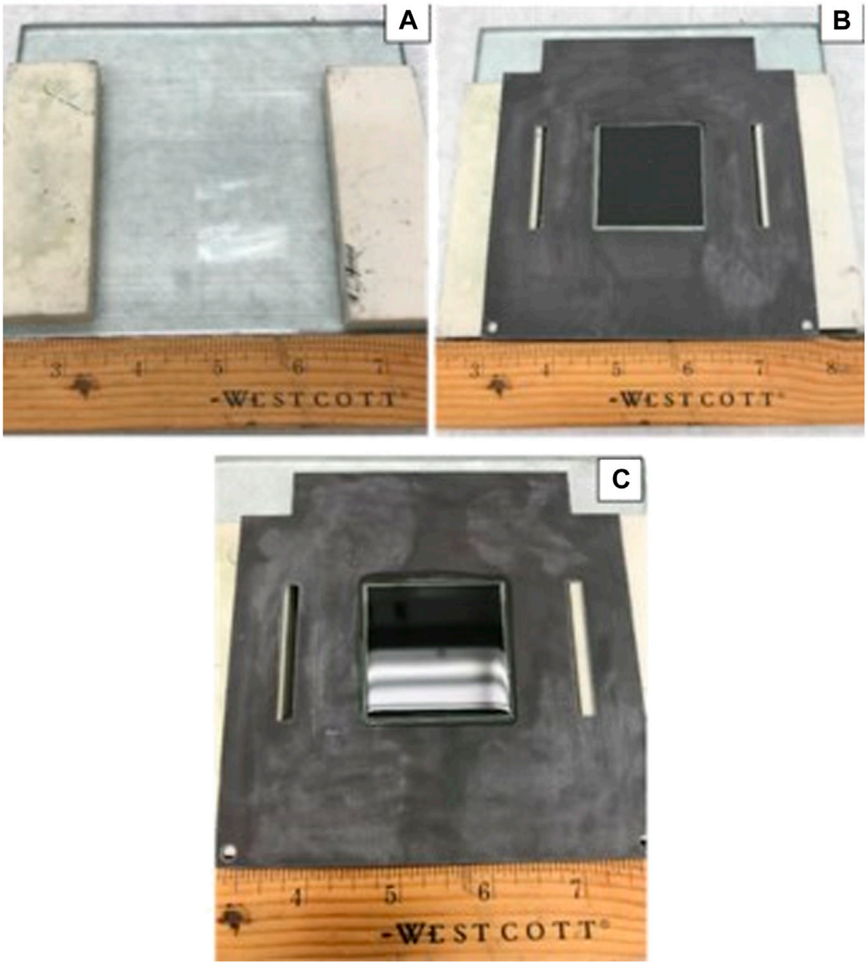

FIGURE 2
Room temperature leak test of a sealed cell/window frame assembly: **(A)** a flat glass plate with two spacers; **(B)** a sealed cell/cell frame assembly with cathode cavity facing up; **(C)** central cavity filled with iso-propanol.

spacers one can use glass slides that are typically used for optical microscopy (about 1 inch wide by 3–4 inch long and 1 mm thick). For high temperature cross-bubbling tests, two bubblers for the exhaust gases are required: one on the anode side and the other on the cathode side. To facilitate visual observation of bubbling, the bubbler should be made of transparent plastic or glass (three to four inches diameter 10–12 inches long) with an aluminum plate on top and bottom. The metal plates are fastened to the transparent bubbler with four long threaded rods and nuts. Teflon seals should be used. Two stainless steel pieces of tubing are inserted into the bubbler (e.g., 1/8 inch diameter): a long one is immersed into the water near the container bottom for gas from the cell and a short one that should not contact the water surface. High temperature leak tests by the OCV technique require a full set of test equipment including a high temperature furnace, a gas control system, an exhaust system for fuel and air, safety valves, an external loading fixture if compressive seals are used, a stack test fixture, and an electrochemical performance instrument such as impedance analyzer or a multi-meter with a resolution of 1 mV or better to measure the OCV.

Step by step procedure

Room temperature leak test of sealed cell to a coated window frame plate

Figure 1 shows a schematic drawing of the cross-section view of a planar cell sealed to a window frame plate with a glass seal between the cell's dense electrolyte layer and the metal frame. A

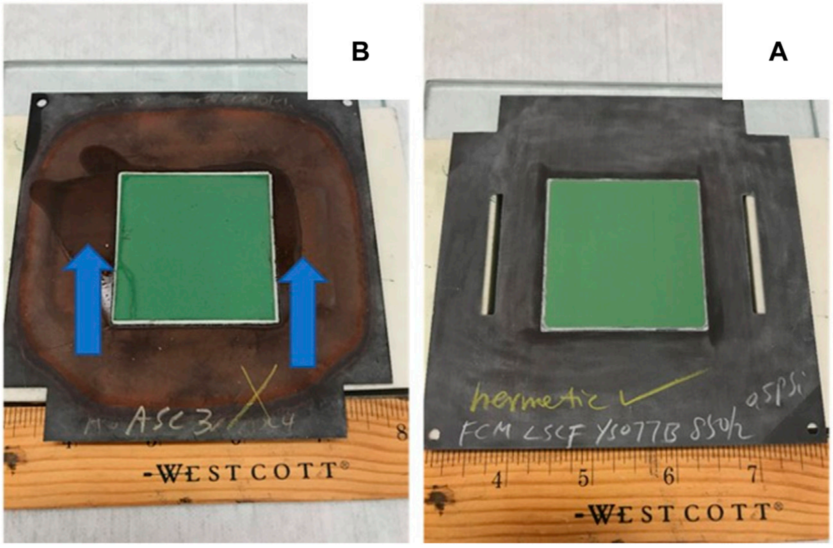

FIGURE 3
Leak test results of a sealed cell/cell frame assembly. Observation at anode side after ~5 min of iso-propanol exposure at cathode side: **(A)** a satisfactory seal where no iso-propanol was observed; **(B)** a failed seal where iso-propanol was observed at anode side (arrows).

commercial silicate-based glass in powder form was mixed with organic binders to make a paste that was applied between the faying surfaces. The couple was then slowly heated to 500°C to burn off the organic binders and heat treated at 800–950°C, per glass manufacturer recommendations, for a few hours for wetting and sealing. A typical example of a 2 inch × 2 inch LSM-based YSZ electrolyte electrode-supported cell glass-sealed onto an aluminized SS441 cell frame is shown in Figure 2. To perform the leak test with isopropanol or ethanol:

1. Place two flat spacers (e.g., alumina flat pieces) of the same thickness on a flat surface with sizing greater than the cell dimensions. The thickness of the spacers should be such that the cell's anode surface does not come in direct contact with the glass plate (Figure 2, A).
2. Place the sealed cell/window frame assembly on top of the spacers with the cathode side cavity (black color) facing up (Figure 2, B).
3. Add some iso-propanol or ethanol into the cathode cavity to cover the entire cathode surface, but not to overflowing (Figure 2, C). In case of overflowing, such that the excess liquid spills over and wets the anode side, drain the alcohol and allow the test sample to dry thoroughly before starting over.
4. Wait about 3–5 min for the iso-propanol or ethanol to penetrate through any potential defects/cracks in the glass seal (add additional isopropanol or ethanol if it becomes depleted due to evaporation).
5. Pour the pool of alcohol out of the cell.
6. Quickly flip the cell/window frame assembly over and check for wet spots. If there are no wet spots, the seal is hermetic (Figure 3, A). If there is a leak, wet spots can be easily spotted (arrows in Figure 3B).
7. Note that observed liquid penetration could also come from a cracked cell or through a pin hole in the ceramic cell; in either case, however, the cell/window frame assembly is not suitable for high-temperature testing. From our experience in testing over 300 cell to window frame seals, the wet spots were very easy to observe without a magnifying glass or optical microscopy. Very few leaks showed small wet spots which evaporated away rather quickly (in less than 5 s). In this case, one should repeat the process by doubling the wait time from 3–5 min to 6–10 min while maintaining the cathode cavity fully covered by the alcohol. Then repeat steps 5 and 6. Since the alcohol is colorless, one may add a dye to the alcohol to facilitate the examination; however, the dye should not contain any metal ions that could contaminate the cell.

Room temperature leak test of tubular cells

One can apply the same alcohol leak test concept to tubular cells. Figure 4 shows the typical sealing geometry of a tubular cell in a metallic manifold plate. The leak test requires a glass, plastic, or metal pipe with an inner

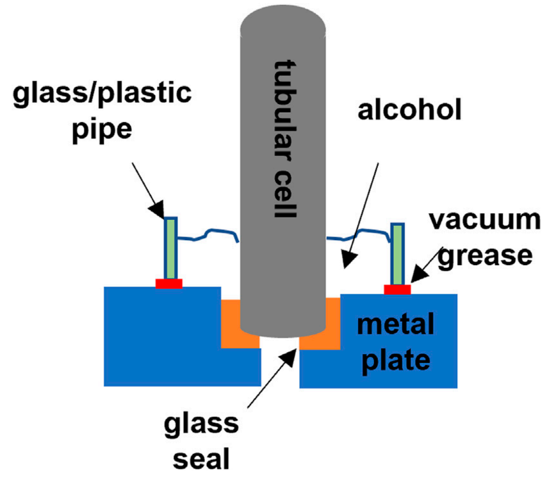

FIGURE 4
Schematic drawing of the leak test for tubular cells.

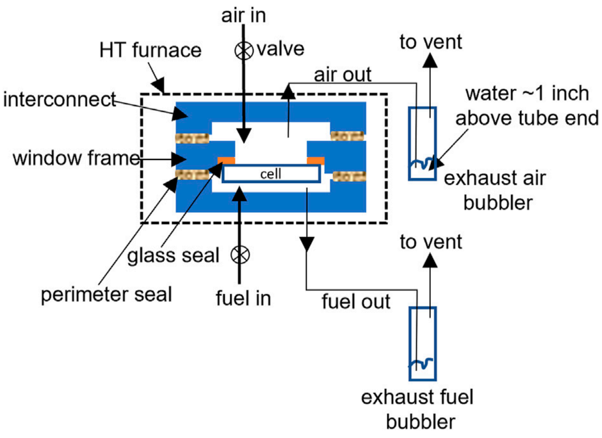

FIGURE 5
Schematic drawing of the setup for high-temperature leak test by cross-bubbling.

diameter larger than the outer diameter of the ceramic tube. The length of the pipe could be just 1–2 inches and the thickness could be several mm for easy handling. The pipe end edges need to be flat so that one can apply vacuum grease and press it down to the manifold plate with a ceramic tube inside to stop the leakage of isopropanol. The leak test can then be conducted similar to the window frame plate (i.e., planar cell) test by filling the pipe's annular space with the alcohol to a half to one inch height. Wait 3–5 min and visually check the bottom of the manifold plate for signs of isopropanol.

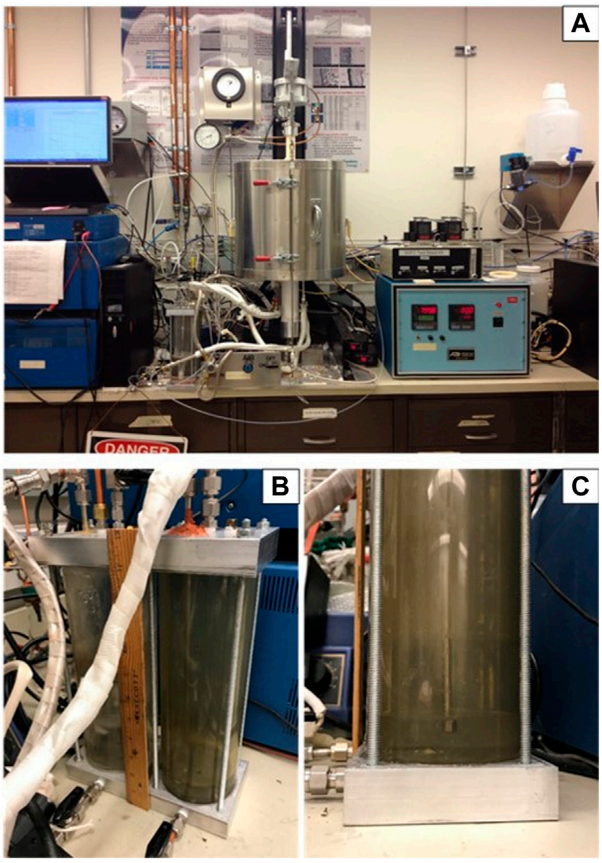

FIGURE 6
Actual set up for a generic stack test, **(A)** full view of the experimental set-up, **(B)**, view of the two exhaust water bubblers (one for fuel and one for air), and **(C)**, enlarged side view of the bubbler with ~0.2–0.5 inch of water above the tubeing end.

High temperature leak test by cross-bubbling for an un-reduced cell

The following leak test procedures are for a generic single cell stack fixture test consisting of an assembled cell/window frame with interconnect plates and gas manifold or compressive loading plates. Figure 5 shows the simplified schematic drawing of the setup where a cell glass-sealed to the window frame plate is sandwiched with two interconnect plates on either side with perimeter seals. Current collector and contact materials at the anode and cathode are not shown. The same principle could be extended to short stacks consisting of 3-5 cells. A full view of a typical generic stack test is shown in Figure 6A. The cell is under compressive loading and the fuel and air exhaust are immersed in the water bubblers (Figure 6, B). A zoomed in view of the bubbler is included in Figure 6C. After the final stack firing is conducted to bond the contact materials, the cell is cooled to the operating temperature (e.g., 800°C), and the following procedure is used to conduct the leak test with air in both channels (before fully reducing the anode):

1. Apply air to the cell at a reasonable flow rate through the air channel with no gas flowing in the fuel side. A typical air flow rate for a 2 inch × 2 inch LSM-based anode-supported YSZ thin electrolyte cell with an active cathode area of 16 cm2 is generally 800–900 sccm. To minimize potential thermal shock, the air flow rate should be increased gradually from zero to the target (e.g., over a period of ~30 min)
2. Adjust the water height above the immersed end of the gas tubing to about 0.2–0.5 inch in both bubblers. This provides a suitably low resistance for bubbling.
3. Bubbling in the exhaust fuel bubbler indicates leakage caused by (1) cell to cell frame glass seal failure, (2) cell fracture (sometimes caused by flattening of the warped cell frame under the stack's compressive loading), or (3) perimeter mica seal failure, if a compressive seal is used as the perimeter seal. Note that it is not common to observe cross-bubbling if the only leakage is through the perimeter mica seal. This is because the leakage through the compressed mica is rather small (Chou et al., 2002), and does not typically contribute to cross bubbling based on our experience of testing over 300 individual cells.
4. Shut down the air flow and wait for any observed bubbling to stop. Depending on the overall gas tubing length, it may take several minutes.
5. Turn on gas flow in the fuel side while no air flows in the other side, in a similar manner to step 1.
6. Watch for cross-bubbling in the exhaust air bubbler, which is indicative of a leak.
7. The cell may still be operable if the cross-bubbling is very minute (e.g., one bubble per second or less when the outer diameter of the metal tubing inside the bubbler is 1/8 inch). One can further repeat the test by increasing the water height from 0.2 to 0.5 inch to about 3–4 inch (typical water height for SOFC/SOEC operation) to observe if the bubbling frequency decreases. If the bubbling decreases, one may still use the cell.

High temperature leak test by OCV for a fully reduced cell

In addition to the cross-bubbling method to detect cell leakage in an unreduced cell, one can also use the open circuit voltage as an alternative leak test for single cells and short stacks that have been fully reduced. In stacks, the voltage loss due to a single cell leak (which could be 20 mV) may be too small to detect in the presence of 10 + additional cells, when the overall voltage could be above 10 V. Such a small voltage deviation (20 mV vs. 10 V) could also come from temperature variations between cells. To overcome this potential uncertainty, one needs to have voltage leads for each individual cell or for subsets of 2-3 cells to reduce the likelihood of significant temperature gradients and their effects on overall voltage. Once the cell is fully reduced, flow the desired fuel (e.g., H2: N2 = 1:1 + 3% H2O) and air at reasonable flow rates. For example, for a 2 inch × 2 inch cell with an active cathode area of 4 cm × 4 cm, one can flow 450 sccm of hydrogen fuel to the anode and 900 sccm of air to the cathode. Depending on the system and furnace, it may take some time to reach this final flow rate in order to minimize the potential for thermal shock. Once the flow rate has stabilized for 30 min, and cell temperature remains constant, one can then measure the OCV to determine whether there is a leak by comparing the measured OCV with the calculated Nernst voltage at the specified temperature and oxygen partial pressures in the fuel and air (dry or moist). If the measured OCV is more than 20 mV lower than the Nernst voltage, it is likely that some leakage is occurring. Table 1 lists the calculated Nernst voltage for hydrogen fuel (pure or diluted with N2) with 3% moisture *versus* air at 700, 750, and 800°C. This information can also be used to confirm the afore-mentioned cross-bubbling technique. It needs to be noted that, if one would also like to run a cross-bubbling test after the cell anode is fully reduced, care must be taken to avoid potential explosion or cell damage resulting from the mixing of air and fuel due to leakage.

TABLE 1 Nernst voltage for hydrogen fuel (pure H_2 or H_2:N_2 = 1:1) with 3% moisture *versus* air at various temperatures.

Temperature C	Pure H_2, 3%H_2O	H_2:N_2 = 1:1, 3%H_2O
800	1.101	1.069
750	1.110	1.079
700	1.118	1.089

Quality control and quality assurance section

In room temperature leak tests with the alcohol penetration method and in high temperature leak tests with the cross-bubbling method, no quality control is required; all observations are visual. In high temperature leak tests using the OCV measurement technique, one would need to calibrate the analytical electrochemical characterization equipment (an impedance spectrometer or a multimeter) using appropriate calibration standards as suggested by the equipment manufacturer. In addition to the voltage measurement, an accurate measurement of cell temperature is vital in the OCV method. An external type K or S thermocouple is often placed near the cell to ensure the correct temperature is obtained for the Nernst equation calculations. The calibration of the external type K or S thermocouples can be obtained from the manufacturer.

Results

Scope and applicability

The proposed room temperature leak test by alcohol penetration is for typical planar cells sealed to a coated metallic window frame. This method is simple, fast, economical, and non-destructive. It is not a quantitative method, however. It does not require special training, expensive equipment, or constant calibrations. The results are easy to interpret without ambiguity as indicated by the arrows in Figure 2B, where the wet stains of alcohol on the anode side are obvious. In this case, leaks were present in both the glass seal (top arrow) and the cell (lower arrow). The concept is also applicable to tubular cells; however, the procedures may require minor modifications to accommodate differences in tubular designs and seal configurations. The high temperature cross-bubbling method is most suitable for a planar single cell geometry and could also be applicable to short stacks. It is most desirable to check the leakage in un-reduced cell/stack conditions where no safety or fire hazard needs to be considered since one can use air on both electrodes. The results are fast and can be semi-quantitative, meaning one can estimate the leak rate by counting the number of bubbles per minute with a known tubing inner diameter. The correlation of cross-bubbling to the leak rate is often very clear when the bubbling frequency is high (e.g., several bubbles per second) in the other channel’s bubbler. This method is not applicable to tubular designs unless all the tubes are enclosed in another pipe with a hermetic seal. The OCV technique is most suitable for planar single cells and may be extended to short stacks with voltage leads on subsets of adjacent cells such that the voltage drops from single cell leakage can be easily resolved from those resulting from temperature gradients.

Health and safety warning

Room temperature leak tests using alcohol need to be conducted in a ventilated space and away from open flames. For safety it is preferred they be conducted in a ventilated hood. All high temperature leak tests require hot surface hazard training. The OCV method also requires proper training for handling flammable gases at elevated temperatures and the emergency shut down procedure.

Cautions

In room temperature leak tests with alcohol, the sealed cell to window frame plate needs to be handled with care since the glass seal and the ceramic cell are generally brittle if the sample is dropped or carelessly handled. In addition, the thin window frame plate may warp slightly after high temperature sealing. Avoid pressing on the window frame plate when placing it on the glass plate for the room temperature alcohol penetration test.

Discussion

For the SOFC/SOEC to operate, one needs to make sure there are no leaks, especially through the cell to window frame plate seal. Early leak detection before stack assembly is more desirable and economical. This protocol introduced three methods to assess leakage: room temperature alcohol penetration, high temperature cross-bubbling, and high temperature OCV measurements. Among them, the first two are fast, with very little ambiguity. The high temperature OCV method is applicable to fully reduced single cells and stacks. The authors have not applied the high temperature OCV method to stacks with a large number of cells and, therefore, could not establish the experimental uncertainty related to this technique. For materials and process development using single cells, the leak tests presented in this protocol would be sufficient to assess leakage. However, new techniques may be required for large full-sized stacks.

Data availability statement

The original contributions presented in the study are included in the article/supplementary materials, further inquiries can be directed to the corresponding author/s.

Author contributions

YC and JH contributed to conception and design of test method. YC and OAM organized the test results and analysis. YC wrote the first draft of the manuscript. All authors contributed to manuscript revision, read, and approved the submitted version.

Funding

This work was funded by the U.S. Department of Energy Solid Oxide Fuel Cell Core Technology Program. Pacific Northwest National Laboratory is operated by Battelle Memorial Institute for the US Department of Energy under Contract no. DE-AC06-76RLO 1830.

Conflict of interest

The authors declare that the research was conducted in the absence of any commercial or financial relationships that could be construed as a potential conflict of interest.

Publisher's note

References

Chou, Y-S., Stevenson, J. W., and Chick, L. A. (2002). Ultra-low leak rate of hybrid compressive mica seals for solid oxide fuel cells. *J. Power Sources* 112 (1), 130–136. doi:10.1016/s0378-7753(02)00356-7

Chou, Y-S., Stevenson, J. W., and Gow, R. N. (2007). Novel alkaline Earth silicate sealing glass for SOFC: Part I. The effect of nickel oxide on the thermal and mechanical properties. *J. Power Sources* 168 (2), 426–433. doi:10.1016/j.jpowsour.2007.03.039

Fergus, J. W. (2005). Sealants for solid oxide fuel cells. *J. Power Sources* 147, 46–57. doi:10.1016/j.jpowsour.2005.05.002

Gunawan, S., Setiawan, I., and Setyawan, I. (2021). Progress in glass-ceramic seal for solid oxide fuel cell technology. *J. Adv. Res. Fluid Mech. Therm. Sci.* 82 (1), 39–50. doi:10.37934/arfmts.82.1.3950

Lessing, P. A. (2007). A review of sealing technologies applicable to solid oxide electrolysis cells. *J. Mat. Sci.* 42, 3465–3476. doi:10.1007/s10853-006-0409-9

Sang, S., Li, W., Pu, J., and Jian, L. (2008). Novel Al_2O_3-based compressive seals for IT-SOFC applications. *J. Power Sources* 177 (1), 77–82. doi:10.1016/j.jpowsour.2007.10.085

Simner, S. P., and Stevenson, J. W. (2001). Compressive mica seals for SOFC applications. *J. Power Sources* 102 (1-2), 310–316. doi:10.1016/s0378-7753(01)00811-4

Singh, K., and Walia, T. (2021). Review on silicate and borosilicate-based glass sealants and their interaction with components of solid oxide fuel cell. *Int. J. Energy Res.* 45, 20559–20582. doi:10.1002/er.7161

Weil, K. S., Hardy, J. S., and Kim, J. Y. (2003). Use of a novel ceramic-to-metal braze for joining in high temperature electrochemical devices. *J. Adv. Specialty Mater. V, Am. Soc. Metals* 5, 47–55.

Nomenclature and definitions

RT room temperature

HT high temperature

LSM lanthanum strontium manganate

YSZ yttrium stabilized zirconia

SOFC solid oxide fuel cell

SOEC solid oxide electrolysis cell

OCV open circuit voltage

sccm standard cubic centi-meter per minute

Frontiers in
Energy Research

Advances and innovation in sustainable, reliable and affordable energy

Explores sustainable and environmental developments in energy. It focuses on technological advances supporting Sustainable Development Goal 7: access to affordable, reliable, sustainable and modern energy for all.

Discover the latest Research Topics

See more →

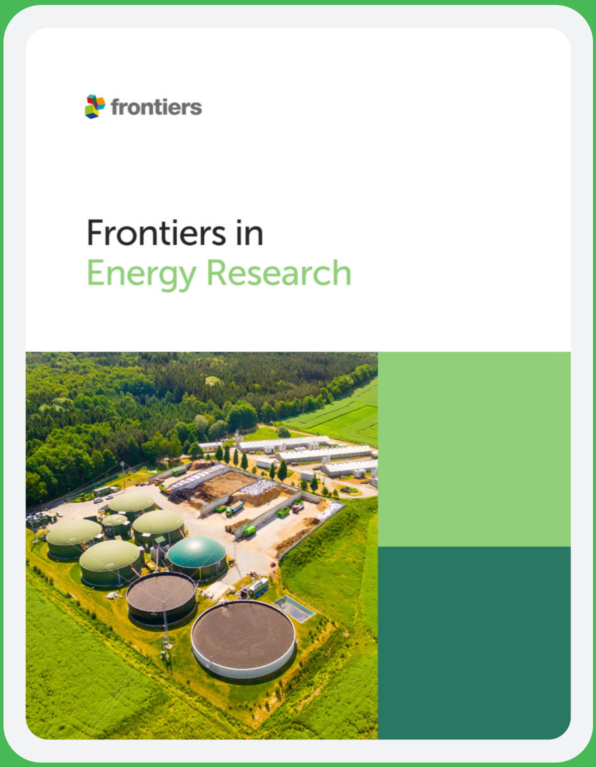

frontiers

Frontiers in
Energy Research

Frontiers

Avenue du Tribunal-Fédéral 34
1005 Lausanne, Switzerland
frontiersin.org

Contact us

+41 (0)21 510 17 00
frontiersin.org/about/contact